UNIVERSIDAD DE CHILE
FACULTAD DE CIENCIAS FÍSICAS Y MATEMÁTICAS
DEPARTAMENTO DE ASTRONOMÍA

IMAGING OF INTERACTIONS BETWEEN CIRCUMSTELLAR DISKS AND EXTRASOLAR PLANETS

TESIS PARA OPTAR AL GRADO DE
DOCTOR EN CIENCIAS, MENCIÓN ASTRONOMÍA
EN COTUTELA CON UNIVERSIDAD DE LIEJA

VALENTIN ANDRÉ CHRISTIAENS

PROFESOR GUÍA:
SIMÓN CASASSUS MONTERO
PROFESOR GUÍA 2:
OLIVIER ABSIL

MIEMBROS DE LA COMISIÓN:
LUCAS CIEZA
JAMES JENKINS
DIMITRI MAWET
JEAN SURDEJ
ZAHED WAHHAJ

Este trabajo ha sido parcialmente financiado por CONICYT-PCHA/Doctorado Nacional/2016-21161112

SANTIAGO DE CHILE
2018

RESUMEN DE LA MEMORIA PARA OPTAR
AL TÍTULO DE DOCTOR EN CIENCIAS, MENCIÓN ASTRONOMÍA
POR: VALENTIN ANDRÉ CHRISTIAENS
FECHA: 24 DE JULIO, 2018
PROF. GUÍA: SIMÓN CASASSUS MONTERO
PROF. GUÍA 2: OLIVIER ABSIL

IMAGING OF INTERACTIONS BETWEEN CIRCUMSTELLAR DISKS AND EXTRASOLAR PLANETS

Se necesitan observaciones para restringir los mecanismos involucrados en el proceso de formación de planetas. Los discos circunestelares ricos en gas y polvo, llamados *discos protoplanetarios*, son el lugar esperado de nacimiento de los planetas. Esta tesis se aprovecha de la sinergia entre ALMA y los instrumentos de imagen de alto contraste (HCI) para estudiar la formación de planetas y la retroalimentación mutua planeta-disco en discos protoplanetarios con grandes huecos, llamados *discos de transición*.

La primera parte de esta tesis está dedicada a la imagen de estos discos. En particular, se realizó un análisis detallado de las espirales encontradas en MWC 758 y HD 142527. Las espirales de MWC 758 son probablemente debidas a la presencia de dos compañeros, con uno de ellos posiblemente detectado dentro de la cavidad en base a nuestros datos. En el caso de HD 142527, las espirales del borde de la cavidad parecen ser, junto con otras características del disco, productos de la interacción dinámica entre la binaria y el disco. Las espirales frías a mayor escala vistas con ALMA podrían estar relacionadas con la inestabilidad gravitacional del disco o las sombras proyectadas por el disco interno inclinado.

Para probar la hipótesis que los huecos grandes en los discos de transición se deben a la presencia de compañeros, se llevó a cabo una encuesta HCI de esos discos utilizando VLT/NACO en IR térmico, presentada en la segunda parte de esta tesis. Se implementaron códigos de reducción de datos que se utilizaron para buscar compañeros en todos los discos ya observados en esta encuesta. Hasta el momento, se han identificado cuatro candidatos compañeros (de 15 fuentes observadas), aunque se requiere seguimiento para confirmar que son verdaderos compañeros. También se presenta mi contribución a la detección de un compañero subestelar joven muy rojo en el disco de escombros de HD 206893.

El potencial de los espectrógrafos de campo integral (IFS) para detectar y caracterizar compañeros de baja masa está investigado en la tercera parte de esta tesis. Se observó una muestra de cinco discos de transición usando VLT/SINFONI en infrarojo cercano. La combinación de imagen diferencial angular y espectral (ASDI) permitió suprimir las imperfecciones del halo estelar de manera eficaz y lograr altos contrastes. Se detectaron tres compañeros y dos sistemas con espirales. En particular, se detectó el compañero de baja masa HD 142527 B en la mayoría de los canales espectrales lo que permitió llevar a cabo una caracterización espectral detallada y estimar sus parámetros físicos.

En conclusión, esta tesis provee nueva información sobre los discos de transición y el posible vínculo entre los grandes huecos y la presencia de compañeros. Un análisis similar al caso de HD 142527 se aplicará a los compañeros confirmados en nuestras encuestas para entender mejor las interacciones compañero-disco y la formación de planetas.

RESUMEN DE LA MEMORIA PARA OPTAR
AL TÍTULO DE DOCTOR EN CIENCIAS, MENCIÓN ASTRONOMÍA
POR: VALENTIN ANDRÉ CHRISTIAENS
FECHA: 24 DE JULIO, 2018
PROF. GUÍA: SIMÓN CASASSUS MONTERO
PROF. GUÍA 2: OLIVIER ABSIL

IMAGING OF INTERACTIONS BETWEEN CIRCUMSTELLAR DISKS AND EXTRASOLAR PLANETS

Observations are required to constrain the mechanisms involved in the process of planet formation. The young gas- and dust-rich circumstellar disks, also called *protoplanetary disks*, are the expected birthplace of planets. This thesis takes advantage of the synergy between the Atacama Large Millimeter Array (ALMA) and high-contrast imaging (HCI) instruments to study planet formation and the planet-disk mutual feedback in protoplanetary disks with large gaps, referred to as *transition disks*.

The first part of my thesis is dedicated to the imaging of transition disks. In particular, I performed a detailed analysis of the spirals found in the transition disks of MWC 758 and HD 142527. The spiral arms of MWC 758, along with other features of the disk, suggest the presence of two embedded companions, with one of them being tentatively detected inside the disk cavity based on our data. For HD 142527, the spirals stemming from the edge of the cavity are, along with other features of the disk, most likely by-products of the disk-binary dynamical interaction. The cold large-scale spirals seen with ALMA could be rather related to gravitational instability or shadows cast by the warped inner disk.

To test the hypothesis that large gaps in transition disks are due to embedded companions, I carried out a HCI survey of those disks using VLT/NACO in thermal IR, presented in the second part of this thesis. I implemented a data reduction pipeline, and used it to search for faint companions in all the disks already observed in this (still on-going) survey. So far, four companion candidates have been identified (out of 15 sources observed), although follow-up observations are required to confirm they are genuine companions. I also present my contribution to the detection of a young extremely red substellar companion in the debris disk of HD 206893 using thermal-IR NACO data.

The potential of integral field spectrographs (IFS) to detect and characterize faint companions is investigated in the third part of this thesis. A sample of five transition disks with large gaps was observed with VLT/SINFONI in near-IR. The combination of angular and spectral differential imaging (ASDI) enabled to efficiently suppress speckles and achieve high contrasts in a range of radial separations. We (re)detected three companions (one new detection to be confirmed) and two spiral patterns (one tentative). In particular, low-mass companion HD 142527 B was redetected in most spectral channels, which allowed me to carry out a detailed spectral characterization and infer its physical parameters.

In conclusion, this thesis has provided new insights into transition disks and the possible link between large gaps and embedded companions. An approach similar to that applied to the case of HD 142527 will be pursued for confirmed companions in our HCI surveys to provide better insight into companion-disk interactions and planet formation.

RESUMEN DE LA MEMORIA PARA OPTAR
AL TÍTULO DE DOCTOR EN CIENCIAS, MENCIÓN ASTRONOMÍA
POR: VALENTIN ANDRÉ CHRISTIAENS
FECHA: 24 DE JULIO, 2018
PROF. GUÍA: SIMÓN CASASSUS MONTERO
PROF. GUÍA 2: OLIVIER ABSIL

IMAGING OF INTERACTIONS BETWEEN CIRCUMSTELLAR DISKS AND EXTRASOLAR PLANETS

Des observations sont nécessaires pour comprendre le processus de formation planétaire. Les jeunes disques circumstellaires riches en gaz et en poussière, appelés *disques protoplanétaires*, sont le lieu de naissance supposé des planètes. Cette thèse tire profit de la synergie entre les instruments d'imagerie à haut-contraste (HCI) et ALMA pour étudier la formation de planètes et comprendre le feedback mutuel planète-disque dans les disques protoplanétaires avec de grandes cavités, appelés *disques de transition*.

La première partie de ma thèse est dédiée à l'imagerie de ces disques. En particulier, j'ai effectué une analyse détaillée des spirales trouvées dans MWC 758 et HD 142527. Mon analyse des bras spiraux de MWC 758 suggère la présence de deux compagnons, dont un seul a possiblement été détecté dans la cavité sur base de nos données. Dans le cas de HD 142527, les spirales issues du bord de la cavité, tout comme d'autres aspects du disque, semblent être des sous-produits de l'interaction dynamique entre la binaire et le disque. Les spirales froides à grande échelle observées avec ALMA pourraient être liées à l'instabilité gravitationnelle du disque ou à des ombres projetées par le disque interne.

Pour tester l'hypothèse que les cavités dans les disques de transition sont dues à la présence de compagnons, j'ai effectué un relevé HCI de ces disques en utilisant VLT/NACO en IR thermique, présentée dans la deuxième partie de cette thèse. J'ai mis en place un pipeline de réduction de données, et l'ai utilisé pour chercher des compagnons dans ces disques. Jusqu'à présent, quatre candidats compagnons ont été identifiés (sur 15 sources observées), bien qu'un suivi soit nécessaire pour confirmer qu'ils s'agit de véritables compagnons. Je présente également la détection d'un jeune compagnon substellaire extrêmement rouge dans le disque de débris de HD 206893 grâce à d'autres données NACO.

Dans la troisième partie de cette thèse, nous avons étudié le potentiel des spectrographes intégral de champ (IFS) pour détecter et caractériser des compagnons de faible masse. Un échantillon de cinq disques de transition a été observé avec VLT/SINFONI en proche IR. Via la combinaison des techniques d'imagerie différentielle angulaire et spectrale, nous avons pu supprimer efficacement les speckles dans l'image et atteindre des contrastes élevés. Nous avons (re)détecté trois compagnons et deux motifs de spirales. En particulier, le compagnon de faible masse HD 142527 B fut redétecté dans la plupart des canaux spectraux, ce qui permit une caractérisation spectrale et l'estimation de ses paramètres physiques.

En conclusion, cette thèse a apporté de nouvelles contraintes sur les disques de transition et leurs possibles liens avec la présence de compagnons. Le même type d'analyse qu'appliqué aux compagnons confirmés dans nos relevés afin de mieux comprendre les interactions entre disque et compagnon et le processus de formation des planètes.

Agradecimientos

I profoundly acknowledge my tutors Olivier Absil and Simon Casassus. Without your wise advice, patience, and continuous positive feedback, all the work presented in this thesis would not have been possible. I will be forever in debt of your guidance and experience. Thank you!

I also express my gratefulness to Lucas Cieza, James Jenkins, Dimitri Mawet, Jean Surdej and Zahed Wahhaj for expressing your support during my thesis, and for taking the time to read this manuscript. I am very thankful to all the postdocs and ESO fellows that I have met, including (but not limited to) Alice, Seba, Gerrit, Matías, Nico, Henning, Julien and Jesús, you guys rule and benefitting from your experience was invaluable! Thank you also to Victor and Hernan for your help in solving my computer-related problems.

Big thanks to the *weonos* for your support and for uncountable good moments and adventures that made this PhD a unique experience worth living until the end: cheers Sudeep, Blake, Robert, Nina and Nathen! I am also thankful to all the other great people I met in Chile. Thank you Seba and Gijs for the awesome trip to Brazil and parties at your respective place! Gracias a David por ayudarme a sobrevivir en el centro y haber sido un gran compañero de depa, a Bica, Chelo, Pablo, Carla y Jonathan por los carretes, a Ricardo por las noches de juego Civilization, a Jorge, Mati y Seba por los kartings y otras actividades outdoor, a Paula, Mari y José por la ayuda con los cursos y el examen de calificación, y a Vachail por la buena onda en 3 continentes distintos. Gracias también a todos los otros estudiantes (no puedo nombrarlos a todos) por crear un ambiente tan bacán en Calan! Agradezco de todo corazón a Marta por la tremenda ayuda al nivel administrativo.

Je suis également reconnaissant envers mes amis en Belgique. Merci Max, Cazo et Matthias pour les bons moments passés ensemble à Liège et à Rio, et merci à Tom, Aurel et Coco pour les joyeuses soirées de retrouvailles lors de mes retours en terres natales. Thanks Aïssa, Brunella, Carlos, Christian, Gilles, Maddalena and Olivier for good moments spent together in the Vortex team both at Liège and at conferences. Pour finir, je suis extrêmement redevable à toute ma famille. Merci pour votre soutien inconditionnel!

I acknowledge support from (1) the Millennium Science Initiative (Chilean Ministry of Economy) through grant RC130007, (2) CONICYT through CONICYT-PCHA/Doctorado Nacional/2016-21161112, and (3) the European Research Council under the European Union Seventh Framework Program (ERC Grant Agreement n. 337569) and from the French Community of Belgium through an ARC grant for Concerted Research Action.

Contents

List of Tables

List of Figures

I Introduction

Stars (Kandinsky, 1938)

For a long time the planets of the Solar System were the only one known in the Universe, and theories of planet formation were very speculative due to the lack of observational data to support them. About 20 years ago, the window to other planet systems was eventually opened. Since then, technological progress and several generations of dedicated instruments have enabled to better constrain the process of planet formation and evolution, either from the direct observation of planet forming environments, or from the statistical properties inferred from the profusion of detected extra-solar worlds. The main goal of this thesis is to provide new observational constraints to the processes of planet formation and evolution with direct observations of the interactions between nascent planets and young circumstellar disks, the cradles of planetary systems.

The first part of this manuscript consists in the introduction of key concepts that are required to put in context the results obtained during this thesis, presented in Parts II, III and IV. To begin, I define what exoplanets (Chap. 1) and circumstellar disks (Chap. 2) are, and explain how they are connected. In Chap. 3, I summarize current models of planet formation and confront them in Chap. 4 with observational constraints gathered from direct imaging at the time I started this thesis. Finally, I explain in Chap. 5 how this thesis inscribes in the context of recent transformative results brought by state-of-the-art instrumentation, and will insist on the synergy of different types of observations required to put together the missing pieces of the puzzle of planet formation.

The story so far: In the beginning the Universe was created. This has made a lot of people very angry and been widely regarded as a bad move.

Douglas Adams (from *The Restaurant at the End of the Universe*)

1 Exoplanets

1.1 History

Speculations about the existence of other worlds have spread throughout several centuries, with avant-garde claims sometimes leading to dramatic outcomes, as exemplified by the infamous trials of Giordano Bruno (1548-1600) and Galileo (1564-1642). The earliest reported attempts of extra-solar planet research is attributed to Huygens (1698), followed by pioneering works of W. Jacob and T. J. J. See in the 19th century, and efforts from P. van de Kamp and collaborators in the mid-20th century's. However, instrumental lack of sensitivity prevented any detection, or more exactly led to numerous false positive claims (e.g. See 1896; van de Kamp 1969). If any lesson should be drawn from the plethora of exoplanet primo-detection claims which sooner or later got refuted, it is to always show extreme caution in this exercise. As will be seen in Chap. 4, false positives are still a well known tune in modern-day exoplanet research.

Until about 20 years ago, the Solar System planets were the only examples of planets in the Universe. Assessing the true place of our system in the Universe, or attempting to draft global planet formation scenarios were hence significantly hindered. Interestingly, the first two confirmed exoplanets (PSR B1257+12 A and B) were detected orbiting a pulsar (Wolszczan & Frail 1992; Wolszczan 1994). A few years later though, an exoplanet orbiting a main sequence (MS) star (51 Peg) was eventually discovered, using the radial velocity (RV) technique (Mayor & Queloz 1995). The first ten years of exoplanet search then saw the supremacy of the RV technique (Fig. 1.1), and hundreds of new exoplanet discoveries.

After years of improvements in the field of high-contrast imaging (HCI), the first directly imaged planetary mass companion was eventually found (Chauvin et al. 2005a). Starting from the late 2000's, more and more exoplanets were found through the transit method, owing to improved photometer sensitivities and dedicated space missions. In particular, space telescope Kepler (Borucki et al. 2004) has provided the largest number of confirmed exoplanet detections to date (more than 2000; e.g. Borucki et al. 2011; Morton et al. 2016).

More than 3000 exoplanets have been confirmed as of 8 March 2018[1]. The field of exoplanets is thus one of the fastest growing discipline in astronomy. In less than 25 years, we passed from the uncertainty on the very existence of planets beyond the Solar System

[1]J. Schneider, "Interactive Extra-solar Planets Catalog", *The Extrasolar Planets Encyclopedia*, available at: `http://exoplanet.eu/catalog/`

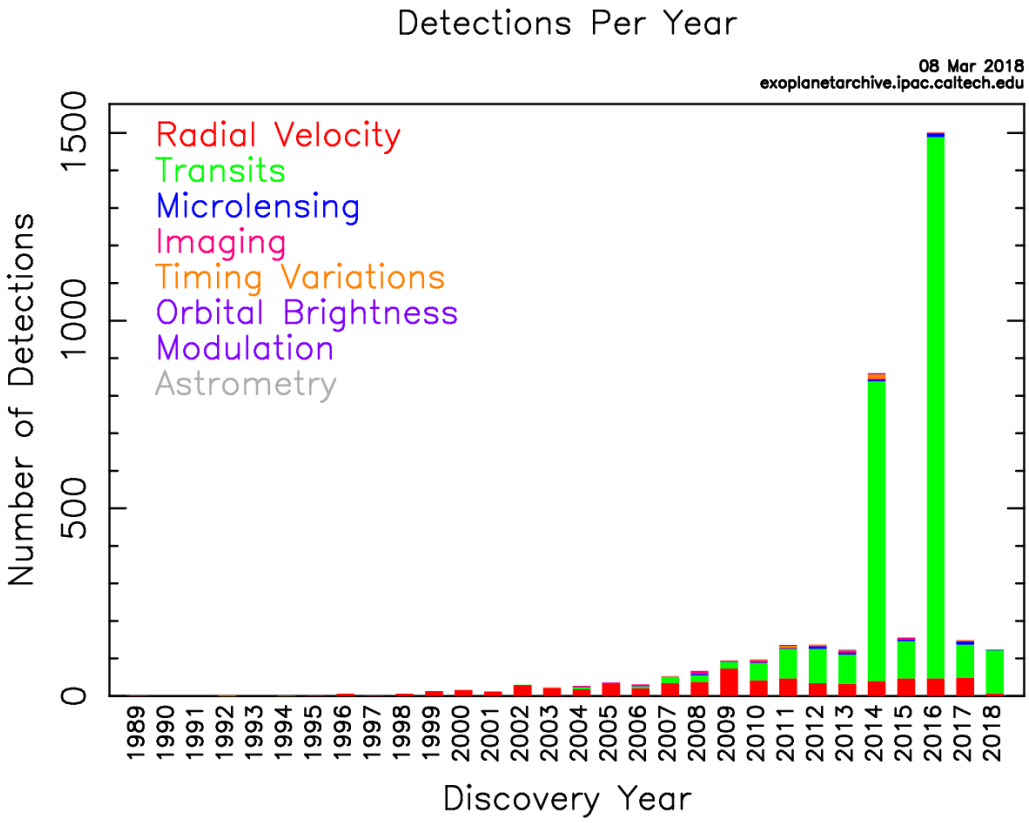

Figure 1.1: Exoplanet detections over time and as a function of the technique used. Credit: Caltech's exoplanet archive plotter (available at `https://exoplanetarchive.ipac.caltech.edu/cgi-bin/IcePlotter/nph-icePlotInit?mode=demo&set=confirmed`).

to the realization that exoplanets are actually abundant in our Galaxy. The direct imaging method mentioned in this section will be explained in more details in Sec. 1.3, while the statistical results obtained with the exoplanet search campaigns using that technique will be discussed in Sec. 4.1 along with their implications for the process of planet formation.

1.2 Definition

Extra-solar planets, or exoplanets, are planets orbiting other stars than our Sun. While this definition seems simple and intuitive, a more thorough look is needed in order to delimit the upper boundary of the planetary range, i.e. regarding the distinction between giant planets and brown dwarfs. Brown dwarfs are, as defined by the IAU, sub-stellar objects too light for sustaining hydrogen-1 fusion reactions in their cores, but contrarily to mere planets, are heavy enough for fusion of deuterium. In the recent years, observational evidence has accumulated in favor of a similar formation process for brown dwarfs and stars (see e.g. the review of Luhman 2012). Young brown dwarfs and low-mass stars share indeed similar properties in terms of multiplicity fraction, circum(sub)stellar disks, mass accretion rates, and kinematic and spatial distributions at birth. In particular, the brown dwarf initial mass function appears to be consistent with the lower-mass end of the stellar

mass function (e.g. Chabrier et al. 2014). Furthermore, pre-brown dwarf core collapse in an isolated environment has also been directly observed (e.g. André et al. 2012), identical to the gravitational collapse mechanism leading to protostars. On the contrary, the formation mechanism which accounts best for the detected population of planets so far appears to be the core accretion mechanism (Sec. 3.2), hence a hierarchical growth mechanism inside a circumstellar disk instead of the top-down gravitational collapse of a larger core.

Since the formation scenario of a detected mature companion is difficult to infer from current observables, a simple pragmatic criterion for their discrimination is needed. Mass is usually considered to be the most suited one (e.g. Schneider et al. 2011). The commonly admitted mass limit is ~ 13 Jupiter masses ($M_{\rm Jup}$), corresponding to the limit below which thermonuclear fusion of deuterium in the core is not supposed to happen anymore, for a solar metallicity (e.g. Burrows et al. 2001; Spiegel et al. 2011). However, Udry (2010) suggested that there was apparently no reason to choose 13 $M_{\rm Jup}$, since it does not correspond to any difference in the mass distribution of RV-detected companions. Moreover, this mass distribution has shown a lack of companions ranging from 25 to 40 $M_{\rm Jup}$ (e.g. Grether & Lineweaver 2006; Udry 2010; Sahlmann et al. 2011), referred to as the *brown dwarf desert*. Based on these statistical results, Schneider et al. (2011) have suggested an *arbitrary* value of $25 M_{\rm Jup}$ as the upper-limit of exoplanets mass. Nevertheless, more recent RV surveys have suggested that the BD desert may not be as "dry" as initially thought (e.g. Duchêne & Kraus 2013a; Guillot et al. 2014; Troup et al. 2016).

Recent studies proposed a classification of celestial bodies based on their location in a mass versus radius (or density) diagram (e.g. Hatzes & Rauer 2015; Chen & Kipping 2017). In that kind of plot, relatively sharp changes in slope are seen between neptunian and jovian worlds and between substellar objects and stars. However, there is no apparent distinction between giant planets and brown dwarfs, as both appear to follow the same R(M) flat slope ($R \propto M^{-0.04 \pm 0.02}$; Chen & Kipping 2017). As far as mass and radius are concerned, brown dwarfs appear thus as high-mass members of a single *jovian world* class, although these conclusions are to be taken carefully considering the brown dwarf desert between 25 and 50 $M_{\rm Jup}$, and the fact that the high-mass end brown dwarfs close to $0.08 M_\odot$ appear to also be consistent with the stellar slope.

Most recent efforts to distinguish between formation scenarios for mature giant planets and brown dwarfs have focused on metallicity and chemical composition (e.g. Ma & Ge 2014; Mata Sánchez et al. 2014; Maldonado & Villaver 2017), and new suggestions of division lines start to emerge (e.g. Schlaufman 2018). It is possible that the final answer to the debate will be brought by GAIA, as it is expected to discover $21,000 \pm 6000$ 1–15 $M_{\rm Jup}$ planets/brown dwarfs orbiting between 1 and 5 au of their star by the end of its 5-year mission, hence $\sim$100 times the amount of objects currently known in that range (Perryman et al. 2014). In the meantime, for the objects where tracing back the formation history is impossible, using a generic term such as *Jovian worlds* might be the most appropriate way to refer to them (e.g. Chen & Kipping 2017). In that sense, Chabrier et al. (2014) argue that, anyway, deuterium burning only happens in the ~ 100 Myr of the life of brown dwarfs and has little effect on neither their formation nor their further evolution, contrarily to hydrogen burning which determines the evolution of stars during most of their life.

1.3 Direct imaging of exoplanets

For a long time, astronomers have not been able to disentangle the light of exoplanets from the bright glare of their parent stars. Therefore, they resorted to indirect methods (i.e. scrutiny of the parent star signal instead of direct signal from the planet) to infer the presence of planets. Stars and planetary companions are all orbiting their common centre of mass, which is further away from the center of the star for more massive companions on larger orbits. In terms of star's observables, this fact causes perturbations in radial velocity, astrometric position and, in the case of pulsars, time of arrival of signals. These three observables are the ones used in the so-called *radial velocity*, *astrometry* and *pulsar timing* methods respectively. In systems with a favorable geometry, the presence of a planet can alter the observed intensity of the incoming flux from the parent star. This is the case for *transit*-related techniques and the *gravitational microlensing* method, which are all based on a fine monitoring of this observable.

Technological improvements in the past decade have eventually enabled to directly detect the signal from a few giant extrasolar planets. Direct imaging is complementary to indirect methods since it probes preferentially giant planets orbiting on wide orbits. Being able to literally *see* the emitted light of planets in other systems presents some attractive advantages. A direct image enables to infer the (projected) separation of the exoplanet with respect to its host star. As the planet moves forward onto its orbit, follow-up observations provide new astrometric points which can be fit to infer all the orbital elements of the exoplanet. Direct imaging enables thus the study of the (large-scale) *architecture* of planetary systems. Furthermore, spectroscopy of the light from the companion can be used to characterize its *atmosphere*, in terms of temperature, surface gravity and chemical composition. Based on available evolutionary models, it is then possible to estimate the mass, radius and age. In turn, sufficient observations enable to feed the models and better constrain them. Direct imaging is particularly appropriate for studying exoplanets around young stars, where exoplanets have not cooled down yet and are hence intrinsically brighter. This technique can thus provide constraints on the *mechanisms of formation and evolution* of planetary systems. However, to benefit from this wealth of information, one has to overcome two major obstacles which are discussed in the next subsections.

1.3.1 Angular resolution

Given the large distances between stars compared to planetary orbits, making direct images of exoplanets requires to reach an exquisite angular resolution. The maximum observable angular separation between a planet of semi-major axis a_p and eccentricity e_p and its star, for a system located at a distance d is:

$$\beta_{\max} = \frac{a_p(1-\mathrm{e}_p)}{\mathrm{d}}. \tag{1.1}$$

Table 1.1 provides typical angular resolutions required to image exoplanets at various separations from their host star, and for different distances to the Earth.

	0.1 AU	1 AU	5 AU	30 AU	
3 pc	30 mas	0.3"	1.5"	9"	*Ground-based AO*
10 pc	10 mas	0.1"	0.5"	3"	*or*
25 pc	4 mas	40 mas	0.2"	1.2"	*spatial telescope*
100 pc	1 mas	10 mas	50 mas	0.3"	
		Interferometry			

Table 1.1: Required angular resolutions in order to resolve an exoplanet for various combinations of planet separation to its host star (0.1 au: *hot Jupiter*, 1 au: Earth, 5 au: Jupiter, 30 au: Neptune) and system's distance to the Sun (close stars, at 3–25 pc, or star formation regions, typically $\gtrsim$100 pc away). The most-indicated high-angular resolution technique is provided in each case, considering NIR observations with today's 10m-class telescopes.

The angular separation of the planet has to be confronted against the angular resolution θ of the telescope:

$$\theta \simeq \sin\theta = 1.22\frac{\lambda}{D} \tag{1.2}$$

which is the angular separation corresponding to the first trough in the radial profile of the Airy pattern, for a mono-pupil telescope of diameter D observing at a wavelength λ. According to Eq. 1.2, in order to observe a planet at 1 AU from its star located 10 pc away, at a wavelength of 10 μm, a telescope diameter of at least 25 m is theoretically needed. In practice however, atmospheric turbulences affect the incoming wavefront, so that the angular resolution is typically limited by the *seeing*. In order to push the angular resolution to its limit, one has to use *adaptive optics* (AO) systems to counter the effect of atmospheric turbulence. More details on AO systems will be provided in Sec. 10.1.

Ground-based mono-pupil telescopes equipped with AO systems are limited to an angular resolution of typically 50 mas at near-infrared (NIR) wavelengths. In order to reach higher angular resolution, one can use *interferometry*. A particular concept relevant for the search of exoplanets is the one of *nulling interferometry*. While this concept enables the theoretical detection of planets, the reconstruction of good-quality images from interferometric observations requires a sufficient amount of baselines. Another type of interferometry, so-called *sparse aperture masking* (SAM) or *non-redundant masking*, has been developed which can be performed on a mono-pupil telescope by the insertion of a mask filled with small holes in an intermediate pupil plane. Since in the rest of this thesis I only focus on non-interferometric high-contrast imaging techniques, I defer the interested reader to Tuthill et al. (2000) and Ireland (2013) for more detailed information about SAM, and to Beichman et al. (1999) and Cockell et al. (2009) for more details about nulling interferometry applied to the search for exoplanets.

1.3.2 Contrast

The second hurdle to be overcome in direct imaging is the luminosity contrast involved between the planet and its star. Planets incoming light $L_{\rm p}$ divides into distinct contributions: the reflected light from their parent star $L_{\rm p,ref}$ (most significant at UV/visible wavelengths),

their intrinsic thermal emission due to the radiation of latent internal heat $L_{\rm p,int}$ (most significant at IR wavelengths), and emission from reprocessed stellar light $L_{\rm p,eq}$ (also typically in IR). In comparison, the contribution of non-thermal features such as auroras is typically negligible.

The brightness corresponding to reflected stellar light is given by

$$L_{\rm p,ref} = \frac{A_{\rm Bond} L_*}{8} \left(\frac{R_p}{a_p}\right)^2 \phi(t) \tag{1.3}$$

where $\phi(t)$ is an orbital phase factor given by $\phi(t) = 1 - \sin \mathrm{i}_p \sin(2\pi t/P)$, and $A_{\rm Bond}$ is the Bond albedo of the planet, defined as the ratio of total reflected light to total bolometric incident light. This reflected luminosity is most significant for very short separation giant planets. In practice, this contribution is usually negligible for directly imaged exoplanets given their large separation.

When planets form, potential energy is transformed into thermal energy due to gravitational contraction. Soon after formation, the contribution from internal heat emission of giant planets can be approximated by the intrinsic luminosity of a brown dwarf (neglecting the effect of lithium and deuterium burning and different atmosphere composition). An expression for the latter was derived in Stevenson (1991), based on polytropic equations of state:

$$L_{\rm p,int} \propto t^{-5/4} M_p^{5/2} \kappa^{0.3} \tag{1.4}$$

where t is the time spent since the formation of the substellar objects, M_p is the mass of the object, and κ is the opacity of the gas. As expected, the younger and the more massive the object, the larger the intrinsic luminosity due to latent heat. Such giant planets for which the effective temperature is much larger than their radiative equilibrium temperature (defined in the next paragraph) are usually referred to as *self-luminous* planets. Not only does the intrinsic luminosity of giant planets peaks at its formation, but the luminosity of the host star is also lower in its pre-main sequence phase than when it is on the main sequence. This is thus even more favorable in terms of planet/star contrast, and explains why young giant planets are one of the primary science niches of direct imaging. From equation 1.4, one can also notice the weak dependency on the opacity of the gas, which suggests that models using different opacity laws should still predict relatively similar luminosities. Giant planet formation models will be explained in more details in Secs. 3.1 and 3.2.

For older (cooled down) planets, the intensity of their thermal emission consists mostly of reprocessed incident stellar light. The effective temperature $T_{\rm eff}$ is roughly equal to the radiative equilibrium temperature $T_{\rm eq}$, and these planets are usually referred to as *mature* planets. The associated luminosity is given by:

$$L_{\rm p,eq} = 4\pi R_p^2 \sigma T_{\rm eq}^4 \tag{1.5}$$

$$= 4\pi R_p^2 \sigma \left(\frac{1 - A_{\rm Bond}}{4f}\right) \left(\frac{R_*}{a_p}\right)^2 T_*^4 \tag{1.6}$$

where factor f is equal to 0.5 for planets unable to redistribute heat from the day side to their night side (i.e. typically tidally locked planets or slowly rotating), and 1 otherwise, and other notations are as in Eq. 1.3. The luminosity of mature planets depends thus mostly

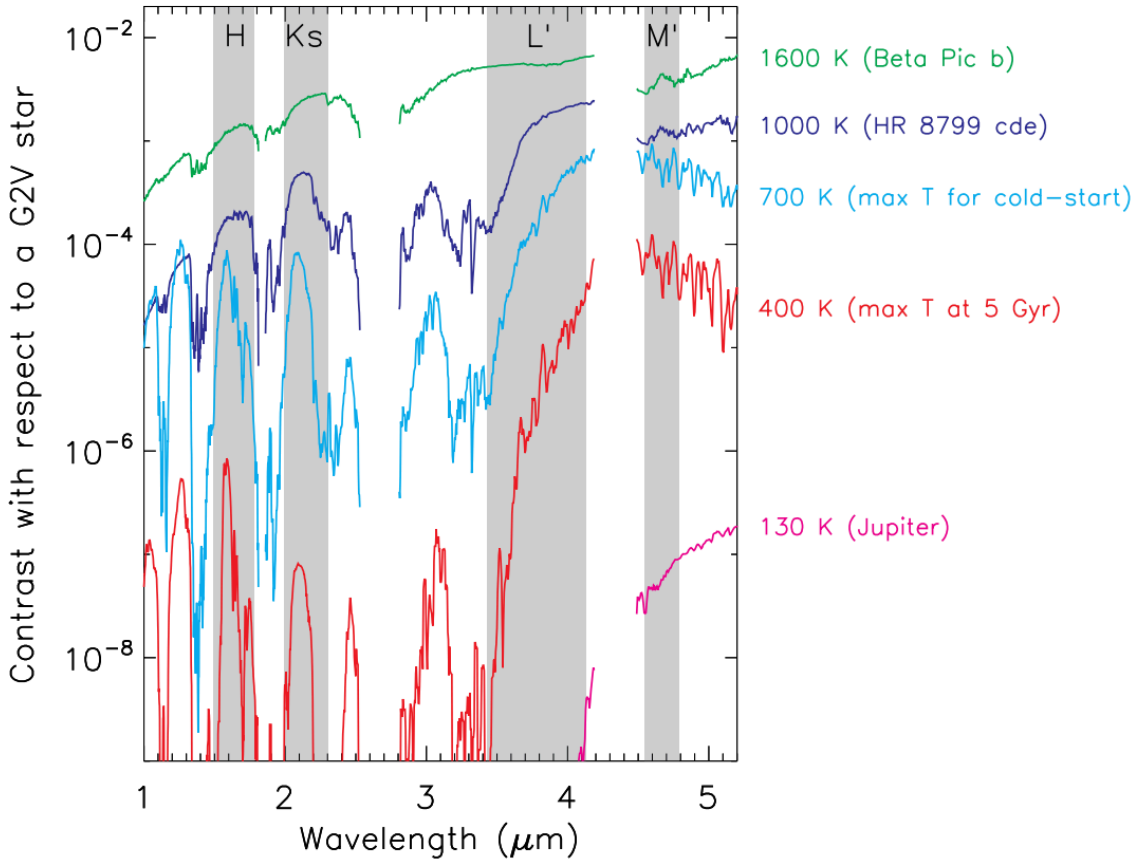

Figure 1.2: Contrast between different (exo)planets and the Sun as a function of wavelength. The contrast ratio is more favorable in thermal infrared. Figure extracted from Skemer et al. (2015).

on the square of their radius, the semi-major axis of their orbit, and on the luminosity of their host star.

From young to adolescent ages, the contrast of giant planets appers optimal around the L' band (Fig. 1.2). The more mature – and colder – the planet, the longer the wavelength at which the contrast is optimal. For example, a mature Jupiter-like planet orbiting at 5 au from its star, the contrast in visible is $\sim 10^{-9}$ (from stellar light reflection; e.g. Traub & Oppenheimer 2010), while it is $\gtrsim 10^{-8}$ in thermal IR (e.g. Skemer et al. 2015, Fig. 1.2). The contrast between a Solar-type star and an Earth-size planet at 1 au is of order 10^{-9} in the visible domain (0.4–0.7 μm), and about 10^{-7} in thermal IR (e.g. Beichman et al. 1999). Based on the above considerations, it appears systematically more advantageous to search for exoplanets at thermal-IR wavelengths. However, for a given telescope diameter, observing at longer wavelengths implies a loss in angular resolution, so a trade-off has to be made. At those wavelengths, additional difficulties for ground-based telescopes include the high atmospheric thermal background emission and the absorption from molecules in the atmosphere.

In direct non post-processed images, a faint companion would typically lie in the photon noise $\sigma = \sqrt{N_{ph}}$ of the rings of the diffraction pattern. The brightness L_p has thus to be compared with the typical brightness of the diffraction ring at angular separation β from

the parent star:

$$L_{ring} = L_*(\beta/\theta)^{-3} \tag{1.7}$$

where θ is defined in equation 1.2. In the case of a Jupiter-Sun system seen at 10 pc, it is possible to infer from equations 1.2, 1.3 and 1.7 that the planet to star's wings brightness ratio is around 5×10^{-6} for an 8m telescope at a wavelength of 3.8 μm at the diffraction limit of the telescope. Ways to deal with this contrast issue include stellar coronagraphy, dedicated observing strategies and post-processing techniques relying on the concept of differential imaging, and will be detailed in Chap. 10.

2 Circumstellar disks

Circumstellar disks are present around young stars, and are labelled depending on their composition and evolutionary stage. *Protoplanetary disks* (also known as *primordial disks*) are gas- and dust-rich, which distinguishes them from older *debris disks*. An intermediate class of disks, so-called *transition disks*, has also been identified. They consist of primordial gas and dust but are characterized by the presence of a dust-depleted cavity. In this chapter, I briefly describe those three types of disk.

2.1 Protoplanetary disks

The existence of protoplanetary disks has been hypothesized for a long time based on the architecture of our own Solar System, where all planets orbit roughly in the same plane (e.g. Cameron 1962). First observational evidence of these objects came from the SED obtained with the NASA InfraRed Telescope Facility (IRTF) at Hawaii and with the InfraRed Astronomical Satellite (IRAS), which showed significant IR excess around T-Tauri variable stars (Lada & Wilking 1984; Rucinski 1985). First resolved images of these disks were obtained with the HST in the Orion nebula (Fig. 2.1a, b and c). In those images, the disks are seen as dark shadows due to the very optically thick dust at optical and IR wavelengths. In the following decades, both IR space telescopes (ISO, Spitzer, Herschel) and sub-mm interferometers, including the Plateau de Bure Interferometer (PdBI), the Sub-Mm Array (SMA), the Combined Array for Research in Millimeter-wave Astronomy (CARMA), and recently the Atacama Large Millimeter Array (ALMA), enabled to build a more complete picture of these objects.

2.1.1 Disk formation in the context of star formation

Protoplanetary disks are a natural outcome of the process of star formation. This process is summarized in Fig. 2.2. When a perturbation breaks the pressure equilibrium of a molecular cloud parts of it can gravitationally collapse, provided the *Jeans criterion* is fulfilled, which depends on the temperature and initial mean density of the cloud. The collapse is initially dynamical. As the density increases, initial inhomogeneities in the cloud (*pre-stellar cores*) can in turn match the Jeans criterion, hence become gravitationally unstable

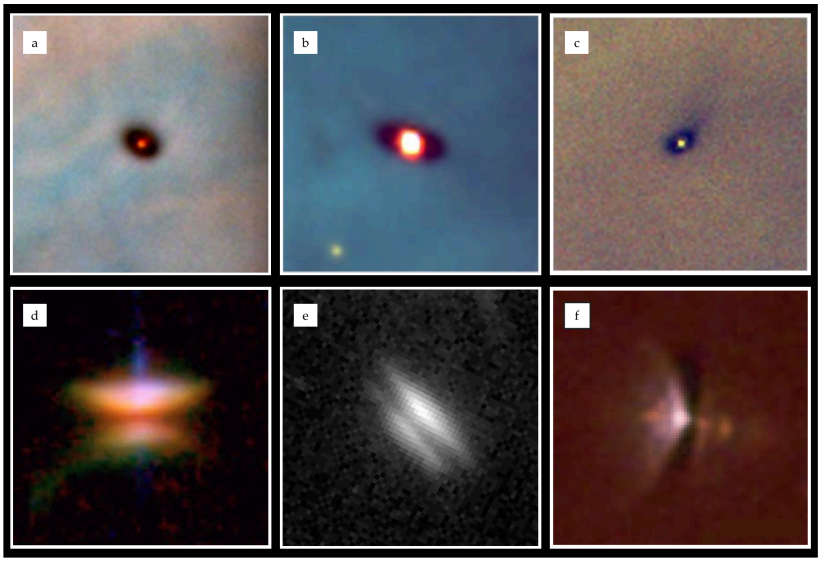

Figure 2.1: **a, b** and **c**: Protoplanetary disks observed with HST in the Orion nebula. The protoplanetary disks are seen in silhouette against the background luminous gas, with typical length scales of several hundreds of au. The bright central spots stem from the protostars (O'dell et al. 1993; McCaughrean & O'dell 1996). **d, e** and **f**: HST images of edge-on protoplanetary disks HH 30, HK Tau and d216-0939, resp. (Burrows et al. 1996; Stapelfeldt et al. 1998; Smith et al. 2005).

and fragment to form protostars. This fragmentation process can be further enhanced by turbulence, which can trigger several consecutive collapses, accounting for the formation of stars in groups, and at a smaller scale, multiple systems (this is the so-called *gravo-turbulent fragmentation* formation mechanism; e.g. Hopkins 2013).

The formation of the protostar is accompanied by the infall of a large quantity of gas from the molecular cloud, which leads initially to spherical accretion. At this stage (*class 0*; Fig. 2.2), the density has increased sufficiently for the gas to be opaque to IR photons, and the collapse is slowed to a quasi-static contraction. This phase is expected to last $\lesssim 10^4$ yrs (Yorke et al. 1993; Hueso & Guillot 2005).

Due to the conservation of angular momentum, the infalling material progressively accumulates in the shape of a disk, which is referred to as *protostellar disk* at these early stages (age ~ 1–5×10^5 years; Evans et al. 2009). Jets or bipolar outflows are observed in this phase, which might be related to the process of angular momentum removal. These *class I* young stellar objects (YSOs) are observationally identified from their rising SED slope towards far-IR wavelengths (Fig. 2.2). Many of these class I objects show short-lived bursts of luminosity, related to sporadic episodes of colossal accretion, and are referred to as *FU Ori* stars. A possible mechanism beneath these accretion bursts is the fragmentation of the massive protostellar disk, driving rapid transport of material onto the protostar (Zhu et al. 2009; Vorobyov & Basu 2010b).

By an age of 0.5–1 Myr, most of the material from the protostellar disk is now inside the protostar. *Protoplanetary disks* are made of these remnants of star formation, which are believed to be used for planet formation, hence their name. These *class II* objects encompass *T-Tauri* stars+disks and *Herbig* Ae/Be stars+disks. T-Tauri stars are young solar

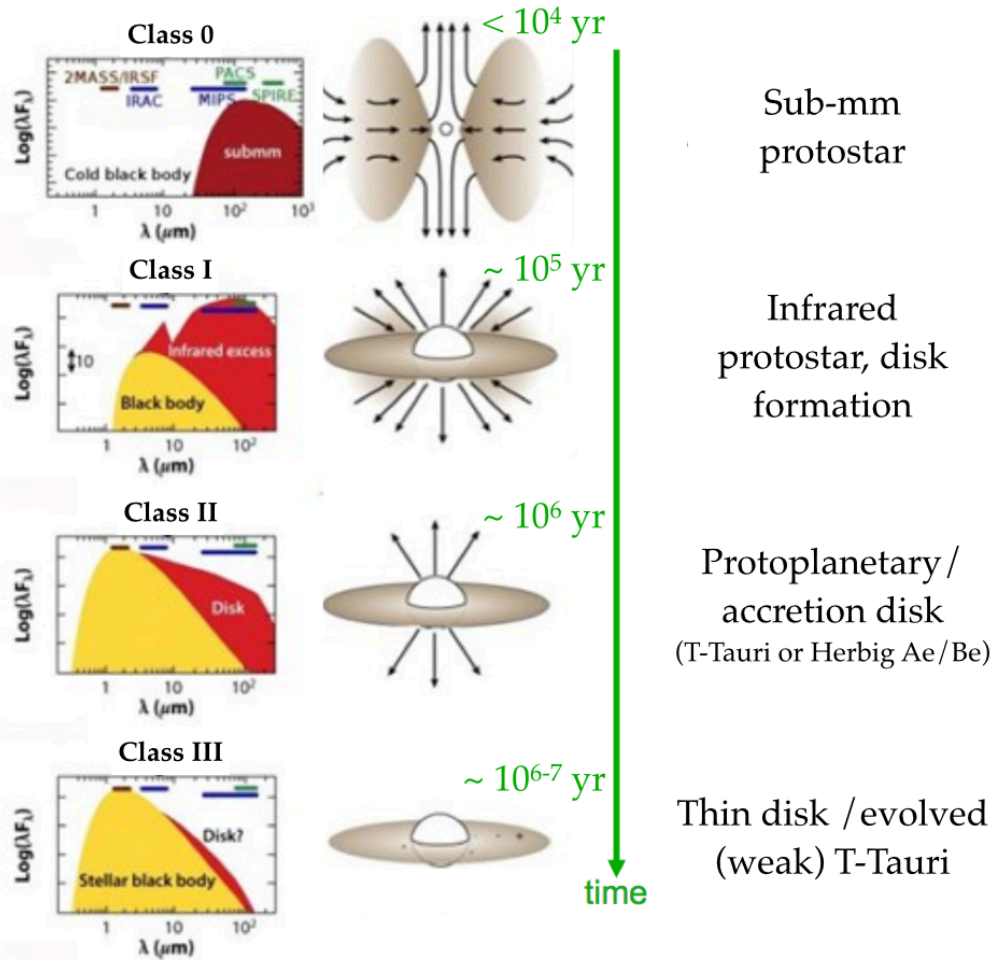

Figure 2.2: Diagram showing the different phases of star and circumstellar disk formation, and corresponding SED observational signature. The classification of young stellar objects (classes 0 to III) is based on the shape of the SED. Figure adapted from André (1994).

analogs with a strong magnetic field due to convection in their envelope, violent stellar activity, and intense FUV and X-rays radiation (Bertout 1989). Herbig Ae/Be stars are the higher mass counterparts (2–8 $M_\odot$) of T-Tauri stars, hence hotter and more luminous, but with weaker magnetic fields and quieter stellar activity owing to their non-convective envelope (Waters & Waelkens 1998). These *class II* objects are identified from (i) their emission lines tracing accretion by the central star, and (ii) strong IR/sub-mm excess due to the reprocessing of the stellar light by dust in the disk. However, contrary to class I objects, the peak of emission is now photospheric. Gravitational energy released by this gas accretion can contribute with an additional component in the SED at optical/UV wavelengths. Mass accretion rates measured for protostars span a large range of values, typically between 10^{-6} and $10^{-9} M_\odot \mathrm{yr}^{-1}$ for Herbig stars, and between 10^{-9} and $10^{-12} M_\odot$ yr^{-1} for T-Tauri stars (Fairlamb et al. 2015; Natta et al. 2006).

Finally, the SED of *class III* objects is characterized by a weak IR excess and weak emission lines. It is believed that this class of objects corresponds to optically thin accretion disks already in the process of being dispersed.

2.1.2 Protoplanetary disk properties

Mass

The bulk mass of protoplanetary disks consists of gas (up to 99% initially), while the remainder consists of dust. It is relatively difficult to probe most of the gas mass though; H_2 only has magnetic quadrupoles transitions in IR, and most of the gas is not warm enough to excite those transitions. Estimates of the gas mass using other species, such as CO, have been performed, but uncertainties arise from the adoption of interstellar H_2:CO and ^{12}CO:^{13}CO abundance ratios (10^4 and 76, resp.; e.g. Perez et al. 2015; Miotello et al. 2016). This is a risky assumption due to the expected freeze-out of a significant fraction of CO on grains in the midplane (Tielens et al. 1991; Qi et al. 2013), and its photo-dissociation close to the surface (van Dishoeck & Black 1988). As a matter of fact, recent studies showed that taking into account chemistry in the disk, CO is indeed likely much less abundant (relative to H_2) than in the ISM, with a decreasing trend with both radial separation and age of the disk (e.g. Yu et al. 2017; Molyarova et al. 2017).

Since the gas is not a reliable option, mass estimates are often inferred from sub-mm (continuum) observations of the dust component, where the emission can be considered mostly optically thin. For that, one has to assume an opacity prescription for the dust, such as Beckwith et al. (1990).

$$\kappa_\nu = 0.1 \left(\frac{\nu}{10^{12}\ \mathrm{Hz}} \right)^\beta \ \mathrm{cm^2\ g^{-1}} \tag{2.1}$$

where κ_ν is the dust opacity at a frequency ν, and β is a power law index which is typically $\sim$1 for protoplanetary disks. Assuming optically thin emission, the mm-flux can be directly converted into a mass, for a certain dust temperature T_{dust} (e.g. Andrews & Williams 2005):

$$M_\mathrm{d} = \frac{F_\nu \mathrm{d}^2}{\kappa_\nu B_\nu(T_{\mathrm{dust}})} \tag{2.2}$$

$$\approx \frac{F_\nu \mathrm{d}^2}{2\kappa_\nu \nu^2 k T_{\mathrm{dust}}/c^2} \tag{2.3}$$

where the second line comes from the Rayleigh-Jeans approximation to the Planck function $B_\nu(T_{\mathrm{dust}})$, which is justified at mm wavelengths. Proceeding in such a way to estimate the disk mass presents several possible biases though:

- the normalization of the opacity prescription in Eq. 2.1 assumes a fiducial interstellar gas-to-dust ratio of 100:1, which might not be true everywhere in the disk or might evolve with time;
- the emission is known to be optically thick in the inner parts of the disk, typically up to ~ 10 au, which implies that the estimate will miss a possibly significant fraction of the total mass;
- the opacity prescription in Eq. 2.1 is valid for grain sizes up to a maximum size $a_{\mathrm{max}} \approx 3mm$ (e.g. Draine 2006), and is known to be significantly smaller for larger (> 3 mm) grains (e.g. D'Alessio et al. 2001), which means that a possibly significant contribution from large grains is not included in the mass estimate.

The neglected mass due to optically thick emission and the inappropriate opacity prescription for large grains tend to underestimate the mass, while the possibility of lower than 100:1 gas-to-dust ratios in parts of the disk tend to overestimate it. Comparison of disk masses measured using Eq. 2.2 and the mass expected from the integration of T-Tauri mass accretion rates during typical disk lifetimes suggests that disk masses might be significantly underestimated (e.g. Hartmann et al. 1998; Andrews & Williams 2007). Using HD (hydrogen deuteride) might be the least biased way to estimate total disk masses (Henning & Semenov 2013). Bergin et al. (2013) used far-IR lines of HD in Herschel data to estimate the mass of the disk of TW Hya to $\sim$50 $M_{\rm Jup}$, suggesting that using either the mm-continuum or CO indeed underestimates the mass by a factor ranging from a few to a few tens. Assuming that the above-mentioned biases would affect the estimation of all disk masses in roughly the same way, there appears to be a linear dependency between stellar and disk mass (Williams & Cieza 2011; Andrews et al. 2013). Regardless of biases, protoplanetary disks are much less massive than their central star, and are thus expected to orbit mostly at *Keplerian velocity*. This prediction was confirmed observationally from CO emission line profiles (e.g. Sargent & Beckwith 1987; Guilloteau & Dutrey 1998).

Radial and vertical profiles

The *radius* of protoplanetary disks was first estimated with the silhouette images of disks obtained with HST in Orion (Fig. 2.1), suggesting a large dispersion of disk sizes (50–200 au; Vicente & Alves 2005). This large dispersion was further confirmed with sub-mm observations ($\sim$10–1000 au; e.g. Hughes et al. 2008; Andrews et al. 2009; Isella et al. 2009; Andrews et al. 2010), which additionally showed an apparent lack of correlation between the physical extent of the disk and stellar properties. CO line observations, probing directly the gas disk, appear to show in general larger extents than sub-mm continuum observations (e.g. Piétu et al. 2007; Andrews et al. 2012).

Protoplanetary disks have a non-negligible vertical height which tends to increase with radius, i.e. disks are *flared*. HST images of almost edge-on disks confirmed that fact early on (Fig. 2.1d, e and f). This is also confirmed from the observed SED slopes of protoplanetary disks, more consistent with a flared disk than a flat disk geometry. The *scale height* of the disk, $H(r)$, is set by the equilibrium between the disk thermal pressure (which tend to make the disk thicker) and the vertical component of the stellar gravity (which tend to make it thinner). There are two main sources of heating accounting for both the radial and vertical temperature profiles of the disk: *viscous* heating and *passive* heating from stellar irradiation. In the case of a passive disk, stellar radiation is absorbed in a thin surface layer by dust, and is then re-radiated in IR. The two-layer passive disk model proposed in Chiang & Goldreich (1997) appears to reproduce well the observed radial temperature profile of disks (e.g. Piétu et al. 2007), suggesting that it is a good representation of the disk, at least in the outer parts. Viscous heating is expected to be increasingly significant in the denser inner parts of the disk, so that models of the whole disk should consider both effects (e.g. Dullemond et al. 2007). More details on the physical properties of protoplanetary disks can be found in the reviews of Williams & Cieza (2011) and Dutrey et al. (2014).

Composition and chemistry

Protoplanetary disks are mainly made of gas (∼99%), with the remaining 1% consisting of dust, at least initially. Although small in mass fraction, the dust makes protoplanetary disks optically thick at most wavelengths. The gas consists mainly of dihydrogen (∼73% in mass) and helium (∼25%). Combined with hydrogen, oxygen, carbon and nitrogen, they form most of the *ices* including water ice, solid methane (CH_4), ammoniac (NH_3), carbon dioxide and monoxide (CO_2 and CO), and carbon hydrates. These compounds have a condensation temperature between 10 and 200 K and are referred to as *volatiles*. Material whose condensation temperature is comprised between 200 and 1500 K such as iron and nickel metallic alloys, and silicates are the fundamental bricks of rocky cores (Sec. 3.2). Finally, some *refractory* materials, such as calcium oxyde and aluminium, have their condensation temperature higher than ∼1500 K.

A summary of the chemical structure of the disk is provided in the right-hand side of Fig. 2.3. At inner radii, high temperatures and densities enable neutral-neutral reactions. At larger radii, the UV/X-rays play a key role as photo-dissociation and photo-ionization of molecules close to the surface foster a rich molecular-ion chemistry. At the same time, the μm-size dust grains in the upper layers are acting as a shield for radiation; heating the adjacent layer to the surface, but keeping the midplane extremely cold ($\sim$ 10–20 K), where the chemistry is dominated by gas-grain surface interaction and grain surface reactions following the freeze-out of volatiles onto the grains. More details on the chemistry in protoplanetary disks can be found in Bergin (2009) and Henning & Semenov (2013).

2.1.3 Mechanisms at work in protoplanetary disks

Hydrodynamic processes and angular momentum transport

Protoplanetary disks are a specific type of accretion disk and, as such, are transporting both mass onto the central star and angular momentum outwards. A large variety of angular momentum transport mechanisms have been proposed, including magneto-hydrodynamical (MHD) turbulence, hydrodynamical instabilities, outflows and gravitational instability (see e.g. Turner et al. 2014, for a review). Their relative importance is still debated and the dominant transport mechanism might be different at different locations in the disk.

Among MHD instabilities, a commonly invoked mechanism to account for angular momentum transport is the *magneto-rotational instability* (MRI; Balbus & Hawley 1991), which stems from the combined effect of differential rotation between proto-star and disk, and the interaction between the (proto)stellar magnetic field and ionized material in the disk. Nonetheless, ionized species are mainly found in the surface layers of the disk, while in the interior a significant portion of the disk could be neutral (the so-called *dead zone*). This dead zone with low turbulence also happens to be overlapping with the location where dust grains settle and grow (see next paragraph). The enhanced density (due to poorer angular momentum transport) and low turbulence in the dead zone could favor both the

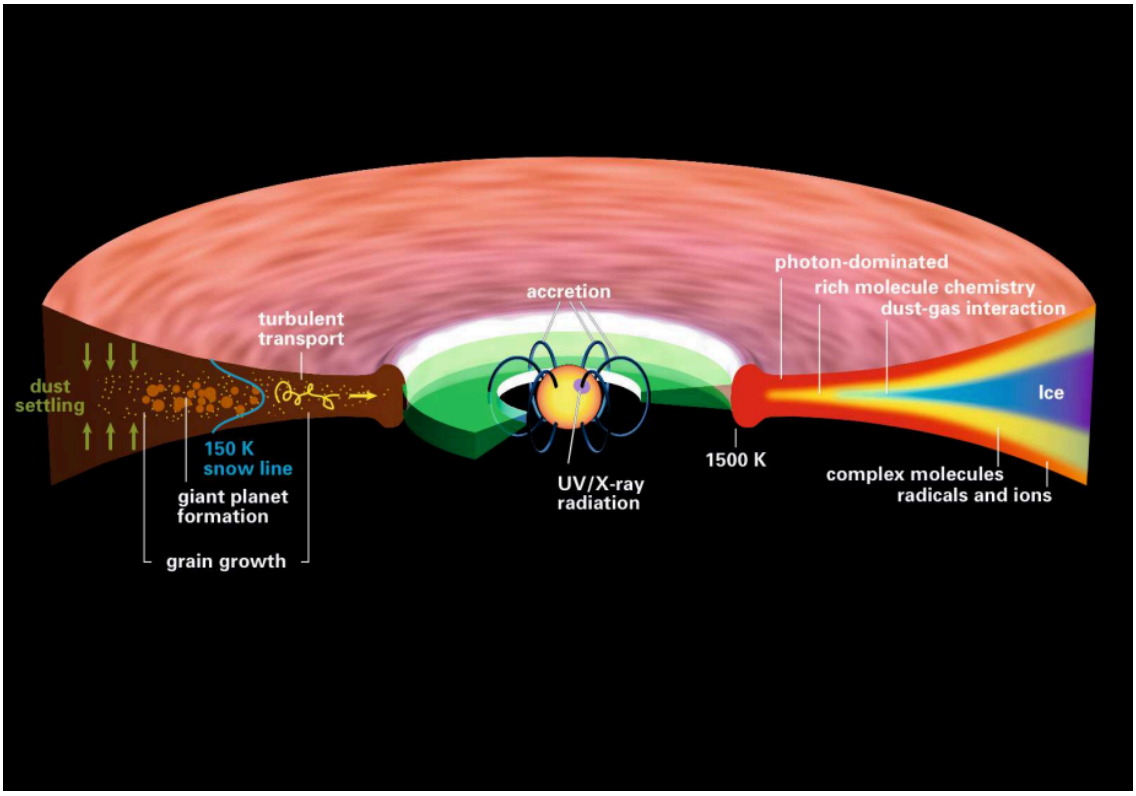

Figure 2.3: Sketch of a protoplanetary disk showing the chemical structure of the disk (right side) and physical processes at work (left side). Figure from Henning & Semenov (2013).

onset of a *Rossby wave instability* (RWI; Lovelace et al. 1999; Li et al. 2000, 2001) and the formation of giant planets (e.g. Varnière & Tagger 2006). The RWI is a special case of Kelvin-Helmholtz instability in the case of a differentially rotating disk, where the extra shear is converted into vorticity. Rossby waves arise where a local extremum in either pressure or a surface density extremum in the disk is found, and their non-linear evolution can lead to vortex formation (e.g. Li et al. 2000, 2001). Vortices in the gas component of the disk, in turn, have been proposed early on as a way to trap solid material and form planetary cores (e.g. Barge & Sommeria 1995; Bracco et al. 1999). This hypothesis appears to be validated by more recent numerical simulations (e.g. Lyra et al. 2009b; Regály et al. 2013) and analytical considerations (Lyra & Lin 2013), and will be discussed in more details in Sec. 6.2.2.

Mechanisms affecting the dust

The evolution of the disk is not only set by the viscous accretion of the gas. A variety of processes affect the dust as well, including dust settling, grain growth, fragmentation and radial migration (see e.g. Blum & Wurm 2008; Henning & Meeus 2011; Blum 2018, for reviews).

Grain growth and *dust sedimentation* towards the midplane are two interconnected mechanisms. Growth by coagulation requires the appropriate range of relative velocity

between the colliding dust grains, which is set by Brownian motion and turbulence stirring in the disk. A common way to estimate how coupled are dust grains to the turbulent eddies is with the *Stokes number* (e.g. Dullemond & Dominik 2004b):

$$St \propto \frac{\Omega \rho_{\rm s}}{\rho_{\rm g} v_{\rm th}} \, a \tag{2.4}$$

where $\rho_{\rm s}$ and $\rho_{\rm g}$ are the densities of the solid grain and the gas resp., a is the radius of the grain, and $v_{\rm th}$ is the isothermal sound speed. When $St << 1$, the dust particle is very well coupled with the turbulence, while $St >> 1$ corresponds to the case where the dust grain does not feel the turbulence. Given the linear dependency of St with the size of the particle, dust grains of different sizes will thus acquire a relative velocity, with the largest grains (or *pebbles*) decoupling more significantly from the gas motion, and sedimenting (or *settling*) towards the midplane, as their motion becomes more dominated by the vertical component of gravity. In addition to vertical settling, the larger the dust grains, the more they feel a headwind from the gas on their orbit around the star, which is due to the gas orbiting almost but not exactly at Keplerian velocity due to the radial pressure gradient. Grains progressively loose angular momentum due to this aerodynamic drag, and hence migrate radially inward.

In practice, experiments show that very small grains (μm-size) are expected to grow easily by coagulation up to mm-sizes (see e.g. Dullemond & Dominik 2004b; Blum & Wurm 2008; Birnstiel et al. 2010). However, larger (cm- to meter-size) blocks are known to be more prone to fragmentation and to fast inward migration (Birnstiel et al. 2011; Weidenschilling 1977, resp.). The inward radial migration is very fast, of the order of 10,000 years to migrate from 1 au into the star for meter-size boulders ($St \sim 1$; Weidenschilling 1977; Brauer et al. 2008). Both the fragmentation and fast inward drift are a significant problem for further growth and the formation of building blocks for planet formation, and are commonly referred to as the *meter-size barrier*. I will briefly discuss in the context of the core accretion scenario the most promising mechanism that has been invoked to bypass the meter-size barrier (Sec. 3.2). This meter-size barrier has indeed to be passed to account for the routine detection of mature giant planets, as the latter must form while the disk is still rich in gas.

Disk dispersal

Several mechanisms are believed to cause the progressive dissipation of protoplanetary disks, including viscous accretion radially inward toward the star, with some material subsequently ejected outward via jets, planet formation (see Secs. 3.1 and 3.2), and dissipation through stellar wind and photoevaporation by the central star, or by neighboring O-type stars (e.g. Alexander et al. 2006; Alexander et al. 2014). Regarding the average lifetime of protoplanetary disks, Haisch et al. (2001) calculated the fraction of stars showing an IR excess in young clusters of different ages. Plotting these fractions in a disk fraction vs. sample age plot (known as *Haisch-Lada plot*), they found that younger clusters had statistically more circumstellar disks and assessed that the overall disk lifetime was $\gtrsim 6$ Myr, based on an exponential fit. More recently, Mamajek (2009) suggested a characteristic disk lifetime

of 2.5 Myr based on a larger sample. Interestingly, some of the most remarkable gas-rich disks have estimated ages well above these average values (see e.g. Sokal et al. 2018, and references therein for the example of TW Hya). Based on these considerations, 10 Myr is usually a good rule of thumb for the division between protoplanetary and debris disks (e.g. Wyatt et al. 2015).

2.2 Debris disks

Debris disks are found around stars of $\sim$10 Myr to several 100s Myr old. These disks have very little amount of gas, as it has been accreted, has dispersed through photoevaporation and stellar winds and/or has been used for the formation of giant planets. While protoplanetary disks are the gas-rich residuals of star formation, *debris disks* cannot simply be defined as the gas-poor residuals of both star and giant planets formation. Indeed, the dust they are made of if most likely not primordial, as they are expected to be quickly removed via radiation pressure, Poynting-Robertson drag, and collisional destruction (e.g. Backman & Paresce 1993; Dominik et al. 2003). Therefore, dust grains must be continuously regenerated, most likely through collisions between planetesimals (hence their name). Quoting Mark Booth (2018): *Debris disks is where what you have spent so long to build planets and planet-forming blocks through complicated and not yet fully understood mechanisms, finally destroy and break up in smaller parts again.*

The first debris disk was inferred around Vega, based on its IR excess compared to the Rayleigh-Jeans tail of the star contribution (Aumann et al. 1984). Since then, a lot of debris disks have been inferred from the IR excess found in their SED thanks to several generations of IR space telescopes. Depending on the amount of excess at each wavelength, the presence of dust belts at different temperatures can be inferred (e.g. Chen et al. 2014). In-depth studies using Spitzer and Herschel have focused mainly on bright debris disks found around A-type (e.g. Su et al. 2006) and FGK-type stars (e.g. Bryden et al. 2006; Eiroa et al. 2013). The detected cold and warm components in debris disks are typically scaled up versions of the Solar System's Kuiper Belt and Zodiacal disk, respectively.

The first resolved image of a debris disk was obtained early on around β Pictoris (Smith & Terrile 1984), owing to the favorable disk-to-star contrast and the large extent of the disk. In comparison, astronomers had to wait more than 15 years for the next resolved images of debris disks (Holland et al. 1998). Nowadays however, new generations of instruments have enabled the routine observations of debris disks with resolved images tracing either the scattered light from their star at near-IR (e.g. Milli et al. 2015; Boccaletti et al. 2015) or the direct thermal emission from dust at longer wavelength (e.g. Su et al. 2017).

A wide diversity of structures has been unveiled in the recent years, including narrow rings, eccentric rings, annular gaps, arcs, warps, clumps, and brightness asymmetries (Fig. 2.4). Debris disks are thus particularly interesting for the study of planet-disk interactions, since an attractive interpretation for either rings or non-axisymmetric structures is gravitational sculpting by planets. Modeling of those disk features can provide dynamical constraints on putativer perturbers (e.g. Faramaz et al. 2015). A remarkable example

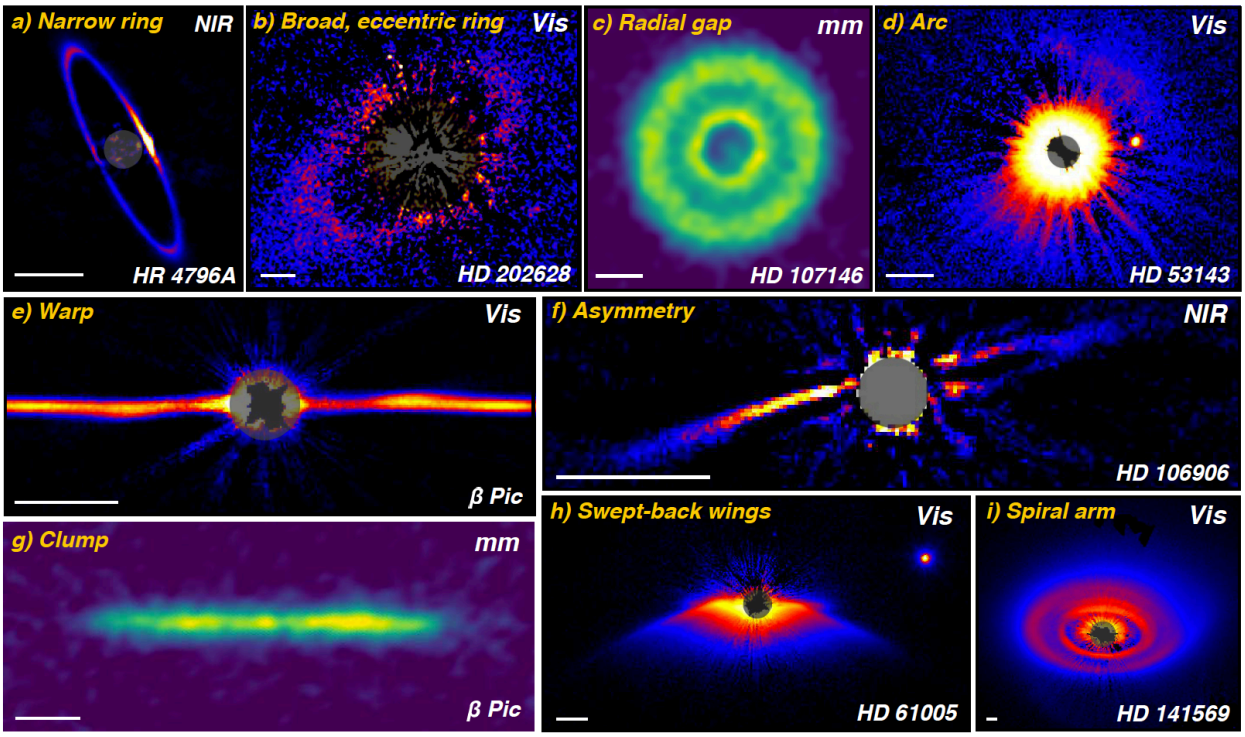

Figure 2.4: Gallery of debris disks compiled in Hughes et al. (2018). A wide diversity of structures can be observed which in some cases might be suggestive of the presence of planets. References: a) Milli et al. (2017b); b) Schneider et al. (2016); c) Marino et al. (subm.); d) Schneider et al. (2014); e) Kalas et al. (2015); f) Konishi et al. (2016); g) Dent et al. (2014); h) Schneider et al. (2014); i) Konishi et al. (2016).

of synergy between the analysis of disk images and exoplanet search is the case of β Pic b, where mounting evidence for the presence of a planet, including a its inner warp (Heap et al. 2000) and the presence of a bright mid-infrared clump (Telesco et al. 2005), have culminated in the eventual detection of the expected giant planet (Lagrange et al. 2009, 2010). Alternative scenarios have also been suggested to account for the diversity of morphologies of other disks, such as recent planetesimal collisions, interactions with the ISM, or gravitational perturbations from stellar flybys (see Hughes et al. 2018, and references therein).

Interestingly, some of the observed features in debris disks such as annular gaps, warps, asymmetric dust distributions and spiral arms, are also observed at earlier stages, in the protoplanetary disk and transition disk phases, so that these structures will be discussed in Part II, in the context of transition disks, the stage at which they might originate. In particular, the only debris disk source in which spiral arms have been detected is very young (HD 141569; e.g. Konishi et al. 2016; Mawet et al. 2017a), and has sometimes been classified as a transition disk given the non-negligible amount of residual gas. Nonetheless, during this thesis I mainly targeted younger disks, except for the case of HD 206893, which will be discussed in Sec. 12.2. Therefore, I defer the interested reader to the recent reviews of Hughes et al. (2018) and Wyatt (2018) for a more comprehensive summary of current knowledge regarding the structure, composition and evolution of debris disks, and possible planet-disk interactions.

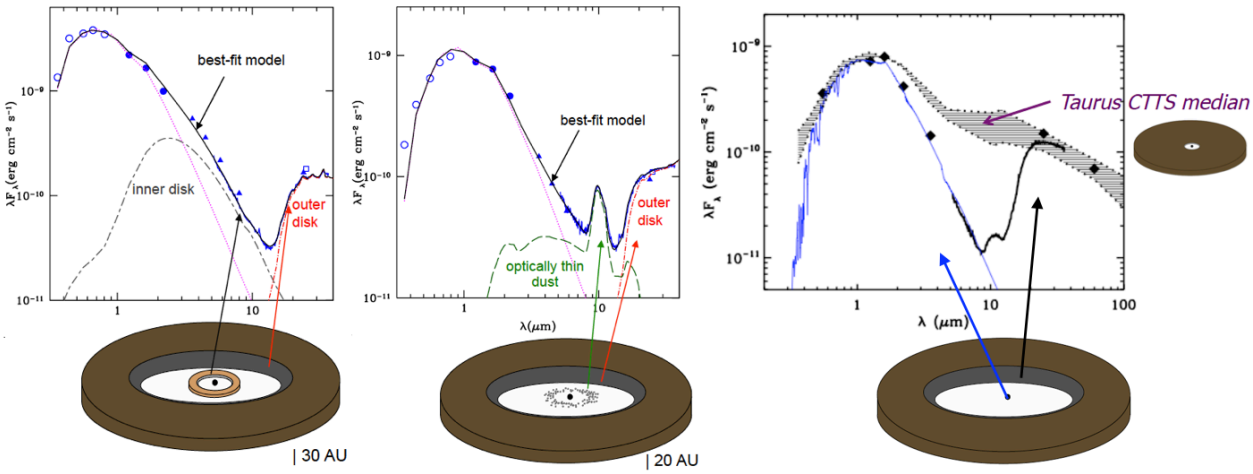

Figure 2.5: Observed SED of pre-transitional (left and middle) and transitional (right) disks, and sketch showing the inferred origin for each component. In the left panel, an optically thick inner disk is still present. In the middle panel, optically thin dust is present, resulting in a significant contribution at $\sim 10\mu$m. In the right panel, the SED shows a significant lack of IR excess compared to the median SED of classical T-Tauri disks in Taurus. Espaillat et al. (2007) suggested that the sub-class of pre-transitional disk could represent a predecessors of transition disks with large cavities. Figure adapted from Espaillat et al. (2007) and Espaillat et al. (2014).

2.3 Transition disks

Transition (or transitional) disks are protoplanetary disks showing evidence for an inner cavity or a large annular gap in their dust distribution. Their first observational identification dates back to the works of Strom et al. (1989) and Skrutskie et al. (1990), who noted a strong mid- to far-IR excess but weak near- to mid-IR excess (compared to photospheric emission) for some young stellar objects, using both ground-based near-IR photometers and mid- to far-IR photometry with IRAS. Since these colors are intermediate between those of class II and class III objects, it was suggested that these objects were in *transition*. The lack of near- and mid-IR excesses in the SED was interpreted as due to the presence of an inner hole (right panel of Fig. 2.5). As Marsh & Mahoney (1992) pointed out, the inner hole does not not necessarily reflect disk dispersal, but could also be consistent with the presence of an inner binary. Large surveys with space telescope *Spitzer* enabled the identification of many more such objects (D'Alessio et al. 2005; Calvet et al. 2005), including a subset of disks showing strong near- and far IR excesses (similar to T-Tauri disks), but a mid-IR excess deficit, suggestive of the presence of an inner disk followed by an annular gap (hence not a fully depleted cavity). Espaillat et al. (2007) refer to these objects as *pre-transitional disks*, suggesting they could trace the first stage of disk clearing towards a large inner cavity (left panel of Fig. 2.5). Some objects also displayed a peak at 10μm, suggesting that very small dust ($< 1\ \mu$m) was present in the cavity (middle panel of Fig. 2.5), which could possibly represent a more advanced stage of clearing towards a full cavity.

At the end of the 2000s, a new generation of sub-mm interferometers (SMA, PdBI), enabled to confirm the presence of inner cavities in the distribution of large grains of most transition disks (e.g. Brown et al. 2008; Andrews et al. 2009). Soon after, near-IR high-contrast imaging instruments tracing the polarized emission from the surface of the

disk have also resolved large clearings in some (but not all) of those disks, mostly using Subaru/HiCiao (as parts of the SEEDS survey; e.g. Tamura 2009; Thalmann et al. 2010; Hashimoto et al. 2012) and VLT/NACO (e.g. Quanz et al. 2011; Avenhaus et al. 2014).

The exact origin of large cavities has been the topic of intense debates. Several explanations have been put forward, including dynamical clearing by stellar or planetary companion(s) (Lin & Papaloizou 1979; Artymowicz & Lubow 1994), photoevaporation (e.g. Clarke et al. 2001; Alexander et al. 2014), dust grain growth (e.g. Dullemond & Dominik 2005), photophoresis (e.g. Krauss et al. 2007), MRI-induced winds or dust flows (e.g. Suzuki & Inutsuka 2009; Chiang & Murray-Clay 2007) and dead zones (e.g. Regály et al. 2012; Flock et al. 2015). Some of these suggestions have lost momentum, such as grain growth which predicts a smooth variation from the optically thin cavity to the thick outer disk, while the typical SEDs of transition disks suggest a sharp transition between the cavity and the outer disk (e.g. Birnstiel et al. 2012).

The formation of giant planets or the presence of (sub)-stellar binary are predicted to involve *dynamical clearing* of the disk (e.g. Marsh & Mahoney 1992; Paardekooper & Mellema 2004; Zhu et al. 2011). *Photoevaporation* on the other hand, is also known to be a dominant process to disperse the disk once the accretion on the star stops (e.g. Alexander & Armitage 2007; Alexander et al. 2014). *Dead zones* are also expected to play an important role for both planetesimal formation and disk evolution via the formation of one or several vortices at the dead zone's outer edge. Those three mechanisms are thus nowadays considered by the community to be the most likely dominant processes at the origin of the observed cavities (e.g. Owen 2016; Pinilla et al. 2018).

Observations of transition disks have been biased towards disks surrounding Herbig Ae/Be stars (owing to their brightness). A line of investigation focusing on the classification of Herbig Ae/Be disks based on their SED, initiated by Meeus et al. (2001), recently resulted in the conclusion that all flared disks (inferred from the SED) were transition disks (Maaskant et al. 2013). These flared disks, labelled group I in the Meeus et al. (2001) taxonomy, are opposed to relatively flat disks, labelled group II. It has been hypothesized that group II disks are a later evolutionary stage than group I, as a result of dust settling (e.g. Dullemond & Dominik 2004b). Alternatively, group I and group II disks might represent two distinct evolutionary paths branching from primordial flared disks (e.g. Maaskant et al. 2013). The question of the possible evolutionary link between these groups is thus still open. Some insight can be obtained from complete surveys of disk populations, which will be briefly discussed in Chap. 8.

3 Models of planet formation and evolution

The nebular hypothesis, initially put forward by Swedenborg (1734) and further developed by Kant (1755) and Laplace (1796), proposes that planets form from the residuals of star formation, and that planetary systems may be common around other stars. While this hypothesis is now largely accepted by the scientific community, different models within that paradigm are still debated, and in particular *gravitational instability* (or *disk instability*) and *core accretion*, which will hence be detailed in this chapter. Gravito-turbulence is able to produce planetary-mass objects, through a "star-like" formation mechanism, and will hence not be discussed here. I defer the interested reader to Padoan & Nordlund (2002) and Hennebelle & Chabrier (2013) for more details.

3.1 Gravitational instability

Historically, gravitational instability (GI) was the first proposed mechanism of planet formation, dating back to the 18th century. This theory has been revived by G. Kuiper in the 50's and A. G. Cameron in the 60's, and further developed in Boss (1997). In essence, the model proposes that giant planets spawn directly from the *gravitational fragmentation* of the protoplanetary disk surrounding the newborn star. Broadly speaking, planet formation through GI is to the protoplanetary disk what stellar formation is to the galactic disk. As a matter of fact, the criterion for disk instability (so-called *Toomre criterion*) was historically derived for stars in the galactic disk, and reads (Toomre 1964):

$$Q \equiv \frac{c_s \Omega}{\pi G \Sigma} < Q_{\text{crit}} \approx 1 \tag{3.1}$$

where c_s is the sound speed, Ω is the angular frequency of the disk and Σ is the surface density. A region of the disk will be gravitationally unstable if the value of Q is lower than a critical value of about 1, reflecting the point where potential energy dominates over thermal pressure and shearing force. Massive (large Σ) and cold (low c_s) parts of the disk are thus more likely to be unstable. A disk that is gravitationally unstable forms spiral arms which efficiently transport angular momentum (e.g. Rice et al. 2003; Forgan & Rice 2013; Dong et al. 2015a, more details in Sec. 6.4.2).

Nonetheless, the Toomre criterion alone is not sufficient to predict whether parts of the

disk can gravitationally fragment or not. A portion of the disk might be gravitationally unstable and not collapse if the cooling timescale for the gas at that location is too long; the criterion reads (Gammie 2001):

$$t_{\rm cool} \equiv \frac{U}{2\sigma T_{\rm disk}^4} \lesssim \beta_{\rm crit}\Omega^{-1} \tag{3.2}$$

where U is the thermal energy content of the disk per unit area, and $\beta_{\rm crit}$ is a factor depending on the properties of the gas. Assuming an ideal gas equation of state, Gammie (2001) found that $\beta_{\rm crit} \approx 3$. If the criterion defined in Eq. 3.2 is not met, a quasi-steady state is reached, where the cooling is compensated by heating through gravitational turbulence.

While observations suggest that GI can form (stellar) binary companions (Tobin et al. 2016), the formation of objects in the planetary mass range appears more complicated. Forgan & Rice (2013) showed that considering heating of the disk by stellar irradiation, only final products of the mass of brown dwarfs or low-mass stars can be produced by fragmentation. Furthermore, these very massive proto-companions might further grow during their inward migration in the massive disk (e.g. Kratter et al. 2010; Stamatellos 2015). Due to the very short timescale for the formation of the proto-companion, it is not expected to open a gap, and it would hence follow a very fast migration (of type I; Sec. 3.4) inward (e.g. Baruteau et al. 2011). Hydro-dynamical simulations suggest that this very fast migration typically does not stop and actually feeds the forming protostar which, when it happens, could correspond to FU Ori bursts (Vorobyov & Basu 2010b). Vorobyov & Basu (2010a) note however that the last generation of clumps produced by disk fragmentation around the end of the protostellar disk phase might survive if they manage to open a gap.

Alternatively, during their inward migration, these gravitationally collapsed clumps could accrete pebbles, which would sediment in their center to form a core and, depending on the core mass and migration rate, could have their envelope tidally disrupted by the parent protostar (Nayakshin 2010). This mechanism, referred to as *tidal downsizing*, might save some of these clumps from a fatal outcome, and form objects with a range of mass and radius, including terrestrial planets. Although still in its infancy, this theory could alleviate some of the shortcomings of the classical GI scenario (see Nayakshin 2017b, for a review).

In summary, although GI is likely to occur in the protostellar disk phase, it is unclear whether some of the clumps formed in such a way can survive to the very quick inward migration, and lead to the formation of planets. The possibility for it to work in the outer parts of protoplanetary disks is also uncertain. Despite these difficulties, the main appeal of disk instability comes from the potential to form giant planets very fast. I defer the interested reader to the recent review in Kratter & Lodato (2016) for more details on GI.

3.2 Core accretion

Core accretion (CA) was a theory initially proposed to account for the formation of both terrestrial and gas giant planets in our Solar System. The bases of this theory were first laid out in Safronov (1969, 1972) for terrestrial planet formation, and was later picked up

by Cameron (1973) to also qualitatively account for the formation of giant planets. The model was further developed by Mizuno (1980), and perfected by Pollack et al. (1996). In broad terms, the theory proposes that formation follows a bottom-up process (contrarily to the top-down GI theory), with a growth in size ranging over 14 magnitudes between sub-μm size dust particles and fully formed giant planets. Five main steps can be identified in the formation of giant planets:

1. Grain coagulation up to centimeter sizes through collisions and efficient sticking (as explained in Sec. 2.1).

2. Growth beyond the meter-size barrier. This has long been the bottleneck of the theory, but an appealing solution has been proposed: *streaming instability* (e.g. Youdin & Goodman 2005; Youdin & Johansen 2007; Johansen et al. 2007) followed by gravitational collapse of pebble clouds (e.g. Simon et al. 2016; Blum et al. 2017; Blum 2018). More work is required to better assess the possible influence of other hydrodynamical instabilities at work in the disk though (e.g. Paardekooper & Johansen 2018).

3. Growth of planetesimals through mutual collisions, in two main steps: runaway accretion followed by (slow) oligarchic growth (Kokubo & Ida 1998; Thommes et al. 2003). The latter could possibly be boosted by *pebble accretion* (e.g. Lambrechts & Johansen 2012; Ormel et al. 2012), eventually leading to the formation of a rocky core.

4. Accretion of gas leading to the formation of an atmosphere, which is initially in hydrostatic equilibrium. This step was predicted to be slow in the initial model of Pollack et al. (1996), and hence suffered major criticism from GI upholders (e.g. Boss 1997). However, it has later been shown that taking into account planetary migration into the disk could significantly accelerate the growth rate (e.g. Alibert et al. 2004; Bitsch & Johansen 2016)

5. Once a critical mass is reached, hydrostatic equilibrium is no longer sustained and *runaway gas accretion* ensues (Mizuno 1980), until no more gas is available in the feeding zone of the planet.

For telluric planets, the growth stops at the end of the third or fourth step, either because the core does not reach a sufficient size, or because not enough gas is available by the time it does reach a sufficient size. The process of giant planet formation might take place preferentially beyond the snow lines of most abundant volatiles where a higher abundance of ices/solids can be found, facilitating a faster core formation.

In summary, the main steps of CA have been well established, and promising solutions have been proposed to address the initial difficulties related to the theory. Similarly to GI, a remaining possible shortcoming of this scenario is the expected very fast inward migration of the planetary core before it reaches a sufficient mass to open a gap (more details on Type I migration in Sec. 3.4.1). Interestingly, this theory which developed mostly from observations of the Solar System have stood up, and actually enables to account very well for, the bonanza of exoplanets found by indirect methods in the recent years and the dearth of exoplanets found at large separations (see e.g. Winn & Fabrycky 2015).

3.3 Predictions from planet formation models

In this section, I briefly summarize some predictions made by detailed formation models of giant planets, such as the expected color and luminosity of these objects, the possible contribution from a circumplanetary disk, and the predicted population of exoplanets that should be found as a whole.

3.3.1 Hot and cold start models

In order to validate a planet formation theory, its predictions have to be confirmed observationally. Early models for the predicted luminosity, spectra, colors, and evolution of giant planets made use of a detailed model of their interior taking into account thermochemistry, opacity sources, radiative and convection zones and temperature/pressure profiles (e.g. Burrows et al. 1997). The effect of stellar irradiation was later included as well (e.g. Baraffe et al. 2003). Given the already high complexity of these models, the addition of another layer of complexity (and uncertainty) related to the formation of these planets has been avoided for a long time. Formation is thus skipped all together and the initial condition in these *hot-start* models consists typically of a fully formed giant planet whose entropy is arbitrarily set to a high value, the giant planet then cools down radiatively over time translating into a slow decay in its luminosity.

Models including the formation history of the giant planets have emerged through the works of Marley et al. (2007) and Fortney et al. (2008), and are referred to as *cold-start* models. Contrary to hot-start models, they take into account a 2–3 Myr time for the growth of the core in the CA scenario. These models typically lead to significantly lower values of entropy than hot-start models when planet formation is completed, hence their name. Cold-start models are thus expected to make more physical sense at early ages (e.g. Spiegel & Burrows 2012). Whether a cold- or hot-start model is considered, the luminosity of the giant planet is predicted to be highest soon after its formation. The expected cooling rate differs for both models though. Cold start models typically predict a slower cooling, while hot-start models predict an initially relatively fast cooling followed by an increasingly slower pace with time.

More recently, Mordasini et al. (2012) have considered a coupled model for both formation and evolution of giant planets to predict in a self-consistent way all physical parameters of the planet and its luminosity. In their work, two physically extreme situations are considered during the runaway gas accretion phase of the giant planet; either it occurs with no radiative losses, or on the contrary all the accretion energy is re-radiated away. They showed that these two assumptions led to similar luminosity predictions as the hot- and cold-start models, resp. (Fig. 3.1). Since in nature, conditions might be found somewhere between those two extreme assumptions, the use of both type of models is motivated. In that sense, Spiegel & Burrows (2012) suggest the use of intermediate (*warm-start*) models, reflecting the large uncertainties involved in the formation process, and including the effect of metallicity which can significantly slow down the cooling process. Although the

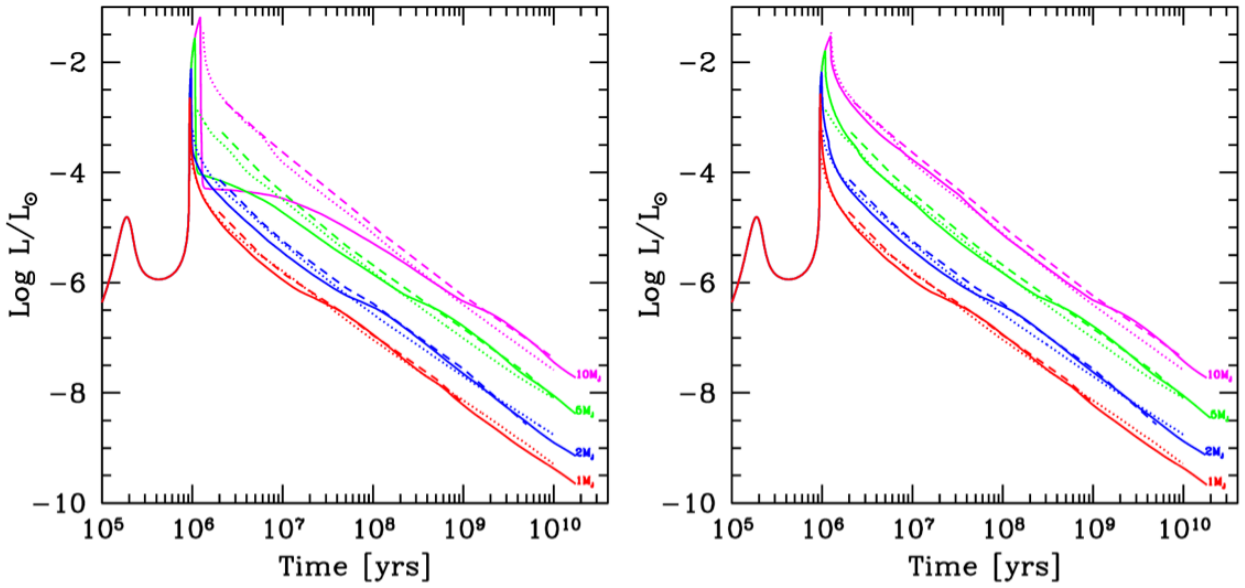

Figure 3.1: Luminosity predictions for gas giant planets of different masses assuming either (1) that all accretion energy is re-radiated away (*left panel*) or (2) that there is no radiative loss (*right panel*) during the runaway gas accretion phase. Models making use of assumption (1) lead to similar luminosity predictions as *cold-start* models, while assumption (2) leads to a high level of entropy in the formed planet, hence similar predictions as *hot-start* models (given by the dotted and dashed lines Burrows et al. 1997; Baraffe et al. 2003, resp.). Plots extracted from Mordasini et al. (2012).

runaway accretion phase is very short, the predicted luminosities by hot- and cold-start models in Fig. 3.1 are significantly different for massive giant planets ($> 5M_{\rm Jup}$) for up to ∼100 Myr. Discriminating between the different models hence requires the direct imaging of very young giant planets.

3.3.2 Circumplanetary disks

The simple observation that the largest moons of the gas giants in our Solar System are found in prograde, circular orbits roughly co-planar with the equator of the planet is a first hint that giant planet formation involves a *circumplanetary* (also called *protolunar*) disk (CPD; e.g. Lunine & Stevenson 1982). Analytical developments and hydro-dynamical simulations have further consolidated that hypothesis (Lissauer 1993; Papaloizou & Nelson 2005; Martin & Lubow 2011). Nevertheless, these long-sought CPDs have remained elusive to date.

While cold, warm or hot-start models consider the luminosity of protoplanets alone, an additional contribution could come from their CPD, which could facilitate their detection. Recently, Zhu (2015) computed the expected luminosity and colors of CPDs as a function of planet mass, mass accretion rate and CPD inner radius, assuming actively accreting disks whose luminosity is significantly larger than the planet irradiation, so that the effect of the latter can be neglected. His results suggest that CPDs have very red colors, which motivates a search with HCI in thermal IR. Eisner (2015) argues that the predictions made in Zhu

(2015) are only valid after the onset of runaway accretion, and provides new luminosity and color estimates for both the hydrostatic growth and runaway accretion phases. While his results are in agreement with that of Zhu (2015) for the latter, he predicts that the earlier phase of hydrostatic growth might only be detectable at much longer wavelength ($> 20\mu$m).

Montesinos et al. (2015) investigated the consequences of not neglecting the feedback of planet irradiation on the disk, which might be a concern for planets with masses $\gtrsim 5M_{\rm Jup}$. They found that a giant planet with a large effective temperature (with a luminosity $\gtrsim 10^{-4}L_{\odot}$), the radiative feedback of the planet could lead to a significantly larger thermal-IR luminosity for the CPD; up to two orders of magnitude for a 5 $M_{\rm Jup}$ planet. This luminosity enhancement is attributed to a positive feedback loop: the planet radiative feedback on the (circumstellar) disk produces an enhancement of the stellocentric accretion stream passing through the location of the protoplanet (likely due to an enhancement of turbulence, enabling a better dissipation of angular momentum; Montesinos et al. private comm.). The enhanced stellocentric accretion heats the CPD, enhancing its luminosity, hence increasing the accretion rate. This positive feedback loop stops when the heating rate is finally compensated by radiative cooling. Their predictions suggest that CPDs could be observed as bright spots in HCI thermal-IR images, with luminosities ranging up to $10^{-3}L_{\odot}$ for a CPD around $5M_{\rm Jup}$, and even redder colors than predicted by Zhu (2015).

A CPD is a miniature Keplerian accretion disk, hence its gas deviates from the global Keplerian pattern of the transition disk. This is detectable in ALMA CO line velocity channels as a dynamical kink (Perez et al. 2015). An invaluable by-product is a dynamical mass estimate of the companion, derived from the measured velocity dispersion at that location, hence independent from evolutionary models. Alternatively, CPDs were also predicted to be detectable using deep band 7 or band 9 continuum observations targeting the enhanced thermal emission from mm-size dust at the protoplanet location (Zhu et al. 2017; Szulágyi et al. 2017). However, searches with continuum observations have led to non-results so far (e.g. Isella et al. 2014; Wu et al. 2017), setting stringent constraints on the dust mass of these disks. These non-detections might be suggestive of very compact optically thick CPDs with higher temperatures than circumstellar disks, implying that thermal-IR observations would be more appropriate to confirm their presence (Wu et al. 2017).

3.3.3 Planet population synthesis

Given the ever growing number of detected exoplanets and the progressive resorption of observational biases in the mass vs semi-major axis diagram, population synthesis is expected to provide increasingly better constraints on the planet formation and evolution processes. The technique, inspired from stellar population synthesis, has bloomed after the pioneering work of Ida & Lin (2004a,b).

As a general rule, planet population synthesis models try to connect the diversity of detected exoplanets to a consistent formation mechanism. Some global end-to-end models have been developed based on a simplification of detailed sub-models which describe for

example the evolution of protoplanetary disks, planetesimal growth, runaway accretion, orbital migration, planetesimals-planet and planet-planet scattering. These global models can predict a final distribution of planets in terms of mass, semi-major axis, radius and luminosities, which can be compared to the statistics of detected exoplanets. While the quality of the predictions reflects the current state of knowledge of the planet formation process, the observed exoplanet statistics can reversely be used to better constrain sub-models of planet formation and evolution. Several generations of population synthesis models have succeeded each other, adding progressively more complexity to the sub-models involved in the adopted global model, in parallel to the advancement of the field. I defer the interested reader to the reviews of Benz et al. (2014) and Mordasini (2018) for more details about planet population synthesis models.

3.4 Migration in a gas-rich disk

Since gas giant planets have to form in the circumstellar disk while it is still gas-rich, there *must* necessarily be interactions between nascent planets and the disk. While the expected effects of the feedback of the planet on the disk will be described in Part II, the most significant effect of the disk on the planet is planetary migration. While in this section I only focus on planet migration due to a gas-rich disk, which is most relevant to the topic of this thesis, it is noteworthy that other mechanisms can lead to planet migration after dissipation of the gas disk, including planetesimal disk scattering (see e.g. Fernandez & Ip 1984; Malhotra 1995; Armitage 2015), and planet-planet scattering (see e.g. Terquem & Papaloizou 2002; Marzari & Weidenschilling 2002; Adams & Laughlin 2003).

3.4.1 Types of migration

Type I migration is illustrated in the left panel of Fig. 3.2. It applies to small planets that do not manage to create a hole in the surface density distribution of the gas in the disk. It stems from the gaseous disk rotating at a different rate than the planet, hence exerting a gravitational torque on the planet, leading to angular momentum exchange between the disk and the planet. The total torque T_p can be expressed as a sum over partial torques evaluated at resonant locations; at the *corotation radius* and at *Lindblad resonances* (Goldreich & Tremaine 1979; Tanaka et al. 2002):

$$T_{\rm p} = T_{\rm CR} + \sum_{\rm ILR} T_{\rm LR} + \sum_{\rm OLR} T_{\rm LR} \tag{3.3}$$

where CR, ILR and OLR, stand for corotation resonance, inner Lindblad resonance, and outer Lindblad resonance, respectively. The amplitude of $T_{\rm CR}$ can be estimated considering that gas particles in the direct vicinity of the planet follow *horseshoe orbits* (in the referential of the planet).

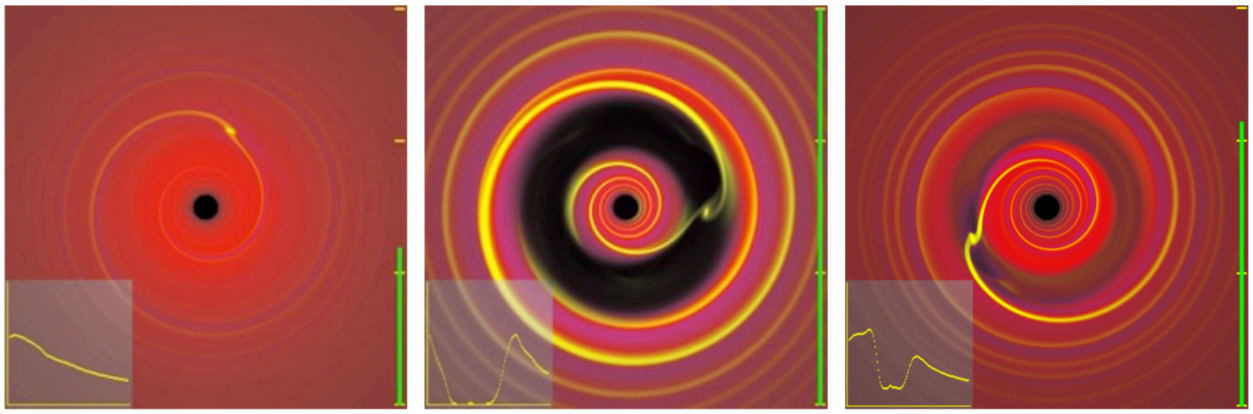

Figure 3.2: Type I (*left*), II (*middle*) and III (*right*) migration. The insets at the bottom left of each image show the average radial surface density profile of the disk. See text for details. Credit: P. Armitage.

The Lindblad resonances of a planet in a Keplerian disk are located at:

$$r_L = \left(1 \pm \frac{1}{m}\right)^{2/3} r_p \tag{3.4}$$

where m is an integer and r_p is the orbital radius of the planet. For resonances with $r_L < r_p$, angular momentum is transferred from the gas to the planet, and the orbital radius of the planet will increase. The reverse happens for resonances with the outer part of the disk ($r_L > r_p$). Goldreich & Tremaine (1979) showed that $T_{\rm LR} \propto \Sigma M_p^2$, where Σ is the gas surface density, M_p is the mass of the planet. The transfer of angular momentum is thus strongest for massive planets in a massive gas disk. The migration timescale $\tau \propto M_p/T_{\rm LR} \propto 1/M_p$ is thus shorter for more massive planets, as long as they do not open a gap.

The relative contribution of each term in Eq. 3.3 is still debated, and type I migration is a topic of active research given its relevance for all planets forming in gas-rich disks (e.g. Bitsch et al. 2013b; Baruteau et al. 2014; Ogihara et al. 2018).

Type II migration corresponds to the case where the planet is massive enough to dynamically carve a gap (right panel of Fig. 3.2). This dynamical carving is a consequence of planet gravity dominating over the effect of disk viscosity; gas is repelled from the Lindblad resonant locations, while in the type I case the viscosity of the gaseous disk is dominant, hence replenishing those resonant locations. This translates in two conditions for a planet to open a gap. The first condition is that the Hill radius of the planet is larger than the scale height of the disk. This is referred to as the *thermal gap opening mass* (Lin & Papaloizou 1993): $M_{\rm th} = c_s^3/G\Omega$. The second condition is that the timescale for the disk to close the gap by viscosity is longer than the timescale for the tidal torque exerted by the planet to open the gap. For planets where these conditions are met, the gas can be assumed to be effectively blocked from passing through the gap, apart from two tidal streams passing through the location of the planet and bridging the gap (Lubow et al. 1999). In first approximation, the migration of the planet will thus follow the viscous evolution of the disk (hence always inward), although taking the tidal streams into account can influence the migration rate (e.g. Duffell et al. 2014; Dürmann & Kley 2017). Nonetheless, the inward migration might

be stopped, or even reversed, in the case of capture in resonance between two protoplanets or when the respective gap of the two protoplanets start to overlap (e.g. Masset & Snellgrove 2001). The Grand Tack model suggests that this happened for Jupiter and Saturn in the protosolar nebula (Walsh et al. 2011). Finally, for such massive planet the feedback of the planet on the disk, consists of a strong spiral density wave (Fig. 3.2). This will be further discussed in Sec. 6.4.

Type III migration was proposed in Masset & Papaloizou (2003) as an additional type of migration that would apply typically to planets between sub-Saturn and sub-Jupiter masses located in massive protoplanetary disks. These planets open a gap or at least create a dip in the surface density distribution of the disk, but the mass of the surrounding disk is still larger than the planet mass. Considering a planet that is already migrating, the asymmetry between the gas particles crossing inward and outward the orbit of the planet (at the ends of the horseshoe) is further enhanced, which accelerates the migration. As the migration rate increases, so does the asymmetry, and a positive feedback loop settles in, leading to runaway migration. Masset & Papaloizou (2003) argue that such migration can account better for the diversity of hot Jupiters found so far.

3.4.2 Eccentricity or inclination excitation in a gas-rich disk

For massive objects found in type II migration, such as brown dwarfs or low-mass binaries (surrounded with a circumbinary disk), numerical simulations indicate that the outer Lindblad resonances from the external part of the disk can significantly excite the *eccentricity* of the companion (e.g. Artymowicz et al. 1991; Papaloizou et al. 2001; Dunhill et al. 2013). For those gapped disks harboring a binary or massive substellar companion, most recent simulations point towards a complex disk evolution possibly explaining companions with a significantly different orbital *inclination* than the disk. Recent studies show indeed that an initially mild relative misalignment between the circumbinary disk and the companion orbital plane can evolve to an almost polar misalignment (Owen & Lai 2017; Martin & Lubow 2017). Owen & Lai (2017) invoke a secular resonance between the precession of the inner disk and the precession of the orbit of the companion as the cause of the misalignment. The simulations of Martin & Lubow (2017) do not involve an inner disk, but they note that the misalignment process appears to operate best for higher binary eccentricity, similarly to Owen & Lai (2017). The results of these hydro-dynamical simulations appear supported by a recent theoretical paper, which suggest that outer/circumbinary disks with a sufficiently high aspect ratio compared to its viscosity will efficiently precess as a quasi-rigid body instead of aligning with the binary orbital plane (Zanazzi & Lai 2018). Putting the different pieces together, it appears that a possible evolutionary sequence for such systems consists first in the outer disk driving a growth in the eccentricity of the massive companion in the gap, followed by a misalignment between the inclination of the disk and the orbit of the companion.

For giant planets, numerical simulations seem to suggest that the eccentricity is also excited but only up to a certain value e $\sim h$, where h is the disk aspect ratio (Papaloizou

et al. 2001; D'Angelo et al. 2006; Duffell & Chiang 2015). Owen & Lai (2017) predict that the misalignment mechanism due to secular resonance between inner disk and companion precession would not work for giant planets with a mass $\lesssim 10 M_{\rm Jup}$ in transition disks. Nonetheless, Bitsch et al. (2013a) found that the outer disk could act as the third body exciting the Kozai-Lidov mechanism, i.e. leading to an eccentricity-inclination oscillation for the companion (Kozai 1962; Lidov 1962). Therefore, in certain conditions interactions between giant planets and gaseous disks might affect their eccentricity and inclination.

4 Constraints on planet formation from direct imaging

Until 25 years ago, the only evidence available to constrain models of planet formation and evolution consisted of Solar System observations. However, the latter do not tell us how frequent is our system at the scale of the galaxy. Since 1995, a plethora of exoplanets have been discovered, mainly by indirect methods (Fig. 4.1). Our knowledge regarding the population of giant planets at short to mid-separation is now relatively complete, while conclusions regarding smaller size planets at all separations and mid-size planets from mid- to large separation still suffer significant observational biases. A major challenge is now to connect this observed diversity of mature extrasolar systems to a consistent planet formation scenario. However, it is likely that this variety is partly or mostly due to significant orbital evolution throughout the life of the system (Sec. 3.4), For example, orbital evolution is required to explain the observed population of *Hot Jupiters*. Conclusions regarding planet formation based on the statistics of mature systems only would thus likely be flawed (e.g. Winn & Fabrycky 2015).

Although few in numbers, and probing a specific locus of the mass versus semi-major axis diagram (*magenta points* in Fig. 4.1), direct imaging detections have enabled some of the most detailed spectral characterization of giant planets in a couple of remarkable systems. Moreover, these detections mostly correspond to young systems, for which the planet to star contrast ratio is more favorable for their detection, hence providing direct constraints on the mechanisms and conditions involved at birth. In this chapter, I will focus on these constraints that are brought by direct imaging, as they are most relevant to the context of this thesis.

4.1 Constraints from direct imaging surveys

A major result of direct imaging surveys is the paucity of giant planets found on large orbits (e.g. Lafrenière et al. 2007; Chauvin et al. 2010; Janson et al. 2012; Galicher et al. 2016; Vigan et al. 2017). In a recent review, Bowler (2016) quotes an occurrence rate of $0.6^{+0.7}_{-0.5}$% for 5–13 $M_{\rm Jup}$ planets between 30 and 300 au. Given that the occurrence of Hot Jupiters is ~ 1% as well (e.g. Mayor et al. 2011; Wright et al. 2012), giant planets appear thus to be as rare in the outer and inner ends of stellar systems, compared in particular to the $\gtrsim 10$%

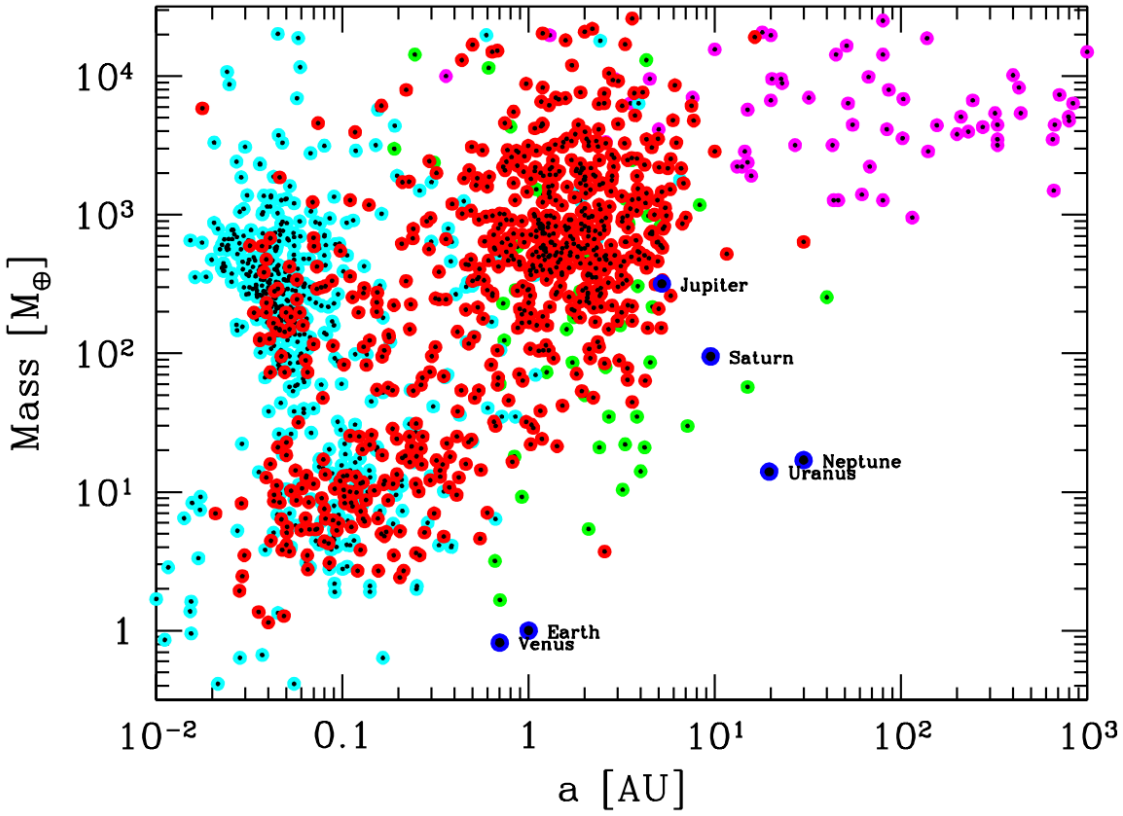

Figure 4.1: All detected exoplanets with a reliable mass estimate (as of 2017) placed in a mass versus semi-major axis diagram. Cyan, red, green and magenta points correspond to detection made with transit, radial velocity, microlensing and direct imaging techniques, respectively. Figure adapted from Mordasini (2018).

detection of GPs at warm separations (Winn & Fabrycky 2015, and references therein).

Considering a larger interval in mass which includes all substellar objects from 0.5 to 75 $M_{\rm Jup}$, Vigan et al. (2017) infer a substellar companion frequency of 0.7–5.7% within 20–300 au of FGK stars, based on a statistical sample consisting of all 199 FGK stars within 100 pc observed in 13 direct imaging surveys. In that study, they compared the few detections of substellar objects to a synthetic population of substellar objects formed by GI following the model of Forgan & Rice (2013). This is shown in Fig. 4.2, where red to yellow pixels correspond to an increasing occurrence rate. The synthesized population includes the effect of planet migration and planet-planet scattering, and predicts that more than 30% of companions between 1 and 75 $M_{\rm Jup}$ would be detectable (Fig. 4.2). The few detections of substellar companions at large separation does not appear compatible with the population of objects synthesized with core-accretion even when including the effect of planet-planet scattering (blue to cyan pixels in Fig. 4.2; Ida et al. 2013). Given that only 3/199 FGK stars were found to harbor a substellar companion, they derive that the fraction of FGK stars forming giant planets by GI is at most a few percent. Nonetheless, I note that this fraction assumes that all the detected companions are formed by disk fragmentation, and not through gravito-turbulent fragmentation (e.g. Hopkins 2013), so that GI might even be less efficient at forming surviving giant planets.

In contrast, Nayakshin (2017a) argues that the result of Vigan et al. (2017) is also com-

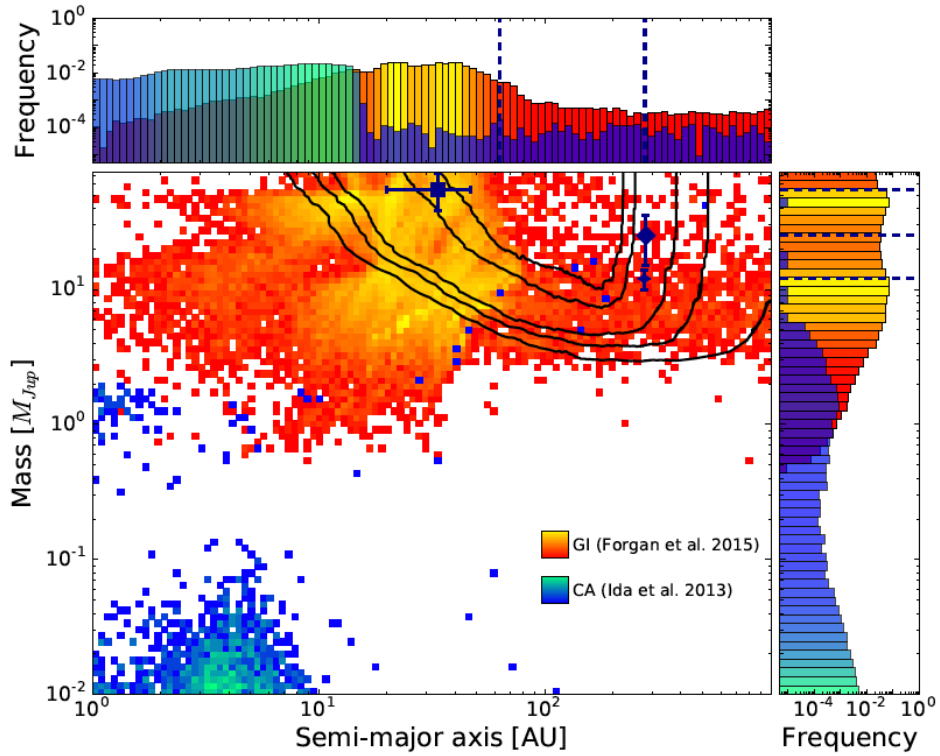

Figure 4.2: Results from direct imaging surveys of substellar companions (3 objects found around 199 FGK stars) and sensitivity limits (black lines correspond to detection probabilities of 5%, 25%, 50%, 90% and 95%), compared to population synthesis models based on GI (Forgan & Rice 2013; Forgan et al. 2015) and CA (Ida et al. 2013). See text for details. Figure from (Vigan et al. 2017).

patible with a scenario in which GI is actually efficient to fragment clumps in the protostellar disk, but the vast majority of them gets destroyed. This possibility is supported by recent models including the effects of scattering and migration after gravitational collapse of the clumps, and gas accretion during migration (e.g. Nayakshin 2017a; Forgan et al. 2018; Müller et al. 2018).

4.2 Constraints from directly imaged young planetary-mass objects

A key benefit of HCI is the possibility to spectrally characterize, and hence probe the atmosphere of, self-luminous giant planets. The characterization typically starts with detection in multiple broad-band filters, which provides color information (e.g. Bonnefoy et al. 2013). The inferred colors can then be plotted in a color versus magnitude diagrams (CMD), and compared for example to mature objects of similar effective temperature (typically brown dwarfs). An example of this kind of plot is provided in Fig. 4.3. Young planetary-mass objects of interest are given with *right-pointing blue triangles*. As can be seen from the plot, a common trait between directly imaged young substellar companions is that they are significantly redder than their field dwarfs counterpart. This is also visible

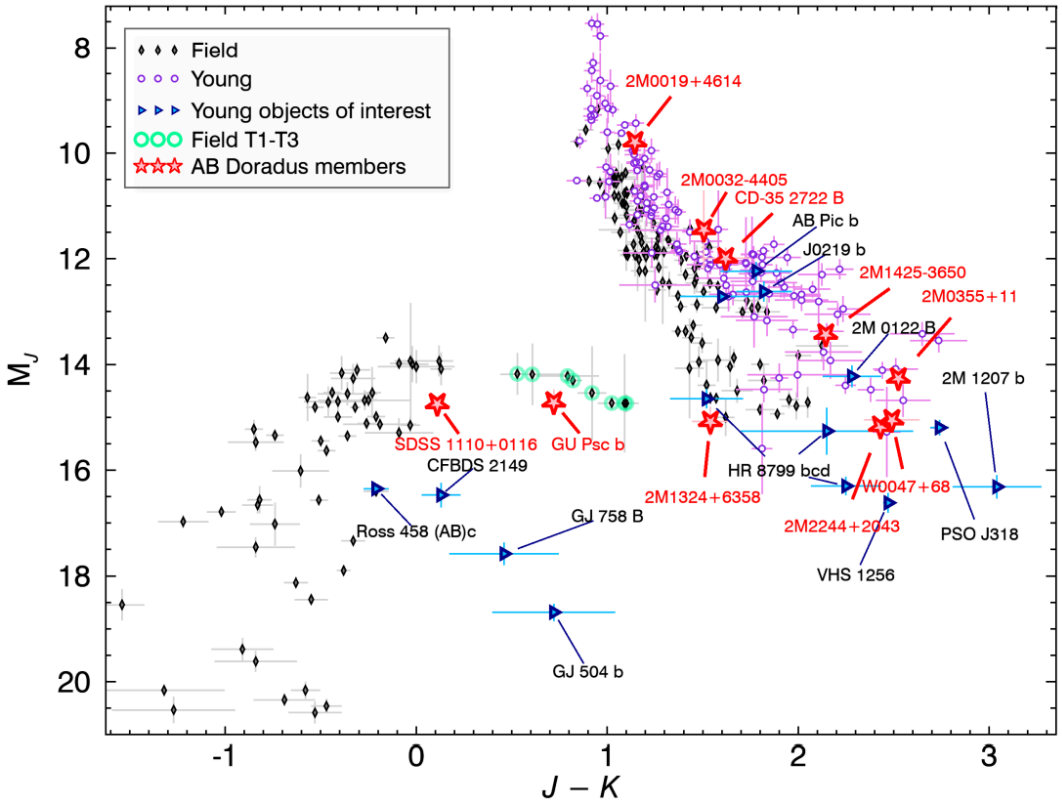

Figure 4.3: Color magnitude diagram of young brown dwarfs and planetary-mass objects (*open purple circles* and *right-pointing blue triangles*, compared to the field sequence of brown dwarfs (*black diamonds*). Particular emphasis is given to members of the young AB Doradus moving group (*red stars*) which are redder to the field sequence. Figure from Gagné et al. (2018).

from the sequence formed by low-mass members of the young AB Doradus moving group (*red stars* in Fig. 4.3), which are systematically redder than their field dwarf counterparts. The origin of these very red colors is still debated. It could be associated to the low-gravity of these objects; lower atmospheric pressure could enable the presence of thick dust clouds in the atmosphere (e.g. Barman et al. 2011; Marley et al. 2012). Another possibility is the presence of a long-lived circumplanetary disk (e.g. Eisner 2015; Zakhozhay et al. 2017).

Depending on the source, a more detailed characterization may or may not be obtained with follow-up observations at higher spectral-resolution. A trade-off is typically to be made between achieved contrast and spectral resolution, given that last generation extreme-AO instruments are mostly equipped with low-spectral resolution integral field spectrographs (IFS; Chap. 14). Apart from a few favorable cases (e.g. Chauvin et al. 2005a; Patience et al. 2012), the retrieval of reliable spectra of directly imaged exoplanets had mostly to wait the last generation of extreme-AO instruments.

Once colors or a spectrum are retrieved, they can be compared to predictions from starting models. Bonnefoy et al. (2013) showed that the mass inferred for β Pic b from cold-start models were incompatible with dynamical constraints from the planet-disk system, hence suggesting that the use of either warm- or hot-start models was more appropriate for this kind of object. Marleau & Cumming (2014) inferred initial entropy values for β Pic b and

the planets of the HR 8799 system based on the observed luminosity, age and mass constraints (inferred from both complementary RV data and dynamical stability constraints) of these systems. These appear incompatible with the values of initial entropy obtained in the coldest start models proposed in Marley et al. (2007), arguing in favor of warm-start models. Recent progress in atmospheric retrieval codes enable now the chemical abundances and temperature-pressure profiles to be inferred from an input spectrum (Lavie et al. 2017). In the case of the HR 8799 planets, this forward modeling enabled to constrain the C/H, O/H and C/O ratios which require a late accretion of ice, and hence appear more consistent with the CA scenario than a formation by GI.

Another invaluable piece of information obtained with direct imaging is the knowledge of the exact orbit of companions. In specific cases where several giant planets are found on large orbits, the inferred orbital elements allow to build a full picture of the architecture of the outer system (see e.g. Zurlo et al. 2016, for the planets of the HR 8799 system). The few directly imaged planetary-mass objects have typically been found at large stellocentric radius, which sometimes appear to defy the CA formation scenario, which involve longer dynamical timescales and hence much slower formation at large radii. Pebble accretion has been suggested to boost planet growth, and hence alleviate this issue (Lambrechts & Johansen 2012). Furthermore, Masset & Snellgrove (2001) showed that pairs of planets where the outer planet is less massive than the inner one would migrate outward when their orbit enters in resonance. This could thus be another qualitative explanation for the configuration of the HR 8799 planets, for which at least the two inner planets appear to be in mean-motion resonance (Zurlo et al. 2016).

Some directly imaged planetary-mass objects appear to be on extremely large orbits, sometimes beyond the typical extent of protoplanetary disks. This is the case of DH Tau b (projected separation of $\sim$335 au Itoh et al. 2005; Patience et al. 2012), AB Pic b ($a \gtrsim 260$ au Chauvin et al. 2005b; Bonnefoy et al. 2010), GSC 06214-00210 b ($a \gtrsim 318$ au Kraus et al. 2008; Bowler et al. 2011), or ROXs 42B b ($a \gtrsim 140$ au Kraus et al. 2014; Daemgen et al. 2017), which all have estimated masses similar or lower than the deuterium-burning limit. While a CA formation followed by dynamical scattering is in theory possible, it would typically require an even more massive companion than the one that is scattered away. In the absence of a central binary, a close stellar flyby might have been responsible for such dynamical ejection of scattering. Interestingly, DH Tau b and GSC 06214-00210 b both show significant hydrogen emission lines in Hα and Paβ and excess optical continuum, consistent with significant ongoing accretion (Bowler et al. 2011; Bonnefoy et al. 2014; Zhou et al. 2014). In the case of GSC 06214-00210 b, a very red K - L' color suggests the presence of a circumplanetary disk (Ireland et al. 2011). A close fly-by would likely have stripped apart the circumplanetary disk, hence in situ formation appears more likely (Bowler et al. 2011). All together, and considering the large stellocentric separation, it appears thus more likely that these objects formed like binary stars, by gravito-turbulent fragmentation of the parent cloud, and represent the low-mass tail of objects formed in such a way. The first imaged exoplanet found around brown dwarf 2M1207 (TWA 27; Chauvin et al. 2005a) is now also considered to fall in this category, considering the mass ratio of the two component, and the impossibility of CA and GI to form giant planets in the protoplanetary disks of brown dwarfs (e.g. Payne & Lodato 2007; Ricci et al. 2014).

Finally, it is worth mentioning in this section the infamous case of FW Tau C. This companion was first reported as FW Tau b in Kraus et al. (2014), who claimed the companion to be a 10 $M_{\rm Jup}$ giant planet orbiting at 330 au from the central M-dwarf binary, based on its faint dereddened K'-band absolute magnitude. However, new ALMA images of the system recently showed an extended close to edge-on disk around the companion. The extended emission from the disk observed in CO lines enabled to infer a dynamical mass of $\sim 0.1 M_{\odot}$ for the companion (Wu & Sheehan 2017). This story can be considered as a warning fable regarding the dangers of relying on optical and/or near-IR direct imaging alone to characterize very young companions since they can be extremely extinct. It also highlights the requirement of using either HCI in thermal IR or sub-mm interferometric images, to probe the earliest stages of planet formation.

4.3 Protoplanet candidates

The strongest constraints on the formation mechanisms of giant planets are likely to be obtained from giant planets caught at birth. Given that protoplanetary disks are mostly optically thick in IR, transition disks, which harbor annular or circular clearings, might be the best targets to look for those protoplanets. Furthermore, a possible explanation for these gaps or cavities is that they are dynamically carved by forming giant planets. As a matter of fact, all protoplanet candidates claimed by the time I started this thesis are located in transition disks and were identified with observations in L' (Fig. 4.4). Nevertheless, recent literature has cast doubt on the possibility that these detections are indeed protoplanets (*right column* of Fig. 4.4). These sources are briefly discussed below.

T Cha Using SAM, Huélamo et al. (2011) were the first to claim the detection of a protoplanet in the transition disk of T Cha, one of the brightest disks in the Chameleon star forming region. However, Olofsson et al. (2013) showed later that this signal could be interpreted as asymmetric disk emission due to forward scattering of an inclined disk.

LkCa 15 A large cavity has been resolved in the transition disk of LkCa 15 in both near-IR polarimetric and sub-mm images (Thalmann et al. 2010; Andrews et al. 2011), suggesting it was sculpted by one or several companions. Soon after, Kraus & Ireland (2012) claimed a protoplanet detection in the cavity using SAM. Based on both SAM L' and Hα detections, Sallum et al. (2015) renewed the claim for the presence of protoplanets. However, a year later Thalmann et al. (2016) showed in new polarimetric images that the companion candidates were all located at the bright inner edge of the disk, suggesting that part or all of their flux is in fact tracing dust-scattered stellar light. The Hα detection might then be tracing the strong Hα emission line from the central star (Manara et al. 2014) scattered commensurately at the inner rim of the disk.

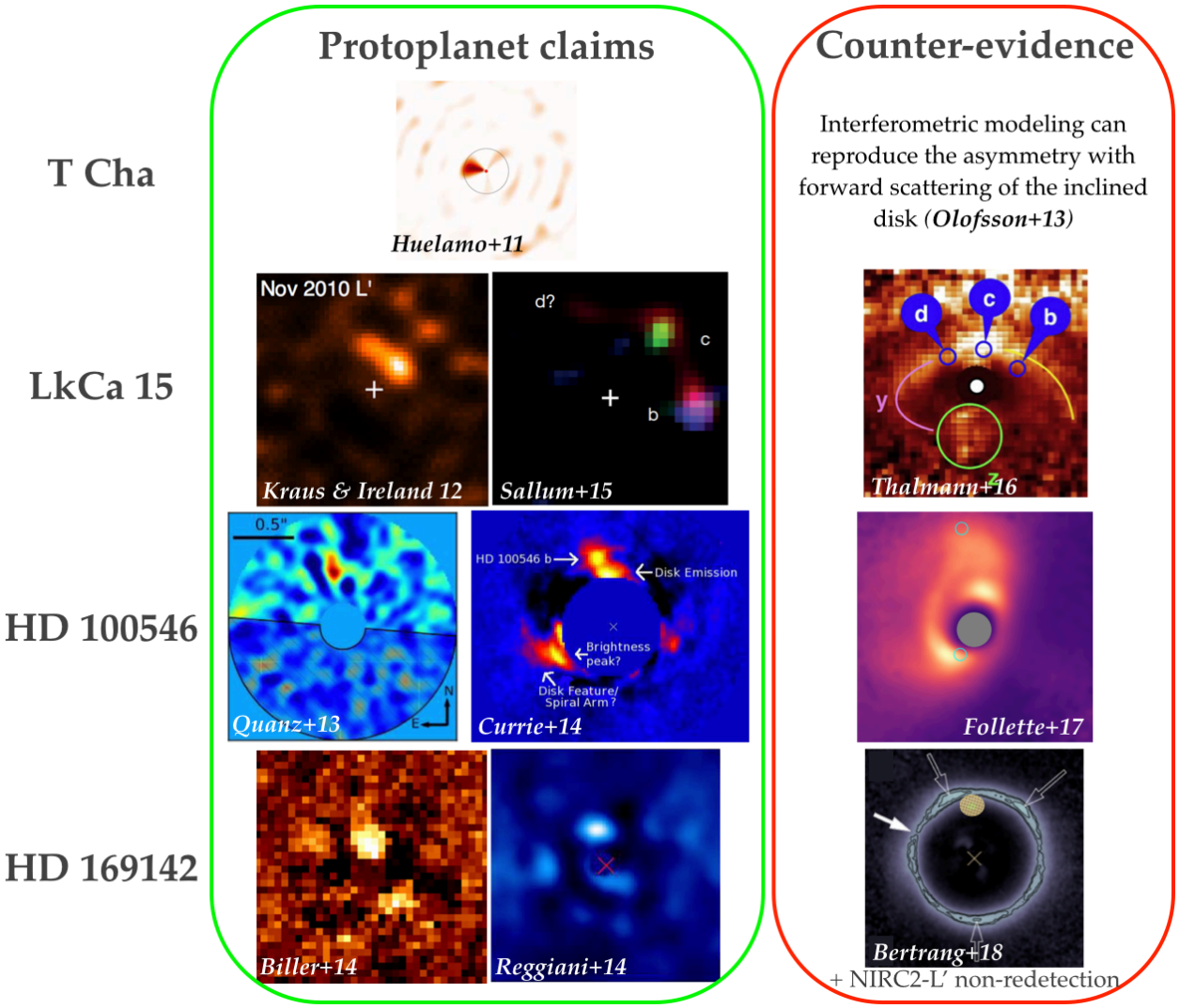

Figure 4.4: Left: protoplanet claims (all in L'-band, with only LkCa 15 with additional K-band and Hα observations). Right: corresponding counter-evidence. See description in text. References: T Cha (Huélamo et al. 2011; Olofsson et al. 2013), LkCa 15 (Kraus & Ireland 2012; Sallum et al. 2015; Thalmann et al. 2016), HD 100546 (Quanz et al. 2013a; Currie et al. 2014; Rameau et al. 2017) and HD 169142 (Biller et al. 2014; Reggiani et al. 2014; Bertrang et al. 2018).

HD 100546 This disk was among the first ones to reveal signposts of planet presence, including spiral arms (e.g. Grady et al. 2001; Boccaletti et al. 2013) and a 13 au gap (Bouwman et al. 2003; Benisty et al. 2010). Quanz et al. (2013a) claimed that the resolved signal they found in L' band at $\sim$0.5″ to the North could be tracing a protoplanet. The re-detection of the L'-source along with a non-detection in K band set color constraints incompatible with photospheric emission, and favored the possibility of emission tracing a protoplanet (Quanz et al. 2015a). Nonetheless, recent observations with GPI and MAGAO with a less aggressive filtering of the image suggest that the compact source could be tracing an extended disk feature (Rameau et al. 2017).

HD 169142 This other transition disk harbors an extended annular gap (40–70 au) observed in near-IR polarimetric images (Quanz et al. 2013b). Observations in L' with NACO equipped with its new AGPM coronagraph (Sec. 10.2.1) revealed the presence of a compact signal at $\sim 0.15''$ to the North of the star (Reggiani et al. 2014; Biller et al. 2014), right within the bright ring seen in polarized light. The new SPHERE polarimetric images suggested that the bright L'-blob could trace the inner rim of the bright ring (the ellipse in the bottom right image of Fig. 4.4 Ligi et al. 2017; Pohl et al. 2017a; Bertrang et al. 2018). The compact signal could not be recovered with new L' observations obtained with Keck/NIRC2 (M. Reggiani, private comm.).

5 This thesis

A major challenge of planetary science is to connect the diversity of detected mature exoplanet systems (Chap. 4) with a consistent planet formation mechanism (Chap. 3). Indirect methods have revealed a large diversity of mature exoplanets, complementing the detailed knowledge gathered from giant planets in our own Solar System. However, the architecture of a lot of mature systems is now believed to be mostly the result of the evolution of the system after formation (e.g. Winn & Fabrycky 2015). Planet population synthesis models (Sec. 3.3.3) can be used to constrain the dominant mechanisms required to reproduce the detected population of exoplanets, but their validity and potential for predictability depend on the quality of the sub-models used regarding both formation (Secs. 3.1 and 3.2) and migration (Sec. 3.4) of planets. The most stringent constraints on both the formation and evolution of planet systems are likely to be inferred from the direct observation of planet formation and planet-disk interactions in-situ. These detections are of foremost importance to constrain formation models whose assumptions are still largely uncertain and lead to significantly different predictions for cold-, warm- and hot-start models (Sec. 3.3.1), and regarding the possible contribution of a circumplanetary disk (Sec. 3.3.2). In this context, the most promising sources to target are thus transition disks (Sec. 2.3), which could trace an intermediate stage between fully optically thick protoplanetary disks (Sec. 2.1) and debris disks (Sec. 2.2).

The recent technological advancement of sub-mm interferometers (and in particular ALMA) and high-contrast imaging instruments has provided new images of primordial disks at unprecedented sensitivity, which is dramatically changing our view of the environment in which planets are believed to form. Given that young giant planets are found to be significantly redder than initially expected based on the field brown dwarf sequence (Sec. 4.1), older-generation thermal-IR HCI instruments (e.g. Keck/NIRC2, VLT/NACO) are expected to still be as competitive as new extreme-AO instruments for the detection of nascent brown dwarf and planetary-mass objects, in particular when equipped with state-of-the-art coronagraphs. The beginning of this thesis coincided with the first observational identification of very asymmetric dust distributions in transition disks thanks to ALMA (Casassus et al. 2013b; van der Marel et al. 2013), the identification of resolved gaps and spirals in optical/IR polarimetric images (e.g. Hashimoto et al. 2011; Muto et al. 2012; Grady et al. 2013) and the first claims of protoplanet detections (e.g. Huélamo et al. 2011; Kraus & Ireland 2012; Quanz et al. 2013a, Sec. 4.3). These first results have suggested that we now have the potential to probe in details the observational properties of different components of planet cradles: gas, dust grains of different sizes, and possibly the protoplanets themselves. In this thesis, I propose to take advantage of the synergy between sub-mm

and optical/IR HCI observations, both reaching unprecedented angular resolution at the most relevant wavelengths to study the formation of giant planets. More specifically, I aim to constrain the answer to several hot questions in the field of planet formation and planet-disk interactions, including:

1) What is the origin of the structures recently imaged in transition disks? A wealth of structures has been found in young circumstellar disks since the advent of ALMA and the new generation of HCI instruments, including large cavities, annular gaps, crescent-shape dust distributions, shadows, warps and spiral arms. Since planet formation is believed to be concurrent to the transition disk phase, a key question is whether (or which of) these structures can be related to the presence of protoplanets. Even if the structures observed in transition disks were not related to giant planet formation, their study would still be invaluable to better understand the environment in which giant planets form.

2) Where and when do giant planets form? High-contrast imaging in thermal IR is particularly appropriate to detect and characterize young self-luminous giant planets. Thermal IR is indeed key since these nascent planet are expected to be very red and likely very extinct by surrounding dust (Sec. 4.2). Furthermore, as seen in Sec. 4.3, a first *bona fide* protoplanet detection is still required.

3) What are the spectral signatures of young companions? There is still a lot of uncertainty regarding synthetic spectra and evolutionary models of low-mass objects at very young age. Obtaining spectra of very young low-mass companions could enable to better constrain these models, and identify their possible weakness. It could also allow to identify possible accretion signatures.

This thesis is divided in three main parts, reflecting the different angles adopted to answer these questions: the imaging of transition disks (Part II), the high-contrast imaging of young companions in thermal infrared (Part III) and the detection and characterization of young companions using a near infrared integral field spectrograph (Part IV)

In Part II, I first provide a review of companion signposts observed in transition disks, including large cavities and annular gaps, asymmetric dust distributions, shadows, warps and spiral arms (Chap. 6). In particular, an account of both observational evidence and possible physical mechanisms at the origin of these structures will be given, with a particular emphasis on spiral arms. Then, in Chap. 7, I detail my personal contributions regarding the characterization of spiral arms. This will include an analysis of the morphology of shadow-induced spiral arms (Sec. 7.1; Montesinos et al. 2016); a detailed study of the morphology of the spiral arms found in the system of MWC 758, including a discussion regarding their origin (Sec. 7.2); and another detailed study of the spirals found in the disk of HD 142527, where I led the characterization of the spirals observed with ALMA (Sec. 7.3.2; Christiaens et al. 2014) and contributed to the characterization of dedicated simulated spirals (Sec. 7.3.3). Finally, in Chap. 8, I will provide a summary of preliminary results of

the study of transition disks within a complete protoplanetary disk population, and briefly describe my contribution to the ODISEA survey.

In Part III, I first present an overview of high-contrast imaging (HCI) techniques (Chap. 10). This is intended as a non-comprehensive review of HCI, with a special emphasis on the tools that I have used. In Chap. 11, I detail the various aspects of the HCI survey that I have led using VLT/NACO to search for protoplanets in transition disks, including the motivation of the study, the target selection, the observations that I carried out, the data calibration and reduction pipeline that I implemented, and the results obtained so far. Chapter 12 will then present my contribution to the analysis of other HCI thermal-IR data, which led in the case of MWC 758 to the detection a protoplanet candidate and a third spiral arm (Sec. 12.1; Reggiani et al. 2018), and in the case of the debris disk of HD 206893, to the detection of a very red substellar companion (Sec. 12.2; Milli et al. 2017a; Delorme et al. 2017).

In Part IV, I first provide a short description of integral field spectroscopy (Chap. 14). Then, I detail the various aspects involved in the work that I carried out with medium spectral resolution IFS VLT/SINFONI, searching for young companions in a selected sample of transition disks (Chap. 15). In particular, I will present the specific observation strategies involved, the data reduction that I carried out, and the results that were obtained for each source. For one of the sources of the sample, PDS 70, an optimal reduction of the data revealed a companion candidate and a tentative spiral arm, possibly connected to the former; this led to a paper submitted to MNRAS (Sec. 15.5.1; Christiaens et al. 2018a). For another source of the sample, HD 142527, we could re-detect low-mass companion HD 142527 B in most spectral channels of SINFONI, which enabled the extraction of the first medium-resolution spectrum of a low-mass companion within $0''.1$ from its central star. Spectral characterization allowed us to infer the physical properties of the companion, including its temperature, surface gravity, mass, radius and age, thereby illustrating the potential for SINFONI+ADI to characterize young low-mass companions (Chap. 16; Christiaens et al. 2018b).

Finally, Part V summarizes the results obtained in this thesis (Chap. 18), and presents an outlook of possible avenues opened by upcoming techniques and instruments to better answer the questions outlined above (Chap. 19).

II Imaging of transition disks

Squares with concentric circles (Kandinsky, 1913)

In this part, I first describe transition disk features that could be indicative of the presence of embedded companions (Chap. 6), namely large annular gaps and cavities, asymmetric dust distributions, shadows and warps, and spiral arms. Other physical mechanisms that can lead to the formation of these features are also discussed. Special emphasis is put on spiral arms, a topic I have worked on in the context of several studies presented in the other chapters of this part.

I briefly describe my contribution to the characterization of shadow-induced spiral arms in Sec. 7.1. The detailed analysis that I carried out for the spiral arms found in the disks of MWC 758 and HD 142527 are then presented in Secs. 7.2 and 7.3.2, respectively. For the spirals of MWC 758, I identified the trace of each spiral, fitted it to the expected shape of companion-induced spirals, measured their pitch angle, the separation angle between each pair of spirals, and performed a proper motion analysis of the main spiral based on observations at different epochs. The results of this analysis fed the discussion regarding their origin (Sec. 7.2.8).

The analysis of the ALMA spirals of HD 142527 fits within the broader study of the origin of the peculiar morphology of the disk, which turned out to harbor almost all the disk features discussed in Chap. 6 and a low-mass stellar companion. For that source, I also characterized observed NIR spirals and spirals obtained in dedicated hydro-dynamical simulations (Sec. 7.3.3). The qualitative origin of most disk features appears now understood as by-products of the interaction with the companion.

In Chap. 8 I explain the importance of studying transition disks within the broader population of protoplanetary disks, and briefly present my contribution to the ODISEA survey.

Finally, a summary of the results and of my future plans in the context of the imaging of transition disks is provided in Chap. 9.

Mmmmmmmmm... doughnuts.

Homer Simpson

6 Possible planet signposts in disk images

6.1 Large gaps and cavities

6.1.1 Observations

Large cavities ($R \gtrsim 20$au) have been resolved for the first time in sub-mm observations of protoplanetary disks thanks to SMA, thereby providing confirmation of the radial clearing interpretation to account for the lack of IR excess in their SED. Since 2012, a few dozens of transition disks with large cavities have also been observed with ALMA. Fig. 6.1 compiles most transition disks with large gaps observed with ALMA in band 6 (1.3mm) and band 7 (0.87mm) continuum between Cycles 0 and 3. Apart from HD 100546, all cavities are estimated to be larger than 20au (Pinilla et al. 2018). A few additional transition disks have been resolved with large annular gaps and rings and are discussed in Sec. 6.1.3.

Some transition disks harbor a cavity seen in near-IR polarized light (e.g. RX J1604 and LkCa 15; Mayama et al. 2012; Thalmann et al. 2014). For those disks, the cavity appears thus to be depleted in both large (mm-size) and small (μm-size) grains, as traced by the sub-mm continuum and polarimetric images, respectively. Nonetheless, the cavity sizes for the mm- and μm-size dust most often do not match (e.g. Garufi et al. 2013; Follette et al. 2013; Pinilla et al. 2015c).

In some disks observed with ALMA, the cavity is seen in both the mm-dust distribution and the gas surface density (e.g. HD 135344 B, DoAr 44 and IRS 48; van der Marel et al. 2016b). An optically thin tracer is used to probe the gas distribution, such as ^{13}CO and its J=2-1 or J=3-2 rotational lines. The gas cavity (similarly to the NIR cavities) is usually observed to be smaller than the sub-mm continuum cavities (RX J1604 and SZ 91; Zhang et al. 2014; Canovas et al. 2015, resp.), which is not surprising given that small dust grains are more coupled to the gas. Nevertheless, often cavities do not appear entirely devoid of gas (e.g. HD 142527 and SR 21; Casassus et al. 2013b; van der Marel et al. 2016b). This is also suggested by IR ro-vibrational CO line observations, providing independent evidence for the presence of residual gas (e.g. Pontoppidan et al. 2008; van der Plas et al. 2009).

Owen (2016) argues that transition disks can be roughly divided in two categories based

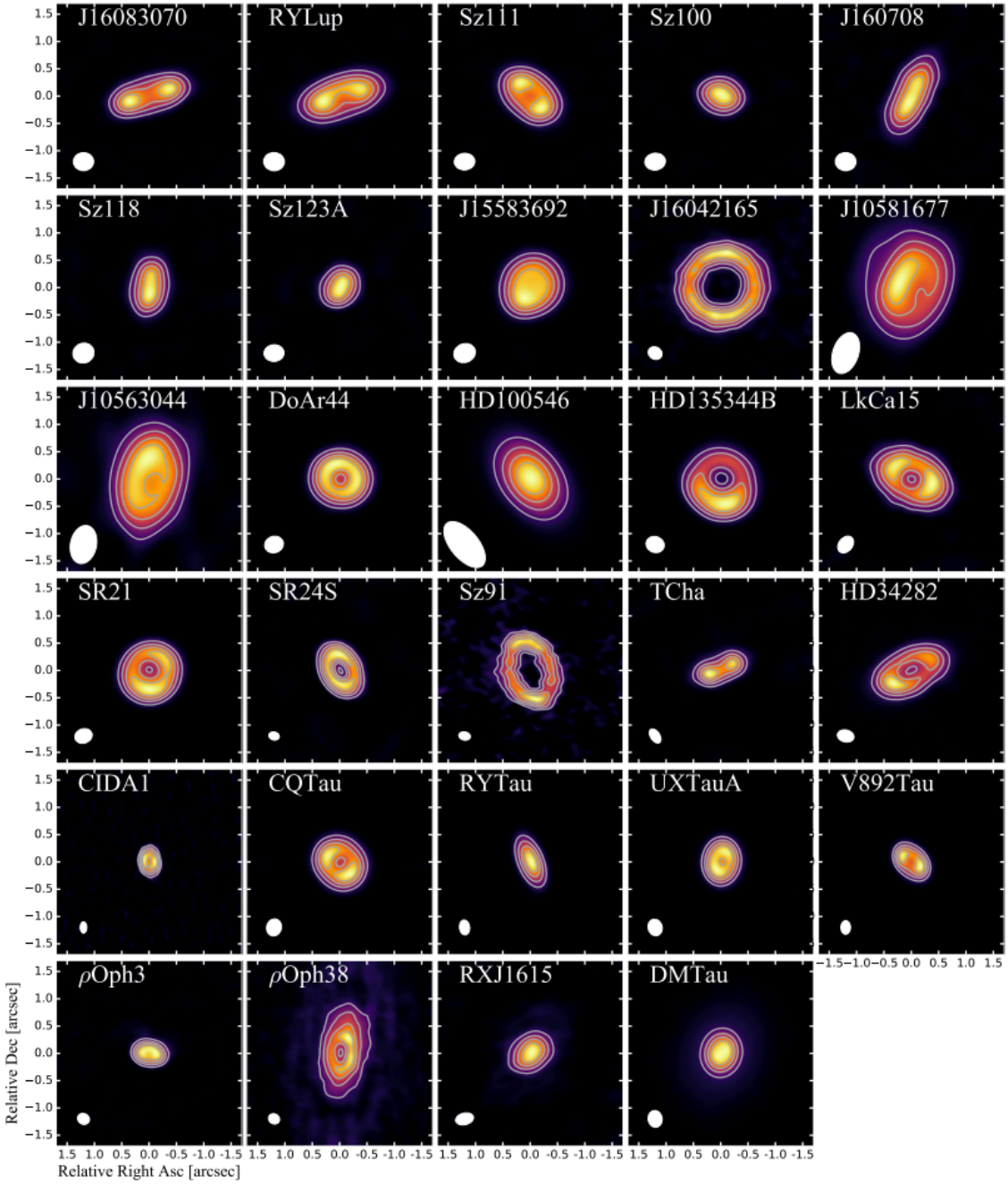

Figure 6.1: Gallery of transition disks observed with ALMA between cycles 0 and 3. Figure extracted from Pinilla et al. (2018). References to individual images can be found therein.

on their mm-flux, hole radius and accretion rates. The global distribution of transition disks in terms of mm-flux shows indeed a bimodal distribution, with a dip in the occurrence of disks with a flux $\sim$ 30 mJy (normalized to a distance of 140pc). About $\gtrsim 60\%$ of known transition disks appear to be mm-faint, while the $\lesssim 40\%$ remaining disks have a flux larger than $\sim$ 30 mJy and are henceforth referred to as mm-bright (Owen et al. 2012; Owen 2016). There appears to be a counter-intuitive correlation between brightness and hole radius; transition disks with larger holes appear to have larger mm-flux (left panel of Fig. 6.2), and are hence likely more massive. Somewhat counter-intuitively as well, the

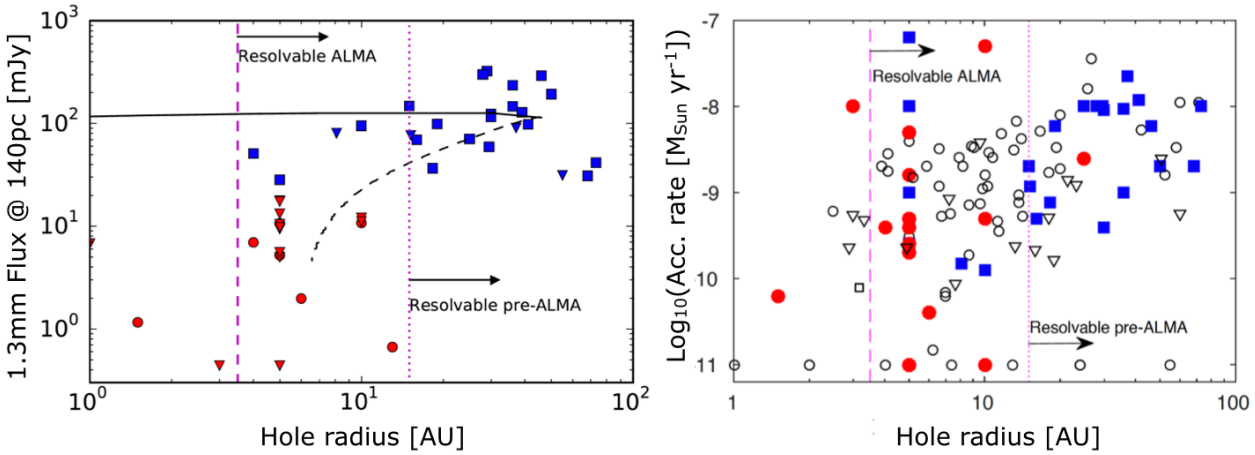

Figure 6.2: Accretion rate and 1.3mm flux of transition disks as a function of the inferred hole size. Blue squares are mm-bright disks (1.3mm flux $\gtrsim$ 30 mJy) and red circles are mm-faint disks. Triangles correspond to upper limits. In the right plot, open circles correspond to disks without a mm-flux estimate for classification. Plots from Owen (2016).

accretion rate does not appear to be affected by the very large holes, as can be visualized in the right panel of Fig. 6.2. There is even a tentative positive correlation between accretion rate and cavity size, contrary to mm-faint disks. Most mm-bright transition disks with large gaps are found around Herbig Ae/Be stars. On the contrary, the occurrence of mm-faint transition disks appears relatively independent of spectral type. Comparing mm-fluxes of transition disks with those of class II objects (Andrews et al. 2013), one finds that mm-bright transition disks have similar mm-fluxes (~ 0.1Jy) as the bright end of the protoplanetary disks surrounding stars of the same spectral type (Herbig Ae/Be), hence suggesting they correspond to the upper-end of the disk mass distribution. Using the same mm-flux to disk mass scaling relation as in Andrews et al. (2013) leads to typical values of 4–12 $M_{\rm Jup}$ for the transition disks around Herbig Ae/Be stars, which suggests a possible underestimation of the disk mass, as already pointed out in Sec. 2.1.

6.1.2 Possible interpretations

The diversity of observed cavities, in terms of size, residual gas/μm-size grains and accretion rate, suggests that transition disks could form a relatively heterogeneous class of objects. It seems reasonable to think that more than one mechanism is at work to account for such diversity. As pointed out in Sec. 2.3, the three major processes now considered by the community to be most likely to cause these cavities are (i) dynamical carving by low-mass (stellar or substellar) companions (e.g. Lin & Papaloizou 1979; Marsh & Mahoney 1992, 1993; Dong et al. 2015c), (ii) dead zone-induced hydrodynamical instabilities (e.g. Flock et al. 2015; Pinilla et al. 2016; Ruge et al. 2016) and (iii) photo-evaporation (e.g. Clarke et al. 2001; Alexander & Armitage 2007; Alexander et al. 2014). These are briefly summarized below.

Photoevaporation

Photoevaporation is expected to unfold in three acts. In the first phase, expected to last up to a few Myrs, the accretion rate is significantly higher than the photoevaporation rate, hence disk evolution is dominated by viscous accretion. When the accretion and photoevaporation rates start to become comparable, the hot gas that is photoionized and whose sound speed is larger than the Keplerian velocity is removed from the disk. This happens at a certain radius which is expected to be of the order of $\sim$10 au for Solar-mass protostars. An annular gap is thus created, and material in the inner disk is progressively drained by viscous accretion, which is expected to last $\sim$0.1 Myr. At the end of this process, the outer disk is directly exposed to stellar radiation, and the dissipation of the outer disk is expected to be very fast. Observationally, gaps formed by photoevaporation can be distinguished from dynamically-carved and vortex-induced gaps as they are expected to efficiently remove the gas from the gap/cavity.

Dynamical clearing by low-mass companions

For a companion to open a gap in the disk, (1) its Hill radius must be larger than the local disk scale height, and (2) the timescale for the opening of the gap by the torque exerted by the planet on the disk must be shorter than the timescale for the closing of the gap by disk viscosity (e.g. Lin & Papaloizou 1993; Bryden et al. 1999). The Hill radius of a planet at separation r_p is given by:

$$r_H = \left(\frac{M_p}{3M_*}\right)^{1/3} r_p \tag{6.1}$$

where M_p and r_p are the mass and radial separation of the planet, and M_* is the mass of the central star. These two conditions are expected to be met for Saturn- or Jupiter-mass planets considering typical protoplanetary disk parameters (e.g. Zhu et al. 2013a), although the exact value of the critical planet mass depends on the mass of the central star, the radial location of the planet (due to disk flaring), and the exact value of the disk viscosity, which is still highly debated. In this hypothesis, the size of the gap or cavity would thus be proportional to the mass of the companion, since a more massive companion exerts a stronger torque on the disk. Gap formation and planet migration are expected to be tightly related (Sec. 3.4.1) due to the torque exerted by the disk on the planet. What starts as a relatively narrow annular gap, can then also widen as the companion migrates. Whether a full gap is carved or not, the companion will create a density bump in the surface density distribution, and can hence lead to the formation of a vortex and dust trap in the outer disk through the RWI (see Sec. 6.2.2).

Gaps dynamically carved by embedded planets are also expected to have a different radial extent for dust grains of different sizes (Pinilla et al. 2012a; de Juan Ovelar et al. 2013). This is due to the larger grains being efficiently trapped at the location of gas surface density bump, while smaller grains remain more coupled to the gas down to a closer separation with the planet. Gaps induced by planets are thus systematically expected to be smaller in near-IR images, tracing μm-size dust, than in sub-mm observations, which reveal the mm-size grains distribution. Furthermore, the more massive the companion, the more efficient

the clearing of the μm-size dust cavity, the larger the radius at which the edge of the sub-mm cavity will be observed, and the sharper the shape of the cavity edge (e.g. Crida et al. 2006; Mulders et al. 2013).

Dead zone-induced dust filtration

Simulations show that the outer edge of dead zones constitutes a radial pressure bump which can effectively prevent dust grains and pebbles (mm- to m-sizes) that are radially drifting inward, hence stopping their migration and leading to the formation of a gap (e.g. Rice et al. 2006; Pinilla et al. 2012b). Unfortunately, the observational prediction for gaps formed by companions and those resulting from this *dust filtration* are very similar: segregation of dust grains of different sizes (Pinilla et al. 2012b; de Juan Ovelar et al. 2013), and sharp transition (or wall) between the gap and the outer disk. A possible way to distinguish them is through the gas distribution. The gas surface density is expected to be only slightly affected by the dead zone, while a (massive) companion is expected to efficiently lower the gas surface density in the cavity (e.g. Zhu et al. 2011; Fung et al. 2014; Pinilla et al. 2016). This could help disentangle the true origin of the observed large cavities where dust segregation is observed (e.g. Brown et al. 2009; Andrews et al. 2011; Garufi et al. 2013; Follette et al. 2013). Nonetheless, predictions on the amount of residual gas vary significantly depending on the assumption made for the disk viscosity and the mass of the companion.

Given the above considerations, it is now possible to better constrain the origin of the two populations of transitions disks identified in Owen (2016). Mm-faint transition disks show relatively small gap sizes ($\lesssim 10$ au) and do not show any dependency between hole radius and accretion rate. This is qualitatively consistent with disks in the process of being photoevaporated. On the contrary, photoevaporation alone does not appear able to account for the properties of mm-bright transition disks. The latter harbor large cavities and display significant accretion rates. They also typically harbor residual gas (e.g. Casassus et al. 2013b; van der Marel et al. 2016b, 2018). and are hence more likely the result of either dynamical sculpting by low-mass companion(s) or dust filtration. A recent survey using SAM led to the conclusion that up to $\sim$40% of transition disks around T-Tauri stars are likely harboring a central binary (Ruíz-Rodríguez et al. 2016). Nonetheless, their survey did not include mm-bright transition disks, for which the occurrence could be higher considering they are mostly found around Herbig Ae/Be stars, which are known to have a larger binary fraction than later type stars (Duchêne & Kraus 2013b). High-contrast imaging is thus necessary to better constrain the possible presence of close-in low-mass stellar companions around Herbig Ae/Be stars. However, a *terra incognita* between 1–10 au in separation (for disks at 140 pc) will likely be impossible to explore until the advent of 30m-class telescopes.

6.1.3 Concentric rings

I note that some disks show evidence for concentric rings or multiple annular gaps in resolved images, but not all of those show evidence of clearing in their SED (e.g. HL Tau, HD 163296 and Elias 2-24; ALMA Partnership et al. 2015; Isella et al. 2016; Cieza et al. 2017). The latter are hence not to be considered as *bona fide* transition disks. Other disks imaged with annular gaps and showing hints of clearing in their SED (such as TW Hya, HD 97048, HD 169142, AS 209 and V1094 Sco; Andrews et al. 2016; van der Plas et al. 2017b; Fedele, D. et al. 2017; Fedele et al. 2018; van Terwisga et al. 2018), hence overlap with the class of *pre-transitional disks* defined by Espaillat et al. (2007, see also Sec. 2.3). Whether disks showing concentric rings (but no SED signature), pre-transitional disks and transition disks with large gaps are tracing an evolutionary sequence is an open question. These ringed disks are not discussed further since they are either not *bona fide* transition disks, or they are pre-transitional disks for which the possible origins discussed in the previous section also hold.

6.2 Asymmetric dust distributions

6.2.1 Observations

First indications of asymmetric dust distributions in disks were found in SMA images (e.g. Ohashi 2008; Brown et al. 2009; Andrews et al. 2011). Nonetheless, apart in the case of LkHα 330 (whose asymmetric dust distribution was partially resolved with SMA; Isella et al. 2013), it is only with the advent of ALMA that a resolved view of these asymmetries was enabled. In particular, ALMA cycle 0 revealed two extremely lopsided disks; Oph IRS 48 and HD 142527 (top row of Fig. 6.3; van der Marel et al. 2013; Casassus et al. 2013b). The asymmetry takes the shape of a crescent or horseshoe, and the contrast in flux density reached therein (compared to the minimum at the same radius) is larger than $\sim$100 in IRS 48 and $\sim$30 in HD 142527. The signal in the horsehose of HD 142527 is now known to be modulated by a decrement in temperature related to the shadow cast by the tilted inner disk with respect to the outer disk, at a PA$\sim -8^\circ$ (Marino et al. 2015b; Casassus et al. 2015b; Casassus 2016, see also Sec. 7.3).

A few other transition disks have been shown to harbor milder asymmetries, of $\lesssim 2$ in contrast, such as SR21, HD 135344 B (middle row of Fig. 6.3; Pérez et al. 2014), and AB Aur (Tang et al. in prep., as mentioned in Tang et al. 2017). In the case of HD 135344 B, it is worth noting that the mm-dust asymmetry is coincident with one of the two near-IR spiral arms (Sec. 6.4.1, Fig. 6.5b). Only in two cases, two dust traps were found at different radii in the same disk: MWC 758 (Marino et al. 2015a; Boehler et al. 2018; Casassus et al. 2018a) and V1247 Orionis (Kraus et al. 2017). The contrast of the outer clump in MWC 758 is $\sim$ 6.5, which makes it the third most lopsided clump in a transition disk (Boehler et al. 2017). The inner clump has a contrast of ~ 2.5, more similar to those of SR21 and HD 135344 B.

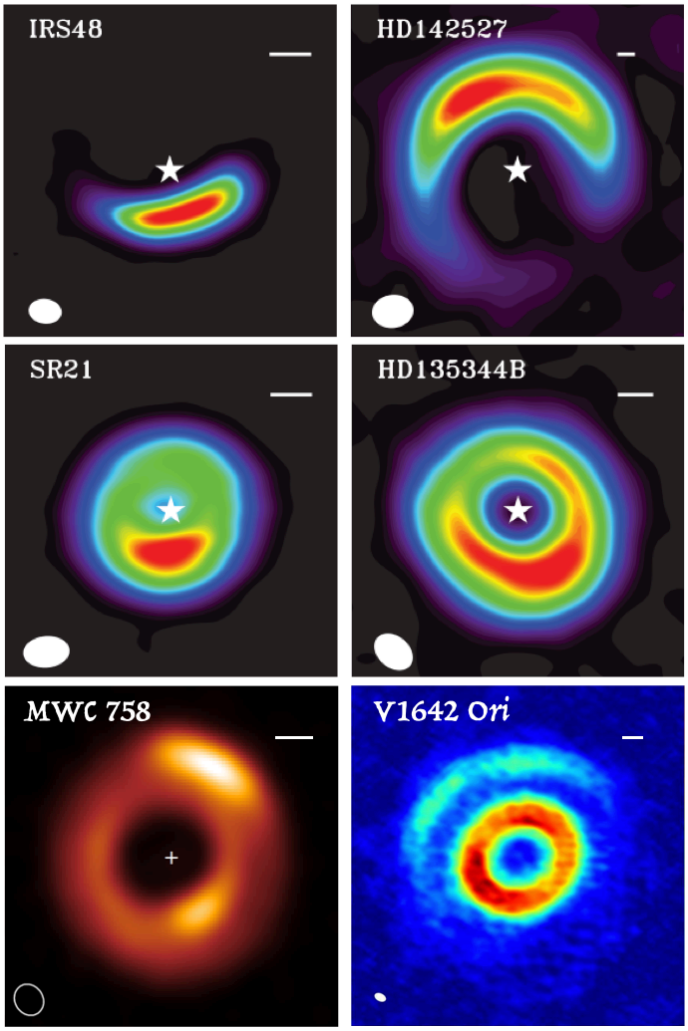

Figure 6.3: Gallery of azimuthally asymmetric distributions of mm-size dust in transition disks imaged with ALMA. The *top row* corresponds to the largest known contrast with respect to disk emission at the same radius ($\gtrsim 100$ for Oph IRS 48 and $\gtrsim 30$ for HD 142527). The middle row shows mild azimuthal asymmetries (contrast factors $\lesssim 2$). The *bottom row* consists in the two transition disks with a known double asymmetric dust distribution at two different radii. References: Top two rows from van Dishoeck et al. (2015), based on observations reported in van der Marel et al. (2013, Oph IRS 48), Casassus et al. (2013b, HD 142527) and Pérez et al. (2014, SR 21 and HD 135344 B). Bottom row: Boehler et al. (2018, MWC 758) and Kraus et al. (2017, V1642 Ori).

Whether high or mild contrast, single or double clumps, when observed at sufficient resolution, the morphology of these asymmetries systematically consists of a wider azimuthal than radial extent. This can be quantified by the aspect ratio $\chi = \sigma_\theta/\sigma_r$ where σ_θ and σ_r are the measured azimuthal and radial widths, respectively. Reported values of χ include ~ 3 for the crescent-shaped sub-mm continua of SR 21, Oph IRS 48 and the inner clump of V1247 Ori (Pérez et al. 2014; van der Marel et al. 2013; Kraus et al. 2017), ~ 5.5 in the outer clump of V1247 Ori (Kraus et al. 2017), and ~ 7 for the crescent of HD 135344 B (Pérez et al. 2014).

In comparison, the gas surface density shows usually no or very low enhancement at the location of the dust asymmetries. Nonetheless, it is also worth noting the difficulty to probe the gas surface density there (e.g. Casassus 2016). CO lines are usually optically

thick, while dense-gas tracers might be affected by complex chemistry (e.g. van der Plas et al. 2017a, for HD 142527). Nonetheless, detailed modeling of both gas and dust ALMA observations of HD 142527 have enabled Muto et al. (2015) to estimate the gas contrast to be $\sim$3, hence 10 times smaller than the dust continuum at the same separation.

Follow-up of the largest asymmetries using ATCA has revealed cm-wavelength counterparts suggesting the presence of large cm-size grains (Casassus et al. 2015b; van der Marel et al. 2015). For both HD 142527 and Oph IRS 48, the distribution of cm-size grains is overlapping with the mm-size grains distribution, but appears to be more compact (Casassus et al. 2015b; van der Marel et al. 2015). A similar conclusion has been reached for the outer clump of MWC 758 initially reported in Marino et al. (2015a), for which new cm-wavelength observations at high resolution have revealed a $\sim$2.3 times more (azimuthally) compact clump at 34 GHz than at 334 GHz (Casassus et al. 2018b). Assuming that the cm-wave continuum at 34 GHz continuum is optically thin (contrary to the sub-mm continuum), it can be used to estimate the cm-size dust mass. For HD 142527, a mass of a few Earth masses was inferred in the cm-wave crescent (Casassus et al. 2015b). The new cm-wave observations of MWC 758 rather suggest an optically thick continuum for the outer clump even at 34 GHz, which precludes this kind of estimate (Casassus et al. 2018b).

6.2.2 Possible origins

Vortex-induced dust trapping

A pressure/surface density bump in the radial disk profile can launch Rossby waves (Sec. 2.1). The presence of unstable modes can induce RWI, i.e., the breaking up of Rossby waves into vortices (Lovelace et al. 1999; Li et al. 2000, 2001). In turn, these vortices are expected to effectively *trap* solids (e.g. Barge & Sommeria 1995; Klahr & Henning 1997; Regály et al. 2012; Lyra & Lin 2013). Hydrodynamical simulations in Regály et al. (2012) managed to qualitatively reproduce the shape of observed asymmetric dust overdensities by considering RWI-induced vortices at the edge of a dead zone. Lyra & Lin (2013) later derived the analytical solution of dust trapping steady-state vortices. When applied to Oph IRS 48, their model appears to predict dust masses and turbulent velocities consistent with observational and numerical constraints (van der Marel et al. 2013; Lesur & Papaloizou 2009; Lyra & Klahr 2011). A strong argument further supporting the dust trap hypothesis is the confirmation that the overdensity is more compact at cm-wavelengths than at mm-waves (Casassus et al. 2015b; van der Marel et al. 2015; Casassus et al. 2018a). Indeed, the efficiency of *dust trapping* is expected to depend on the Stokes number, which is closer to 1 for pebbles approaching meter sizes.

Milder contrasts for the mm-overdensity appear to correspond to more azimuthally extended emission, as can be seen in the cases of HD 135344 B and the outer component of V1247 Ori (Fig. 6.3). How can this be explained in the RWI-induced vortex scenario? Ragusa et al. (2017) performed simulations involving companions of different mass ratios with respect to the primary star. For companions of less than $\sim 10 M_{\rm Jup}$ (assuming a 1 $M_\odot$ primary star), there is almost no noticeable azimuthal asymmetry and a ring-like shape

mm-size dust distribution is produced (as predicted in Pinilla et al. 2012a, where radial dust filtration alone is expected). On the contrary, more massive companions lead to increasingly azimuthally concentrated dust traps. Therefore a single physical mechanism – dynamically carved gaps by companions of different masses – appears to be sufficient to account for the variety of mm-continuum morphologies in transition disks. and lopsided disks of varying aspect ratios. This would also explain the two systems observed with double dust traps (MWC 758 and V1642 Ori, Fig. 6.3), which would simply require the presence of two planets at different radii (e.g. Barraza et al. 2018, in prep. for MWC 758). These predictions for dust traps triggered by planet-induced gaps should nonetheless be compared with new predictions for dead-zone induced dust traps.

Alternative origins

To account for large azimuthally asymmetric dust distributions, Mittal & Chiang (2015) suggested the presence of a gravitational global mode of azimuthal wavenumber $m = 1$ for sufficiently massive disk that can shift the center of mass of the star+disk system. The resulting effect would appear morphologically similar to the large crescents of HD 142527 and Oph IRS 48. However, the inclusion of disk self-gravity appears to dampen the expected contrast of such kind of dust trap, making it harder to reconcile with observations (Baruteau & Zhu 2016).

Circumplanetary disks are expected to be very compact (a few R_H at best) and hence unresolved (e.g. Martin & Lubow 2011). On the contrary, all mm-dust overdensities appear to be both spatially resolved and azimuthally extended in recent observations, which hence argue against the possibility that the observed dust clumps trace circumplanetary disks.

Spiral density waves are an alternative explanation for asymmetries found at milder contrast, such as those of HD 135344 B and V1247 Ori (Pérez et al. 2014; Kraus et al. 2017). In those sources, a near-IR spiral arm appears indeed to roughly connect with the observed dust trap (e.g. Muto et al. 2012; Ohta et al. 2016). The enhanced mm-dust emission could trace either dust trapping due to pressure/density bump associated with the spiral itself or shock heating from the spiral wave (e.g. Lyra et al. 2016). On the other hand, Rafikov (2016) does not predict spiral shock heating to be significant, unless the spirals are due to a central binary. In the latter case, a significant dust trap is expected due to the gap-carving binary itself, as seen in the previous subsection. As will be seen in Sec. 7.3.3, an alternative origin for the significant dust trap in HD 142527 could be a strong spiral density wave launched by the central binary (Price et al. 2018), hence not requiring vortices. In a similar vein, Bae et al. (2017) proposed that companion-induced spiral shocks could open gaps through angular momentum exchange with the disk, further arguing that these rings, consisting of local density maxima, could hence also lead to efficient dust trapping.

6.2.3 Potential for second-generation planet formation

Giant planets are expected to open a gap (Sec. 3.4.1), and hence lead to a density and pressure maximum at the outer edge of the gap which, as seen in the previous section, can lead to dust trapping in the outer disk. These *dust traps* can efficiently capture migrating pebbles from mm to metre sizes. It is thus natural to imagine that they could lead to a second-generation of planets. In fact, the potential of long-lived vortices in protoplanetary nebula to effectively trap dust and hence enable planet formation has been identified early on (e.g. Barge & Sommeria 1995; Adams & Watkins 1995; Tanga et al. 1996), before the exact mechanism to create such vortices was well understood. Hydrodynamical simulations in Lyra et al. (2008, 2009a,b); Sándor et al. (2011); Ayliffe et al. (2012) all suggest that vortices might indeed be a viable formation scenario of planetary cores through enhanced accumulation of large pebbles.

The main uncertainty however concerns the question of whether material inside the vortex reaches a sufficient density for gravitational collapse. In the case of HD 142527, one of the best characterized dust trap, gas does not appear to reach a sufficient density for gravitational instability (Fukagawa et al. 2013; Muto et al. 2015). Another possibility is that the solid density reaches a sufficient level close to the center of the vortex, in a similar way as the streaming instability gathers pebbles sufficiently close together to provoke their gravitational collapse (Sec. 3.2). A lot of pebbles appear indeed to be trapped, about a few Earth masses of cm-size dust (which is thus a lower limit f the total dust mass) based on cm-wave emission (Casassus et al. 2015b). It appears thus a priori conceivable that the streaming instability could work along the closed streamlines of the vortex as it gathers more and more drifting solid material from the outer part of the disk. New hydrodynamical simulations are required to test this hypothesis though.

6.3 Shadows and warps

6.3.1 Shadows

Three types of shadows have been observed in transition disks so far; secular two-sided shadows, single-sided moving shadows, and transient individual shadows. A gallery of all detected shadow-like features is provided in Fig. 6.4.

The shadow in the circumbinary disk of GG Tau A was the first one reported in literature (Silber et al. 2000; Potter et al. 2001; Itoh et al. 2002, Fig. 6.4f). Based on a >10 years baseline, Itoh et al. (2014) measured the rotation rate of the shadow to be $\sim 5.5°$ in 12 years. This is much faster than the Keplerian rotation rate at the edge of the circumbinary disk. The shadow also appears to be counter-rotating with respect to the disk (e.g. Guilloteau et al. 1999) and the orbital motion of the central binary (e.g. Köhler 2011). Itoh et al. (2014) suggest it is due to the precession of an inclined and asymmetric inner disk around one of the components of the binary.

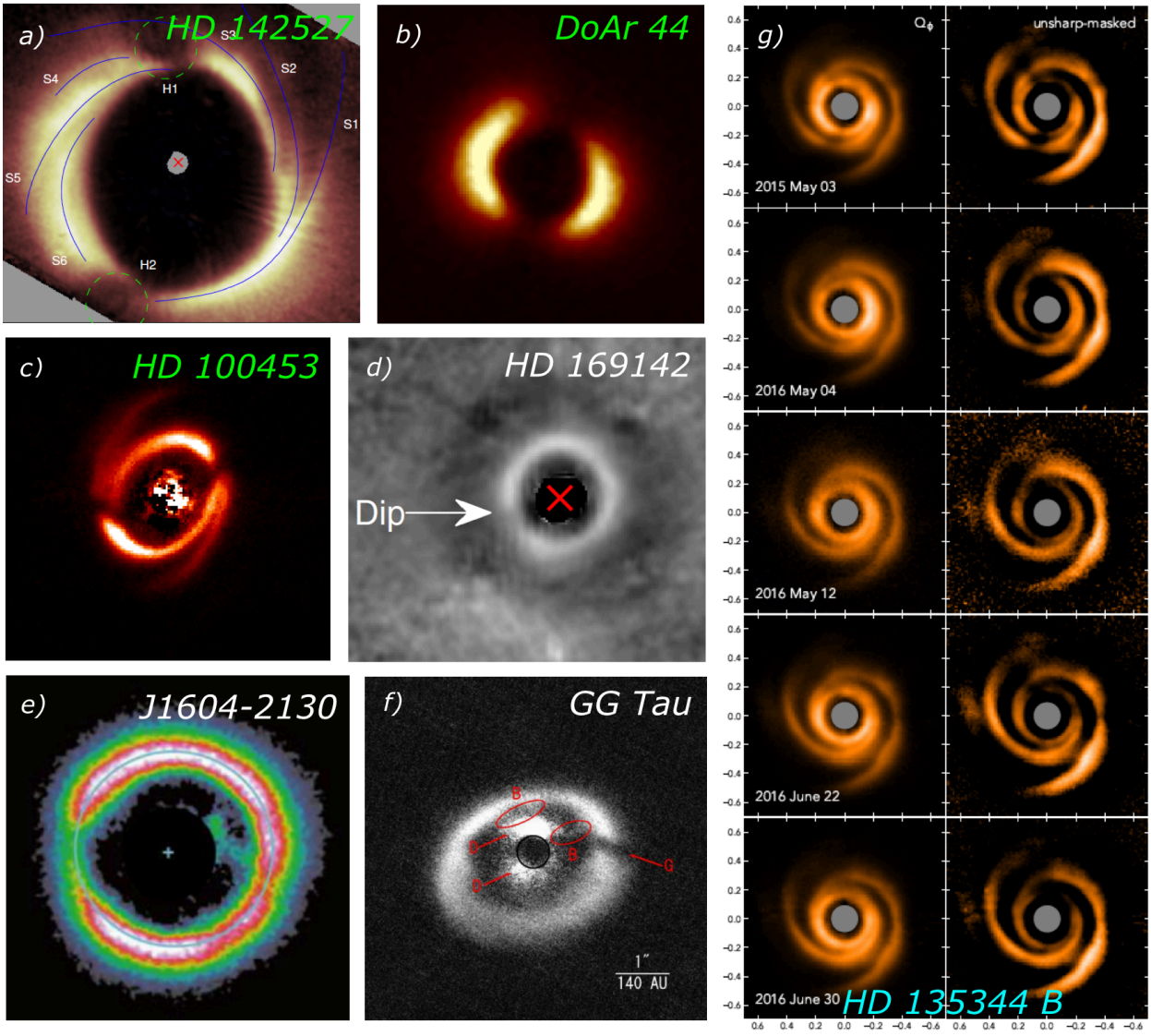

Figure 6.4: Gallery of shadows observed in transition disks. Several types of shadows can be identified: secular two-sided shadows (*green* labels), long-lived single moving shadow (*white* labels), and transient individual shadows (*cyan* labels). References: DoAr 44 (Casassus et al. 2018b), HD 142527 (Avenhaus et al. 2014), HD 100453 (Benisty et al. 2017), HD 169142 (Quanz et al. 2013b), J1604-2130 (Mayama et al. 2012), GG Tau (Itoh et al. 2014) and HD 135344 B (Stolker et al. 2017).

Similarly, a dip in the annular emission of the disk of J1604-2130 has been observed to be moving at different epochs. First detected in Mayama et al. (Fig. 6.4e; 2012) towards the East, it was found a few years later to the NE, both in Pinilla et al. (2015a) and Canovas et al. (2017), which suggests it is rotating at a rate of $\sim 22^\circ$ yr^{-1}. A similar shadow has been reported in the main ring of HD 169142 (Fig. 6.4d; Quanz et al. 2013b), and found a few years later at a significantly different PA in Bertrang et al. (2018). Both Canovas et al. (2017) and Bertrang et al. (2018) argue that the rotation rate of these fast-moving shadows are compatible with an object orbiting at a few au separation from the star, and speculate that it could be a circumplanetary disk given the large extent required to cast a shadow.

The first two-sided shadows have been observed in HD 142527 as dark dips in the scat-

tered light distribution at the edge of the cavity (Fukagawa et al. 2006; Casassus et al. 2012; Canovas et al. 2013; Avenhaus et al. 2014, labeled H1 and H2 in Fig. 6.4a). Since then, two additional transition disks have shown similar two-sided dips: HD 100453 and DoAr 44 (Benisty et al. 2017; Casassus et al. 2018a, Fig. 6.4b and c). These shadows on both sides of the disk do not appear exactly symmetric with respect to the central star. They also do not appear to "cut" the outer disk radially, but rather with a certain angle.

Finally, evidence for transient shadows has been found in the disk of HD 135344 B (Stolker et al. 2017). The timescale of the variability appears to be on the order of less than a day, with different shadows quickly appearing and disappearing at different PAs in the outer disk (Fig. 6.4e).

6.3.2 Warps

A common explanation for the observed shadows is the presence of an inclined optically thick inner disk with respect to the outer disk, namely a *warp*. Using a 3D radiative transfer code, Whitney et al. (2013) showed that different relative misalignments between inner and outer disks could create two-sided shadows similar to those observed. When more realistic parameters are considered for the tilted inner disk, an almost perfect agreement between radiative transfer predictions and observations is obtained for a difference in inclination of $\sim 70^{\circ}$ (e.g. Marino et al. 2015a; Min et al. 2017, for HD 142527 and HD 100453, resp.). Furthermore, in the case of HD 142527 observational confirmation of the warp hypothesis has been provided by ALMA observations of CO rotational lines (Casassus et al. 2015a). The velocity maps show indeed almost free-fall velocities in the vicinity of the warp. In the case of HD 100453, constraints on the orientation of the inner disk based on NIR interferometry are consistent with the misalignment required to cast the observed shadows (Min et al. 2017). Radiative transfer predictions on the system of DoAr 44, which presents similar two-sided shadows as HD 142527 and HD 100453, also suggest the shadows are due to a misaligned inner disk (Casassus et al. 2018a). In summary, it appears thus evident that two-sided dips correspond to shadows cast by a significantly misaligned inner disk with respect to the outer disk.

What can produce these warps? The most commonly invoked mechanism involves the presence of a massive companion. Hydrodynamical simulations have indeed shown that misalignments can be caused by the dynamical interaction between the disk and a companion on an inclined orbit (e.g Mouillet et al. 1997; Arzamasskiy et al. 2018). Owen & Lai (2017) proposed that a massive companion ($\sim$0.01-0.1$M_{\odot}$) on an eccentric orbit in the gap of a transition/circumbinary disk would drive a significant misalignment of the inner disk if their respective precession periods (of the companion and inner disk) enter in resonance, which might happen during the inward migration of the companion. Alternatively, other studies have shown that an initially mildly misaligned outer disk around a system containing a massive companion on an eccentric orbit could be excited to an almost polar plane with respect to that of the binary (Martin & Lubow 2017; Zanazzi & Lai 2018). More details on possible inclination–eccentricity excitation mechanisms are provided in Sec. 3.4.2.

Alternative mechanisms have been proposed in the literature to account for warps. Simulations in Nixon & Pringle (2010) showed that a fly-by is able to warp the outer part of a disk. Their simulations suggest that such warp can survive up to a Myr. As will be seen in Sec. 6.4.2 in the context of spirals, flybys are rare, except perhaps in the densest star-forming clusters, which suggests that the observation of warps would be unlikely in the flyby hypothesis. Another possibility at early stages is a warp of the innermost parts of the disk by a strong magnetic field whose dipole is misaligned with the orbital axis of the disk (e.g. Esau et al. 2014). Nonetheless, this is expected to warp only the portion of the disk lying at less than a fraction of au from the star. While this is a possibility that cannot be excluded for transient shadows, it appears unable to account for large scale warps involved in two-sided shadows or observed in debris disks.

Finally, it is interesting to notice that warps have also been observed in debris disks, such as AU Mic (e.g. Boccaletti et al. 2015) and β Pic, where in the latter case β Pic b was shown to account for the observed warp (e.g. Dawson et al. 2011; Chauvin et al. 2012). All in all, given our current knowledge, warps inferred from the observation of double shadows, sub-mm line velocity maps, or directly imaged, appear to be a strong indication for the presence of a (massive) companion in the disk.

6.4 Spiral arms

6.4.1 Observations

A variety of spiral patterns has been observed in transition disks, starting with HST images of AB Aur and HD 100546 (e.g. Grady et al. 1999, 2001). A gallery summarizing the observations of spirals found in transition disks so far is provided in Fig. 6.5. The vast majority of conspicuous spiral arms has been observed in polarimetric images (top two rows of Fig. 6.5), hence tracing small grains at the surface of the disk. With the advent of ALMA, a few spiral arms have now also been detected in sub-mm continuum and gas lines (bottom row of Fig. 6.5). The sub-mm continuum image of Elias 2-27 (Fig. 6.5*k*) suggests that the spiral pattern is imprinted in the mid-plane. ALMA images of AB Aur (Fig. 6.5*l*) and HD 142527 (Fig. 6.5m) correspond to the CO J=2-1 line integrated and peak intensity maps, respectively. This line is typically optically thick in young disks, although it is unclear up to which radial separation this assumption still holds. The CO spirals of HD 142527 are studied in details in Sec. 7.3.2.

Based on their morphology, I propose to divide the spirals observed in transition disks in three categories: grand-design (*white labels* in Fig. 6.5), flocculent (*yellow labels*), and single (large-scale) spiral arms (*red labels*). Depending on the wavelength and angular resolution of the observation, some sources might fall in different categories. This is the case of AB Aur which shows a flocculent spiral morphology in near-IR and another grand-design spiral pattern in the cavity as seen in the CO image obtained with ALMA (e.g. Hashimoto et al. 2011; Tang et al. 2012, 2017). Another example is HD 142527 which harbors all three types of spiral arms: flocculent spiral arms at the outer edge of the cavity (e.g. Avenhaus

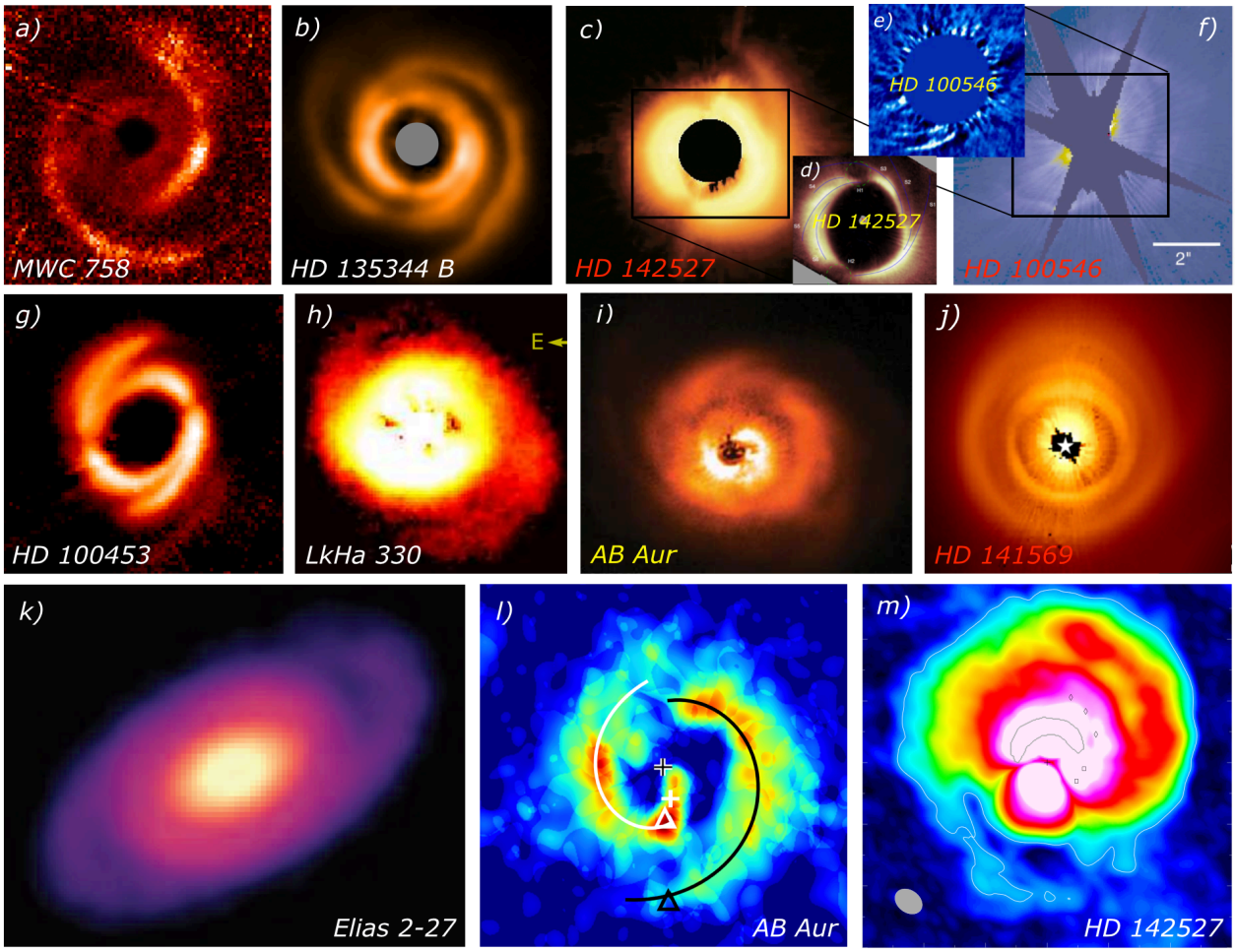

Figure 6.5: Gallery of spiral arms observed in transition disks. The top two rows correspond to observations in near-IR, while images from the bottom row were obtained through sub-mm interferometry with ALMA. The spirals can be classified in three broad categories: grand-design (*white* labels), flocculent (*yellow* labels) and single spiral arms (*red* labels). See text for details. References: a) Benisty et al. (2015); b) Stolker et al. (2016); c) Fukagawa et al. (2006); d) Avenhaus et al. (2014); e) Boccaletti et al. (2013); f) Grady et al. (2001); g) Benisty et al. (2017); h) Uyama et al. (2018); i) Hashimoto et al. (2011); j) Konishi et al. (2016); k) Pérez et al. (2016); l) Tang et al. (2017); m) Christiaens et al. (2014, see also Sec. 7.3.2)

et al. 2014, 2017), a larger single spiral also stemming from the edge of the cavity (e.g. Fukagawa et al. 2006) and a large-scale grand-design spiral pattern seen in CO (Christiaens et al. 2014).

A common quantity used to characterize the morphology of spiral arms is the *pitch angle*, which is defined at each point of the spiral as the angle between the tangent to the spiral and the local azimuthal vector. A meaningful pitch angle measurement requires a face-on view of the disk, and hence previous deprojection of the disk using its inclination and PA of semi-major axis. Measured values of pitch angle can vary greatly from a disk to another, between spirals within a same disk or even throughout the length of a single spiral arm (see e.g. MWC 758; Sec. 12.1.1), ranging typically from $\sim 10^\circ$ to $\sim 30^\circ$.

Another observable used to characterize spirals is their *contrast*. It is typically defined as the ratio between the peak of emission along the arms and the background surface

brightness. Likewise the pitch angle, the contrast can also vary throughout the length of the spiral arm. Reported contrast values for the spirals span 1.5 to 3 (e.g. Garufi et al. 2013; Pérez et al. 2016; Dong & Fung 2017b).

Finally, in the case of multiple spirals, another observable is the *separation angle* between the different arms, and its evolution with radial separation. The grand-design spirals of Elias 2-27 are roughly axisymmetric, i.e. they have a constant separation angle $\sim$180° at all radii (Pérez et al. 2016). The main spirals of HD 135344 B also have a relatively constant separation angle, but closer to $\sim$130° (Garufi et al. 2013; Fung & Dong 2015).

Spirals have also been observed at much younger ages than transition disks. For example, in systems of multiple Class 0/I protostars spiral streams have been observed connecting the different components (e.g. Tobin et al. 2016). The infall of parts of the envelope around Class 0/I protostars, identified based on velocity (dispersion) maps, has also been shown to follow spiral-like shapes (e.g. Tobin et al. 2011). In the case of transition disk AB Aur, large scale spiral arms extending up to 700 au were found with a velocity pattern suggesting counter-rotation with respect to the disk, and were hence attributed to the same origin (Tang et al. 2012).

On the other hand, they have also been imaged up to the early debris disk stage (e.g. HD 141569; Konishi et al. 2016; Mawet et al. 2017a) or with no sign of velocity dispersion (e.g. Christiaens et al. 2014; Pérez et al. 2016). This diversity could suggest that not a single mechanism is at the origin of all observed spirals.

6.4.2 Possible origins

Since my main contributions in the context of transition disk imaging concerns the characterization of spiral arms (Secs. 7.1 to 7.3), it is worth dwelling on the possible mechanisms leading to their formation, and on possible ways to disentangle them. However, before discussing possible spiral-inducing mechanisms, it is worth understanding their exact nature. Similarly to the arms observed in spiral galaxies, the spiral arms seen in protoplanetary disks are expected to trace density waves rather than material arms rotating at Keplerian velocity. If the arms were material, the inner part of the observed spirals would rotate several times faster than their outer part, implying that within a few orbital periods they would wind up and disappear. As density waves, spirals would hence have their own rotation period. Their observation is hence believed to trace either genuine density enhancement or increased temperature/pressure which puffs up the vertical scale height of the disk. In the latter case, a larger vertical scale height captures more light from the star, accounting for a more efficient scattering of small grains. Juhász et al. (2015) showed that a relative change of only 0.2 in pressure scale height was enough to account for the observed contrast of spiral arms in near-IR (contrasts $\gtrsim 1.5$), while a density improvement of $\delta\Sigma/\Sigma \sim 3.5$ would be required to reach the same observed contrast.

What can excite these density and/or pressure/temperature waves? Several mechanisms have been proposed, and are briefly described below.

Embedded companions

Forming planets interact gravitationally with the disk in which they form. Lin & Papaloizou (1979) were the first to show that binaries with extreme mass ratios embedded in an accretion disk would exchange angular momentum with the disk, predicting that the interaction would result in the formation of a spiral arm. Goldreich & Tremaine (1979) showed independently that any rotating external gravitational potential (e.g. a planet) embedded in the disk would lead to the formation of *density waves*, mostly at the Lindblad and corotation resonances (Sec. 3.4.1). However, one had to wait the analytical studies of Ogilvie & Lubow (2002) and Rafikov (2002) for the exact shape of the density wave to be calculated analytically. This shape is that of a single spiral arm corresponding to the locus of constructive interferences between the density waves launched from Lindblad resonances in the disk (Ogilvie & Lubow 2002). For a planet at location (θ_p, r_p), the spiral is expected to follow (Rafikov 2002):

$$\theta(r) = \theta_p + \frac{\text{sign}(r - r_p)}{h_p} \times \left\{ \left(\frac{r}{r_p}\right)^{1+\beta} \left[\frac{1}{1+\beta} - \frac{1}{1-\alpha+\beta}\left(\frac{r}{r_p}\right)^{-\alpha}\right] - \left(\frac{1}{1+\beta} - \frac{1}{1-\alpha+\beta}\right) \right\} \tag{6.2}$$

where h_p is the disk aspect ratio at radius r_p. It is assumed that the disk angular frequency Ω and sound speed c_s can be expressed as power laws: $\Omega \propto r^{-\alpha}$ and $c_s \propto r^{-\beta}$. This equation has 5 free parameters. Two parameters correspond to the position of the companion (r_p, θ_p), assumed to be in the same plane as the disk. In practice, they define the location of the *twist* that is seen in the morphology of the spiral (see e.g. Fig. 7.4b, where the twist in the spiral model is on top of the companion candidate). The three other parameters (h_p, α and β) define the shape of the spiral propagating inward and outward from that location, and depend on the disk; $\alpha = 3/2$ and $\beta = 0.25$ for Keplerian, passively heated disks.

It is possible to fit the measured polar trace of a particular spiral to Eq. 6.2 in order to determine the position of a putative companion launching it. Nonetheless, the best-fit parameters are usually degenerate (at least when no twist is observed in the image, which has been the case for all spiral observations so far). Even when α and β are fixed to represent a passively heated Keplerian disk, any combination of (r_p, θ_p) lying in the rough continuation of the spiral can lead to similar quality fits, with only minor variations of the best-fit h_p value (e.g. Muto et al. 2012; Boccaletti et al. 2013; Christiaens et al. 2014). Furthermore, the best-fit value of h_p usually corresponds to significantly larger temperatures than expected from SED fitting (e.g. Benisty et al. 2015; Stolker et al. 2016).

Equation 6.2 can also be written in terms of pitch angle evolution with radius (Rafikov 2002; Juhász & Rosotti 2018):

$$\psi(r) = \pi/2 - \tan^{-1}\left\{ \text{sign}(r_p - r)\frac{1}{h_p}\left(\frac{r}{r_p}\right)^{\beta+1}\left[\left(\frac{r_p}{r}\right)^{\alpha} - 1\right]\right\} \tag{6.3}$$

Fitting of the measured pitch angle evolution of an observed spiral to Eq. 6.3 has not yet been reported in the literature, but would likely suffer less degeneracy on the planet position and yield a better estimate of the companion location (provided a sufficiently long

spiral trace). This is because the pitch angle of the spirals tend to decrease away from the planet (either inward or outward), thus tracing the evolution of the pitch angle along the spiral trace should enable to infer the location of the companion launching it more reliably (e.g. Bae & Zhu 2017b; Juhász & Rosotti 2018).

Equations 6.2 and 6.3 describe the evolution of waves in the linear regime, i.e. without/before the formation of a shock and its corresponding nonlinear dissipation of angular momentum. Goodman & Rafikov (2001) and Rafikov (2002) argue that the evolution of spiral density waves might always lead to shock formation and hence nonlinear dissipation of angular momentum between the planet-induced wave to the disk. Rafikov (2002) estimated that the shock forms at a radial separation $r_{\rm sh} - r_p \approx 0.93(\frac{m_p}{M_{\rm th}})^{-2/5}$, where the thermal mass $M_{\rm th} \equiv \frac{2}{3}h_p^3 M_*$ is roughly of the order of $\sim 0.1 M_{\rm Jup}$ (resp. $1 M_{\rm Jup}$) for a disk aspect ratio of 0.05 (resp. 0.1) at the location of the planet. For relatively massive planets with $M_p \gtrsim M_{\rm th}$, the shock thus forms in the direct vicinity of the planet, and the observed spiral wake beyond the shock does not follow the linear predictions, as it propagates faster than the local sound speed and is hence expected to lead to a more open pitch angle. This is a first hint towards explaining the large observed pitch angles, which in the linear regime would correspond to unrealistic disk scale height / temperatures compared to predictions based on SED fitting (e.g. 250K at 70 au for MWC 758; Benisty et al. 2015).

Hydrodynamical simulations have enabled to better investigate the non-linear regime by analyzing the effect of the injection of massive planets in realistic protoplanetary disks, first through 2D simulations (e.g. Dong et al. 2011; Juhász et al. 2015), and more recently with 3D disk simulations as well (e.g. Zhu et al. 2015; Dong et al. 2015b; Dong & Fung 2017a, Fig. 6.6). These simulations showed that the pitch angle of spirals launched in the nonlinear regime was indeed larger than predicted by Eq. 6.3. They also showed that a single planet with $M_p \gtrsim M_{\rm th}$ could launch multiple inner spirals, each with a significantly larger pitch angle than predicted in the linear regime (e.g. 12-20° instead of ∼7° for a $6 M_{\rm Jup}$ planet Zhu et al. 2015; Dong et al. 2015b). However, only a single conspicuous outer spiral is expected even in the nonlinear regime, and its pitch angle is moderately larger than the linear regime prediction (e.g. 7° instead of ∼4°for a $6 M_{\rm Jup}$ planet Zhu et al. 2015). More recent hydrodynamical simulations also suggest that the thermal heating due to shocks might be observable (e.g. Richert et al. 2015; Lyra et al. 2016). Radiative transfer of those simulations suggest nonetheless that considering the enhanced scale height due to the temperature increase, the contribution from scattering is expected to dominate over the contribution from thermal emission itself, even at thermal-IR wavelengths (Hord et al. 2017).

An observational diagnostic that can possibly be used to estimate the mass of a spiral-launching companion is the observed contrast of the arm. As expected, more massive companions induce brighter arms. Dong & Fung (2017a) inferred the following empirical relationship based on their hydrodynamical + radiative transfer simulations:

$$\delta_{\rm max} = \left(\frac{M_p}{h_p^{1.38}} \right)^{0.22} \tag{6.4}$$

where $\delta_{\rm max}$ is the face-on arm maximum contrast with respect to the average disk emission at that radius, and M_p is the mass of the planet expressed in $M_{\rm Jup}$.

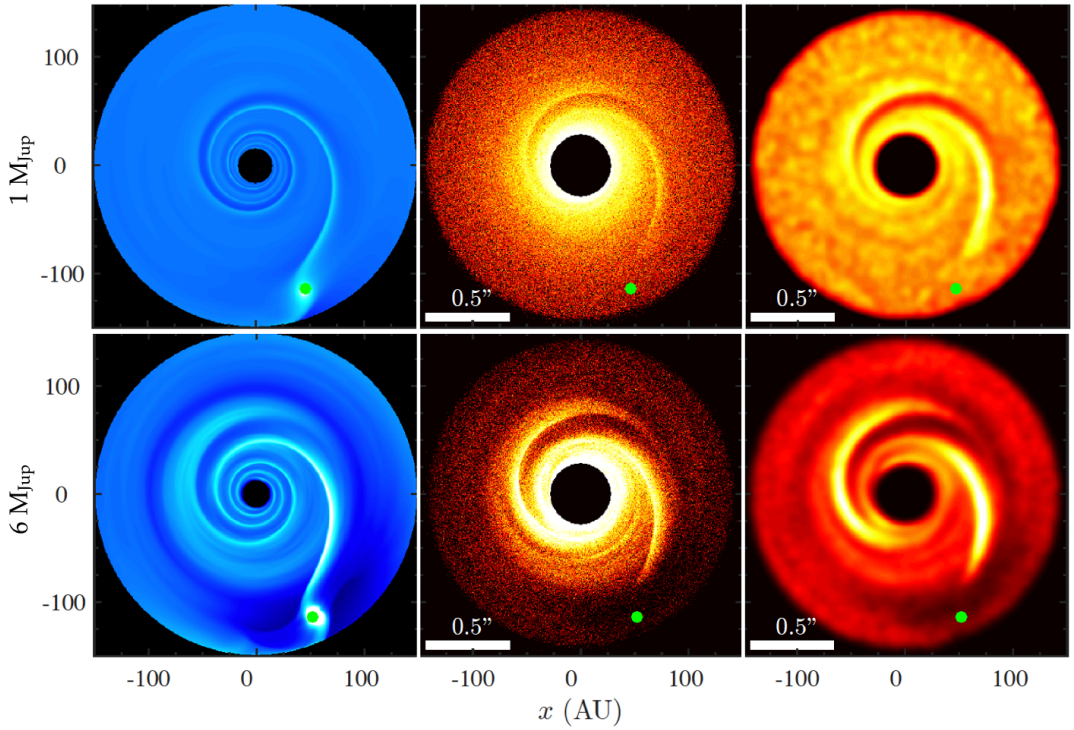

Figure 6.6: Spiral arms induced by planets of 1 $M_{\rm Jup}$ (top row) and 6 $M_{\rm Jup}$ (bottom row), whose locations are indicated by the green dot. The different columns (from left to right) show the surface density, the radiative transfer at H band at native resolution and the radiative transfer convolved with a gaussian PSF with FWHM $=$ 0.″06 and r^2-scaled. A faint third spiral can be discerned in the $1M_{\rm Jup}$ case, while the $6M_{\rm Jup}$ planet is expected to produce a two-arm spiral pattern. Simulations from Dong et al. (2015b).

As argued in Bae & Zhu (2017a), the exact number of observed spiral arms can also be used to estimate the mass of the perturber. For planets with $M_p > 3M_{\rm th}$ a grand-design 2-spiral-arm pattern is expected to dominate, while a tertiary arm can be observed for $M_p \lesssim 3M_{\rm th}$ (Fig. 6.6). Moreover, the separation between primary and secondary spiral arms has also been shown to depend on the mass of the companion. Fung & Dong (2015) inferred the following empirical relationship:

$$\phi_{\rm sep} = 102^\circ (\frac{q}{0.001})^{0.2} \tag{6.5}$$

where $\phi_{\rm sep}$ is the separation angle between the primary and secondary spiral, and q is the mass ratio between the companion and the primary star. The separation angle converges towards 180° for increasing companion mass, and plateaus at that value for $q \geqslant 0.016$ (i.e. $16M_{\rm Jup}$ for a $1M_\odot$ primary star). Measuring the separation angle between multiple spiral arms can thus provide a constraint on the mass of the putative perturber launching them.

Finally, the spiral arm(s) launched by a planet are expected to be co-rotating with it since they are density waves (and not material arms). Given a sufficiently long baseline, measuring the proper motion of observed spiral arms should thus enable to constrain the radial location of the companion that is producing them.

Dust traps

Dust traps (Sec. 6.2.2) correspond to local maxima in the dust surface density distribution and, as such, might launch spiral density waves in the same way as embedded planets. The estimated mass of trapped cm-size dust can reach several Earth masses – which is thus a lower limit of the total dust mass in the trap (e.g. Casassus et al. 2015b, for HD 142527). Dedicated simulations are nonetheless required to better investigate the possibility of spirals launched by a dust trap.

Interestingly, several transition disks show spiral arms passing through the location of the observed dust trap. The possibility of a causal relationship was first raised in van der Marel et al. (2016a) to account for the spiral arm of HD 135344 B that is passing through the location of the dust trap seen in ALMA data. The near-IR spiral arm of V1642 Ori also appears to point towards the lopsided mm-continuum in the outer ring of the disk (Ohta et al. 2016; Kraus et al. 2017). In the case of MWC 758, spiral arm S3 in Reggiani et al. (2018, Sec. 12.1.1) is passing roughly through the inner dust trap, and spiral arm S1 passes at the edge of the outer dust trap. Similarly, the spiral arms identified in LkHα 330 (Akiyama et al. 2016; Uyama et al. 2018) appear to be located at the inner edge of the tentative dust traps seen with SMA in LkHα 330 (Isella et al. 2013).

There appears to be a tentative correlation between the occurrence of dust traps and spiral arms in transition disks, however this does not necessarily involve a relation of causality. They could indeed both be induced by the presence of a giant planet carving a gap, which would trigger the RWI at the origin of the dust trap. The planet could launch a spiral and, as mentioned in Sec. 6.2.2, a mm-continuum enhancement might be expected to be roughly colocated with the spiral due to shock heating (Lyra et al. 2016; Rafikov 2016). The question is thus: what came first? The dust trap (e.g. originating at the edge of the dead-zone) or the giant planet(s) which can induce both spirals and large dust traps?

Gravitational instability

If the disk is massive, its own gravity might lead to the formation of spirals (e.g. Durisen et al. 2007). The condition for gravitational instability (GI) is set by the Toomre parameter, defined in Eq. 3.1. As seen in Sec. 3.1, the fulfillment of Eq. 3.1 is the only requirement for the formation of spiral arms, while the condition for the formation of low-mass companions by gravitational fragmentation of the disk also requires a fast cooling timescale. The morphology of the GI-induced spirals depends on the mass ratio between the disk and the primary. More massive disks tend to enhance low-m modes such as the grand-design (m=2) pattern, while disks with a more modest mass ratio with respect to the central star will tend to produce a flocculent spiral structure (e.g. Forgan & Rice 2013; Dong et al. 2015a). Recent 3D hydrodynamical simulations showed that the condition to form two-armed spirals was a disk-to-star mass ratio of $q \gtrsim 0.25$ (Dong et al. 2015a). These spirals show a relatively wide pitch angles ($\sim$ 10–15°). The efficient angular momentum transport in the grand-design case is also expected to lead to high mass accretion rate onto the star, of the order of $10^{-6} M_\odot$ yr^{-1}. Nonetheless, Dipierro et al. (2014) showed that even

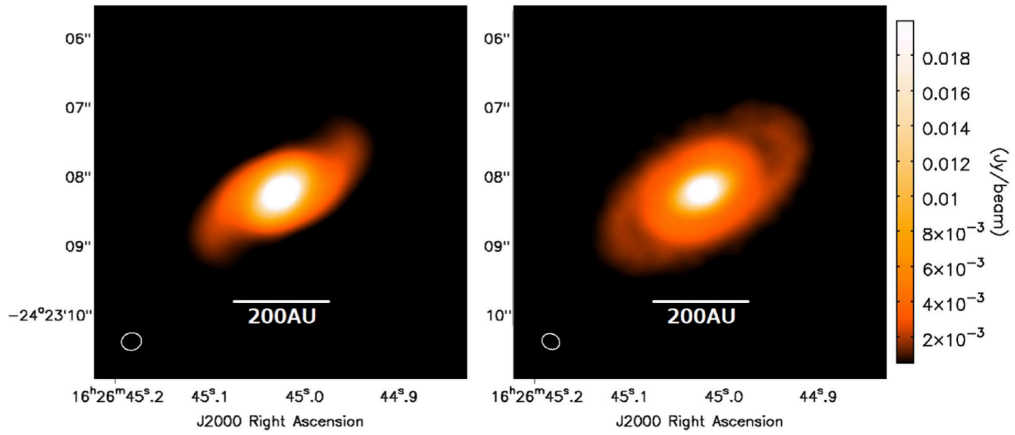

Figure 6.7: Radiative transfer prediction in sub-mm continuum based on the output of an MHD simulation of a gravitationally unstable disk (*left*) compared to the ALMA image of Elias 2-27 (*right*; Pérez et al. 2016). These simulations suggest that the arms are material rather than density waves. Figure from Tomida et al. (2017).

flocculent spiral patterns could appear like a two-arm grand-design morphology due to beam convolution. This effect might be particularly significant for inclined disks observed at poor angular resolution.

These morphological characteristics are inferred assuming that GI-induced spirals correspond to density waves such as those induced by embedded companions (e.g. Dong et al. 2015a). Nonetheless, based on new MHD simulations, Tomida et al. (2017) have challenged this assumption, proposing that GI-induced spirals rather corresponded to material arms (Fig. 6.7). These authors argue that although material arms would tightly wind up and disappear after a few rotations, they are expected to recurrently re-appear in Class 0/I disks due to frequent fulfillment of the GI condition with the continuous addition of infalling material. Whether spirals produced by GI are density waves or material arms is thus an open debate. In either case, the evolution of primordial disks might be dominated by angular momentum transport from the spirals (e.g. Rafikov 2016; Tomida et al. 2017).

What about more evolved disks such as transition disks? For class II disks, the requirement for GI might be more difficult to meet, apart possibly in their outer parts. It is nonetheless interesting to note that transition disks have mass estimates corresponding to the high-mass end of the protoplanetary disk distribution (Chap. 8). However, both the mass estimates of grand-design spiral-bearing disks HD 135344 B or MWC 758 obtained from their sub-mm flux ($q \sim 0.01$ for both; Andrews et al. 2011; Lyo et al. 2011; Garufi et al. 2013) and their mass accretion rates ($\sim 10^{-8} M_\odot$ yr^{-1}; Eisner et al. 2009; Grady et al. 2009) appear to be incompatible with the requirements of $q \gtrsim 0.25$ and $\dot{M} \gtrsim 10^{-6} M_\odot$ yr^{-1} derived in Dong et al. (2015a). The disk mass would have to be underestimated by at least a factor of 25 to lead to sufficient disk gravity to form two-arm spirals, and about 99% of the material losing angular momentum would have to be captured by other bodies (e.g. forming planets) to account for the measured accretion rates. Furthermore, GI-driven spiral arms are expected to show relatively small and constant pitch angle ($\sim 7^\circ$ in the simulations of Bae et al. 2014) throughout their length, which is not the case of the main spirals of MWC 758 or HD 135344 B, displaying an increasing pitch angle with radial separation (e.g. Benisty et al. 2015; Stolker et al. 2016). Spirals in these disks are thus most likely not

due to GI alone. Can they be due to the combined effect of embedded companions and GI? Pohl et al. (2015) showed that low-mass companions in marginally stable disks could drive the outer part of the disk gravitationally unstable and excite open spiral arms with a significantly larger contrast than those due to companions in gravitationally stable disks. Nonetheless, in gravitationally unstable disks, they showed that the inclusion of embedded companions led to more tightly wound arms, suggesting that self-gravity dominates (with a similar morphology to the spirals seen in Bae et al. 2014).

Stellar flybys

Stellar encounters are extremely unlikely in the field given the ratio between typical stellar radii and the distances between stars (e.g. Binney & Tremaine 1987). The probability is significantly larger in star-forming clusters, considering both the higher stellar density and the $\sim 10^4$ times larger cross-section of protoplanetary disks. The effect on the disk of a stellar flyby has been studied both analytically and numerically. The analytic approach is typically only possible for closest approach distances that are sufficiently large (at least 2 disk radii; Ostriker 1994) since the violent interaction at closer separations involves highly non-linear processes. Flybys have thus been much more studied with numerical tools (e.g. Clarke & Pringle 1993; Hall et al. 1996; Hall 1997; Boffin et al. 1998). A variety of test cases have been considered: penetrating (in the disk) vs non-penetrating, co-planar vs non-coplanar, prograde vs retrograde. First simulations rather aimed to answer the question of binary capture, however the first detections of spiral arms and warps in circumstellar disks with HST (e.g. Grady et al. 2001; Clampin et al. 2003) motivated the study of the morphological implications for the disk of a stellar flyby. In general, only roughly co-planar and prograde flybys lead to a conspicuous two-armed spiral pattern (e.g. Boffin et al. 1998; Pfalzner 2003). This particular case has thus been investigated in greater details in the studies of Pfalzner (2003), Pfalzner et al. (2005) and Quillen et al. (2005).

Figure 6.8 shows the expected morphology of spiral arms due to a stellar co-planar and prograde flyby, as presented in Quillen et al. (2005). These spirals are similar in morphology (contrast and pitch angle) to those due to bound substellar companions external to the disk. Since the dynamical interaction happens only once, the mass of the perturber typically requires to be larger to produce the same effect as a bound giant planet. A flared disk leads to a less pronounced spiral pattern, as can be seen in the bottom row of Fig. 6.8. The typical lifetime of the spirals induced by the flyby is of the order of an orbital period, with a better and slightly longer visibility for more massive perturbers. This implies that testing the flyby origin for specific spirals only requires the measurement of the proper motion of stars lying within a few arcmin separation of the disk (considering typical stellar proper motion rates of $\lesssim 50mas$ yr^{-1} for stars at $\gtrsim 100$ pc). The results of Quillen et al. (2005) were obtained based on a 2D hydrodynamical code similar to FARGO (Masset 2000). Pfalzner (2003) obtained spirals with qualitatively similar morphology in SPH simulations. In comparison, Pfalzner et al. (2005) considered the disk-disk flyby scenario and showed that transfer of material between the disks through their tidal tails could occur for massive disks and/or relatively close encounters, but would otherwise lead to similar results as the star-disk case. During the flyby, the angular momentum exchange typically

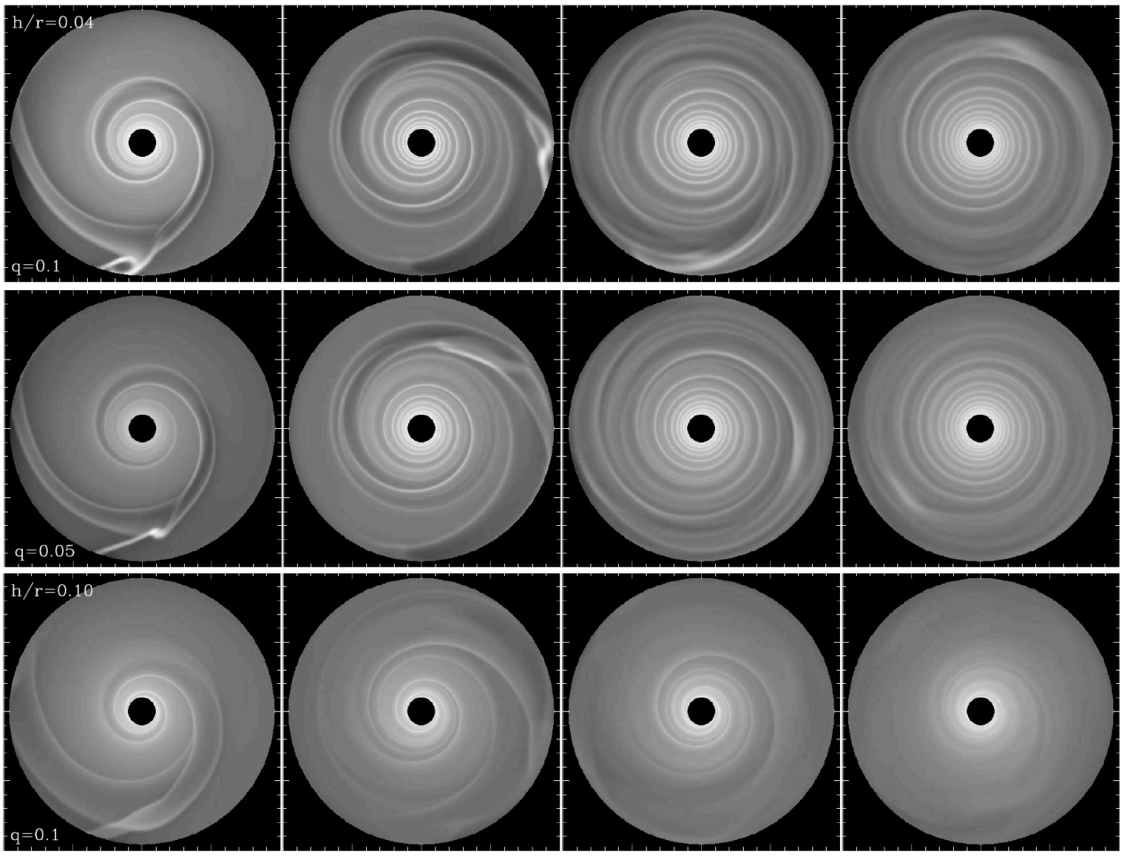

Figure 6.8: Expected imprint of a stellar flyby on the disk surface density as a function of time (left to right: 1/4, 1/2, 1 and 2 orbital periods at 300 au after the flyby). The first two rows show the effect of decreasing the external star mass ratio with respect to the primary star (q), and the bottom row considers the effect of a more flared disk ($h = 0.1$ instead of $h = 0.04$). Simulations from Quillen et al. (2005).

removes angular momentum from material in the disk, which enhances mass transport and boosts stellar accretion (Pfalzner 2003; Pfalzner et al. 2005). Flybys are thus expected to accelerate the evolution of the disk.

Hydro-dynamical simulations enable to probe the predicted effect of a flyby on the disk, but what is the probability of observing flyby-induced spiral arms in young disks? Here, I consider a back-of-the-envelope estimate based on the encounter rates calculated in Clarke & Pringle (1991) and the typical survival time of the spiral structure inferred from the simulations in Pfalzner (2003) and Quillen et al. (2005). In their Table 1, Clarke & Pringle (1991) computed star-disk encounter rates considering environments of different stellar densities and a range of disk models with different masses and radii. I only kept in my Table 6.1 their two models whose properties are most similar to typical class I and II disks, resp., based on current constraints on those disks, and only considered the typical density and stellar velocity dispersion (V_*) of open cluster cores (first column; based on Binney & Tremaine 1987) and their mean values throughout a giant molecular cloud (right column; based on Solomon et al. 1987). The different rates they calculated are (i) the rate at which passing stars strike the disk ($\Gamma_{\rm hit}$), (ii) the rate of stellar capture into the system ($\Gamma_{\rm cap}$) which also requires that the velocity difference is lower than the escape velocity, and (iii) the probability of capture at a certain time given that the disk has not been hit by a pre-

Table 6.1: Flyby occurrence rate.

			$n_o = 10^2 pc^{-3}$, $V_* = 1$km s^{-1}			$n_o = 12 pc^{-3}$, $V_* = 2$km s^{-1}		
Model	M_d/M	R_d(a.u.)	Γ_{hit}	Γ_{cap}	Γ_{bin}	Γ_{hit}	Γ_{cap}	Γ_{bin}
II	0.3	1000	3.2×10^{-2}	7.7×10^{-3}	1.8×10^{-3}	5.0×10^{-3}	2.0×10^{-4}	7.9×10^{-6}
VI	0.07	500	1.2×10^{-2}	2.4×10^{-3}	5.0×10^{-4}	1.5×10^{-3}	5.4×10^{-5}	2.0×10^{-6}

Notes: Star-disk encounter rates are expressed in Myr $^{-1}$. Two disk models are considered, corresponding roughly to protostellar and protoplanetary disk parameters (models II and VI resp.). The encounter ($\Gamma_{\rm hit}$) and capture rates ($\Gamma_{\rm cap}$ and $\Gamma_{\rm bin}$) are computed for two star-forming environments of different stellar density and stellar velocity dispersion. See text for details. Extracted from Table 1 in Clarke & Pringle (1991).

vious encounter before ($\Gamma_{\rm bin}$). This is because the encounter is likely to remove or truncate significantly the disk. All values are expressed in Myr^{-1}.

Class I disks are expected to last up to 0.1 Myr and class II disks have median lifetimes of ∼3 Myr (Sec. 2.1). We immediately note from Table 6.1 that even in the denser case of open cluster cores, hitting rates are low and the occurrence rate of a direct encounter over the whole lifetime of the disk (integrating over both class I and II phases) is $\lesssim 0.07$ and $\lesssim 0.01$ in dense open cluster cores and throughout giant molecular clouds, respectively. Nonetheless, the formation of spirals does not require a penetrating encounter (i.e., the external star striking the disk). In fact, flybys can typically induce spirals if the closest approach is separated by up to ∼3 disk radii (e.g. Pfalzner 2003). Therefore, considering a ∼10 times larger cross-section, the possibility that such flyby occurs over the whole lifetime of the disk becomes more significant.

However, assessing the observability of such event requires considering the expected survival time of the spirals after the dynamical interaction. I consider the optimistic case of a large disk and a relatively massive stellar perturber, for which the spirals can survive up to $\sim 10^4$ yrs (Fig. 6.8; Quillen et al. 2005), hence ∼100 times shorter than the typical lifetime of class II disks. Finally, I estimate the probability of observing spiral arms due to a flyby in a given transition disk at a given time considering the overall occurrence rate of an encounter over the whole lifetime of the disk (provided in the previous paragraph), multiply it by 10 for the enhanced cross-section, and by the ratio of spiral survival timescale over disk lifetime (∼1/100). This yields probabilities $\lesssim 0.7$% and $\lesssim 0.1$% for disks in open cluster cores and giant molecular clouds resp., and severely lower values for isolated disks. Prograde co-planar encounters are the type of flybys leading to the most conspicuous spiral arms, with a pattern similar to those produced by bound companions (e.g. Boffin et al. 1998). Considering the additional constraints of being prograde and co-planar would make the flyby scenario extremely unlikely to account for even a fraction of all observed spirals.

Warps

Quillen (2006) showed that the large-scale spiral arms seen in the disk of HD 100456 could be due to a warp (Fig. 6.9). Based on her study, a slight differential tilt of the outer parts

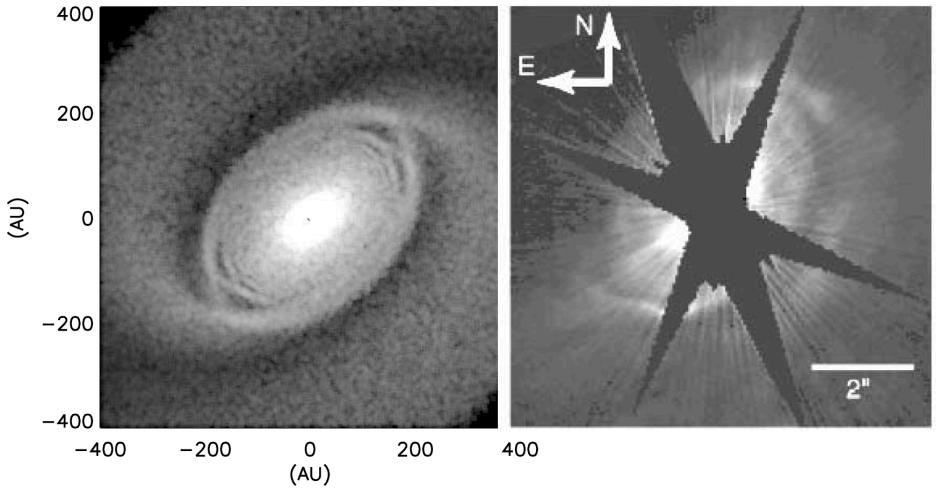

Figure 6.9: (Left) Simulation of a warp in the outer disk of HD 100456, observed as two large-scale spiral arms. (Right) HST image of HD 100546 (Grady et al. 2001) showing a remarkable similarity with the simulated warp. Figure from Quillen (2006).

of the disk by $\sim 10^{\circ}$ is sufficient to create illumination/shadowing effects such that the disk would appear to display two large-scale spiral arms in scattered light images. She also argues that this minor warp can occur if the outer disk is initially slightly misaligned with respect to the orbital plane of embedded planets or planetesimals. Alternatively, Larwood & Kalas (2001) showed that a flyby could also lead to a warping of the outer disk. However, the simulations in Nixon & Pringle (2010) suggest it would survive less than $\sim$1 Myr, which makes this possibility unlikely (in particular given the discussion in the previous subsection). Morphologically, the brightest parts of the two spirals do not appear symmetric with respect to the central star, but rather appear along the same PA range, separated radially by a dark lane. This is somewhat different to the double spirals observed in most disks (*white labels* in Fig. 6.5).

Another situation where warps and shadows can lead to the formation of spiral arms is for a significantly tilted optically thick inner disk casting shadows on the outer disk (Montesinos et al. 2016). Since I contributed to that study, I will detail it separately in Sec. 7.1.

6.4.3 Summary

As seen in the previous section, a variety of different mechanisms are theoretically able to produce spiral arms in disks. These mechanisms can lead to different predictions in terms of morphology, kinematics, proper motion, presence of associated disk features (e.g. shadows) or even regarding their intrinsic nature (e.g. GI-induced spiral arms might be material instead of density waves; Tomida et al. 2017), which can be used to constrain the origin of observed spirals. Based on these considerations, I reviewed literature and compiled in Table 6.2 the most likely processes accounting for all conspicuous spirals observed so far in transition disks. A detailed discussion of each particular source is beyond the scope of this thesis. Instead, I will focus on the sample of transition disks for which I performed the

Table 6.2: Favored origin for the spiral arms found in different transition disks

	Compa-nion(s)	Disk self-gravity	Warp or shadows	Stellar flyby	Late infall	Refs.
AB Aur						
Flocculent	**?**				✓	a
Grand-design	✓	✗			✗	b
Elias 2-27	✗	✓			✗	c,d
HD 100453	✓		**?**			e,f,g
HD 100546						
Flocculent	**?**			✗		h,i,j
Large-scale	✗		✓	✗		j,k
HD 135344 B	✓	✗	**?**			l,m,n,o
HD 141569	**?**			**?**		k,p
HD 142527						
Flocculent	✓		**?**	✗		q,r,s
Single	✓		**?**	✗	✗	s,t,u
Grand-design		**?**	**?**	✗	✗	u,v
LkHα 330	**?**					w,x
MWC 758	✓	✗				n,y,z,aa
PDS 70	✓	✗				ab
V1247 Ori	✓					ac,ad

✓: favored dominant mechanism. ✗: ruled out or very unlikely.

?: (other) possible mechanism at work. *blank*: unconstrained or not investigated.

References: (a) Tang et al. (2012); (b) Tang et al. (2017); (c) Pérez et al. (2016); (d) Tomida et al. (2017); (e) Dong et al. (2016); (f) Benisty et al. (2017); (g) Wagner et al. (2018); (h) Boccaletti et al. (2013); (i) Follette et al. (2017); (j) Quillen (2006); (k) Quillen et al. (2005); (l) Muto et al. (2012); (m) Garufi et al. (2013); (n) Dong et al. (2015b); (o) Stolker et al. (2016); (p) Reche et al. (2009); (q) Casassus et al. (2012); (r) Casassus et al. (2012); (s) **Price et al. (2018)**; (t) Fukagawa et al. (2006); (u) **Christiaens et al. (2014)**; (v) **Montesinos et al. (2016)**; (w) Akiyama et al. (2016); (x) Uyama et al. (2018); (y) Benisty et al. (2015); (z) **Reggiani et al. (2018)**; (aa) Bae & Zhu (2017b); (ab) **Christiaens et al. (2018b, Sec. 15.5)**; (ac) Ohta et al. (2016); (ad) Kraus et al. (2017).

spiral arm analysis (bold references in Table 6.2). In the specific cases of the spirals of MWC 758 and HD 142527, the detailed analyses of the spirals that I carried out are presented in Secs. 7.2 and 7.3.2, respectively. I also found a tentative spiral-like feature in the disk of PDS 70, possibly connected to a protoplanet candidate (see Sec. 15.5).

Based on Table 6.2, it appears that the properties of most observed spirals are compatible with the arms being dynamically induced by companions. Some disks harbor several types of spirals, with different morphologies and at different scales, which could suggest that several simultaneous spiral-inducing processes are at work. For example, in the case of AB Aur, the large-scale flocculent spirals in the outer disk and the grand-design arms in the cavity appear most compatible with a late-envelope infall and companion(s) in the cavity (Tang et al. 2012, 2017). Pohl et al. (2015) also showed that marginally gravitationally unstable disks excited by low-mass companions could lead to spiral arms with a larger contrast with respect to the disk than gravitationally stable disks. As discussed previously, the

mass of disks is typically underestimated, and transition disks do correspond to massive protoplanetary disks, so that this possibility cannot be totally excluded.

In the previous subsection, I showed that flybys were a very unlikely cause for the observed spiral arms. In comparison, we know that giant planets are relatively common in mature systems ($\gtrsim$ 10% of main-sequence stars harbor giant planets Winn & Fabrycky 2015). Therefore, it appears globally as a more likely origin for most observed spirals. The higher occurrence of spirals in systems showing other signposts of companion presence such as dust traps or warps might be another hint in that direction.

7 Spiral arm characterization

7.1 Morphology of shadow-induced spirals

As mentioned in Sec. 6.4, one of the different mechanisms proposed to explain the observation of spiral arms in transition disks is shadowing from the inner disk on the other disk. This was investigated in Montesinos et al. (2016), where I contributed with the geometric characterization of the shadow-induced spirals. The exact disk morphology considered in this study consists of an optically thick inner disk with a polar orientation with respect to the outer disk, so that the shadows cast by the inner disk can be considered roughly symmetric on the outer disk. Material from the outer disk crossing periodically those shadows suffer a corresponding perturbation in temperature. The corresponding lower pressure accelerates the material crossing the shadows. Hydro-dynamical simulations in Montesinos et al. (2016) show that this effect leads to the formation of noticeable spiral density waves after a few hundred orbits. Fig. 7.1 shows the resulting spirals obtained for a 0.25 $M_\odot$ disk illuminated by a 100 $L_\odot$ (*top row*) and 1 $L_\odot$ (*bottom row*) star, for increasing number of orbits, where a pair of symmetric shadows is cast on both sides of the disk. The resulting spirals are more pronounced in terms of density contrast for more massive, marginally unstable, disks. This suggests that some contribution can be attributed to self-gravity. In such case, the spirals are predicted to be conspicuously observable in scattered light. In the case of less massive disks, spiral arms are also created, but their observability might be compromised due to the low density contrast expected.

In order to characterize geometrically the spirals, I first identified their trace as local radial maxima in azimuthal steps of 1°, and then performed a least-square fit of the spiral trace to the general Archimedean spiral equation: $r = A_0 + A_1\theta^n$. The best-fit Archimedean spiral to the SW arms are provided with *red solid lines* in Fig. 7.1. The *red dashed lines* correspond to the point-symmetric locus of the best-fit spirals with respect to the central star; they show that the spirals produced in the simulations are rigorously symmetric, as expected from the symmetry of the shadows. I also fitted the spiral traces to the logarithmic spiral equation ($r = a + \mathrm{e}^{b\theta}$) and to the equation inferred from spiral density wave theory (Eq. 6.2), but noticed that the fits were of lower quality than obtained with the general Archimedean spiral equation. Nonetheless, the logarithmic spiral fit to short portions of the spiral traces allowed me to estimate the pitch angle (Π)) and its variation across the length of the spirals. Both the best-fit general Archimedean spirals parameters and the measured pitch angles are compiled in Table 7.1. The pitch angle values range from $\sim$11° to

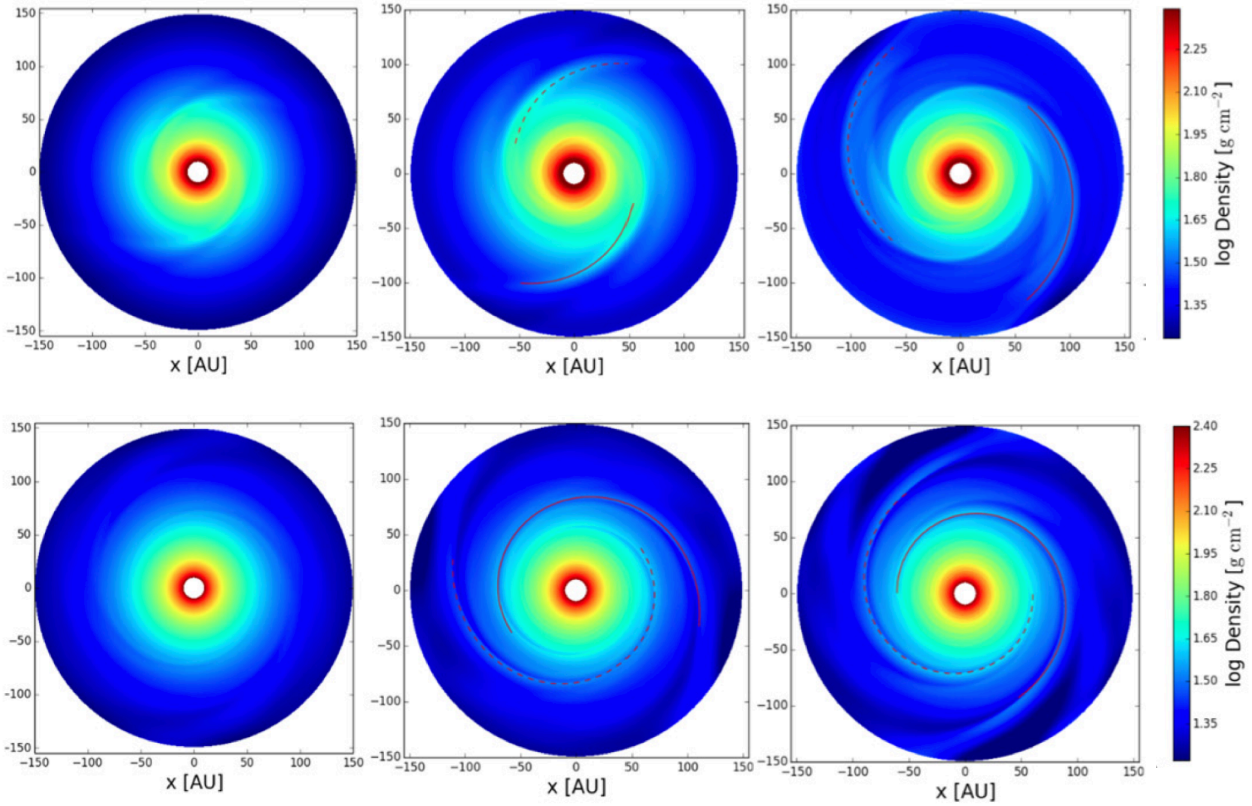

Figure 7.1: Simulations of shadow-induced spirals in a 0.25 $M_\odot$ disk, provided in logarithmic surface density scale. Top row corresponds to a central star of 100 $L_\odot$ after 150, 250 and 500 orbits respectively. Bottom row corresponds to a central star of 1 $L_\odot$ after 2500, 3500 and 4000 orbits respectively. Figure adapted from Montesinos et al. (2016).

23°, with increasing values for increasing radius (i.e. opening spirals). There is also a slight increasing trend for the pitch angle of spirals produced around more luminous central stars, which can be interpreted as due to a larger pressure difference in the shadow, leading to an enhanced acceleration on the material crossing the shadow.

Similarly to dust traps, there is also a tentative correlation between the occurrence of shadows and that of spirals in transition disks (as can be readily seen from comparing Figs. 6.4 and 6.5). For example, HD 142527 and HD 100453 both have an inner disk warp and show spiral arms. Could one trigger the other, or could they have similar origins? As discussed in Sec. 6.3.2, the presence of an inner warp is a strong indication for the presence of a massive companion. Morphologically, the pitch angles of simulated spirals appear similar to the measured pitch angle in the aforementioned disks. Furthermore, shadow-induced spirals are launched from the PA where the shadow is cast, which is the case of the spirals of HD 100453 (Fig. 6.4b) and the main spirals originating from the edge of the cavity of HD 142527 (S1 and S5 in Fig. 6.4a). However, for both HD 100453 and HD 142527 a known low-mass M-dwarf companion has been detected, and its gravitational effect alone appears able to produce spirals with the observed morphology (e.g. Dong et al. 2016; Price et al. 2018, see also Sec. 7.3.3). Assessing which effect dominates – shadows or dynamical excitation by the companion – requires new dedicated simulations considering both mechanisms together.

Table 7.1: Parameters of shadow-induced spirals: best-fit parameters of the fit to the general Archimedean and pitch angle values, for different models and after a different number of orbits.

Model Parameters	Orbit Number	Spiral Parameters A_0, A_1, n, Π°
$M_d = 0.05\ M_\star$; $L_\star = 1\ L_\odot$	3500	n/a
	4000	n/a
$M_d = 0.05\ M_\star$; $L_\star = 100\ L_\odot$	250	68.7; 14.6; 2.1; $22.^\circ59 \pm 3.5$
	500	56.9; 4.2; 1.64; $13.^\circ82 \pm 3.5$
$M_d = 0.25\ M_\star$; $L_\star = 1\ L_\odot$	3500	70.3; 4.6; 1.68; $13.^\circ82 \pm 3.5$
	4000	60.3; 5.4; 1.45; $11.^\circ35 \pm 3.5$
$M_d = 0.25\ M_\star$; $L_\star = 100\ L_\odot$	250	60.3; 28.2; 1.35; $15.^\circ04 \pm 2.5$
	500	87.2; 17.8; 1.43; $13.^\circ09 \pm 2.0$

Finally, I note that a more recent study considered the effect of moving shadows, in particular due to the precession of an inclined inner disk (Montesinos & Cuello 2018). They found that the spiral is launched at the co-rotating radius, where precessing shadow and Keplerian gas rotate at the same azimuthal velocity. Nonetheless, in both Montesinos et al. (2016) and Montesinos & Cuello (2018) the results are inferred based on 2D hydrodynamical simulations. A more accurate treatment might require 3D simulations, given the 3D geometry of shadows cast by the inclined inner disk.

7.2 Analysis of the spirals of MWC 758

In this section, I provide a detailed analysis of the spirals of MWC 758 observed in L'-band with NIRC2+AGPM data. Part of these results are published in Reggiani et al. (2018, provided in Sec. 12.1.1), along with the protoplanet candidate detection found in the same data. However, only the most relevant parts of the spiral analysis were summarized and included into the paper for the sake of clarity and conciseness. Therefore, I provide the full details of the spiral arm analysis in this section. I defer the reader to Sec. 12.1.1 for details on the observations, data processing and analysis of the protoplanet candidate.

7.2.1 Identification of disk features in the IR images

In our final images of MWC 758 obtained with NIRC2 at two different epochs, we detect a third spiral arm (S3), in addition to the two previously known spirals seen in H- and Y-band polarized light images (Grady et al. 2013; Benisty et al. 2015). This is shown in Fig. 7.2, where the left panel corresponds to the SPHERE polarized light observations in

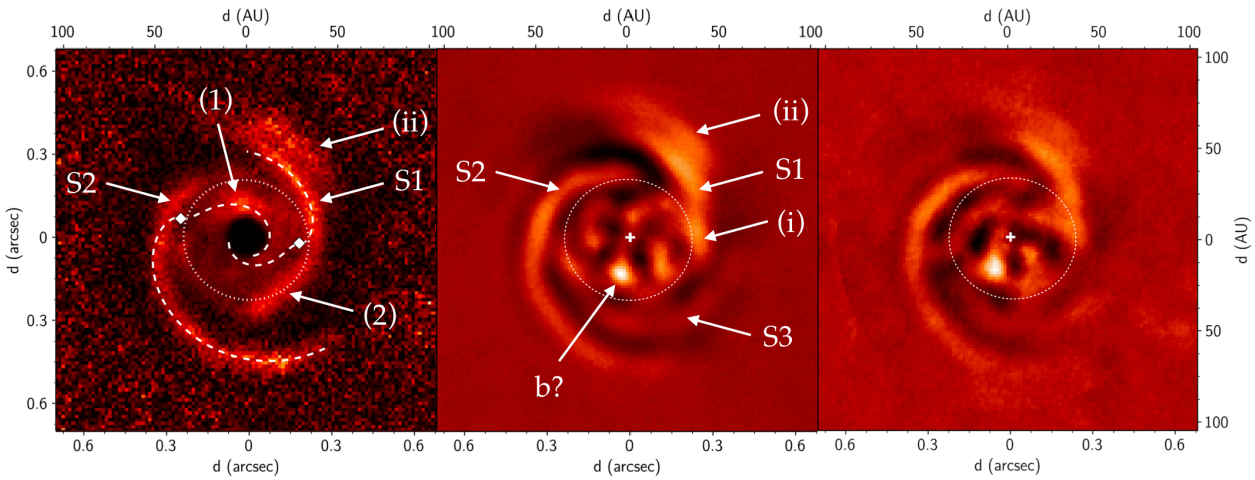

Figure 7.2: (Left panel): SPHERE polarized light observations of MWC 758 obtained in Y band (1.04μm) in Mar. 2015, as reported in Benisty et al. (2015). (Middle and right panels) NIRC2 L'-band observations (3.8μm) at two different epochs: Oct. 2015 and Oct. 2016, respectively. The dotted ellipse corresponds to a deprojected circle of 0.″25 radius. The dashed lines in the left panel correspond to the best-fit spiral models forcing companions to be located inside the sub-mm cavity (which can be visualized in Fig. 6.3).

Y band (1.04μm) reported in Benisty et al. (2015), and the middle and right panels correspond to the L'-band (3.8 μm) NIRC2 final PCA-ADI images obtained at in October 2015 and October 2016, respectively. The spiral arms detected at L'-band most likely trace scattered stellar light by sub-micrometer size dust. The detection of S3 in L'-band and its non-detection with polarized light at shorter wavelength could be explained by the different dust scattering properties at different wavelengths. If the emission traces Rayleigh scattering of sub-micrometer size grains, the scattering cross-section is $\propto \lambda^{-4}$ (hence the mean free path of photons is $\propto \lambda^{4}$). Then Y-band would trace mostly the disk surface, while L'-band could probe deeper layers of the disk. Therefore, the non-detection of S3 at Y-band could mean that it has a smaller scale height than S1 and S2.

The different effects of Rayleigh scattering at Y and L' bands can be seen comparing of left and middle panels of Fig. 7.2. At a PA$\sim$45°, it is possible to see by eye that the crest of S2 is closer to the dotted ellipse in the Y-band image than in the L'-band image. At a similar location, one can also notice that the root of S2 appears to extend further in (towards the West) in the L' image compared to the polarized light image. A bright feature, labelled (1) in the polarized light image, appears to subtend the same PA range as the root of S2, but at shorter separation, and could hence be shadowing the root of S2 for the same reason that S3 is not seen at shorter wavelength: significantly larger scattering cross-section at shorter wavelength, hence correspondingly shorter mean free path. A minor warp has been inferred for the inner disk of MWC 758 based on near-IR interferometric data (e.g. Isella et al. 2006, 2008; Lazareff et al. 2017), which could also account for an extended diffuse shadow cast on one side of the outer disk (contrary to the shadows cast by an almost polar misalignment of the inner disk). This would likely have a stronger shadowing effect at shorter wavelengths. The possibility of a mild inner warp is further supported by the kinematics measured in recent sub-mm gas lines (Boehler et al. 2017).

Comparison of our image with the polarized light images of Benisty et al. (2015) re-

veals several other differences. First, the bright Y-band arc located at $\sim$0$''$.2 separation and covering a PA range of 180°–270° (labelled feature (2)) appears much less prominent in L'-band, but is still recovered at the same location as in the polarized light image. A possible reason for the significant damping of the arc in our image is the tendency of ADI to self-subtract extended axi-symmetrical signal. Second, while S1 and the Y-band arc appear smoothly connected in the polarized image, this is not the case in our L'-band images, where a clumpy structure is distinguished close to the root of S1 (labelled feature *i* in the middle panel of Figure 7.2). Part of the reason for such discontinuity could be the ADI filtering of a slightly over-illuminated area of the spiral, as ADI is known to produce negative azimuthal lobes and distort azimuthally extended features (e.g. Milli et al. 2012). Alternatively, this could indicate that it is tracing a different physical process (e.g. the merging of S1 and S2). The different appearance of feature (*i*) at Y- and L'-band could also be due to the tracing of different disk layers. Part of the L'-band emission could also trace shocks occurring in the spiral wake, as they might heat the disk locally (e.g., Richert et al. 2015; Lyra et al. 2016). However, Rafikov (2016) argues that the increase in temperature due to shocks should be negligible, meaning that the observed spirals would only trace scattered stellar light.

Apart from the spirals, a common feature that is recovered in both the polarized light images and L' images is the bright second arc, shifted radially outward from S1, at PA $\sim 325°$. We refer to it as feature (*ii*) in Figure 7.2. Regarding its origin, we note a resemblance with the double arc seen in the disk of HD 100453 (Benisty et al. 2017, Fig. 6.5g). In the latter case, it was suggested to correspond to the scattering surface of the bottom side of the disk. We note that in the case of MWC 758 this explanation is consistent with the estimated inclination and PA of the outer disk (i $\sim 21°$, PA $\sim 65°$). Such double arc is indeed expected to be most prominent in the direction of the semi-minor axis of the disk, towards the closer side of the inclined disk (with respect to the observer). This disk orientation has recently been confirmed with new mm-line observations (Boehler et al. 2017). This interpretation further requires the truncation of the optically thick disk, which could be due to a companion outside the disk, which could also trigger the spiral pattern (e.g. Dong et al. 2018a). Alternatively, Boehler et al. (2017) rather suggest that both features (*ii*) and (2) trace in fact the wall of dust at the edge of the two dust traps seen in that system (Fig. 6.3).

7.2.2 Reliability of the spiral arm detection

Before proceeding further with the analysis of the spiral arms, I provide here the results of a test that aims to assess the reliability of S3 in our images. ADI is known to be an aggressive algorithm that can introduce biases in the results of disk image processing (Milli et al. 2012). We tested the effect of ADI on spiral features, by injecting two artificial spiral arms (similar to S1 and S2) into an ADI cube obtained in similar conditions for a different source showing no disk emission. For this object, a reference star was also observed before and after the target observations to allow for reference star differential imaging (RDI, Mawet et al. 2013). In the residual images after PCA analysis, the injected spirals in the ADI data reduction appear to be sharper, but unchanged in shape, compared to RDI (see Figure 7.3). No tertiary arm is generated by the injections of the two spiral arms. These tests give us

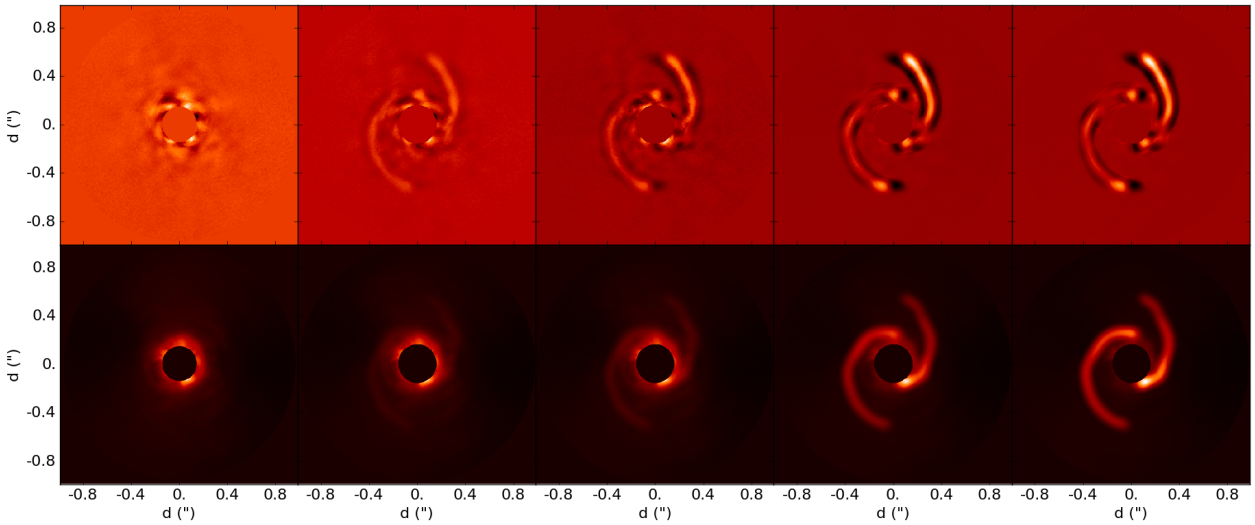

Figure 7.3: ADI and RDI comparison on artificial spirals. Top and bottom row show the results of PCA-ADI and PCA-RDI, respectively, on artificially injected spirals. The injected spiral flux increases from left to right.

confidence that the third spiral arm detected in the final PCA-ADI images is real.

7.2.3 Trace of the spirals

Considerations on the morphology (shape in polar coordinates, pitch angle, separation angle) of spirals in disks are most meaningful with face-on geometry. It also enables direct comparison with predictions from theoretical or numerical studies of spirals. Therefore a first step before analyzing the spirals was to deproject our final image using the orientation of the disk inferred in previous studies, in order to produce a face-on view of it. Based on resolved CO emission, Isella et al. (2010) inferred an inclination of $21° \pm 2°$ and a PA of semi-major axis of $65° \pm 7°$. This orientation would be the one of the outer disk, while IR-interferometric observations suggest a possible mild misalignment of the inner disk (Isella et al. 2006, 2008; Lazareff et al. 2017). Given that the inner disk is not expected to be resolved in our L'-band observations, we only use the orientation of the outer disk for the deprojection. The deprojected image is shown in the different panels of Fig. 7.4. Only the Oct. 2015 PCA-ADI final image was used, as it reaches better sensitivity than the Oct. 2016 data set, reflecting the better conditions at the time of the observation. To characterize the spiral arms and features (*i*) and (*ii*), we then identified their trace as radial intensity maxima in azimuthal steps of 1°. These are marked with crosses in Fig. 7.4a.

7.2.4 Fits to the spiral density wave equation

I performed a least-square fit of the trace of the different spirals to the predicted shape of spiral density waves in the linear regime (Eq. 6.2; see Sec. 6.4.2 for more details). In order to reduce the degeneracy between the 5 free parameters, I fixed two of the parameters

for the disk: α to 1.5, which is equivalent to assuming a disk in Keplerian rotation, and β to 0.25, corresponding to a passively heated disk. Even if the assumption on β is not completely accurate, I noticed, similarly to Benisty et al. (2015), that the exact value of β within a physically meaningful domain (from 0.05 to 0.5), did not affect significantly the shape of the spiral. The parameter affecting most significantly the morphology of the spiral is h_p, the disk aspect ratio at the location of the companion, which is let as a free parameter in all our fits.

I performed two kinds of fit: (A) fits where the position of the perturber (r_p, θ_p) is fixed to the location of the companion candidate in our image, and (B) letting those two parameters, along with h_p, free. Therefore, type A fits tackled the question of whether any of the observed spirals could be due to the companion candidate, and check whether the best-fit models could correspond to physically meaningful values of h_p. Type B fits simply aimed at finding the spiral models reproducing at best the morphology of the observed spirals, disregarding the physical meaning of the best-fit parameters.

For type A fits, the only spiral that could be fitted with a physically meaningful value of h_p was S2. Indeed, to match S1 a spiral model launched from the companion location would require $h_p > 0.25$, i.e. unphysically high temperatures for the disk at that location. The best fit model to Eq. 6.2 for the trace of S2 (*black dashed line* in Fig. 7.4b) is achieved with $h_p = 0.13 \pm 0.02$ (i.e., $h(r = 20$ au) = 0.13) which is roughly compatible with the best-fit disk models inferred from previous sub-mm observations ($h(r = 100$ au) = 0.18; Andrews et al. 2011). One has to keep in mind nonetheless that the best-fit values of h_p obtained from Eq. 6.2 are to be considered as upper limits, which could be in better agreement with the colder estimated temperatures inferred for the gas in the cavity (Isella et al. 2010). Indeed, only spirals in the non-linear regime are expected to be observable (Dong & Fung 2017b), and inferring h_p based on the best-fit linear spiral model is expected to overestimate h_p (Zhu et al. 2015). However, a major problem of the best-fit linear model is that it appears clearly suboptimal and cannot reproduce the full trace of S2, with an insufficient opening for the outer half of the spiral trace.

Therefore, I investigated whether spiral S2 could be consistent with a spiral density wave launched by the companion in the weakly non-linear regime, instead of the linear regime. The analytical studies of Goodman & Rafikov (2001) and Rafikov (2002) have explored the weakly non-linear regime and inferred in particular that the azimuthal distance between the spiral shock front and the path predicted by Eq. 6.2 in the linear regime would scale with t^2, where the quantity t is (Rafikov 2002, based on their Eq. 43, with α = 3/2):

$$t \propto \left| \int_1^{r/r_p} |s^{3/2} - 1|^{3/2} s^{-13/8} \mathrm{d}s \right| \tag{7.1}$$

where s is a dummy variable used for integration. This relationship was used in Zhu et al. (2015) to show that the shape of their simulated 3D spiral density waves induced by $\geqslant 1 M_{\rm Jup}$ injected companions was indeed consistent with the analytical prediction of Rafikov (2002) for the weakly non-linear regime, and that in comparison the shape defined by Eq. 6.2 underestimated the opening of the spiral.

In practice, using Eq. 7.1 to fit an observed spiral requires to make several assumptions,

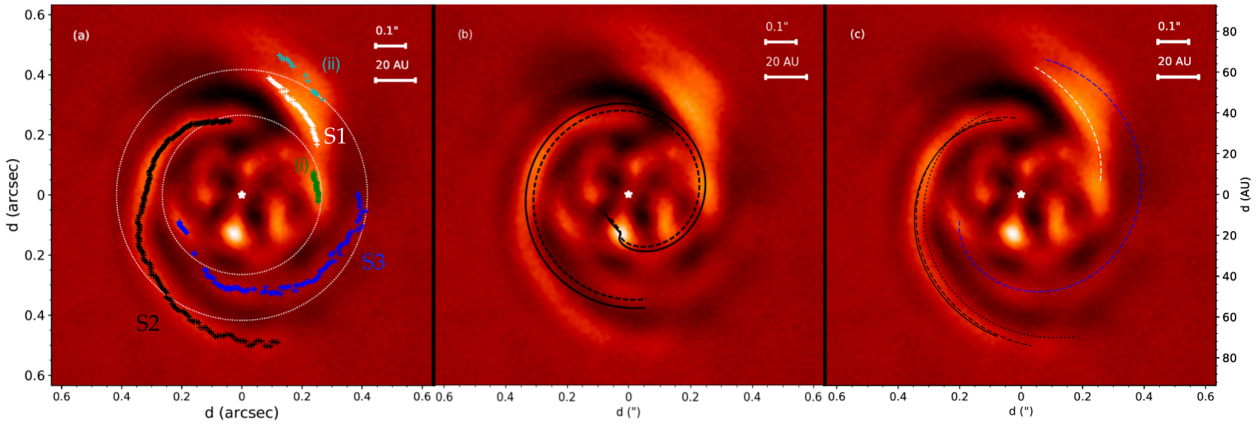

Figure 7.4: (a) Spiral traces. **(b)** Best-fit spiral models to S2 using the spiral density wave theory (*dashed line*) and the correction for the weakly non-linear regime (*solid line*), forcing the location of the perturber to be that of the companion candidate. **(c)** Best fit spiral models to each spiral trace, without any constrain on the parameters. *Dashed lines* correspond to the best-fit models in the 2015-epoch image. The *dotted* and *solid lines* correspond to the best-fit model of S2 in the 2011 H-band image of Grady et al. (2013, using the best-fit parameters reported in their paper), and in our 2016-epoch L'-band image.

which limits its usefulness. First, one needs the knowledge of the exact linear spiral density wave model that would stem from the location of the companion (i.e., in addition to assumptions on α and β, both the companion location and h_p have to be known). Typically, h_p can be estimated from either SED fitting or resolved mm-line observations probing the radial temperature profile in the disk. Based on the SED fit in Andrews et al. (2011), I considered h_p = 0.1. A second assumption has to be made in order to use Eq. 7.1, which is the azimuthal deviation between the (true) weakly non-linear regime spiral shock and the path predicted by Eq. 6.2 at a certain point of the shock. The decision of which point to consider is arbitrary. However, this decision should not matter if the observed spiral follows indeed the deviation predicted for the weakly non-linear regime. In the case of our observation, I set the point to be in the middle of feature (i), considering that if S2 is the spiral shock launched by the companion, it would necessarily pass through feature (i). This choice is further motivated by the possibility that the peculiar morphology of feature (i) could be due to the intersection of S2 with S1. Using these assumptions, the best-fit weakly non-linear spiral model is given by the *black solid curve* in Fig. 7.4b. This best-fit model still appears to be suboptimal compared to the observed morphology of S2 which is more open in its outer half. This suggests one of the following possibilities: (a) S2 is not launched by the companion candidate, (b) the spiral is launched by the companion but in the completely non-linear regime (hence not predictable analytically), or (c) the companion's orbit is not circular and/or not co-planar with the outer disk (which is the assumption made in all analytical studies of companion-induced spirals so far).

In this reasoning, I made the additional assumption that a shadow-like feature must account for the dark area at a PA$\sim$320° that appears to be truncating S2. As mentioned before, there might be a mild warp from the inner disk, which could be occulting part of the outer disk. All together, and considering the suboptimal fit obtained in the weakly non-linear regime, it appears however unlikely that S2 is launched by the companion candidate, at least if the companion is on a co-planar circular orbit with respect to the outer disk. As

will be seen in the case of HD 142527 though, this is not necessarily always true or expected for massive companions (Sec. 7.3.3).

Nonetheless, it is interesting to note that any spiral model launched from the companion candidate location with a reasonable value of h_p, including in particular the best-fit weakly non-linear spiral model would necessarily pass through feature (2), i.e. the almost circular arc that is best seen in Fig. 7.2a. The typical predicted pitch angle of outer spiral arms (outer with respect to the companion location) happens to be $\lesssim 5°$ (e.g. Dong et al. 2015b), hence almost circular in appearance as well. This suggests that if the orbit of the companion is circular and co-planar with the outer disk, feature (2) might be the only spiral shock effectively induced by the companion in the disk.

I also considered the best-fit spiral models obtained for each spiral trace in case B, when both the companion position (r_p, θ_p) and the disk scale height at that location, h_p, are let as free parameters. These are shown with *dashed lines* in Fig. 7.4c. Interestingly, the best-fit models of S1 and S2 would connect roughly at the location of feature i, if the model for S2 was extended radially inward. Another interesting fact is that the best-fit model of S3, when extended radially outward, passes through feature ii, which might suggest they are both parts of the same spiral structure, but truncated by a shadow in the middle (possibly due to feature i). In that scenario, the merging of S1 and S2 shown as feature i could create a stronger shock, with the increased temperature leading to an enhanced scale height, shadowing the outer part of the disk in that PA range. Alternatively, this might be a coincidence, and feature ii could be unrelated to S3, tracing either the backside of the disk or the illuminated wall of dust at the edge of the outer dust trap.

7.2.5 Proper motion

Another application I made from the best-fit spiral model of S2, is the study of its proper motion over a 5-year baseline. In Fig. 7.4c, in addition to the best-fit model obtained for the 2015 image (given with a *dashed line*), I also give the best-fit spiral model of S2 in the NIRC2 2016 image (*solid line*) and in the HICIAO image obtained on Dec. 24, 2011 (*dotted line*; Grady et al. 2013), which corresponds to the first detection of S2. Grady et al. (2013) performed the same fitting procedure as I did to the trace of S2 and provided the best-fit parameters they found in their study, which I then used to plot their best-fit model in Fig. 7.4c. S1 was not conspicuous in their image, hence the analysis could only be performed on S2. All models lead to a visually convincing match with S2 at their respective epoch, tracing the central crest of the spiral. The amount of rotation to be applied to the 2015 and 2016 models to match the 2011 model is $17° \pm 5°$and $19° \pm 6°$, respectively. This is consistent with the expected rotation of the companion candidate around a $1.5 \pm 0.2 M_\odot$ central star on a 20 ± 1 au radius circular orbit ($19° \pm 1°$ and $24° \pm 1°$ in 3.83 and 4.83 years, respectively), and would be an argument in favor of MWC 758 b as the origin of S2. Indeed, we would not expect any observable rotation of S2 if it were due to an external companion.

We identified a weakness in this tentative analysis, which incited us to not include it in Reggiani et al. (2018). The HiCIAO image was obtained at H band (1.6μm), while our

NIRC2 images were obtained at L' band (3.8μm). As mentioned earlier, the Rayleigh-scattering cross-section is extremely dependent with wavelength, so that different disk layers are traced at different wavelengths (as confirmed by the comparison of S2 between Fig. 7.2a and b; Sec. 7.2.1). Therefore, one could expect that the best-fit model in H band is shifted radially inward toward the star compared to the L'-band models in Fig. 7.4c. The quoted uncertainties in the previous paragraph do not take into account this possibility. Therefore, all together, the detection of proper motion appears too tentative.

More recently, another study based on the same idea reached the conclusion that the spiral pattern in MWC 758 does not show any significant sign of rotation between 2005 and 2015 (Ren et al. 2018). This temporal baseline corresponds to observations made with the HST and NIRC2, at wavelengths of 1.1μm and 3.8μm, respectively. Although their study made use of a proper mathematical treatment of the spiral, I identified two possible sources of bias in their study which inspire caution. First, the spiral pattern is not seen as such in the HST image (see their Fig. 1). The pattern seen with HST is better described as a truncated circle with brightness asymmetries due to the lower angular resolution of HST. The two individual rolls that they average to produce a final image are not very similar, apart from the bright signal likely corresponding to S1. Second, the observations that they considered for the proper motion estimate are at two significantly different wavelengths, which can lead to different radial separation (as argued in the previous paragraph) and different possible truncation locations for the spirals (as can be seen at the root of S2 in the SPHERE and NIRC2 images, Fig. 7.2). The main assumption in their mathematical treatment is that the spiral pattern is rigorously identical in shape, and only rotates azimuthally, however as argued above the observed pattern in the HST and NIRC2 images are visually different. Therefore, their result is likely to be considered with caution. More definitive conclusions on the proper motion of S2 would be obtained from the comparison of new H-band polarized images with the 2011 HICIAO image of the system reported in Grady et al. (2013), which is the first observation with a conspicuous detection of S2.

7.2.6 Pitch angle

In addition to fits to spiral equations, the trace of the spirals also allowed us to measure their pitch angle, defined at each point as the angle between the tangent to the spiral and the local azimuthal vector. For each trace, the pitch angle ψ was estimated in two different ways: (a) we considered the average value of the pitch angle computed from all pairs of consecutive points in the trace, and (b) we derived the pitch angle of the best fit logarithmic spiral given by $r = a\mathrm{e}^{b\theta}$. Logarithmic spiral arms have the property of keeping a constant pitch angle throughout their length, given by $\psi = \tan^{-1} b$. Both methods yielded consistent measurements, although method (a) led to larger uncertainties.

Figure 7.5 shows the pitch angles measured with method (b) for each feature identified in Fig. 7.4a. We measured the evolution of the pitch angle over S2 and S3 using method (b) on consecutive sections of the spirals separated by 5° and subtending each 50°. A single measurement using method (b) is provided for S1, features (*i*) and (*ii*), due to the short PA range they subtend. We first notice that the pitch angle of feature (*i*) is slightly negative

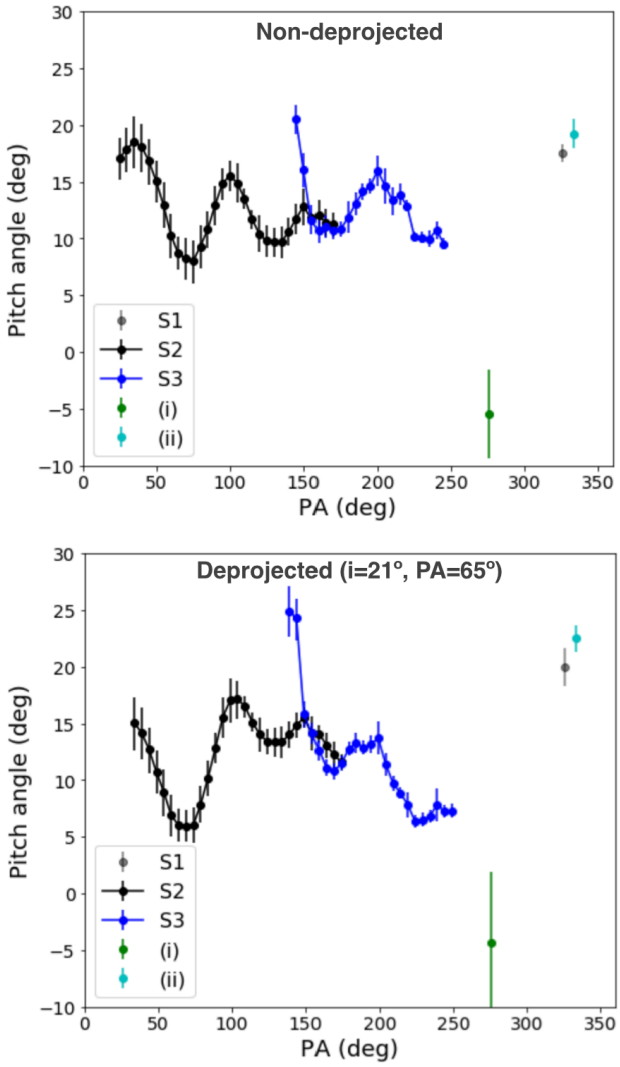

Figure 7.5: Pitch angle of each spiral, in the non-deprojected (top) and deprojected image (bottom). For each measurement, we considered either the whole trace (for S1, features *i* and *ii*), or consecutive arcs subtending 50° (for S2 and S3) to trace the evolution of the pitch angle along the trace in order to provide reliable pitch angle estimates. The estimate for feature (*ii*) has a larger uncertainty because its trace only subtends ∼25°, instead of ∼50° for S1 and feature (*ii*).

(quasi-null), which suggests that it is more likely related to the Y-band circular arc rather than to S1. Globally, S2 and S3 appear to show significant fluctuations in pitch angle. In particular, the root of S3 (PA <150°) shows a more significant pitch angle than the rest of S3. This could imply that it is either tracing a feature of the disk unrelated to S3, or that ADI filtering significantly alters the shape of S3 at such close separation. Overall, S1 and feature (*ii*) present a slightly larger pitch angle than both S2 or S3. The difference is more significant after deprojection (∼20° instead of ∼7–16°). It appears thus more likely that feature (*ii*) is related to S1 rather than S3.

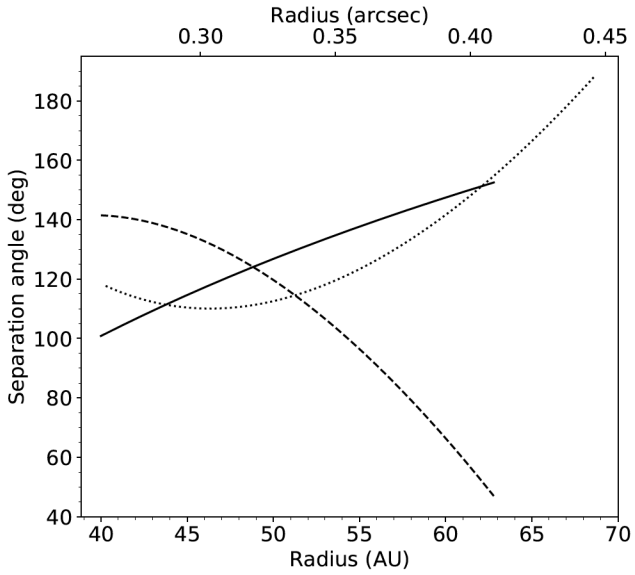

Figure 7.6: Separation angle between S1 and S2 (*solid line*), between S1 and S3 (*dashed line*), and between S2 and S3 (*dotted line*).

7.2.7 Separation angles

Finally, a last measurable quantity that will be useful for the discussion on the origin of the spirals (next subsection), is the separation angle between each spiral. For massive companions able to launch multiple spirals, an empirical relationship has recently been established between the mass of the companion and the separation angle $\phi_{\rm sep}$ between primary and secondary inner spiral arms: $\phi_{\rm sep} = 102°(q/0.001)^{0.2}$, where q is the mass ratio between the companion and the star (Fung & Dong 2015, hereafter FD15). Therefore, I measured the separation angle $\phi_{\rm sep}$ between each pair of spiral arms between 40 and ∼63 au (delimited by the two dotted lines in Fig. 7.4a), where all spirals are clearly defined in our final PCA-ADI image. These separation angle measurements are based on the geometrical fits of the spirals shown in Fig. 7.4c.

In the FD15 simulations, the separation angles are relatively constant with radius, with only a slight decreasing trend for all models with $\phi_{\rm sep} > 80°$. Here, for each pair of spirals, the observed separation angle appears to vary significantly with radius. Only in the limited range of radii ∼40–55 au, are the $\phi_{\rm sep}$ for the S1-S3 and S2-S3 pairs relatively constant and hence comparable to the FD15 predictions. Considering that radial range, the FD15 models corresponding to $q = 4 \times 10^{-3}$ and $q = 10^{-3}$ lead to the closest match to the measured $\phi_{\rm sep}$ of the S1-S3 and S2-S3 pairs, respectively. Considering a stellar mass of $1.5 M_{\odot}$, these mass ratios would correspond to a companion mass of $\sim 6 M_{\rm Jup}$ (for S1-S3) and $\sim 2 M_{\rm Jup}$ (for S2-S3). The first possibility is consistent with our detection limits inside 90 au, while the second is compatible with our sensitivity limits at any radius (Fig. 12.3). Nevertheless, these predictions require the presence of a giant planet at large separation (> 80 au), which is expected to be very rare (Sec. 4.1). Furthermore, in the case that S1-S3 (resp. S2-S3) are launched by an external companion, another companion would yet be required to account for S2 (resp. S1), except if S2 (resp. S1) happens to be a very bright tertiary arm, even

brighter than the secondary arm (i.e. S3 in both cases).

7.2.8 Origin of the spiral arms

In this subsection, I first attempt to interpret all the results inferred from the different aspects of the spiral arm analysis presented in the previous paragraphs in the perspective of embedded companion(s). Other possible origins for the spirals, not related to embedded companions, are then briefly discussed.

Companion-induced spirals

Two main possibilities exist regarding the putative companion(s) launching the observed spiral arms: (1) it is located in the outer disk, beyond the extent of the observed spirals; (2) it is located in the sub-mm cavity, hence accounting for both the cavity and the spirals.

Case 1: could the spirals be launched by a companion in the outer disk? Hydrodynamical simulations and corresponding radiative transfer models have suggested that observable spirals in NIR could only be launched by companions massive enough ($\gtrsim 1 M_{\rm Jup}$) for the linear spiral density wave theory to break down (e.g. Juhász et al. 2015; Dong & Fung 2017b). Such massive companions are expected to launch several arms inward from their location, either two or three, depending on its mass (e.g. Zhu et al. 2015; Bae & Zhu 2017b). The m=2 mode is expected to dominate for the most massive companions, while the m=3 mode corresponds typically to $M \lesssim 5 M_{\rm Jup}$. As argued in Bae & Zhu (2017b), a companion launching all three spirals could be compatible with our sensitivity limits in the outer disk (Fig. 12.3). The predicted pitch angle of these inner spirals range between 10-15°, hence also roughly consistent with the observed spirals of MWC 758 (e.g. Dong et al. 2015b). The separation angle between the primary and secondary inner spirals is expected to be relatively constant with radius and follow the relation inferred in FD15 (see previous subsection). Nonetheless, in the case of MWC 758, based on the separation angle (Fig. 7.6), the only pairs of possible primary-secondary spirals are S1-S3 and S2-S3, which appears slightly at odd with the fact that S1 and S2 are the brightest spirals in all IR images. A companion at that separation would not lead to a significant rotation of the spirals, as also tentatively inferred in Ren et al. (2018). Finally, dedicated hydro-dynamical simulations including a planet of a few Jupiter masses at ∼100 au appears to reproduce qualitatively but not perfectly the observed spiral pattern (Dong et al. 2015b, 2018a). For example, the simulated secondary spiral appears like a single arm whose trace is equivalent to a blend of S3 at short radius and S1 at large radius.

Globally, the scenario involving a 2-5 $M_{\rm Jup}$ companion in the outer disk appears thus plausible, and might be the dominant effect at the origin of the spirals, given the rough agreement between simulation and observation. Such outer planet would be just below our sensitivity limits (Fig. 12.3), considering that our limits might also be slightly optimistic

given the adoption of hot-start models for the magnitude to mass conversion. Nonetheless, this hypothesis presents a few minor weaknesses as well: (1) as mentioned above, their simulated secondary spiral does not reproduce perfectly S1 neither as seen in Benisty et al. (2015) nor as in our observations, but rather as composed of parts of the observed S3 and S1 in our images; (2) it involves a giant planet at a separation (> 80au) where they are known to be very rare (Sec. 4.1); (3) the measured separation angles between S1 and S2 are not consistent with that pair being the primary-secondary, which appears at odd with the fact that they are the brightest IR spirals – all simulations of multiple inner arms predict secondary arms to be brighter than tertiary arms (e.g. Dong et al. 2015b); (4) another companion is still required to account for the eccentric sub-mm cavity (Andrews et al. 2011; Boehler et al. 2017; Dong et al. 2018a).

Case 2: could the spirals be launched by a companion in the cavity? In particular, could the companion candidate seen in our L' images be at the origin of the spirals? It has been well established that companions on circular and co-planar orbits with the disk can only launch one spiral outward from their location (e.g. Dong et al. 2015b; Zhu et al. 2015) – in contrast with the possibility of multiple inner spirals. Our fits to the spiral density wave equation suggest that only feature (2) could possibly be induced by the companion candidate if on a circular orbit co-planar with the outer disk. Therefore, if a single companion in the cavity is to induce multiple outer spirals, its orbit must break one or both of these assumptions – co-planarity or circularity. Recent simulations in the case of the disk of HD 142527 indicate indeed that the close-in companion with an inclined and eccentric orbit (Lacour et al. 2016) is able to qualitatively reproduce the multiple spiral arms stemming from the edge of the eccentric cavity (Price et al. 2018, Sec. 7.3.3). In the case of MWC 758, several studies based on near-IR interferometric data have suggested that the inner disk is likely misaligned with respect to the outer disk, with the difference in inclination estimated between 10°and 30°, while the PA does not appear well constrained (Isella et al. 2006, 2008; Lazareff et al. 2017). It is thus conceivable that the orbit of the companion candidate lies in the same plane as this mildly misaligned inner disk. In that case, the large fluctuations in the measured pitch angle along S2 and S3 could also be considered as a clue that the spirals are launched by a companion whose orbital plane is different than the plane of the outer disk (Fig. 7.5). Indeed, if the spirals were seen face-on after deprojection, one would not expect significant fluctuations in their opening angle (apart in the direct vicinity of the companion, Zhu et al. 2015; Juhász & Rosotti 2018). Nevertheless, this interpretation has to be mitigated with the fact that our deprojection does not take into account the flaring of the disk, which may slightly bias the measured pitch angles – the spiral pressure waves at the surface of the disk are indeed expected to "lean" towards the star due to the flared geometry of the disk.

As in case 1, this scenario is not devoid of weaknesses. A possibly major uncertainty in this scenario is that it is unsure whether the conclusions based on HD 142527 B can easily be extended to MWC 758 b, which is estimated to be ∼70 times less massive than the former ($\sim 5\ M_{\rm Jup}$ vs $\sim 0.35 M_\odot$, see Secs. 12.1.1 and 16.1, resp.). Another possible weakness of this scenario is the fact that a single planet in the cavity would not be able to account for the two dust traps, nor for a possible truncation of the outer disk (required if feature *ii* is indeed the backside of the disk; Dong et al. 2018a). Dedicated simulations in the giant planet mass

regime are required to better probe the effects of orbital inclination and eccentricity on the induced spiral pattern.

Case 1+2 A possible way to solve the weaknesses inherent to each scenario is the presence of two companions, one in the cavity and one outward from the spirals. Cases 1 and 2 are indeed not mutually exclusive. Indirect surveys of exoplanets have found an abundance of multiple giant planet systems (e.g. Winn & Fabrycky 2015, and references therein). New simulations in Barraza et al. (2018, in prep.) suggest that two companions, one in the cavity and one in the outer disk are required to account for the double dust trap (Sec. 16.1). Furthermore, these new simulations also manage to reproduce better the three spiral arms seen in our observations, hence explaining the minor disagreement between the simulations of Dong et al. (2018a) and the observed L' spirals.

Alternative origins

For the sake of completeness, we also considered the possibility that the observed spiral pattern is induced by one or several other physical mechanisms. There is no conspicuous detection of long-lived shadow, as in the cases of HD 142527 (Avenhaus et al. 2014; Marino et al. 2015b) and HD 100453 (Benisty et al. 2017), which makes the possibility of shadow-induced spirals unlikely.

The flyby by an external star is also known to produce a one- or two-arm spiral pattern (e.g., Quillen et al. 2005). We investigated the possibility that MWC 758 could have undergone a fly-by from the source located at $2\farcs3$. As detailed in Sec. 12.1.1, the color and magnitude of the object are not compatible with a young object at the distance of Taurus, and could either correspond to an early red dwarf at the distance of MWC 758, or a red giant star much farther away. The probability that an old red dwarf happens to cross the star forming region of Taurus is very small, we hence favor the second hypothesis.

Based on mm-dust continuum observations and assuming a fiducial gas-to-dust ratio of 100, the disk mass was estimated to 0.008 $M_\odot$ (Andrews et al. 2011). Considering a stellar mass of 1.5 $M_\odot$, the disk is about 50 times less massive than required to form spiral arms by self-gravity (Dong et al. 2015a). However, as noted in Sec. 2.1, the disk mass is likely underestimated. While it is not possible to completely rule out an hypothetical impact due to a marginally unstable disk, it is interesting to note that in the case of TW Hya, disk mass estimates based on HD (expected to be the most reliable tracer of gas mass) have led to a factor $\sim$5 larger mass estimate than obtained with sub-mm continuum or CO lines (Bergin et al. 2013). If a bias of the same amplitude applies to the disk of MWC 758, it would thus still be gravitationally stable.

7.3 Case of HD 142527

In this section, I present the special case of HD 142527, which features both all disk structures discussed in Chap. 6, and a close-in low-mass binary star (characterized in Sec. 16.1). I first summarize the information known about the source in Sec. 7.3.1. The investigation I led of the large-scale CO spiral arms seen with ALMA in this disk is then presented in Sec. 7.3.2. Finally, in Sec. 7.3.3, I detail my contribution to characterize the spiral arms obtained in new hydro-dynamical simulations of the disk, which fits within the broader study of the impact of the binary companion on the disk, published in Price et al. (2018).

7.3.1 The source

The system of HD 142527 has drawn progressively more attention as observations probing different components of the disk have successively unveiled a very unique morphology. Given its extensive study over the years, it is now possible to build a relatively complete picture of what is going on in the disk. A summary of the most relevant observations of the system and the model inferred from them is provided in Fig. 7.7.

Waelkens et al. (1996) classified HD 142527 as an Herbig Ae star of F6 III spectral type (hereafter "Herbig Fe" star). The isochrones of Palla & Stahler (1999) suggest a mass and age of 1.9 $\pm$ 0.3 $M_{\odot}$ and 2^{+2}_{-1} Myr. The distance, initially estimated to 200 pc by Hipparcos (de Zeeuw et al. 1999) and later considered to be closer to $\sim$140 pc due to probable membership to the Upper Centaurus Lupus group (Teixeira et al. 2000), is now confirmed by Gaia to be 157$\pm$1 pc (Gaia Collaboration et al. 2018). The peculiar SED of the system, consisting of a lack of mid-IR excess but a larger far-infrared excess than stellar luminosity (Waelkens et al. 1996), motivated Fukagawa et al. (2006) to obtain the first high contrast images which enabled to resolve the circumstellar environment in H and K bands. In these first images, they reported two bright and asymmetric arcs on both sides of the star, and a large-scale spiral arm stemming from the western arc (top left panel of Fig. 7.7). Based on both the asymmetries seen in these images and in SMA observations, Ohashi (2008) suggested that HD 142527 was a promising laboratory to study the process of planet formation in-situ.

The gap has been resolved in multiple NIR follow-up images (Casassus et al. 2012; Canovas et al. 2013; Avenhaus et al. 2014, top-middle panel of Fig. 7.7). The record-sized gap for a gas-rich disk, with an estimated radial width of $\sim$ 130 au, adds to the peculiarity of HD 142527, and contributed to foster interest on the source. The advent of ALMA has enabled to confirm the large gap in the mm-size dust distribution, and to identify even more distinguishing features in the system, including one of the largest dust traps (Sec. 6.2, middle left panel of Fig. 7.7; Casassus et al. 2013b; Fukagawa et al. 2013; Muto et al. 2015), tentative gap crossing filaments (Casassus et al. 2013b) and large scale gaseous spiral arms (described and analyzed in the next section; Christiaens et al. 2014, bottom-left panel of Fig. 7.7). First inferred from SED modeling in Verhoeff et al. (2011), the presence of an inner disk was observationally confirmed in the ALMA sub-mm continuum data of Fuka-

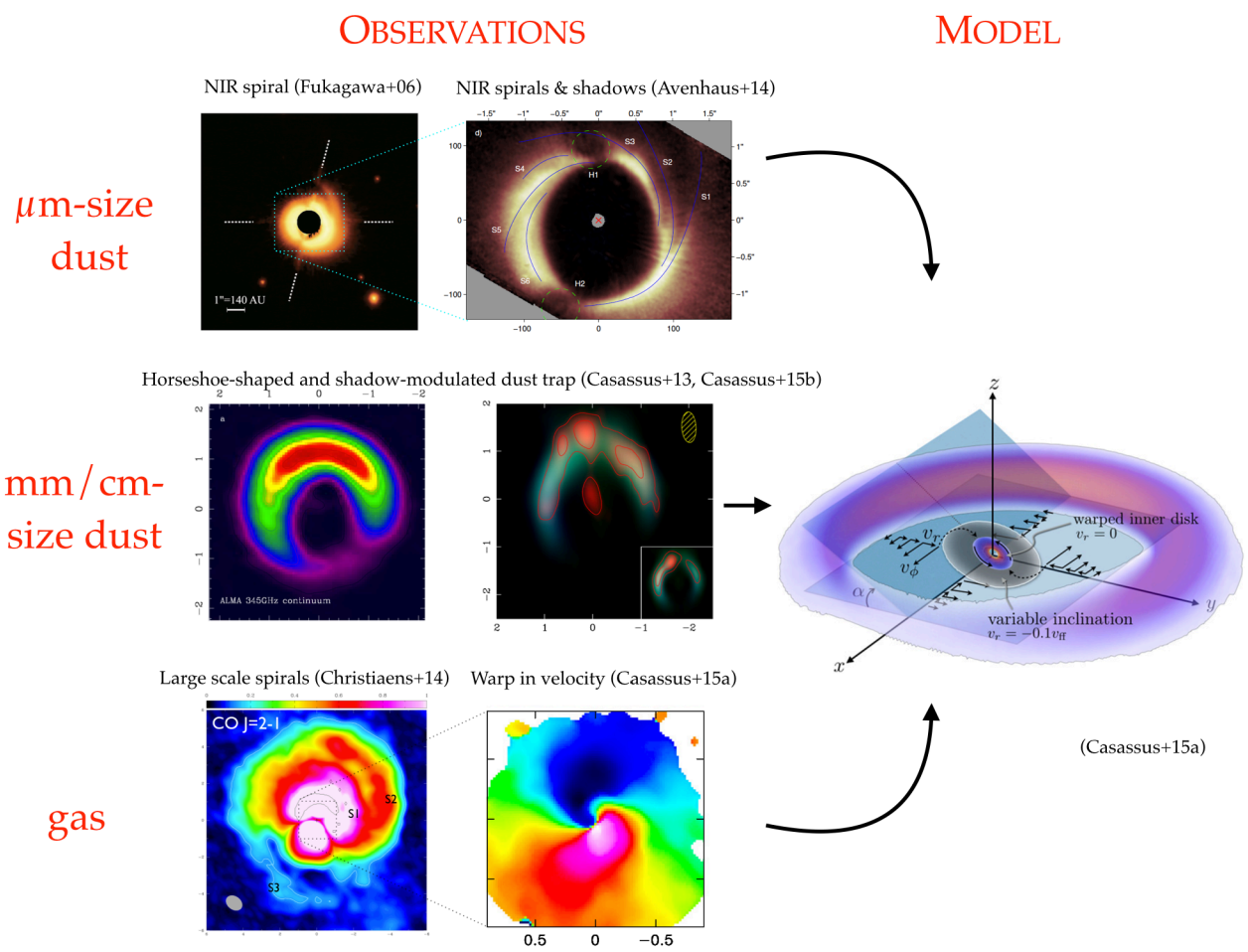

Figure 7.7: Observations (left) and model (right) of the disk of HD 142527. The different rows show the different components of the disk probed by observations obtained with a diversity of techniques and at various wavelengths (see details in the text). The model depicts the orientation of the inner and outer disk, the corresponding velocity field, and the large dust grain distribution (pink). References: Observations from Fukagawa et al. (2006); Avenhaus et al. (2014); Casassus et al. (2013b, 2015b); Christiaens et al. (2014); Casassus et al. (2015a) from top left to bottom right. Cartoon model from Casassus et al. (2015a).

gawa et al. (2013). The dust trap nature of the asymmetric mm-size dust distribution was confirmed with cm-wave interferometric observations, showing a more compact cm-size distribution (Casassus et al. 2015b, central panel of Fig. 7.7).

The two-sided shadows initially seen in Casassus et al. (2012), a puzzling mystery for several years, was eventually elucidated in Marino et al. (2015a), who showed that it was most likely caused by an optically thick inclined inner disk with respect to the outer disk. The warp was observationally confirmed in mm-line velocity maps (Rosenfeld et al. 2014; Casassus et al. 2015a, bottom-middle panel Fig. 7.7).

In parallel to the flow of peculiarities successively encountered in the disk, a companion candidate was announced in Biller et al. (2012) and later confirmed in Close et al. (2014) and Rodigas et al. (2014). In particular, Close et al. (2014) showed that it was significantly accreting based on its Hα emission. A first astrometric study and SED fitting were reported in Lacour et al. (2016), which suggested that the companion had a mass of only

$\sim$0.1 $M_\odot$ and was likely on an inclined and eccentric orbit, hence possibly shepherding the inclined inner disk. A more detailed spectral characterization of the companion, presented in Christiaens et al. (2018a; Sec. 16.1), has since then enabled to further constrain the physical properties of the companion, suggesting it is a M2.5$\pm$1.0 red dwarf with an estimated mass and age of 0.34$\pm$0.06 $M_\odot$ and 0.5-3 Myr, respectively.

In the next section, I detail the results of my analysis of the spiral arms seen in CO mm-lines with ALMA. Then, in Sec. 7.3.3, I summarize the recent results of Price et al. (2018) demonstrating that all the main characteristics of the disk can in fact all be qualitatively accounted for by the low-mass stellar binary companion.

7.3.2 Spiral arms in the disk of HD 142527 from CO emission lines with ALMA

V. Christiaens, S. Casassus, S. Perez, G. van der Plas & F. Ménard
ApJ, 785, 12 (2014)

Abstract

In view of both the size of its gap and the previously reported asymmetries and near-infrared spiral arms, the transition disk of the Herbig Fe star HD 142527 constitutes a remarkable case study. This paper focuses on the morphology of the outer disk through ALMA observations of ^{12}CO J=2-1, ^{12}CO J=3-2 and ^{13}CO J=2-1. Both ^{12}CO J=2-1 and ^{12}CO J=3-2 show spiral features of different sizes. The innermost spiral arm (S1) is a radio counterpart of the first near-infrared spiral observed by Fukagawa et al. (2006), but it is shifted radially outward. However, the most conspicuous CO spiral arm (S2) lies at the outskirts of the disk and had not been detected before. It corresponds to a cold density structure, with both brightness and excitation temperatures of order 13$\pm$2 K and conspicuous in the ^{12}CO J=2-1 peak-intensity map, but faint in ^{12}CO J=3-2. There is also a faint counterarm (S3), point-symmetrical of S2 with respect to the star. These three spirals are modelled separately with two different formulae that approximate the loci of density maxima in acoustic waves due to embedded planets. S1 could be fit relatively well with these formulae, compared to S2 and S3. Alternative scenarios such as gravitational instability or external tidal interaction are discussed. The impact of channelization on spectrally and spatially resolved peak intensity maps is also briefly addressed.

Introduction

The young circumstellar disks that host a large annular gap or central cavity, the so-called *transition disks* (TDs), could be crucial in the context of planetary formation as their morphologies may result from dynamical clearing due to planet(s) (Dodson-Robinson & Salyk

2011; Zhu et al. 2012, 2013b), rather than dust grain growth or photo-evaporation alone (Rosotti et al. 2013).

Asymmetric features, warps or spirals in TDs can also evidence the presence of stellar or planetary companions (e.g. Goldreich & Tremaine 1979). Spiral features have mostly been detected in optical or near-infrared (NIR) wavelengths (e.g. Grady et al. 2001; Clampin et al. 2003; Fukagawa et al. 2004; Muto et al. 2012; Grady et al. 2013), and in the disk of AB Aur at radio wavelength (Corder et al. 2005; Lin et al. 2006), although in counter-rotation with the disk, thus probably stemming from a late envelope infall (Tang et al. 2012).

The disk around the Herbig Fe star HD 142527 constitutes an outstanding example of a nearly face-on TD (i$\sim$28$\pm$3°; Pérez et al. 2014), showing both a large asymmetric dust depleted gap and a spiral arm observed in NIR scattered light (Fukagawa et al. 2006). Its mass and age were estimated to respectively $\sim$1.9-2.2 $M_\odot$ and 1-12 Myr old (Fukagawa et al. 2006; Verhoeff et al. 2011), for a distance of 145$\pm$15 pc (de Zeeuw et al. 1999; Acke & van den Ancker 2004). Fujiwara et al. (2006) concluded that the disk's rotation axis was inclined so that the east side was the far side, with a position angle (PA) of $\sim$-20°. With K-band imaging, Casassus et al. (2012) reported the presence of smaller spiral structures at the outer edge of the gap, confirmed by Rameau et al. (2012) and in NIR polarized intensity studies (Canovas et al. 2013; Avenhaus et al. 2014, the latter work identifies two new spirals).

ALMA provided substantial insight into the structure of HD 142527. Casassus et al. (2013b) found gap-crossing HCO^+(4-3) filaments, diffuse CO(3-2) inside the cavity, and confirmed the horseshoe morphology of the dust continuum reported by Ohashi (2008), which they interpreted as a dust trap. Fukagawa et al. (2013) reported on another ALMA dataset in ^{13}CO J=3-2, C^{18}O J=3-2 and underlying continua. Here we focus on the outskirts of the HD 142527 disk and report on the discovery of several CO spiral arms.

Observations

Datasets The observations were obtained with ALMA on June 2012 (Cycle 0), and cover ^{12}CO J=2-1 (230.538 GHz, hereafter CO 2-1), ^{12}CO J=3-2 (345.796 GHz, CO 3-2) and ^{13}CO J=2-1 (220.399 GHz, ^{13}CO 2-1), with baselines comprised between 21 (resolution of $\sim$12.8″) and 379 m ($\sim$0.71″). For details on the instrumental setup and calibration we refer to Pérez et al. (2014) and Casassus et al. (2013b), respectively for bands 6 (CO 2-1 and ^{13}CO 2-1) and 7 (CO 3-2).

Spectral line imaging was achieved with the `CASA` package. The continuum was first subtracted in the visibility domain. We binned the original spectral channels to 0.2 km s^{-1} bin-width. Next, visibility data were *clean*ed (Cotton-Schwab `CLEAN`). As faint extended structures were seeked, natural weighting was preferred over Briggs weighting, and masks were drawn manually in the dirty maps for each velocity channel. To avoid spurious detections, the masks delimited signal at $\sim 5\sigma$. For comparison, an elliptical mask identical in all velocity channels, embracing the whole butterfly pattern, yielded similar moment maps.

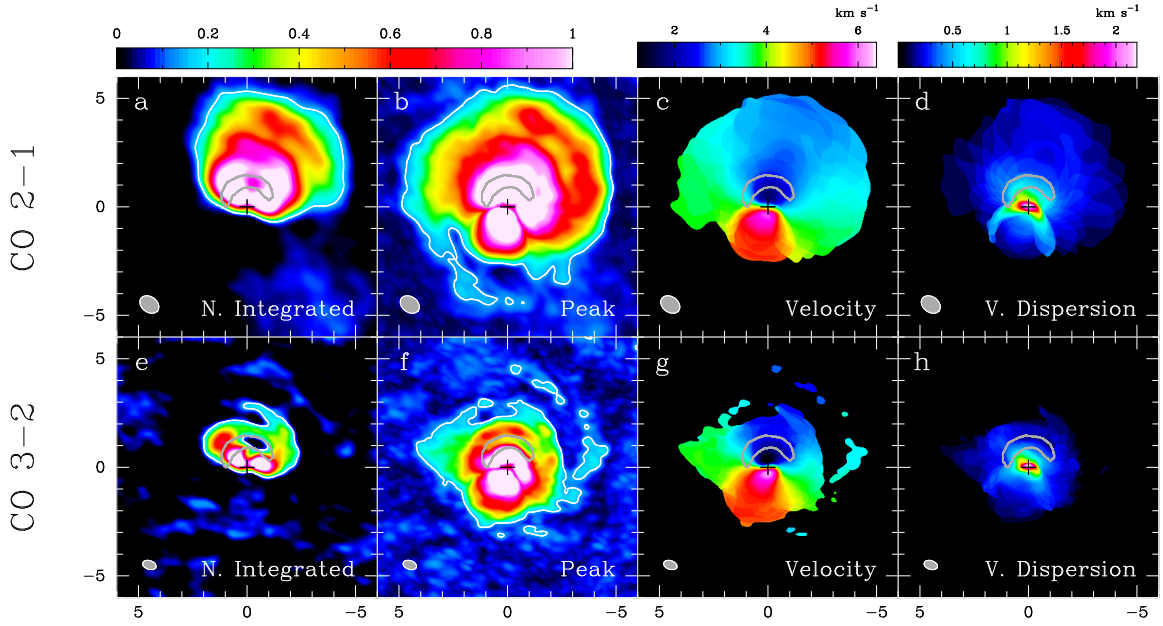

Figure 7.8: Moment maps for CO 2-1 and CO 3-2. Respective beam sizes are 0.96×0.72 and 0.63×0.40 arcsec^2. North is up and east is to the left. $x-$ and y axis indicate angular offset from the star along R.A. and Dec. from the position of the star. A continuum contour at 180 mJy beam^{-1} (half-maximum, from Casassus et al. 2013b) is overplotted in *light gray*. **a** and **e**: *Velocity-integrated intensity maps*. For CO 2-1 and CO 3-2, the 1 σ noise levels are respectively 14 and 17 mJy beam^{-1}; and the color scales are both normalized to 20 σ. The 3σ contour is shown in white. **b** and **f**: *Peak-intensity maps*. With $I_{\rm peak}$ maps, the mean of the noise is non-null; it equals respectively 27 and 42 mJy beam^{-1} for CO 2-1 and CO 3-2. The 1 σ values are respectively 11 and 15 mJy beam^{-1}; and the color scales are both normalized to 40 σ. The relevant contour, mean(noise)+3σ, is shown in white. **c** and **g**: *Velocity centroid map*. **d** and **h**: *Velocity dispersion map*.

Moment Maps Inspection of the channel maps for the different CO transitions confirms the LSR systemic radial velocity of 3.7±0.2 km s^{-1} (Casassus et al. 2013b; Pérez et al. 2014). Both CO 2-1 and CO 3-2 (but not ^{13}CO 2-1) channels with velocity higher than the systemic velocity show a decrement in the specific intensity levels between 4.2-4.8 km s^{-1} (*southern* velocities). These velocities correspond to an extended diffuse cloud best detected in single-dish data (Casassus et al. 2013a).

For CO 2-1 and CO 3-2 lines, maps of the velocity-integrated intensity ($I_{\rm int}$), the peak intensity ($I_{\rm peak}$), and the velocity centroid and dispersion are computed in order to further characterize the outer disk (Figure 7.8). The intensity scale is chosen to emphasize the fainter structure in the outer disk, at the expense of saturation in the brighter central regions, discussed in Casassus et al. (2013b) and Pérez et al. (2014). We restrict the velocity range to $2.6 < v_{\rm lsr}/{\rm km\ s^{-1}} < 3.6$ (northern velocities) for the computation of the $I_{\rm int}$ maps because of the intervening cloud.

The computation of the $I_{\rm peak}$ maps revealed an unknown issue. As seen in Figure 7.9a, the signal in the disk appears segmented for CO 2-1 (this is also the case for CO 3-2). This might be due to the discretization of the velocity field in channel-averaged visibilities. To prove that the segmentation is spurious, we computed two (resp. four) $I_{\rm peak}$ maps with the same velocity bin width (0.2 km s^{-1}), but shifted by half (resp. a quarter of) the bin width, and then averaged them. The fragmentation follows the velocity channels, and is almost

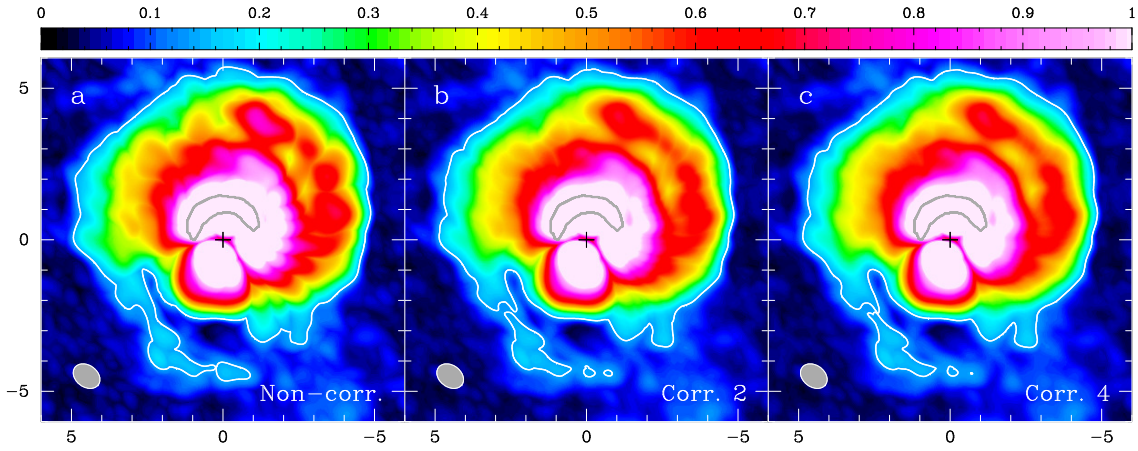

Figure 7.9: CO 2-1 $I_{\rm peak}$ maps: unsmoothed (**a**), smoothed using two (**b**) and smoothed using four (**c**) shifted datacubes. Legends follow from Figure 7.8*b*. The rest of the paper implicitly shows $I_{\rm peak}$ maps smoothed using four shifted datacubes.

completely smoothed-out when averaging the different binnings (Figure 7.9b and c).

From the CO 2-1 $I_{\rm int}$ map in the north (Figure 7.8a), an arc-like structure in the NW of the image, already hinted in the channel maps, is detected at very large distance from the star ($\sim$3.6″). Closer-in, at about 2.4″, the intensities are higher and more extended to the NNW than to the NNE. In the $I_{\rm peak}$ map (Figure 7.8b), the closer-in structure turns out to be roughly shaped as a spiral arm (hereafter S1), whereas the large scale arc is revealed as a conspicuous tightly wound spiral (S2). At an approximately point-symmetric location of S2 with respect to the star, we also detect a remarkable counterspiral (S3).

We estimated an upper limit on the flux loss due to interferometer filtering by aperture photometry in the relevant channels of a LIME (Brinch & Hogerheijde 2010) model of HD 142527 (Pérez et al. 2014). Cleaning the model, sampled at the uv-coverage of our observation, and comparing with the original model yields flux losses $\lesssim$16%. While this result suggests that filtering-out is minor for S2, the faintness of S3 stems probably from absorption due to the intervening cloud.

Bridge-like features in the central regions of the $I_{\rm peak}$ maps (Figure 7.8b and f), also seen in the velocity dispersion map (Figure 7.8d and h), are due to this intervening cloud. The kinematics in CO 2-1 appear to be Keplerian, even under spirals S1 and S2. The spirals do not have counterparts in velocity dispersion, i.e. there is no local enhancement of the velocity gradient or turbulence.

The CO 3-2 $I_{\rm int}$ map in the *north* (Figure 7.8e) displays S1 more evidently, and the $I_{\rm peak}$ map (Figure 7.8f) also confirms its presence. Some faint extended patches of signal, just above the mean(noise)+3σ level also follow relatively well S2 detected in Figure 7.8b.

However, the outer disk seems too faint to enable detection of extended structures in ^{13}CO 2-1.

Spiral arms The three spiral arms extend, in projected angular separations but deprojected physical distances:

- from ∼1.9″(∼290 AU) at PA∼-110° to ∼2.8″(∼380 AU) at PA∼0° for S1;
- from ∼3.0″(∼520 AU) at PA∼-100° to ∼4.2″(∼640 AU) at PA∼0° for S2;
- from ∼3.2″(∼520 AU) at PA∼100° to ∼4.4″(∼670 AU) at PA∼190° for S3.

They all subtend ∼100° in azimuth. S2 and S3 have radial widths ranging 0.6-1.1″ (90-160 AU), and are thus globally resolved radially.

Physical Diagnostics in the Spiral Arms Except for S3, whose signal is absorbed, several physical parameters describing the spirals may be derived. In $I_{\rm peak}$(CO 2-1), the maximum intensities are ∼450 mJy beam^{-1} for S1 (at PA∼-70°, R∼330 AU), and ∼280 mJy beam^{-1} for S2 (at PA∼-80°, R∼530 AU). In $I_{\rm peak}$(CO 3-2), the maximum intensities, roughly at the same locations as for CO 2-1, are ∼320 mJy beam^{-1} for S1, and ∼120 mJy beam^{-1} for S2.

Assuming that ^{12}CO is optically thick, the peak intensities provide brightness temperatures, which approximate the kinetic temperatures at the unit-opacity surfaces, of $T_{b,S1}$∼20 K (from both CO 2-1 and CO 3-2 maximum intensities) and $T_{b,S2}$∼11-15 K (the upper value stems from CO 2-1 maximum intensity). Assuming LTE, the excitation temperatures derived from the ratio of CO 2-1 and CO 3-2 maximum intensities are $T_{{\rm ex},S1}$∼22-27 K and $T_{{\rm ex},S2}$∼13-15 K. CO gas is expected to condensate on dust for T$\lesssim$19-20 K (e.g. Qi et al. 2011; de Gregorio-Monsalvo et al. 2013). The observation of CO gas at lower temperature in S2 may suggest that dust grains are depleted, or mainly settled in the mid-plane (e.g. Dullemond & Dominik 2004a), or that CO desorption is efficient at the surface of dust grains (e.g. Hersant et al. 2009), at that radial distance.

The gas temperature in the gap is ∼41-43 K (Fukagawa et al. 2013; Pérez et al. 2014). Using this value at 80 AU, 20-27 K at 330 AU ($T_{b,S1}$-$T_{{\rm ex},S1}$) and 13-15 K at 530 AU ($T_{b,S2}$-$T_{{\rm ex},S2}$), the best fit to the law $T \propto r^{-q}$ yields q∼0.5-0.6. This range of values is steeper than q∼0.3 found by Pérez et al. (2014) up to ∼300 AU.

Sound speed and scale height are defined respectively as $c_s^2 = k_B T_b/(\mu m_p)$ and $H = c_s/\Omega$, where k_B is the Boltzmann constant; μ is the mean molecular weight of the gas in terms of proton mass m_p, namely ∼2.3 for H_2 with 10% of He; and Ω is the angular frequency at the physical radius where the temperature is derived. With T_{S1}∼20-27 K and T_{S2}∼13-15 K, and assuming Keplerian rotation, we find scale heights of H_{S1}∼38-44 AU and H_{S2}∼66-76 AU, hence a disk aspect ratio h_S∼0.12-0.13 at the location of both spirals. Verhoeff et al. (2011) quoted a scale height of 60 AU at the inner rim of the outer disk (h∼0.46). However, considering a disk with i∼28±3° (Pérez et al. 2014) instead of 20° leads to a scale height of 20±7 AU (h∼0.15±0.05) in the inclination/inner rim scale height relation of Avenhaus et al. (2014), thus in agreement with our result.

We can also obtain lower limits on the mass of each spiral assuming LTE. The integrated flux was computed in S1 and S2 from $I_{\rm peak}$(CO 2-1) by defining an aperture 1″ wide in radius, and centered on the best fit model spiral to Kim (2011) equation (see section 7.3.2). We

obtain integrated fluxes of 1.41 Jy and 1.27 Jy for S1 and S2 respectively. Using these values with $T_{ex,S1}$ and $T_{ex,S2}$, a velocity dispersion of ∼0.3 km s^{-1} (see Figure 7.8d), and assuming [H_2]/[CO] = 10^4, the total gas mass in each spiral is $M_{S1} \gtrsim 1.38 \times 10^{-6} M_\odot$ and $M_{S2} \gtrsim 1.23 \times 10^{-6} M_\odot$.

Modelling of the Spiral Arms An elliptical grid is defined to match the inclination and PA of the projected disk, with deprojected bins of 0.125″ in radius and 5° in azimuth. The trace of each spiral is identified with radial cuts in $I_{\rm peak}$, using local maxima for S2 and S3, and local inflection points for S1 (second-derivative nulls). We obtain 16, 20 and 20 points tracing respectively S1, S2, and S3 in the CO 2-1 $I_{\rm peak}$ map (Figure 7.10a); and 17 and 14 points respectively tracing S1 and S2 in the CO 3-2 $I_{\rm peak}$ map (Figure 7.10c). Uncertainties in the measured positions of the spirals were set to max{bin size, quarter of the beam size}. We then perform least-squares fits to each spiral independently using two different parametric formulae, as follows.

The polar coordinates of an acoustic wave created by a planet in a gaseous disk can be approximated by Eq. 6.2. First fits with equation 6.2 were computed by fixing the values of α to 1.5 (Keplerian rotation) and β to 0.25 (see q in section 7.3.2). We found plausible values of h_c (between 0.01 and 1.0) with the points of CO 2-1 $I_{\rm peak}$ map for S1 (h_c = 0.15) and S3 (h_c = 0.27), but not for S2, and for neither spiral with the points of CO 3-2 $I_{\rm peak}$ map. In order to further reduce the parameter space, a second set of fits was run fixing as well the value of h_c to 0.15. The best fit models are shown in *solid dark gray* lines in Figure 7.10b and d; the inflection point in the spiral curves represents the best fit location of the planet. The values of the best fit r_c, θ_c, and χ^2 are given in Table 7.2.

Sweeping β from 0.15 (Pérez et al. 2014) to 0.30 ($q = 0.6$) does not significantly change χ^2 (relative to the spread of values for different spirals) and the value of the other parameters. On the contrary, the best fit parameters depends strongly on h_c; a difference of a few hundredths induces significantly different results, confirming the degeneracy already noted by Muto et al. (2012) and Boccaletti et al. (2013). Since χ^2 depends on the estimated error bars, which are not independently determined, we use χ^2 to compare different models rather than assess their statistical significance. The best fit spiral appears to be S1, while S2 and S3 provide χ^2 values a factor of several times larger.

Another formula suggested by the theoretical work of Kim (2011) approximates the shape of the spiral wake created by an embedded planet on a circular orbit to an Archimedean spiral:

$$r(\theta) = a\theta + b \tag{7.2}$$

where a corresponds to r_p/M_p with r_p the launching radius of the planet and M_p its Mach number, and b is a constant. Parameters for the best fit of each spiral are given in Table 7.2. With a χ^2 value at least twice smaller than the two other spirals, it is again S1 that is best fit. Equations 6.2 and 7.2 are fundamentally different - $\theta(r)$ vs $r(\theta)$, so that χ^2 obtained with each equation should not be mutually compared.

The similar slopes a of S3 and S1 may suggest that S3 is prolongating S1. Conversely, models for S2 and S3 do not share the same slope, even though the point-symmetric of

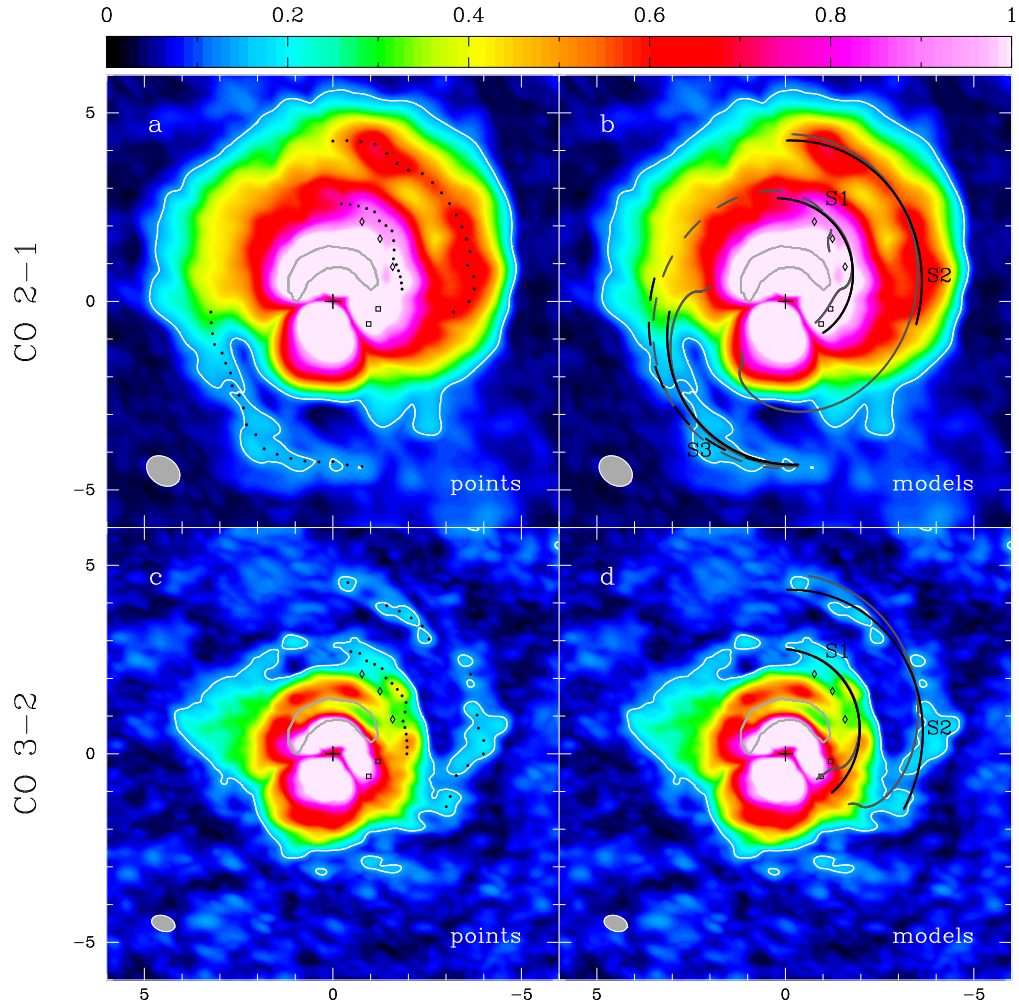

Figure 7.10: Modelling of the spirals observed in the CO 2-1 and CO 3-2 $I_{\rm peak}$ maps. Legends follow from Figure 7.8*b* and *f*. For comparison, we indicate the position of the H-band spiral arm from Fukagawa et al. (2006, *diamonds)*, and the Ks-band spiral root from Casassus et al. (2012, *squares)*.**(a)**: Points tracing the spirals used for the modelling. **(b)**: Modelling of the spiral arms as in Muto et al. (2012, *solid dark gray lines)* and Kim (2011, *solid black lines)*. The *dashed dark gray* and *dashed black* spirals represent the point-symmetric of S2 models with respect to the star. **(c)** and **(d)**: Identical to (a) and (b) with the CO 3-2 $I_{\rm peak}$ map.

S2 with respect to the star roughly coincides with S1 and S3 (*dashed dark gray* curve in Figure 7.10b).

Comparison with NIR Spiral Arms Although S2 and S3 had not been detected before, a spiral arm similar to S1 had already been reported in NIR H and K bands by Fukagawa et al. (2006). Also in NIR, closer-in observations in Ks-band (Casassus et al. 2012), L'-band (Rameau et al. 2012), H- and K-bands polarimetric intensities (Canovas et al. 2013; Avenhaus et al. 2014), all led independently to the detection of spiral structures closer to the star, originating at the outer edge of the gap. In Figure 7.10 we register the contour crests from the spiral of Fukagawa et al. (2006, their Figure 2), as well as the most prominent spiral feature from Casassus et al. (2012, spiral #2 in their Figure 2). Our S1 model extends the radio spiral to its NIR root, suggesting that the H-band spiral arm, its

Table 7.2: Values of the best fit parameters with equations (6.2) and (7.2).

Equation (6.2)		S1	S2	S3
CO 2-1	r_c [arcsec]	1.71 ±0.04	2.13 ±0.24	2.62 ±0.08
	θ_c [deg]	283 ±5	146 ±64	83 ±10
	χ^2	2.38	18.0	4.66
CO 3-2	r_c [arcsec]	1.62 ±0.04	2.69 ±0.38	/
	θ_c [deg]	255 ±7	235 ±45	/
	χ^2	2.05	36.0	/

Equation (7.2)		S1	S2	S3
CO 2-1	a [arcsec rad^{-1}]	0.58 ±0.05	0.20 ±0.05	0.65 ±0.06
	b [arcsec]	-0.86 ±0.29	3.05 ±0.29	2.34 ±0.16
	χ^2	0.16	0.30	0.40
CO 3-2	a [arcsec rad^{-1}]	0.45 ±0.03	0.25 ±0.10	/
	b [arcsec]	-0.02 ±0.17	2.88 ±0.52	/
	χ^2	0.18	2.94	/

[a] For Eq. (6.2), we fixed $\alpha = 1.5$ (Keplerian rotation), $\beta = 0.25$ (from q found in section 7.3.2) and $h_c = 0.15$ (best fit value when h_c is set free for S1 in the CO 2-1 $I_{\rm peak}$ map).

Ks-band root, and the inner rim of S1 are part of the same structure.

Discussion: origin of the spiral arms

Several scenarios have been proposed for the occurrence of spirals in TDs (see e.g. Boccaletti et al. 2013, for a summary). HD 142527, with its well-defined tightly coiled radio spirals in Keplerian rotation, provides an interesting case study suggesting a different origin than the CO spirals in the disk of AB Aur.

S1 could be fit with equations (6.2) and (7.2) assuming an embedded companion (section 7.3.2), although its location on the model spiral could not be precisely constrained. An object has been discovered by Biller et al. (2012) and re-detected in Hα by Close et al. (2014) at ∼12 AU. Extending S1 inwards does not allow us to confirm a possible relationship. Nevertheless, the clearing of a gap as large as 140 AU should involve several planets (e.g. Dodson-Robinson & Salyk 2011). For S2 and S3, both the *relatively* poor least-square fit with equations (6.2) and (7.2) and their very large scales argue in favor of a different cause.

Simulations in the context of protoplanetary disks have shown that two-armed spirals, such as S2 and S3, could be induced by stellar encounters (e.g. Larwood & Kalas 2001; Quillen et al. 2005). Similarly, simulations of Augereau & Papaloizou (2004) and Quillen et al. (2005) reproduce the large scale (∼325 AU) tightly wound spiral observed in the disk of HD 141569 A, by tidal induction from its M-dwarf companions (external to the disk).

Tidally induced spiral structures are transient and vanish within a few orbits, which implies either a very recent encounter or a bound companion external to the disk periodically exciting spirals. For HD 142527 no such object has been detected.

Gravitational instability (GI) is an alternative scenario able to create a grand-design two-armed spiral structure (e.g. Boss 1998). The stability of a disk is characterized by Toomre's parameter, Q (Toomre 1964). Fukagawa et al. (2013) computed an upper limit of 1-2 for Q in the dust continuum horseshoe, so that depending on the gas-to-dust ratio, fragmentation of either the gas or the dust or both components due to GI may occur. Approximating $Q \approx \frac{M_\star}{M_\mathrm{d}} h_S$ (Gammie 2001), with the mass of HD 142527 $M_\star$ set to 2 $M_\odot$, the disk mass M_d set to 0.1 $M_\odot$ (Verhoeff et al. 2011) and the aspect ratio at both spirals h_S∼0.1 (section 7.3.2), we find Q∼2.0 similarly to Fukagawa et al. (2013). This suggests that the outer disk in general, not just the horse-shoe, is stable but close to the instability regime.

7.3.3 Characterization of dedicated simulated spirals

As an increasing amount of observational evidence accumulated on the case of HD 142527, the likely culprit for the distinctive morphology of the disk became progressively more evident. To confirm the suspicions, a set of hydrodynamical simulations were carried out using 3D smoothed particle hydrodynamics code PHANTOM (Price et al. 2017). In this section, I summarize the results of the study presented in Price et al. (2018), focusing on the part that I led: the spiral arm analysis.

The simulations were set up considering the characteristics of the companion and the disk as constrained by the large amount of observations available on the source (detailed in Sec. 7.3.1). The mass of the primary and the companion were set to 1.8 $M_\odot$ and 0.4 $M_\odot$, as suggested by the modeling of the gas kinematics and spectral characterization of the SINFONI spectrum of HD 142527 B, resp. (Casassus et al. 2015a, Sec. 16.1, resp.). Tested orbits for the companion were limited to a range of likely orbits inferred from the astrometric modeling in Lacour et al. (2016). For the disk, a similar model as presented in Casassus et al. (2015a) was used to set the initial conditions. Hydrodynamical simulations were followed by radiative transfer using MCFOST (Pinte et al. 2006, 2009), which enabled a direct comparison of the results with observations at different wavelengths.

For all tested orbits, three or more prominent spiral arms are seen around the cavity (Fig. 7.11). The companion thus already explains why spiral arms are present around the cavity without needing to invoke GI or other physics. Visual comparison of our results with scattered light (Avenhaus et al. 2014, 2017), 2 μm (Casassus et al. 2012, 2013b) images of HD 142527 shows that the blue orbits (top row of Fig. 7.11) tend to produce spirals less consistent with the observations.

In this study, my contribution consisted in the characterization of these simulated spiral patterns and their quantitative comparison to observed spirals. I first started by identifying the trace of the main spirals stemming from the edge of the cavity, by isolating radial local maxima in the appropriate PA and radial ranges. "Main spirals" refer to the "inner" and

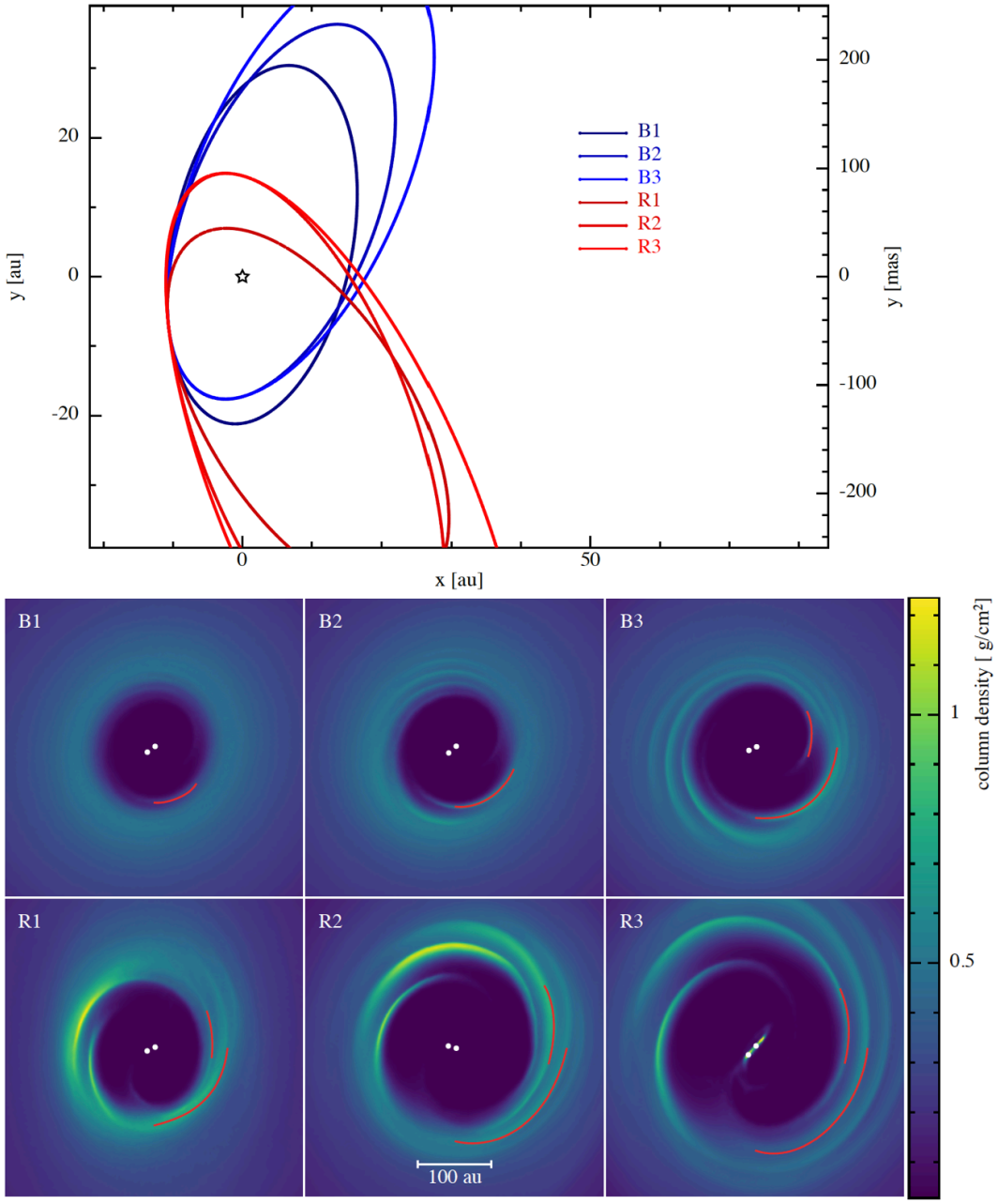

Figure 7.11: Results of the simulations of the disk of HD 142527 with PHANTOM in terms of column density (bottom panels), obtained for different tested orbits of the companion (shown in the top panel) after 50 binary orbital periods. Figure adapted from Price et al. (2018).

"outer" spiral arms, corresponding to the two spirals seen to the SW of the cavity in several of the simulations and in the scattered light observation of the disk (which is provided in Fig. 7.12a). They span position angle ranges of [260°, 305°] and [180°, 270°].

I considered fits of the spiral traces to the various following equations in order to determine how the morphology of the spirals was best reproduced:

- the logarithmic spiral equation: $r = a\mathrm{e}^{b\theta}$;
- the general Archimedean spiral equation: $r = a\theta^{1/n} + b$;

Table 7.3: Characteristics of the spirals obtained with different possible orbits for the companion.

	M (< 90 au) ($\times 10^{-3} M_\odot$)	Pitch ang. (PA 265°)	Pitch ang. (1st half)	Pitch ang. (2nd half)	SW Fork?
Obs	1.7 ± 0.6	4.8°	-3.6°	9.9°	Yes
B1	2.0	1.5°	3.1°	0.0°	No
B2	1.9	1.3°	3.2°	2.5°	No
B3	1.6	5.1°	7.1°	3.2°	No
R1	2.1	-1.8°	-4.0°	0.6°	Yes
R2	1.5	6.0°	6.4°	5.7°	No
R3	1.4	3.6°	6.8°	0.4°	No

Notes: M stands for the residual gas mass in the cavity. The last column reports whether a fork/bifurcation is seen between the spirals at the SW of the cavity. Table from Price et al. (2018).

- the equation derived from spiral density wave theory (Eq. 6.2);
- a polynomial of the form $r = \sum_{i=0}^{4} a_i \theta^i$, which can be considered as a "generalization" of the general Archimedean spiral equation.

Contrarily to the other spiral characterization studies I led (Secs. 6.4.2, 7.2 and 15.5.1), here the disk images (simulated and observed) were not deprojected. The spiral density waves are expected to be launched in the orbital plane of the companion, which is inclined with respect to the outer disk in all tests considered here. The morphology of the companion-induced spirals in the outer disk will thus likely be significantly different than predicted by the spiral density wave equation provided in Eq. 6.2, which considers the case of a companion on an orbit coplanar with the disk. Since the goal here is only to reproduce at best the morphology of the spirals and not necessarily to connect it to the physics, the spiral density wave equation was considered on the same level as the other equations. Only the polynomial led to good visual fits of the spirals when considered on their whole length. Best fit models corresponding to the best fit polynomial equations are thus shown in red in Fig. 7.11.

To compare more quantitatively the simulated spirals with the observed ones, I measured the pitch angle of the outer spirals using the best-fit logarithmic spiral on a short section centered on PA $\sim$ 265°. These values are provided in Table 7.3. I also considered fits to the first and second half of the length of the spiral traces, corresponding to PA ranges of [180°, 225°] and [225°, 270°] (or shorter sections in that range when necessary). These pitch angle estimates over half-lengths enable to infer the trend of the spiral: opening or closing with increasing radius. In order to determine the simulated spirals that are most similar to the observed one, and hence constrain the orbit of the companion, I performed the same least-square fit to the observed spirals reported in Avenhaus et al. (2017, Fig. 7.12a), and reported the results in the top row of Table 7.3.

Orbits B1 and B2 show pitch angles too small and little or no asymmetry in the gas distribution around a cavity which is close to circular. Orbit B3 shows promising spirals to the NE of the cavity, but the spiral arms to the SW show a series of almost-circular tightly wrapped arms not seen in the observations. The red orbits, by contrast, produce a bright

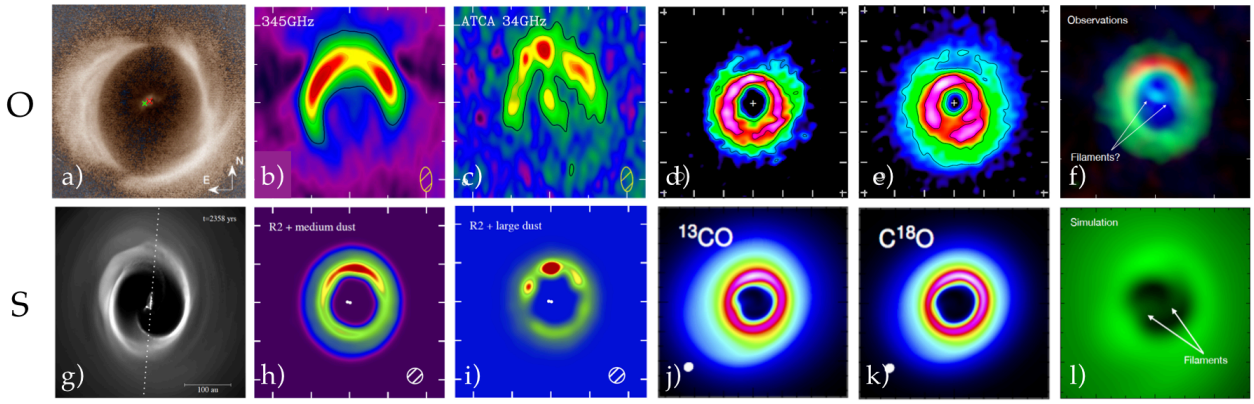

Figure 7.12: Observations (top row) vs simulations of the disk of HD 142527. Details on each panel are provided in the text. References: top row (from left to right): Avenhaus et al. (2017), Casassus et al. (2015a, twice), Boehler et al. (2017, twice) and Casassus et al. (2013b). Bottom row: Price et al. (2018).

spiral structure and asymmetry in both the cavity and the gas distribution more similar to what is observed. In particular, orbit R1 is the only simulation to show a bifurcation in the spiral arms to the SW of the cavity, similar to what is seen in the scattered light image. Orbit R2 is closest to the observed cavity size and develops an eccentric cavity similar to those found in previous circumbinary disc simulations (e.g. Farris et al. 2014; D'Orazio et al. 2016; Ragusa et al. 2016) and used by Ragusa et al. (2017) to explain dust horseshoes. Orbit R3 shows the most open spirals but the overdensity around the cavity is less prominent, making it less promising for the observed dust structures. The cavity size produced in that simulation is also too big. Based on these considerations, we infer that the orbit of the companion must be part of the "red" family, most likely with intermediate orbital parameters between R1 and R2.

The fact that the most likely orbit for the companion has a very large eccentricity and consists of a polar alignment with the outer disk appears to confirm observationally the mechanisms that have been proposed to excite orbital eccentricity (e.g. Artymowicz et al. 1991; Papaloizou et al. 2001; Dunhill et al. 2013) and inclination (Martin & Lubow 2017; Zanazzi & Lai 2018). More details on these physical mechanisms are provided in Sec. 3.4.2.

Interestingly, R2 shows a significant gas overdensity spiral coincident with the location of the dust trap. As seen in Sec. 6.2.2, a pressure or density bump is what is expected to give rise to dust traps. In order to check whether these could be related, two new hydrodynamical simulations were run including grain sizes of 100 μm and 1 mm, resp., and using orbit R2 for the companion. The results of these simulations (shown in Fig. 7.12h and i) compare very well with ALMA and ATCA observations (Fig. 7.12b and c). Therefore, the spiral density wave induced by the companion alone appears able to account for the azimuthally asymmetric dust trap, without recourse to vortices or additional companions.

Apart from the spirals and the dust trap, a range of other diagnostics were used in the study to evaluate the resemblance between simulation results and observations, including the size of the cavity, the profile at the edge of the cavity, the gas surface density, the velocity profile and gap-crossing filaments. Some of these qualitative comparisons are provided in Fig. 7.12. For example, the expected ^{13}CO and C^{18}O line intensity maps (Fig. 7.12j and k,

resp.) are similar to the observed ones (Fig. 7.12d and e, resp.; Boehler et al. 2017). Simulations also predict observable gap-crossing streamers, which might have been hinted at in ALMA data (Fig. 7.12f and l, resp.; Casassus et al. 2013b). All together, the results of the simulations all compare qualitatively well with the observations, with the only sources of discrepancy accountable by the lack of shadows in the simulation. Indeed, the parameters of the inner disk used in the simulation did not lead to an optically thick inner disk. In summary, the dynamical interaction of the binary, on its inclined and eccentric orbit, with the disk can account alone for the observed disk morphology.

8 Transition disks within disk population studies

8.1 Complete surveys of protoplanetary disks

As summarized in Sec. 2.3, transition disks are a particular type of protoplanetary disks, showing large annular gap(s) or a cavity in their surface density distribution. As such, they became prime targets for studies of individual remarkable targets using state-of-the-art instruments at all wavelengths. The observed population is biased towards very bright targets (typically Herbig Ae/Be/Fe disks). This observational bias fits within the natural pattern followed by astronomers when they study a specific type of object with new instruments: the community first focuses on the bright shiny objects (in this case the Herbig transition disks), more easily observed, before tackling more challenging/fainter objects. As the observational bias resorbs with time, complete surveys of the whole population of disks can provide the most useful information. A statistical analysis of the results of the survey enables to put the shiny objects into context, and infer whether they are a common output of disk evolution or whether they are rather outliers in the distribution.

First studies of transition disks within complete surveys of protoplanetary disks relied on SEDs. Results from *Spitzer* suggest that about 10–20% of 3–10 Myr old protoplanetary disks are transition disks (Muzerolle et al. 2010). The large uncertainty on that estimate stems from the fact that it can be difficult to draw a clear boundary between transition disks and young significantly depleted debris disks just from the SED. Large scale studies of disks within a single population have recently started with ALMA (e.g. Ansdell et al. 2016; Barenfeld et al. 2017, for Lupus and Upper Sco, resp.), and are likely to provide much better constraints regarding possible disk evolutionary paths, thanks to direct comparison between primordial and transition disks within the same population. In particular, the results of the first *resolved* study of disks within a complete population (that of Lupus) have recently brought insightful perspectives on the nature of transition disks (van der Marel et al. 2018). Transition disks with a large cavity ($\gtrsim 20$ au) appear to constitute $\gtrsim$11% of all disks in Lupus (hence within the range inferred from SED modeling), lie at the high-end in terms of protoplanetary disk masses (based on mm-flux and outer disk radius), show similar accretion rates as primordial disks, and are found preferentially around early type stars (Ansdell et al. 2016; van der Marel et al. 2018). The amount of residual gas in the observed cavities appears more compatible with the gap being dynamically carved by

companions rather than being induced by the dead zone.

How can the occurrence rate of $\gtrsim 11\%$ be interpreted? Assuming that all protoplanetary disks pass through a transition disk phase, this ratio can be used to infer the average timescale involved for the dispersal of the primordial disk. A ∼11% occurrence rate of depleted disks would then suggest that disk dispersal typically lasts 0.3–1 Myr, as was already inferred based on the results obtained from SED modeling (e.g. Haisch et al. 2001; Mamajek 2009). However, the facts that (1) the resolved gas and dust distribution in these disks suggest they are dynamically carved by embedded companion(s) rather than being induced by photoevaporation or dead zones (van der Marel et al. 2018), and (2) only a fraction of all mature systems appear to harbor giant planets (e.g. Winn & Fabrycky 2015) could suggest that not all protoplanetary disks will pass through a transition disk phase; possibly only those forming massive giant planets or forming substellar companions. This option appears also more compatible with transition disks mostly overlapping with the high-mass end of the protoplanetary disk mass distribution (since more massive disks are more likely to form massive companions). Therefore the assumption that transition disks constitute an evolutionary phase through which *all* primordial disks pass might be flawed, and hence previous disk lifetime estimates could be significantly biased.

Nonetheless, the interpretation that transition disks lie at the high mass end of protoplanetary disk distribution has to be considered with caution. While it is possible that transition disks present the same bias as other (non-gapped) class II disks, it is also possible that they suffer much less from this bias due to the assumption of optically thin sub-mm continuum being more appropriate in this gapped disks. In the latter case, the inferred masses for transition disks would be closer to their true values, but would make them appear similar in mass as the significantly biased masses estimated for non-gapped disks.

To test the hypothesis that transition disks represent the outcome of only one of several possible evolutionary branches, conditioned by the occurrence of a particular mechanism such as the formation of giant planets, it is useful to compare their occurrence rate to that of giant planets, as constrained from surveys using indirect and direct detection techniques. Radial velocity surveys have found giant planets around about $\sim 10\%$ of main sequence stars (Cumming et al. 2008; Howard et al. 2010), while direct imaging surveys constrain the occurrence of giant planets with a mass $> 5 M_{\rm Jup}$ beyond 10 au to be 1–3 % (Brandt et al. 2014, see Sec. 4.1;). It is noteworthy to recall that the two methods are intrinsically biased to giant planets on short and large orbits, resp., so that the demographics in the ∼3-20 au range are in practice poorly constrained. This separation range precisely overlaps with the extent of the large gaps found in mm-bright transition disks (and resolved with ALMA). Comparison with the ∼10% occurrence rate of transition disks with large gaps found in van der Marel et al. (2018) requires thus caution. Nevertheless, it is interesting to note that this occurrence rate appears similar to that of giant planets found at close separation, and discrepant with that inferred from the fraction of directly imaged giant planets at large separation. If large gaps are indeed carved by multiple giant planets, this result would suggest one or several of the following possibilities: (1) the occurrence of giant planets at 5–20 au is more consistent with an extrapolation of the occurrence found by indirect detection methods at short separation (hypothesis also suggested in Dong & Dawson 2016); (2) giant planets are significantly less luminous than predicted by formation and evolution models

at an adolescent/mature age (Sec. 3.3), so that direct imaging surveys are underestimating their occurrence (hypothesis also suggested in Dong et al. 2018b, to account for the non-detection of spiral-inducing companions); or (3) most giant planets migrate significantly inward in these large cavities, so that by an adolescent age, they would mostly lie within a few au separations from the star, either due to gravitational interaction with the gaseous disk or (later) with a disk of planetesimals (see e.g. Sec. 3.4).

Another possibility is that undetected low-mass binary stars at short separation, also dynamically carving large cavities (see the example of HD 142527 B, Sec. 7.3), contribute to a non-negligible fraction of these 11% transition disks with large gaps. Not only are these binary companions still difficultly detectable at short separation, but they are also known to be more abundant around earlier type stars (e.g. Duchêne & Kraus 2013b), which might also be related to the fact that transition disks with large gaps are preferentially found around Herbig Ae/Be stars. This contribution is difficult to assess, but might help making up to the $\sim$11% fraction of disks with large gaps compared to the 1–3 % systems with directly imaged giant planets on very large orbits. To gain more insight, a more detailed comparison of occurrence rates as a function of spectral type and age of the cluster could be helpful, and would hence require the study of other star-forming regions to improve the statistics.

Finally, while the study of van der Marel et al. (2018) suggests that transition disks with large cavities trace a specific evolution path affecting mostly massive primordial disk, the question is still open for lower mass disks. Only new higher resolution ALMA images of those disks will enable to test whether they do evolve forming smaller cavities (unresolvable yet) or whether they generally slowly dissipate without creating a cavity.

8.1.1 ODISEA

Complete surveys in other star forming regions are required to corroborate these first results obtained in Lupus. These would provide a more accurate occurrence rate of transition disks with large cavities (for comparison with giant planet occurrence rates) and enable to study the dependence of that rate with the star forming environment and age. In particular, the Ophiuchus DIsk Survey Employing ALMA (ODISEA; Cieza et al. in prep.) could provide some useful new constraints. This project consists of a complete survey of all disks in the Ophiuchus molecular cloud, obtained with ALMA in band 6 continuum (1.3mm) at an angular resolution of $0\farcs2$ ($\sim$25 au), complemented with multi-wavelength data on all sources. A specific aspect of this large endeavour is an IR direct imaging snapshot survey of all members of the region, which will enable to corroborate disk images with the presence of binaries. Sources were divided between VLT/NACO (70 targets) and Keck/NIRC2 (51 targets) not only to lighten the observational load requested on each instrument, but also to take advantage of the specificities of each instrument; NACO has an IR wavefront sensor providing AO correction for sources up to K = 12 mag, while NIRC2 is equipped with a laser guide star.

In this context, Dr. Alice Zurlo and I prepared the proposal and performed the obser-

vations for the NACO part. The observations with NACO were carried out from April 8 to April 11, 2017 (4 half-nights), as part of program 099.C-0465 (PI: Zurlo). The atmospheric conditions were in general favorable, especially during the last night, with a stable DIMM seeing between 0″.5 and 0″.7 and a coherence time $\gtrsim$ 5ms. For time efficiency, we made use of the *star hopping technique* between each target (detailed in Sec. 11.3.1). We divided our sample of 70 stars into 10 groups of 7 stars each. In each group, the maximum brightness difference was 1 mag. The groups were also made based on proximity of the stars in the sky.

We managed to observe 88 stars in total, hence more than the 70 sources initially foreseen, overlapping with the sources to be observed with NIRC2. Along with Alice, I then supervised undergrad student Antonia Fernandez for the reduction of the NACO data. The data reduction enabled to unveil the presence of 11 binaries (hence $\sim$12.5% of the sources). The fraction is higher in the NIRC2 sample, so that the total average is $\sim$18%. In these multiple systems, not all components are detected with a disk in the ALMA images and the fraction of resolved disks is much lower (Cieza et al. in prep.), which appears in agreement with the fact that disks in multiple systems tend to be less massive and smaller in extent. The stellar multiplicity and the impact of (sub)stellar companions on the disks will be presented in Zurlo et al. (in prep.).

9 Summary and future plans

9.1 Planet signposts in transition disks

In Chap. 6, I reviewed literature to show that large annular gaps/cavities, asymmetric dust distributions, shadows, warps and spiral arms, could be produced by a range of different physical mechanisms, but that all of them also shared the common trait of being accountable for by the dynamical interaction of the disk with an embedded companion. Furthermore, for some of these companion signposts, such as large dust cavities observed with a decrement in gas surface densities (Sec. 6.1.2) and warps (Sec. 6.3.2), there does not appear to be any physical mechanism other than dynamical interaction with a companion to account for their observed morphology. Therefore, large dust cavities with residual gas, warps and two-sided shadows (indicative of an inner warp) can be considered the strongest morphological indicators of companion presence in the disk. The companion producing these features is not necessarily in the planet-mass regime though, as testified by the examples of HD 142527 (Sec. 7.3) and HD 100453 (Wagner et al. 2015; Benisty et al. 2017). Another source where two-sided shadows are observed and a warp is inferred, but no companion is found yet is DoAr 44 (Casassus et al. 2018a), which makes it an ideal source for HCI follow-up in order to detect the companion.

9.2 Origin of the observed spirals

Among different companion signposts, I focused specifically on the origin of spiral arms, and the information that can be inferred from their morphology. Our estimations suggest that *flybys* are a very unlikely origin for the observed spirals. The *late-envelope infall* hypothesis, testable with velocity dispersion maps, so far appears able to explain only the large-scale spirals in AB Aur (Tang et al. 2012). Similarly, only the large-scale spirals of HD 100456 could correspond to a large-scale warp, but the characteristic double spirals separated by a dark lane is not observed in other disks. *Shadow*-induced spirals have a similar morphology as companion-induced spirals, although showing in general larger pitch angles (as inferred from my contribution presented in Sec. 7.1). However, they require the presence of two-sided shadows, associated with an inner warp. Only three disks correspond to that case, and hydro-dynamical simulations suggest that the observed spirals in two of them could be dynamically induced by the M-dwarf companion (HD 142527 and

HD 100453).

Gravitational instability can generate spirals provided that parts of the disk comply with the Toomre criterion. The morphology of the spirals of Elias 2-27 are most compatible with such an origin, although Elias 2-27 is arguably closer to a protostellar disk than a *bona fide* transition disk (Pérez et al. 2016; Tomida et al. 2017). For bona fide transition disks, the process has been considered unlikely to be at play given the disk mass requirements to reproduce the morphology of observed spirals (e.g. Dong et al. 2015a). However, I argue conservatively that it might have an impact if the known biases affecting disk mass estimates turn out to be larger than expected (Sec. 2.1). This conservatism is somewhat justified by (1) the fact that transition disks with large gaps could overlap with the upper-end of the mass distribution of protoplanetary disks (Sec. 8.1), and (2) the high stellar accretion rates measured for Herbig disks with spiral arms (e.g. Hartmann et al. 1998; Andrews & Williams 2007).

Apart possibly from GI and two-sided shadows when present, *embedded companions* appear as the most amenable explanation for two-arm spirals observed in transition disks (as has been proposed by many authors, see Table 6.2). Numerous hydro-dynamical simulations have suggested that spirals similar to observed ones could indeed be launched by companions located outward from the spirals (e.g. Dong et al. 2015b; Zhu et al. 2015). Embedded companions could also intrinsically account for a certain variety in spiral morphologies, given the different possible combinations of mass, number of companions and orbital parameters (e.g. inclination and eccentricity). Several mechanisms might be at play at the same time, as suggested in Pohl et al. (2015) for planet-induced spirals in a marginally unstable disk, which might also account for the observed diversity.

Compared to other planet signposts discussed in Chap. 6, I argue that spiral arms might contain the most information about the companion that is launching them – if that is indeed their origin. The global shape of the spiral (Ogilvie & Lubow 2002; Rafikov 2002), its pitch angle (e.g. Zhu et al. 2015; Dong et al. 2015b), its contrast (Dong & Fung 2017b), the number of observed arms (e.g. Bae & Zhu 2017b) and the separation angle between primary and secondary arms (Fung & Dong 2015; Bae & Zhu 2017b) can all be used to constrain the mass and location of the perturber. Its location can also be constrained through proper motion measurement given a sufficient time baseline since the spirals are expected to be co-rotating with the progenitor body (Lomax et al. 2016; Ren et al. 2018).

9.2.1 Case of MWC 758

I used most of the above-mentioned metrics in the case of the spirals of MWC 758 (Sec. 7.2): the trace of each spiral was identified and fitted to the spiral equation inferred from density wave theory (Rafikov 2002; Muto et al. 2012, Sec. 7.2.4), the evolution of the pitch angle was measured for each spiral (Sec. 7.2.6), the separation angle was measured between each pair of spirals (Sec. 7.2.7), and a tentative proper motion analysis was performed between observations of the spirals obtained at two different epochs (Sec. 7.2.5). The results obtained from this in-depth characterization of the spirals morphology then fed the dis-

cussion on their possible origin. We reached the conclusion that with the images at hand it was not possible to disentangle unambiguously which mechanism is indeed producing the observed spiral pattern. However a scenario involving two companions, where only one candidate was possibly detected so far in the cavity (Sec. 12.1.1; Reggiani et al. 2018), would account best for the full morphology of the disk (eccentric cavity+spirals+double dust trap), and be compatible with the current constraints on the mass of the disk (disfavoring the GI scenario). This two-companion hypothesis appears supported by recent hydro-dynamical simulations (Barraza et al. 2018, in prep.).

9.2.2 Case of HD 142527

Based on ALMA observations of the CO J=2-1 and J=3-2 lines obtained on HD 142527, we discovered some of the first sub-mm gaseous spirals in a transition disk (Sec. 7.3.2). They appear to be very cold, with estimated brightness temperatures lower than the freeze-out temperature of CO, which could suggest efficient desorption from the grains (e.g. Hersant et al. 2009), dust settling (Dullemond & Dominik 2004a) or that dust is depleted at those large separations. These spirals are found at very large scale ($\gtrsim$500 au), which appears difficult to reconcile with an origin related to dynamical interaction with a companion. Given that $Q \sim 2.0$ for the whole disk, an underestimation of the disk mass could make the disk marginally unstable. Therefore, they might be induced by GI or by the shadows (which are known to create more conspicuous spirals in gravitationally unstable disks; Sec. 7.1).

For that system, I also characterized the spirals produced in hydro-dynamical simulations probing the dynamical effect of the binary companion on the disk. I characterized both the simulated and observed spirals in terms of pitch angle evolution and best-fit geometric model. An important result from that study is that the characterization of the spiral arms enabled to provide new constraints on the orbital parameters of the companion. Another conclusion from that analysis is that an inner companion appears able to launch one or several spirals in the outer disk if it is on an inclined and eccentric orbit. Finally, the strongest spiral density wave launched by the companion in the outer disk could trigger the large dust trap (due to the associated gas surface density bump), instead of requiring a vortex (Sec. 6.2.2). This mechanism might deserve more thorough investigation as it could account for the morphology of other systems where a spiral arm is coincident with an elongated dust trap (i.e., HD 135344 B and V1642 Ori; van der Marel et al. 2016a; Kraus et al. 2017).

9.3 Future plans

9.3.1 Origin of the large scale spirals of HD 142527

Hydro-dynamical simulations presented in Sec. 7.3.3 reproduce most of the features of the disk, but were inconclusive regarding the origin of the CO spirals lying at $\gtrsim$500 au from the star. Whether these spirals are due to shadows or GI will be further investigated during my postdoc by comparing the results of new hydro-dynamical simulations with ALMA cycle 3 data acquired at higher angular resolution, that I had no time to analyze yet.

9.3.2 Spirals launched by companions on orbits non-coplanar with the disk

An interesting result from the hydro-dynamical simulations presented in Sec. 7.3.3 is that a companion in a cavity appears able to launch spirals in the outer disk if its orbit is eccentric and misaligned with the outer disk. This conclusion incentivizes new hydro-dynamical simulations to test whether spiral arms observed in other disks could be due to inclined/eccentric companions in the cavity, rather than in the outer disk, where they have been elusive so far despite stringent constraints on their mass (e.g. Sec. 12.1.1, Reggiani et al. 2018; Maire et al. 2017, for MWC 758 and HD 135344 B, resp.). This possibility is further supported by recent hydro-dynamical simulations suggesting that both the orbital eccentricity and inclination of low-mass companions located within the gap of a transition/circumbinary disk could be excited by an initially mild perturbation (Sec. 3.4.2). To my knowledge, apart from the simulations presented in Sec. 7.3.3, only Arzamasskiy et al. (2018) have considered the shape of the spirals launched by a companion on an inclined orbit with respect to the disk. However, the companion they injected was 10^{-4} times the mass of the central star, and the resulting outer spiral appears faint. Therefore, during my post-doc I plan to use 3D simulations considering more massive companions to test whether the spirals of MWC 758 or HD 135344 B could be due to such kind of companion in the cavity.

III High-contrast imaging of companions in thermal infrared

Several circles (Kandinsky, 1926)

High-contrast imaging (HCI) in thermal IR can test the hypothesis that transition disks with large dust cavities are dynamically induced by embedded companions. In this part, I first summarize different HCI techniques used in this thesis, including adaptive optics, coronagraphy, dedicated observing strategies and algorithms, and the tools used to assess the achieved contrast in post-processed images (Chap. 10). This review does not intend to be comprehensive, but rather aims to provide the necessary information to understand the results from my personal contributions, which are presented in the other chapters of this part.

Chapter 11 presents the survey that I led with VLT/NACO to search for protoplanets in transition disks. The target selection, observations, data reduction process, results and future perspectives to complete this on-going survey will be described in details. A significant fraction of the chapter is devoted to the discussion of the results obtained for selected targets of interest, showing either a protoplanet candidate or scattered light emission from the disk.

In Chap. 12, I present my contributions to the detection of companions in datasets obtained outside the context of the VLT/NACO survey. A companion candidate has been found in the transition disk MWC 758 using Keck/NIRC2 data similar to the ones obtained with VLT/NACO. This discovery is presented in Sec. 12.1, along with the detection of a third spiral arm in that system, although the in-depth spiral arm analysis is provided in greater details in Sec. 7.2.

Finally, I briefly describe the detection and spectral characterization of a very red substellar companion in the debris disk of HD 206893 (Sec. 12.2), to which I contributed through the confirmation of the companion in VLT/NACO+AGPM data in thermal IR, and the independent extraction of the spectrum of the companion in SPHERE/IFS data.

A summary of the results and of my future plans regarding the HCI survey I carried out with NACO is provided in Chap. 13.

Observing in thermal IR has been likened to observing visually through a telescope lined with luminescent panels and surrounded by flickering light as though the telescope were on fire.

Low & Rieke, 1974

10 Overview of high-contrast imaging techniques

In order to maximize the chances of detecting exoplanets, the HCI planet hunter employs a specific set of tools both in terms of hardware and software. In addition, an appropriate observing/hunting strategy is required to take advantage of the available tools. The "prey" is indeed elusive; a faint blob, several orders of magnitude fainter than its parent star, camouflaged among similar looking blobs, so-called *speckles*, which are due to imperfections of the instrument. The challenge is often compared to detecting a firefly 1 m away from a lighthouse, when observed 1000 km away. Nonetheless, the task is not impossible as testified by the different detections obtained so far (Sec. 4.2).

In this Chapter, I present a brief overview of the content of the HCI exoplanet hunting bag, namely adaptive optics (AO) systems (Sec. 10.1), coronagraphs (Sec. 10.2), and advanced post-processing algorithms (Sec. 10.4). The latter are specifically designed for the adopted hunting strategy: *differential imaging* (Sec. 10.3). In Sec. 10.5, I will finally briefly explain how to estimate the significance of any potential detection and the contrast achieved in the final images.

10.1 Adaptive optics

In order to image exoplanets, the larger the telescope the better. Not only does a larger primary mirror enable to collect more light, but angular resolution is inversely proportional to the diameter of the telescope. This second assertion is conditional though. While a larger diameter does involve a smaller theoretical diffraction limit, in practice *atmospheric turbulence*, if not treated, will distort the incoming wavefront in such a way that the angular resolution of the largest telescopes can be reduced to that of a mere 20-cm amateur device. AO systems deal with turbulence in real-time, in order to restore the (almost full) potential of angular resolution of the telescope. An alternative to bypass the atmospheric turbulence issue is to go to space, where the absence of atmosphere enables to achieve the telescope's full resolving power. However, given that space telescopes are generally of smaller size than ground-based ones, a trade-off is to be made between stability/sensitivity and angular resolution.

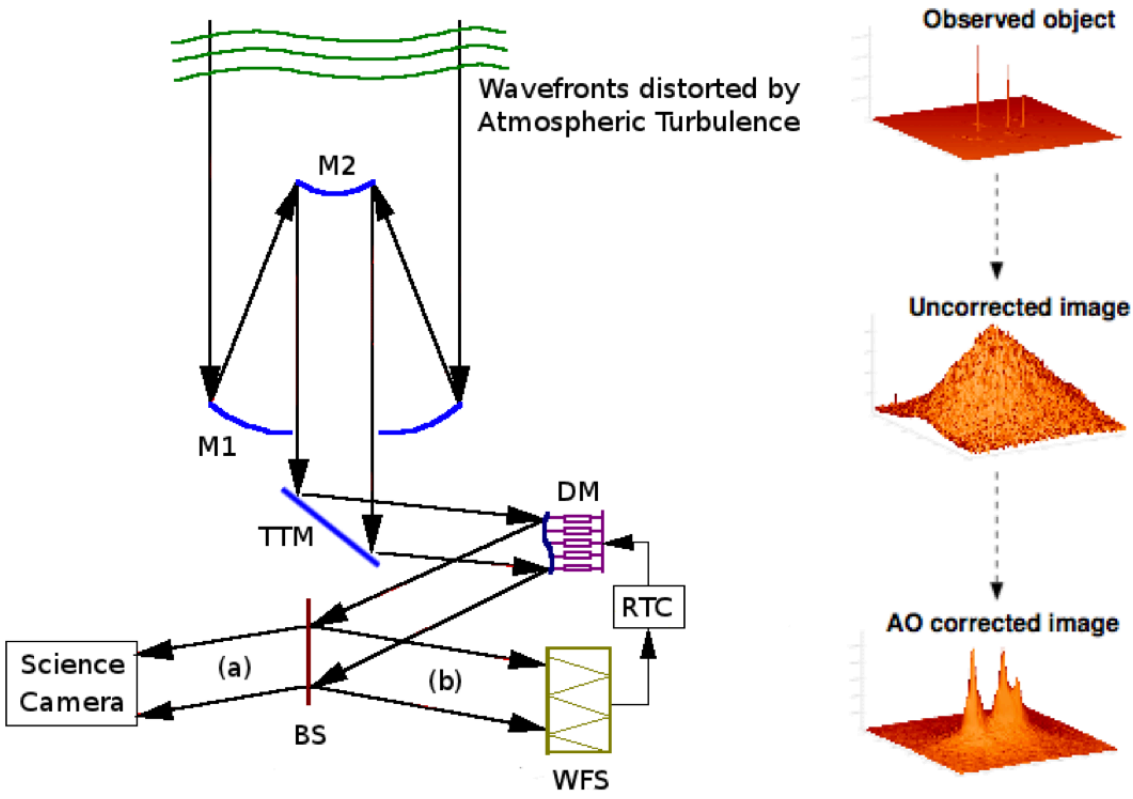

Figure 10.1: (*left*) Simplified diagram of an AO System. See text for details. (*right*) Intensity field in the image plane for multiple punctual sources before and after AO correction. Credit (right panel): NACO manual, ESO.

Before exploring in more details what AO systems are made of, I define what it is not. Adaptive optics is not to be confused with *active optics*, which is also an indispensable component of 8m-class telescopes. The latter is the technology used to prevent deformations of the primary mirror and operates to compensate larger amplitude aberrations. These distortions can be due to mechanical shear, temperature variations or wind. The timescale of these corrections is relatively longer (~ 1 s) as those variations are slower than atmospheric turbulence.

Figure 10.1 shows a sketch of the different components of an AO system. Incoming wavefronts from the observed target are distorted by turbulence in different layers of the atmosphere. When they arrive at the telescope, they are reflected by the primary and secondary mirror (M1 and M2), and then by the tip-tilt mirror (TTM) and the deformable mirror (DM). This is where the AO loop begins. The TTM and DM correct the overall wavefront tilt wobbles and higher orders fluctuations, respectively. The light is then divided by a beam splitter (BS). The transmitted part of the light goes to the science camera, but can still pass through several optical elements on its way there (such as a coronagraph). The reflected part is used to feed the wavefront sensor (WFS), which measures the amplitude of the wavefront distortions. These measurements are then processed by a Real-Time Computer (RTC), which provides the required corrections to the actuators of the DM and to the TTM in order to flatten the wavefront.

In the next subsections, I briefly describe the concepts of Strehl ratio and speckles,

which will be most relevant for the discussion of the results presented in Secs. 11.3 and 15.2. A detailed technical description of the different components of an AO system is beyond the scope of this thesis. I defer the interested reader to Rigaut (2015) and references therein for more details.

10.1.1 Performance of AO systems

Excluding the random variable that represents atmospheric conditions, the overall performance of an AO system depends on the characteristics of each of its components, including the number of subapertures in the WFS, the number and accuracy of the actuators behind the DM or the rate at which the wavefront is reconstructed (e.g. Girard 2011). The main figure of merit used to quantify the overall performance of an AO system is the *Strehl ratio* (hereafter Sr). It is defined as the peak intensity of a measured PSF to the peak intensity of a perfect diffraction-limited PSF for the same optical system:

$$\mathrm{Sr} = \frac{I(\mathbf{x}=0)}{P(\mathbf{x}=0)} \tag{10.1}$$

where $\mathbf{x}$ stands for the position vector, $I(\mathbf{x}=0)$ for the maximum intensity of the measured PSF and $P(\mathbf{x}=0)$ for the maximum of the diffraction-limited PSF. An equally often used way of estimating Sr is the so-called Maréchal approximation, which gives an alternative expression based on wavefront errors: $\mathrm{Sr} = \exp[-\sigma_\phi^2]\exp[-\sigma_\chi^2]$, where σ_ϕ^2 is the wavefront phase variance and σ_χ^2 is the variance of the log-normal amplitude at the pupil plane (Marechal et al. 1994).

For exoplanet detection, the quality of the AO correction is primordial as uncorrected aberrations lead to a swarm of speckles in the vicinity of the star (see next subsection), which significantly degrades the achieved contrast in the image. Second generation AO instruments such as SPHERE at the VLT ($\sim$ 1000 actuators) routinely reach Sr $\sim 85\%$ in H band (e.g. Fusco et al. 2006; Beuzit et al. 2008). By comparison, current on-sky performance of first-generation AO instrument such as NACO at the VLT (14x14 WFS subapertures, 185 actuators) reach about $\sim$40% in H-band, $\sim$60% in Ks-band and $\sim$80% in L'-band for observations with average seeing and coherence time.

10.1.2 Speckles

Speckles are the manifestation of residual wavefront aberrations in the image plane. They take the form of bright spots of typical size $\sim \lambda/D$ and whose brightness depends on the brightness of the star, the fraction (1-Sr) of residual light in the halo, and the angular separation to the star. They are due to both atmospheric and instrumental causes. AO can reduce significantly, but not totally, aberrations due to atmospheric turbulence. The timescale of their variation is $\sim$1-10 ms, *atmospheric speckles* are thus said to be *short-lived*. Therefore, the straylight pattern averages itself out into a smooth halo over the course of the observation.

On the other hand, the so-called *quasi-static speckles* are typically due to the secondary mirror's mechanical support (the "spiders"), imperfections of the telescope mirrors, and non-common path aberrations in the instruments (i.e. wavefront aberrations occurring downstream from the beamsplitter and hence not sensed by the WFS). They are more problematic to deal with as they slowly vary with time, on a timescale ranging from a few minutes to a few hours (e.g Fitzgerald & Graham 2006; Hinkley et al. 2007), because of temperature or pressure fluctuations, mechanical flexures, moving optics, guiding errors, differential refraction effects depending on altitude, or other phenomena (see e.g. Marois et al. 2005, 2006), hence the *quasi-static* denomination. In the case of high-contrast imaging, quasi-static speckles add themselves up over the whole observing sequence, and become dominant over signals that average out, such as photon noise of the diffraction wings and the sky, readout noise and atmospheric speckles (Macintosh et al. 2005), thereby forming a central bright quasi-static pattern. This fact prevents the sensitivity to off-axis companion from increasing with integration time and has the undesirable effect that true companions cannot be distinguished from those artifacts (e.g. Marois et al. 2005). In particular, a major problem consists of *pinned speckles*, which are speckles resulting from an amplification of the variance levels of the stellar PSF at the radial locations corresponding to the bright Airy rings (e.g. Bloemhof et al. 2001; Soummer et al. 2007).

The bright swarm of quasi-static speckles can be dampen thanks to better non-common path aberration calibrations applied to the instrument, through the use of coronagraphy (Aime & Soummer 2004; Soummer et al. 2007), and by appropriate observing strategy and data reduction (described in the next sections).

10.2 Coronagraphy

Pupil edges are responsible for diffraction effects as they correspond to an abrupt transition in intensity between the pupil interior and exterior. Since image and pupil planes are Fourier transforms of each other, this transition results in strong oscillations (diffraction rings) in the impulsive response of the telescope, or point-spead function (PSF). As mentioned in Sec. 1.3, the brightness ratio between a putative planet (say a *Jupiter*) and the stellar diffraction rings is $\sim 10^{-6}$ for an 8m-class telescope at a wavelength of 3.8 μm at the first diffraction ring. To reduce the stellar photon noise against which the planet signal must be distinguished, it is thus necessary to separate the planet and stellar signals with resolved imaging (AO contributes to that respect), but also to reduce the level of these diffraction wings, and this is where *coronagraphy* is useful. Coronagraphs do not only reduce the photon noise, but also the quasi-static speckle noise level, thereby reducing the brightness of *pinned speckles* (e.g. Aime & Soummer 2004; Soummer et al. 2012). Finally, since coronagraphs decrease the stellar flux arriving on the detector, longer integration times can be used in the observations before reaching saturation, which implies less readouts, and hence less overheads. An additional benefit of using coronagraphs is thus that they enable more time-efficient observations, which in turn results in more time spent to accumulate precious photons from putative companions. A great diversity of coronagraphs exist, involving amplitude masks (e.g. the Lyot mask), phase masks, hybrid masks (ampli-

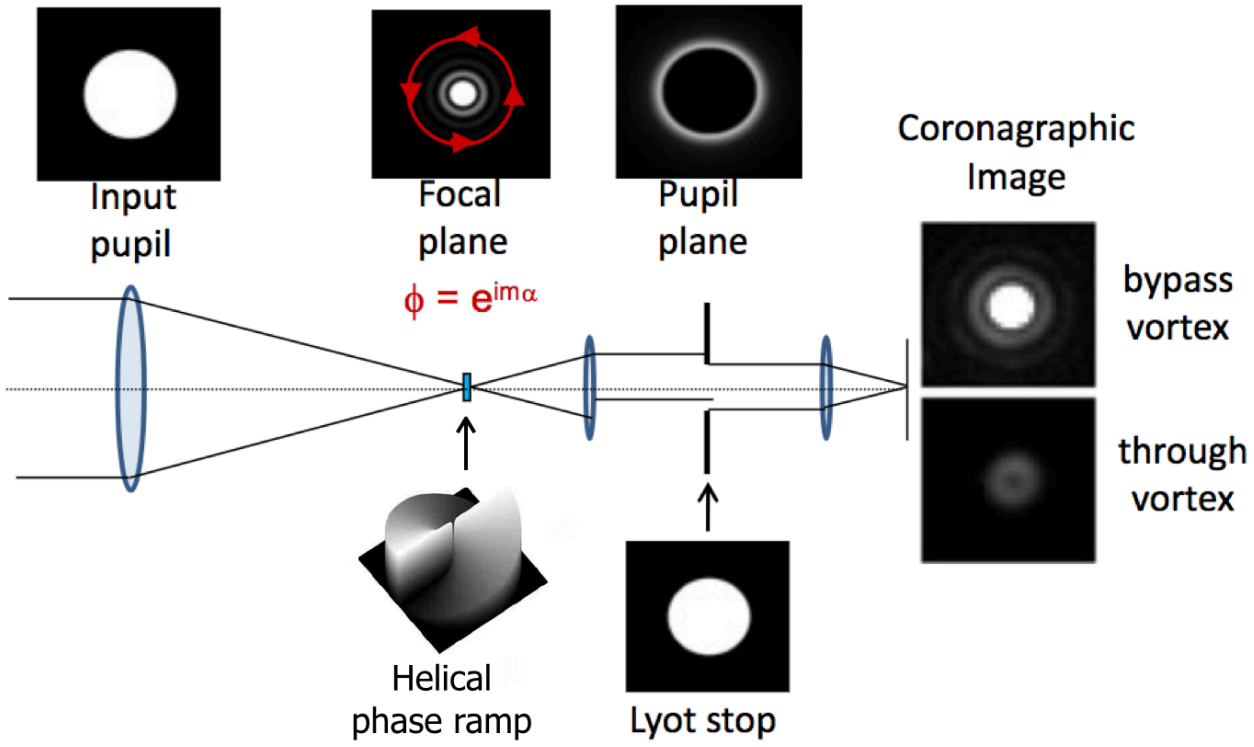

Figure 10.2: Working principle of the vortex coronagraph. A vortex phase mask is placed in an intermediate focal plane. It induces a helical phase shift, forming a singularity in its center which efficiently removes on-axis stellar light when adding a diaphragm in a downstream pupil plane. See text for details. Credit: G. Serabyn.

tude and phase) or interferometric coronagraphs. A summary of all types of coronagraphs is beyond the scope of this thesis, and I defer the interested reader to Mawet et al. (2012) for a review of small angle coronagraphs. Instead, I only provide a description of the Annular Groove Phase Mask (AGPM), as it is the coronagraph that I used in the survey of transition disks presented in Sec. 11.

10.2.1 The Annular Groove Phase Mask coronagraph

The AGPM is a particular implementation of vector vortex phase mask, whose working principle is presented in Fig. 10.2. A vortex phase mask is placed in an intermediate focal plane of the optical path of the telescope, and applies a helical phase ramp to the light passing through; the amount of phase shift depends on the azimuth angle with respect to the optical axis. Due to the helical phase shift, a singularity forms at the center of the mask; on-axis light interferes destructively producing a so-called *optical vortex*. This singularity propagates to the downstream pupil plane, such that all the on-axis light is rejected outside the geometric pupil area (Mawet et al. 2005). A slightly undersized Lyot stop in the downstream pupil plane then enables to remove the diffracted stellar light.

The creation of an optical vortex using annular grooves etched onto a transparent substrate with a sub-wavelength period was first proposed in Mawet et al. (2005). Other work-

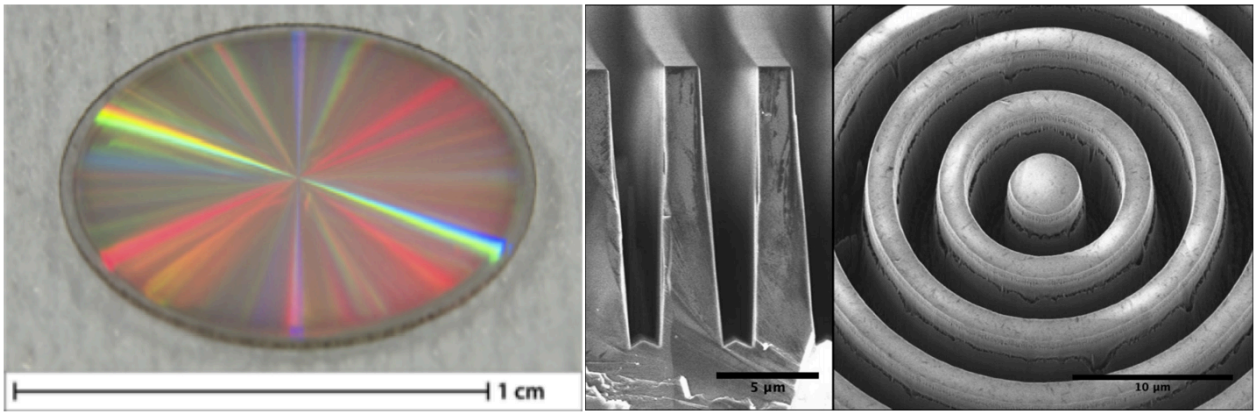

Figure 10.3: AGPM coronagraph at different scales and angles. The middle and right images are obtained with a scanning electron microscope. Credit: VORTEX team (Absil et al. 2016).

ing concepts have been proposed since then, using liquid crystal polymers (Mawet et al. 2009) or photonic crystals (Murakami et al. 2012). The concept of AGPM exploits both (1) the property of *sub-wavelength gratings* to induce *form birefringence* (e.g. Kikuta et al. 1997; Nordin & Deguzman 1999), and (2) the circular symmetry of *concentric grooves*, which enable to induce a a spatially variant half-wave plate with an orientation equal to the azimuthal angle. Sub-wavelength gratings are also referred to as zeroth-order gratings since only the zeroth diffraction order is propagated. Such gratings are birefringent, that is to say that their refractive index depends on the polarization vector and propagation direction of light. Indeed, the electric and magnetic field vectors of light will "see" two different media depending on whether they are parallel or perpendicular to the sub-wavelength grating lines. The subsequent phase shift affecting the two polarization components can be made *achromatic* by tweaking the parameters of the grating: the depth of the grooves, the width of the grating ridges, and the filling factor (Mawet et al. 2005). For the AGPM, the phase ramp consists of a helical pattern of amplitude 4π for one revolution around the optical axis (i.e. it is said to be of topological charge 2).

Figure 10.3 shows a manufactured AGPM, at two different scales and angles. It is a $\sim$1cm-diameter coin made of diamond, with sub-μm-size annular grooves. The exact steps of the etching process are detailed in Vargas Catalán et al. (2016). The choice of synthetic diamond is motivated by its ideal optical, mechanical and thermal properties. After fabrication, the AGPMs are tested in laboratory. I participated to one of these laboratory tests where, along with Christian Delacroix, we measured peak-to-peak attenuation factors of the order of several hundreds at the center of the AGPM (Delacroix et al. 2013). On-sky operations led however to slightly more modest peak attenuation ratios ($\gtrsim$ 50:1 Mawet et al. 2013).

Compared to other coronagraphs, the main strengths of the AGPM include: (1) a high throughput and very small *inner working angle* (separation where the throughput of off-axis light gets lower than 50%): $\sim 1\,\lambda/D$; (2) its achromaticity; (3) a clear 360° field of view (compared e.g. to its predecessor, the four-quadrants phase mask; Rouan et al. 2000). A possible weakness is the very fine alignment required with the star in order to reach an optimal peak attenuation. To alleviate this difficulty, a closed-loop pointing algorithm,

QACITS, has been implemented (Huby et al. 2015). It automatically computes the required shifts to be applied after each exposure based on the residual intensity measured in four quadrants at the location of the donut-shape PSF. This algorithm was proven very effective to recenter the star in quasi-real time behind the AGPM of NIRC2 (Huby et al. 2017). However, tests with the AGPM of NACO did not lead to conclusive results because we could not get access to real time data which could have enabled a correction of the lack of stability of the AGPM. For all observations presented in Sec. 11.3, the AGPM alignment with the star was thus performed manually, and updated every 6-8 min to correct for the drift of the star behind the AGPM.

10.3 Observing strategies

In the field of direct imaging, each and every aspect of an observation must be optimized in order to meet our goal: maximize the contrast to the star and thereby the chance of finding a companion. Some observing strategies have turned out more successful than others, such as *pupil-tracking* and *differential imaging techniques*, which are briefly described below.

10.3.1 Pupil-tracking

To point at a given star, an alt-az telescope is tilted vertically to match the target's *altitude* angle, as well as rotated horizontally to match its *azimuth* angle. Due to this construction, the telescope pupil always remains upright. On the contrary, the orientation of the observed field of view (FOV) changes as the celestial sphere rotates across the observation, in such a way that true North will be "upright" in the FOV only when the object is crossing the meridian.

Telescopes in modern observatories are equipped with a *derotator*, which can compensate for the rotation of the field during the night. The observer has thus the option to observe either with a fixed field (i.e. *field-tracking*), which involves the use of the derotator, or with a fixed pupil (i.e. *pupil-tracking*), where the derotator can be set to track the pupil (and hence to let the field rotate) during the observation. Pupil-tracking is also referred to as *pupil-stabilized* mode or angular differential imaging mode. In pupil-tracking, the relative rotation of the field with respect to the pupil is given by $-p$, where p is the parallactic angle. Field rotation is fastest when the target passes the highest point of its trajectory, i.e. when it transits the local meridian. The field rotation rate around transit also depends on the declination of the target. It is largest for targets transiting close to zenith, i.e. whose declination is close to the geographic latitude of the telescope.

Field tracking is the conventional way of using telescopes in astronomy, as images taken during the night are field-stabilized and can be readily stacked to increase the SNR. However, pupil-tracking has a strong advantage to field-tracking in the context of HCI compared, as speckles due to the telescope (spiders, telescope mirrors) and to the instrument do not move with respect to each other. The resulting speckle halo is significantly more

stable during the observation which, as will be seen in the next subsection, can be taken advantage of for the optimal removal of this bright halo.

10.3.2 Differential imaging

As astronomers got limited by bright swarms of quasi-static speckles to find faint exoplanets, the idea of subtracting reference frames to achieve a better contrast quickly emerged (e.g. Racine et al. 1999). A wide diversity of *differential imaging* techniques have been proposed to build optimal reference/model images for subtraction. Optimal PSF models share two important characteristics: (1) they have to be as correlated to the target image as possible in order to allow for the most effective subtraction of the stellar halo, including its speckles, and at the same time (2) they must present some *diversity* in order to preserve at best from self-subtraction putative faint signals of interest that are sought after (companion or circumstellar disk signals). The source of diversity depends on the chosen observing strategy. In this section, I briefly review a non-exhaustive list of differential imaging techniques, focusing only on those I used in this thesis, namely angular differential imaging (hereafter ADI), reference star differential imaging (RDI), binary differential imaging (BDI), dual-band imaging (DBI) and spectral differential imaging (SDI). Other techniques have been used with different levels of success: *polarized differential imaging* (Mauron & Dole 1998; Kuhn et al. 2001), currently considered by the community as the best technique to image disk structures; *(fast) coherent differential imaging* (e.g. Guyon 2004; Gerard et al. 2018), a promising technique to reach extremely high contrasts; *roll subtraction* (the precursor of ADI in space, Schneider & Silverstone 2003), and *orbital differential imaging* (Males et al. 2015), possibly useful for future space telescopes with extremely stable PSFs. I defer the interested reader to Mawet et al. (2012) for more details on differential imaging techniques.

Angular differential imaging

ADI is the archetypal differential imaging method. As described in the previous section, the idea is to use the differential rotation between FOV and pupil, both to keep speckles due to the pupil and the instrument fixed, and to obtain frames differentiated by angular diversity. The evolution of this rotation is dictated by the parallactic angle. The principle of ADI is illustrated in Fig. 10.4. A PSF reference frame is built from the observed (non-derotated) datacube, it is then subtracted from each individual frames. The individual frames are then derotated to be aligned with a similar field orientation (typically North up in the image), and eventually stacked to form a single final image. *Classical-ADI* or *median-ADI* proposes to build the reference frame with a simple median over the whole datacube; given enough field rotation a putative companion would not be captured in the median (Marois et al. 2006). As will be seen in the next section, more advanced techniques have been proposed since then to create better reference images based on ADI.

ADI has been extensively used by the HCI community since the original concept was

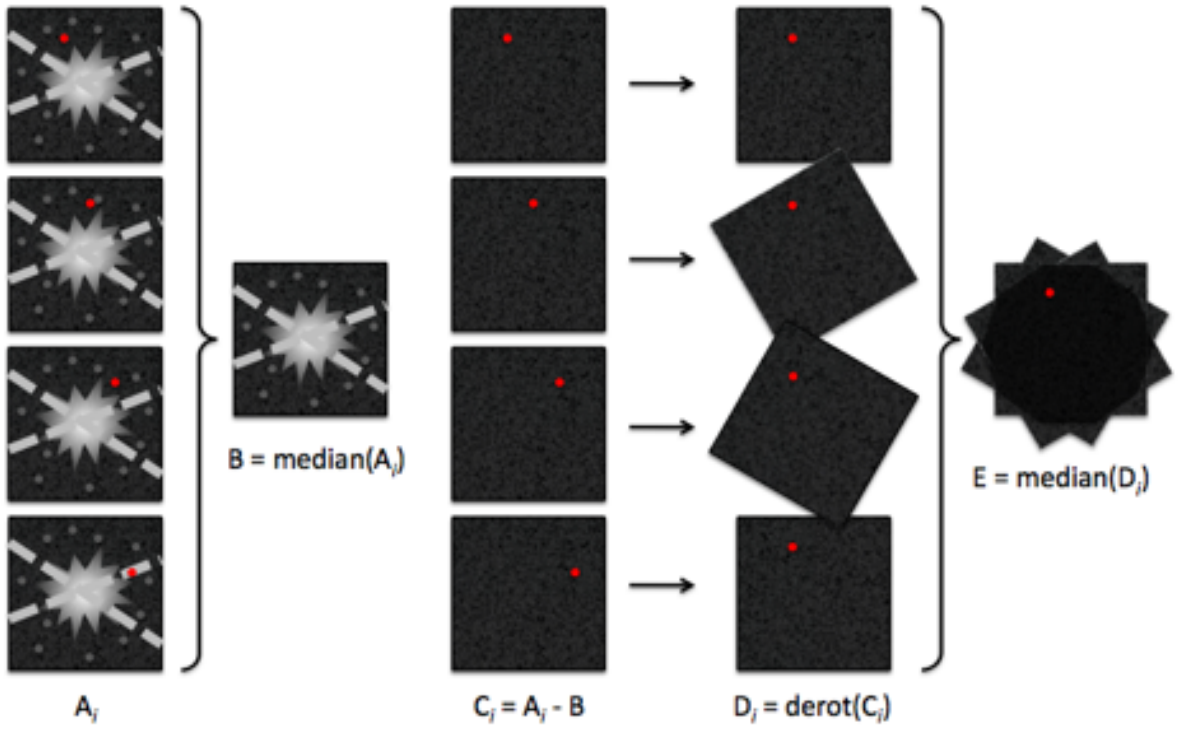

Figure 10.4: Principle of classical ADI (credit: Thalmann).

proposed in Marois et al. (2006). The spectacular direct detection of four giant planets around HR 8799 might have contributed to the subsequent popularity of the technique (Marois et al. 2008, 2010b). As a matter of fact, the technique has allowed the detection of the largest fraction of all directly imaged exoplanets/substellar companions (e.g. Lagrange et al. 2009; Lafrenière et al. 2010; Rameau et al. 2013; Macintosh et al. 2015). It has also enabled the detection of debris disks (e.g. Buenzli et al. 2010; Boccaletti et al. 2012; Currie et al. 2012).

However, it is noteworthy that when extended objects (and in particular azimuthally extended ones), such as disks, are imaged, ADI typically builds reference frames that include a significant amount of flux from the disk. This problem is referred to as *self-subtraction*. Note that this issue also affects point-like sources, to a lower but still problematic extent, so that estimating the true flux of a point-source found in ADI-processed images requires some precaution, and the use of specific tools such as the negative fake companion technique (NEGFC; e.g. Marois et al. 2010a; Lagrange et al. 2010; Wertz et al. 2017). In the case of disks, not only does self-subtraction lead to a lower signal-to-noise ratio for the disk but it also biases the final image of the disk. This issue was investigated in details in Milli et al. (2012). They concluded that ADI can very easily create artificial features without involving additional astrophysical sources. In Christiaens et al. (2018a, Sec. 15.5.1), I extended this analysis to ASDI (ADI+SDI) images.

Dual-band imaging

DBI was historically the first proposed method of differential imaging (e.g. Smith 1987; Racine et al. 1999). Its principle relies on the simultaneous acquisition of two images thanks to a beam splitter in two adjacent filters or spectral windows. One of them is typically centered on an expected absorption line in the spectrum of the exoplanet, e.g. CH_4 at 1.6 μm (Rosenthal et al. 1996; Burgasser et al. 2002), and the other on the nearby continuum. The two images are then subtracted to each other. The presence of a planetary companion would then provide a non-null difference as the absorption feature would lead to a brighter signal in one filter compared to the other. Practical implementation of DBI only requires a beam splitter, two filters and two detectors.

An improvement to the original technique was proposed in Marois et al. (2000), who showed that using three adjacent spectral bands instead of two could improve the achieved contrast. Compared to ADI, the cross-correlation between the PSFs is expected to be higher given the simultaneous acquisitions. However, the limitation in achieved contrast arises from non-common path aberrations downstream from the beam splitter (e.g. Marois et al. 2005). Furthermore, the success of this technique relies on the expected presence and significance of specific spectral features in the spectrum of the companion sought after, which is a major uncertainty for some type of objects (e.g. very young planets). To my knowledge, this technique has led to a single successful detection based on the methane line so far (GJ 504 b; Janson et al. 2013). This companion is likely the coldest exoplanet directly imaged to date. This technique has regained popularity with searches for evidence of accretion around young companions using the Hα line. Using a combination of ADI and DBI across the Hα line, Close et al. (2014) could confirm companion candidate HD 142527 B claimed in Biller et al. (2012) and estimate its accretion rate.

Note that DBI has also been referred to as (simultaneous) *spectral differential imaging* (e.g. Marois et al. 2005), or in the case of combination with ADI, as *ASDI* (e.g. Close et al. 2014). To avoid confusion with the technique presented in the next paragraph, I prefer the use of DBI throughout this thesis.

Spectral differential imaging (with an IFS)

Pushing the concept of DBI further, Sparks & Ford (2002) proposed the use of integral field spectrographs (see Sec. 14 for a brief description) to acquire a large amount of images simultaneously at different wavelengths. As the stellar halo - and its speckles - scales with wavelength ($\sim \lambda/D$), this datacube of multi-wavelength images can be rescaled to a common size. Typically, the reference channel is chosen to be the last wavelength of the datacube, for an upscaling of all other spectral channels. In that rescaled cube, the PSF is very well cross-correlated while the rescaling has induced a radial modulation on the location of any putative faint signal of interest. The PSF model is then built from the rescaled cube and subtracted from each re-scaled image, where the amount of self-subtraction of signals of interest will depend on the amount of radial motion (i.e. on both the wavelength range of the IFS and the radial separation of the signal of interest). After subtraction, each spectral

frame is scaled back to its original size, and the spectral cube can be median-collapsed to increase the SNR of any signal of interest.

As for ADI, the PSF model that is subtracted can be built either from a simple median taken across the wavelength dimension (*classical SDI*) or based on more sophisticated algorithms, which are presented in Sec. 10.4. The correlation between the observed and model PSFs created in such a way is expected to be larger than for ADI given the simultaneity of the spectral frames, which capture the same instantaneous speckle pattern. To reach higher contrast than ADI or SDI alone, it is now a common practice to use both (ASDI) on IFS data obtained with extreme-AO instruments (e.g. Macintosh et al. 2015; Zurlo et al. 2016). Chapter 4 will present the use of ASDI on medium-resolution (non-extreme) AO-fed integral field spectrograph VLT/SINFONI.

Reference star differential imaging

The concept of RDI is very simple; the reference PSF is built based on observations of another star, referred to as *reference star*. In classical RDI, the reference star PSF is simply scaled in flux before subtraction to the target star. For a maximum efficiency, RDI should involve the observation of a reference star (1) obtained as close in time as possible from the science observation; (2) located as close in the sky as possible from the science star – in particular in terms of declination (for similar effects due to e.g. mechanical flexures and differential atmospheric refraction), (3) with similar magnitudes and colors as the target source (to get the most similar level of AO correction and for the stellar halo to be at approximately the same SNR), (4) not harbor a bright circumstellar disk, which could otherwise bias the final image of the target star. Conditions (1) and (2) are also important for the atmospheric conditions to be as similar as possible (e.g. in terms of seeing), as they affect the shape of the AO-corrected PSF.

Despite its simplicity, using RDI in an optimal way requires overcoming several possible shortcomings. First, it is not always possible to find appropriate reference stars close enough from the target of interest, in particular if the target is very bright and/or isolated. A trade-off is usually to be made between separation in the sky and similarity between target and reference stars, so that the subtraction can often result in average quality contrast. RDI usually works better for targets located within star formation clusters, since a similar reference source will often be found close-by. Another possible caveat is that all the time spent on the reference star is not spent on the science target to try to accumulate precious photons from a putative companion. Moreover, overheads can become particularly significant if one has to regularly switch between two stars across the night. An alternative consists in gathering a large amount of archival heteroclite observations of stars of similar magnitudes with the same instrument, and build a reference library based on a certain threshold in cross-correlation. This can be computer-intensive and the effective gain for ground-based observations is still to be assessed. It has been proven very relevant for space-based observations though, characterized by a higher PSF stability (see e.g. Lafrenière et al. 2009; Choquet et al. 2014, 2016). Despite possible caveats, it might the most indicated observing strategy to probe very short separations where ADI and SDI are not applicable, in particular for sources with slow field rotation rates.

Binary differential imaging

BDI has been proposed in Rodigas et al. (2015) as an alternative differential imaging strategy. The principle is very similar to RDI, except that the reference star is the binary companion of the target star (their roles are typically intervertible). This technique has the potential to reach the highest cross-correlation between the PSF of the reference and target stars (and hence achieve the deepest contrast) given that both PSFs are captured at the same time on the same image. Rodigas et al. (2015) infer indeed a $\sim$0.5 mag contrast gain compared to ADI. Nonetheless, for an optimal contrast to be reached, not only must the binary components be sufficiently separated for their PSFs to not overlap, but they should ideally share similar brightness. The latter is a relatively weak constrain though, as scaling up/down in flux the respective PSFs will only introduce noise on the brighter of the two components (i.e., it is still more useful than ADI alone for the fainter component). A survey based on the use of BDI to investigate the occurrence of giant planets in multiple systems is currently on-going using MagAO (Rodigas et al. 2015).

10.4 Data reduction

The first step in data reduction consists in a *basic treatment*, or *basic calibration*, which corrects for the systematics involved in the acquisition of astronomical images. This is briefly described in the next subsection. In HCI, more advanced processing methods have also been developed to exploit at best data obtained using differential imaging strategies, as presented in the previous section. These post-processing algorithms are also described below.

10.4.1 Basic treatment

The main steps of basic treatment involve dark subtraction, flat-field division, bad pixel and cosmic rays correction, in this order. For observations in thermal IR, an additional major contribution comes from the background, hence a sky subtraction is also required.

The first systematics to be corrected in any image are the *bias level* and the *dark current*. The bias is the image obtained with zero exposure time, thus only containing noise due to the electronics. On the contrary, the dark current is the relatively small current due to charge accumulation within the detector even when no photons are entering it, during a given integration time. For each of these effects, there is a fixed number of counts erroneously added to each pixel. These effects are corrected by the acquisition of *dark* frames, obtained with closed shutter and the same integration time as the science images. The median of these dark frames can then be subtracted from science images to correct for the noise pattern caused by both bias level and dark current.

At IR wavelengths, the background thermal emission form both the atmosphere and

the telescope/instrument itself contribute significantly to the flux measured by the detector and have thus to be subtracted as well. The acquisition of frames on empty sky regions is thus performed. Since these sky frames include the signal from bias, dark current and background thermal emission, their subtraction appears *a priori* justified as a first calibration step for IR images. As will be seen in Sec. 11.4 though, the presence of additional sources of bias in VLT/NACO images forced us to consider a different strategy where the sky subtraction is performed later on, after all systematic biases are corrected separately in the science and sky frames. Since the thermal background emission evolve during the night, the rate of sky acquisition should be sufficiently high for an optimal sky subtraction (one every 5-10 min ideally).

Pixels of a given CCD show different quantum efficiency (i.e. sensitivity) at different scales. Pixel-to-pixel variations are usually small (less than a few percent), but the large-scale variations can be more significant. Moreover, any impurity located near the focal plane creates regions of low quantum efficiency on the CCD. The goal of *flat-fielding* is to correct these sensitivity variations. A flat-field consists of the image of a uniform source of light. In thermal IR, it is common to use sky flat-fields obtained around twilight. The flat-field is first normalized based on its median value. After dark subtraction, science frames are thus divided by this normalized flat-field.

Detectors are far from perfect. They present *dead*, *stuck*, and *hot pixels*. The latter have higher than normal dark current and result in brighter pixels than others, especially on long-exposure acquisitions. A bad pixel map is typically obtained as a by-product of the normalized flat-field frame, where pixels are flagged as bad if their normalized efficiency lies below or above a certain threshold (e.g. below 0.67 and above 1.5). Once the bad pixel map is created, bad pixels are replaced by the median of the values of neighboring pixels. Cosmic rays and hot pixels are dealt with a sigma-filter.

10.4.2 Post-processing

Once calibration is over, post-processing consists in the combination of all the data together to produce a final image at the highest possible contrast. Since the typical observing strategy involves differential imaging, an important step of the post-processing is the construction of an optimal PSF model, as correlated to the observed PSF as possible, for subtraction in each image. Residual images are then collapsed in a single, final image. Given that the observing strategies described in Sec. 10.3 already imply the presence of some *diversity* in the data to disentangle faint signals of interest from speckles, a simple way to built the PSF model involves a median of the observed datacube. For ADI, this is referred to as *classical-ADI* (Marois et al. 2006). This method can be slightly tweaked to enhance the final contrast. For example *smart-ADI* divides the field in annuli, and builds a specific PSF model for each annulus of each frame based on the median of the annulus in other frames with a sufficient parallactic angle difference. This is to minimize self-subtraction of any putative companion (e.g. Lagrange et al. 2012). In practice, this strategy involves a trade-off between cross-correlation (highest for frames acquired close in time) and self-subtraction (minimal for frames acquired far in time), so that a limited amount of other

frames in the cube are selected for the construction of the reference image. More refined algorithms have been proposed to better build this reference image, and are described below.

LOCI

The Locally Optimized Combination of Images (LOCI) algorithm was introduced by Lafrenière et al. (2007). As its name suggests, LOCI builds the reference image that is subtracted to each frame from a linear combination of other images of the datacube. This combination is *optimal* in the sense that it finds the coefficients of the linear combination that minimize the least-square residuals. It does so *locally*, that is to say, the least-square minimization is performed in small portions of the image at a time. The shape of the patches is typically chosen to be segments of annuli. In order to limit over-subtraction (over-fitting of the patches), the optimization zone is chosen to be significantly larger than the actual region that is subtracted.

This algorithm represents a significant improvement compared to classical-ADI, as it enables to better deal with speckle decorrelation with time across the observation. Nonetheless, it still presents some weaknesses, including the required tweaking of its free parameters, such as the aspect ratio of the optimization regions (radial vs azimuthal width) or the ratio of sizes between subtraction and optimization regions. Moreover, it significantly affects the flux of true companions (by construction). A last caveat is that it is very computer-intensive.

Several upgrades have been brought to LOCI, such as *damped LOCI* or *TLOCI* (Pueyo et al. 2012; Marois et al. 2014). Compared to the original LOCI, proposed for use on ADI datasets, damped LOCI is compatible with SDI-IFS data, and better deals with companion flux loss; besides the least-square minimization of residuals it adds the condition of maximizing the companion flux (Pueyo et al. 2012). In comparison, TLOCI injects fake companions following specific template spectra and determines the coefficients of the linear combination in such a way that the shape of the retrieved spectrum of the fake companions matches at best the injected one (Marois et al. 2014).

PCA

Principal component analysis (PCA) is a very old method proposed to reduce the number of variables required to model a specific dataset (Pearson, 1901). Its application to datasets obtained with a differential imaging strategy is very recent though (Soummer et al. 2012; Amara & Quanz 2012). In essence, PCA uses the observed datacube to build an orthogonal set of images (so-called *principal components*), which are ordered by decreasing variance (i.e., the first principal components account for as much of the variability in the data as possible). The reference PSF model that is then subtracted to each frame corresponds to the projection of the frame itself on that orthogonal basis. More specifically, the decomposition is made on a lower-rank sub-space; i.e., the basis is truncated to the first $n_{\rm pc}$ principal

components.

In order to build that orthogonal basis, one can use the Karhunen-Loève transform (see e.g. Soummer et al. 2012) or singular value decomposition (SVD; see e.g. Amara & Quanz 2012). Both methods are closely related and lead to an equivalent result: an orthogonal basis ordered by decreasing variance. Below I briefly summarize the SVD method, as it is how PCA is implemented in the Vortex Imaging Package (Gomez Gonzalez et al. 2017), which I used for the processing of my data:

1. All frames of the datacube are mean-centered, i.e. the temporal mean is subtracted to each frame so that the new mean is zero.
2. The mean-centered 3D datacube is transformed into a 2D matrix $\mathbf{S}$ with dimensions $m \times n$; each of the m frames of the cube is now represented as a 1D vector of length n.
3. Matrix $\mathbf{S}$ is decomposed in singular values: $\mathbf{S} = \mathbf{U}\mathbf{W}\mathbf{V}^{\mathbf{T}}$ where $\mathbf{W}$ is a $m \times n$ diagonal matrix with only positive (or zero) elements, and $\mathbf{U}$ and $\mathbf{V}$ are $m \times m$ and $n \times n$ unitary matrices respectively. The non-zero values on the diagonal of $\mathbf{W}$ are the *singular values*[1] of $\mathbf{S}$, while the columns of $\mathbf{V}$, $\phi_{\rm i}$, constitute a set of orthonormal eigenvectors (or principal components) of the covariance matrix $\mathbf{M}^{\mathbf{T}}\mathbf{M}$.
4. The PSF references $R(\overrightarrow{x})$ are built for each image $I(\overrightarrow{x})$ as:

$$R(\overrightarrow{x}) = \sum_{\rm i=1}^{n_{\rm pc}} a_{\rm i} \phi_{\rm i}^{n_{\rm pc}}(\overrightarrow{x}), \tag{10.2}$$

   where the coefficients $a_{\rm i}$ are found from the projection of the image on the orthonormal basis of $\phi_{\rm i}$ truncated to its $n_{\rm pc}$ first elements:

$$a_{\rm i} = < I(\overrightarrow{x}), \phi_{\rm i}^{n_{\rm pc}}(\overrightarrow{x}) > . \tag{10.3}$$

5. Finally, the reference images are subtracted to each frame, and the resulting residual images are derotated and stacked.

This approach provides comparable PSF-suppression quality to LOCI, although with slightly less self-subtraction for companions and with a significant speed enhancement for computation. In practice, the speed enhancement becomes marginal when PCA is applied on concentric annuli where a parallactic angle threshold is used (as in smart-ADI and LOCI). The only free parameter is $n_{\rm pc}$ which basically determines how much of the variance present in the dataset should be included. Through injection of fake companions in the raw image, one can test which value of $n_{\rm pc}$ is optimal to reach the highest contrast in the final image. The optimal value of $n_{\rm pc}$ varies with radial separation Meshkat et al. (2014), so that images corresponding to a range of $n_{\rm pc}$ values should be computed for an optimal testing of the presence of companions at different separations.

PCA is the algorithm that was favored throughout this thesis to take advantage at best of the differential imaging datasets acquired with VLT/NACO, where PCA was coupled with ADI, RDI or BDI (Sec. 11.5) and with VLT/SINFONI, where PCA was coupled to ADI and SDI (Sec. 15.3).

[1]They are the square roots of the *eigenvalues* found by the Karhunen-Loève transform.

10.4.3 VIP

The Vortex Imaging Package is an open source package[2] compiling a large set of routines written in Python, useful for the calibration and post-processing of HCI datasets (Gomez Gonzalez et al. 2017, Gomez Gonzalez et al. 2018, in prep.). VIP started as the effort of Carlos Alberto Gomez Gonzalez, a former PhD student of the VORTEX team. I extensively used the package during this thesis, and contributed to it with the addition of several routines (described in Secs. 11.4 and 15.3), testing and debugging.

10.5 Performance assessment

10.5.1 SNR and significance of detections

Given a final image obtained with the application of PCA on a differential imaging dataset, how to measure the significance of any particular signal seen in that image? Answering this question requires the knowledge of the probability density function of the noise in the image. Speckle noise in raw images follows a positively skewed modified Ricci distribution (e.g. Perrin et al. 2003; Aime & Soummer 2004; Soummer et al. 2007). However, by subtracting the correlated component of the stellar noise, differential imaging algorithms have the beneficial effect of whitening the noise in the residual images. Residual noise is further whitened by the final combination of the frames by virtue of the central-limit theorem (Marois et al. 2008). Therefore, the noise in the final image can be assumed in first approximation to be normal at most locations, and the use of Gaussian statistics is usually justified in order to estimate signal to noise ratios and detection significance. However, it is unsure whether this is still true at very short separation (within a few FWHM) from the star, given the temporal and spectral variability of the noise, and the difficulty of using normality tests at such close separation (Jensen-Clem et al. 2018).

Given the radial dependance of residual noise, it makes most sense to use concentric annuli to estimate the noise in the final image. In order to estimate the SNR of a particular signal in the image, one can consider the flux measured in a 1-FWHM aperture centered on that signal, x_1, to the mean ($\bar{x_2}$) and standard deviation (s_2) of the fluxes measured in independent resolution elements at the same radius (Fig. 10.5), so that SNR $\approx \frac{x_1-\bar{x_2}}{s_2}$ (e.g. Rameau et al. 2013). At small separation though, the number of such apertures is too small (e.g. 6 at 1 FWHM radial separation) for the estimate to be meaningful, and Mawet et al. (2014) suggest that a Student t-test is more appropriate to estimate the SNR. The SNR of a signal x_1 at a certain separation from the star, or equivalently the corresponding value in the associated t-distribution p_t, would then be (Mawet et al. 2014):

$$p_t(x, n_2 - 1) = \frac{x_1 - \bar{x_2}}{s_2\sqrt{1 + \frac{1}{n_2}}}, \tag{10.4}$$

[2]Available at `https://github.com/vortex-exoplanet/VIP`

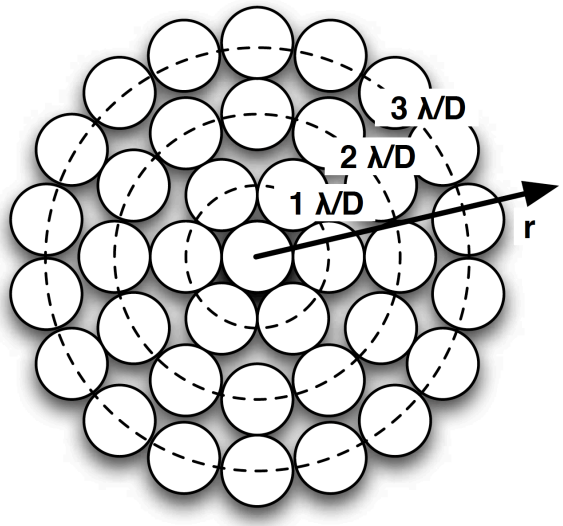

Figure 10.5: Apertures used for SNR estimates. The small number of independent apertures at small angle advocates the use of Student statistics. Sketch from Mawet et al. (2014).

where $\bar{x_2}$ and s_2 are the mean and standard deviation of the fluxes measured in the n_2 other independent resolution elements located at that radial separation. This definition significantly differs from the classic definition of SNR only at short separation, due to the $\sqrt{1+1/n_2}$ factor. To assess the significance of a detection, one has to compute the false positive fraction (FPF) associated to that t-distribution (Mawet et al. 2014):

$$FPF = \int_{\tau}^{+\infty} p_t(x, n_2 - 1)\mathrm{d}x, \tag{10.5}$$

where τ is the chosen threshold. It is then common to convert back this FPF into a Gaussian "$n\sigma$"-confidence level. For example, a FPF $\approx 3 \times 10^{-7}$ corresponds to a 5σ Gaussian confidence level.

10.5.2 Contrast curves

The standard way to assess the sensitivity to faint physical signals in the vicinity of a star in a given observation is through *contrast curves*. Contrast curves provide at each radial separation an estimate of the contrast (with respect to the star) above which a companion would likely be detected. Originally, this was performed by simply measuring the noise in concentric annuli in the final image, and compare it to the flux of the star. This, however, does not reflect the *throughput* of the processing algorithm, which represents the fraction of the off-axis companion signal making it through to the final image.. Differential imaging processing algorithms are indeed known to not only subtract the stellar halo, but also to significantly alter the flux of faint signals of interest in the vicinity of the star. The estimation of the throughput is thus typically performed by injecting fake companions at different radii and at a known flux in the raw cube, and comparing the latter with the flux retrieved in the post-processed image.

The noise measured in the final image, corrected by the throughput, enables thus to compute a contrast curve corresponding to a certain detection threshold. The final contrast curve also has to consider Student statistics at small separation, in a same way as mentioned in the previous section. Concretely, for all datasets presented in Secs. 11.6 and 15.4, I chose to compute 5σ-contrast curves, i.e the contrast level for which a companion would be detected with a FPF $\sim 3 \times 10^{-7}$.

The contrast curve can then be converted into a planet-mass sensitivity curve using evolutionary models which predict the expected magnitude of low-mass objects (from giant planets to low-mass stars) for different masses and ages. Hot-start models commonly used in that purpose include COND (Baraffe et al. 2003) or BT-SETTL (Allard et al. 2012). One has to keep in mind that the masses inferred with these hot-start models estimates might be optimistic at very young ages compared to more physically realistic cold- or warm-start models (Sec. 3.3).

11 Survey of transition disks with VLT/NACO

In this chapter, I describe the transition disk survey that I carried out in thermal IR to search for protoplanets. I detail the motivations of this endeavor (Sec. 11.1), the target selection (Sec. 11.2), the observations carried out (Sec. 11.3), the data calibration and post-processing (Secs. 11.4 and 11.5), and the results obtained for all targets observed so far (Sec. 11.6).

11.1 Motivation

As seen in Chap. 3, giant planet formation is believed to occur in protoplanetary disks before the primordial gas is dissipated (e.g. Haisch et al. 2001). Although several mechanisms are able to open gaps in the surface density of disks, the properties of transition disks with large gaps ($\gtrsim 20$ au), including their measured mass accretion rates and sub-mm fluxes are best accounted for by the presence of embedded companions dynamically carving the cavity (Sec. 6.1; Owen 2016). Current trends in theory also contemplate the possibility of second-generation planet formation, whose formation mechanism requires the existence of (first-generation) giant planet(s) at shorter orbital radius (e.g. Sándor et al. 2011; Ayliffe et al. 2012, Sec. 6.2). These second-generation planets could be related to observed dust traps, also found in these transition disks with large gaps (Sec. 6.2). Thus, transition disks are optimal candidates to search for both first-generation (proto)planets in the gap and second-generation protoplanets in the outer disk.

As a matter of fact, all protoplanet candidates proposed so far were detected in transition disks (Sec. 4.3). Nonetheless, caution is required to interpret these bright IR blobs. Recent literature has indeed shown that some, if not all, of those claims could also be interpreted as aggressively filtered disk signal (Fig. 4.4; Thalmann et al. 2016; Rameau et al. 2017; Follette et al. 2017). A first bona fide detection of a protoplanet is thus still required. New HCI observations of transition disks with large gaps would enable to test both hypotheses of giant planets in the gap, and second-generation planets in the outer disk. Furthermore, some of these disks could also be the result of the dynamical interaction with a close-in low-mass binary star (see e.g. the case of HD 142527 B, Sec. 7.3.3), which may also be detected in the survey.

Thus far, theoretical progress has mostly been driven by the study of dynamical effects of the planet's gravitational field onto the parent disk, such as gaps and spirals (see Secs. 6.1 and 6.4). Nonetheless, in light of the first few protoplanet detection claims (Fig. 4.4), several studies have reconsidered the question of the expected luminosity and color of forming giant planets, including the possible contribution from an accretion circum-planetary disk (CPD; e.g. Zhu 2015; Eisner 2015; Montesinos et al. 2015). The latter appears indeed as a possible solution to account for the very red colors of the protoplanet candidates observed so far, typically found in L' (3.8 μm). Various color and luminosity predictions have been calculated based on different assumptions on the accretion (see details in Sec. 3.3.2). New detections are thus required to better test and refine these models, as well as other hot-/cold-/warm-start models planet formation models (Sec. 3.3.1).

Further insight on the formation mechanism of giant planets can be obtained from the statistics of detected protoplanets in this survey. Core accretion is known to be inefficient at large separation, while gravitational instability is expected to work better in the outer parts of the disk, although subsequent migration could bring GI-formed planets closer in (e.g. Forgan & Rice 2013). Filling the mass-semi-major axis space with new detections and comparison with synthetized populations from both models will enable to better constraint the mechanism at work (e.g. Vigan et al. 2017, see Sec. 4.1).

Our survey of transition disks include systems with an estimated age ranging from a fraction of a Myr up to $\sim$ 10 Myr. The age of the systems where protoplanets are found in our survey will provide both a new estimate of the timescale of giant planet formation and another clue for the formation process involved. Indeed, gravitational instability is expected to occur very rapidly ($\sim$ 10^3–10^5 yrs) in the early stages of the disk, while core accretion is expected to be significantly slower, despite a possibly faster pace enabled by pebble accretion (Ormel et al. 2012; Lambrechts & Johansen 2012).

Finally, another by-product of this survey might come in the form of new images of the disks at L' band, which will enable us to look for shadows, warps or any asymmetry in the disks (see e.g. Rameau et al. 2013; Hashimoto et al. 2012, for L' spirals and disk edges). If both a companion and disk features are present, comparison with hydrodynamical simulations might further constrain the mass and orbit of the companion (see e.g. Dong et al. 2015b; Price et al. 2018, Sec. 7.3.3).

11.2 Targets

The target sample has significantly evolved since the project started in 2015 due to external factors. A sample of 16 transition disks bearing strong planet signposts had initially been accepted for observation in period P95 (first semester of 2015). However, due to a major technical failure of NACO, the run was cancelled and NACO became unavailable for almost a year. When it was available again to the community in P97, a GTO had been granted by ESO to the ISPY consortium (first called Prima-DDL) to exploit the AGPM, effectively blocking most disks bearing strong planet signposts. We noted that the ISPY consortium does not focus only on transition disks (21 transition disks out of 141 targets blocked).

Their main focus is much broader, including debris disks and class II disks in general. In particular, their list of transition disks would not enable a meaningful statistical study of transition disks in itself. Therefore, we requested the observation of transition disks in P97, P99 and P101 to build a more statistically significant sample of these objects (programs 097.C-0653, 099.C-0883, 0101.C-0924), and study the occurrence of companions in their cavities.

The current target selection is based on 5 criteria. All sources are transition disks which (i) have a gap expected to be resolved with NACO in L'-band ($r \gtrsim 0\farcs1$), (ii) are observable with the VLT at an elevation $> 40°$, (iii) are sufficiently bright for good AO correction ($K < 10$ mag), (iv) are not in the ISPY Guaranteed Time Observation (GTO) protected target list, and (v) are not yet observed with NACO in L' at an optimal contrast. These criteria yield a final sample of 21 transition disks, whose physical properties are provided in Table 11.1, including the parent star forming region, their new Gaia DR2 distance (Gaia Collaboration et al. 2018), spectral type, radial separation of the annular gap ($r_{\rm sep}$) when relevant, radial width of the clearing ($r_{\rm cav}$), and L magnitude as proxied by the flux measurement in the $W1$ band of WISE (Wright et al. 2010).

Complying to criterion *i* was verified in two ways. We first considered disks that had already been resolved either in sub-mm or in near-IR, and whose image show evidence for a cavity larger than 0$\farcs$1 or a gap located further than 0$\farcs$1. Given that disks with the largest gaps were mostly blocked by ISPY, only HD 135344 B (Muto et al. 2012; Garufi et al. 2013) and 6 sources identified from the ODISEA survey (Cieza et al. in prep.; Sec. 8.1.1) were included in such a way. A significant fraction of transition disks has not been imaged with HCI instruments yet. Therefore, I also added transition disks for which SED fitting suggested that the cavity size or gap separation was resolvable, as estimated in van der Marel et al. (2018). The sample presented in van der Marel et al. (2018) constitutes indeed in the largest collection of transition disks identified so far. Given the typical separation of transition disks ($\gtrsim$ 100 pc), our selection naturally favored transition disks with relatively large gaps. Since extremely large gaps are uncommon (and blocked by ISPY), criterion *i* also naturally trimmed out disks at larger distances than $\sim$ 200 pc. The only exception to criterion *i* is RU Lup, which was observed due to the lack of other available sources with larger gaps that night.

Criterion *ii* implied that we did not include any source from Taurus or at norther declinations in our survey. A complementary survey of transition disks is led by Drs. Gary Ruane and Dimitri Mawet using Keck/NIRC2 in L', which will enable to explore transition disks in the northern hemisphere.

NACO is equipped with an infrared WFS, which was particularly useful for these very red sources. Although the nominal limit for AO correction is $K = 12$ mag, in practice closing the AO loop on such faint targets is only possible in very good observing conditions. Therefore we limited the sample to targets brighter than K=10 mag (criterion *iii*).

Criterion *iv* forced us to discard most disks bearing strong planet signposts (presented in Chapter 6) from the sample. Nonetheless, several datasets acquired by ISPY are already available in the archive. Among those, I reduced their data on HD 100453, which is hence also shown in Table 11.1. This source was privileged given the presence of a large cavity,

Table 11.1: Physical properties of the sources included in the survey.

Name	RA (h:m:s)	DEC (d:m:s)	Region[a]	Dist. (pc)	Sp.T.	$r_{\rm sep}^{\rm (b)}$ (arcsec)	$r_{\rm cav}^{\rm (c)}$ (arcsec)	$r_{\rm cav}^{\rm (c)}$ (au)	$L^{\rm (d)}$ (mag)	Refs. (gap & dist.)
SZ Cha	10 58 16.77	-77 17 17.1	Cha I	190	K2		0.16	30	7.0	1 & 2
T 25	11 07 19.15	-76 03 04.9	Cha I	197	M2.5		0.15	30	9.7	1 & 2
WW Cha	11 10 00.11	-76 34 57.9	Cha I	192	K5		0.26	50	4.9	1 & 2
HD 98800 B	11 22 05.29	-24 46 39.1	TW Hya	42	K5		0.12	5	5.5	3,4 & 5
HD 100453	11 33 05.58	-54 19 28.5	Iso	104	A9V		0.18	19	4.7	6 & 2
T Cha	11 57 13.53	-79 21 31.5	ϵ Cha	110	K0		1.27	140	5.9	1 & 2
ISO-ChaII29	12 59 10.19	-77 12 13.7	Cha II	196	M0		0.97	190	9.0	1 & 2
PDS 66	13 22 07.55	-69 38 12.2	Iso	99	K1	0.55	0.35	35	6.6	7 & 2
HD 135344 B	15 15 48.44	-37 09 16.0	UCL	142	F4		0.18	26	5.0	8 & 2
RU Lup	15 56 42.31	-37 49 15.5	Lup I	160	G5V		0.03	4	6.0	9 & 2
Sz84	15 58 02.50	-37 36 02.8	Lup I	153	M5		0.46	70	9.7	1 & 2
J1622-3724	16 22 53.10	-37 24 37.4	Lup V	150	M5.5		1.13	170	7.4	1 & 1
J1623-2417	16 23 09.22	-24 17 04.6	Oph	161	M		0.2	32	7.2	10 & 2
J1623-4015	16 23 28.09	-40 15 36.9	Lup VI	150	M3.5		0.33	50	9.8	1 & 1
ROXRA 3	16 25 38.12	-24 22 36.3	Oph	144	M0		0.5	72	8.5	10 & 2
DoAr21	16 26 03.03	-24 23 36.4	Oph	134	K1		0.52	70	5.8	1 & 2
Elias 2-24	16 26 24.07	-24 16 13.5	Oph	136	K6	0.44	0.2	27	6.6	10 & 2
ROXRA 22	16 26 36.83	-24 15 51.9	Oph	136	M0		0.12	16	8.5	10 & 2
EM* SR 13	16 28 45.28	-24 28 19.0	Oph	82	M2		0.11	9	7.2	10 & 2
WSB 82	16 39 45.45	-24 02 03.9	Oph	156	M3.5		0.3	47	6.5	10 & 2

Table 11.2: Physical properties of the sources included in the survey (continued).

Name	RA (h:m:s)	DEC (d:m:s)	Region[a]	Dist. (pc)	Sp.T.	$r_{\rm sep}^{\rm (b)}$ (arcsec)	$r_{\rm cav}^{\rm (c)}$ (arcsec)	$r_{\rm cav}^{\rm (c)}$ (au)	$L^{\rm (d)}$ (mag)	Refs. (gap & dist.)
J1842-3532	18 42 57.95	-35 32 42.7	Upp Sco	154	K2		1.04	160	7.6	1 & 2
J1900-3645	19 00 58.05	-36 45 05.0	Cr A	153	M0.75	0.5	0.09	14	9.0	1 & 2

Notes:

Bold font corresponds to sources that have been observed so far. The few remaining sources will be observed between July 1 and 3, 2018.

[a] Cha: Chameleon. TW Hya: TW Hydra. Iso: Isolated. UCL: Upper Centaurus Lupus. Oph: Ophiuchus. Upp Sco: Upper Scorpius. Cr A: Corona Australis dark cloud.

[b] When provided, corresponds to the radial separation of the annular gap.

[c] When $r_{\rm sep}$ is provided, it corresponds to the width of the annular gap. Otherwise, it is the radius of the cavity.

[d] Magnitude measured in the W1 channel ($\sim$3.7 μm) of WISE (Wright et al. 2010)

References: (1) van der Marel et al. (2016c); (2) Gaia Collaboration et al. (2018); (3) Furlan et al. (2007); (4) Akeson et al. (2007); (5) Boden et al. (2005); (6) Wagner et al. (2015); (7) Wolff et al. (2016); (8) Stolker et al. (2016); (9) Takami et al. (2001); (10) Cieza et al. (in prep.).

shadows and spirals. I have not had the time to reduce more datasets from the archive yet.

Regarding criterion *v*, I noticed that several transition disks had already been observed with NACO in L'. However, some bright sources were not yet observed with the AGPM (such as T Cha and HD 135344 B). Since the AGPM can bring a significant contrast gain at very short angle compared to observations with other masks or without coronagraph (e.g. Mawet et al. 2013; Absil et al. 2013), we also included them for re-observation.

The total of 21 sources matching our criteria will add to the 24 transition disks already observed with NACO in L' in optimal contrast conditions ($\sim$20 of which by ISPY), which will be retrieved from the archive to form a total sample of 45 transition disks. This will constitute the first large sample of transition disks, from which it will be possible to infer useful statistics on the occurrence of protoplanets in these gapped disks. The occurrence of protoplanets as a function of the estimated age of the system will provide new independent observational constraints on the giant planet formation timescale. The dependency with spectral type will also be investigated; two out of the three claimed protoplanet candidates at the time this survey started were found around late B-type stars (HD 100456 and HD 169142; Quanz et al. 2013a, 2015a; Reggiani et al. 2014; Biller et al. 2014). Nevertheless, observations of transition disks have been significantly biased towards Herbig Ae/Be stars so far (including regarding those already observed in the archive). The addition of our 21 sources will enable to investigate as well the occurrence of protoplanets around later type stars (as it comprises of 10 FGK and 11 M type stars), and across star forming regions of different ages (namely Ophiuchus, Chameleon, Lupus, and Upper Sco).

11.3 Observations

Table 11.3 provides a log of all visitor mode observations of this survey, while the log of service mode observations can be found in Table 11.4, along with an entry for the observation of HD 100453. I performed all the visitor mode observations and prepared all the observing blocks, except for HD 100453, which was observed by the ISPY consortium. In both tables, I provide the number of exposures (NEXP) obtained on each source, the integration time (DIT) and the number of co-adds (NDIT) used in the sequence. The range of airmass, mean DIMM seeing value (seeing at λ=500 nm and at zenith) and parallactic angle range obtained during the sequence are also given. The last column denotes the adopted differential imaging strategy - ADI, RDI or BDI (Sec. 10.3) - and whether the AGPM (Sec. 10.2.1) was used or not. A few datasets were amenable for post-processing with either RDI or ADI; these are labelled *ARDI*.

All observations were obtained in the so-called *cube mode*, which enables to save each individual integration (*co-add*) separately instead of stacking them. The amount of time spent on each source was constrained by the need for sufficient parallactic rotation (1.5 FWHM at $\sim$0$''$.15 separation, equivalent to $\sim$60°) to reach useful contrasts with ADI. We set a minimum on-source time of 1h to reach a good sensitivity in the background-limited regions. For stars that do not reach a sufficient parallactic angle rotation in 1h30 or passing through the zenith hole, we intertwined the observation of the target with reference

stars in order to apply RDI. For these sources, we typically spent two thirds of the time on the science target, and one third on the reference stars. Optimal practices for RDI, including *star hopping*, are briefly discussed in the next subsection. As this technique is not standard, the observations had to be performed in visitor mode. Finally, the close quadruple system of HD 98800 (two resolvable components of the same magnitude), for which a transition/young debris disk is predicted around the B component, was observed without coronagraph for a reduction based on BDI.

Apart from HD 98800, sources brighter than L' = 7mag were observed with the AGPM (Sec. 10.2.1), as it provides a significant reduction of stellar speckle noise down to an inner working angle of $\sim$0$''$.1 (e.g. Mawet et al. 2013; Absil et al. 2013). Observations with the AGPM on NACO involve significant overheads though, due to the manual recentering of the AGPM and the acquisition of dedicated sky frames. We noticed that the star appeared to drift behind the AGPM so that a manual recentering was required every 5-10 min in order to maintain a centering accuracy of $\lesssim$0.3 pixel. The drift rate appeared to depend on the field rotation rate, so that I increased the recentering frequency around transit. Since an optimal sky subtraction also requires sampling every 5-10 min (the typical timescale for background variation in IR), in practice both steps (sky acquisition+AGPM recentering) were performed consecutively.

For sources fainter than L' = 7 mag, the gain in contrast brought by the AGPM is minor, in particular considering the lower throughput due to the combination of AGPM and Lyot stop. In addition, the attenuation of the faint source is such that it is more difficult to align the AGPM with the star, leading to more time wasted during the manual alignment. Therefore, for those sources we preferred to observe without the coronagraph. During those observations, the sources were simply dithered between the two or three good quadrants of the detector (see Sec. 11.4.1 for more details on the bad quadrants), which hence did not require the acquisition of dedicated sky images.

11.3.1 Strategies used for RDI observations

As mentioned in Sec. 10.3.2, it is crucial for reference stars to have a PSF as correlated as possible to that of the science target, for the construction of an optimal PSF model for subtraction during post-processing. This typically requires the reference star to be as identical to the target as possible in terms of magnitude, color and position in the sky. A similar L' magnitude will lead to a same signal to noise ratio for the stellar flux with respect to the background. In practice, if the condition of similar brightness cannot be fulfilled in the vicinity of the target, it is better to choose a slightly brighter reference star to avoid introducing additional noise during reference subtraction. A similar magnitude in the band used for AO correction is also important, in order to reach a similar quality level for the AO correction (i.e., a similar Strehl ratio, Sec 10.1.1). It is also crucial to choose the reference star to be as close to the target star as possible, in particular in terms of elevation. Differential mechanical flexures (e.g. when the telescope is inclined towards different altitudes) can lead to different quasi-static speckle patterns. Finally, because quasi-static speckle pattern do evolve (albeit slowly), it is also important to sample the reference star as often

Table 11.3: Log of the visitor mode observations obtained with VLT/NACO

Date	Source	NEXP[a]	DIT[b] (s)	NDIT[c]	INT[d] (min)	Airmass	Seeing[e]	Par. Ang.[f] (Start/End)	Obs. Strat.[g]
2016/04/30	TWA 7	33	0.4	100	22	1.0-1.0	0″.80	+20°/+60°	AGPM+ADI
	HD 98800	66	0.18	100	20	1.0-1.1	0″.90	+92°/+95°	BDI
	PDS 66	60	0.4	150	60	1.4-1.6	0″.75	+12°/+43°	AGPM+RDI
	RU Lup	100	0.4	120	80	1.0-1.2	0″.65	+6°/+78°	AGPM+ADI
2016/08/08	DoAr 21	40	0.3	200	40	1.0-1.1	0″.95	-93°/+96°	AGPM+ADI
2017/05/05	WW Cha	24 (10)	0.16	350	26	1.7-1.6	0″.70	-25°/+9°	AGPM+RDI[i]
	T Cha	33 (12)	0.2	300	33	1.7-1.8	1″.0	+3°/+32°	AGPM+RDI[h,i]
2017/05/06	Sz Cha	42 (16)	0.35	170	42	1.7-1.8	1″.65	-14°/+46°	AGPM+ARDI[h,i]
2017/05/07	Ass Cha T 2-25	34 (10)	0.22	270	34	1.7-1.6	0″.65	-21°/-1°	RDI
	HD 135344 B	18 (4)	0.35	170	18	1.2-1.1	1″.30	-91°/-62°	AGPM+RDI[h,i]
2018/06/01	WW Cha	40 (10)	0.25	250	42	1.6-1.7	0″.35	-4°/+36°	AGPM+RDI
	HD 135344 B	58	0.25	250	60	1.1-1.0	0″.40	-62°/+15°	AGPM+ADI[i]
2018/06/02	ISO-ChaII29	12 (4)	0.15	330	10	1.6-1.6	0″.45	-8°/+2°	RDI[h]
	HD 135344 B	64 (20)	0.25	250	67	1.1-1.1	0″.40	-67°/+70°	AGPM+ARDI[i]

Notes:

[a] Number of data cubes acquired. When provided the number in parenthesis corresponds to the number of cubes obtained on the reference star(s).

[b] Detector integration time for each individual spectral cube.

[c] Number of co-adds in each data cube.

[d] Total integration time on source.

[e] Mean value of DIMM seeing during the observation.

[f] Parallactic angles at start and end of sequence.

[g] Observing strategy.

[h] Observation acquired in very poor conditions and/or interrupted due to poor conditions (e.g. high wind, bad seeing or thick clouds).

[i] Bad columns in the quadrant where the AGPM is located (Fig. 11.2c).

Table 11.4: Log of the service mode observations and archival data obtained with VLT/NACO

Date	Source	NEXP[a]	DIT[b] (s)	NDIT[c]	INT[d] (min)	Airmass	Seeing[e]	Par. Ang.[f] (Start/End)	Obs. Strat.[g]
2016/05/09	HD 100453	274	0.25	100	114	$1.2 - 1.4$	$> 1''.5$	-33°/+60°	AGPM+ADI[h]
2017/05/23	HD 135344 B	72	0.15	337	61	1.0-1.2	$1''.25$	+44°/+76°	AGPM+ADI[i]
	J1842-3532	68	0.08	416	38	1.0-1.0	$1''.50$	-40°/+28°	ADI[i]
2017/05/29	J1622-3724	74	0.08	423	42	1.0-1.1	$0''.90$	-25°/+45°	ADI[j]
2017/08/26	J1900-3645	62	0.1	453	47	1.1-1.1	$0''.55$	+51°/+76°	ADI
2018/04/17	Sz84	74	0.21	216	56	1.0-1.0	$0''.80$	+6°/+58°	ADI[k]
2018/04/19	J1623-4015	74	0.21	216	56	1.1-1.0	$0''.50$	-63°/-21°	ADI

Notes:

[a] Number of data cubes acquired.

[b] Detector integration time for each individual spectral cube.

[c] Number of co-adds in each data cube.

[d] Total integration time.

[e] Mean value of DIMM seeing during the observation.

[f] Parallactic angles at start and end of sequence.

[g] Observing strategy.

[h] Very poor observing conditions; the dataset was significantly trimmed during data reduction.

[i] Despite the poor seeing, Strehl ratio was $> 60\%$ and the run was classified 'A'.

[j] Vertical bands on the detector suggesting a defective readout (Fig. 11.2d).

[k] Very elongated PSF (Fig. 11.2e).

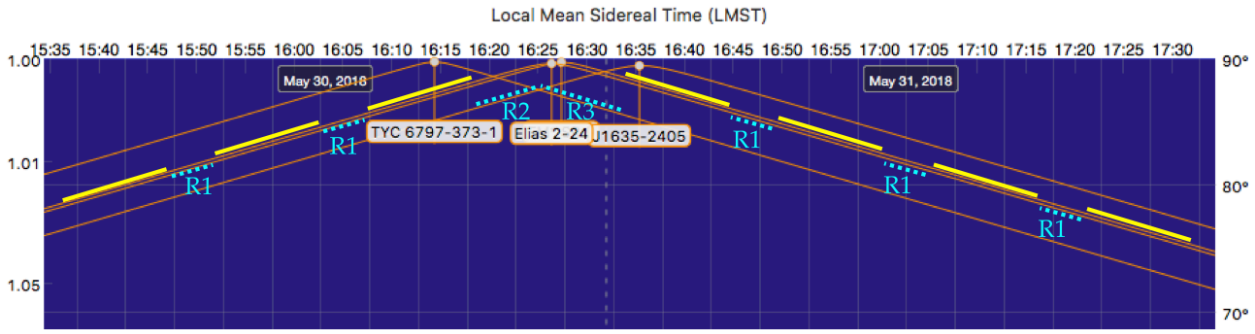

Figure 11.1: Example strategy for an observation with reference stars, where the science target passes through the zenith hole, which is the case of all the Ophiuchus sources of our sample. The thick yellow lines shows the lapses of time spent on the science target (Elias 2-24 in this example). The dashed cyan lines show the lapses spent on the different reference stars R1, R2 and R3. In this example, R1 is EM* SR 9 (label hidden behind Elias 2-24), R2 is TYC 6797-373-1 and R3 is J1635-2405. See details in the text.

as possible.

The criteria I typically defined are: $\Delta L < 0.2$mag, Δ RA $< 0.2°$and Δ DEC $< 0.1°$. I used the All-sky WISE catalog[1] to find reference stars matching these criteria. Reference stars for sources passing through the zenith hole (see next paragraph) comply to the same conditions but the range of accepted RA is shifted by $\sim$10 arcmin. These criteria typically lead to a few potential reference stars per science target, but in the case of very bright and/or isolated sources, may require to be loosen up. At least two reference stars are prepared for each observation, in case one of them turns out to be a binary.

Zenith hole observations

The *zenith hole* is a blind spot within $\sim 3°$ from the zenith where an altaz telescope cannot point, due to the very fast motion that would be involved for the telescope to track an object passing through it. Up to 20-25 min can be lost if one simply waits for the source to cross the hole. In practice, these precious VLT minutes can be put at better use by observing an appropriate reference star. An example RDI strategy involving three reference stars is shown in Fig. 11.1. Reference star R1 has practically the same coordinates as the target, while R2 (resp. R3) has a positive (resp. negative) difference in RA of $\sim$10 arcmin. The observation can be optimized by observing R2 and R3 in the zenith hole of the science target (Elias 2-24 in the example). The strategy can also be reduced to two reference stars, replacing reference R1 by R2 before the transit, and by R3 after the transit.

As will be seen in Fig. 11.6.1, it appears crucial to use RDI for sources passing through the zenith hole in order to optimize the achieved contrast. All 6 sources to be observed in July 2018 (marked with non-bold font in Table 11.1) are located in Ophiuchus, and will hence pass through the zenith hole. For these sources, I plan to apply a strategy similar to that presented in Fig. 11.1.

[1]Available at `http://irsa.ipac.caltech.edu/Missions/wise.html`

Star hopping

For RDI observations, I optimized the slewing time between target and reference stars by performing *star hopping*. This technique consists in entering manually the shifts in coordinates between the two stars directly to the telescope, and skipping the acquisition on the new target. In practice, this can only be done for stars with very similar magnitudes (so that the AO configuration can stay the same) and sufficiently close in the sky (the amplitude of a single *hop* has to be less than 15′). These practical requirements also happen to maximize the correlation between the speckle patterns of the reference and science stars, as discussed above. Star hopping enables to significantly reduce the overheads from 10-15min to only 3-5min. In order to maximize the correlation between science and reference targets, after every six datacubes spent on the science target (6-8 min), I would typically *hop* and acquire two datacubes on a reference star.

To compute the exact shifts to be applied to the telescope, I used a routine implemented by Dr. Sylvestre Lacour. Targets with similar magnitudes but separated by more than 15′ can still be reached in theory by two or more consecutive hops. However, I noticed in practice that the risk of not landing on the desired target increased for more than two consecutive hops, due to cumulated uncertainties on the proper motions of the sources which are not taken into account in the shift estimation. This risk is lowered for sources in a same star-forming region.

11.4 Data calibration

I implemented a pipeline to handle the basic processing of NACO data. The pipeline is composed of a main jupyter notebook, which facilitates visualization of intermediate products, and separate python scripts, used for CPU-intensive tasks. While the plan was to make an automatic pipeline, it turned out to be impractical due to the varying biases in different datasets. For example, some datasets present bad detector columns, some others are made of incomplete cubes (i.e., containing less co-adds than the nominal NDIT), and the dust grains and AGPM center are found at different locations for data at different epochs. The pipeline is thus only semi-automatic, and requires visual inspection of intermediate products at several key steps in the process. Since not all systematic effects were identified at once, the pipeline has significantly evolved through time. Finally, specific characteristics of the observation (e.g. use of the AGPM, presence of reference stars) or of the source (e.g. the presence of a binary companion) also led to different versions of the pipeline. Below is a summary of the main steps of the calibration process, provided in the same order as they are performed in the pipeline.

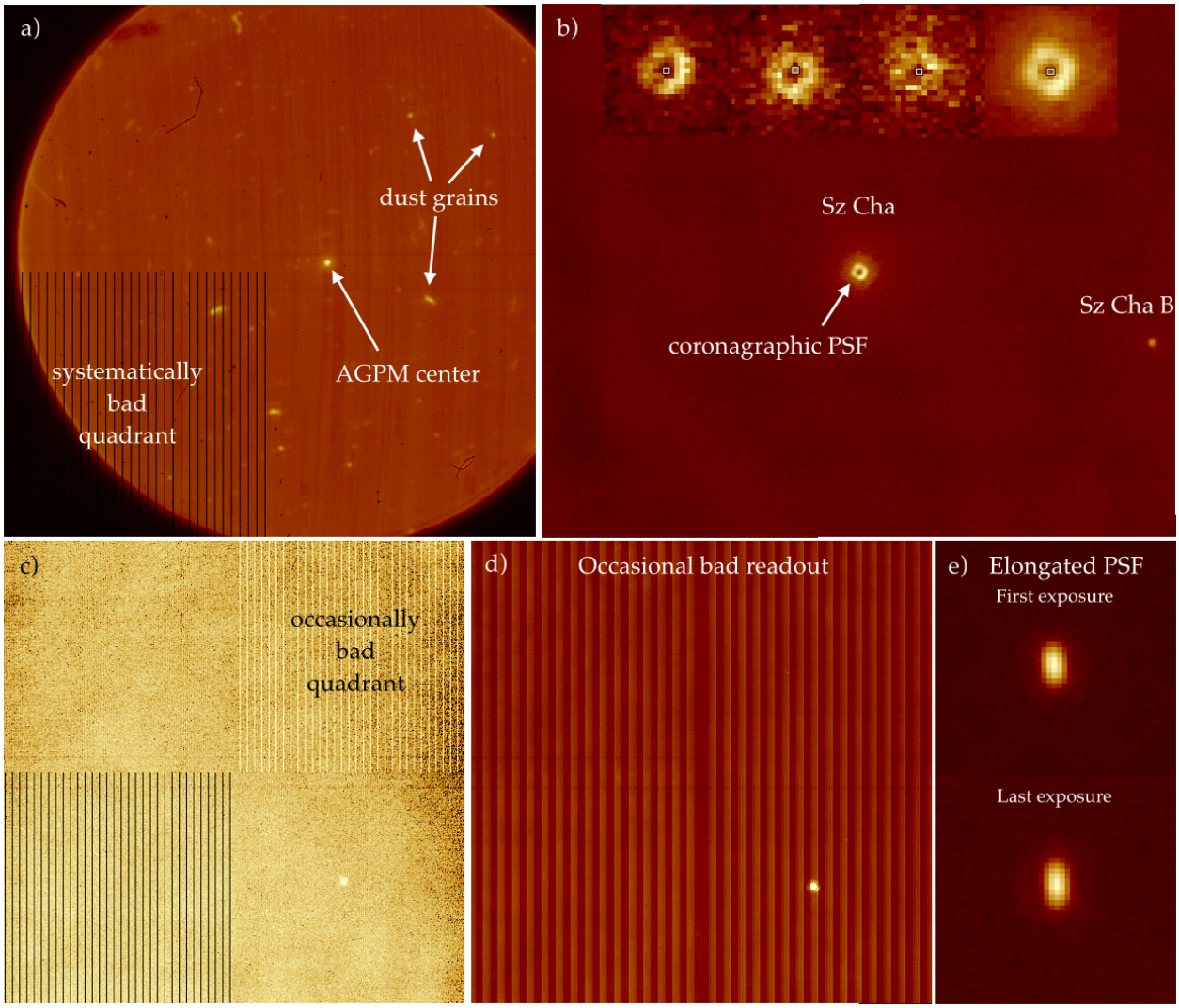

Figure 11.2: Illustration of some of the biases affecting images acquired with NACO. **(a)** Raw image obtained with NACO+AGPM. The bottom-left quadrant is systematically affected by bad columns of pixels. **(b)** Coronagraphic PSF image of Sz Cha and its M-dwarf companion. The image is obtained after median-collapse of an exposure obtained in cube mode; where individual frames are not co-added. The insets on top of the image provide an idea of the coronagraphic PSF in individual non-coadded frames (three insets on the left) and the median-collapsed one (right inset). **(c)** Non-coronagraphic image obtained after dark subtraction, flat-fielding and sky subtraction. The top-right quadrant is sometimes defective as well. **(d)** Bad readout affecting the dataset of J1622-3724. **(e)** Elongated PSF, with a three times larger FWHM along one axis compared to the other, affecting the dataset of Sz 84.

11.4.1 Systematic biases of NACO

As described in Sec. 10.4.1, the first steps of the calibration consists in a dark subtraction, flat-fielding and bad pixel correction (which also include the correction of NaN values). In addition to these, I encountered several sources of systematic biases that are specific to NACO, and which are subsequently corrected in the following order.

Bad columns of the detector

The lower left quadrant of the detector is plagued by columns of stuck pixels. They are easily flagged in the bad pixel map that is built from the flat fields, and are hence median-filtered accordingly during the bad pixel correction.

However, columns of the upper right quadrant do also sporadically show a hot pixel behavior during the night (Fig. 11.2c). The effect is occasional and usually not captured in the flat fields taken during twilight. They are only evident after dark subtraction and flat-fielding, and are not all corrected with a sigma-filter. Therefore, a visual inspection of intermediate frame is required to know whether a specific correction is to be applied. Given their periodicity (every 8 columns) and specific location (totality of the upper right quadrant), providing as input to the pipeline the coordinates of a single hot pixel enables to flag them all. Once flagged, they are corrected with a median-filter.

DIT instability in cube mode

Another source of bias is illustrated in the left plot of Fig. 11.3. It shows the normalized PSF flux measured in a 1-FWHM aperture centered on the star in each co-add of a 100-frames long datacube. The measured flux shows an exponential decay, with a total variation of $\sim 1.5\%$ between the first and last frame. Furthermore, visual inspection of the first few frames also shows significant residuals suggestive of an inappropriate dark subtraction. I suspect these behaviors to be due to an inconstant DIT value used for the different co-adds acquired in cube mode. This explanation is indeed consistent with the dark subtraction (performed using the median of all dark frames) leaving significant residuals in the first few frames of each cube. Despite the small ($\lesssim$0.1%) relative variation for the blue points of the left plot of Fig. 11.3, naively discarding the first few frames of each cube (red dots in Fig. 11.3) would still lead to a significant variation in the background after sky subtraction (right panel of Fig. 11.3). While the median of the flux measured far from the star is indeed zero over the whole cube, in individual frames the flux is discrepant from zero by several hundreds of ADU.

The optimal solution is thus to scale each frame to a same DIT, assuming that the measured flux is directly proportional to the true DIT. The first 1-3 frames are still removed from the cube due to the presence of strong residuals from an inappropriate dark subtraction. Since sky frames are also obtained in cube mode, a similar scaling is applied to them before subtraction. The flux in an aperture far from the star, sampling the background, is used to scale the sky frames to the same level as the science frames. I noticed that the shape of the exponential decay depended on the number of co-adds (NDIT) in the cube; for a sky cube with the same nominal value of DIT but only 50 co-adds, the shape of the exponential decay is significantly different. I alerted ESO about this issue and recommended the acquisition of dark frames in cube mode at the end of the night, with not only the same DIT as science/sky cubes, but also the same values of NDIT.

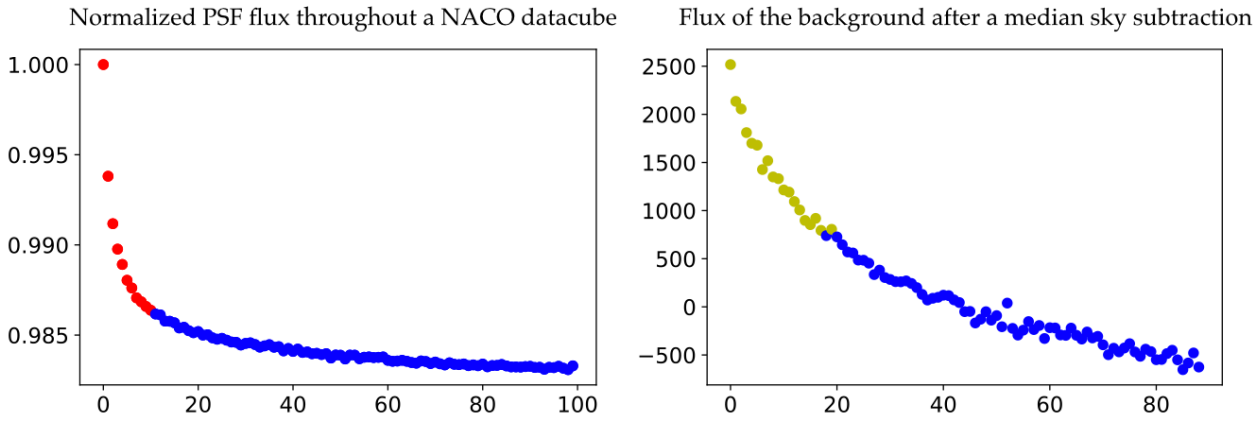

Figure 11.3: Flux measurements reflecting the Instability in the effective DIT used in the cube mode of NACO. (*left*) Flux measurements of a non-coronagraphic PSF in the non-coadded frames of a typical NACO datacube. *Red points* show the measurements that are larger than the median plus a standard deviation, which I discarded from the cube in the first implementations of my pipeline. (*right*) Flux measurements in a background portion of the field after median sky subtraction. Even when only the blue points from the left graph are kept, the subsequent sky subtraction leads to a wide range of background levels throughout the cube, between 2500 ADUs and -650 ADUs.

Dust grains on the AGPM

As can be seen in Fig. 11.2a, when the AGPM is used a large amount of bright blobs are crowding the field. These correspond to tiny *dust grains* located on the substrate of the AGPM, which appeared magnified due to the location of the AGPM in an intermediate focal plane. They are removed by the sky subtraction. Unfortunately, they appear to drift slowly on timescales of minutes (along with the apparent drift of the AGPM with respect to the camera). Therefore, to avoid strong positive-negative residuals during sky subtraction due to misaligned dust grains, the sky frames are first registered with the science frames. The rough coordinates of a few dust grains (typically 5-7 of them scattered on the detector) are provided as input to the pipeline, so that 2D Moffat fits are performed in boxes centered on those locations to measure the centroids of the dust grains. Comparing the value of the centroids found in such a way for science and sky frames enables to register them. Typical amplitude for the shifts is of the order of $\lesssim$0.05 pixel. However, a misalignment of that order is already able to produce significant positive-negative residuals in the sky subtracted image at the location of the dust grains. This is another bias which impeded the pipeline to be fully automatic because the location of dust grains can slightly change from epoch to epoch.

11.4.2 Sky subtraction

At this point, coronagraphic science and sky frames are registered with respect to each other based on the dust grains, so that the sky can be subtracted to the science frames without leaving residuals. Depending on both the frequency with which skies were obtained and the variability of the atmospheric conditions, the use of PCA to build an optimal

sky frame can sometimes lead to better results. For a good sky sampling though, subtraction of the median of the sky cube obtained closest in time typically leads to slightly better results (based on visual inspection of sky-subtracted frames).

For non-coronagraphic observations, the star was dithered in a different quadrant of the detector after each exposure. Therefore sky subtraction was simply performed by subtracting the median of the closest science cube in time. The frames were then cropped to the size of a single quadrant.

11.4.3 Centering on the star

Non-coronagraphic PSF centering

The position of the star on the detector is affected by jittering throughout the observations. This is readily observable and fixable for non-saturated non-coronagraphic frames using Gaussian or Moffat fits to determine the exact location of the centroid. I have noted however that fits to a 2D Moffat function were slightly more robust than to a 2D Gaussian, which sometimes leads to aberrant results even for visually good-looking PSFs (typically a handful of outliers out of thousands of frames, against 0 outlier for the Moffat fit). This incited me to favor the use of the 2D Moffat fit for all other datasets.

An example of good non-coronagraphic PSF can be seen in Fig. 11.21. In comparison, one of our datasets (Sz 84) was affected by an extremely elongated PSF. While the median of the co-adds show the elongated shape provided in Fig. 11.2e, in some individual frames the PSF even appeared to be made of two separate centroids. Nonetheless, given the 52° field rotation and the absence of rotation of the elongation axis throughout the observation, I suspect the cause of the elongated shape to be due to either an instrumental artifact or poor AO correction, rather than tracing e.g. a close binary. For that dataset, the recentering was performed using the centroid found with Moffat fits of the median-collapsed cubes, and significant trimming to reject the double-centroid PSFs.

Coronagraphic PSF centering

For coronagraphic data, the combination of jittering and the fact that the star is hidden behind the mask significantly hinders the possibility of a straightforward optimal centering. Figure 11.2b shows an example of the coronagraphic PSF obtained in NACO observations with the AGPM. That image is obtained after median collapse of the co-adds in one datacube. The insets on top of the image correspond to close-up views on the coronagraphic PSF; the first three insets represent typical individual co-adds of the cube, and the right inset is a close-up view of the coronagraphic PSF after median collapse. As can be seen from the typical quality of the PSF obtained in individual co-adds, any recentering routine would rather have to rely on the median of each cube. Given the morphology of the coronagraphic PSF, I will refer to the dip in intensity created by the AGPM as *hole* and to the

bright ring surrounding it as *donut*.

I first attempted to recenter the star assuming that it was relatively well-centered behind the AGPM hole (as we estimated the manual centering to have an accuracy of ∼0.3px during the observations), and just fitted the hole with negative 2D Gaussian and negative 2D Moffat functions. In practice, these fits considered a small box centered on that location, where I tested fits both with or without preemptive thresholding of the donut. I also considered to perform these fits with or without oversampling the frames (using x1, x2, x4 and x8 the original pixel scale). I noticed that without oversampling by at least x4, the 2D fits often led to significant outliers ($>$ 10 pixels), which I attributed to the very small size of the AGPM hole (only $\sim$ 4 pixels wide) not enabling an accurate 2D fit of the hole.

In parallel, recentering tests with the AGPM installed in NIRC2, carried out by Drs. Mickael Bottom, Gary Ruane and Dimitri Mawet suggested that a more accurate way of recentering the star in all the frames could be achieved by proceeding in two separate steps: (1) find the relative shift between the cubes using the cross-correlation of the speckle pattern, and (2) find the exact position of the center of the AGPM with a negative 2D Gaussian fit in the median-combined frame and assume that it is the stellar location. I performed tests on the NACO+AGPM dataset of HD 206893, which harbors a faint companion at 0″.27 separation (Sec. 12.2), to pinpoint the most appropriate algorithm to recenter coronagraphic images obtained with the AGPM. Using the technique proposed by the NIRC2 team led to slightly better SNR for the companion, and contrast achieved at $>$ 0″.3 separation, with also better results when frames are not oversampled. The method was thus adopted in my pipeline, and the two steps are detailed in the next two paragraphs.

Relative alignment of AGPM frames The registration of the frames with respect to each other is basically performed via cross-correlation of the speckle pattern. For this technique to work, the first step consists in removing the spatial frequencies that do not correspond to the typical sizes of speckles in the image. This is done with a high-pass filter, removing all large scale variations ($>$ 4 FWHM) due to imperfect background subtraction, followed by a spatial binning of the frames by a factor corresponding to a FWHM. In order to boost the contribution from the speckle halo compared to the core, the image is converted to logarithmic scale. The algorithm then finds the shifts that maximize the cross-correlation between these subsampled log-scale images and the median of the whole cube. The procedure is iterative; after all the frames are shifted, the median of the whole cube is computed again, and new shifts are computed. In practice, five iterations are sufficient and lead to a good alignment of the frames. This algorithm was first coded by Mickael Bottom, and then adapted to Python by Gary Ruane, who made it available in the VIP package.

Centering on the AGPM hole The second part of the centering process consists in locating the star, and placing it at the center of all images. This is important for an optimal post-processing, final derotation of the frames and stacking. Since the star is hidden behind the AGPM, there is in fact no direct way to infer its precise location. However, given that the star was frequently and manually recentered behind the AGPM down to a precision

of ∼0.3 pixel during the observations (based on visual symmetry of the donut), it is likely that the median position of the star over the whole sequence lies very close to the center of the AGPM. Therefore, fitting the AGPM hole should be a good proxy. Since the AGPM is a phase mask, there is no hard blocking of the light as in an amplitude mask. As mentioned earlier, it is better represented with a 2D Gaussian or Moffat function. In practice, this step is encapsulated within the iterative process described in the previous paragraph. Before all frames are aligned with respect to the median of the whole cube, the algorithm implemented by M. Bottom and G. Ruane fits a 2D negative Gaussian to the AGPM hole and shifts the median frame to place the centroid in the middle of the image.

Based on earlier recentering tests with the AGPM of NACO involving 2D Gaussian and Moffat fits, I suspected that this step could be suboptimal for NACO. This routine was indeed implemented for the AGPM of NIRC2, while the pixel scale of NACO is ∼3 times broader (27.1 mas px^{-1} instead of 9.9 mas px^{-1}), leading to ∼9 times less pixels in the AGPM hole available for the 2D fit. Therefore, I investigated another option for the centering taking advantage of the annular symmetry of the AGPM donut. I designed a routine which finds the location of the center of the donut based on the annular mask that maximizes the mean flux measured in the donut, by iterating on the center of the annular mask in steps of 0.2 pixels in a grid of a few pixels wide along x and y. After a few tests, I set the default values for the annulus width and radial separation to FWHM/2 and 1 FWHM, resp. (i.e., typically an annulus spanning 3 to 5 pixels separation).

Figure 11.4 shows a comparison of the shifts computed with the annular fit (ann), and the 2D negative Gaussian (ng) and negative Moffat (nm) fits for 6 datasets acquired on different reference stars (shown with thick bars in the right-hand panels) at various epochs. Each reference star was observed in pairs of two consecutive datacubes (delimited by small ticks on the right-hand plots), as a result of the star hopping strategy. The top and bottom panels correspond to shifts in x and y, resp., while the left and right columns show the same information but at two different scales. On the left panels one can notice what was already mentioned earlier; the 2D negative Gaussian (ng) and negative Moffat (nm) fits lead to several outliers (shifts larger than 10 px) among different cubes. On the contrary, the maximal annular flux method never finds shifts larger than 2 pixels. This is to be expected; although the AGPM coordinates on the detector vary from epoch to epoch, this variation is never larger than a few pixels. Furthermore, we notice that the shifts found with the annulus method are always consistent within ∼0.3px for pairs of consecutive cubes, which is expected given that they were obtained consecutively during the observations (without manual recentering in between). Finally, visual inspection of the frames also suggested a satisfactory recentering. Altogether, the global recentering of the cube based on the maximal annular flux applied on its median-combined frame appears thus to be the most appropriate strategy for NACO+AGPM data.

The annular method appears optimal for coupling with the speckle halo cross-correlation alignment (where it replaces the 2D negative Gaussian fit centering part) to align together science and reference stars observed during a typical high-correlated RDI sequence. However, I noticed that the maximal annular flux centering method was most appropriate for a use on its own when the goal is to build a large cube of reference frames obtained at various epochs and in significantly different conditions. Indeed, I attempted to use the speckle

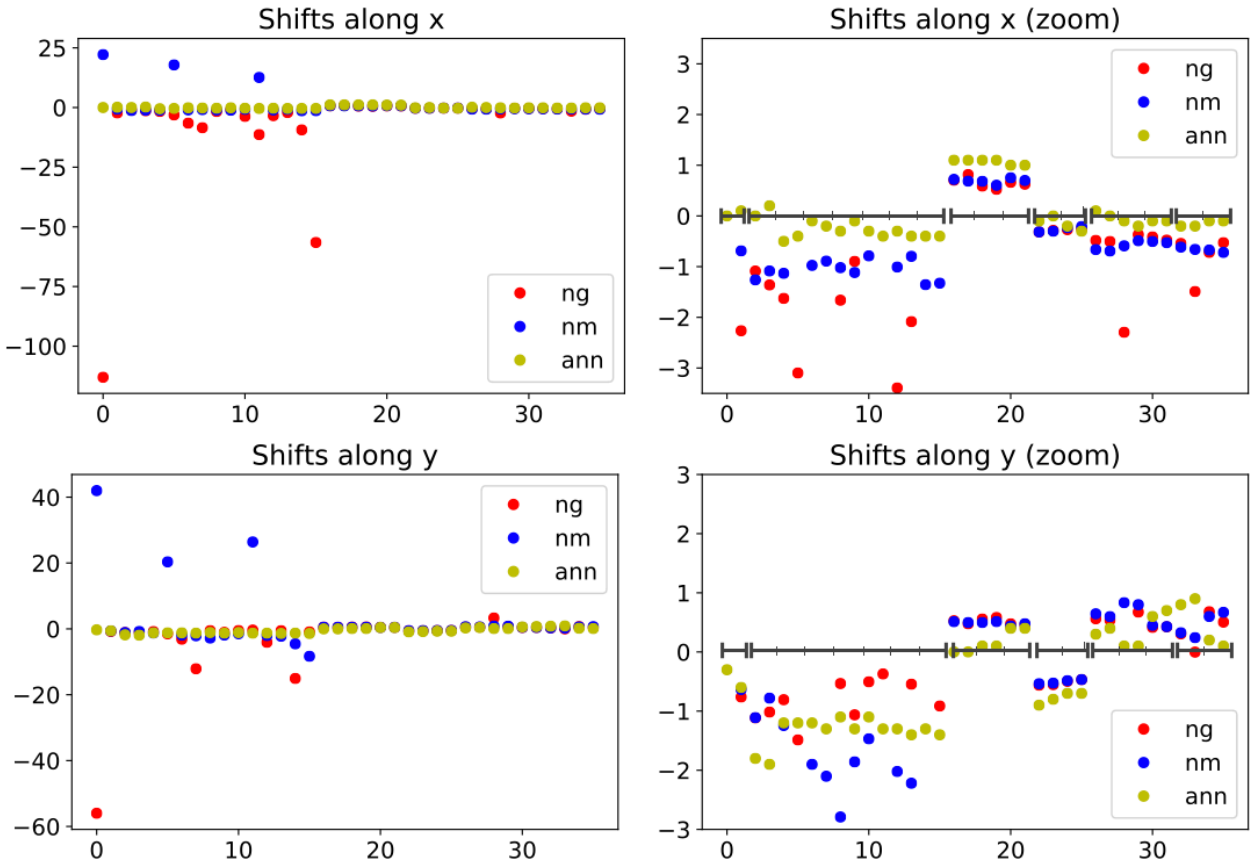

Figure 11.4: Measured centering shifts for 6 reference star datasets obtained with NACO+AGPM. Different centering techniques are compared: 2D negative gaussian or negative moffat fitting (*ng* and *nm* resp.) to the central AGPM hole, and annulus fit to the donut (*ann*). Compared to the negative gaussian and negative moffat, the annulus method does not yield any significant outliers (best seen in the left panels), and appear to provide consistent shifts for each pair of datacubes within a same sequence (indicated with thin ticks along the y = 0 axis). See text for more details

halo cross-correlation method to align all my reference star observations obtained at different epochs into a master reference cube and it lead, as somewhat expected, to visually poor centering (pixel-wise misalignement). This master reference cube could later be useful for the application of RDI on any dataset obtained with NACO in L', where frames used for building of the PCA library would be selected based on a cross-correlation criterion.

Coronagraphic PSF centering using a binary companion If a binary companion is present, it can be used to accurately recenter the coronagraphic PSF. I implemented a subroutine within my pipeline which enables to perform the centering based on a 2D Moffat fit of the centroid of the companion. These centroids correspond to a roughly circular trajectory during the night due to field rotation. My recentering algorithm takes advantage of that fact to fit the trace formed by the centroids with a circular arc. The deviations of the centroid locations with respect to the best-fit circle are then used to recenter each frame. The accuracy of the centering is proportional to the amount of field rotation available during the sequence, the brightness of the companion and its radial separation.

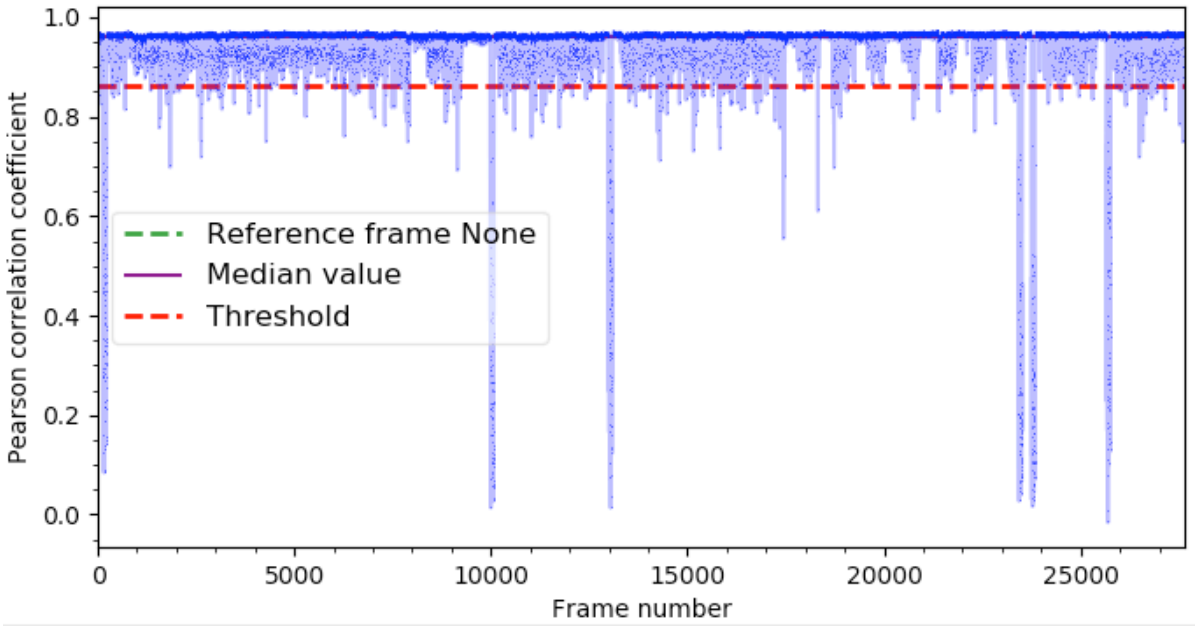

Figure 11.5: Example of bad frame trimming based on cross-correlation, on the dataset of J1900-3645. The threshold was such that 3% of frames in the whole observation were rejected.

The routine was tested on the datasets of HD 100453 and Sz Cha, and the resulting PSF of the companions appeared very sharp and round after post-processing, suggesting that the method performed well. This can be visualized in Fig. 11.8 in the case of HD 100453 B.

11.4.4 Bad frames rejection

During the observation, it can happen that the loop opens during acquisition, or that conditions get momentarily worse, leading to a poorer AO correction. It is thus better to remove these bad frames in order to keep the PSF as correlated as possible for an optimal model. For an automatic rejection of bad frames, I used the routine implemented in VIP which performs a cross-correlation of each frame of the cube with either a user-defined good-quality frame, or the median of the whole datacube. The level of correlation is measured with the Pearson correlation coefficient (r), a measure of the linear correlation between variables. Frames can then be trimmed according to a user-defined threshold for r, or for the percentile of frames to be rejected. An example is provided in Fig. 11.5, corresponding to the dataset of J1900-3645, where 3% of frames got rejected. For each source, I typically aimed to keep frames with $r \gtrsim 0.8$ with the median frame of the sequence. Frames with a significantly smaller value of r correspond mainly to images obtained in opened AO loop.

On average, between 1 and 5% of frames were flagged as bad and rejected, depending on the conditions. A higher ratio of bad frames were rejected for some datasets. This is the case of Sz Cha and HD 100453, both obtained in poor conditions. Both also happened to be surrounded by an M-star binary in the field of view, therefore I rather based the frame rejection on the measured flux of the companion. For those datasets, I rejected frames where the flux was lower than a standard deviation below the median.

11.5 Post-processing

At this point, the calibration has left us with a 3D datacube composed of correlated PSFs, with the star located on the central pixel of each frame. Different post-processing techniques are then used depending on the adopted observation strategy. Each calibrated datacube either contains sufficient angular diversity to apply an ADI-based algorithm, or is associated to a reference star datacube, which followed the same calibration process (and in particular a common alignment with the science cube) to enable the application of RDI. For the dataset of HD 98800, the binary acted as reference star for the application of BDI. As for the data calibration, I made an intensive use of the different tools implemented in VIP for the post-processing (Gomez Gonzalez et al. 2017). Given the large amount of data I obtained, I could contribute to the testing, debugging and minor improvement of some routines of the open source package. These include the addition of a more robust cropping algorithm (`get_square_robust()`), slight improvements to the PCA algorithms (e.g. an automatic loop implemented for the parallactic angle threshold used in PCA-ADI in annuli), additional options to both the routine calculating a normalized PSF template and the function computing the contrast curve. Additional minor contributions to VIP were also developed in the context of the VLT/SINFONI survey, and are mentioned in Sec. 15.3.

The typical first step in the post-processing of thermal IR observations consists of a *high-pass filtering* of all the frames in the calibrated cube (also referred to as *unsharped masking*, e.g. Wahhaj et al. 2013). In practice, the high-pass filter consists in the subtraction of a median-filtered image using a 4-FWHM-size box. This is to remove spatial frequencies corresponding to background variations that are related to an imperfect sky subtraction. This step can also be followed by smoothing using a Gaussian kernel of 1 FWHM to enhance signals at that spatial frequency. Nonetheless, given the extremely large sizes of our datasets (5000-20000 frames), either of these steps involved prohibitive CPU time and resources. Therefore, in practice, all datasets were first reduced without these preliminary steps. However, for sources where the images of the first reductions revealed something potentially interesting (i.e., the sources that are discussed in Sec. 11.6), I did came back to this preliminary step, and applied a high-pass filter after cropping the frames to a relevant size. This typically led to an improvement of the significance of possible detections.

11.5.1 PCA

Regarding the post-processing, I made use of PCA (Sec. 10.4.2). PCA is implemented in VIP with different flavors regarding the geometry of the area it is applied on. I tested both PCA in full frames and in concentric annuli. PCA in full frame is as described in Sec. 10.4.2.

Specificities of PCA-ADI

The annular version of PCA-ADI first divides the field in concentric annuli and applies PCA separately in each of these annuli. In addition, it also considers a parallactic angle threshold so that the PCA library built for each annulus only contains annuli of other frames in which a putative planet has sufficiently rotated to minimize self-subtraction. It is thus CPU-intensive and leads in practice to prohibitive calculation time for large non-binned datacubes.

Specificities of PCA-RDI

PCA can be coupled to RDI, either in full frame or in annuli. An additional parameter that is relevant to PCA-RDI is the so-called *scaling* of the reference cube. By default, the scaling can be set to "None", which tells PCA to use the reference cube as is to compute principal components. It can also be set to "temp-mean", which consists in removing a temporal mean of the pixels in the time direction. This option performs thus a kind of median-ADI to the data before RDI. A last possibility is to set the scaling to "temp-standard", which not only removes the temporal mean, but also scales the flux in order to make the pixels have the same rms over time. The advantage of this option is that it gives more weight to the outer parts of the image when applying RDI.

11.5.2 Post-processing scheme

For each dataset, I carried out several sets of reductions using different algorithms and parameters, such that the results could be obtained within a reasonable timeframe. These are detailed in the following paragraphs.

Original cube

I applied both median-ADI and PCA (coupled with either ADI or RDI) in full frame for a range of n_{pc} that is commensurate with the size of the dataset. For example, for cubes made of thousands of frames of 300x300 px, I explored values of n_{pc} geometrically spaced between 2 and several hundreds. The cube is not binned temporally as the sensitivity towards faint companions is optimal without binning. This is a conclusion I reached based on fake companion injection tests and based on the SNR of the companion candidates presented in the next section (tests leading to the same conclusion are shown in Gomez Gonzalez et al. 2017).

Cube cropped in size

On a cube where the frames are cropped to 1″ raidus (71x71 px), I also applied median-ADI and full-frame PCA for a range of values in $n_{\rm pc}$. A first contrast curve is computed for median-ADI. I injected fake companions at various radial separation at 0.8 times the 5σ level contrast inferred with the median-ADI contrast curve. These fake companions were typical injected at 0″.2 and spaced radially by 0″.2 and spaced azimuthally by 120°, so that their injection follows a spiral geometry. Then I searched for the optimal $n_{\rm pc}$ which enabled to optimize the SNR of those companions at different separations. Finally, I computed PCA-ADI contrast curves using the optimal $n_{\rm pc}$ inferred above; the final optimal contrast curve considers for each separation the highest contrast inferred in the different contrast curves.

Cube both cropped in size and binned temporally

On a cube where the frames are cropped to 1″ radius (71x71 px) and binned temporally by a factor 10, I applied the same procedure as described in the previous paragraph, but using PCA-ADI in annuli. As this flavor of PCA is extremely CPU-intensive on cubes made of several thousand frames, results can be obtained within a reasonable timescale only after temporal binning of the input cube. I noticed that in practice the contrast curve of PCA-ADI in annuli reached similar levels as PCA-ADI in full frame, which could suggest that the detrimental effects of temporal binning and selecting frames far in time for the PCA library, and beneficial effect of minimizing self-subtraction tend to average out.

Characterization of companions

For cases where a companion candidate was found, I also used PCA in a single annulus centered on the radial location of the companion candidate, and studied the evolution of its signal with varying $n_{\rm pc}$ values. I estimated the SNR and significance of companion candidates as explained in Sec. 10.5.1. I also used the technique of the negative fake companion (NEGFC, e.g. Lagrange et al. 2010; Wertz et al. 2017) in order to retrieve the astrometry and photometry of the companion candidate seen in the image. ADI-based algorithms are indeed known to significantly alter the flux and affect the geometry of the PSF of companions in the post-processed image. NEGFC bypasses these biases allowing for a more robust estimate of the position and flux of companions. This is done by injecting negative PSF templates in the calibrated cube (before post-processing) at the rough location of the companion, subsequent application of (PCA-)ADI, and minimization of a certain figure of merit in the post-processed image. The figure of merit can be chosen to be either the residual absolute flux or the standard deviation measured in an aperture centered on the companion in the post-processed image. The process is iterative regarding the location and flux of the injected negative PSF templates, until the figure of merit is minimized. In practice, the search can be performed with a simplex or a Monte-Carlo Markov Chain (MCMC) sampler, as implemented in VIP.

11.6 Results

In this section, I first present global results of the survey in terms of achieved sensitivity, and then specific results obtained for outstanding targets separately. All observed datasets obtained before June 2018 were post-processed and are discussed in this section. Known disk features were redetected around HD 100453, T Cha and HD 135344 B. Out of 15 transition disks observed so far, four have led to the tentative detection of point-like sources (not reported in the literature yet): WW Cha, HD 135344 B, J1622-3724, and J1900-3645. Finally, I also present the results of the application of BDI on HD 98800 B.

11.6.1 Contrast curves of all ADI sources

For all sources observed with the ADI strategy, the sensitivity achieved in the final images was estimated with contrast curves, as per the procedure described in the previous section. These are shown in Figs. 11.6 and 11.7. Each curve is built from a combination of the optimal contrast reached at different separations with different $n_{\rm pc}$. The optimal $n_{\rm pc}$ is typically lower at shorter separation, as larger values of $n_{\rm pc}$ start to overfit the image from the inside out, leaving pixel noise at high spatial frequency in an increasingly larger circular area centered on the star.

In Fig. 11.6, the deepest contrast is achieved with the HD 100453 dataset between 0$''$.3 and 0$''$.8 separation, which is not surprising considering that it is both the brightest target of our sample (L=4.7 mag) and the one with the longest integration (117 min). The bump in contrast around 0$''$.18-0$''$.2 is likely due to bright signal from the edge of the cavity, including from the spirals (Fig. 11.8). The increase in the contrast curve towards a separation of $\sim$1$''$.0 is due to the bright M-dwarf companion, which was not removed from the datacube.

The second deepest contrast is obtained with HD 135344 B, which is also the second brightest source in our sample (L=5.0 mag). When compared with the final image of the system (Fig. 11.16c), the humps in the contrast curve at $\sim$0$''$.19 and $\sim$0$''$.32 are likely to be due to extended disk signals, including a bright spiral arm. For a better comparison with previous L' NACO+AGPM contrast curves shown in Mawet et al. (2013) and Absil et al. (2013), which did not consider Student statistics, I also provide the 5σ Gaussian contrast curve (i.e., not corrected considering small-sample statistics) with a *red dashed curve*. In Mawet et al. (2013) and Absil et al. (2013), the contrast achieved at 0$''$.1 separation were 7.5 mag and 8.8 mag respectively. The source in Mawet et al. (2013), HR 4691, is slightly fainter than HD 135344 B, while β Pic whose NACO+AGPM contrast curve is presented in Absil et al. (2013) is 1.5 mag brighter. Considering these facts, the contrast achieved in the HD 135344 B dataset is in good agreement with these early results. The discrepancy at larger separation is most likely due to strong disk signal in the HD 135344 B image between 0$''$.18 and 0$''$.3.

Datasets obtained on DoAr 21, TWA 7 and RU Lup corresponded to my first observations with NACO+AGPM, and the observation likely suffered from my inexperience, that

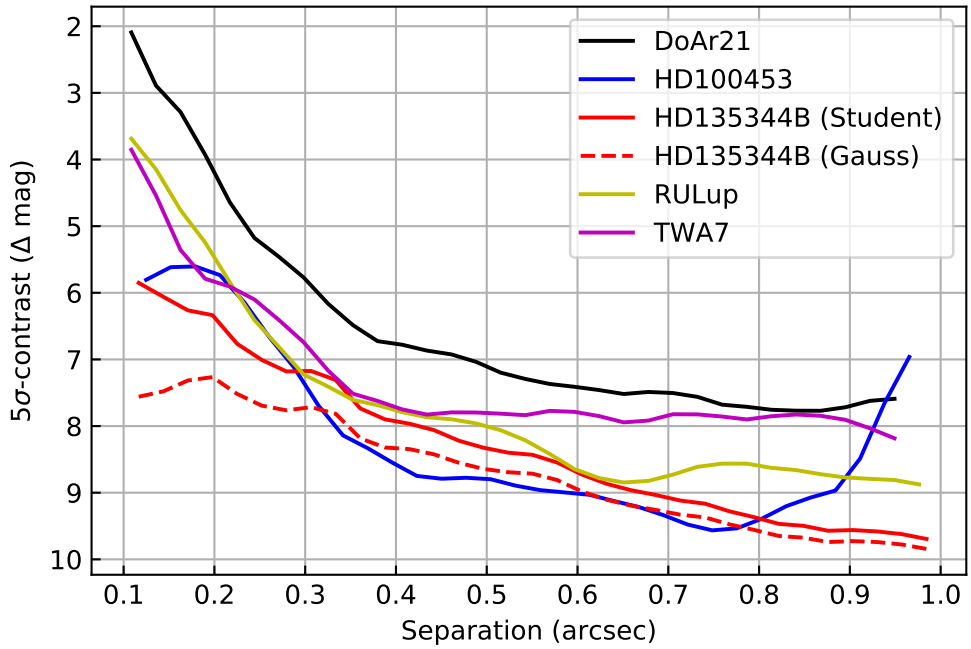

Figure 11.6: Optimal contrast curve for all the sources observed with AGPM+ADI (the brighter sources of our sample). See text for details.

of the support astronomer, and our ignorance of the AGPM drift problem. In particular, I suspect the alignment of the AGPM to be sub-optimal throughout the observations, with alignment accuracies of 0.5-0.7 px compared to ∼0.3 px for the HD 135344 B dataset obtained a year later. Furthermore, I suspect that the particularly shallow contrast obtained with the DoAr 21 dataset is due to an additional effect. This target was observed on both sides of the zenith hole, however without appropriate reference star observation in the middle. Given the ∼180° field rotation between the two halves of the dataset, but the very small amount of rotation ($\lesssim 5°$) within each half, I forced the PCA library of each frame to be built from frames of the other half. The observing conditions changed significantly while the target was transiting, and I suspect the quasi-static speckle patterns of both subsets to be significantly decorrelated. Visual inspection of the calibrated cube shows indeed tentative differences between the PSF before and after the zenith hole. Therefore, this result suggests that for targets passing through the zenith hole, the use of an appropriate RDI strategy (such as shown in Fig. 11.1) is necessary to optimize the final contrast.

The contrast curves obtained for fainter sources ($L \geqslant 7$ mag), which did not involve the use of the AGPM, are shown in Fig. 11.7. One can notice the more abrupt shape of the contrast curve at small angle ($r \lesssim 0\farcs3$) compared to the contrast curves obtained with the AGPM. The achieved contrast is best at small angle for the dataset of J1623-4015, which benefitted from the best observing conditions and largest field rotation. The spread in the contrast curves at large separation ($r \gtrsim 0\farcs5$) reflect mostly the spread in brightness of the central star, which sets the contrast level at which the background noise is reached. The dataset of Sz 84 was affected by an extremely elongated PSF. It is also one

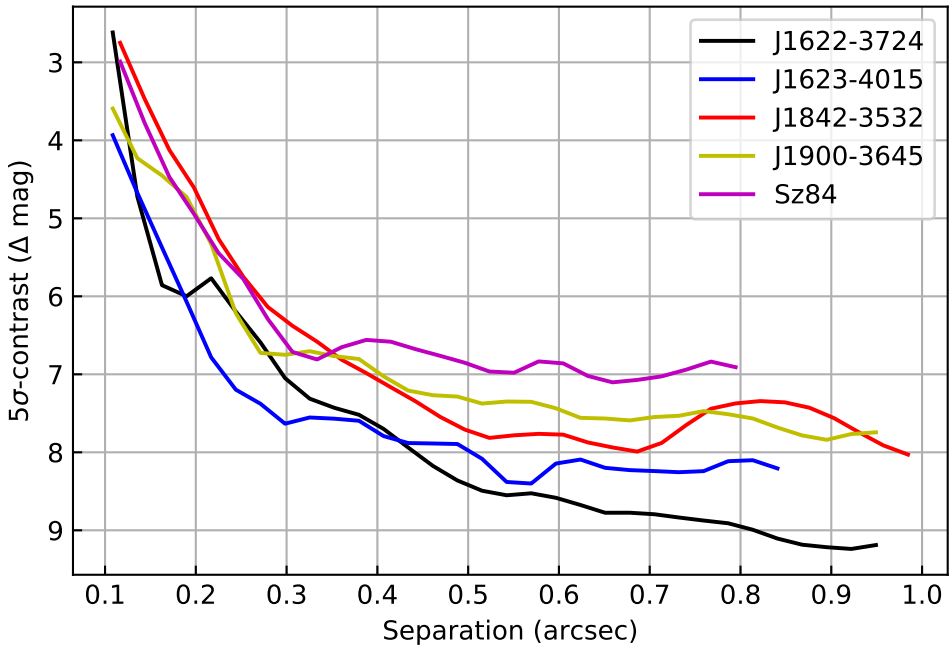

Figure 11.7: Optimal contrast curve for the sources observed with ADI, but without AGPM (the fainter sources of our sample). See text for details.

of the faintest sources of our sample. Both factors likely contribute to make it the shallowest contrast curve of our survey. The contrast achieved at large separation ($r > 0\farcs6$), in the background-noise-dominated regime, appears globally better than that of datasets obtained with the AGPM (considering the central stars are significantly fainter than those presented in Fig. 11.6). This is likely due to (1) a much better sky sampling, obtained every minute with the star dithering strategy, resulting in an optimal background subtraction, and (2) a larger number of photons acquired for a given total integration time, due to a higher throughput in the absence of AGPM and Lyot stop. Although the datasets of Sz 84, J1842-3532 and J1900-3645 were also acquired in service mode, they were affected by an extremely elongated PSF, mediocre (and variable) observing conditions and small amount of total field rotation, resp., which might account for the shallower contrasts.

11.6.2 Contrast curves for RDI datasets

For RDI datasets, a bug appears to be affecting the contrast estimated by the routine implemented in VIP. This conclusion was also suggested by results obtained on other NIRC2 datasets (Maddalena Reggiani, private comm.). I could recently pinpoint the source of the problem thanks to the RDI dataset on T Cha (see dedicated subsection). Nonetheless, the implementation of the solution is not straightforward, and requires some significant change in the code. I mentioned the problem to Carlos Gomez, and plan to tackle the implementation of a solution after completion of my thesis. In the meantime, this implies

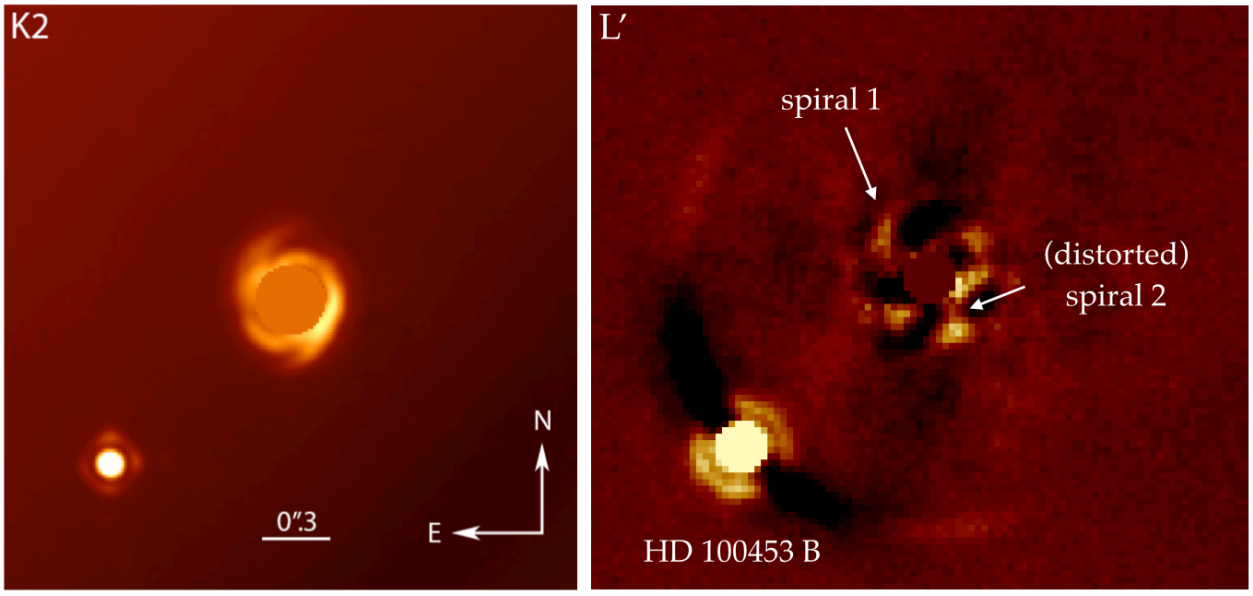

Figure 11.8: (left) SPHERE/IRDIS K-band image of HD 100453 (extracted from Wagner et al. 2015). (right) Final image obtained using median-ADI on the NACO L' dataset (which is similar to the PCA-ADI reduction with $n_{\rm pc} = 1$, after centering of the cube using the binary companion.

that contrast curves obtained on the RDI datasets of this survey are not reliable. They are thus not shown.

11.6.3 HD 100453

HD 100453 is an isolated Herbig Ae star located at ∼104 pc (Gaia Collaboration et al. 2018), with an M-dwarf binary companion. Its disk harbors a ∼0″.18 cavity and a conspicuous pair of spirals (Wagner et al. 2015; Benisty et al. 2017, Fig. 6.5g). A pair of shadows, best seen in polarimetric images of the disk (Benisty et al. 2017, Fig. 6.4c), are located at the root of the spirals, which could suggest the shadows are triggering the spirals (Montesinos et al. 2016, Sec. 7.1). Nonetheless, the results of the analyses of Dong et al. (2016) and Wagner et al. (2018) are compatible with the hypothesis of the spirals being launched by the binary companion. However, the companion does not account for the shadows, which rather suggests the presence of a warped inner disk. The latter was recently confirmed through modeling of NIR interferometric data (Min et al. 2017). The large gap and warp could suggest the presence of an additional companion inside the cavity as in the case of HD 142527 (Sec. 7.3). This source was thus a prime target to be included in the survey.

I retrieved the data acquired by ISPY from the ESO archive after they became public. The absence of sky frames in the dataset forced me to use the first principal component of the whole datacube as a proxy for sky subtraction. Our final image obtained with median-ADI is shown in the right panel of Fig. 11.8. The bright M-dwarf companion appears sharp and round; which suggests that the method implemented to recenter the raw cube, based on a fit of the binary trajectory with a circular arc (Sec. 11.4.3), appears to perform well. For

this bright companion, it is possible to see clearly the biases introduced by ADI at the same radial separation as the companion; a strong negative-positive residual pattern spanning a similar azimuthal extent as the parallactic angle range.

The reduction using median-ADI and PCA-ADI with few $n_{\rm pc} < 3$ shows some tentative counterparts to the known spirals in this system (Wagner et al. 2015; Benisty et al. 2017), as labelled in Fig. 11.8. It appears that ADI is enhancing the bright part of spiral 2, thereby distorting its morphology. Increasing $n_{\rm pc}$ totally self-subtracts the extended structures, which reminds us of the dangers of using ADI to analyze extended disk features (see also Milli et al. 2012, and Sec. 15.5.1). No other companion is found in the image. I noticed that a new dataset was acquired by ISPY on this source, in much better conditions, and is now available in the archive. I plan to reduce these new data as well.

11.6.4 T Cha

T Cha is a bright nearby (d $= 109.6 \pm 1.0$ pc; Gaia Collaboration et al. 2018) transition disk located in the ϵ Cha star-forming region. One of the first protoplanet candidate claims was made in that disk using SAM (Huélamo et al. 2011, Sec. 4.3), but was later refuted as combined SED and SAM modeling rather suggested the asymmetry could be accounted for with forward scattering of an inclined disk (Olofsson et al. 2013). New SPHERE images have recently enabled to resolve the disk for the first time in NIR (Pohl et al. 2017b, left panel of Fig. 11.9). This new image was the opportunity to test our RDI reduction on that dataset, considering the SPHERE DPI image as proxy of the ground truth image of the disk (i.e., not affected by geometric biases due to post-processing).

In Fig. 11.9, I compare the SPHERE image to the final images obtained with NACO+AGPM using different *scalings* for the PCA-RDI reduction and two different values of $n_{\rm pc}$ (see Sec. 11.5.1 for a description of the scaling parameter). The NACO images are roughly cropped to the same size as the SPHERE image. The disk image is not clearly recovered for the no-scaling reduction, and increasing $n_{\rm pc}$ does not enable to retrieve a good image from the disk before it gets self-subtracted. On the contrary, the disk image is well recovered with temp-mean and temp-std scaling for $n_{\rm pc}$ values ranging from 2 to almost 100. Some negative lobes are seen on the sides of the disk signal, which are likely due to the scaling, which can be described as an ADI-preprocessing step before doing RDI. The results of these tests suggest that, when the reference cube is not very well correlated with the science cube (as is the case here), temp-mean and temp-std scaling are crucial to increase the contrast achieved with RDI.

The associated contrast curves computed for the different values of the scaling parameter suggeste the presence of a bug in VIP, as previously noted based on NIRC2 RDI datasets (M. Reggiani, private communication). This can be directly inferred from the shape and values of the temp-std contrast curve, which do not appear to make sense. This is also hinted by the fact that the contrast curves obtained with no scaling and temp-mean scaling differ by only $\sim$0.5 mag, while the final images obtained with these two parameters suggest a more significant difference. In light of the disk images, I re-inspected the VIP

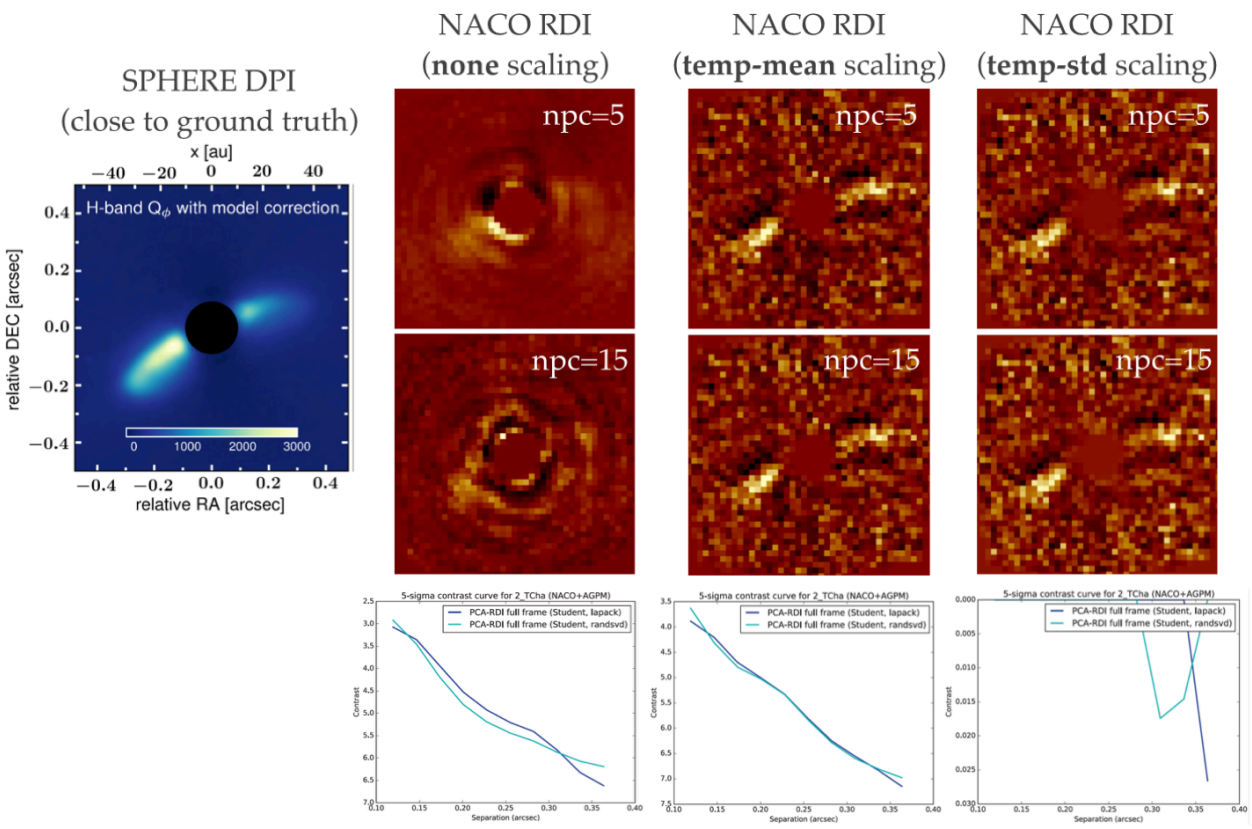

Figure 11.9: RDI tests on the dataset of T Cha. (left panel) The recent image obtained with SPHERE provides a proxy of the ground-truth image of the disk (Image extracted from Pohl et al. 2017b). Then, from left to right, the three columns of NACO images correspond to reductions with *no scaling*, *temp-mean scaling* and *temp-std scaling*, for two different values of $n_{\rm pc}$. The bottom row of these columns corresponds to the contrast curves calculated by the routine implemented in VIP. See text for details.

code and deduced that the origin of the problem was an inappropriate computation of the throughput in the calculation of the contrast curve in the temp-mean and temp-std cases. The throughput associated to a particular post-processing algorithm (i.e., the percentage of flux of any true companion that is preserved in the final image) is typically computed by comparing the flux of injected fake companions in frames before and after post-processing. The problem is that temp-mean and temp-std *re-scale* the cube *after* the first measurement of the flux. Therefore, the flux measured in the final processed frame is not directly comparable with the frame in the original non-rescaled frames. However, since this rescaling is done within the PCA function, the correction of the problem is not straightforward and requires some careful modification of the contrast curve function. I have not had the time to implement the solution yet, nonetheless, a meeting with Carlos Gomez is planned in order to fix this issue. The conclusion is that only the contrast curve inferred for no scaling is reliable. The fact that that contrast curve is shallow appears in agreement with the poor quality of the corresponding disk image.

11.6.5 WW Cha

WW Cha is located at a distance of 192.1 ± 1.5 pc (Gaia Collaboration et al. 2018), and is the brightest transition disk in the Chameleon I star forming region (L=4.9 mag). Its extremely red color (V = 14.1 mag) suggests that the source is significantly self-embedded. There is no published resolved image of the disk, which could be partly due to the difficulty of using an AO instrument with a visible WFS on such red source.

Applying PCA-RDI with temp-mean and temp-std scaling on that dataset reveals a point-like source at $\sim$0.″47 separation and PA$\sim$185° (left panel of Fig. 11.10). Considering the separation of the point-source and Student statistics, the significance of the detection is 4.6σ. Its contrast, as estimated with NEGFC, is 9.1$\pm$0.2 mag with respect to the parent star. The NEGFC estimate should not be affected by the throughput issue mentioned in the previous subsection; although the negative fake companion injection is performed in the cube before scaling, but the scaling should not affect the relevance of the figure of merit in the final frame. Although the companion is less significant in a PCA-ADI reduction only, I tested NEGFC with PCA-ADI, PCA-RDI (temp-mean scaling) and PCA-RDI (temp-std scaling) and they all lead to $\sim$9.1 mag contrast, which appears to confirm the previous statement.

Assuming it traces an authentic companion, the absolute magnitude of the point-like source ($M_{L'} \sim 7.6$mag) would correspond to a $\sim 16 M_{\rm Jup}$ planet, assuming pure photospheric emission from the COND hot-start model (Baraffe et al. 2003), and considering the estimated age of the Cha I region ($\sim$ 2 Myr). I note that this mass estimate is optimistic due to the use of a hot-start model, and could be even more so considering how embedded the parent star is; a more massive companion might be lurking in the disk with its light being significantly affected by extinction, such as in the case of FW Tau C (Kraus et al. 2014; Wu et al. 2017, Sec. 4.2).

Assuming the signal is authentic, it could also trace a filtered disk feature. The first resolved images of the disk using polarimetry have recently been obtained as part of the DARTTS survey (Avenhaus et al. 2018), and will be presented in a future publication (Avenhaus et al., in prep.). The SPHERE/ZIMPOL polarized H-band image displays a large scale spiral-like feature which appears to pass through the location of the blob (H. Avenhaus, private comm.). Therefore, the new dataset that I acquired on June 1, 2018, and which I have not had the time to reduce yet, will enable to test the authenticity of the blob. If the signal is re-detected, follow-up with ALMA gas line observations would enable to infer the mass of the companion based on the kinematics of the gas and without being biased by extinction (e.g. Perez et al. 2015; Pinte et al. 2018). Such ALMA data already exist for WW Cha but are still in proprietary time (PI: T. Muto).

11.6.6 HD 135344 B

HD 135344 B (SAO 206462) is a Herbig Fe star located at a distance of $\sim$142 pc (Gaia Collaboration et al. 2018) with an estimated mass and age of $1.7 \pm 0.2 M_{\odot}$ and 8^{+8}_{-4} Myr, resp. (Müller et al. 2011). This system has been extensively studied in the recent years as the disk

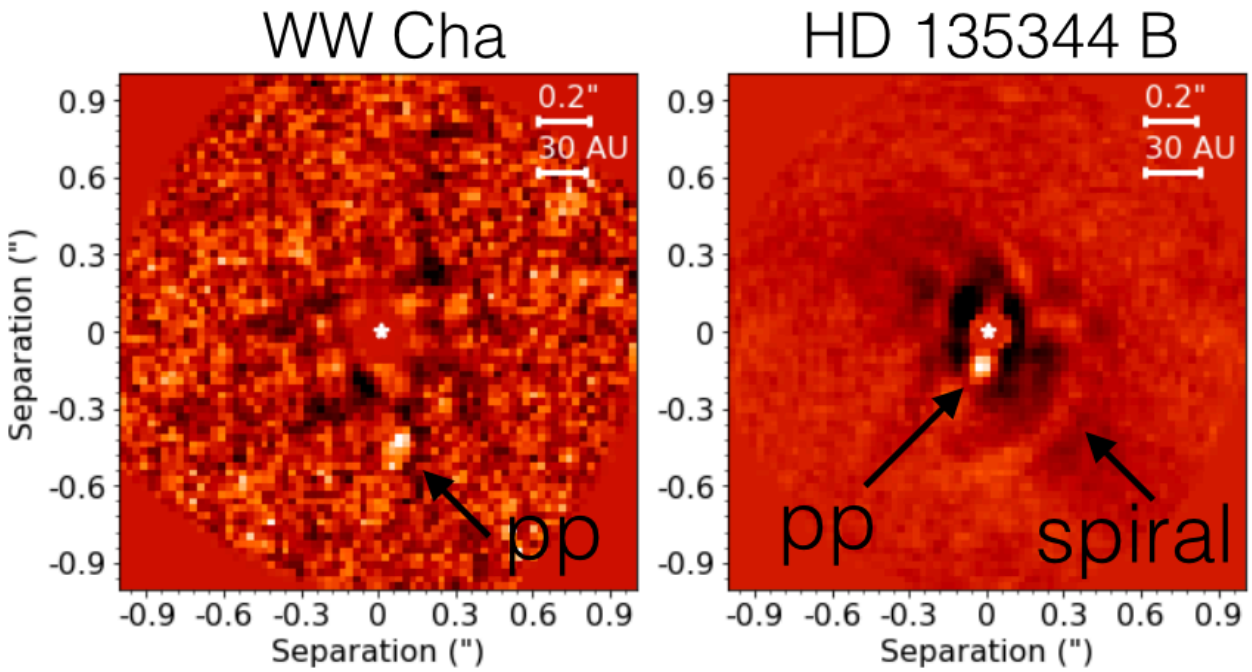

Figure 11.10: Final images obtained on the datasets of WW Cha and HD 135344 B, both obtained using the AGPM. The WW Cha image is obtained using PCA-RDI, with the temp-std scaling. The HD 135344 B image corresponds to a PCA-ADI reduction. See text for details.

turned out to harbor strong planet signposts: a cavity significantly depleted in small dust, large dust and gas but with different gap sizes inferred for each component (Brown et al. 2009; Garufi et al. 2013; van der Marel et al. 2016b); prominent spiral arms (Muto et al. 2012; Garufi et al. 2013; Stolker et al. 2016) and an asymmetric mm-size dust distribution (Pérez et al. 2014). A significant accretion rate was measured for the primary star ($\sim 10^{-7}$–$10^{-8} M_{\odot}\mathrm{yr}^{-1}$), requiring material to cross the cavity (Garcia Lopez et al. 2006; Fairlamb et al. 2015). In addition, the disk shows shadows that are quickly varying in time (on the timescale of less than a day), suggesting an origin to be related to optically thick material in the inner parts of the disk (Stolker et al. 2016, 2017). A large variety of scenarios have been put forward to account for the peculiar morphology of the disk, involving different predictions regarding the mass and location of companions:

- Muto et al. (2012) proposed that each spiral arm was launched by a planet in the outer part of the disk.
- Garufi et al. (2013) suggested the presence of a planetary mass companion inside the cavity to account for the different gap sizes in gas and mm-size dust.
- Based on a joint SED and IR-images fit, Carmona et al. (2014) have inferred that inside the cavity, the surface density of the gas must increase radially outward, suggesting the presence of a migrating giant planet.
- The hydrodynamical simulations in Dong et al. (2015b) reproduce well the double spiral arms with a planet at a radial separation of $\sim$ 100 a. Based on the observed contrast of the spirals, Dong & Fung (2017a) suggested that the mass of the planet must be $\sim$ 5–10 M_{Jup}. This mass estimate is consistent with the prediction of a $\sim 6 M_{\mathrm{Jup}}$ companion causing the relatively constant separation angle of $\sim$130° between

the two main spiral arms (Fung & Dong 2015).

- Similarly, the simulations in Bae et al. (2016) suggested that a single massive planet ($\sim 10 M_{\rm Jup}$) in the outer disk could launch both spirals and trigger the dust trap, which in turn would prevent further large grains to migrate inward, hence creating the cavity.
- van der Marel et al. (2016a) proposed on the contrary that a single massive companion in the cavity could be at the origin of the spiral pattern. More exactly, the companion would trigger both a spiral arm outward and a ring-shape dust trap at the edge of the cavity. The latter would then create a secondary vortex dust trap outward, launching a second spiral arm (the one coincident with the vortex location; see images in Pérez et al. 2014; van der Marel et al. 2016b).

Nonetheless, the putative planets have eluded direct detection so far (e.g. Vicente et al. 2011; Maire et al. 2017), which has prevented to find out which of these scenarios is indeed happening. Armed with the AGPM of NACO, we observed the system in L' in order to reach a higher sensitivity to faint red companions at small separation. Any detection might enable to untangle the true scenario at play, and be of possibly significant importance to explain the origin of similar features seen in other Herbig transition disks (e.g. MWC 758, HD 100546, AB Aur; Benisty et al. 2015; Reggiani et al. 2018; Follette et al. 2017; Tang et al. 2017). HD 135344 B has thus the highest priority among all targets of our sample, and multiple epoch observations with different instruments have been obtained, as detailed below.

Two datasets were obtained with NACO+AGPM on HD 135344 B in 2017 (see Tables 11.3 and 11.4). The visitor mode observations were obtained in mediocre and variable seeing conditions, and short coherence time, leading to a PSF of poor quality, visually varying over time. The service mode observations, although obtained with only 33° field rotation and mediocre seeing, had a longer coherence time and benefitted from more stable conditions, which led to a good PSF quality, relatively stable throughout the observation. Both datasets were reduced but, as expected, the contrast achieved in the service mode images was significantly better. The final PCA-ADI image obtained on the service mode dataset is shown in the right panel of Fig. 11.10. A bright blob is visible to the SE of the image, at a separation of $0\farcs125 \pm 0\farcs010$, PA $\sim 171 \pm 3°$, and 5.3±0.3 mag contrast, as estimated by NEGFC. In addition, the brightest of the two spiral arms in that system can also be distinguished to the SW, at ∼0″.30-0″.55 radial separation. In order to check the authenticity of the blob, I carried out a series of tests, described in the next paragraph.

Speckle tests - assessing the authenticity of the NACO L' blob

When a bright blob is found at such small separation (here at ∼1.2FWHM), additional precautions have to be taken to ensure the signal does not correspond to a residual speckle. In practice, the tests do not enable to fully discard the possibility of a pinned speckle, but can reject the hypothesis of an authentic companion if any of the tests yields a negative result.

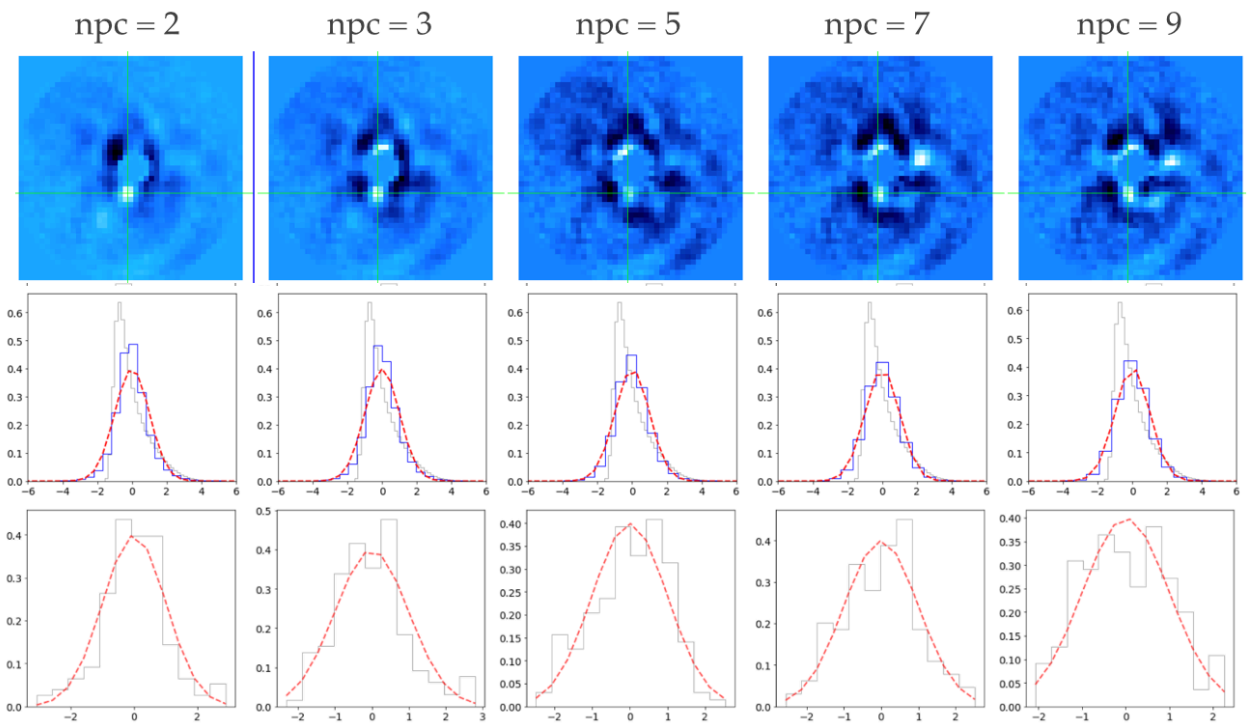

Figure 11.11: First speckle test: survival of the blob with varying number of principal component, and test of the normality of the pixel value distribution in an annulus of a 1-2 FWHM separation (the blob is at . The blue curve corresponds to the measured pixel distribution, compared to a normal distribution (*red dashed* curve) and an MR distribution (*gray curve*). All distributions are normalized to a zero-mean and unit standard deviation. See text for details.

The first test consists in checking the survival of the blob with the number of principal components used for the PCA-ADI reduction. The presence of the blob for a single value or in a very short range of $n_{\rm pc}$ would strongly suggest that the blob is a speckle; so would its sudden disappearance from one value of $n_{\rm pc}$ to another instead of a progressive self-subtraction with increasing $n_{\rm pc}$. This test is shown in the top row of Fig. 11.11. The blob appears to survive for all $n_{\rm pc}$ values from 2 to a dozen, and appears progressively self-subtracted with increasing $n_{\rm pc}$. Another test consists in checking the distribution of pixel values in an annulus encompassing the location of the companion. A spreading closer to a modified Rician (MR) than to a Gaussian distribution would suggest that the correlated noise has not been well subtracted/whitened, and that most of the signal seen would trace the residual speckle field (e.g. Soummer et al. 2007). Statistics of a modified Rician distribution are strongly in disfavor of an authentic companion, as the possibility of a bright residual speckle would be much more likely (e.g. Soummer et al. 2007). The distribution of pixel values in a 1-2 FWHM annulus in the cube obtained after subtraction of the PCA model to each individual frame is shown in the middle row of Fig. 11.12. The normalized distribution of pixel values, shown with a *blue curve*, appears closer to the unit Gaussian distribution (*red dashed curve*) than to the normalized MR distribution (*gray curve*), with a better agreement for increasing values of $n_{\rm pc}$ (representative of a better subtraction of the correlated noise). The distribution of pixel values in the same annular region of the final collapsed frames is provided in the bottom row of Fig. 11.12, where one can notice that the final distribution is further whitened by means of the central limit theorem and follows

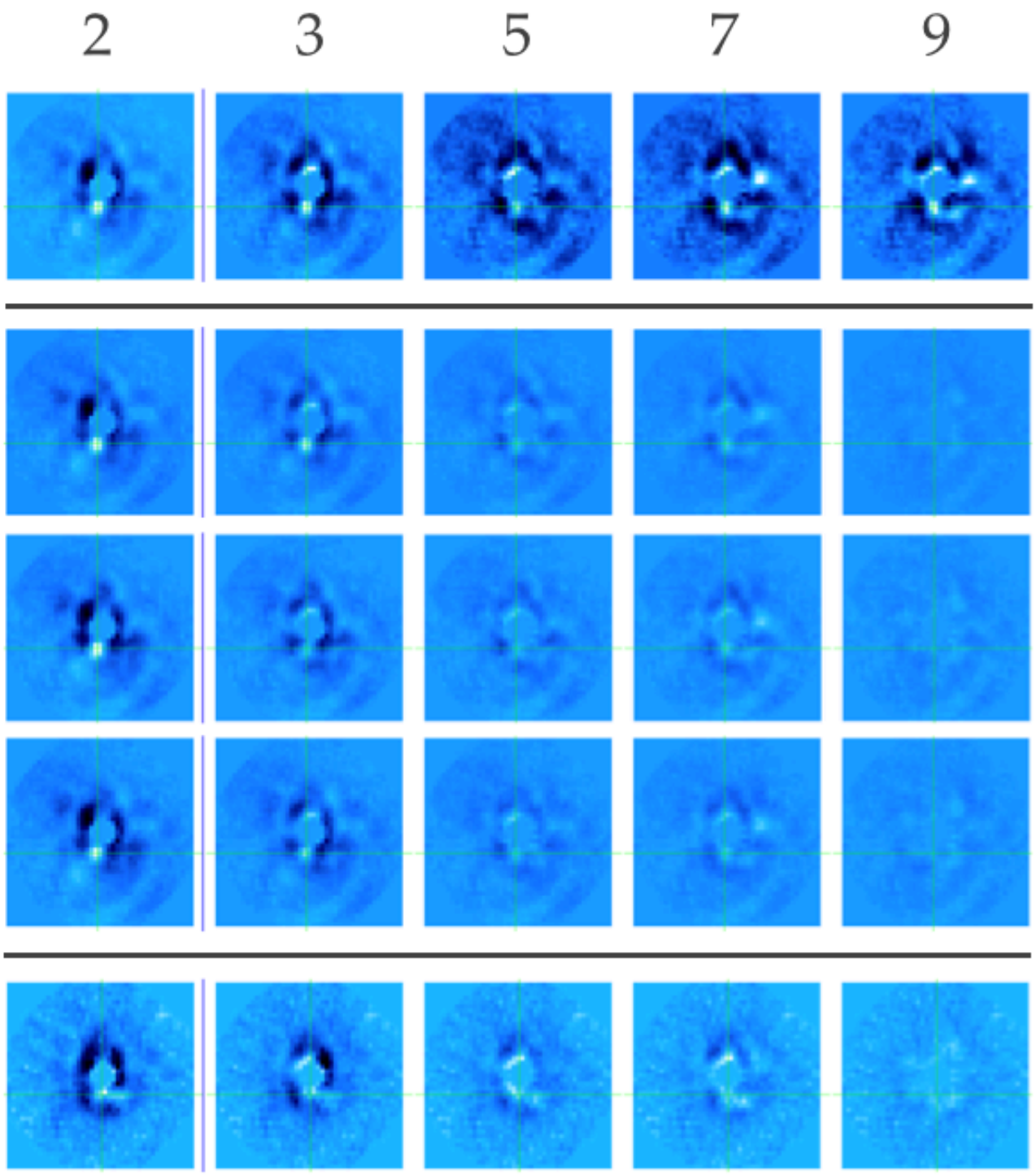

Figure 11.12: Second speckle test: comparison of the results obtained with the original cube (*top row*), with different partitions of the cube keeping only half of the frames but preserving the whole parallactic angle range (*middle rows*) and with a partition of the cube keeping only half of the frames and dividing in half the whole parallactic angle range (*bottom row*). See text for details.

relatively well (considering the small number of pixels in the annulus of a single image) a unit normal distribution. From these tests, it is thus not possible to discard the possibility of an authentic companion signal.

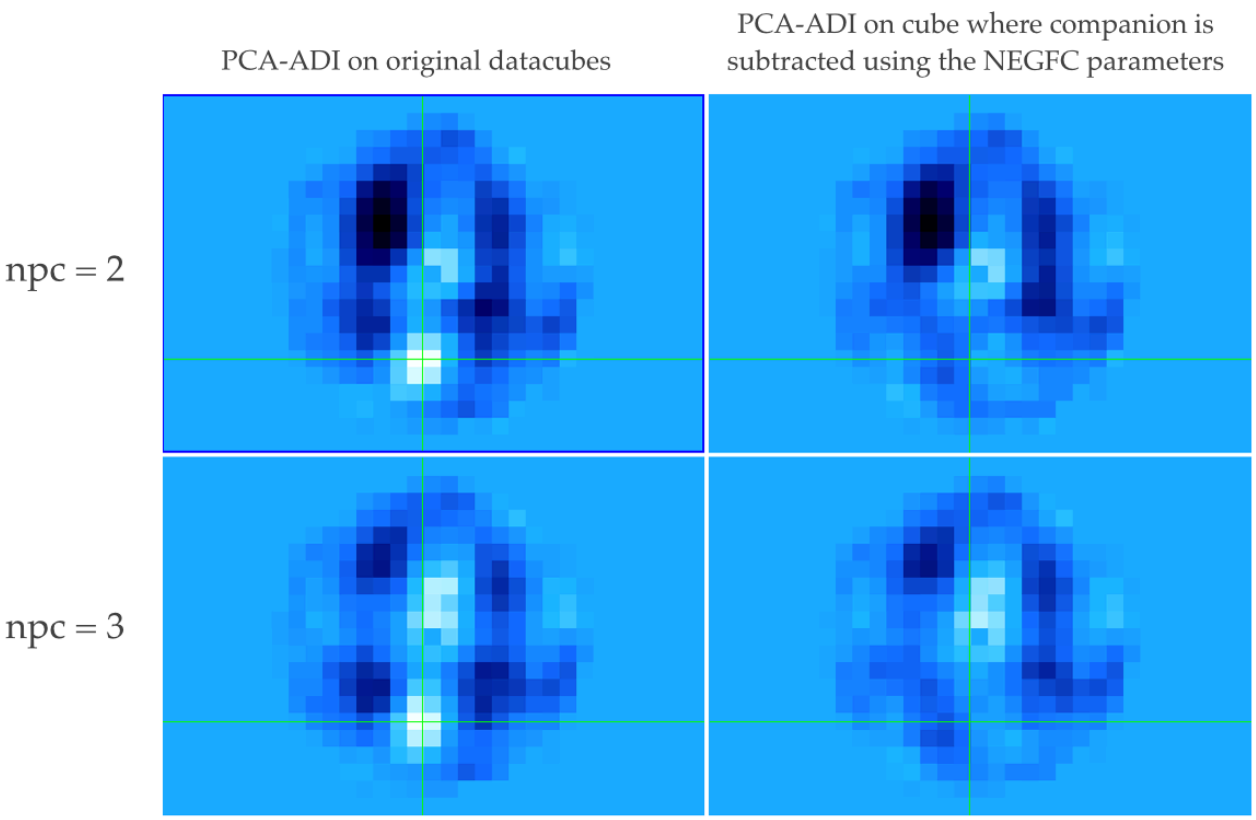

Figure 11.13: Third speckle test: subtraction of the companion from the original cube. The negative lobes framing the blob seem to disappear, which is the expected behavior if they were tracing negative ADI side lobes in the first place. See text for details.

Next, I tested the survival of the blob when PCA-ADI is applied to different partitions of the datacube. The detectability of a truthful companion with ADI depends on the total parallactic angle range of the sequence; a shorter range will lead to more self-subtraction. Here, the total field rotation is only 32°, leading to only ∼0.7 FWHM linear motion at the location of the companion candidate, so that self-subtraction is expected to be significant and could account for the total self-subtraction of the companion for $n_{\rm pc}$ values larger than a dozen. In Fig. 11.12, I show the reduction obtained with various $n_{\rm pc}$ values ranging from 2 to 9, for the original cube (top row), different partitions of the cube keeping only half of the frames but preserving the whole parallactic angle range (*middle rows*), and a partition of the cube consisting of half of the frames such that the total parallactic angle range is divided in two. For the middle and bottom rows, the color scale of each frame corresponds to the linear minimum-maximum stretch of the leftmost image of the row. In all reductions preserving the whole parallactic angle range, the blob is recovered. In the reduction where the same number of frames is kept but the parallactic angle range cut in half, the blob appears almost fully self-subtracted. This is consistent with the expected behavior for an authentic companion.

A third test was carried out, consisting in the subtraction of the companion from the raw cube using the photometry and astrometry estimated by NEGFC and followed by the application of PCA-ADI on that new cube. This is shown in Fig. 11.13 for the two values of $n_{\rm pc}$ where the companion is most conspicuous. This time the PCA-ADI reductions are

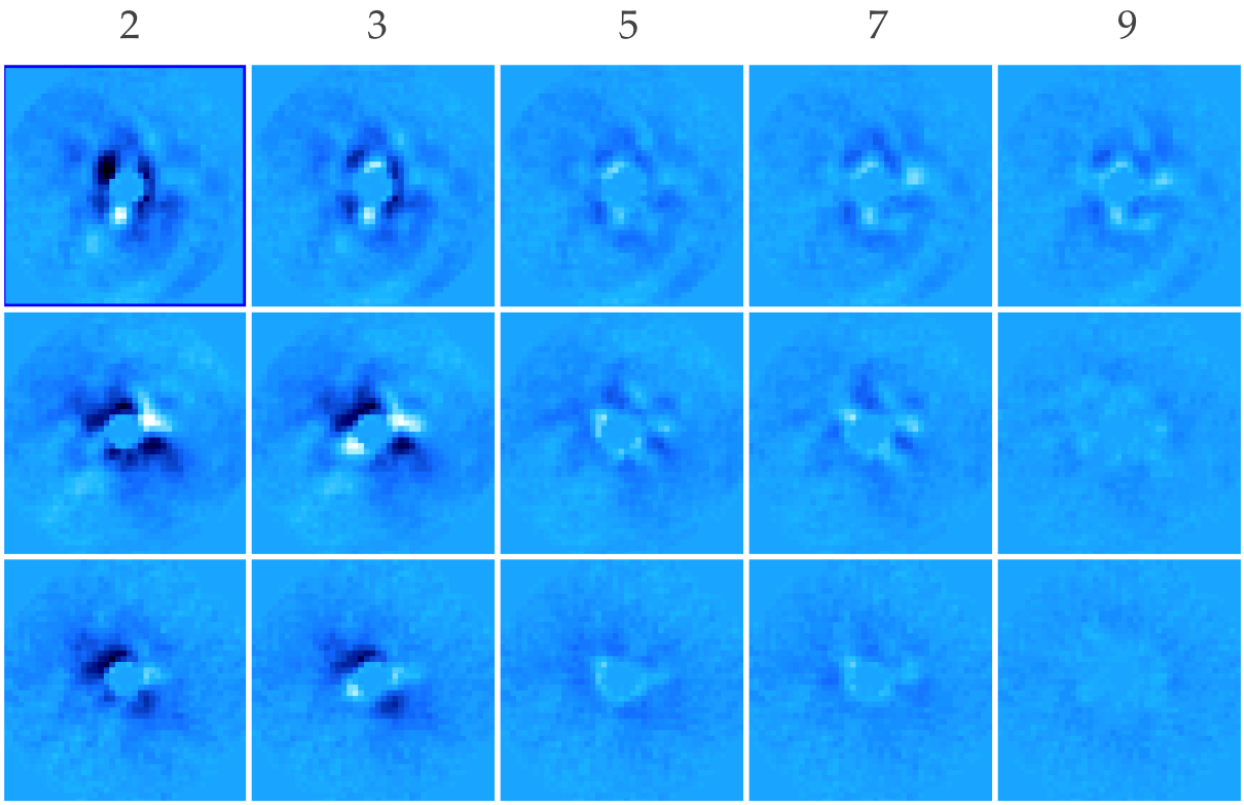

Figure 11.14: Fourth speckle test: PCA-ADI reductions for various values of $n_{\rm pc}$ using the normal (*top row*) and opposite (*middle row*) values of derotation angles. The *bottom row* consists of the PCA-ADI images obtained from the cube where the companion candidate was subtracted using the NEGFC parameters, and using the opposite values of derotation angles. The results are more ambiguous for this test. See text for details.

performed on a single 2-FWHM-wide annulus at the radial location of the companion candidate. The reduced images obtained after subtraction of the companion candidate in the raw cube not only subtract well the bright signal of the blob, but also the negative signals that were flanking the blob. This suggests that these negative contributions corresponded to the characteristic negative ADI side lobes (see e.g. Fig. 11.8 for a dramatic example corresponding to an extremely bright companion). This behavior is more likely to trace an authentic signal from a companion than from a speckle.

A fourth and last test was performed to assess the authenticity of the blob. It is shown in Fig. 11.14. The final PCA-ADI images obtained with various values of $n_{\rm pc}$ are compared to the PCA-ADI images obtained when using the opposite derotation angle values. In the latter case, the derotation and final recombination should not lead to significant constructive signal, while the level of residual speckle noise is preserved (using random derotation angles would smooth it). One can note from the middle row of Fig. 11.14 that using negative derotation angles also leads to some relatively bright signal at the same separation as the companion candidate. This looks *a priori* like a red flag regarding the authenticity of the possible companion. Nonetheless, a more careful look at the range of derotation angles, [-30°,-62°], suggests that the companion candidate itself might be causing the bright and azimuthally extended signal to the NW. The same test applied on the cube where the signal from the companion candidate was removed does not lead to any significant blob in

the final images. I checked this assumption by removing the companion candidate from the raw cube using the photometry and astrometry inferred by NEGFC, before applying PCA-ADI with negative derotation angles. This is shown in the bottom row of Fig. 11.14, where one can see that the bright signal to the NW is indeed subtracted.

In conclusion, while the L' blob appears to have passed all the tests, it is noteworthy that this does not rule out completely the possibility of a speckle yet. In order to confirm the companion, we requested follow-up time with NACO+AGPM. Our proposal got accepted and led to new observations in June 2018.

NIRC2 L' blob

After submission of the follow-up proposal, I was notified by collaborators that a similar blob had been observed one year earlier in a NIRC2+AGPM dataset. However, due to low significance, the latter was not followed up. Interestingly, the PCA-RDI reduction of the NIRC2 dataset shows a blob at a very similar location as the NACO blob. This is shown in Fig. 11.16, where the L' images are also compared to SPHERE/ZIMPOL polarimetric images of the disk.

The parameters of the blob inferred by NEGFC for the NIRC2 blob are $r \sim 0\farcs113$ (resp. 0$\farcs$123), PA $\sim 266.0°$(resp. 266.0°) and $\Delta L' \sim 3.9$ mag (resp. 5.0 mag) as inferred using PCA-RDI with no scaling and temp-mean scaling, resp. (M. Reggiani, private comm.). The small amount of rotation in the NIRC2 dataset (∼20°) and the fact that the companion looks more conspicuous in the no-scaling image suggest that the no-scaling results should be preferred. The difference in PA between the two epochs (2016/05/27 and 2017/05/24 for the NIRC2 and NACO datasets, resp.) is compatible with Keplerian motion on a circular orbit at ∼18 au from a 1.7 $M_\odot$ central star, in the direction expected for trailing spiral arms. Comparison of the L' images with the ZIMPOL polarimetric images shows that both blobs appear to be located right within the ∼0$\farcs$18 radius cavity (Stolker et al. 2016), which suggests that they do not correspond to filtered disk features (which is not expected from PCA-RDI without scaling anyway).

However, a discrepancy between the NACO and NIRC2 blobs is the contrast inferred by NEGFC: $\Delta L' \sim 5.3 \pm 0.3$ for the NACO blob versus $\Delta L' \sim 3.9$ mag for the NIRC2 blob (when favoring the no-scaling solution). A possible explanation is that the PCA-RDI (no scaling) estimate could be affected by residual signal by an improper subtraction of the halo at the location of the companion, which might happen if the reference star is not exactly of the same brightness. In the example of T Cha, I showed indeed that PCA-RDI without scaling could lead to significant spurious residuals in the final image which are likely due to a suboptimal correlation level between science star and reference. These would thus affect significantly the estimation of the contrast of the companion using the sum figure of merit (Sec. 11.5.2 for details on NEGFC). Nonetheless, such spurious structures are not evident in the final PCA-RDI image of NIRC2. This discrepancy requires thus a more thorough investigation.

Despite the discrepancy in contrast, the astrometry argues in favor of the two blobs

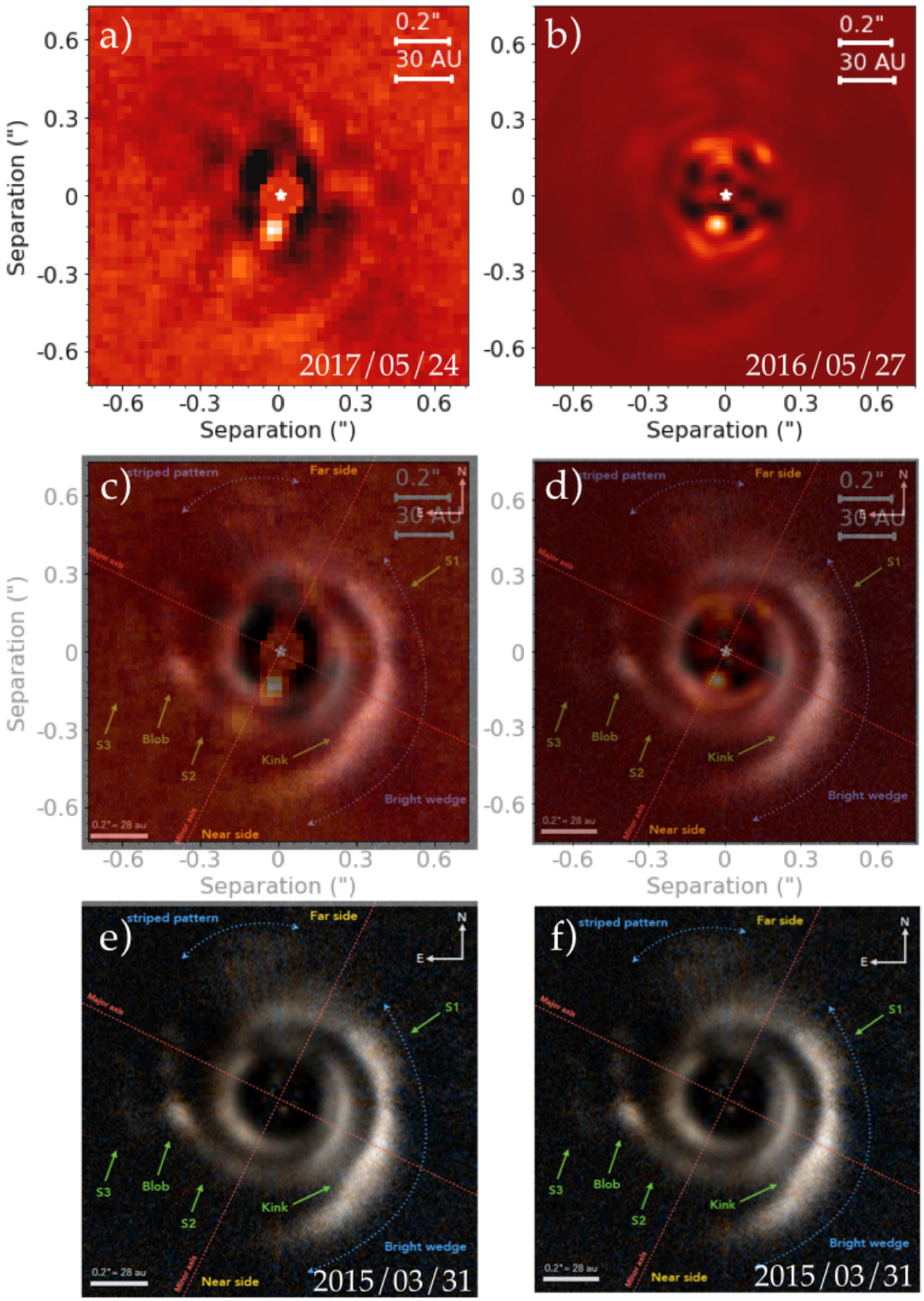

Figure 11.15: Comparison between NACO and NIRC2 L' images (top row) and polarimetric images obtained with SPHERE ZIMPOL (bottom row) of HD 135344 B. The middle row shows both sets of images together with a 50-50% opacity. Credit for the polarimetric image: Stolker et al. (2016).

tracing the same signal, and that the discrepancy in estimated contrast could reflect either a bug in the contrast estimate or simply variability of the object. Therefore, in the next paragraph, I estimate the significance of the separate and combined detections.

Significance of the L' blobs

The SNR of each blob, as estimated per the method presented in Sec. 10.5.1, is 4.1 and 4.7 for the NIRC2 and NACO detections, respectively. Since they are located at 1.5 and 1.2 FWHM from the star, I used Student statistics to estimate the confidence level of each detection to be 2.8σ and 2.9σ in the NIRC2 and NACO images respectively. The two signals are thus not significant when taken separately.

Given the two independent tentative detections in L' band at the same location, it is sound to compute the odds ratio that both signals are tracing an authentic companion (hypothesis H_1) rather than a false positive (H_0). I followed the same reasoning as presented in Reggiani et al. (2018, Eq. 12.1 in Sec. 12.1.1) for the protoplanet candidate found at two epochs around MWC 758, and inferred the odds ratio for the L' blob of HD 135344 B to be 680:1. This calculation is based on the probability of finding a companion of 5-20 $M_{\rm Jup}$ between 15-22 au, considering the planet mass vs semi-major axis distribution inferred from direct imaging surveys Brandt et al. (2014): $p(M, a) \propto M^{-0.65} a^{-0.85}$ for 5-70 $M_{\rm Jup}$ between 10-100 au. The normalization factor used for the integration is found considering the 6% probability for a $2 M_{\odot}$ to host a 5-13 $M_{\rm Jup}$ planet in 10-100 au separation (Nielsen et al. 2017).

Considering the 680:1 odds ratio, the planet hypothesis appears more likely than a false positive. Nonetheless, given the uncertainties in contrast inferred in the two datasets, a new dataset of higher quality was required.

Follow-up with SPHERE

We obtained Directory Discretionary Time (DDT) on VLT/SPHERE using the IRDIFS_EXT mode ($YJH + K1K2$ bands) on March 27, 2018. In order to probe the radial separation of the L' blob, we requested the observations to be made without coronagraph. Indeed, Maire et al. (2017) showed that bright diffraction blobs at the edge of the apodized Lyot mask hindered their search for companions at $\lesssim 0''.135$ separation in that disk. Observations were acquired in good and stable conditions (DIMM seeing $\sim 0''.5$ and coherence time $\sim$10 ms). The total integration time was 40 min (resp. 54 min) with IRDIS (resp. IFS), resulting in $\sim 63^{\circ}$ field rotation. The IRDIS data were calibrated by Dr. Alice Zurlo, resulting in an ADI cube of 140 frames, while the IFS data were calibrated by Dr. Dino Mesa. I subsequently post-processed the IRDIS data while Dr. Carlos Gomez analyzed the IFS data. The latter are not presented in this thesis, but preliminary results do not reveal signal other than the spiral arms in YJH. Below I rather focus on the K-band IRDIS data that I reduced.

The final images obtained with IRDIS are shown in the bottom row of Fig. 11.16, and are

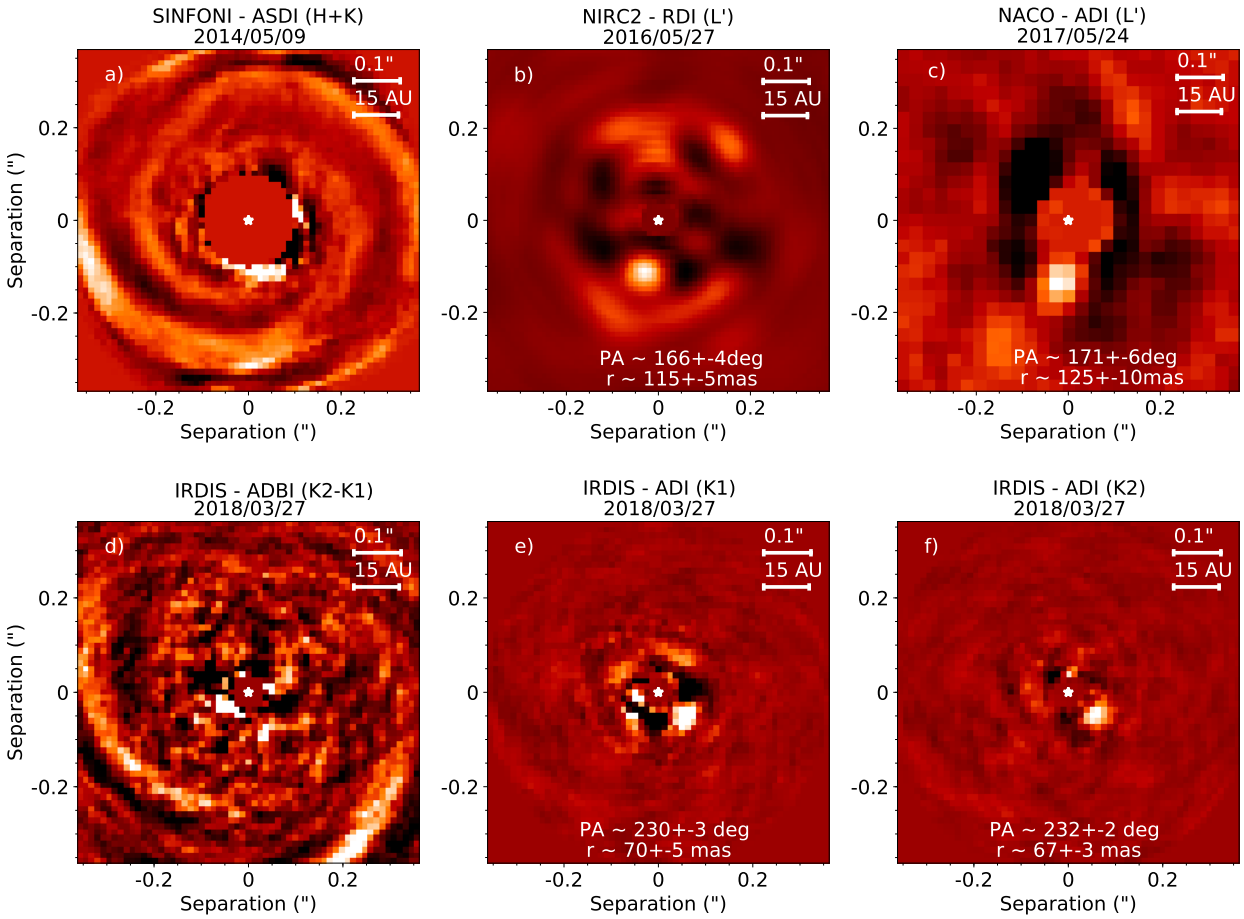

Figure 11.16: Final images of HD 135344 B obtained at different epochs with different instruments: **a)** Final SINFONI HK ASDI image (see details in Sec. 15.4); **b)** L' NIRC2 image obtained with the AGPM and using RDI; **c)** L' NACO image obtained with the AGPM and using ADI, as part of this survey; **d)** SPHERE/IRDIS PCA-ADBI image obtained between the $K1$ and $K2$ images; **e), f)** SPHERE/IRDIS PCA-ADI images obtained in the $K1$ and $K2$ filters, respectively.

compared to the SINFONI final H+K ASDI image (Sec. 15.4.1), and the L' images obtained with NIRC2 and NACO, with all images set to the same scale for better comparison. I first reduced the data using PCA-ADBI, as described in Sec. 15.3.2, using the $K1$ ($\lambda = 2.110\mu$m) and $K2$ ($\lambda = 2.251\mu$m) channels instead of the H and K bands. Then, I applied PCA-ADI in annuli (Sec. 11.5.1) to the ADI cube corresponding to each channel separately. The final image obtained with PCA-ADBI (Fig. 11.16d) does not reveal any significant signal apart from the outer part of the two spirals. Applying PCA-ADI separately in $K1$ and $K2$ did not reveal any counterpart to the L' blob detected with NACO and NIRC2. However, a new blob is seen at shorter separation and significantly different PA, in both $K1$ and $K2$ final images. Its significance is discussed in the next paragraph.

The non-detection of the L' blob in deep K band images is intriguing. Our IRDIS contrast curve discards any companion with a contrast $\Delta K < 8.8$ mag at the separation of the L' blob which, assuming photospheric emission, restricts the companion to a mass lower than $\sim 19\ M_{\rm Jup}$ according to the COND hot-start models (Baraffe et al. 2003). However, if the L' luminosity was photospheric, it would correspond to a $\sim 0.35 M_{\odot}$ for an age of ~ 8

Myr. This possibility can thus be safely discarded. If the L' blob was tracing accretion luminosity from a circumplanetary disk, our color constraint ($L' - K > 4.4$ mag) implies that the CPD is more than 2 mag redder than predicted in Zhu (2015). The assumption used in Zhu (2015) is that the CPD is actively accreting, with a negligible feedback of the planet on the disk In practice, based on hot-start models, his models would thus be valid only for planets with a mass smaller than 5-10 $M_{\rm Jup}$. Montesinos et al. (2015) considered the case of non-negligible flux from the planet and argued that by including this contribution, it could lead to a positive feedback loop between accretion rate, temperature and luminosity of the CPD (see Sec. 3.3.2). Recent color predictions based on this model show that the CPD is expected to be bright only in thermal IR, with a peak flux between 5 and 25 μm depending on the feedback efficiency (Gárate et al. 2017). In that case, the short wavelength tail of the blackbody function would imply extremely red colors between L' and K and possibly be compatible with the observation. In summary, the new IRDIS observations restrict the interpretation of the L' blob to three possibilities: (1) despite the odds (it passes all the speckle tests and is independently detected by two instruments at roughly the same location, using two different post-processing techniques), the signal does correspond to a speckle; (2) the luminosity from the blob traces a sporadic event (e.g. episodical accretion) and the variability might then also explain the discrepancy in the measured contrast of the blob with NIRC2 and NACO; (3) it traces a circumplanetary disk significantly redder than predicted in Zhu (2015), possibly rather in agreement with the assumptions made in Montesinos et al. (2015).

Authenticity of the K-band blob

Table 11.5: Characteristics of the point-like sources found in our images of HD 135344 B

	L' blob	L' blob	$K1$ blob	$K2$ blob
Date	2016/05/27	2017/05/24	2018/03/27	2018/03/27
Instrument	NIRC2	NACO	IRDIS	IRDIS
λ (μm)	3.8	3.8	2.110	2.251
Algorithm	PCA-RDI[a]	PCA-ADI	PCA-ADI	PCA-ADI
r (mas)	$\sim$113	125$\pm$10	70$\pm$5	67$\pm$3
r (FWHM)	$\sim$1.5	$\sim$1.2	$\sim$1.2	$\sim$1.1
r (au)	$\sim$16.0	17.8$\pm$1.4	9.9$\pm$0.7	9.5$\pm$0.3
PA (deg)	$\sim$166	171$\pm$3	229.6$\pm$3.3	231.8$\pm$1.6
Contrast (Δmag)	$\sim$3.9	5.3$\pm$0.4	7.46$\pm$0.29	7.33$\pm$0.08
SNR	4.1	4.7	6.1	5.9
Significance (σ)	2.8	2.9	3.3	3.2
Odds ratio	683:1[b]			

Notes:

[a] Without scaling.

[b] Odds ratio for the combined detection in the NIRC2 and NACO datasets (see text for details).

Regardless of the authenticity of the L' blob, it is interesting to test whether the new blob found with IRDIS in K band is to be trusted. NEGFC coupled to PCA-ADI yields

the following photometry and astrometry for the blob seen in the $K1$ (resp. $K2$) spectral channels: $r \sim 70 \pm 5$ mas (resp. 67 ± 3 mas), PA $\sim 229.6° \pm 3.3°$(resp. 231.8 ± 1.6) and $\Delta K1 \sim 7.46 \pm 0.29$ (resp. $\Delta K2 \sim 7.33 \pm 0.08$). The detection appears visually more conspicuous in the $K2$ channel than in the $K1$ channel. The $K2$ blob is slightly more round, and its subtraction leads to less residuals in its surroundings which accounts for the smaller uncertainties. Given the separation of only ∼70 mas, no counterpart is expected to be found in the L' images due to the coarser angular resolution. The parameters inferred for the L' and K blobs are compared in Table 11.5.

Before applying speckle tests, it is useful to keep in mind that compared to coronagraphic observations (such as those obtained with NACO/NIRC2+AGPM), images obtained without a coronagraph have a higher chance to contain bright *pinned speckles* (e.g. Bloemhof et al. 2001; Bloemhof 2004, see Sec. 10.1.2). The probability of pinned speckle is significantly larger on the bright diffraction rings than in the troughs of the Airy pattern; the distribution of pixel values follow indeed an MR distribution that is several times narrower in a through than on a peak of the Airy pattern (see e.g. Fig. 7 of Soummer et al. 2007). Fortunately, the high stability of the observing conditions and the very high Strehl ratio achieved by SPHERE significantly reduce the probability of getting pinned speckles (by definition a high Sr involves less stellar flux contributing to speckles). Furthermore, comparison of the location of the K-band blob with the median PSF of the star, shows that it is located within the first trough of the Airy pattern, and hence has a lower chance of tracing a pinned speckle. Nonetheless, this argument alone does not discard the possibility of a speckle. Therefore, I carried out similar speckle tests as presented for the NACO L' blob. These are shown in Figs. 11.17 and 11.18.

The first speckle test consisted in evaluating the survival of the blob when $n_{\rm pc}$ is varied, and in comparing the reductions with images obtained with the opposite derotation angles. The companion candidate is detected for $n_{\rm pc}$ values ranging from 10 to 23 (resp. 26) in the $K1$ (resp. $K2$) ADI cube (for comparison the total number of frames in the ADI cube is 140). The result is shown for $K2$ in the top row of Fig. 11.17), where one can notice a progressively stronger self-subtraction for increasing values of $n_{\rm pc}$. When the opposite derotation angles are used, no signal as strong as the blob is recovered, although there appears to be residual signal spread out in the N/NW at a similar radial separation as the blob (second row of Fig. 11.17). I performed the same test after subtraction of the blob in the original ADI cube, and noticed that these residuals are significantly damped (bottom row of Fig. 11.17), to a same level as the residuals found in the images obtained after using the normal derotation angles (but subtracted companion; third row of Fig. 11.17). Similar results were obtained with the $K1$ datacube. The result of this test is compatible with an authentic companion, although it does not rule out the possibility of a speckle.

The second test that was carried out is shown in Fig. 11.18. I used the photometric and astrometric parameters of the companion derived by NEGFC to subtract it from the original datacube, and post-processed the new cube with PCA-ADI. This is also shown in the third row of Fig. 11.17 with smaller frames but a larger range of $n_{\rm pc}$ values. The conclusion is the same for all images: the negative signals originally flanking the blob have almost completely disappeared in the $K2$ images, and are significantly damped as well in the $K1$ images. This is also a behavior that is expected for an authentic companion.

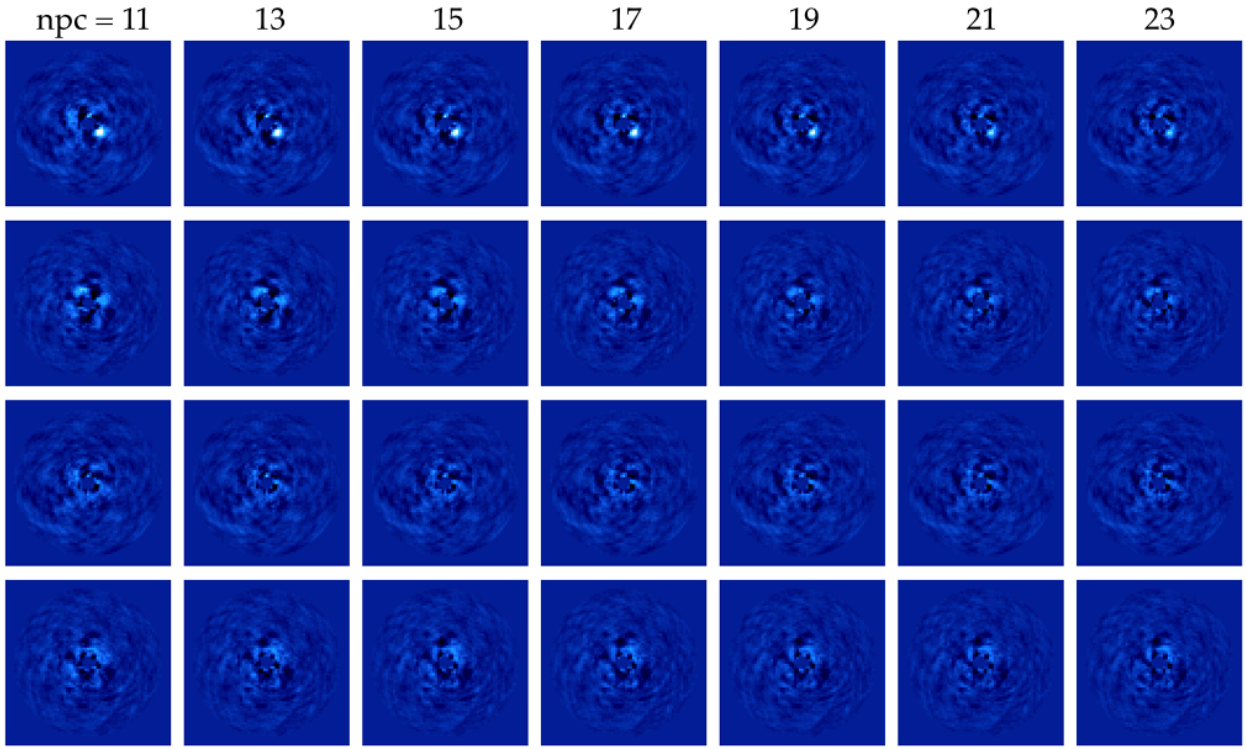

Figure 11.17: Speckle test #1 on the IRDIS dataset of HD 135344 B ($K2$ channel). PCA-ADI images for various values of $n_{\rm pc}$ using the normal (*top row*) and opposite (*second row*) values of derotation angles. The *third* and *bottom rows* consist of the PCA-ADI images obtained from the cube where the companion candidate was subtracted using the NEGFC parameters, and using the normal and opposite values of derotation angles respectively. Using the opposite derotation angles no signal as bright as the companion candidate is found. All images share the same color scale, corresponding to a linear minimum-maximum stretch in the top left panel. See text for details.

Significance of the K-band blob

To estimate the significance of the $K1$ and $K2$ blobs, I first slightly tweaked the function implemented in VIP to estimate the SNR of each detection (i.e., tweaked compared to what is explained in Sec. 10.5.1). The first change concerns the negative side lobes. Considering the lack of independent apertures on an annulus at very short separation ($\sim$6 at $\sim$1 FWHM separation; Fig. 10.5), including apertures overlapping with the ADI negative lobes significantly increase the standard deviation of the fluxes measured in the apertures at that radius. Therefore, I removed the two apertures which overlap with the two negative side lobes. This practice appears justified to me only if the second speckle test (shown in Fig. 11.18) is passed; i.e. that the negative side lobes disappear in the final image obtained after subtraction of the companion candidate in the raw cube. The second modification to the code consisted in adding the possibility of considering a second image for the computation of the flux in apertures at the same separation. This second image should be the final processed image obtained with the opposite derotation angles after the companion is subtracted from the raw cube. Indeed, this keeps the same speckle noise level while removing the companion from the image, as can be seen from the comparison of the third and fourth rows of Fig. 11.17. Therefore, considering this second image effectively double the number

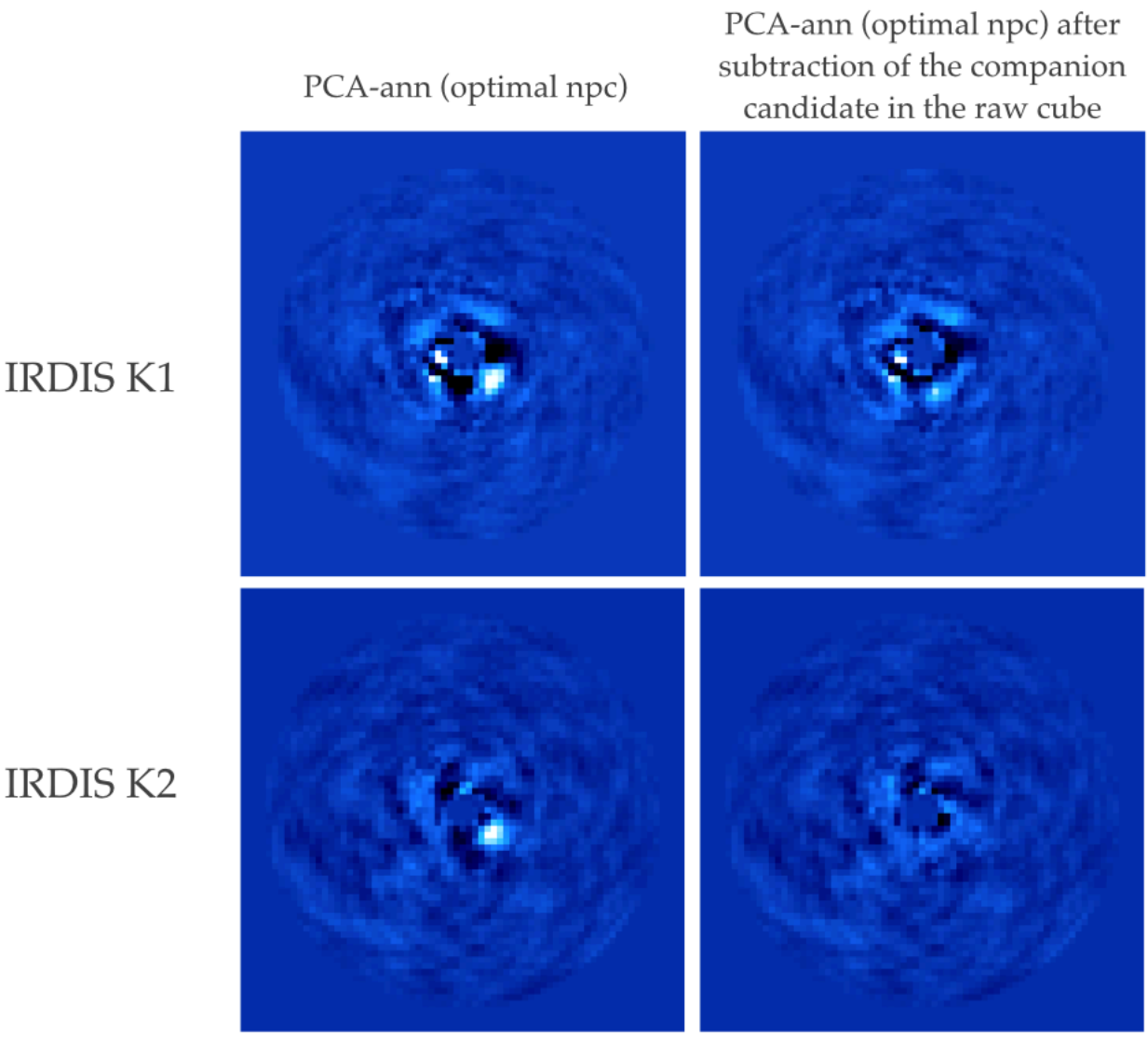

Figure 11.18: Speckle test #2 on the IRDIS dataset of HD 135344 B. The negative signals flanking the $K1$ and $K2$ blobs appear significantly damped in the final image obtained after the companion candidate was subtracted from the raw cube using the photometry and astrometry inferred by NEGFC.

of apertures to check the noise, and slightly mitigate the penalty factor. Considering these two modifications, the SNR of the companion candidate is estimated to ∼6.1 (resp. ∼5.9) in the $K1$ (resp. $K2$) final image. These correspond to 3.3 and 3.2σ detections at 1.2 and 1.1 FWHM separation, resp., based on Student statistics. Follow-up with another epoch observation with IRDIS is thus required to confirm the authenticity of the blob. The new epoch observation could also provide insight on the nature of the observed signal, depending on the presence or absence of Keplerian proper motion.

Future plans

On June 1 and 2, 2018, I re-observed the system of HD 135344 B using NACO in L' band. During both nights, observing conditions were excellent (DIMM seeing $\sim$ 0″.35 and coherence time $\gtrsim 5$ ms). The first dataset corresponded to an ADI sequence reaching $\sim 80°$ rotation, while the second dataset corresponded to an ADI+RDI sequence (140° rotation, with interspersed observations of a reference star). A quick reduction of the first dataset after the first night did not recover the L' blob. I plan to carry out a deeper analysis of the second dataset in order to reach better conclusions regarding the nature of the L' blob.

We have also submitted an ALMA proposal to probe the kinematics of the gas in the disk. This technique was proposed to detect the presence of CPDs based on observations at fine angular and spectral resolution of an optically thin line of the disk (see e.g. Perez et al. 2015). At the time this thesis is being written, we are waiting for the decision of the ALMA time allocation committee. This promising technique might be more appropriate to detect deeply embedded protoplanets, and first detections have recently been claimed in the disk of HD 163296 (Teague et al. 2018; Pinte et al. 2018).

11.6.7 J1622-3724

J1622-3724 is a young stellar object in the Lupus V region, at a distance of $\sim$ 150 pc (Gaia Collaboration et al. 2018). There is no reported resolved observation of the disk yet. Nonetheless, based on SED modeling (shown in Fig. 11.19e), van der Marel et al. (2016c) have classified it as low-mass disk with large hole and very low scale height: $r_{\rm cav} > 100$ au, $M_{\rm disk} < 5 M_{\rm Jup}$, and $h_c \sim 0.01$, where h_c is the disk aspect ratio in the dust cavity of radius $r_{\rm cav}$.

Observations were obtained on 29 May 2017 in average conditions (stable 0″.9 DIMM seeing), with 70°total field rotation (Table 11.4). A point source is found to the NW of the star after post-processing using either median-ADI (Fig. 11.19a) or PCA-ADI with a large range of $n_{\rm pc}$ (2 to >60). Using NEGFC, I constrained the astrometry and photometry to be: $r = 2''.644 \pm 0''.010$, PA = -28.95°$\pm$ 0.11, and $\Delta L'$ = 8.97 $\pm$ 0.15 mag. I double-checked that using these parameters for a negative injected companion would lead to an appropriate subtraction in the final frame (Fig 11.19b vs d). The uncertainty on the radial separation is dominated by the uncertainty on the plate scale (27.12$\pm$0.11 mas px^{-1}; Milli et al. 2017a), while the error on the PA reflects both the residual background noise and the uncertainty on the true North (offset of -0.56 $\pm$0.07 °; Milli et al. 2017a).

The SNR of the point-like source is ~ 7.5 (Fig 11.19c), which corresponds to a 6.9σ detection. The radius of $\sim$2″.6 would correspond to a projected separation of 390 au. Follow-up is required to check whether the source is bound or a background object. If bound, the contrast of almost 9 mag and distance of 150 pc would imply an object of $M_{L'} \sim 10.5$ mag. Using COND models (Baraffe et al. 2003) and considering an age of 5 Myr for Lupus V (e.g. Spezzi et al. 2011), the $M_{L'}$ magnitude would correspond to a mass of $\sim 4 M_{\rm Jup}$.

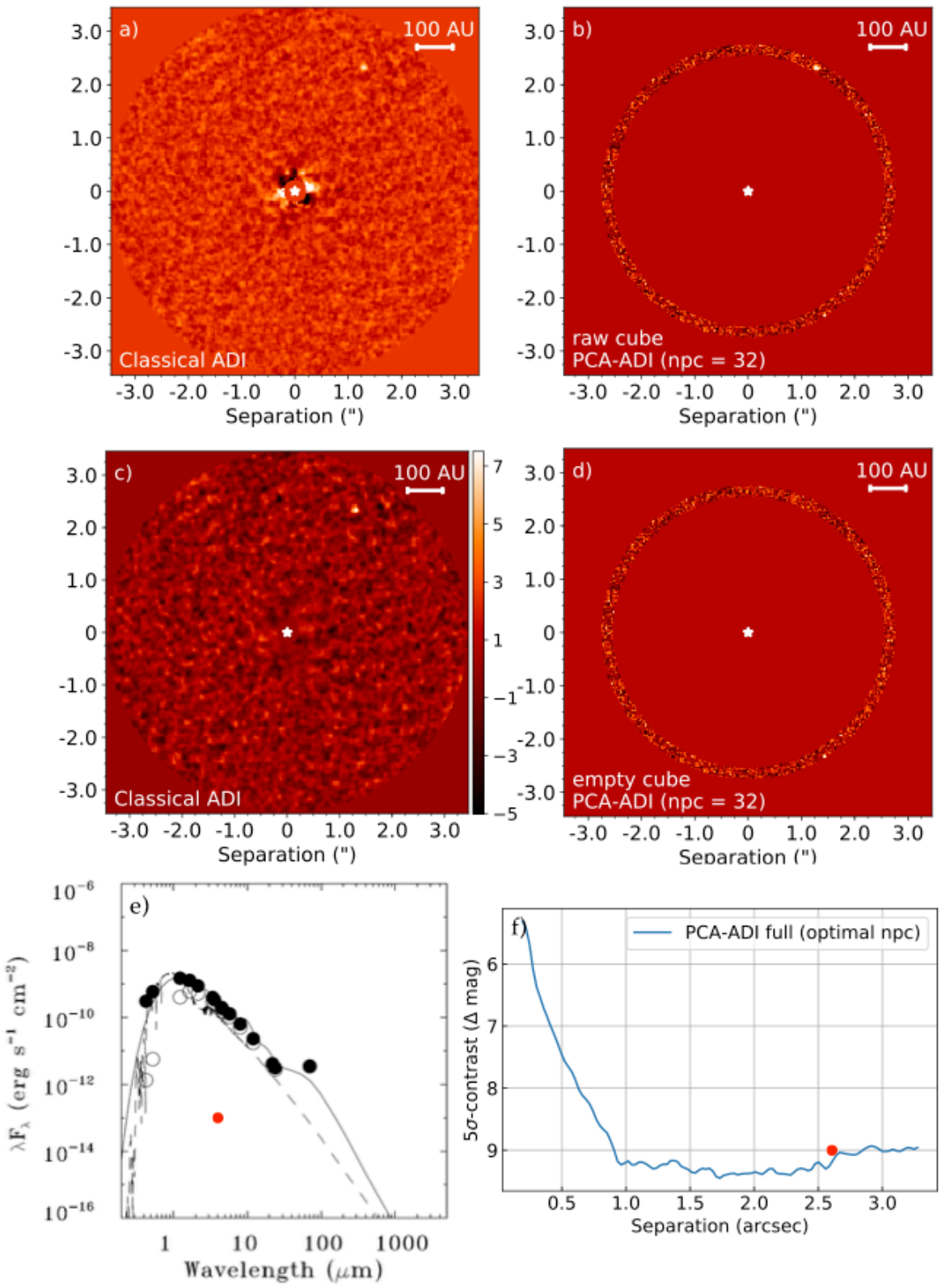

Figure 11.19: Summary of the results obtained on J1622-3724. **a), c)** Image obtained with classical-ADI and corresponding SNR map. A point-like feature is found at $\sim$2.″6 to the NW with an SNR $\sim$7.9 ($\sim$6.9σ). **b), d)** Final image obtained with PCA-ADI in an annulus, with the original datacube (b), and the cube where the companion was removed using the photometry and astrometry inferred by NEGFC (d). **e)** SED of the source (van der Marel et al. 2016c). **f)** 5σ optimal contrast curve. Red dots show the location of the companion candidate in the SED and the contrast curve. See text for details.

11.6.8 J1900-3645

J1900-3645 is a young M0.75 accreting star, located at a distance of 153 pc, as estimated by Gaia (Gaia Collaboration et al. 2018). It is part of the young Corona Australis dark cloud (0.3-3 Myr; Meyer & Wilking 2009; Gutermuth et al. 2009). There is no published resolved observation of the disk yet. However, the SED of the source is typical of a transition disk with a large hole (Fig. 11.20e). Romero et al. (2012) recognized it as the transition disk of their sample whose SED characteristics are most compatible with giant planets dynamically carving the gap, based on the positive slope of the IR excess, suggestive of a sharp inner hole, and the high stellar accretion rate. SED fitting suggests the presence of a ~ 14-au-wide annular gap at a separation of $\sim$72 au (van der Marel et al. 2016c).

A non-coronagraphic dataset was obtained on the source in service mode in excellent conditions on 26 August 2017 (stable DIMM seeing $\sim$0$''$.5), but with only 25° field rotation. Using either median-ADI or PCA-ADI for a large range of $n_{\rm pc}$ values enables to recover a point-like source at a separation of 0$''$.7 to the east (Fig. 11.20a and b). At that separation, 25° rotation translates into $\sim$3.5 FWHM linear motion which is compatible with the recovery of a point-like source with ADI, while the inner regions ($r < 0''.3$) appear completely self-subtracted in the image. The SNR of the point-like source is $\sim$6.9, which corresponds to a 5.6σ detection considering Student statistics at a 6.5 FWHM separation. The exact astrometry and photometry retrieved by NEGFC are: $r = 0''.699 \pm 0''.015$ (107 ± 2 au), PA $= 91.0° \pm 0.5°$ and $\Delta L' = 7.55 \pm 0.30$. Assuming the object is bound to J1900-3645, its absolute magnitude $M_{\rm L'} \sim 10.6$ would suggest a protoplanet of 1.9-3.2 $M_{\rm Jup}$ according to COND models for an age range of 0.3-3 Myr (Baraffe et al. 2003). Nonetheless, the companion might be partly embedded and an unknown fraction of its flux might be extinct, hence leading to an optimistic mass estimate. Alternatively, if the observed flux stems mostly from a circumplanetary disk, it would be compatible with a $0.3 - 3 \times 10^{-6} M_{\rm Jup}^2$ yr^{-1} (e.g. a 1 $M_{\rm Jup}$ accreting at $10^{-6} M_{\rm Jup}$ yr^{-1}; Zhu 2015).

Interestingly, the radial separation of the point-like source is relatively similar to the prediction made for the location of the annular gap based on SED fitting (0$''$.7 vs 0$''$.5), given that typical uncertainties affecting gap radii estimated from the SED can lead to up to a factor 2 discrepancy with measured gap radii in resolved observations (van der Marel et al. 2016c). Follow-up with NACO in L' is required to confirm that the companion is indeed bound, and not a background star. Given the preliminary hints of protoplanet presence in that disk and its radial separation, the companion candidate in this system has a higher chance of being a forming planet or brown dwarf than our other 3 companion candidates found in this survey.

Observations with SPHERE/IRDIFS ($YJH + K1K2$) would enable to probe its color, while observations with SPHERE/ZIMPOL in Hα could constrain the accretion rate of the object, and hence provide insight on the presence of a circumplanetary disk. Finally, ALMA follow-up observations of gas lines might enable to independently estimate the mass of the companion. Considering the very young age of the system and the large separation at which the companion candidate is found (107 au), if the source is confirmed to be bound, it might correspond to one of the first detections of protoplanet caught soon after formation by GI.

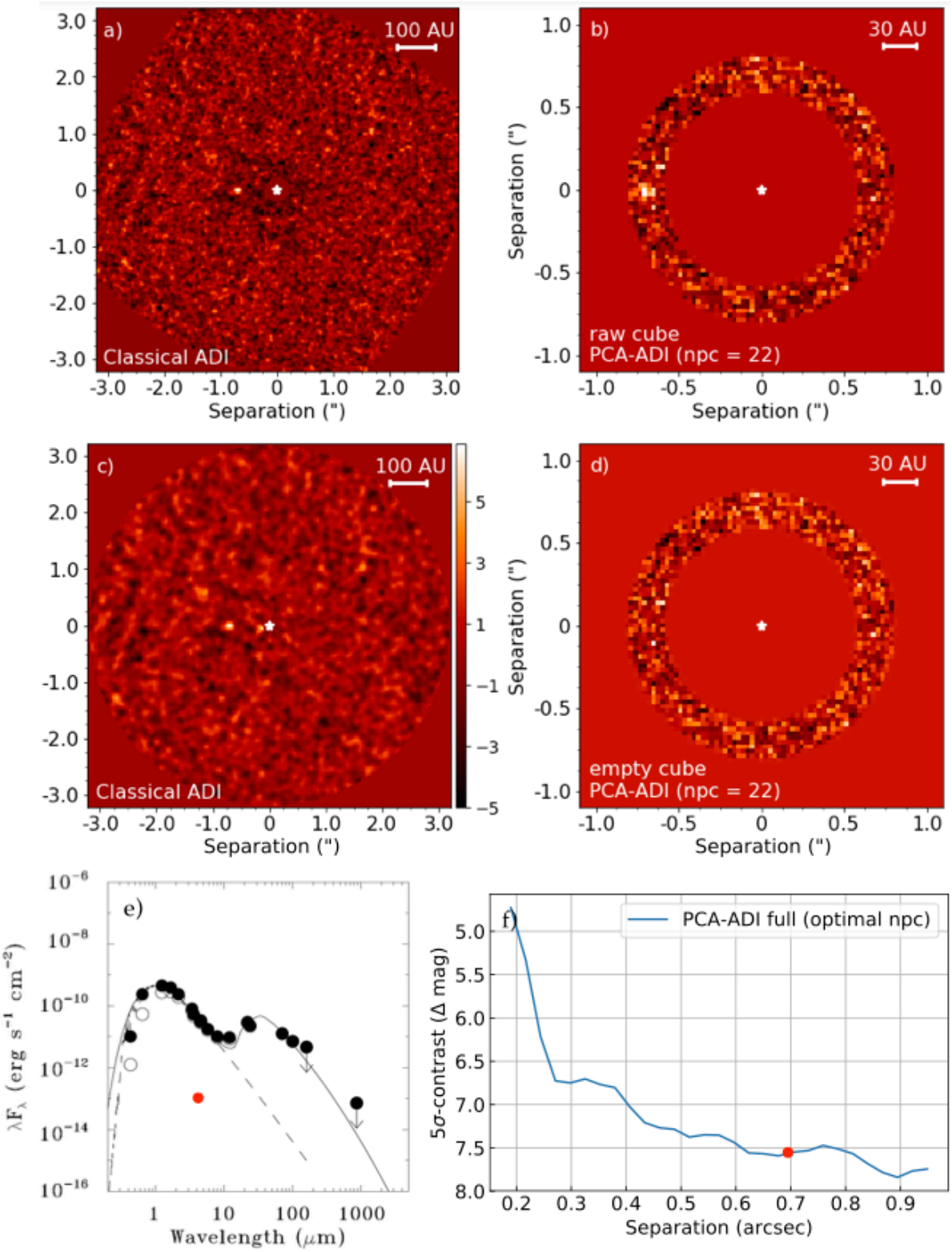

Figure 11.20: Summary of the results obtained on J1900-3645. **a), c)** Image obtained with classical-ADI and corresponding SNR map. A point-like feature is found at $\sim$0.″7 to the E with an SNR $\sim$6.9 ($\sim$5.3σ detection) **b), d)** Final image obtained with PCA-ADI in an annulus, with the original datacube (b), and the cube where the companion was removed using the photometry and astrometry inferred by NEGFC (d). **e)** SED of the source (extracted from van der Marel et al. 2016c). **f)** 5σ optimal contrast curve. Red dots show the location of the companion candidate in the SED and the contrast curve. See text for details.

11.6.9 HD 98800 B

HD 98800 is a nearby (42.2 $\pm$ 4.7 pc; Boden et al. 2005) quadruple system composed of a double spectroscopic binary, as illustrated in Fig. 11.21a. Modeling of the SED suggests that the unresolved HD 98800 B pair is surrounded by a circumbinary/transition disk (Furlan et al. 2007; Akeson et al. 2007). Furlan et al. (2007) inferred the presence of optically thin dust from the SED and argue that the survival of dust in the cavity, in the absence of gas, might point to the presence of a planet that is holding up the dust by resonances. The individual stars in each double pair is not expected to be resolved in L'-band observations. However, the similar flux of the two pairs of binaries (taken together as unresolved sources) motivated us to include the source in the survey in order to attempt the application of BDI to reach high contrast at very short separation from the binaries (Rodigas et al. 2015, Sec. 10.3.2).

Observations were carried out in good conditions (DIMM seeing $\sim$0$''$.9). We did not use any coronagraph, used a value of DIT ensuring the centroid would not get saturated, and simply dithering the pair of binaries in a different quadrant of the detector after each exposure in order to optimize the sky subtraction. The derotator was reset in the middle of the sequence, which contributed to the very small amount of total field rotation ($\sim$3°).

Figure 11.21b shows the binary in individual calibrated frames of the sequence. It is evident from visual comparison that both PSFs are extremely well correlated, with the same portions of Airy rings standing out in the same exposures, but slightly varying through time. Nonetheless, it is also apparent that both stellar halos are overlapping owing to their very close separation ($\sim 0''.54$), which holds the promise of a complicated post-processing.

Figure 11.21c further quantifies the similarity between the two PSFs. The *left* plot shows the normalized flux of both component, which is the same within $\sim$5%, and show same variations across the sequence. The *right* plot shows the Pearson cross-correlation coefficient which enables to assess how well correlated are the reference frames to the science frames in the cases of BDI and ADI. For BDI (*blue points*), the cross-correlation coefficient is measured between the two PSFs in each co-add. For ADI (*red points*), the cross-correlation is measured between the PSF of HD 98800 B (north component) in each co-add and the same PSF in the co-add corresponding to the middle with the sequence (the red point with $r = 1$ on the top of the graph). Although both estimates lead to very high correlation coefficients ($\gtrsim 0.99$), the correlation is systematically higher when using the binary captured at the same time, than using the source itself at different times of the sequence, which suggests that BDI might eventually reach a slightly better contrast than ADI (assuming we had sufficient field rotation for a fair comparison). No temporal binning was performed in order to keep the correlation between primary and secondary PSFs as high as possible. I kept 6050 frames out of the 6500 frames acquired initially (NEXP = 65, NDIT = 100), only rejecting the first frame of each cube (strongly affected by inappropriate dark subtraction) and the frames where the AO loop opened.

I cropped images of 21x21 px around each component, thereby cutting at half the separation between the two components. The cropping was performed in such a way to place the centroid (measured with Moffat fits) on the central pixel of each stamp image. I subse-

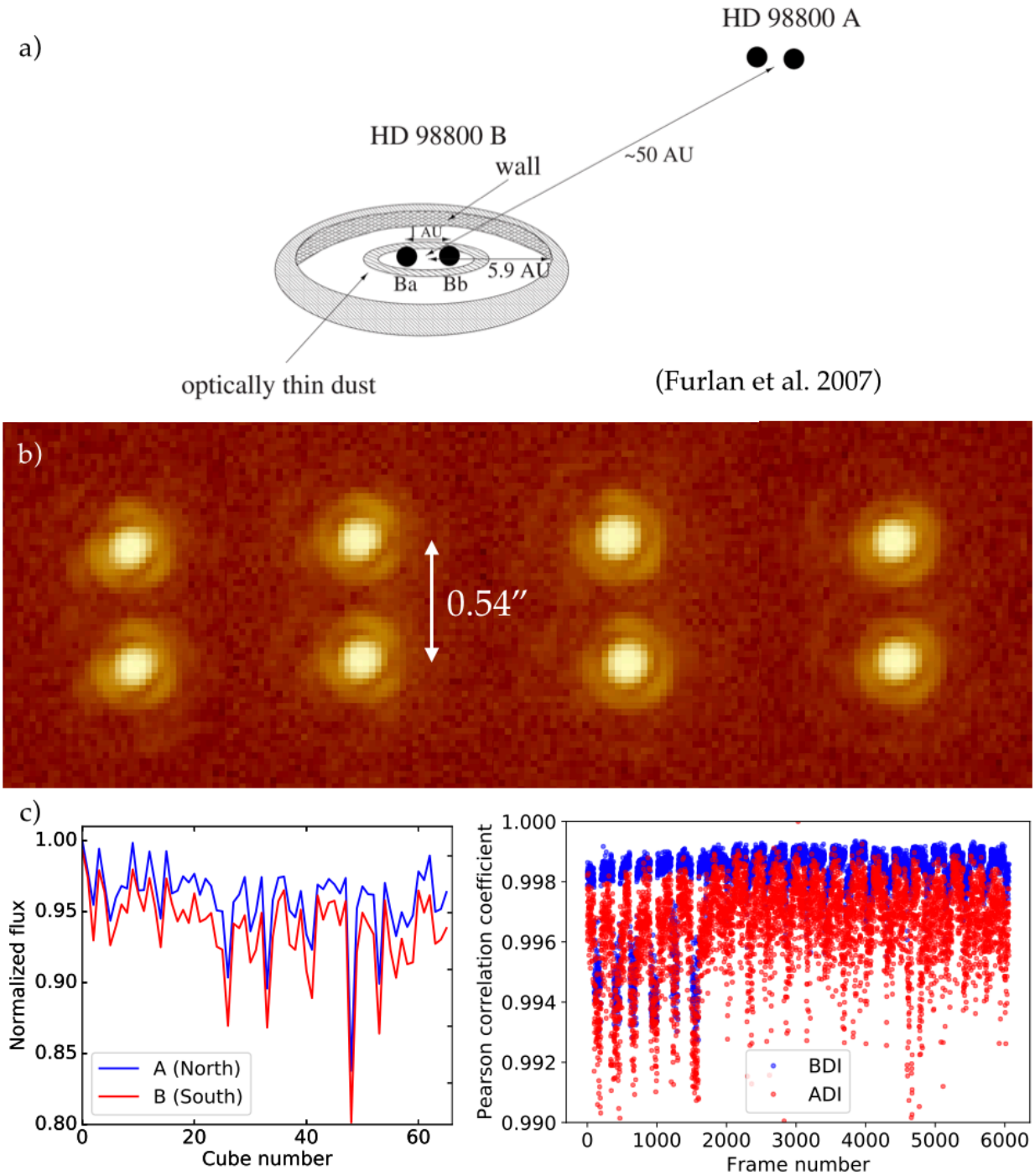

Figure 11.21: Illustration of the application of BDI on HD 98800. **(a)** Sketch of the system from Furlan et al. (2007). Each double binary is not expected to be resolved in our L'-band observations given the distance of 42.7 ± 4.7 pc and the deprojected physical separations inferred from the orbital fit in Boden et al. (2005). **(b)** Illustrative PSF images obtained with NACO in L' band at different times. Although the shape and speckle pattern in the stellar halos change with time, a visually high cross-correlation can be seen at any moment between each component. The binary was separated by $\sim 0\farcs54$ at the time of our observation. **(c)** (left) Normalized flux measured in the median of each cube. (right) Pearson cross correlation coefficient measured between the PSF of the primary in each frame and (1) the PSF of the secondary in the same frame (*blue points*, BDI), and (2) the PSF of the primary in the central frame of the whole sequence (*red points*, ADI). See details in the text.

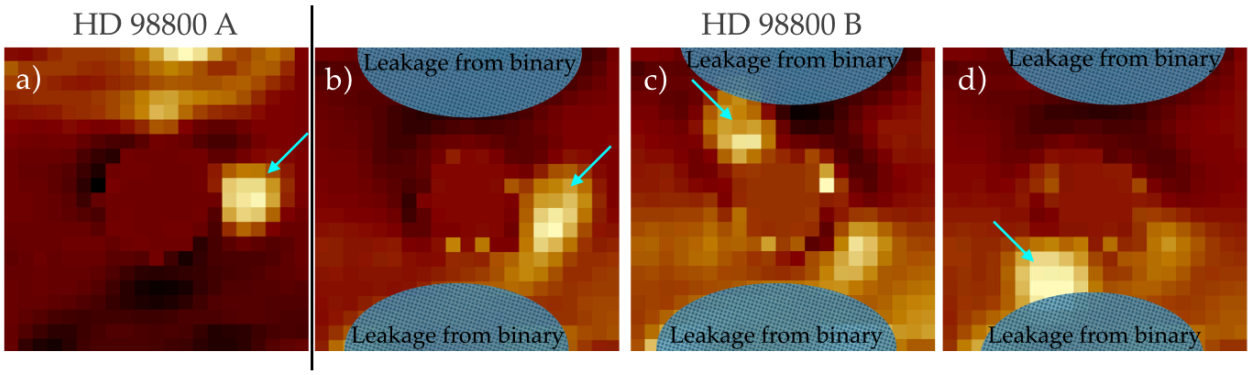

Figure 11.22: Results of PCA-BDI on the HD 98800 system. The cyan arrows indicate the location of injected fake companions at 5 magnitude contrast, corresponding to a 3σ detection in the image of HD 98800 A. See details in the text.

quently measured the flux of the PSF in each of the 2x6050 frames. Then, for each component, I built a reference cube using the other component. The measured fluxes were used to rescale each frame of the reference cube to the same level as the corresponding science frame. I first applied a simple BDI, frame per frame, and median-stacked the residual images. However, this resulted in significant bright residuals in the direction of the other component and negative residual in the opposite direction, as can be seen in Fig. 11.22a. This is the signature of a significant overlap of the two PSFs. I subsequently applied BDI in combination with PCA, using the algorithm for PCA-RDI, in the hope it would enable to somewhat damp the artifacts due to overlapping. However, this did not improve significantly the results.

In the final frame obtained with PCA-BDI on HD 98800 A, no significant signal is found in the direct vicinity of the star, apart from the overlapping artifacts. I estimated the contrast achieved by injecting repeatedly a fake companion in the raw cube at different contrasts, and inferring the value of contrast that would lead to a 3σ re-detection in the final frame. The contrast achieved is $\sim$5.0 mag at $0''.17$ separation. This is shown in Fig. 11.22a, where the fake companion is indicated with an arrow.

Contrarily to HD 98800 A, the final PCA-BDI frames of HD 98800 B are dominated by some bright residuals. In order to estimate the significance of these signals I injected the 5.0 mag contrast fake companion, known to lead to a 3σ detection in the final image of HD 98800 A, in the raw cube of HD 98800 B. I compared the level of the fake companion injected at different PA values in the PCA-BDI frames of HD 98800 B with the residual signal, and inferred that the residual signal was not significant. This can be seen in Fig. 11.22b, c and d, where I also masked the areas most affected by overlapping artifacts for clarity.

In an attempt to get rid of the overlapping artifacts, I built a PCA library containing the same amount of vertically flipped and normal reference images of the other component. I also tested a PCA library made uniquely of vertically flipped images. Both tests led to worse results, based on the contrast of the injected fake companion required for a 3σ detection in the image of HD 98800 A.

In summary, the poor results despite the high correlation between the PSFs is most

likely attributable to the overlapping of the PSFs. Although the level at which they overlap is small compared to the peak values, this effect becomes dominant after reference PSF subtraction. However, given the extremely high levels of correlation between the two components, I suspect that the technique could be very efficient for more separated binaries. This source might be ideal for BDI with future instrument ELT/METIS, as the binaries will be more separated in terms of FWHM, which would hence minimize overlapping effects.

12 Contribution to the detection of companions in thermal IR

12.1 Case of MWC 758

Transition disk MWC 758 was observed with Keck/NIRC2 equipped with its new AGPM coronagraph in the context of a transition disk survey in the North (PIs: Ruane/Mawet) complementary to the survey that I am leading in the South. The observations were obtained by G. Ruane, and the data reduction was performed by M. Reggiani using VIP. M. Reggiani led the analysis of the protoplanet candidate found in our final images at two epochs. My contribution in this study consisted in the analysis of the spiral arms: I measured the spirals pitch angle, performed a geometrical fit of the spiral trace to different equations derived from the spiral density wave theory, estimated the proper motion of the spirals between different epochs, and measured their azimuthal separation. The results did not enable to converge on a clear-cut origin, although the most likely origin is likely to be related to the presence of one or several embedded protoplanets; either the one discovered if on an inclined an eccentric orbit and/or a yet undetected companion outward from the spiral arms. I defer the reader to Sec. 7.2 for a detailed account of the spiral arm analysis; only the most relevant results were included in the published version of the paper, whose content is provided below as is.

12.1.1 Discovery of a point-like source and a third spiral arm in the transition disk around the Herbig Ae star MWC 758

M. Reggiani, V. Christiaens, O. Absil, D. Mawet, E. Huby, E. Choquet, C. A. Gomez Gonzalez, G. Ruane, B. Femenia, E. Serabyn, K. Matthews, M. Barraza, B. Carlomagno, D. Defrère, C. Delacroix, S. Habraken, A. Jolivet, M. Karlsson, G. Orban de Xivry, P. Piron, J. Surdej, E. Vargas Catalan & O. Wertz

A&A, 611, 74 (2018)

Abstract

Transition disks offer the extraordinary opportunity to look for newly born planets and investigate the early stages of planet formation. In this context we observed the Herbig A5 star MWC 758 with the L'-band vector vortex coronagraph installed in the near-infrared camera and spectrograph NIRC2 at the Keck II telescope, with the aim of unveiling the nature of the spiral structure by constraining the presence of planetary companions in the system. Our high-contrast imaging observations show a bright ($\Delta L' = 7.0 \pm 0.3$ mag) point-like emission, south of MWC 758 at a deprojected separation of ∼20 au ($r = 0\farcs111 \pm 0\farcs004$) from the central star. We also recover the two spiral arms (south-east and north-west), already imaged by previous studies in polarized light, and discover a third one to the south-west of the star. No additional companions were detected in the system down to 5 Jupiter masses beyond 0$\farcs$6 from the star. We propose that the bright L'-band emission could be caused by the presence of an embedded and accreting protoplanet, although the possibility of it being an asymmetric disk feature cannot be excluded. The spiral structure is probably not related to the protoplanet candidate, unless on an inclined and eccentric orbit, and it could be due to one (or more) yet undetected planetary companions at the edge of or outside the spiral pattern. Future observations and additional simulations will be needed to shed light on the true nature of the point-like source and its link with the spiral arms.

Introduction

Understanding how planet formation takes place is a fundamental question in astronomy today. The ∼3000 planets discovered in the last two decades thanks to various techniques allow astronomers to study planet mass and orbital parameter distributions, and their dependence on the properties of the host stars. Despite the important advancements made in the knowledge of planetary systems, many aspects concerning the initial conditions for planet formation and evolution still remain unknown. High angular resolution imaging of young protoplanetary disks in the closest star forming regions could provide answers to these questions. A variety of disk structures have been detected through infrared scattered light or mm-wave imaging. Circumstellar disks may present large cavities (e.g., Andrews et al. 2011), gaps and bright rings (e.g., Quanz et al. 2013b), asymmetries (e.g., van der Marel et al. 2013), and spiral arms (e.g., Garufi et al. 2013; Benisty et al. 2015). In some cases the combination of polarized scattered light and millimeter measurements has even shown spatial segregation, which could be directly linked to the presence of planets (Pinilla et al. 2012a). Direct images of young planets embedded in protoplanetary disks would offer the possibility of investigating the link between the initial stages of planet formation and the final outcomes of the process.

In this context, MWC 758 (HD 36112) offers a unique environment to probe the existence of planetary companions and to explore the connection between disk structures and planet formation. MWC 758 is a young stellar object (3.5 ± 2 Myr, Meeus et al. 2012) at a distance of 151^{+9}_{-8} pc (Gaia Collaboration et al. 2016) close to the edge of the Taurus star-forming region (stellar properties are given in Table 12.1). Measurements of resolved CO emission around the star determined the stellar mass to be $2.0 \pm 0.2 M_{\odot}$ and the disk to

have an inclination of $21^\circ \pm 2^\circ$ and a position angle of the semi-major axis of $65^\circ \pm 7^\circ$ (Isella et al. 2010). The mass and age estimates were based on the previously adopted Hipparcos distances of 200 pc (van den Ancker et al. 1998) and 279 pc (van Leeuwen 2007). Given the revised Gaia distance, the star could be older and lighter than thought so far. In this paper, we assume a stellar mass of $1.5 \pm 0.2 M_\odot$, reflecting the scaling of the dynamical mass estimate to the new Gaia distance. Based on its SED, MWC 758 has been classified as pre-transition disk (Grady et al. 2013). Although a cavity of 55 astronomical units (au) in radius has been inferred from dust millimeter emission (Andrews et al. 2011), infrared polarized intensity observations found no clear evidence for a cavity in scattered light (Grady et al. 2013; Benisty et al. 2015). Using Ks-band (2.15 μm) direct imaging and H-band (1.65 μm) polarimetric imaging with the High Contrast Instrument with Adaptive Optics (HiCIAO) at the Subaru Telescope, Grady et al. (2013) detected two spiral arms and polarized light down to 0$''$.1 (15 au) from the star. Recent VLT Spectro-Polarimetric High-contrast Exoplanet REsearch (SPHERE) observations in the Y band (1.04 μm) have confirmed the presence of scattered light at least down to 14 au (Benisty et al. 2015). The asymmetries observed by Isella et al. (2010) in the mm-dust distribution and in CO emission suggest that the disk may be gravitationally perturbed by a low mass companion orbiting within a radius of 23 au (assuming a distance of 151 pc). The asymmetric cm-dust distribution was shown to follow the location of the mm-dust (Marino et al. 2015a), hinting towards the hypothesis of a dust trap, which could also be created by such companion in the gap through the Rossby wave instability (e.g., Pinilla et al. 2012b). Hydro-dynamical simulations of the disk indicate that the observed spirals could instead be launched by a massive planet or brown dwarf at larger separations ($\sim$100 au based on the revised Gaia distance, Dong et al. 2015b). The presence of stellar companions down to a mass limit of 12 $M_{\rm Jup}$ at 0$''$.25 and of planets outside 0$''$.5 (5 $M_{\rm Jup}$ at 0$''$.5, and 3 $M_{\rm Jup}$ at 1$''$, according to the BT-SETTL models; Allard et al. 2012) has been ruled out based on a combination of sparse aperture masking observations at L' band and angular differential imaging at K' and Ks bands (Grady et al. 2013).

In this paper we present high contrast imaging observations of the Herbig Ae star MWC 758 obtained with the NIRC2 camera at the Keck II telescope in the L' band (3.8 μm). Thanks to the use of the Keck adaptive optics system, combined with the recently commissioned vortex coronagraph and with high-contrast differential imaging techniques, the observations of MWC 758 presented in this paper achieved unprecedented sensitivity in the innermost 0$''$.25 and allowed us to probe the existence of planetary companions down to 0$''$.08.

Observations and Data Reduction

MWC 758 was observed twice (see Table 12.2) with the Keck II telescope at W. M. Keck Observatory, taking advantage of the L'-band vector vortex coronagraph installed in the near-infrared camera and spectrograph NIRC2 (Serabyn et al. 2017). This vector vortex coronagraph is a phase-mask coronagraph enabling high contrast imaging close to the diffraction limit of the telescope ($\sim$0$''$.08). On October 24, 2015 we obtained 33 minutes (80 frames) of on-source integration time and 129° of field rotation (see Table 12.2) to allow for angular differential imaging (ADI, Marois et al. 2006). Each frame is the sum of

Table 12.1: Stellar Properties

Properties	Values
RA (J2000)	$05^{h}30^{m}27^{s}.530$
DEC (J2000)	$+25°19''57''.082$
Age (Myr)	3.5 ± 2.0 (1)
Mass ($M_{\odot}$)	1.5 ± 0.2 (2)
L' (mag)	4.75 (3)
Distance (pc)	151^{+8}_{-9} (4)

References: (1) Meeus et al. (2012); (2) we scaled the dynamical mass estimate in Isella et al. (2010) to a distance of 151 pc; (3) Malfait et al. (1998); (4) Gaia Collaboration et al. (2016).

Table 12.2: Observations

	First epoch	Second epoch
UT date (yyyy/mm/dd)	2015/10/24	2016/10/24
DIT (s)	0.5	0.25
Coadds	50	160
Number of frames	80	80
Total Int. Time (s)	2000	3200
Plate scale (mas/pix)	9.942	9.942
Filter Coronagraph	L'	L'
Par. angle start/end (°)	-128/+103	-90/+97
Mean airmass	1.012	1.074
Median seeing ($''$)	0.64	0.75

50 internally co-added frames of 0.5 s discrete integration time (DIT) each. During the coronagraphic acquisitions, the sky (DIT $= 0.5$ s) and the unsaturated stellar point-spread function (PSF, DIT $= 0.018$ s) were also measured for background subtraction and photometric calibration purposes, respectively. The alignment of the star onto the coronagraph center is crucial for high contrast at small angles. In this case it was performed using the tip-tilt retrieval technique QACITS (Huby et al. 2015, 2017), as already implemented for HD 141569 (Mawet et al. 2017a). Thanks to QACITS, we could reach a centering accuracy of $0.03\lambda/D$ rms (3 mas rms). MWC 758 was then re-observed on October 24, 2016, following the same observing strategy as for the first epoch of observations (detailed information are given in Table 12.2). Due to cirrus clouds the weather conditions during this run were not as good as in the 2015 run.

Both data sets were preprocessed using the Vortex Image Processing package (VIP, Gomez Gonzalez et al. 2017). Images were divided by a flat field obtained without the vortex phase mask and the background emission (sky) was subtracted based on principal component analysis (PCA, Gomez Gonzalez et al. 2017; Hunziker et al. 2017). Bad pixel correction and bad frame removal were also applied to the data. Finally, the frames were re-centered through Fourier shift operations. For each epoch, the stellar PSF was subtracted by performing PCA (Amara & Quanz 2012; Soummer et al. 2012) to the full set of frames.

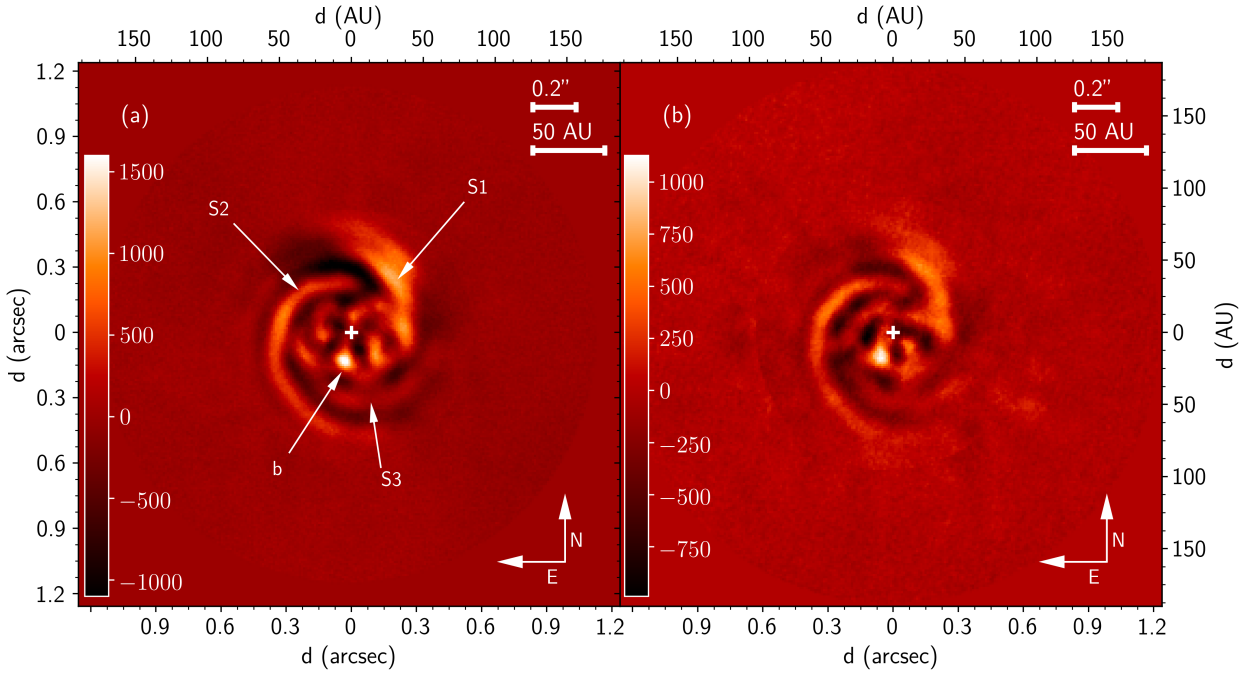

Figure 12.1: Final PCA-ADI images for the 2015 (a) and 2016 (b) data sets. Three spiral arms and a bright point-like feature are detected in the images. The three spiral arms and the point-like source are labeled with S1, S2, S3, and b, respectively.

Results

The final PCA-ADI L'-band images (Figure 12.1) show a bright point-like emission source, detected south of MWC 758 (labeled b in Figure 12.1a), at $\sim$0″.1 from the central star. The images also recover the two spiral arms (S1 and S2) already observed in near-infrared polarized light (Grady et al. 2013; Benisty et al. 2015), and reveal an additional one to the SW (S3).

In the following sections, we present the results in details.

The point-like source in the disk In the PCA-ADI residual images for both epochs, a bright L'-band emission source is located at the same position interior to the spiral arms (see Figure 12.1). For each dataset, the final image corresponds to the number of principal components that maximize the signal to noise ratio (S/N) of the point-like feature (3 and 9 components, respectively). To compute the S/N, we follow the Mawet et al. (2014) prescription, where the signal is summed in a 1 full width at half maximum (FWHM) aperture around a given pixel, and the noise is computed as the standard deviation of the fluxes inside 1 FWHM apertures covering a 1 FWHM-wide annulus at the same radial distance from the center of the frame, taking into account the small sample statistic correction. In both data sets, the point-source is recovered with a S/N of $\sim$5. Figures 12.2a and 12.2b show the S/N maps for the 2015 and 2016 final PCA-ADI images, respectively. None of the other bright features in the inner part of the disk (within 0″.2), is recovered with a SNR $>$ 3.

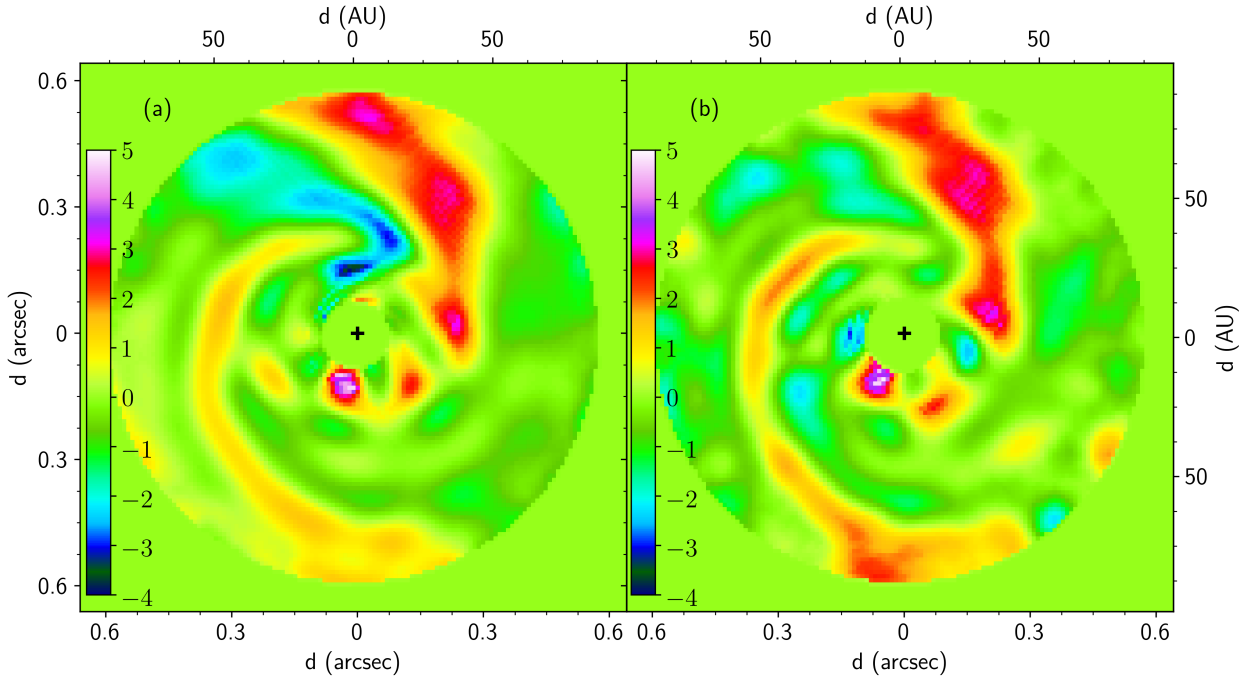

Figure 12.2: SNR maps for the 2015 (a) and 2016 (b) data sets. Apart from b, none of the other bright features in the inner part of the disk (inside 0.″2, down to the inner working angle at 0.″08), is recovered with a S/N > 3

To assess the reliability of the detection, we performed a series of tests. We both varied the number of PCA coefficients and divided the two data sets into subsets containing either half or a third of the frames, but covering the full field rotation. In both cases, the emission source south of MWC 758 appears to be the most significant feature in the final PCA-ADI images. We also inverted the parallactic angles of the frames, but we could not artificially generate any feature as bright as the one we detected.

The astrometry and photometry of the source are determined by inserting negative artificial planets in the individual frames, varying at the same time their brightness and location. The artificial companions are obtained from the unsaturated PSF of the star, which was measured without the coronagraph. The brightness and position that minimize the residual in the final images are estimated through a standard Nelder-Mead minimization algorithm. In the first epoch, the source is located at a distance $r = 0.''112 \pm 0.''006$ from the central star at a position angle PA $= 169° \pm 4°$, with a magnitude difference $\Delta L = 7.1 \pm 0.3$ mag. In the second dataset, the estimated position is $r = 0.''110 \pm 0.''006$ and PA $= 162° \pm 5°$, and the flux ratio is $\Delta L' = 6.9 \pm 0.5$ mag. The magnitude difference takes into account the vortex transmission (∼50%) at these separations. The uncertainties on the quantities due to speckle noise were determined by injecting fake companions around the star in the raw, companion-subtracted cube at the same radial distance, and calculating the median errors of the retrieved distributions. Variations of the total flux in the unsaturated PSF during the observing sequence were also included in the uncertainty on the brightness difference. The two measurements of separation, position angle and contrast are consistent with each other within 1σ. If the spirals are trailing, a companion in the disk is expected to rotate clock-wise. Given the distance of the source from the star and the time difference between the two epochs (1 year), orbital motion on a circular orbit would

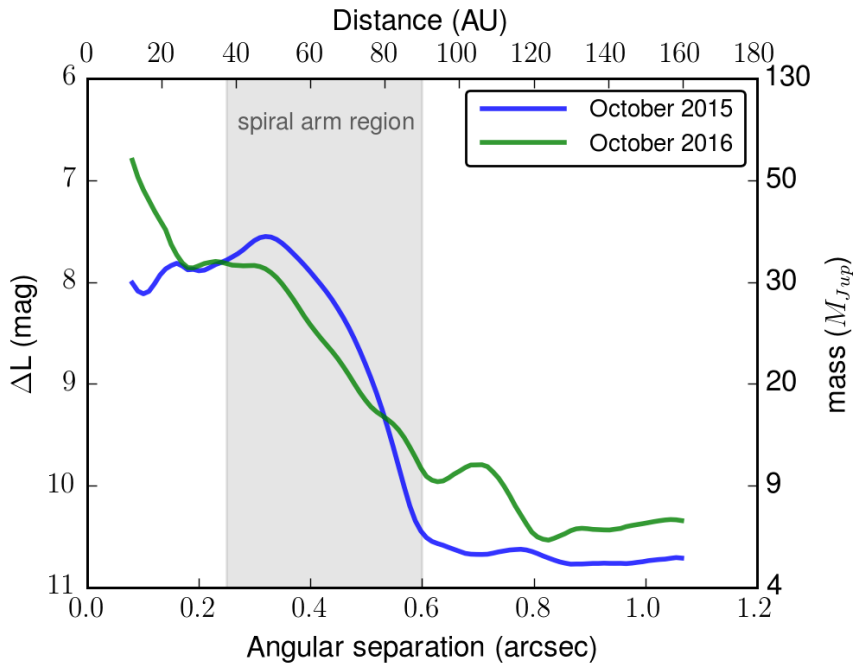

Figure 12.3: Detection limits at 95% completeness around MWC 758 for the Oct. 2015 (*blue line*) and the Oct. 2016 (*green line*) data sets. A false alarm probability of 1% is allowed in our field of view. The inner region indicated by the gray area is dominated by the presence of the spirals arms. Outward, our detection limits for the Oct. 2015 data set are close to 5 $M_{\rm Jup}$, according to the BT-SETTL evolutionary model (Allard et al. 2012).

produce a displacement of $\sim 5^{\circ}$, which is in line with our measurements.

Upper limits on other companions Apart from b, the only other point-like source observed in the field of view is the star located at 2.″3 to the NW, identified by (Grady et al. 2013) as background source. In order to calculate robust detection limits, assess the mass constraints for other companions around MWC 758, and mitigate some of the shortcomings of standard contrast curves, we adopted the concepts of false positive fraction (FPF) and true positive fraction (TPF, Wahhaj et al. 2013; Ruane et al. 2017).

In the hypothesis that after subtracting the stellar PSF the noise in the image can be considered Gaussian (Mawet et al. 2014), and that we set an acceptable fraction (1%) of false positive in our field of view (a region of $1'' \times 1''$), we computed the signal level corresponding to a given completeness level (Ruane et al. 2017). We adopted a 95% completeness, or TPF $= 0.95$, which means that such a signal would be detected 95% of the time. The contrast curve at 95% completeness is plotted as a function of angular distance in Figure 12.3. In the inner 0.″6, the sensitivity is limited by the scattered light emission from the spirals between 30 and 90 au. Beyond 0.″6, the sensitivity becomes almost constant (background-limited) and we can exclude planetary-mass companions down to ~ 5 $M_{\rm Jup}$ (see Figure 12.3) according to the BT-SETTL evolutionary model (Allard et al. 2012).

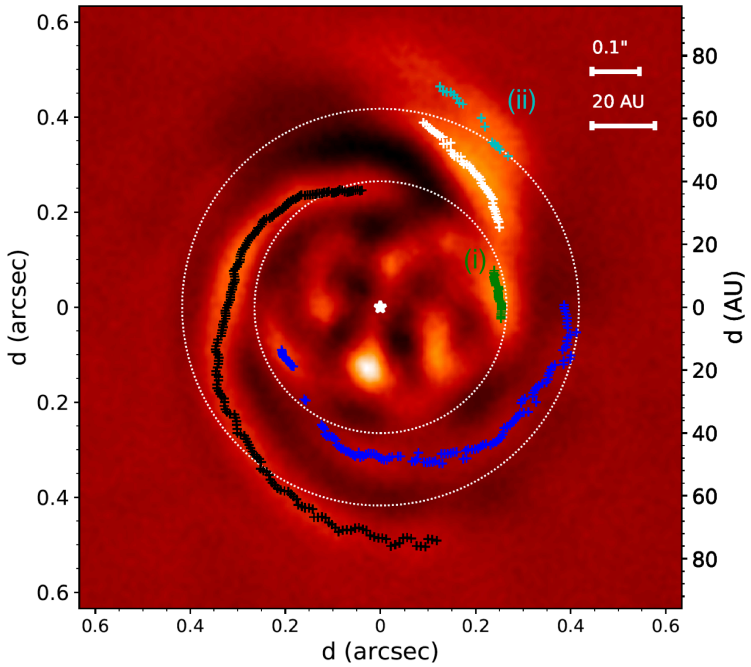

Figure 12.4: Deprojected disk image from the 2015 data set showing the trace of S1 (*white*), S2 (*black*), S3 (*blue*), features *i* (*green*) and *ii* (*cyan*). The dotted circles have 40 au and 63 au radial separations, and represent the limits within which the separation angle is computed between each pair of spirals (Figure 12.7).

Spiral arms Both the Oct. 2015 and Oct. 2016 final images (Figure 12.1a and b) show the two bright spiral arms (S1 and S2) already detected in H- and Y-band polarized light (Grady et al. 2013; Benisty et al. 2015), and a third fainter spiral to the SW (S3), which has not yet been reported. A detailed discussion on the reliability of the detection of the third arm is given in Appendix B. In addition to the three spirals, we recover the bright second arc, shifted radially outward from S1, observed in polarized light at PA $\sim 325°$ by Benisty et al. (2015). We refer to it as feature *ii* in Fig. 12.4.

Comparison of our image with the polarized light images of Benisty et al. (2015) also reveals several differences. First, the bright Y-band arc located at $\sim$0$''$.2 separation and covering a PA range of 180°– 270°(feature (2) in Benisty et al. 2015) appears much less prominent in L'-band, but is still recovered at the same location as in the polarized light image. A possible reason for the significant damping of the arc in our image is the tendency of ADI to self-subtract extended axi-symmetrical signal. Second, while S1 and the Y-band arc appear smoothly connected in the polarized image, this is not the case in our L'-band images, where a clumpy structure is distinguished close to the root of S1 (feature *i* in Fig. 12.4). Part of the reason for such discontinuity could be the ADI filtering of a slightly over-illuminated area of the spiral, as ADI is known to produce negative azimuthal lobes. Alternatively, this could indicate that it is tracing a different physical process (e.g. the merging of S1 and S2).

To characterize the spiral arms and features *i* and *ii*, we identified their trace as radial intensity maxima in azimuthal steps of 1°. This was done both in the final PCA-ADI image and in a deprojected one, based on a disk inclination of 21° and a PA of the semi-major axis of 65° (Isella et al. 2010). The deprojected image is shown in Figure 12.4. Only the

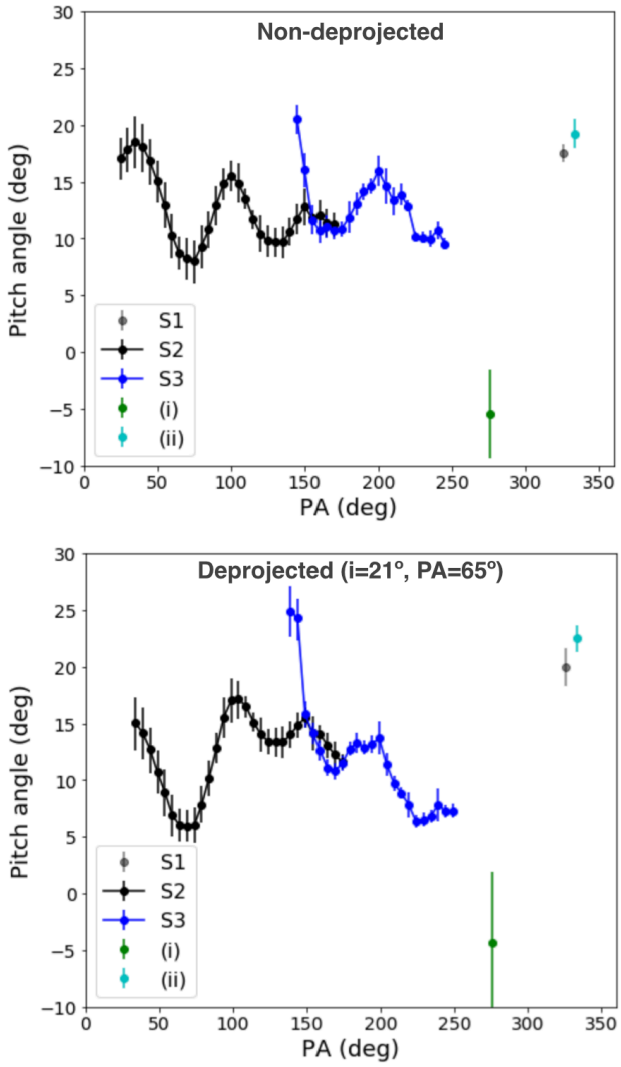

Figure 12.5: Pitch angle of each spiral, in the non-deprojected (top) and deprojected image (bottom). For each measurement, we considered either the whole trace (for S1, features *i* and *ii*), or consecutive arcs subtending 50° (for S2 and S3) to trace the evolution of the pitch angle along the trace in order to provide reliable pitch angle estimates. The estimate for feature *ii* has a larger uncertainty because its trace only subtends ∼25°, instead of ∼50°for S1 and feature *ii*.

Oct. 2015 PCA-ADI final image was used, as it reaches better sensitivity than the Oct. 2016 data set. The trace of the spirals then allowed us to measure their pitch angles, defined at each point as the angle between the tangent to the spiral and the local azimuthal vector. For each trace, the pitch angle was estimated in two different ways: (a) we considered the average value of the pitch angle computed from all pairs of consecutive points in the trace, and (b) we derived the pitch angle of the best fit logarithmic spiral given by $r = a\mathrm{e}^{b\theta}$. Logarithmic spiral arms have the property of keeping a constant pitch angle throughout their length, given by the complementary of $\arctan(1/b)$. Both methods yielded consistent measurements, although method (a) led to larger uncertainties.

Figure 12.5 shows the pitch angles measured with method (b) for each feature identified in Figure 12.4. We measured the evolution of the pitch angle over S2 and S3 using method

(b) on consecutive sections of the spirals separated by 5° and subtending each 50°. A single measurement using method (b) is provided for S1, features *i* and *ii*, due to the short PA range they subtend. We first notice that the pitch angle of feature *i* is slightly negative (quasi-null), which suggests that it is more likely related to the Y-band circular arc rather than to S1. We also note that the root of S3 (PA <150°) shows a more significant pitch angle than the rest of S3. This could imply that it is either tracing a feature of the disk unrelated to S3, or that ADI filtering significantly alters the shape of S3 at such close separation. Overall, S1 and feature *ii* present a slightly larger pitch angle than both S2 or S3. The difference is more significant after deprojection (∼20° instead of ∼7–16°). It appears thus more likely that feature *ii* is related to S1 rather than S3, although the possibility that feature *ii* traces the outer tip of S3 cannot be completely ruled out in view of the strong fluctuations in the pitch angle of both S2 and S3 (up to 10°). The distortion of the spirals induced by the disk deprojection also appears to enhance the drop in pitch angle along the PA of the semi-major axis ($65 \pm 7°$and $245 \pm 7°$) for both S2 and S3. Implications are further discussed in Sec. 7.2.8.

Discussion

The nature of the point-like source If we take a mean weighted by the errors of the estimates of the two epochs, the point-like source is located at an angular separation of $0\farcs111 \pm 0\farcs004$ with a magnitude difference of $\Delta L' = 7.0 \pm 0.3$ mag. Given the distance of the star (151 pc; Gaia Collaboration et al. 2016), and assuming the disk to be nearly face on (Isella et al. 2010), the physical separation from the central star is 16.7 ± 0.6 au. Taking into account the inclination of the disk, the bright emission would be at 20±1 au (assuming co-planarity, as shown in Fig. 12.4).

To explain the nature of the point-like source, we explored different possibilities. Comparing the separation and the brightness of the source with the TRILEGAL tridimensional model of the galaxy (Girardi et al. 2012), we can safely reject the hypothesis that the bright emission is a background star (probability $\simeq 10^{-6}$). If the L'-band emission came from the photosphere of a low-mass companion, its mass would range between 41-64 Jupiter masses ($M_{\rm Jup}$), according to the BT-SETTL evolutionary models (Allard et al. 2012). However, the non-detection of a fully depleted cavity in micrometer-size dust, requiring a steady replenishment of small particles, restricts the mass of companions in the inner disk of MWC 758 to be $\lesssim$ 5.5 $M_{\rm Jup}$ (Pinilla et al. 2015b), or even smaller depending on the assumed model (e.g. a $1 M_{\rm Jup}$ planet should already start opening a gap in the gas distribution, Dong & Fung 2017b; Fouchet et al. 2010; Paardekooper & Mellema 2004). With such mass constraints, only a protoplanet (hence MWC 758 b) surrounded by a circumplanetary accretion disk could account for the observed brightness. According to the circumplanetary disk accretion models of Zhu (2015), its L'-band luminosity is compatible with a 0.5-5 $M_{\rm Jup}$ planet accreting at a rate of 10^{-7}-10^{-9} $M_\odot$ yr^{-1} (see Figure 12.6). The corresponding K-band magnitude difference with the star (∼7–9 mag) would be consistent with the non-detection of MWC 758 b in previous images at this wavelength (Grady et al. 2013). Due to the highly structured nature of the inner disk, we cannot discard the possibility that the point-like source is associated with an asymmetric disk feature, as recently suggested for HD 169142

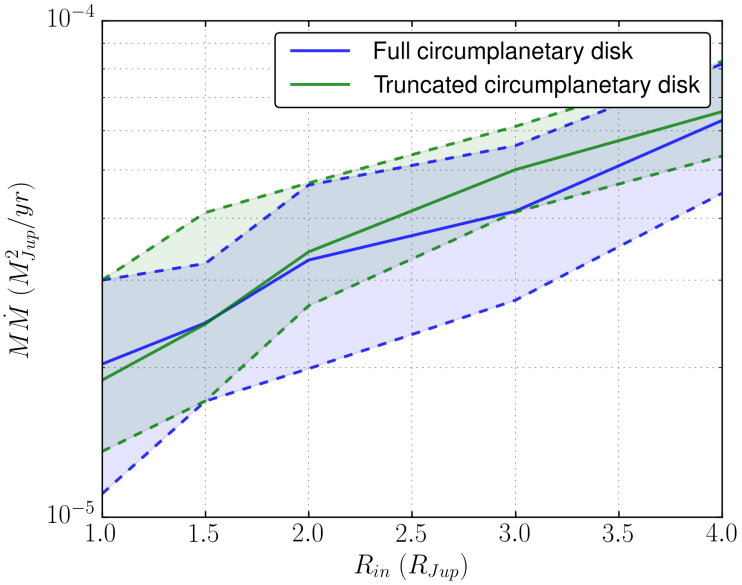

Figure 12.6: Circumplanetary disk accretion models from Zhu (2015). The product of the mass of the planet and the disk accretion rate ($M_p\dot{M}$) changes as a function of the disk inner radius (R_{in}). The solid blue and green lines represent the $M_p\dot{M}$ vs. R_{in} curve for the measured L'-band absolute magnitude ($M_{L'} = 5.9$ mag), in the case of a full or a truncated circumplanetary disk, respectively. The dotted lines indicate the 1σ error bars.

(Ligi et al. 2017). However, only future observations, as for instance the lack of orbital motion or the detection (or not) of Hα emission, can test this hypothesis.

Besides these potential astrophysical origins, we also consider the possibility that the point-like source corresponds to a false positive detection, i.e., a bright speckle appearing twice at the same location. We show in Appendix A that, under Gaussian noise assumption, the astrophysical explanation is favoured at an odds ratio of ~1000:1 with respect to the false positive hypothesis.

The spiral arms Three spiral arms are detected at L'-band, which most likely traces scattered stellar light by sub-micrometer size dust. The detection of S3 in L'-band and its non-detection with polarized light at shorter wavelength could be explained by the different dust scattering properties at L'-band (3.8 μm) compared to Y-band (1.04 μm). If the emission traces Rayleigh scattering of sub-micrometer size grains (cross-section $\propto \lambda^{-4}$), then Y-band would trace mostly the disk surface, while L'-band could probe deeper layers of the disk. Therefore, the non-detection of S3 at Y-band could mean that it has a smaller scale height than S1 and S2. The different appearance of feature *i* at Y- and L'-band could also be due to the tracing of different disk layers, or to ADI filtering. Part of the L'-band emission could also trace shocks occurring in the spiral wake, as they could significantly heat the disk locally (e.g., Richert et al. 2015; Lyra et al. 2016). However, Rafikov (2016) argues that the increase in temperature due to shocks should be negligible, meaning that the observed spirals would only trace scattered stellar light.

Regarding the origin of feature *ii*, we note a striking resemblance with the double arc seen in the disk of HD 100453 (Benisty et al. 2017). It was suggested that such feature

can be explained as the scattering surface of the bottom side of the disk. We note that in the case of MWC 758 this explanation is consistent with the estimated inclination and PA of the outer disk (i $\sim 21°$, PA $\sim 65°$), since such double feature is expected to be more prominent along the semi-minor axis of the disk. If this interpretation is correct, the NW side of the outer disk is closer to us than the SE side.

Could any of the observed spirals be launched by the candidate companion? Hydrodynamical simulations and corresponding radiative transfer models suggest that observable spirals in near-infrared light could only be launched by companions massive enough for the linear spiral density wave theory to break down (Juhász et al. 2015; Dong & Fung 2017b). In this case, the planet responsible for the spiral structure would be located at the edge of or outside the spiral arms in order to be able to reproduce the observed pitch angles (Dong et al. 2015b), indicating that the protoplanet candidate is most likely not responsible for the observed disk structure. However, the possibility that the candidate companion is on an inclined, eccentric orbit cannot be ruled out. Recent simulations suggest that a mild perturbation on the inclination of a companion in the inner disk can lead to a polar orbit within a few Myr (Owen & Lai 2017; Martin & Lubow 2017). In such case, spiral predictions from circular orbits co-planar with the disk would not be valid. Recent simulations in the case of the disk of HD 142527 indicate that the close-in companion with an inclined and eccentric orbit (Lacour et al. 2016) is able to qualitatively reproduce the spiral arm pattern in the outer disk (Price et al. 2017, in prep.). Similarly, some or all of the observed spirals in MWC 758 could be launched by the candidate companion if in the same plane as the inner disk, which is likely misaligned with respect to the outer disk. The difference in inclination is estimated between 10°and 30°, while the PA does not appear well constrained (Isella et al. 2006, 2008; Lazareff et al. 2017). Finally, the large fluctuations in the measured pitch angle along S2 and S3 could also be considered as a clue that the spirals are launched by a companion whose orbital plane is different than the plane of the outer disk. Indeed, if the spirals were seen face-on after deprojection, one would not expect significant variations in their opening angle (apart in the direct vicinity of the companion, Zhu et al. 2015; Juhász & Rosotti 2018). Nevertheless, our deprojection does not take into account the flaring of the disk, which may bias the measured pitch angles.

In case a massive, yet undetected companion located outside of the spirals is needed to account for the observed multiple spiral pattern, an empirical relationship has recently been established between the mass of the companion and the separation angle $\phi_{\rm sep}$ between primary and secondary spiral arms: $\phi_{\rm sep} = 102°(q/0.001)^{0.2}$, where q is the mass ratio between the companion and the star (Fung & Dong 2015, hereafter FD15). In order to investigate the origin of the spirals of MWC 758, we measured the separation angle $\phi_{\rm sep}$ between each pair of spiral arms between 40 and ∼63 au, where all spirals are clearly defined in our final PCA-ADI image (Figure 12.7). These measurements are based on geometrical fits of the spirals, to be presented in Barraza et al. (2017, in prep.). In the FD15 simulations, the separation angles are relatively constant with radius, with only a slight decreasing trend for all models with $\phi_{\rm sep} > 80°$. Here, for each pair of spirals, the observed separation angle appears to vary significantly with radius. Only in the limited range of radii ∼40–55 au, $\phi_{\rm sep}$ for the S1-S3 and the S2-S3 pairs are comparable to the FD15 models for $q = 4 \times 10^{-3}$ and $q = 10^{-3}$, respectively. Considering a stellar mass of $1.5 M_{\odot}$, this would correspond to a companion mass of $\sim 6 M_{\rm Jup}$ (for S1-S3) and $\sim 2 M_{\rm Jup}$ (for S2-S3). The first possibility is

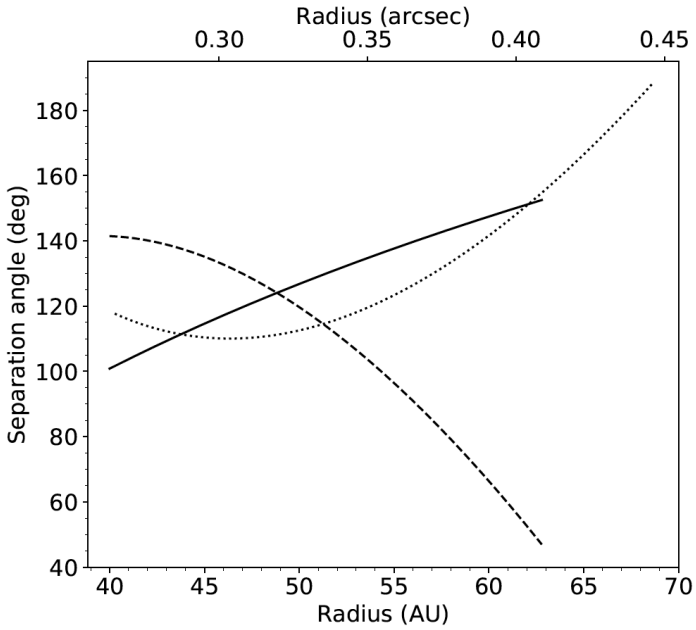

Figure 12.7: Separation angle between S1 and S2 (*solid line*), between S1 and S3 (*dashed line*), and between S2 and S3 (*dotted line*).

consistent with our detection limits inside 90 au, while the second is compatible with our sensitivity limits at any radius (Figure 12.3). Nevertheless, these predictions require the presence of a giant planet at large separation (> 80 au), which is expected to be very rare (e.g. Vigan et al. 2017). Furthermore, in the case that S1-S3 (resp. S2-S3) are launched by an external companion, another companion would yet be required to account for S2 (resp. S1), except if S2 (resp. S1) happens to be a very bright tertiary arm, even brighter than the secondary arm (i.e. S3 in both cases).

For the sake of completeness, we also consider the possibility that the observed spiral pattern is induced by one or several other physical mechanisms. Hydro-dynamical simulations have suggested that shadows producing a periodical perturbation in temperature on the outer disk could be able to launch large scale symmetrical spiral arms (Montesinos et al. 2016). In the case of an inclined inner disk with respect to the outer disk, two shadows are cast and a relatively symmetric two-arm spiral pattern forms in the outer disk. Nevertheless, there is no detection of conspicuous shadows similar to the case of HD 142527 (Avenhaus et al. 2014; Marino et al. 2015b) or HD 100453 (Benisty et al. 2017), which makes this possibility unlikely.

The flyby by an external star is also known to produce a one- or two-arm spiral pattern (e.g., Quillen et al. 2005). We investigated the possibility that MWC 758 could have undergone a fly-by from the source located at 2.″3. As detailed in Appendix C, the color and magnitude of the object are not compatible with a young object at the distance of Taurus, and could either correspond to an early red dwarf at the distance of MWC 758, or a red giant star much farther away. The probability that an old red dwarf happens to cross the star forming region of Taurus is very small, we hence favor the second hypothesis.

Based on mm-dust continuum observations and assuming a fiducial gas-to-dust ratio of

100, the disk mass was estimated to 0.008 $M_\odot$ (Andrews et al. 2011). Considering a stellar mass of 1.5 $M_\odot$, the disk is about 50 times less massive than required to form spiral arms by self-gravity (Dong et al. 2015a).

Conclusions

The L'-band vortex coronagraph installed on Keck/NIRC2 was used to discover a point-like source with ∼7.0 mag contrast in L'-band at only ∼0.″11 from the central star, and to reveal an additional spiral arm in the disk. Although the possibility of an asymmetric disk feature cannot be excluded, we argue that the $L' \sim 11.7$ mag apparent magnitude emission ($M_{L'} \sim 5.9$, assuming a distance of 151 pc) is most likely due to an embedded protoplanet. In this case the newborn planet would be sourrounded by an accreting circumplanetary disk, which may account for most of the observed luminosity. The presence of scattered light down to 15 au (Benisty et al. 2015) indicates that the planet should be small enough to have only marginally affected the inner part of the disk.

We considered several possibilities for the origin of the spiral arms. Neither disk self-gravity nor the source at ∼2.″3 (most likely a background red giant) appear to be able to account for the observed structures. Our analysis suggests that the most likely explanation for the observed spiral pattern involves either (i) the candidate companion itself if it is on an inclined and eccentric orbit, possibly co-planar with the inner disk; (ii) the presence of an undetected $\sim 6 M_{\rm Jup}$ planet at the outer tip of S1; (iii) the presence of an undetected $\sim 2 M_{\rm Jup}$ planet at or outside the outer tip of S2; or a combination of the above explanations. Both the second and third cases are compatible with our sensitivity constraints. The second case is similar to the prediction based on previous hydro-dynamical simulations of the disk of MWC 758 (Dong et al. 2015b).

New dedicated simulations considering the revised distance of MWC 758 (151 pc, Gaia Collaboration et al. 2016), and including the protoplanet, the third spiral arm and our mass constraints in the outer disk, will enable to further constrain the origin of the observed spiral pattern. Future re-detection (or non-detection) of the companion at other wavelengths will help us constraining its properties thanks to the comparison with SED predictions (Zhu 2015; Eisner 2015). Follow-ups with ALMA could probe the dynamics of the disk and also provide new insight on the nature of the bright L'-band point-source. If the observed feature is an accreting circumplanetary disk, it is expected to leave an observable kinematic signature in ALMA observations (Perez et al. 2015). Its accretion nature could also be confirmed with direct imaging in the Hα line, as for HD 142527B (Close et al. 2014) or LkCa 15 (Sallum et al. 2015).

Appendix A: The odds ratio calculation

To evaluate in a more rigorous way the confidence of the detection we built an odds ratio (OR) between the likelihood of the planet (H_1) and the false positive (H_0) hypothesis. Based

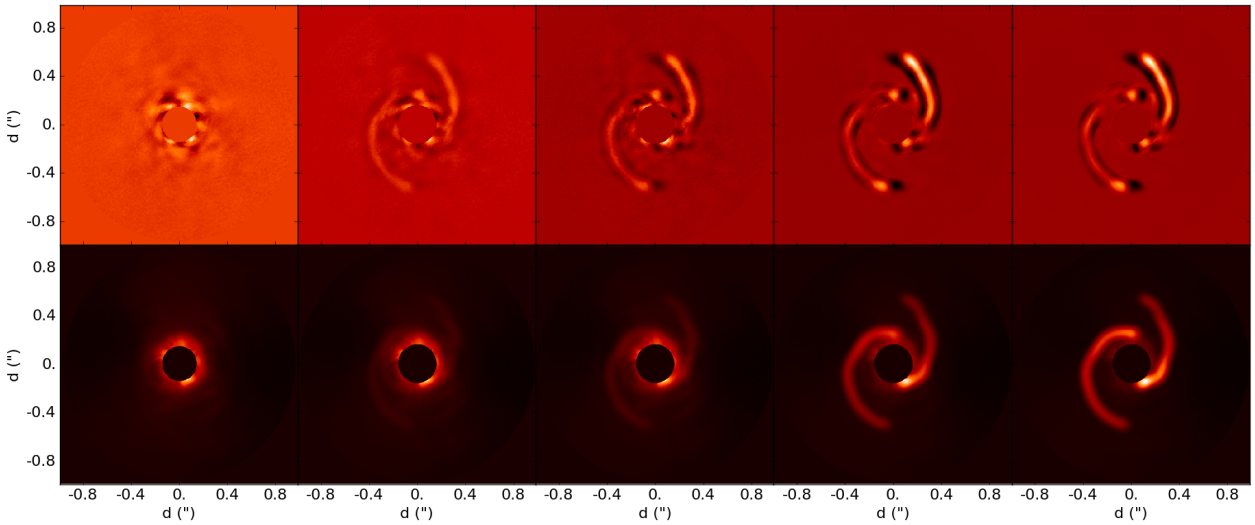

Figure 12.8: ADI and RDI comparison on artificial spirals. Top and bottom row show the results of PCA-ADI and PCA-RDI, respectively, on artificially injected spirals. The injected spiral flux increases from left to right.

on the Bayes theorem, it can be computed as:

$$\mathrm{OR} = \frac{\mathrm{P}(H_1|x)}{\mathrm{P}(H_0|x)} = \frac{\mathrm{P}(x|H_1,\mu_c)}{\mathrm{P}(x|H_0)} \times \frac{\mathrm{P}(H_1)}{\mathrm{P}(H_0)} \tag{12.1}$$

where $\mathrm{P}(x|H_1,\mu_c)$ and $\mathrm{P}(x|H_0)$ are the likelihood of the data given the signal with flux μ_c and the likelihood of the data given a false positive, respectively. $\mathrm{P}(H_1)/\mathrm{P}(H_0)$ is the ratio of the priors for H_1 and H_0. $\mathrm{P}(x|H_0)$ can be evaluated from the S/N of the bright emission under Gaussian noise assumption. In this case, a 5 sigma detection corresponds to a probability of 0.12% using the Student t-distribution with 6 degrees of freedom (defined as the number of independent and identically distributed samples at a radial distance r, i.e. $(2\pi r/\mathrm{FWHM}) - 2$). $\mathrm{P}(x|H_1,\mu_c)$ can be estimated after removing the bright emission. There is a 50% chance for the noise to be higher, and 50% chance to be lower at that location, meaning $\mathrm{P}(x|H_1,\mu_c)$=0.5. To estimate the prior ratio, we considered the expected number of planets in a given mass and separation range around a ~2 $M_\odot$ star. Preliminary analysis of the Gemini Planet Imager Exoplanet Survey gives a 6% probability of 2 $M_\odot$ star hosting a planet between 5-13 M_{Jup} in the 10-100 au separation range (Nielsen et al. 2017). The disk geometry and its L'-band luminosity constrain the mass of the protoplanet around MWC 758 to be ~1–6 M_{Jup}. Assuming that planets follow the mass and semi-major axis distributions measured by RV surveys (Cumming et al. 2008), we estimated the likelihood of having a planet between 1-6 M_{Jup} and between 19-21 au to be $\mathrm{P}(H_0)$= 0.006 (hence, $\mathrm{P}(H_1) = 1 - \mathrm{P}(H_0)$=0.994). Considering that we detected the point-source in two epochs, indicated here by the subscript a and b, the odds ratio becomes:

$$\mathrm{OR} = \frac{\mathrm{P}(x_a|H_1,\mu_c)}{\mathrm{P}(x_a|H_0)} \times \frac{\mathrm{P}(x_b|H_1,\mu_c)}{\mathrm{P}(x_b|H_0)} \times \frac{\mathrm{P}(H_1)}{\mathrm{P}(H_0)} = 1048. \tag{12.2}$$

The planet hypothesis is thus favored at an odds ratio of 1048:1, providing high confidence that this is, indeed, a true companion.

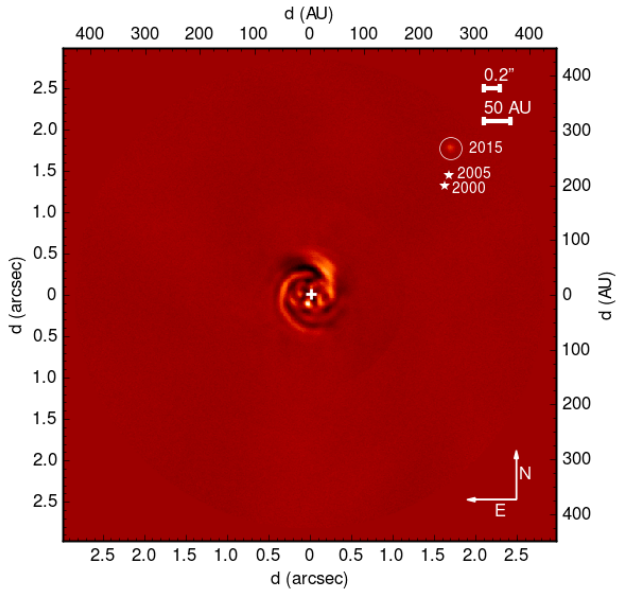

Figure 12.9: Wide field view of MWC 758 from our L'-band 2015 data. A source is detected at 2.″3 from the star. Positions of the same object in the 2000 (Grady et al. 2005) and 2005 (Grady et al. 2013) HST observations are plotted on the image, too. North is up and east is toward the left.

Appendix B: Reliability of the observed spirals

ADI is known to be an aggressive algorithm that can introduce biases in the results of disk image processing (Milli et al. 2012). We tested the effect of ADI on spiral features, by injecting two artificial spiral arms (similar to S1 and S2) into an ADI cube obtained in similar conditions for a different source showing no disk emission. For this object, a reference star was also observed before and after the target observations to allow for reference star differential imaging (RDI, Mawet et al. 2013). In the residual images after PCA analysis, the injected spirals in the ADI data reduction appear to be sharper, but unchanged in shape, compared to RDI (see Figure 12.8). No tertiary arm is generated by the injections of the two spiral arms. These tests give us confidence that the structures detected in the final PCA-ADI images are real.

Appendix C: The source at 2.3"

After PSF subtraction, a source at a distance $r = 2.''315 \pm 0.''002$ and PA = 316°±2° is recovered in the final 2015 image (see Figure 12.9). Its L'-band magnitude is $L' = 14.4 \pm 0.1$ mag. This source was previously classified as non-comoving (Grady et al. 2013) and as background object based on its V-magnitude (Grady et al. 2005). A re-analysis of the archival STIS and NICMOS data sets (Choquet et al. 2014) results in magnitudes $V = 17.74 \pm 0.03$ and $J = 15.8 \pm 0.1$ assuming a Kurucz (Kurucz 1993) A2V stellar model, and $V = 18.37 \pm 0.03$ and $J = 15.5 \pm 0.1$ for a M2V spectral-type. The color information and absolute magnitudes are inconsistent with a young object at the distance of Taurus. They would rather suggests either an M4 main sequence star at the distance of MWC 758, or a red giant much further

away. Considering that the probability of an old M dwarf crossing the Taurus star forming region is small, we believe that the source at 2″.3 is most likely a background red giant.

12.2 Case of HD 206893 B

In this section, I present the peculiar case of HD 206893 B, the reddest companion found to date in a debris disk. This source is thus older than other objects discussed in this thesis. In the next two sections, I summarize my contributions to the discovery of the companion and its spectral characterization, which were presented in Milli et al. (2017a) and Delorme et al. (2017) respectively. The discovery paper presents the detection with VLT/SPHERE and the confirmation in L' band with VLT/NACO using the AGPM coronagraph. In that work, I carried out the observations, data reduction and analysis of the NACO data. In the spectral characterization paper, my contribution consisted in retrieving the spectrum of the companion using the routines implemented in VIP. The extracted spectrum was then compared to results obtained with other algorithms.

12.2.1 Discovery

HD 206893 is an F5V star surrounded by a large debris disk, as inferred from its SED (Moór et al. 2006; Chen et al. 2014), but undetected in scattered light. Its age is relatively poorly constrained, with estimates ranging between 200 Myr and 2 Gyr (Zuckerman et al. 2004; David & Hillenbrand 2015). The source was observed with SPHERE/IRDIS in H band on 5 October 2015, as part of the SPHERE High Angular Resolution Debris Disc Survey (SHARDDS, PI: Julien Milli) which aims to resolve for the first time the disk of sources whose SED suggests the presence of a massive debris disk. A bright companion candidate was detected at S/N $\sim$ 14 at $\sim$ 0″.27 towards the NE of the star (Fig. 12.10a).

In this context, a re-detection was required to confirm companionship. This is when I got involved in the project. After discussion with Olivier Absil and Julien Milli, we decided to attempt re-detecting the companion candidate with NACO+AGPM in L'. Below I describe the observations, data reduction and analysis of the NACO data that I carried out, as provided in Milli et al. (2017a). Then I briefly discuss the conclusions that could be reached from the comparison between the NACO and SPHERE results.

Observations and data reduction with NACO

HD 206893 was observed with VLT/NaCo on 8 August 2016, taking advantage of its AGPM coronagraph (e.g. Mawet et al. 2005, 2013). This observation was part of program 095.C-0937(B) (PI: O. Absil). HD 206893 was observed in pupil-stabilised mode using the 27.1 mas pixel^{-1} plate scale and the L'- band filter (3.8 μm). The seeing (0″.7-0″.8) and the coherence time ($\sim$5 ms) were stable throughout the observation. A total of 90 science data

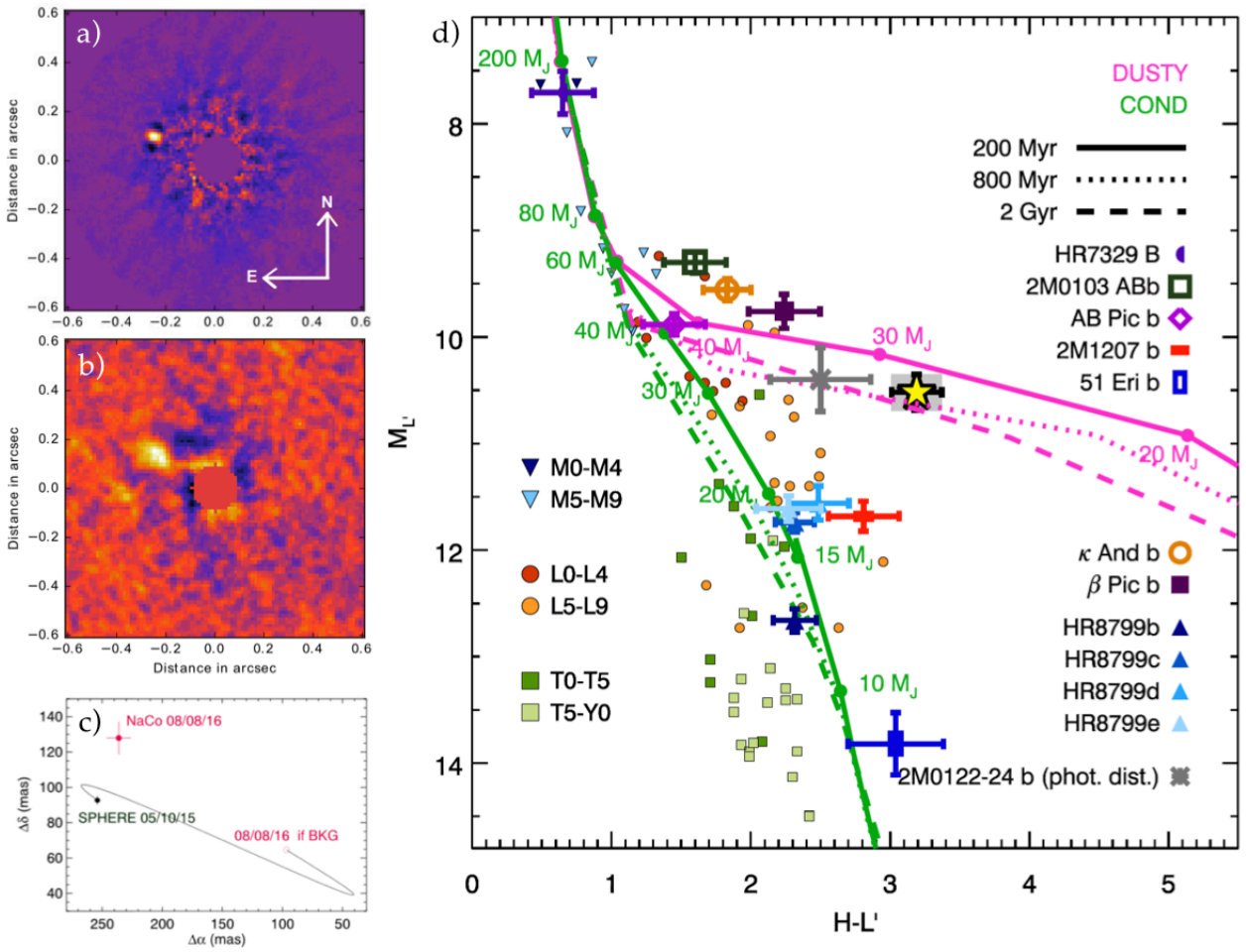

Figure 12.10: Detection of HD 206893 B. **a)** SPHERE/IRDIS H-band image. **b)** NACO L'-band image. **c)** Proper motion analysis: the companion is not a background object. **d)** $H - L'$ color-magnitude diagram showing the location of HD 206893 B (yellow star) compared to other directly imaged companions. Figures presented in Milli et al. (2017a).

cubes of 0.3s (DIT) exposure and 200 (NDIT) frames were obtained, corresponding to 1h30 on-source and a 107° total parallactic angle variation. Sky data cubes were obtained every 10-12min. The star was carefully re-centered behind the coronagraph after each sky observation to a ∼0.2-0.3 pixel accuracy. Four data cubes were also obtained with a shorter exposure time and the star offset from the coronagraph centre (but still behind the AGPM substrate), to obtain unsaturated PSF images. These data cubes were used for photometric calibration and to generate fake companions.

After standard calibrations (Sec. 11.4), the frames were re-centered by fitting a negative gaussian to the AGPM central hole as done in Absil et al. (2013). The frame selection process, essential to reach the best contrast, kept the 12879 most correlated frames with the lowest level of residual speckle noise, out of 18000 original frames. These 12879 frames were binned four by four, to yield a final ADI cube of 3219 frames. The final cube was reduced using PCA-ADI as implemented in VIP (Gomez Gonzalez et al. 2017), with seven principal components removed, which was found to optimize the companion SNR (SNR ∼ 6). The resulting image is provided in Fig. 12.10b.

Results obtained with NACO

In order to infer reliable astrometry and photometry for the companion, the negative fake companion technique (NEGFC) was used, as implemented in VIP (Wertz et al. 2017). The exploration of the three parameters (radial separation, PA and contrast) was performed with a simplex algorithm minimizing the residual standard deviation in an aperture at the location of the companion.

The parameters inferred by NEGFC for the NACO dataset are: $r = 268.8 \pm 10.4$ mas (∼10 au at a distance of 38.3±0.8 pc van Leeuwen 2007), PA $= 61.6 \pm 1.9°$, and $L' = 13.43^{+0.17}_{-0.15}$ mag. The uncertainties reflect (1) residual speckle noise (for all 3 parameters), (2) the error on the plate scale (for the radial separation), and (3) the error on the true north (for the PA). Residual speckle noise uncertainties were estimated in a similar way as described in Wertz et al. (2017), and summarized below. First, the companion was removed from the raw cube using the parameters mentioned above. Next, we injected 360 fake companions separately in the (empty) raw cube, and applied NEGFC in each of these new cubes. The companions are injected at different PAs but at the same separation and contrast as the companion. The distribution of deviations between the parameters used for the injection and the retrieved NEGFC parameters for the 360 fake companions finally enabled to estimate the residual speckle noise uncertainty.

Conclusions based on the NACO and IRDIS results

Julien Milli applied the same technique as described in the previous subsection to extract the astrometry and photometry of the companion in the SPHERE data. This led to $r = 270.4 \pm 2.6$ mas, PA $= 69.95 \pm 0.55°$, and $H = 16.79 \pm 0.06$ mag.

A first conclusion that can be inferred from the astrometric parameters retrieved for the NACO and SPHERE datasets, is that the companion is most likely bound to the system, at a projected separation of ∼ 10 au. A background object would have been found at a significantly different location (Fig. 12.10d).

Second, the H and L' magnitudes suggest that the companion is very red ($H - L' \sim 3.3$). In fact, the comparison to other directly-imaged young companions suggests that it is the reddest companion known to date (Fig. 12.10c). This peculiarity made the source particularly interesting for spectral follow-up.

12.2.2 Spectral characterization

Follow-up observations with SPHERE-IFS were obtained on September 16, 2016 as part of the SpHere INfrared survey for Exoplanets (SHINE) GTO (PI: G. Chauvin). These observations enabled to infer a YJH+$K1K2$ spectrum of the companion which, along with L' photometric points were considered for comparison with a large set of atmosphere models.

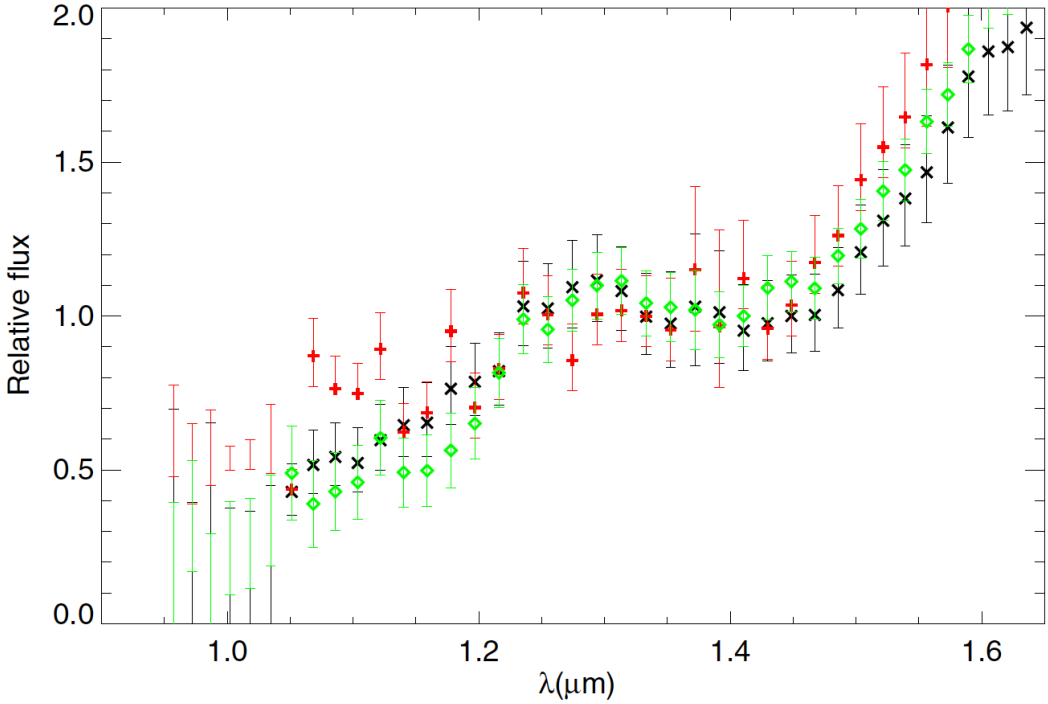

Figure 12.11: Spectrum of HD 206893 B, as extracted from VIP/PCA-ADI (*red*), TLOCI (*black*) and ANDROMEDA (*green*). Plot from Delorme et al. (2017).

Results are presented in Delorme et al. (2017). The spectral analysis from Y to L' is that the companion is either an extremely dusty and red 1300-1400K, 15-30 $M_{\rm Jup}$ L dwarf, or a more massive L dwarf embedded within an extremely dusty environment which absorbs a significant portion of its light, such as a circum-companion disk or a dust cloud released by a recent giant impact. This study also included an in-depth analysis of the properties of the host star. In particular, the age of the system was slightly refined to be between 50 and 700 Myr. An orbital fit of the companion was also performed including constraints from the outer debris disk, suggesting that the semi-major axis of the companion is $\sim$ 14.5 au and its eccentricity $\sim$ 0.31.

In that study, my contribution consisted in the independent extraction of the spectrum of the companion using routines of VIP, and is detailed below, as included in Delorme et al. (2017). For each spectral channel, I first applied PCA-ADI on a single 3-FWHM wide annulus at the radial location of the companion and determined the number of principal components ($n_{\rm pc}$) that would maximize the SNR of the companion in the PCA-ADI processed image. Then, I used NEGFC in each spectral channel, with the same PCA-ADI parameters and $n_{\rm pc}$ as inferred above. Instead of letting 3 free parameters (radial separation, PA and contrast), I fixed the radial separation and PA to be the median value inferred for all spectral channels. I noticed that this led to more robust photometric retrieval in the channels where the companion was found only at low SNR (the blue channels of the spectrum), while it did not affect significantly the flux inferred in other channels. The spectrum I obtained in such a way is shown in red in Fig. 12.11. It is compared to the spectrum inferred by TLOCI (Marois et al. 2014) and ANDROMEDA (Cantalloube et al. 2015).

All three reductions show a very red spectra, with non-detection or marginal detections in the blue part of the spectrum and high signal-to-noise detections in the red channels. According to the estimated error bars, the difference between the extracted fluxes are mostly consistent with Gaussian noise, with a few exceptions in some consecutive channels. This is not surprising given that different algorithms subtract the stellar halo in different ways, leaving slightly different residual speckle noise pattern. Since speckle noise is correlated from channel to channel and that for a separation of $\sim 8\ \lambda/D$, it takes $\sim$8-12 channels for a speckle residual to move radially by one FWHM. This explains why some non-Gaussian differences can be seen over contiguous channels.

Nonetheless, whether the VIP-optimal-PCA or the TLOCI spectrum is used for the fit to BT-SETTL models leads to almost identical results: $T_{\rm eff} = 1550$K (resp. 1600K), $\log(g) = 3.5$ (resp. 3.5) for VIP (resp. TLOCI). Therefore, conclusions regarding the physical properties inferred for the companion are not significantly affected by systematic biases affecting different processing algorithms.

13 Summary and future plans

13.1 Summary of the results

In Chap. 11, I detailed the various aspects of the HCI survey of transition disks that I carried out with VLT/NACO in search for protoplanets. In order to reach the highest contrasts in thermal IR, observations and data reduction were optimized through the use of state-of-the-art tools and techniques (Chap. 10), including the AGPM coronagraph (Sec. 10.2.1), differential imaging techniques (Sec. 10.3.2), star hopping (Sec. 11.3.1), and principal component analysis (Sec. 10.4.2). A full pipeline was implemented for the data calibration and post-processing (Sec. 11.4). It deals with the identified biases affecting NACO, and makes an extensive use of the Vortex Imaging Package (Gomez Gonzalez et al. 2017).

All datasets obtained before June 2018 were calibrated, and reduced using PCA coupled to either ADI, RDI or BDI. This led to the detection of 4 companion candidates out of 15 transition disks (around HD 135344 B, WW Cha, J1622-3724 and J1900-3645), and the re-detection of disk signal around T Cha, HD 100453 and HD 135344 B. All companion candidates still require confirmation with new data. Although the candidates at larger separation are found at higher significance (J1622-3724 and J1900-3645), they also have a higher chance to trace background objects. It is interesting to note though that the separation of the point-like source found around J1900-3645 falls close to the predicted location of the annular gap inferred from SED fitting (van der Marel et al. 2016c). If these two companions at large separation are confirmed they would correspond to 2-4 $M_{\rm Jup}$ companions according to COND models, and might trace protoplanets formed soon after gravitational collapse.

At the other end of the separation range, we could not rule out the possibility that the intriguing point-like source found at short separation (1.2-1.5FWHM) from the star HD 135344 B was a speckle. Despite tentative detections in L' at two epochs with two different instruments using two different differential imaging techniques, the point-source found at a separation consistent with a companion in the gap of the disk was not re-detected in high-sensitivity K-band images obtained with SPHERE, nor recovered in a preliminary reduction of new L' data obtained in June 2018 with NACO. This inspires caution not only regarding this particular source, but also for other claimed protoplanet candidates based on L' blobs at very short separation (e.g. HD 169412 "b" or MWC 758 "b"; Reggiani et al. 2014; Biller et al. 2014; Reggiani et al. 2018, Sec. 12.1). A point in common though is that all those bright blobs are found in the dust cavity of Herbig Ae/Be transition disks. Alter-

natively, this apparent point in common might just be due to the fact that they are among the brightest L' sources observed with the AGPM so far. Assessing whether these bright blobs trace speckles or authentic episodic signals might require gathering a larger sample of observations with the AGPM on similarly bright sources that are not expected to show bright signal coming from their direct vicinity..

Apart from the NACO survey, I also contributed to the confirmation of a substellar companion found in the debris disk of HD 206893, through observations with NACO+AGPM (Sec. 12.2). The reduction of the L' NACO data, and later the spectrum inferred from SPHERE/IRDIFS, revealed that this intriguing young brown dwarf is the reddest substellar companion known to date (Sec. 12.2.2). In general, the unexpected significantly redder colors of young companions compared to the field brown dwarf sequence (Fig. 4.3) makes older-generation thermal-IR HCI instruments (e.g. Keck/NIRC2, VLT/NACO) still as competitive as new extreme-AO instruments for the detection of young brown dwarf and planetary-mass objects, in particular when equipped with state-of-the-art coronagraphs such as the AGPM.

13.2 Future plans

13.2.1 PCA-RDI contrast curves

Once this thesis is completed, I plan to discuss with Carlos Gomez for a solution to be implemented regarding the contrast curve issue for PCA-RDI reductions using temp-mean or temp-std scalings. As seen in the example of T Cha, scaling is important to reach high contrast when the reference and science PSFs are not well correlated. When this issue is solved, I will be able to compute meaningful contrast curves for the sources observed with the RDI strategy, and include them in my statistical survey of the occurrence of protoplanets in transition disks (see below).

13.2.2 Continuation of the survey

Six additional sources, corresponding to promising transition disks identified in the ODISEA survey (non-bold sources in Table 11.1), are planned for observation with NACO between June 29 and July 2, 2018. Except in the case of inclement weather or technical mishap, this new run should bring the number of observed transition disks to 21. Most transition disks with the largest cavities and presenting the most conspicuous signs of companion presence, such as spiral arms, asymmetric dust distribution and warps (Chap. 6), could unfortunately not be included in the survey as they are blocked by the ISPY consortium. However, these datasets have started to become public, therefore I plan to reduce them for inclusion to this survey (about 24 additional targets – 20 from ISPY). This sample might be further expanded after publication of the results of the twin survey of transition disks in

the northern hemisphere using Keck/NIRC2+AGPM (Ruane et al. in prep.). This would bring the size of the total sample to $\sim$ 60 transition disks. With such sample, I plan to carry out a similar statistical analysis as performed in Meshkat et al. (2017) for the occurrence of giant planets in debris disks. The latter study found that debris disks are more likely to host giant planets (about 10 times more likely at a 88% confidence level) than stars of the same age without disk. A similar study at younger age, i.e. in transition disks, would be invaluable to constrain where, when and how giant planets form, before the system has had the time to significantly evolve. Different models will be used to convert contrast limits into mass and mass accretion rate constraints (e.g. Baraffe et al. 2003; Allard et al. 2012; Zhu et al. 2015; Montesinos et al. 2015).

The success of this survey will also require the acquisition of complementary multi-wavelength data. Indeed, as was shown in the case of HD 135344 B, confirming that a blob is tracing a protoplanet can be tricky, and both speckle tests and multi-epoch observations might not be enough to enable to unveil the true nature of observed signals (e.g. if the source of the emission is episodic). Independent detections with other techniques and at other wavelengths would not only enable to confirm companion candidates, but would also bring a lot of new insight regarding the process of planet formation based on the synergy of gathered information. In particular, observations of gas lines with ALMA might provide independent mass estimates of any embedded companion based on the kinematics of the gaseous disk (e.g. Perez et al. 2015; Teague et al. 2018; Pinte et al. 2018). Comparison with any counter part in L' light would enable to better constrain planet formation and evolution models. Other observational techniques including spectral cross-correlation (e.g. Hoeijmakers et al. 2018) and the search for accretion signatures using high-contrast observations in the Hα filter (e.g. Close et al. 2014; Sallum et al. 2015) may also be used.

IV | Detection and characterization of companions with an integral field spectrograph

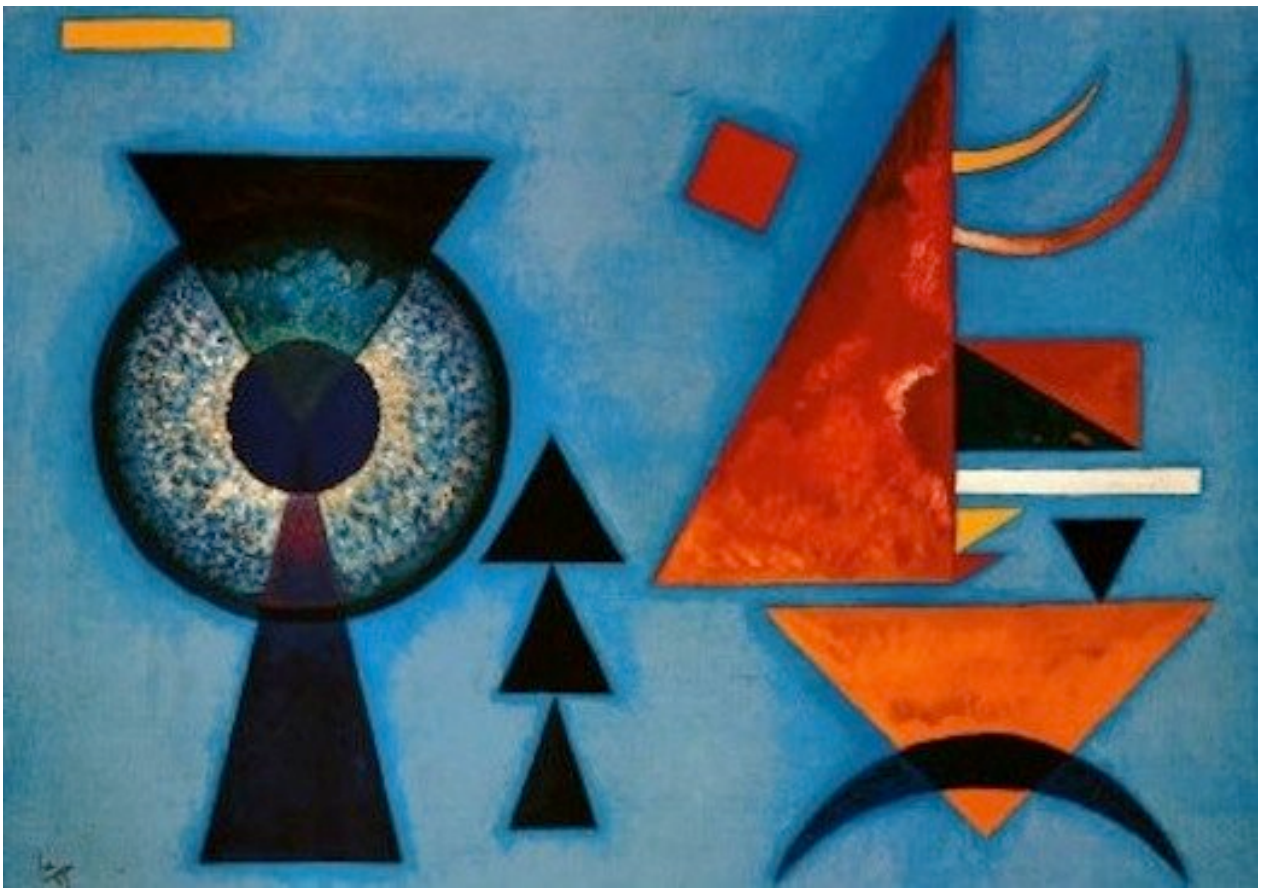

Soft hard (Kandinsky, 1927)

This part is devoted to the use of a medium spectral resolution integral field spectrograph to detect and characterize companions in transition disks. I first provide a brief summary of the concept of integral field spectroscopy (Chap. 14), along with a short description of instrument VLT/SINFONI. Then, the observations, data reduction and results obtained from a mini-survey of transition disks using VLT/SINFONI are presented in Chap. 15. In particular, detailed results will be provided on each individual source of the sample, and

For one of the sources of the sample, PDS 70, the final images obtained after an optimal collapse of the datacube in both temporal and spectral dimensions suggest the tentative detections of both a protoplanet candidate and a spiral-like feature, possibly connecting the former to the outer disk. These results led to a submitted paper to MNRAS, provided in Sec. 15.5.

For HD 142527, the low-mass binary companion was re-detected separately in most spectral channels of the IFS which allowed us to retrieve its spectrum. In-depth spectral characterization, enabled to constrain the physical parameters of the companion, including its effective temperature, surface gravity, mass, age and radius. These results are presented in an A&A paper (in press), which is provided in Sec. 16.

Finally, Chap. 17 provides a summary of the results and future plans related to this part.

In the heavens we discover stars by their light, and by their light alone … the sole evidence of the existence of these distant worlds … that each of them is built up of molecules of the same kinds we find on earth. A molecule of hydrogen, for example, whether in Sirius or in Arcturus, executes its vibrations in precisely the same time. Each molecule therefore throughout the universe bears impressed upon it the stamp of a metric system as distinctly as does the metre of the Archives at Paris, or the royal cubit of the Temple of Karnac.

James Clerk Maxwell

14 Integral field spectroscopy

In this section, I briefly describe the concept of integral field spectroscopy, and more specifically the case of integral field units equipped with an image slicer. This will help understand the optimal use that can be made from it in the context of the high-contrast imaging search and characterization of faint companions.

An integral field spectrograph (IFS) is a device able to obtain spatially resolved spectroscopic information. How is the 3D information captured on a 2D detector? The field of view is divided in different segments, so-called *spaxels*, which are then decomposed in wavelength using a diffraction grating, a prism or a combination of both (grism). Several concepts of IFS have been proposed corresponding to different ways of splitting the field in separate sections; based either on a microlens array, a fibre array (with or without lenslet) or image slicers (see e.g. Westmoquette et al. 2009). Here, I will focus on the latter type, *image slicers*, such as VLT/SINFONI which I used to obtain the results presented in this chapter.

The idea of an image slicer was first presented in Bowen (1938) and consisted of an array of segmented mirrors pointing at slightly different angles. However, its application inside an IFS was only proposed in Weitzel et al. (1996) and Content (1997). The principle of an image slicer-based IFS is depicted in Fig. 14.1. After the field is divided in slices (spaxels), light is decomposed in wavelength using a dispersive device (e.g. a diffraction grating for VLT/SINFONI) in order to produce a set of spectra on the detector. The information on the 2D detector is then typically re-arranged into a 3D spectral cube. This 3D cube can then be used to either produce a multi-color 2D image or to infer the spectrum of each 2D pixel.

In near-IR, two ground-based instruments on 8m-class telescopes currently use this design: VLT/SINFONI (Eisenhauer et al. 2003; Bonnet et al. 2003) and Gemini-N/NIFS (McGregor et al. 2003). Instrument NIRSpec, soon in space on board of JWST, was also manufactured based on this design (Posselt et al. 2004). The upcoming successor of SINFONI, VLT/ERIS will contain a refurbished version of the IFS currently in use in SINFONI (SPIFFI).

Given their design, IFS are particularly used for extended sources or crowded fields, such as galaxies, the Galactic center, planetary nebulae or star-forming regions. In the context of the spectral characterization of faint companions, three flavors of IFS are currently in use: either very low spectral resolution but high-contrast IFS (e.g. SPHERE/IFS,

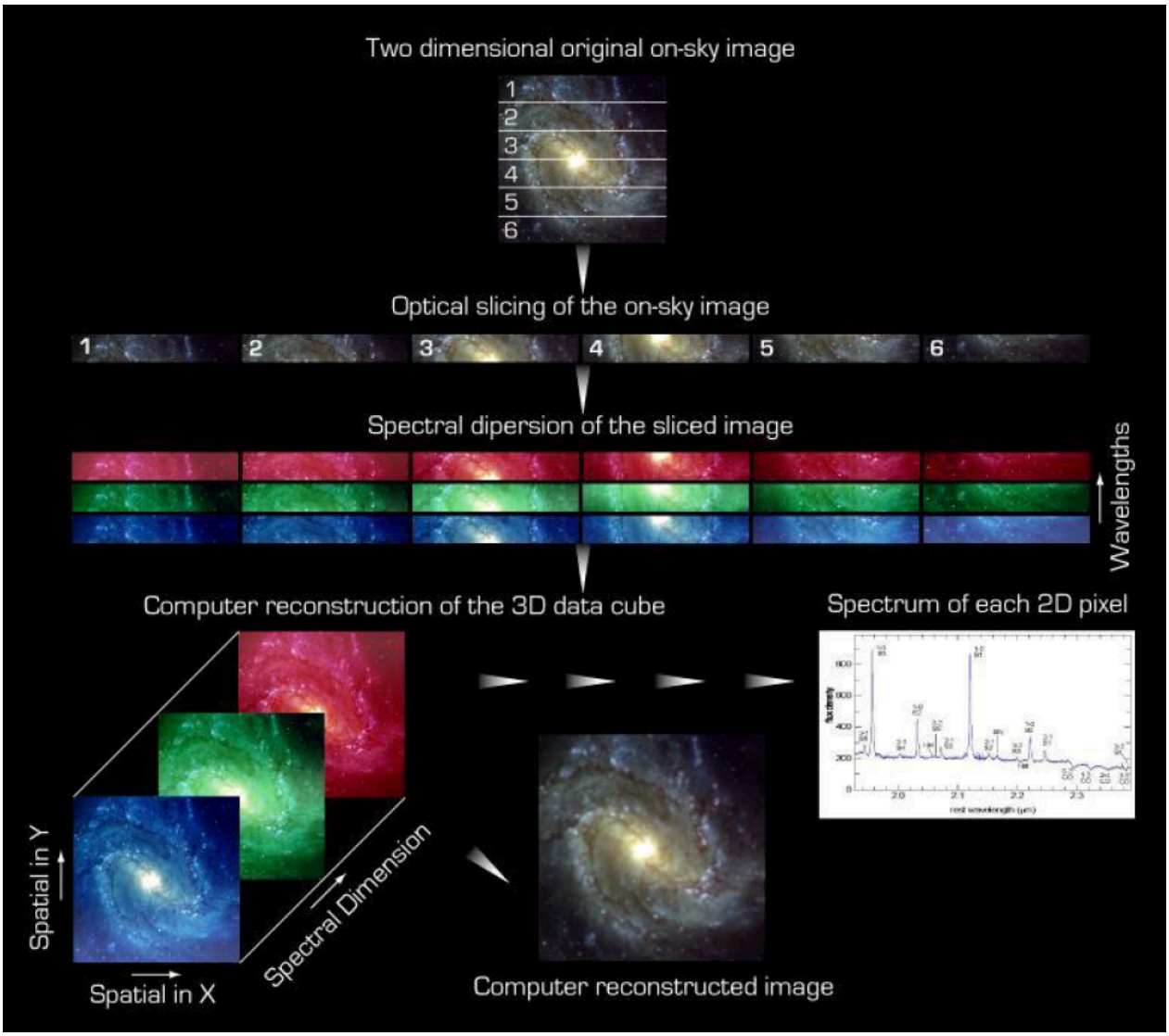

Figure 14.1: Principle of integral field spectroscopy with an image slicer. See text for details. Figure extracted from the VLT/SINFONI manual (ESO).

GPI, CHARIS, ALES; Beuzit et al. 2008; Macintosh et al. 2014; Skemer et al. 2015; Groff et al. 2017, resp.), long-slit spectrographs providing low spectral resolution and intermediate raw contrast (e.g. SPHERE/LSS; Vigan et al. 2008; Hinkley et al. 2015), and moderate-spectral resolution IFS (e.g. VLT/SINFONI and Keck/Osiris; Eisenhauer et al. 2003; Larkin et al. 2003, resp.). In this chapter, I will demonstrate that even medium-spectral resolution IFS can still reach final contrasts close to what is obtained with last-generation extreme-AO systems when data are optimally handled. Other strategies have been / are still in use for spectral characterization; for example a grism (prism + diffraction grating) was installed in NACO and has enabled to retrieve the spectra of planetary-mass companions, such as 2M1204 b and AB Pic b (Chauvin et al. 2005a,b).

14.1 VLT/SINFONI

SINFONI is currently mounted at the Cassegrain focus of UT4 at the VLT, and is composed of two modules: an adaptive optics systems, MACAO (Multiple Application Curvature Adaptative Optics; Bonnet et al. 2003), and an image slicer-based IFS, SPIFFI (SPectrograph for Infrared Faint Field Imaging; Eisenhauer et al. 2003). Light is first corrected from atmospheric turbulence-induced wavefront anomalies in MACAO (see Sec. 10 for a synopsis of AO systems), before being sent to SPIFFI. Either a natural or laser guide star can be used for the AO correction, which provides near diffraction-limited images. The IFS can operate with four different gratings (J,H,K and H+K) in near-IR, enabling to sample a wavelength range comprised between 1.1 and 2.45 μm. Depending on the grating used, the achieved spectral resolution $R_\lambda = \frac{\lambda}{\Delta\lambda}$ ranges between $\sim$1600 (H+K) and $\sim$4400 (K), with intermediate R_λ of $\sim$1900 and $\sim$2600 for the J and H gratings, respectively.

The field-of-view is split in 32 slices (also referred to as *slitlets*) which are then imaged on 64 pixels of the 2048x2048 px Hawaii 2RG detector. Spaxels are thus 32 pixels long and 2 pixels wide. Options for the plate scale include 0$''$.125, 0$''$.05 and 0$''$.0125 px^{-1} along the x-axis, and a twice broader sampling along the y-axis (due to the image slicing). These three options lead to field of views of 8$''$x8$''$, 3$''$x3$''$, and 0$''$.8 x 0$''$.8, respectively.

15 Mini-survey of transition disks with VLT/SINFONI

In this section, I first present the motivation behind the observation of five transition disks using VLT/SINFONI. Then I describe the observing strategy, observations, data reduction process and final results obtained for each source.

15.1 Overview of the project

The basic motivation of this study is the same as the VLT/NACO survey presented in Chapter 3: to search for protoplanets/companions in transition disks. The particular choice of SINFONI was motivated by the new implementation of a pupil-tracking mode (new when the project started in 2014), enabling to process data with both ADI- and SDI-based algorithms. A first example of this technique had recently been applied to extract the spectra of HR 8799 b, c, d and e using Palomar observations (Oppenheimer et al. 2013). Due to the orthogonality of the ADI and SDI biases, ASDI appeared as a promising technique to detect faint companions and also image extended disk features, in particular given the medium-spectral resolution of SINFONI and large wavelength coverage of the H+K mode (1.45-2.45 μm). Furthermore, an additional advantage of using SINFONI is that any companion detection would also likely bring for free some spectral information.

15.1.1 Sample selection

For this pilot study, we focused on five transition disks showing some of the most conspicuous signposts of companions: HD 100456, HD 135344 B, HD 142527, HD 179218 and PDS 70. We further limited the sample to bright objects (R<<14mag) in order to benefit from a good AO correction. Their properties are summarized in Table 15.1. All sources but HD 100546 were believed to harbor a large ($> 0\farcs2$) gap. HD 100456, HD 135344 B and HD 142527 all have spiral arms (Fig. 6.5). Furthermore, HD 135344 B and HD 142527 have asymmetric dust distributions (Fig. 6.3). As seen in Chapter 1, since each of these features can be dynamically induced by the presence of a companion, the combination of several of these features in some of these disks can be considered a strong indicator of

companion presence. Finally, HD 100546 and HD 142527 had claimed companion candidates at the time the project was initiated Quanz et al. (2013a); Biller et al. (2012), although only HD 100546 b was initially expected to be confirmed in our new observations given its larger separation ($\sim$0$''$.5). A detailed description of HD 135344 B, HD 142527 and PDS 70 are provided in Secs. 11.6.6, 7.3.1 and 15.5.1, respectively. Therefore, I defer the reader to the relevant sections for those sources, and only provide a brief description of HD 100456 and HD 179218 below.

HD 100546 is an isolated Herbig Be star (B9V) located at 110 $\pm$1 pc (Gaia Collaboration et al. 2018). Compared to the other sources of the sample, HD 100546 has a relatively small gap $\lesssim$10 au (e.g. Brittain et al. 2009; Benisty et al. 2010; Tatulli et al. 2011). Nonetheless, several spiral arms have been observed to extend in the outer disk, at different scales (Grady et al. 2001; Ardila et al. 2007; Boccaletti et al. 2013). Furthermore, one of the first protoplanet detections was claimed in this disk at a separation of $\sim$ 0$''$.5, using NACO/L' observations (Quanz et al. 2013a, see also Sec. 4.1). The possibility of confirmation and characterization of the companion with SINFONI hence made HD 100546 our first-priority target in the sample.

HD 179218 is a bright Herbig Ae star located at $\sim$ 266 pc (Gaia Collaboration et al. 2018). It has a strong IR excess believed to be associated to a large flaring of the small grain distribution in the disk, which places it as a member of group I Herbig disks (Meeus et al. 2001). Radiative transfer modeling suggests that those disks probably host a very large gap (Maaskant et al. 2013), which is why the source was included in the sample. However, the size of its near-IR gap was recently inferred to be only $\sim$12 au based on modeling of interferometric visibilities (Kluska et al. 2018).

15.2 Observations

For all our observations, the H+K grating was chosen in order to maximize the wavelength coverage, and hence enable a better SDI reduction. We also opted for the finest pixel scale, 12.5 mas px^{-1} (25 mas px^{-1} along the y axis), in order to reach closer angular separations from the star. A drawback of this mode is the small size of the field of view (0$''$.8 $\times$ 0$''$.8), which incited us to adopt specific observing strategies for some objects of the sample (as described in the next subsection).

Observations with SINFONI are affected by significant overheads for short integration times (DIT). For example, the duty cycle efficiency is lower than $\sim$30% for DIT $<$3s and NDIT (number of co-adds) such that the readout occurs every minute (i.e. 70% of the observing time is lost in overheads). On the other hand, if the DIT is too long, saturation can lead to persistence effects on the detector, which can last from a couple of hours (when flirting with the saturation limit) up to several days (when significantly saturated). Therefore, a very careful choice of DIT and NDIT was required in order to minimize overheads

Table 15.1: Physical properties of the sources observed with VLT/SINFONI

Source	Sp.T.	Dist. (pc)	Age (Myr)	Near-IR gap radius	Signposts of companion presence
HD 100546	B9Vne	110±1[a]	5–10[b]	0.″1[c]	Protoplanet candidate[d,e], spirals[f,g]
HD 135344B	F8V	142±2[a]	8±4[h]	0.″18[i,j]	Spirals[i,j,k]
HD 142527	F6III-V	157±1[a]	2–5[l,m]	1″[n,o]	Companion candidate[p,q], spirals[o,r]
HD 179218	A0V	266±4[a]	∼1[s]	0.″05[t]	
PDS 70	K5	113±1[a]	5–10[u]	0.″5[v]	Velocity dispersion peak[u]

References: [a]Gaia Collaboration et al. (2018); [b]Guimarães et al. (2006); [c]Panić et al. (2014); [d]Quanz et al. (2013a); [e]Quanz et al. (2015a); [f]Ardila et al. (2007); [g]Boccaletti et al. (2013); [h]Müller et al. (2011); [i]Garufi et al. (2013); [j]Stolker et al. (2016) [k]Muto et al. (2012); [l]Mendigutía et al. (2014); [m]Lacour et al. (2016); [n]Fukagawa et al. (2006) [o]Casassus et al. (2012); [p]Biller et al. (2012); [q]Close et al. (2014); [r]Avenhaus et al. (2014); [s]Seok & Li (2017);[t]Kluska et al. (2018); [u]Long et al. (2018); [v]Hashimoto et al. (2012)

while both maximizing SNR and avoiding saturation. For fast rotators (typically sources transiting between 60° and 85° altitude), an additional constraint consists in setting the detector readout to at least once per minute in order to minimize smearing due to field rotation (i.e. DIT $\times$ NDIT $<$ 1 min).

A log of all the observations is provided in Table 15.2. At least one useful dataset was obtained for each planned target. Nonetheless, for HD 100546, the first sequence had to be discarded due to a significantly different PSF before and after the interruption by the head of science. For HD 142527, we also discarded the sequences obtained in significantly worse seeing conditions and higher airmass. All observations were obtained in photometric conditions except that of PDS 70, which corresponds to clear conditions. A standard star was also observed either immediately before or after each science target. The chosen standard stars typically corresponded to B-type stars, observed at a similar airmass as our targets. Indeed, since B-type stars show a very smooth continuum only affected by a few hydrogen recombination lines of the Brackett series in H+K, their continuum can easily be fit to a black-body curve and hence enable the calibration of the wavelength response of the instrument.

15.2.1 Specific observing strategies

HD 100546

A specific strategy, designed by Dr. Julien Girard and illustrated in Fig. 15.1, was followed for the observation of HD 100456. Since for this target the goal was to re-detect and possibly perform a spectral characterization of the protoplanet candidate found at 0″.5 separation from the star, the star had to be shifted from the center of the field of view. The possibility of using the 50mas px^{-1} plate scale was also considered, but would have involved a very short DIT (1s) to avoid saturation. In turn, this very short DIT would have led to only $\sim$10% efficiency, instead of $\sim$33% efficiency with the 12.5mas px^{-1} plate scale with the star off-centered. To further optimize the observation, the field was oriented with an initial PA of 180° (i.e. North towards the bottom of the detector). In this way, the rotation of the companion candidate would mostly correspond to a linear motion along the x axis, which has a twice finer pixel scale than the y axis, in the bottom part of the detector where less bad pixels are present.

Four-points dithering pattern

After discussion with Julien, we decided to opt for a four-points dithering strategy for the two disks with gaps that are larger than the field of view of SINFONI: HD 142527 and PDS 70. This strategy is depicted in Fig. 15.2. It consists in placing the star at a different corner of the field of view in consecutive exposures. In this way, a theoretical radius of $\sim$0″.65 can be probed around the star. As the field is rotating during the sequence, a specific part of the field of view can end up in different subsets, which will have to be taken into

Table 15.2: Log of the observations with VLT/SINFONI

Date	Source	UT time	NEXP[a]	DIT[b] (s)	NDIT[c]	INT[d] (min)	Airmass	Seeing[e]	Par. Ang.[f] (Start/End)
2014/05/08	**HD 100546**	23:28-00:15[g,h]	18	4	8	9.6	1.5-1.4	0.″65	-34°/-16°
		00:28-02:55	100	4	8	53.3	1.4-1.5	0.″65	-12°/+38°
2014/05/09	**HD 135344 B**	03:35-06:50	77	3	13	50.1	1.0-1.1	0.″75	-31°/+72°
	HD 179218	07:25-10:10	82	6	7	57.4	1.3-1.4	0.″50	-162°/+151°
2014/05/10	**PDS 70**	01:25-04:20[i]	116	60	1	116	1.1-1.1	0.″65	-68°/+32°
	HD 142527	04:35-06:40[i]	40	1.5	30	30	1.1-1.1	0.″65	-34°/+38°
		06:40-07:40[h,i]	20	1.5	30	15	1.1-1.2	0.″95	+38°/+68°
		07:40-08:40[h,i]	20	4.0	10	13.3	1.2-1.4	>1.″10	+68°/+83°

Notes:

[a] Number of data cubes acquired.

[b] Detector integration time for each individual spectral cube.

[c] Number of co-adds in each data cube.

[d] Total integration time.

[e] Mean value of DIMM seeing during the sequence (corrected from the overestimation bias affecting pre-2016 measurements at the VLT).

[f] Parallactic angles at start and end of sequence.

[g] Interrupted by the head of science due to elongated PSF. The problem could not be solved and the observation was resumed 15 min later.

[h] Discarded for the analysis due to a significant difference in quality with respect to the bulk of the data.

[i] Four-points dithering pattern strategy, to sample at best the large gap.

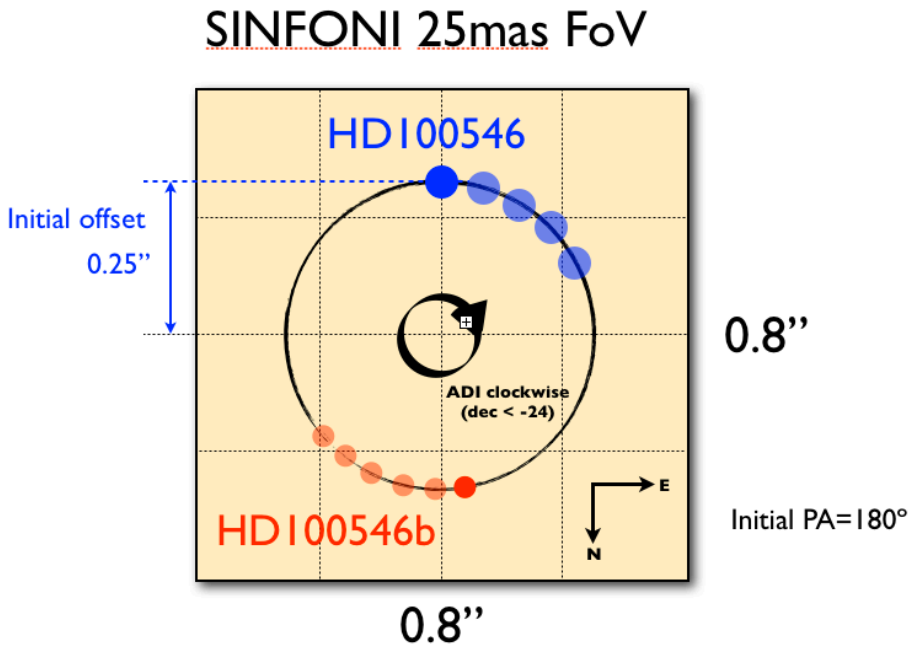

Figure 15.1: Observing strategy used for HD 100546. Given the $0\farcs5$ separation between the star and protoplanet candidate and the $0\farcs8 \times 0\farcs8$ field of view, the star had to be offset from the center in order to keep the protoplanet candidate within the field of view. Credit: Julien Girard.

account during data reduction. The main advantage of this strategy is that it enables to reach a higher spatial resolution than simply using the mode with the next wider field of view ($3'' \times 3''$) which involves a 50 mas px^{-1} plate scale. The global time efficiency is also typically not significantly worse than using the 50 mas px^{-1} plate scale, since the latter requires a corresponding reduction in DIT to avoid saturation, which is accompanied by an augmentation of overhead times.

15.3 Data reduction

15.3.1 Calibration

For the data reduction, I downloaded the ESO Recipe Execution Tool (*EsoRex*), and used the official SINFONI pipeline provided by ESO. The SINFONI pipeline consists in the application of a series of EsoRex *recipes* performing specific operations that are to be performed in a specific order. This is also referred to as *reduction cascade*. The main steps of this reduction are detailed below, together with other steps that are run separately from the ESO pipeline.

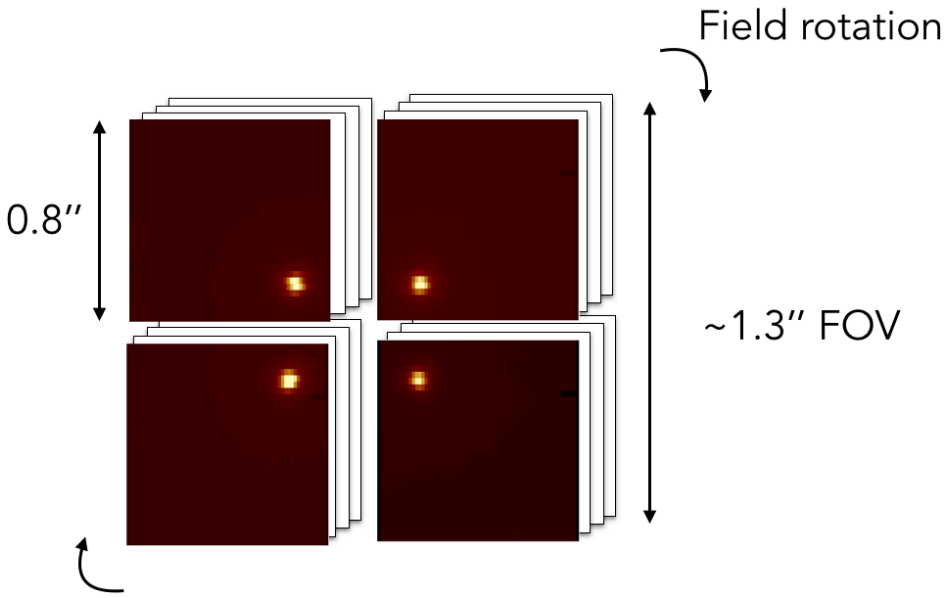

Figure 15.2: Four-points dithering strategy: the star was placed in a different corner of the field of view, while the field is rotating during the observation.

Bad lines correction

The 2048x2048 px Hawaii 2RG detector of SINFONI is plagued by a few bad lines, which result from an inappropriate subtraction of the *bias* estimated for those lines. The bias is estimated with the first 4 columns of the detector, and for long integrations (typical of the observation of faint targets), some of these columns get affected by hot pixels, leading to an overestimation of the bias, causing the appearance of dark rows on the detector. Their correction is the very first step of the calibration process and is performed outside EsoRex, using a dedicated IDL script written by Dr. Christophe Dumas.

Basic cosmetic

The first step of the SINFONI pipeline consists in checking the *linearity* of each pixel with exposures of different DITs, using recipe `sinfo_rec_detlin`. The identified non-linear pixels will be considered in the creation of a bad pixel map. The next step consists in the computation of a master *dark* based on the input of three dark frames using recipe `sinfo_rec_mdark`. Another by-product of this recipe is a hot pixel map. A master flat frame and another bad pixel map (consisting of pixels with a quantum efficiency below or above a certain user-defined threshold) can subsequently be computed using recipe `sinfo_rec_mflat`.

Distortion

The geometric distortion of the detector is calculated using recipe `sinfo_rec_distortion` based on a series of input fiber frames that are progressively moved along the y-direction. This recipe also computes the distance between each slitlet, which will be necessary for cube reconstruction.

Wavelength calibration

Arc lamp frames are provided in input of recipe `sinfo_rec_wavecal`, which subsequently computes the wavelength solution; i.e. each pixel on the detector is assigned a wavelength value.

Cube reconstruction

This is the last step of the SINFONI pipeline, and consists in using all the files created in the previous steps (master dark frame, master flat-field, master bad pixel map, etc.) to calibrate the detector frame and re-arrange it into a spectral cube of 2048x64x64 (spectral and spatial axes, respectively). This is performed using recipe `sinfo_rec_jitter`. This recipe has the option to perform a sky subtraction if sky datacubes are provided as input along with the science cubes. However, Ricardo Ramirez and I noticed that the sky subtraction was sub-optimal and led to residual structures in the final cube. We hence performed the sky subtraction in a separate python script before running the recipe (with the option of sky subtraction in the recipe turned off this time).

Crop in wavelength

The spectral channels at the short- and long-wavelength ends of the spectral cube are typically full of NaN values, and hence contain no useful information. They are cropped out of the cube. Typically this leaves $\sim$ 2000 spectral channels per cube, hence the dimensions of each 3D cube are now 2000x64x64.

NaN correction

NaN values are still sparsely present within the 3D spectral cubes even after cropping in wavelength. They have to be replaced before any further processing of the data. They are identified and replaced by the median of neighbor pixels using the relevant function implemented in the Vortex Imaging Pipeline (VIP; Gomez Gonzalez et al. 2017). This process is iterative, which enables the correction of clumps of NaN values.

Residual bad pixel correction

I noticed that a significant amount of bad pixels typically survive the bad pixel correction performed in the SINFONI pipeline. Given their tendency to appear as clumps in the data cube, they are not well-corrected by sigma-filtering. Therefore, I implemented an algorithm which takes advantage of the circular geometry of the PSF to detect bad pixels as outlier values in concentric annuli centered on the star, and added the function to VIP.

Centering and ASDI cube creation

At this point, the location of the star is different in each frame of each cube due to (i) atmospheric differential refraction (ADR; e.g. Roe 2002) which causes the centroid of the star to "drift" with wavelength ; (ii) the parallactic rotation (in combination with the effect of ADR); (iii) instrumental jitter; (iv) in the case of HD 100546, HD 142527 and PDS 70, the off-centering strategy. The centroid of the star is determined in each spectral channel using a 2D Moffat fit. I noticed that Moffat fits are slightly less prone to yield outlier values for the stellar centroid than Gaussian fits, although the median centroid values found by 2D Moffat and Gaussian fits over a SINFONI datacube typically agree within $\lesssim$ 0.05 px. I implemented the Moffat fit centering routine following the example of the function already implemented in VIP based on Gaussian fits, and later added that routine to VIP.

Once the star is centered in each frame, an ASDI (4D) cube is then created, considering the temporal dimension to join all spectral cubes, so that the final dimensions of the 4D cube are typically NEXPx2000x64x64, where NEXP is the number of acquired spectral cubes. This straightforward construction of the 4D cube was only applied to datasets where the star was left roughly at the center of the field during the observation (HD 135344B and HD 179218), but not for the other three datasets (see below).

Additional precautions in the centering of images with an off-centered star

In order to center the star on the central pixel of frames where the star is initially significantly off-centered (i.e. in the cases of HD 100456, HD 142527 and PDS 70), I implemented a more elaborate procedure than simply using the routine implemented in VIP. Indeed, the VIP routine (`vip.preproc.frame_shift()`), which can perform subpixel-accuracy shifts using bicubic interpolations, is appropriate for relatively small shifts but can introduce artificial signals for significant shifts, that I refer to as *edge effects*. These edge effects consist in the appearance of alternative dark/bright "ripples" in the background frame, just outside the edges of the injected shifted frames. These effects, shown at the location of *magenta arrows* in Fig. 15.3a, are likely due to the bicubic interpolation performed during subpixel-accuracy shifts. Therefore, it was particularly important for frames with off-centered star to use a more careful way of centering the frames. Another bias I noticed consists of the higher signal level contained in columns and rows at the edge of original frames. Given their location at the edge of the field, regardless of the presence of edge effects or not, I

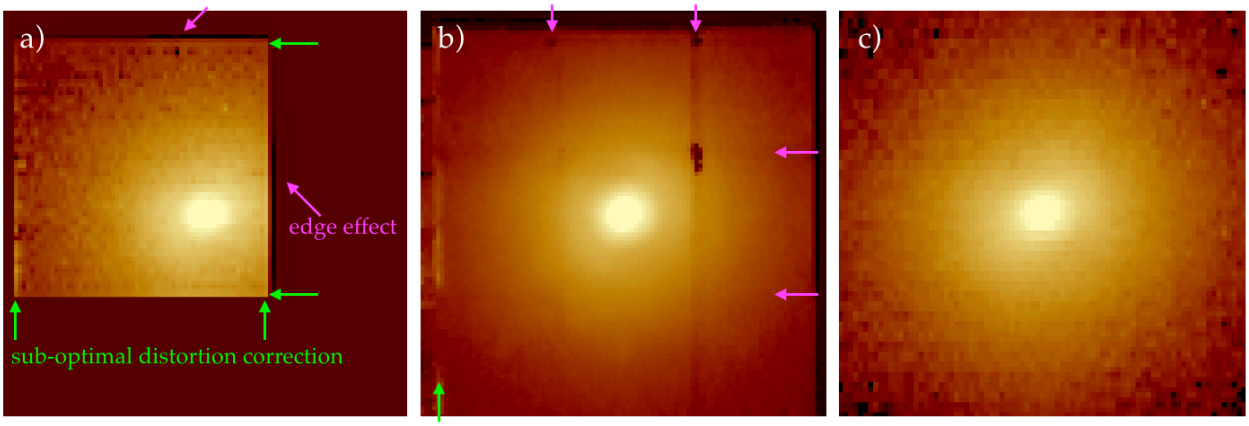

Figure 15.3: Illustration of the biases affecting the centering of frames where the star is significantly off-centered during the observation. **a)** Edge effects (*magenta arrows*) appear at the edge of the science frame due to subpixel-accuracy shifts using a bicubic interpolation with a significantly different background (zero values). Columns or rows close to the edge of the science frame also show a higher level, which I speculate could be due to a sub-optimal distortion correction (*green arrows*). **b)** Median-combination of all frames taken in the four-points dithering pattern strategy (channel at a single wavelength). Significant residuals are left. **c)** Combined four-points dithered frames after additional precautions are taken during the centering and median combination (see text for details). No significant residuals are left in the frame. Color scale is logarithmic for all panels.

speculate that they might be due to a sub-optimal distortion correction. They are shown with *green arrows* in Fig. 15.3a. While these two kinds of effect are minor for observations where the star is placed at the center of the field (since they would only create bright spurious signals at the edges of the field), the non-correction of these features for frames obtained with the four-points dithering strategy which are later median-combined four by four can lead to significant biases in the middle of the recombined frame (Fig. 15.3b).

It is thus crucial to use a more appropriate way to center frames with a significantly off-centered star and get rid of those biases. I figured out that an optimal way to center and combine these frames required the application of the following steps:

1. First create two large 4D cubes, containing zero values so far. One will correspond to the final ASDI cube and the other is temporary. The physical dimensions of the frames in those cubes are larger than 64x64 px by an amount that depends on how off-centered is the star in the field. For the PDS 70 dataset, the dimensions of the first cube are set to NEXP/4 x 2000 x 91 x 91, where NEXP corresponds to the total number of spectral cubes. The second cube has dimensions of 4 x 2000 x 91 x 91.
2. Determine the centroid of the star in each individual 64x64 px spectral frame using Moffat fits, and compute the required shift to place it in the center of the large frames created in step 1 (but do not shift yet).
3. Divide the calculated shifts in an integer and decimal contributions. Perform the sub-pixel shift directly in the 64x64 px frames.
4. Crop out the four columns and rows at the edge of each 64x64 px frames, which contain a higher signal level.
5. Then, inject the original 64x64 px frames of each set of 4 consecutive spectral cubes in the cube of 4 x 2000 x 91 x 91, simply replacing the appropriate lines and columns

of the array so that the star centroid would now end up at the center of the large frame (i.e. no subpixel shift is performed in that step, since it is done in step 2).

6. Compute the non-zero median over the first axis of 4 x 2000 x 91 x 91, this will be the first spectral cube of the NEXP/4 x 2000 x 91 x 91 cube.
7. Repeat steps 5 and 6, until the final 4D cube is filled.

The result of this procedure applied to the PDS 70 dataset is shown in Fig. 15.3c. The previously identified biases appear now to be corrected as no significant spurious signal is seen in the recombined frames.

In the specific case of the HD 142527 dataset, the companion is located sufficiently close from the star in all frames ($\sim$ 6.5 px) so that it is present in all NEXP spectral cubes, despite the star being close to the edge of the frames. Therefore, the analysis of the companion presented in Sec. 16.1 did not require to make use of the above-described centering procedure. Instead, I simply cropped all frames to a stamp size around the centroid of the star determined with Moffat fits, and considered a NEXP x 2000 x 17 x 17 final cube. Nonetheless, for the results on HD 142527 presented in Sec. 15.4.3, using PCA-ASDI and PCA-ADBI, I did use the above-described centering procedure.

15.3.2 Post-processing

Once a 4D cube was created for each source, I compared a variety of post-processing algorithms in order to determine the best way to reach the highest contrast in the final image. Another figure of merit considered in the comparison of the different algorithms was the *aggressiveness* towards extended disk features. Below I provide a very brief description of the different algorithms that were tested, which are all based on the combination of PCA with either ADI and/or SDI. I defer the reader to Sec. 10.3 for a more detailed explanation of how PCA, ADI and SDI work. The tested algorithms are all implemented in VIP.

PCA-ADI (in annuli)

This algorithm is described in Gomez Gonzalez et al. (2017). For each annulus, the PCA library is built in such a way to only include frames where any putative companion would rotate by at least 1 FWHM. In practice, this corresponds to setting a threshold in parallactic angle to accept frames in the library. This frame selection in the construction of the PCA library enables to minimize the self-subtraction of faint signals of interest. This algorithm was applied to the two 3D cubes obtained after collapsing the spectral channels of the H and K bands separately.

Only for HD 179218 was the total field rotation insufficient to use PCA-ADI in annuli because of the parallactic angle threshold. In that case, we considered PCA-ADI in full frame, which is similar to PynPoint (Amara & Quanz 2012); the principal components are determined by singular value decomposition of a library consisting of all the ADI frames without any selection constraint.

PCA-SDI

I implemented a first version of this algorithm, which is very similar to PCA-ADI in full frame, except that the discrimination between faint signals of interest and speckles stems from the radial motion of the former when frames are scaled with wavelength, instead of their azimuthal motion. Compared to the basic principle of SDI, explained in Sec. 10.3, the stellar halo model subtracted from each spectral frame consists of the frame projection on principal components. I put my version of PCA-SDI on VIP, which Carlos Gomez later refined to be integrated within a single versatile full-frame PCA function (with the option of using either ADI, SDI, RDI or a combination of these, depending on the input dataset). It is the results obtained with that latter function (with the option set to SDI only) that are presented in this chapter. The input 3D spectral cube corresponds to the temporally collapsed 4D cube; obtained after a simple derotation followed by median collapse. The amount of radial motion in our H+K channels (1.45-2.45 μm) is such that a putative speckle or stellar halo ring is located $2.45/1.45 \approx 1.7$ times further away from the star in the last channel compared to the first channel.

PCA-ASDI (in one step)

This algorithm will be presented in Gomez Gonzalez et al. (2018, in prep.). It consists in a full-frame PCA in a single step considering both the angular and spectral variation together. I slightly tweaked the algorithm to be compatible with SINFONI data, given that the original behavior was cropping too much of the rescaled frames in the SDI part. The new version of the algorithm with an option making it compatible with SINFONI data was then added to the version of VIP available online.

PCA-ASDI (in two steps)

This algorithm will also be presented in Gomez Gonzalez et al. (2018, in prep.). It consists in the consecutive application of PCA-SDI and PCA-ADI (both in full frame) in two separate steps, and in that order. The output of PCA-SDI consists of a single frame for each spectral cube. PCA-ADI is then applied to the set of all these output frames in the second step.

PCA-ADBI

Finally, I also tested PCA-ASDI on the spectrally collapsed H- and K-band cubes (hence with only 1 principal component for the SDI part). This is similar to PCA-ADI with dual-band imaging and will hence be referred to as *PCA-ADBI*.

As explained in Sec. 10.5, the contrast curve is the standard tool used by the HCI com-

munity to estimate the contrast achieved in a specific image at each radial separation from the star. VIP contains a function to compute the contrast curve for images obtained with PCA-ADI and PCA-SDI. I slightly adapted that code so that it could also compute contrast curves for PCA-ASDI/PCA-ADBI. The changes in the code were such that it now accepts a 4D input cube, and relevant other input files with an extra dimension (e.g. the input PSF template is now a 3D spectral cube).

As will be seen in the next section, the typical throughput of a double-pass PCA (ADI+SDI) is much lower than in a single pass PCA at short separation ($\lesssim 0\farcs15$), this required to add the option of a user-definable value of SNR for the injected fake companion that depends on radius. A fake companion is typically injected at higher SNR at short separation to account for the strong self-subtraction. This way, the throughput estimate is as accurate as possible at all radii.

By default the final PCA-ASDI contrast curve is computed assuming a flat input spectrum, i.e. the same contrast factor is applied to all frames of the input PSF template cube. In order to estimate the sensitivity of PCA-ADBI to red companions, I did not adapt the contrast curve code, but rather modified the input (spectral) PSF templates. These consist normally of a PSF template in H and another in K band, obtained from median-collapse of the relevant spectral channels and subsequent normalization. However, I implemented the option of scaling the PSF templates so that the difference in flux between the H and K band would correspond to a user-defined $H-K$ color, while their average flux (over H and K together) remains normalized. In practice, for all PCA-ADBI contrast curves shown in the next section, I considered $H-K$ = 1, i.e. red companions, as expected for young low-mass substellar objects. In comparison, the PCA-ASDI contrast curves correspond to the achieved contrast towards companions/disk features with an hypothetical flat spectrum.

15.4 Results

Given the variety of observing strategies, I will provide the results for each individual source and discuss them separately. The cases of PDS 70 and HD 142527 already led to a submitted and an accepted paper, resp., and are hence presented in Secs. 16.1 and 15.5. Nonetheless, the contrast curves and PCA-ASDI/ADBI images obtained for HD 142527 were not presented in the paper, and are thus provided in this section as well.

15.4.1 HD 135344 B

The system of HD 135344 B is the ideal source to start the comparison between the different considered algorithms because it has already been extensively studied with other HCI instruments and a detailed view of its disk, including its conspicuous spiral pattern, is now known (see e.g. recent images in Stolker et al. 2016; Maire et al. 2017).

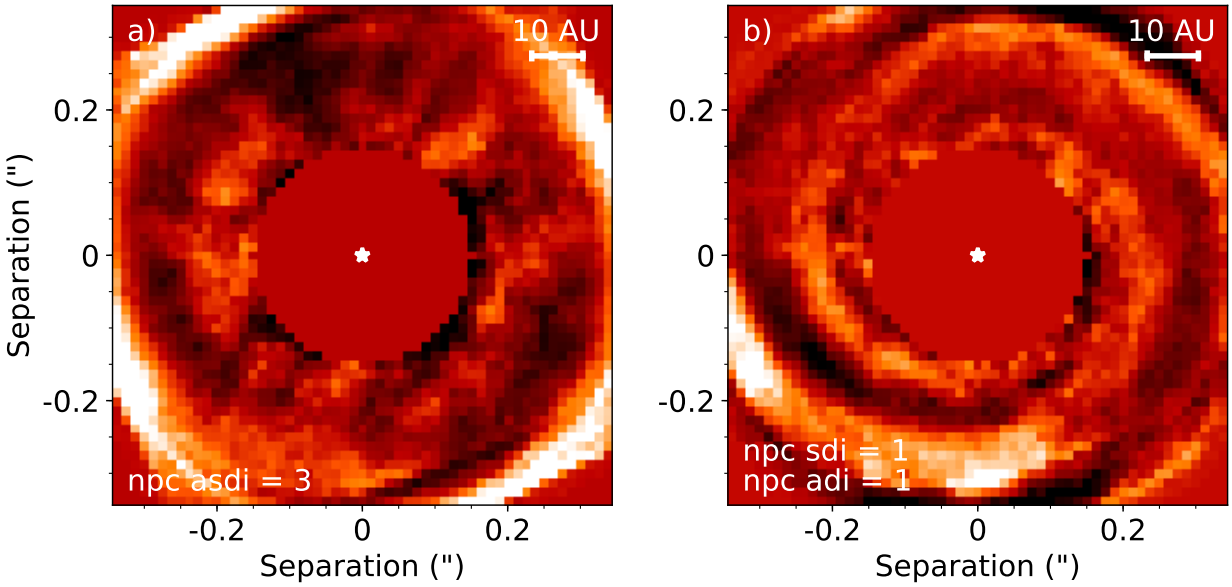

Figure 15.4: Final images of HD 135344 B obtained with PCA-ASDI in one (left) and two steps (right), for the number of principal components that recovers at best the known spiral pattern of HD 135344 B (see e.g. Fig. 15.6).

Comparison between ASDI in one and two steps

In the two panels of Fig. 15.4, I provide a comparison of the final image obtained with PCA-ASDI in a single and two separate steps, respectively. For each reduction, I chose to show the image obtained with the number of principal components ($n_{\rm pc}$) that enables to reproduce at best the known spiral structure. From Fig. 15.4, it appears clear that PCA-ASDI in two consecutive steps leads to a much better recovery of the spiral arms. Why is that so? I suggest that this is due to the combination of two factors: (1) the asymmetry of the dataset (2000 spectral channels vs 77 temporal cubes) and (2) the fact that the cross-correlation between spectral channels (after rescaling) is significantly higher than between temporal cubes. Therefore, less principal components are required for SDI to model well the stellar halo, and diluting the higher cross-correlation between spectral channels in a larger PCA library with both temporal and spectral variation is likely to account for the worse result obtained with PCA-ASDI in a single step. For SPHERE-IFS data, this conclusion would does not necessarily hold given that (1) the number of spectral channels (39) and temporal cubes is typically of the same order of magnitude, and (2) the AO correction leads to a PSF of much higher quality (high Strehl ratio), leading to a higher cross-correlation between temporal cubes. For the rest of this chapter, *PCA-ASDI*, or *ASDI* for short, (without any precision on the number of steps) will refer to the two-steps version of PCA-ASDI.

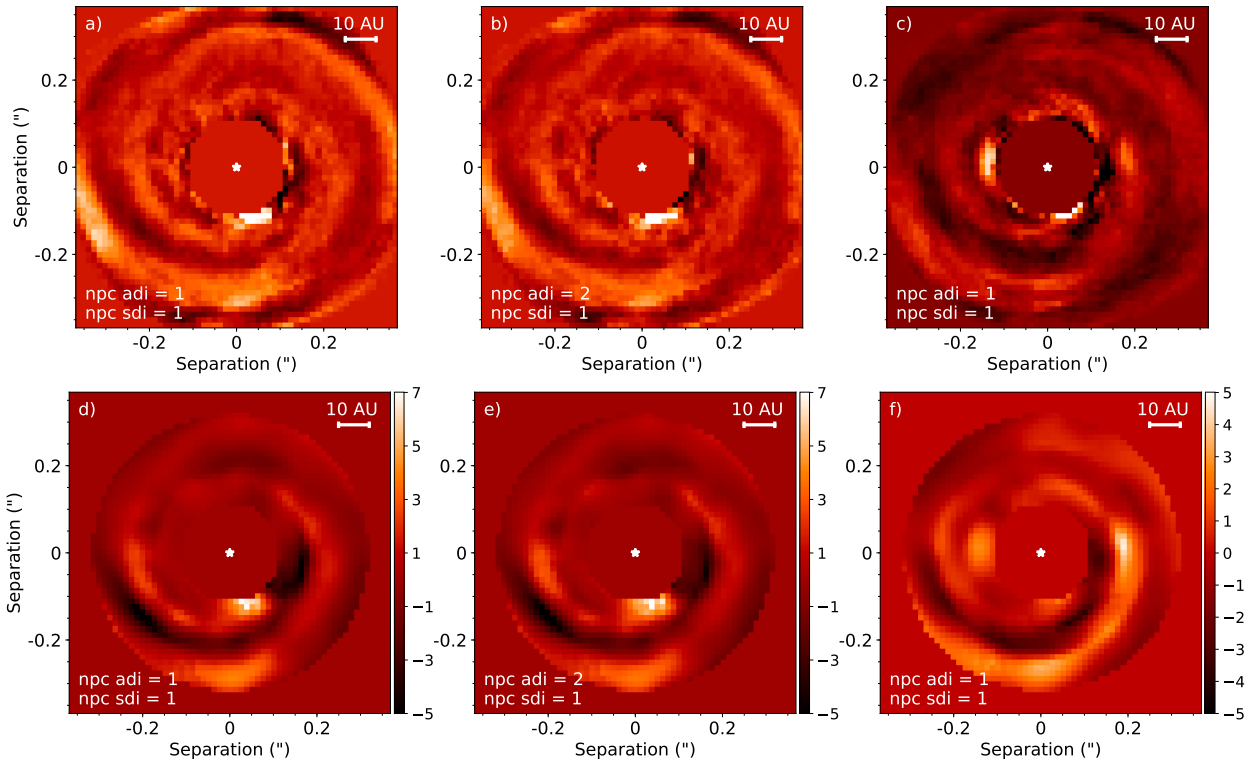

Figure 15.5: Final images and corresponding SNR maps for HD 135344 B when using a slightly smaller numerical mask and a different color scale. These images correspond to the deepest contrast reached between 0.″10 and 0.″15 (see Figs. 15.7 and 15.8). **a)** and **b)** were obtained with PCA-ASDI in two steps, and **c)** was obtained with PCA-ADBI with optimal number of principal components.

Comparison between ASDI and the different algorithms

I also tested the application of PCA-ADI, PCA-SDI and PCA-ADBI. Final images obtained using PCA-ADI alone or PCA-SDI alone do not show any sign of the spirals, for any number of principal components, and are hence not shown. The result obtained with PCA-ADBI is compared to that of PCA-ASDI in Fig. 15.5, for different values of $n_{\rm pc}^{\rm ADI}$. The top row corresponds to the final images obtained with $n_{\rm pc}^{\rm ADI}$=1 and 2 for PCA-ASDI and $n_{\rm pc}^{\rm ADI}$=1 for PCA-ADBI, respectively. The bottom row shows the corresponding SNR maps, computed as defined in Mawet et al. (2014) and as implemented in VIP. The final image obtained with PCA-ADBI recovers the spiral arms although the faint Northern spiral appears less conspicuous than in the PCA-ASDI images. I suspect that collapsing the stellar halo spectrally over the whole H and K bands smears it radially. Collapsing the stellar halo spectrally over the whole H and K bands is expected to create two radially smeared stellar halos. Therefore the PCA-SDI part of PCA-ADBI might not be as optimal as in PCA-ASDI, which would explain the slightly poorer job of PCA-ADBI at recovering the spiral arms, using the same number of principal components.

The value of $n_{\rm pc}^{\rm SDI}$ was set to 1 in all PCA-ASDI reductions. I indeed noticed that increasing its value led to the appearance of concentric dark/bright rings in the final image at a higher spatial frequency than expected from either speckle or true signal (which have ex-

pected spatial scales $\sim$ FWHM). I interpret this behavior as a consequence of the overfitting of individual images in the model created by PCA for subtraction. This appears as another clue that the cross-correlation between (rescaled) spectral channels of a same cube is very high, such that the stellar halo is very well captured with a single $n_{\rm pc}^{\rm SDI}$.

Increasing the value of $n_{\rm pc}^{\rm ADI}$ in all PCA-ASDI/ADBI reductions leads to broken spirals in the final image. This is due to the aggressiveness of ADI towards extended disk features (particularly azimuthally extended ones), as already noted in Milli et al. (2012). (PCA-)ADI tends to flank brighter physical signals in the image with characteristic negative side lobes, which likely account for the broken spiral aspect. Altogether, this means that to recover extended features, a low value for $n_{\rm pc}^{\rm ADI}$ should be used. Specific tests further proving this point are shown in the PDS 70 paper, in Sec. 15.5.1.

Search for a counterpart to the L' blob

In order to check whether a HK counterpart could be found to the L' blob seen with NIRC2 and NACO at $\sim 0\farcs12$ radius separation (Sec. 11.6.6), I set the size of the numerical mask to 0$\farcs$1 radius in the panels of Figs. 15.5 and 15.6. The final PCA-ASDI images show the tentative detection of an extended and bright signal at the root of one of the spirals (at a PA$\sim$190°, and 0$\farcs$12 separation). It appears to be recovered with an SNR $\sim$ 7 in the PCA-ASDI images, which corresponds to a 4.0σ detection considering Student statistics at a 1.8FWHM separation (e.g. Mawet et al. 2014). At that separation, the radial motion of faint signals of interest in the rescaled frames (during SDI) is $\sim$1.2 FWHM. Given that this is the maximal radial motion between the first and last spectral channel, some radial self-subtraction effects is still possible. To better assess the authenticity of this signal, the spectral channels were also reduced one by one with PCA-ADI. Images obtained with $n_{\rm pc}^{\rm ADI}$=1 show a bright speckle at a similar separation but at a PA $\sim$170, identified as such given a radial motion proportional to wavelength throughout the spectral channels. However, as can be seen in the PCA-ASDI images, its contribution appears to have been correctly removed by the SDI part, since no significant signal is found at PA$\sim$170°. No other bright speckle is seen in the PCA-ADI, in particular none at the PA of the feature identified in the PCA-ASDI images. Nonetheless, caution is still required given the low significance of the signal.

I also compared the PCA-ASDI image to a polarimetric image of the disk in order to better interpret the signal seen with PCA-ASDI. This comparison is provided in Fig. 15.6, where the SINFONI image is placed on top of a SPHERE/ZIMPOL image and shown at 100, 50 and 0 % opacity, respectively. The polarimetric image obtained with ZIMPOL, and presented in Stolker et al. (2016), is likely to correspond to the highest quality (most unbiased and detailed) image of the disk of HD 135344 B obtained so far. The PDI technique (Sec. 10.3) is indeed very efficient to image extended disk signals without the introduction of any azimuthal or radial bias. Interestingly, the PCA-ASDI image compares very well with the ZIMPOL image. The main spirals are recovered at the same locations with a nearly identical morphology down to the edge of the cavity. Furthermore, what is identified as a blob in the polarimetric image also appears brighter in the PCA-ASDI image.

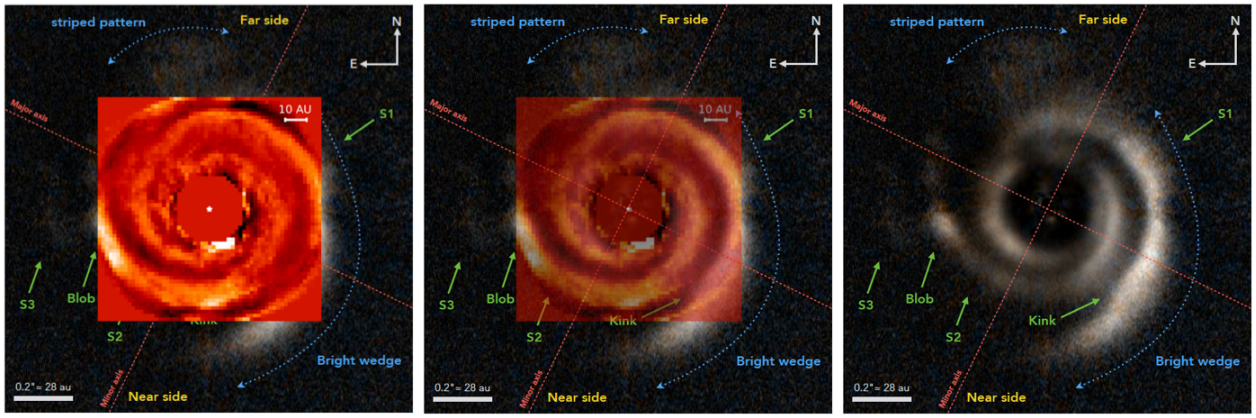

Figure 15.6: Comparison of the SINFONI PCA-ASDI image with the ZIMPOL composite R and I polarimetric image of HD 135344 B. The SINFONI image is re-scaled and centered with the ZIMPOL image. From left to right: the SINFONI image is at 100, 50 and 0 % opacity, respectively. A good agreement is obtained between the SINFONI and ZIMPOL images, suggesting that PCA-ASDI (with low $n_{\rm pc}$) is a non-aggressive algorithm that is appropriate to image disks. ZIMPOL image extracted from Stolker et al. (2016).

The spirals, in particular S2, appear nonetheless to show a different width in the SINFONI image, which is not surprising considering the difference in wavelength (and FWHM) between the two images and the fact that the Rayleigh scattering cross-section is $\propto \lambda^4$ (hence that the mean free path of stellar photons is $\propto \lambda^{-4}$). The different scattering phase function at different wavelengths might also partly account for this effect.

However, a major difference between the two images is that the bright signal seen with SINFONI at $\sim$0$''$.12 separation and PA$\sim$190°does not have any counterpart in the ZIMPOL image. If the signal was tracing scattered light, it would have been detected in the ZIMPOL image. On the other hand, the signal is unlikely to trace thermal emission given its absence in the L' images at that PA (Fig. 11.16). The L' blob is indeed found at PA$\sim$166° and $\sim$171° in the 2016 NIRC2 and 2017 NACO datasets, respectively. If not a speckle artifact, the only remaining option would be that it is tracing a transient event, such as an illumination effect from the warped inner disk (which is known to produce quickly varying shadow patterns; Stolker et al. 2017), or a temporary shock at the rough location where the spiral meets the edge of the cavity (e.g. Hord et al. 2017). Only new observations can further test this hypothesis.

Contrast curves

Next, I computed the 5σ-contrast curve for each tested algorithm (Fig. 15.7). As shown in Meshkat et al. (2014), the number of principal components which enables to reach the deepest contrast in the image changes with radius. Therefore, each contrast curve shown in Fig. 15.7 is in fact built from the combination of different contrast curves, considering the value of $n_{\rm pc}$ optimizing the contrast at each radial separation. The considered $n_{\rm pc}^{\rm ADI}$ values ranged from 1 to 10. For PCA-ADI and PCA-ADBI, the optimal $n_{\rm pc}^{\rm ADI}$ values ranged between 6 and 9. For PCA-ASDI, the optimal $n_{\rm pc}^{\rm ADI}$ values varied between 1 and 2. Larger values of $n_{\rm pc}^{\rm ADI}$ appeared to lead to significant self-subtraction. The value of $n_{\rm pc}^{\rm SDI}$ was fixed

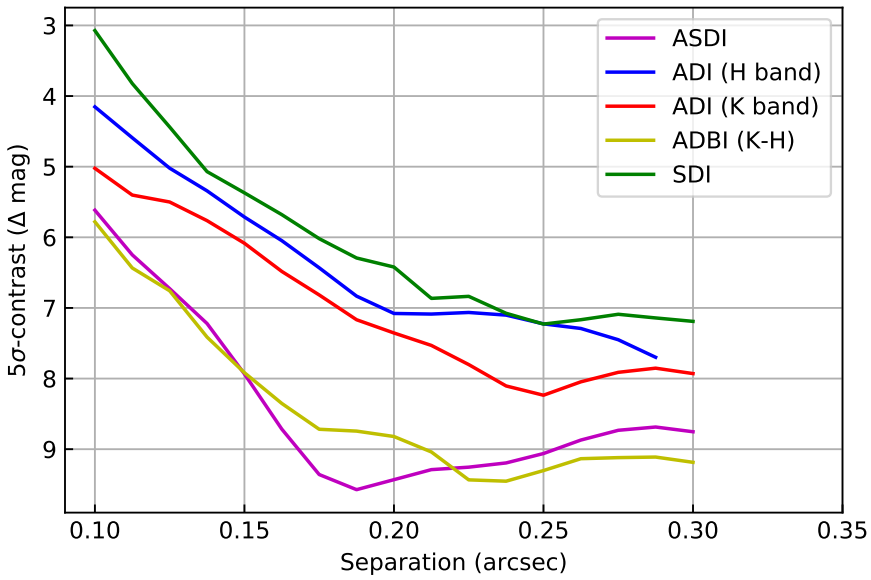

Figure 15.7: Contrast curves obtained with different ADI- and SDI-based algorithms applied to the HD 135344 B dataset. See text for details.

to 1 for PCA-ASDI and PCA-ADBI. For PCA-SDI, the allowed range was between 1 and 5. For values larger than 5, I noticed that most of the frame corresponded to pixel noise at high spatial frequency, suggestive of overfitting of individual frames by the PCA model.

In Fig. 15.7, it is readily evident that the deepest contrast curve is achieved (as expected) from the combination of ADI and SDI, with 1-2.5 mag contrast gain between PCA-ASDI/ADBI and PCA-ADI/SDI alone. This explains why the spirals were not recovered in the PCA-ADI and PCA-SDI final frames, but only in the PCA-ASDI and PCA-ADBI frames. The lowest contrast is obtained with PCA-SDI. This looks a priori counter-intuitive given the very high cross-correlation between rescaled spectral channels of a same cube. However, this can be explained by the temporal collapse of the 4D cube. For each spectral channel, derotating and median-collapsing over the temporal direction (77 datacubes) is expected to lead to a significantly lower cross-correlation between the median spectral channels than between the spectral channels of individual cubes.

PCA-ADI on the spectrally collapsed H and K bands appears to do better than PCA-SDI alone, with a gain of 0.5-1 mag in contrast. The slightly poorer contrast in H band compared to the K band is probably due to a combination of two factors: the central star is 0.7 mag brighter in K and the AO correction (Strehl ratio) is poorer at shorter wavelength.

PCA-ASDI and PCA-ADBI appear to reach similar contrast ratios, although I noticed that the optimal value of $n_{\rm pc}^{\rm ADI}$ was different in each case. As explained before, the radial smearing of the stellar halo inherent to the spectral collapse of H- and K- band channels is likely to slightly lower the efficiency of the SDI part of the PCA-ADBI algorithm. However, this appears to be compensated by increasing $n_{\rm pc}^{\rm ADI}$ in the second step. The fact that the PCA-ASDI and PCA-ADBI contrast curves appear to stagnate (and even going up again for

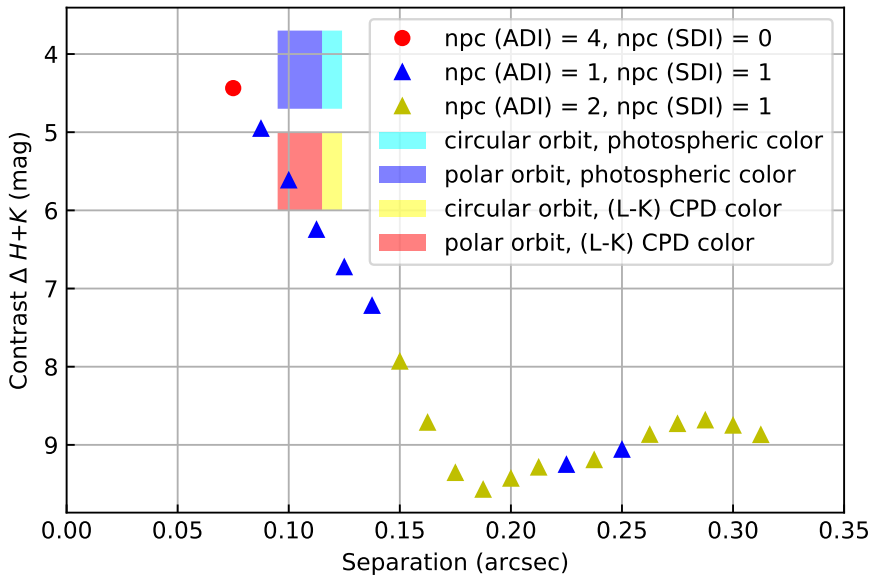

Figure 15.8: Optimal 5σ-contrast curve obtained for HD 135344 B, considering for each separation the algorithm and the number of principal components that optimizes contrast. The location of the companion candidate identified with NACO and NIRC2 in L' band is also shown in the contrast curve, for various assumptions regarding its orbit and $K-L'$ color: circular vs polar, and photospheric vs accreting circumplanetary disk, respectively.

PCA-ASDI) beyond $\sim$0$''$.2 separation is to be attributed to the bright spiral arms. The two small humps at 0$''$.21 and 0$''$.28 radii in the PCA-ASDI contrast curve most likely correspond to the Eastern portion of S1 and the bright blob at the outer tip of spiral S2, resp. (Fig. 15.6).

For comparison, at a separation of 0$''$.18 the contrast reached by PCA-ASDI is similar to that obtained by SPHERE/IRDIS in K1/K2 and falls short of the SPHERE-IFS YJH contrast by only $\sim$ 0.5mag (Maire et al. 2017). An exact comparison is not entirely possible given the different filters used. However, the apparent similarity in the contrast achieved by SINFONI and that obtained with SPHERE in good conditions (seeing $\sim$0$''$.5, τ_0 $\sim$8 ms, ΔPA $\sim$ 64°; Maire et al. 2017) demonstrates the power of PCA-ASDI. Beyond 0$''$.18, the bright cavity edge and spirals affect the SINFONI contrast curve, and to a minor extent the SPHERE contrast curve obtained with ADI (more aggressive towards the spirals), so that the comparison is more difficult. At shorter separation, the SPHERE contrast curve goes much deeper, by $\sim$2 mag, than the SINFONI contrast curve. This is because PCA-ASDI requires sufficient radial motion, and a 2FWHM radial motion (i.e. at least 1FWHM motion even for spectral channels located in the middle of the H+K range) is only obtained beyond 0$''$.19 separation in our SINFONI data. This estimate is obtained considering that 1FWHM$\approx$0$''$.07 in the last channel of K band, to which all other spectral channels are rescaled.

Figure 15.8 shows a composite contrast curve for HD 135344 B, where at each radial separation I considered the deepest contrast obtained from either PCA-ADI (in the collapsed K band) or PCA-ASDI, and reported the corresponding values of $n_{\rm pc}^{\rm ADI}$ and $n_{\rm pc}^{\rm SDI}$ ($n_{\rm pc}^{\rm SDI}$=0 corresponds to PCA-ADI). Compared to Fig. 15.7, the contrast curves were extended slightly

inward (down to $\sim$1 FWHM) and outward (up to $\sim$ 1 FWHM from the edge of the frames). As mentioned previously, the highest contrast is obtained with PCA-ASDI, for $n_{\rm pc}^{\rm ADI}$ = 1 at very short separation, and $n_{\rm pc}^{\rm ADI}$ = 1 or 2 at larger separation. However, at 1 FWHM separation ($\sim$ 0$''$.07 radius) the contrast achieved by PCA-ADI alone appears to be slightly better. This is because at too short separation, the throughput of the double pass PCA (ADI+SDI) is extremely low ($\lesssim$0.005 even for the combination $n_{\rm pc}^{\rm ADI}$ = 1 and $n_{\rm pc}^{\rm SDI}$ = 1) due to the lack of radial and angular motion. It is thus not surprising that PCA-ADI alone performs better at sufficiently small separation (in particular for this dataset obtained with $\sim$100° field rotation in relatively stable conditions).

In Fig. 15.8, I also show the expected location of the L' blob seen in the NACO and NIRC2 image, assuming different $K-L'$ colors and different orbits. For the $K-L'$ colors, I considered two cases: the photospheric colors predicted in the hot-start COND models (Baraffe et al. 2003) and the accreting circumplanetary disk colors presented in Zhu (2015). For the type of orbit, I considered a circular and a polar orbit, the two extreme cases in terms of projected separation of the companion at the epoch of the SINFONI observations. The latter case is justified by the case of companion HD 142527 B (Sec. 7.3.3; Lacour et al. 2016; Price et al. 2018). I considered a 1 mag uncertainty on the L' contrast of the companion owing to the discrepancy between the NACO and NIRC2 measurements. Given the PCA-ASDI contrast curve, it is very likely that the companion candidate would have been seen in the final PCA-ASDI images in any of the considered scenarios (as it would also have been re-detected in the IRDIS K1/K2 observations presented in Fig. 11.16). This other non-detection at shorter wavelength than L' does not help to confirm the detection, but does not enable to rule out the possibility of a redder signal than expected or of a sporadic signal in nature. The L' blob is discussed in more details in Sec. 11.6.6, based on multi-wavelength/instrument/epoch observations.

15.4.2 HD 100546

The dataset of HD 100546 was the most tricky to reduce adequately among the whole sample. This is mainly due to the large offset of the star with respect to the center of the field in a specific part of the detector which, contrary to the four-points dithering datasets, led to biases difficult to correct. Several additional effects further limited the possibility of reaching an optimal contrast. These are described below:

- The observation of that source got interrupted by the head of science at Paranal. After the interruption, I did the mistake of using the same template as in the first sequence, which placed the star at the same initial location with the same initial detector position angle. Furthermore, the PSF also looked different after the interruption. The first sequence was thus discarded. Keeping only the sequence acquired after the interruption only led to 50° field rotation.
- The star globally stayed in the same area of the detector, therefore contrary to the case of observations taken with the four-points dithering strategy, I could not find an optimal way to avoid edge effects in the final image, due to the combined effect of (1) a sharp transition between inserted frames and background, and (2) the bicubic

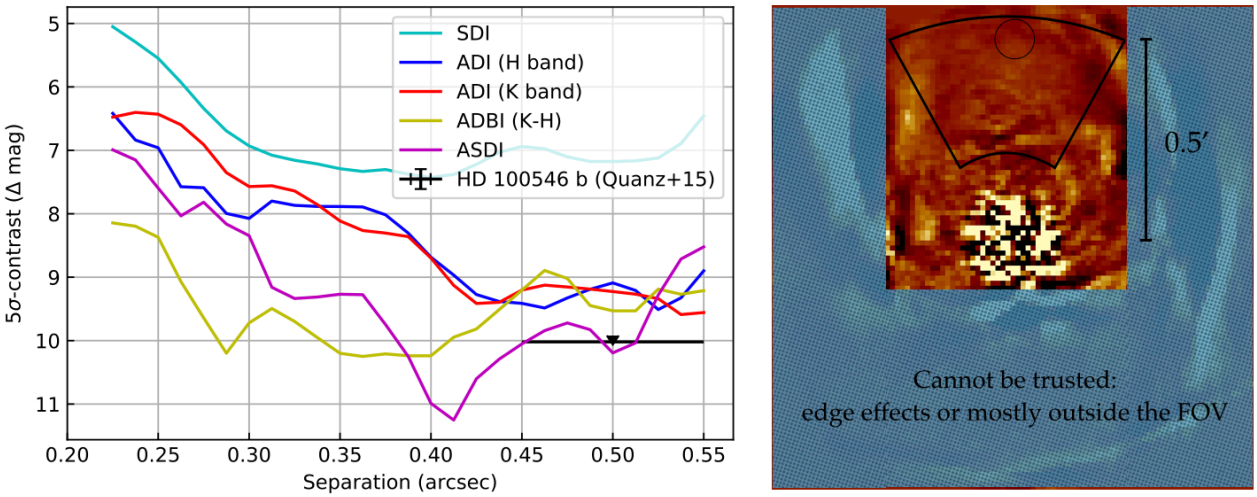

Figure 15.9: (*left panel*) Optimal contrast curve obtained with different algorithms for the SINFONI dataset on HD 100546. (*right panel*) Final image obtained with PCA-ASDI. Grayed area corresponds to parts of the image that cannot be trusted, the wedge in which the contrast curve is computed, and the expected location of protoplanet candidate HD 100546 b.

interpolation performed during final derotation to align North up.

- Atmospheric differential refraction affected all spectral cubes acquired with SINFONI. Its net effect is that the star is not located on the same pixel in different spectral channels, typically the amplitude of the offset is 6-7 pixels across the H+K spectral cubes. However, for this dataset, given the offset of the central star, the star ended up in some spectral channels at only $\sim$ 6 pixels from the edge of the frame, similarly the putative companion also ended up in some channels at $\sim$6 pixels from the edge, at the other side of the field. Cropping frame edges, possibly affected by a sub-optimal distortion correction (Fig. 15.3), was thus not an option. Furthermore the effect of ADR hindered the application of an alternative reduction strategy based on the subtraction of full-frame PCA models before star centering.
- After the interruption, the PSF looked elongated in H band channels but with a progressively more circular symmetry in channels of increasing wavelength, until reaching a circular Airy-like pattern in the middle of the K band. The cross-correlation of the PSF between different spectral channels of the same datacubes was thus not optimal.

I applied all algorithms mentioned in Sec. 15.3 and, as expected, edge effects could not be avoided in the final images. The companion candidate HD 100546 b was not re-detected with any of the considered algorithms, for a large range of tested $n_{\rm pc}$ values. The right panel of Fig. 15.9 shows the final frame obtained with PCA-ASDI, leading to the highest contrast at the expected location of the companion (indicated by a thin circle in that image). Areas that cannot be trusted either due to edge effects or for being mostly outside of the initial field of view are grayed. The contrast curve obtained with the different tested algorithms is shown in the left panel of the same figure. It was computed in the wedge shown with a thick solid line in the right panel. It is useful to keep in mind that due to the wedge, the contrast curves are likely increasingly optimistic towards shorter separation due to the decreasing number of resolution elements.

Regarding the contrast curves, similar qualitative conclusions can be drawn as for the case of the HD 135344 B dataset: PCA-SDI leads to the shallowest contrast among the tested algorithms, and the combination of both ADI and SDI yields the best contrast. Nonetheless, I suspect PCA-ASDI to not perform optimally at close ($\lesssim 0\farcs30$) separation due to the PSF elongation that is present in roughly half of the spectral frames (while a roundish shape is found in the other half). The fact that all algorithms using SDI have a progressively shallower contrast curve beyond $\sim$0$\farcs$40 separation is due to the different rescaling of spectral frames at different wavelengths. Indeed, this effect causes the PSF model that is created and subtracted by PCA to be sub-optimal beyond a certain radial separation. Despite the complications, a similar contrast was obtained at 0$\farcs$5 with PCA-ASDI than inferred in Quanz et al. (2015a) using NACO K-band data, where they did not re-detected the companion candidate either.

Retrospectively, if the observations were to be performed again, I would recommend the use of the four-points dithering strategy as for PDS 70 and HD 142527, as it would lead to significantly less biases and to the creation of a better PSF model for differential imaging.

15.4.3 HD 142527

In this subsection, I only present the results that are not included in Christiaens et al. 2018a (in press, Sec. 16.1), namely the final images obtained with PCA-ASDI and PCA-ADBI and the contrast curves obtained for all tested algorithms. Figure 15.10 shows the PCA-ASDI and PCA-ADBI images obtained with $n_{\rm pc}^{\rm ADI}$=1 and $n_{\rm pc}^{\rm SDI}$=1, and $n_{\rm pc}^{\rm ADI}$=2 and $n_{\rm pc}^{\rm SDI}$=1, resp., which are the combinations optimizing the SNR of the companion HD 142527 B. The algorithms were applied on the full recombined frames, but for a better visibility of the companion, are shown in Fig. 15.10 after significant cropping. No other significant signal is indeed found at larger radius. Despite the very short separation of the companion ($\sim$ 80 mas; $\sim$1.1 FWHM), and the expected significant self-subtraction (due to the lack of radial motion for the SDI part), the signal of HD 142527 B is recovered by both PCA-ASDI and PCA-ADBI. The SNR of the detection is $\sim$ 4.5 for PCA-ASDI, and $\sim$7.5 for PCA-ADBI. It proves that both PCA-ASDI and PCA-ADBI are capable to recover close-in point-like sources, however, as also shown for the PDS 70 dataset (Sec. 15.5.1), PCA-ADBI appears slightly more sensitive to those point-like sources than PCA-ASDI, despite a possibly larger distortion affecting the PSF of the retrieved companion. In fact, the SNR of the detection in the PCA-ASDI image is slightly lower than the average value of SNR in images obtained from applying PCA-ADI separately in each spectral channel (Sec. 16.1). This appears to somewhat corroborate the previous conclusion, inferred from Fig. 15.8, that at very short separation (r $\sim$1 FWHM) the throughput of PCA-ASDI in two-steps is so low that PCA-ADI becomes competitive in terms of achieved contrast. Nonetheless, this conclusion has to be also mitigated by the fact that the PCA-ADI detection of the companion presented in Sec. 16.1 was obtained using 40 cropped temporal cubes instead of 10 cubes resulting from median recombination of cubes four by four.

Figure 15.11 corresponds to the contrast curves obtained with the different algorithms applied to the 4D cube. I note that the PCA-SDI contrast curve is at roughly the same level

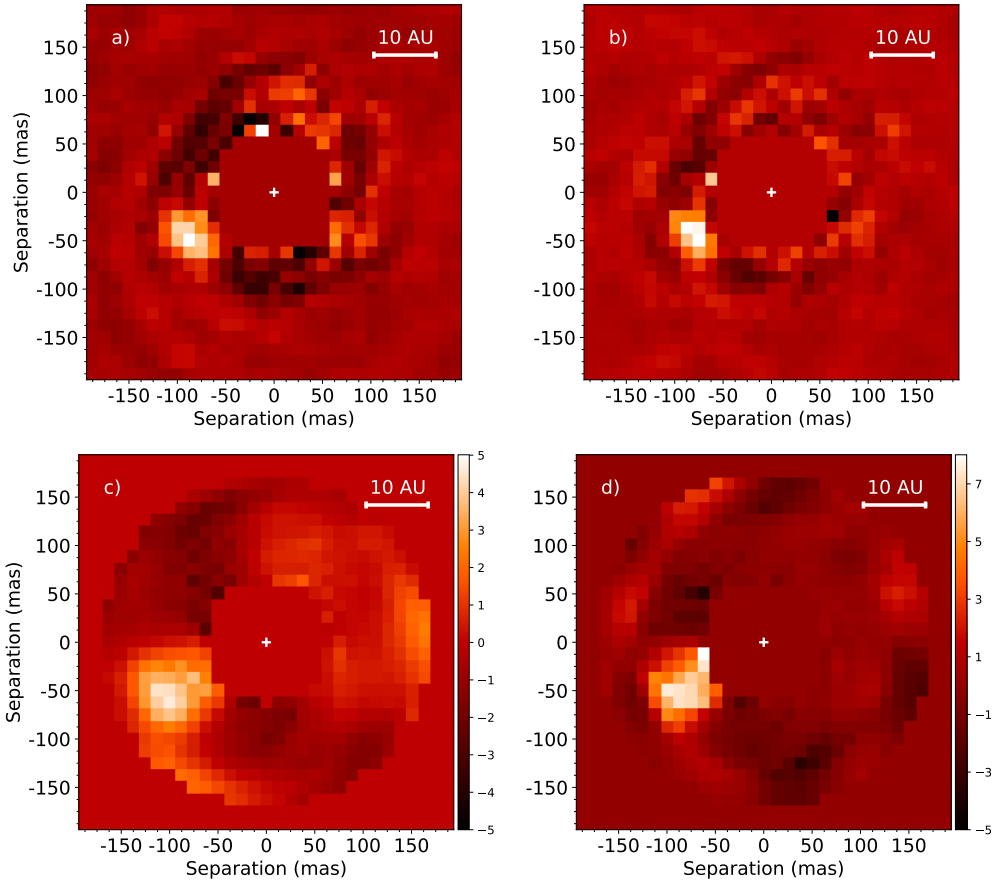

Figure 15.10: a), b) PCA-ASDI and PCA-ADBI images of HD 142527, obtained with $n_{\rm pc}^{\rm ADI}$=1 and $n_{\rm pc}^{\rm SDI}$=1, and $n_{\rm pc}^{\rm ADI}$=2 and $n_{\rm pc}^{\rm SDI}$=1, respectively. **c), d)** SNR maps of a) and b), respectively. The companion is detected at SNR∼4.5 and ∼7.5 respectively.

as the PCA-ADI contrast curves, contrary to the HD 135344 B and HD 100546 datasets where it was slightly underperforming. This can be explained by a higher stability and smaller number of temporal cubes, which lead to a better conservation of the high cross-correlation between spectral frames even after taking the median through the temporal sequence. As for HD 135344 B and HD 100546, the contrast curve of PCA-ASDI and PCA-ADBI are very similar and much deeper than PCA-ADI or PCA-SDI. This time the contrast gain compared to PCA-ADI is up to 2mag deeper, this is likely due to the higher level of stability of the PSF during the sequence.

15.4.4 HD 179218

The images obtained with PCA-ASDI and PCA-ADBI on the dataset of HD 179218 are shown in Fig. 15.12. As for HD 135344 B, the observations were obtained with the star placed roughly at the center of the field. Therefore, compared to the datasets of HD 142527 and PDS 70, PCA-ASDI/ADBI is only useful in a relatively narrow annulus between $\sim 0\farcs15$ and $\sim 0\farcs3$. The image obtained with PCA-ASDI does not reveal any significant signal.

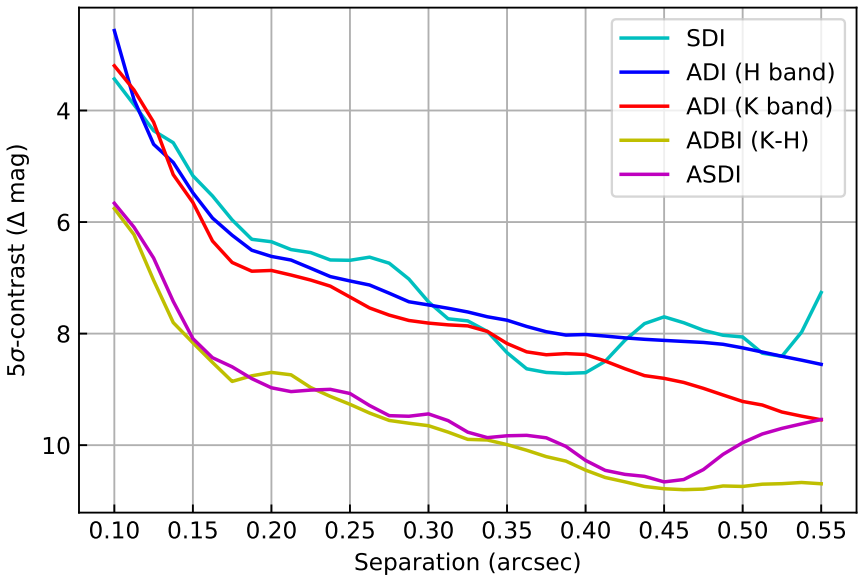

Figure 15.11: Optimal contrast curves obtained for HD 142527, considering for each algorithm the number of principal components that optimizes the contrast achieved at each radial separation.

However, the PCA-ADBI image shows a point-like source at a separation of 0″.16 to the SW of the frame, which appears to be flanked with two negative side lobes. Its SNR is ∼8.0 which corresponds to a 4.7σ detection at a separation of 0″.16, using Student statistics.

Nonetheless, PCA-ASDI images obtained with varying $n_{\rm pc}^{\rm ADI}$ does not lead to any significant detection at that location. Furthermore, making the 0″.15-radius numerical mask slightly smaller reveals a lot of artifacts related to self-subtraction. Given that the tentative blob is at the edge of the numerical mask, one should be cautious with the detection claim. I have not had the time to run further tests on this dataset yet, in order to better constrain the authenticity of the point-like source. Nevertheless, it appears that a tentative blob at a similar location was found in L' using NIRC2 (Gary Ruane, private comm.), which is encouraging. SPHERE/IFS data on that source do not reveal anything (Gerrit van der Plas, private comm.), however they were obtained in poor conditions, far from transit ($\lesssim$2° field rotation). I have noticed that an archival NACO+AGPM dataset in L' is also available on that source, obtained by ISPY in good conditions, with a long integration and a lot of rotation. Therefore, my plan is to reduce the NACO dataset and check if a point-like source can be recovered at that location as well (this dataset will be included in my transition disk survey anyway). As seen in Sec. 11.6.6 in the case of HD 135344 B, speckle tests alone might not be able to provide a clear-cut answer regarding the authenticity of bright close-in signals. However, comparing the results obtained with 3 different instruments is likely to be the best way to check the authenticity of the point-source.

Given that the observations were acquired at different epochs, ranging from 2014 to 2017 for the SINFONI and NACO datasets resp., it will also be possible to test whether the signal comes indeed from a bound object on a Keplerian orbit, or whether it is an extended disk feature. Kluska et al. (2018) determined indeed that the disk was likely significantly

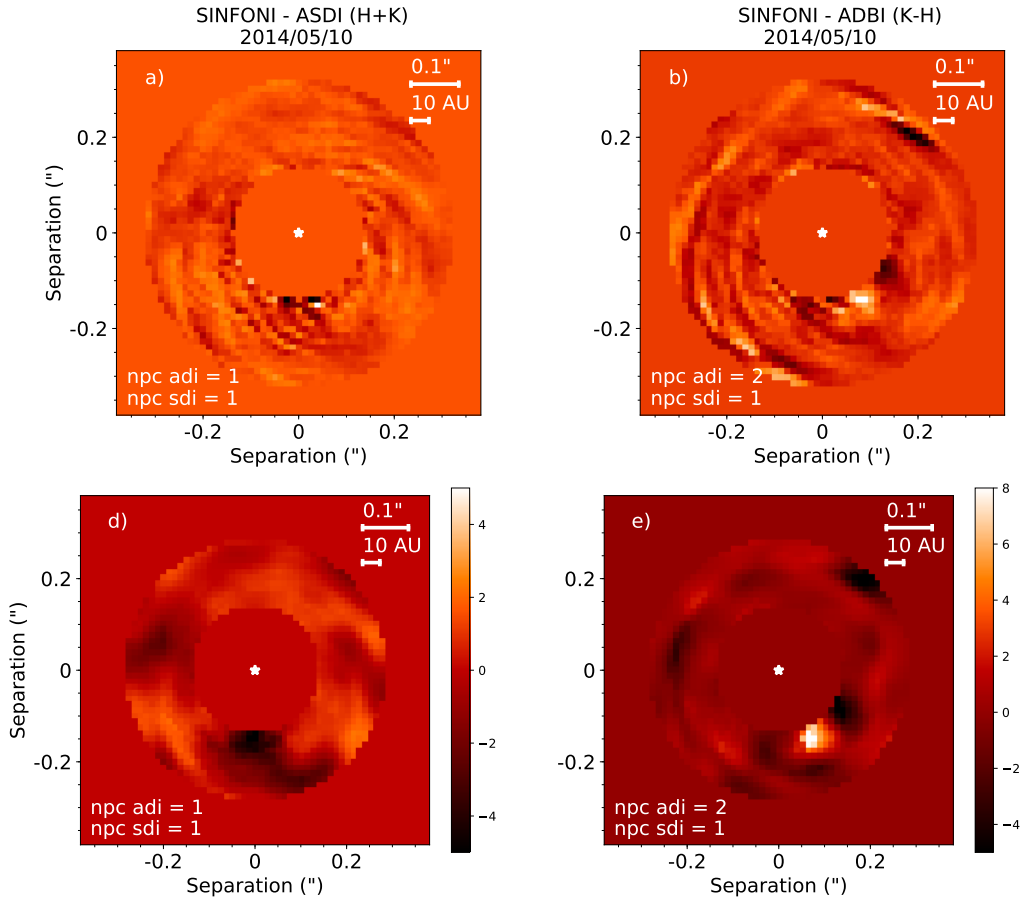

Figure 15.12: **a), b)** PCA-ASDI and PCA-ADBI images of HD 179218, obtained with $n_{\rm pc}^{\rm ADI}$=1 and $n_{\rm pc}^{\rm SDI}$=1, and $n_{\rm pc}^{\rm ADI}$=2 and $n_{\rm pc}^{\rm SDI}$=1, respectively. **c), d)** SNR maps of a) and b), respectively. A companion candidate is detected only in the PCA-ADBI image at SNR ∼8.

inclined with the PA of its semi-major axis between ∼20-30, which means that the location of the blob is roughly along that same axis. Disk modeling suggests that its extent (as would be seen in thermal-IR) is expected to be ∼3 times smaller than the separation of the companion (Kluska et al. 2018). The reduction of the different datasets obtained at various epochs would thus enable to check whether the point-like source corresponds to a companion or to the outer tip of the tilted disk (based on the proper motion of lack therof).

If the companion is confirmed, this would be another evidence that PCA-ADBI is more sensitive at recovering point-like sources, as already shown for HD 142527 B and PDS 70 b (Figs. 15.10 and 15.14). Given that the estimated contrast curves of PCA-ASDI and PCA-ADBI appear in general relatively similar (e.g. Fig. 15.12 for HD 179218), this could suggest that the PCA-ASDI contrast curve is too optimistic and/or that the fact that a companion is red makes it easier to detect with PCA-ADBI. Indeed, as a reminder, all contrast curves obtained with PCA-ADBI shows the detectability towards companions with a red color (H-K = 1), while PCA-ASDI contrast curves show the detectability towards companions with a flat spectrum. Tests I made have shown that the PCA-ADBI contrast curve is roughly ∼0.5 mag shallower when assuming a flat spectrum. I have not had the time to test how PCA-ASDI contrast curves change for red spectra of fake companion. However, this kind

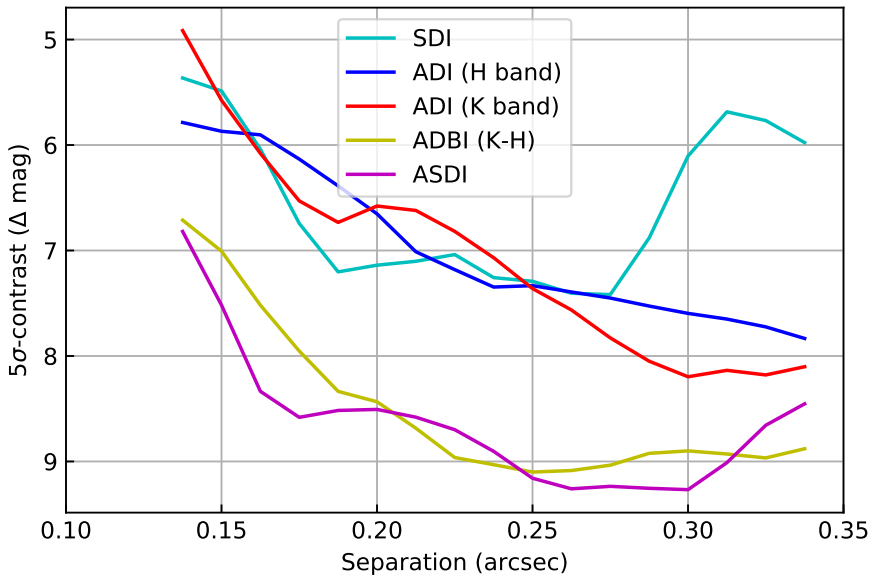

Figure 15.13: Optimal contrast curves obtained for HD 179218, considering for each algorithm the number of principal components that optimizes the contrast achieved at each radial separation.

of tests has been carried out in Rameau et al. (2015), who show a significant dependency of the achieved sensitivity with the slope of and features present in the spectrum. Their results suggest for example that the sensitivity of PCA-ASDI is higher for highly methaned objects (strong absorption band at 1.62μm), while the contrast curve might overestimate the sensitivity towards methane-free companions.

15.5 Case of PDS 70

For PDS 70, the ADBI and ASDI reductions led to the detection of a compact signal, interpreted as a possible companion, and a tentative spiral-like feature possibly connecting the companion candidate with the outer disk. Below is the content of the paper submitted to MNRAS reporting these results. Only the "Observations and data reduction" section was summarized compared to the submitted version.

15.5.1 A possible gap-crossing bridge linked to a companion candidate in the transition disk of PDS 70

V. Christiaens, S. Casassus, O. Absil, C. Gomez Gonzalez, R. Ramírez, J. Girard, S. P. Quanz, V. Salinas, A. Jordán, D. Mawet and Z. Wahhaj
submitted to MNRAS

Abstract

The formation of planets is still mostly a theoretical field which requires critical input from observations. Protoplanetary disks with evidence of large inner clearing (transition disks) are prime targets to look for protoplanets and study their interaction with the disk. Here we present observations of PDS 70, a transition disk with a large gap, obtained with VLT/SINFONI. We take advantage of the significant angular and spectral diversity present in our data for an optimal PSF modeling and subtraction using principal component analysis. Our images reveal the presence of a companion candidate in the cavity and a possible spiral-shaped bridge connecting the candidate and the outer disk. The point-like source is found at $r = 199.5 \pm 12.5$mas (22.5 ± 1.4 au) and PA $= 158.0° \pm 2.4°$, with a contrast of 7.43±0.35 mag in K band and > 7.1mag in H band. We cannot rule out the possibility that the companion candidate is a filtered extended structure. However, if the signal is confirmed to be point-like it could correspond to one of the first detections of a forming giant planet. We argue that recent ALMA observations provide tentative hints supporting the companion+bridging material hypothesis.

Introduction

Protoplanetary disks are the expected birth place of planets. *Transition disks* (TDs) are a specific kind of protoplanetary disks showing evidence of inner clearing. These inner clearings were first inferred from the SED, showing a lack of near- to mid-IR excess (e.g. Strom et al. 1989), and were confirmed through resolved sub-mm observations (e.g. Andrews et al. 2011). Owen (2016) recently highlighted the distinct properties of TDs with very large gaps/cavities ($\gtrsim 20$ au), which show both high accretion rates and bright sub-mm fluxes, in contrast to mm-faint TDs which harbour smaller gaps. These TDs with large gaps/cavities appear incompatible with a photo-evaporation origin, but are most likely due to the dynamical carving by embedded companions. Yet, direct and conspicuous evidence of forming planets is still lacking in these disks despite multiple claims in the recent years (Kraus & Ireland 2012; Quanz et al. 2013a; Reggiani et al. 2014; Biller et al. 2014; Sallum et al. 2015; Reggiani et al. 2018). Indeed, recent literature has shown that aggressive filtering on bright and extended disk emission could create point-like features (e.g. Thalmann et al. 2016; Follette et al. 2017; Rameau et al. 2017), which could be confused with substellar companions.

While the direct observational confirmation of giant planets in transition disks has turned out to be more difficult than expected, mounting indirect evidence of planet presence has been found in transition disks (Casassus 2016, and references therein). Large gaps of different sizes at near-IR and sub-mm wavelengths (e.g. Garufi et al. 2013), asymmetric dust distributions (e.g. Casassus et al. 2013b; van der Marel et al. 2013) and spiral arms (e.g. Muto et al. 2012; Christiaens et al. 2014; Benisty et al. 2015) can be produced through a range of different mechanisms, but they also all have in common to be potential by-products of planet-disk interactions. Price et al. (2018) recently showed that in the case of the transition disk around HD 142527, the characteristics of the disk including the gap size, the banana-shape mm-dust trap and the spiral arms at the gap edge, could all be qualita-

tively accounted for by the low-mass binary (e.g. Biller et al. 2012; Lacour et al. 2016). Are low-mass companions at the origin of similar features observed in other transition disks? Among the different potential signposts of planet presence, spiral arms might provide the most information about the companion that is launching them – if that is indeed their origin. Their global shape, pitch angle and contrast, the number of observed arms and the separation angle between primary and secondary arms can all be used to constrain the mass and location of the perturber (e.g. Ogilvie & Lubow 2002; Rafikov 2002; Zhu et al. 2015; Fung & Dong 2015; Dong & Fung 2017b; Bae & Zhu 2017b).

High-contrast imaging is one of the most suitable techniques to detect faint signals such as nascent planets or circumstellar disk features in the close vicinity of young stars (Absil & Mawet 2010; Bowler 2016). In order to optimize the contrast reached at small angle, astronomers rely on differential imaging techniques. Here, we focus on the combination of angular (ADI; Marois et al. 2006) and spectral differential imaging (SDI; Sparks & Ford 2002) applied to medium-spectral resolution integral field spectrograph (IFS) data obtained with VLT/SINFONI on the transition disk of PDS 70.

PDS 70 is a TTauri star surrounded by a disk with a remarkably large dust-depleted cavity. Previous literature has used a distance of ∼140 pc, assuming membership of PDS 70 to the Upper Centaurus Lupus association (Riaud et al. 2006). However, the new Gaia DR2 distance places it at only 113 ± 1 pc (Gaia Collaboration et al. 2018), which might alter previous stellar parameter estimates. The near-IR JHK spectrum of the star is compatible with an M1V pre-main sequence star (Long et al. 2018), although UBVRI photometry suggests a K5V star (Gregorio-Hetem & Hetem 2002). An M1V spectral type would be compatible with a mass and age of ∼0.5 $M_{\odot}$ and ~ 2 Myr resp., while a K5V spectral type would imply an older and more massive star (∼10 Myr and ∼1.1$M_{\odot}$ resp.; Long et al. 2018). Considering the new distance throughout this paper, the size of the μm-size and mm-size dust cavities are ∼53 au and ∼65 au (Hashimoto et al. 2012, 2015; Long et al. 2018). Near-IR polarimetric images suggest an outer disk inclination of 45-50° and a PA of the semi-major axis of ∼159°. SED modeling hints at the presence of a small optically thick inner disk (Dong et al. 2012). The different gap sizes for μm-size and mm-size dust are suggestive of the presence of one or several companions inside the large annular gap (e.g. Pinilla et al. 2012a; de Juan Ovelar et al. 2013).

In this paper, we present VLT/SINFONI images of PDS 70 and report the detections of a companion candidate and a tentative spiral-shaped bridge connecting the companion and the outer disk. The presence of a planetary-mass companion around PDS 70, at the same position and contrast as our SINFONI candidate companion, was first announced by the SPHERE team (Keppler et al., in press), which casts confidence on the authenticity of the signal we detected.

Observations and data reduction

The observation and data calibration procedure of the PDS 70 dataset are described in Secs. 15.2 and 15.3 respectively. For an optimal post-processing, we used PCA-ASDI and PCA-ADBI as described in Sec. 15.3.2, and PCA-ADI in annuli in each spectral channel, as

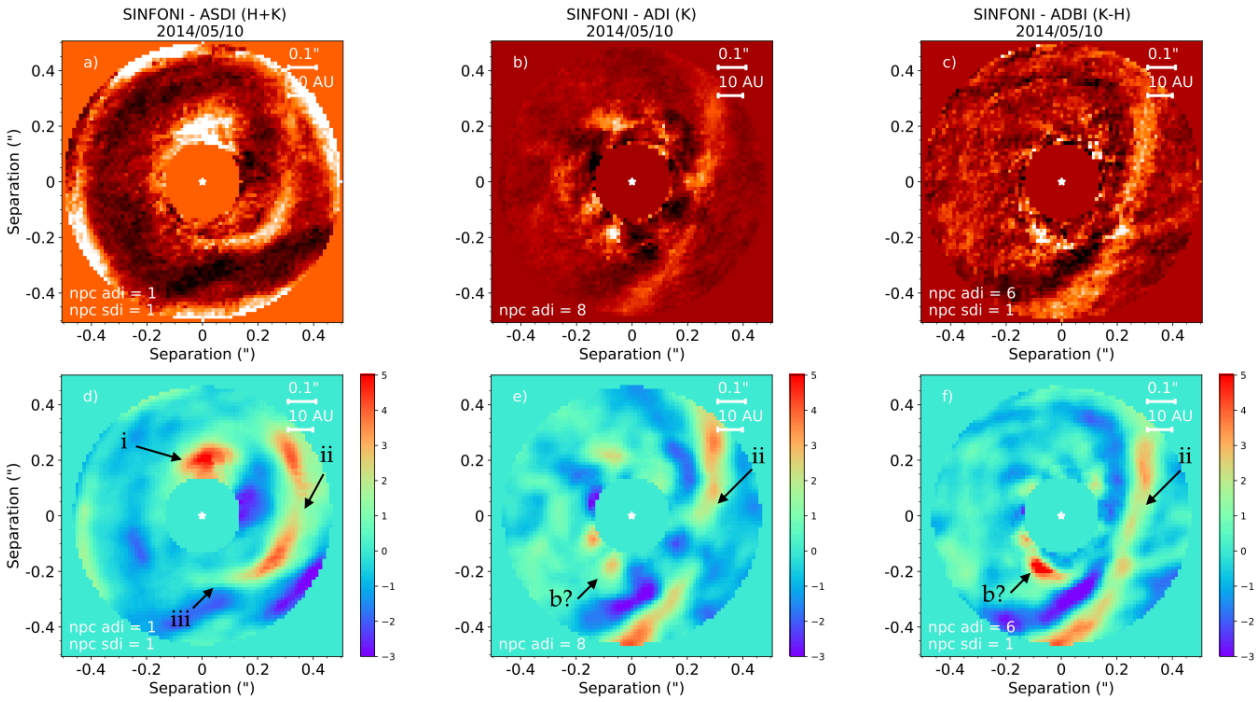

Figure 15.14: Final images obtained with **(a)** PCA-ASDI on the full H+K 4D datacube, **(b)** PCA-ADI in concentric annuli in the K band, and **(c)** PCA-ADBI between the K- and H bands. See Sec. 15.5.1 for details on the algorithms used. **(d), (e)** and **(f)**: SNR maps of (a), (b) and (c) resp., as defined in Mawet et al. (2014). The scale of all images is linear.

described in Sec. 11.5.1.

Results

The final images obtained with PCA-ASDI on the whole 4D cube, PCA-ADI in annuli on the collapsed K-band cube and PCA-ADBI ($K-H$) are shown in Fig. 15.14. The SNR maps are computed as defined in Mawet et al. (2014) and implemented in VIP (Gomez Gonzalez et al. 2017), taking into account a small angle penalty factor.

Figure 15.14a corresponds to our least aggressive reduction in terms of filtering out azimuthally extended signals (see tests in Appendix A), which still reaches a high contrast. It is thus privileged for the study of extended signals. Several features stand out in this image: (i) a bright component protruding from the numerical mask to the north and extending up to 0″.25 separation at an SNR $\sim$ 5, (ii) the bright edge of the outer disk to the west, with its brightest part peaking at an SNR $\sim$ 4–5, and (iii) a spiral-like feature which appears to originate from a PA $\sim$ 180° and a radial separation $r \sim$ 0″.23, and connecting with the edge of the outer disk at PA $\sim$ 225°and $r \sim$ 0″.31. All labeled features are qualitatively recovered for PCA-ASDI reductions obtained with different combinations of number of principal components $n_{\rm pc}^{\rm ADI} \in [1,3]$ and $n_{\rm pc}^{\rm SDI} \in [1,2]$, although progressively filtered out with increasing $n_{\rm pc}$. Based on Fig. 15.14a alone, features (ii) and (iii) are undistinguishable and appear as a single, continuous component. We also note that although feature (iii)

is bright in the final image, it does not appear significant in the SNR map (SNR $\sim$ 2–3). However, the definition in Mawet et al. (2014) was originally designed for evaluating the SNR of point-like features, moreover in the ideal case of absence of bright and extended physical signal at similar radii. Both feature (i) and the signal from the spiral itself at similar radii contribute to lower the estimated SNR. For comparison, with the same definition, spirals seen in the L' band in MWC 758 also show SNR $\lesssim 3$ (Fig. 12.2) but are conspicuous in polarized light (Benisty et al. 2015). Our spiral-like feature is nonetheless still tentative at this point and to be considered with care.

Figure 15.14b is the result of PCA-ADI applied to the cube obtained after collapsing spectral channels of the K band. It is a more aggressive reduction for azimuthally extended signal, but enables to enhance point-like and radially extended signals. The most conspicuous feature in this image is a long arc extending from the NW to the S which traces the bright edge of the outer disk (Hashimoto et al. 2012). Besides the arc, three point-like sources at SNR$\sim$3 can be seen at PA $\sim$ 20°, 115° and 160°. The latter one appears brighter but is not more significant according to the SNR map. We notice that feature (iii) is not seen anymore, and the portion of the arc that lies at an almost constant (projected) radial separation from the star also appears moderately self-subtracted. We ran a series of tests where we injected a fake spiral arm in our dataset (Appendix A) and noticed that, as expected, the injected spiral gets significantly filtered out by PCA-ADI. The final PCA-ADI image in H-band (not shown) is of poorer quality than Fig 15.14b, which we assign to poorer AO-correction at shorter wavelengths. No significant point-like source is found in that image and the conspicuous arc seen in K band is barely recovered in the final $H-$band image.

In order to further boost our potential for detecting red companions, we performed PCA-ADBI between the K and H bands which, compared to PCA-ADI alone, enables to subtract efficiently radially moving speckles. The result is shown in Fig. 15.14c. Out of the three blobs with SNR$\sim$3 in Fig. 15.14b, only one is recovered at SNR $\sim$ 6 (4σ-detection using Student statistics). The signal does not appear very compact, which might be the result of multiple processing and filtering steps and/or mean that the signal is intrinsically extended.

We retrieved the parameters of the companion candidate using the negative fake companion technique (NEGFC; e.g. Marois et al. 2010b; Wertz et al. 2017) in combination with PCA-ADI (where the companion candidate is most point-like). The estimated astrometry obtained by NEGFC is: $r = 199.5 \pm 12.5$ mas and PA=158.0 ± 2.4°, where the uncertainties reflect residual speckle noise in our image and were estimated as in Wertz et al. (2017). In comparison, the uncertainties associated to true North and plate scale (see details in Christiaens et al. 2018, subm.) are substantially smaller. Given the PA of the outer disk (PA$\sim$159°), both the projected and deprojected physical separations are 22.5$\pm$1.4 au. The contrast of the point source inferred by NEGFC is 7.43 ± 0.35 mag in K band, where the uncertainty reflects both residual speckle noise in our image and the variable conditions across the observation. This contrast corresponds to an apparent magnitude of $K = 15.97 \pm 0.35$ mag ($M_K = 10.70 \pm 0.35$ mag), where the uncertainty on the magnitude of the star is negligible in the balance. The non-detection in H band yields a 3σ-upper limit of 7.1 mag contrast, which corresponds to an apparent magnitude $H > 15.90 \pm 0.35$ mag

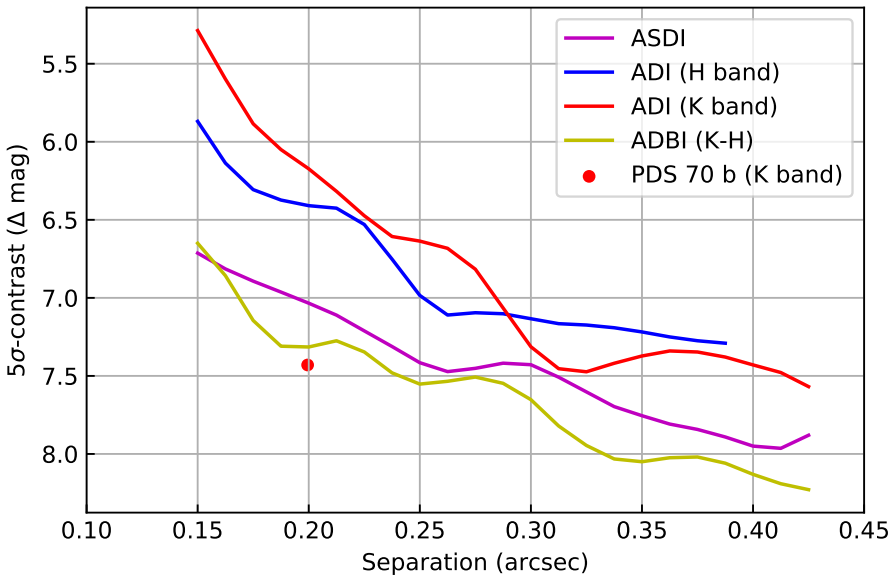

Figure 15.15: 5σ-contrast curves obtained with the different algorithms tested in this work. These curves are compared to the 4σ companion detection in the ADBI image.

($M_H > 10.63 \pm 0.35$ mag). This implies a color constraint of $H - K > 0.07 \pm 0.35$.

Figure 15.15 shows the contrast curves computed for the different algorithms tested in this work. For the calculation of the ADBI contrast curve, we slightly tweaked the code in VIP to consider red fake companions (1 mag brighter in K band than in H band). With this assumption, the 5σ contrast of $\sim$7.3 mag reached at 0$''$.2 separation appears consistent with the 4σ detection seen in Fig. 15.14c.

Given the inferred location of the companion candidate, the tentative spiral arm seen in Fig. 15.14a appears to be connecting the companion and the outer disk edge. This argument incited us to further investigate the tentative spiral despite its low significance. We show in Appendix 15.5.1 that only in our least aggressive reduction an injected synthetic spiral arm similar to the observed one survives post-processing. When $n_{\rm pc}^{\rm ADI}$ is too large, the characteristic negative imprint of ADI truncates the spiral near the bright edge of the outer disk. While these tests do not allow us to fully confirm the authenticity of the observed spiral-like feature, they do account for its absence in the final images where the companion candidate is detected. Alternatively, we also tested the injection of fake companions at the same contrast and radial separation as the companion candidate, but different PAs. In the final ASDI image (with $n_{\rm pc}^{\rm ADI} = 1$) it is not possible to distinguish these fake companions from extended features, as they share roughly the same residual flux level. On the contrary, using larger values of $n_{\rm pc}^{\rm ADI}$ recovers the injected fake companions, with an optimal significance obtained with ADBI. Both the fake spirals and fake companions tests suggest thus that the sensitivity to extended and point-like sources are optimal in the ASDI and ADBI reductions, with low and large $n_{\rm pc}^{\rm ADI}$ values, respectively.

Assuming the spiral is authentic, we used the final ASDI image to analyze it based on

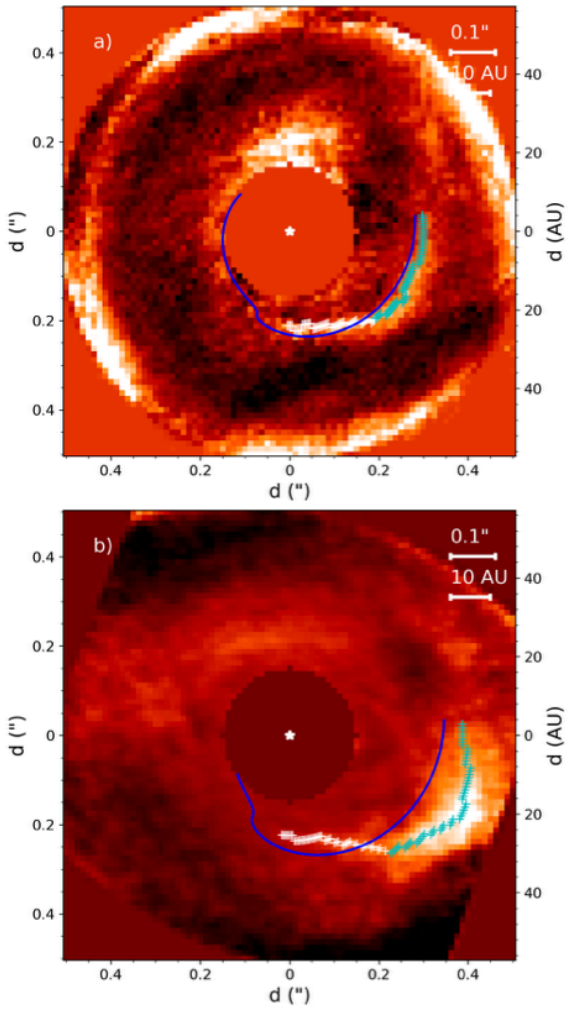

Figure 15.16: (a) Trace of the spiral (*crosses*) and best-fit to Eq. 6.2 (*solid line*) in the final image obtained with PCA-ASDI. *White* and *cyan crosses* indicate the location of radial maxima in steps of 1°; only the *white crosses* are used for the fit to Eq. 6.2. **(b)** Same as (a) in the image obtained after disk deprojection and r^2-scaling.

the spiral density wave theory. The shape of the spiral density wave launched by a planet can be approximated geometrically with Eq. 6.2. While Eq. 6.2 is strictly valid only in the linear regime, which typically corresponds to companions whose mass is insufficient to open a gap, 3D hydrodynamical simulations probing the non-linear regime have shown that the spiral arm launched outward from the companion location is still relatively well approximated by this equation (e.g. Zhu et al. 2015). There is a known degeneracy between the 5 parameters of Eq. 6.2, θ_p, r_p, α, β and h_p (e.g. Muto et al. 2012; Christiaens et al. 2014; Benisty et al. 2015, see Sec. 6.4.2 for details). We fix thus α to 1.5, β to 0.25, and the location of the companion (θ_p, r_p) to that of the point-source found in our images, and just let h_p as a free parameter. Setting α to 1.5 is equivalent to assuming a Keplerian disk, and $\beta = 0.25$ corresponds to the expected temperature profile of a passively heated disk, which is a valid hypothesis given the low accretion rate on the star (Gregorio-Hetem & Hetem 2002).

We considered two different cases, either (A) the spiral is launched in the same plane as the outer disk (i.e. the companion's orbit is coplanar with the outer disk) or (B) it lies in an almost face-on plane (i.e. the orbit of the companion is closer to polar with respect to

the outer disk). To investigate case A, we deprojected our image using the inclination and PA of semi-major axis of the outer disk: i $\sim 50^\circ$ and PA $\sim 159^\circ$ (Hashimoto et al. 2012). The deprojected disk image is shown in Fig. 15.16b, where we also scaled the image by r^2 to compensate for the expected flux dilution of scattered stellar light. In both images, we identified the trace of the spiral-like feature with radial maxima in steps of 1°, and fit the portion that does not overlap with the edge of the outer disk (*white crosses*) to Eq. 6.2. The spiral trace is better fit by Eq. 6.2 in the non-deprojected image ($\chi^2_r \sim 0.3$ vs 0.5), with also a more reasonable best-fit value for h_p (0.050) than the best fit model in the deprojected image ($h_p \sim 0.116$). These values of h_p are upper limits since only spirals in the non-linear regime are expected to be observable (Dong & Fung 2017b), and inferring h_p based on the best-fit linear spiral model is expected to overestimate h_p (Zhu et al. 2015). In comparison, SED fitting suggests $h_p \sim 0.015$ at 22.5 au separation (Dong et al. 2012).

Discussion

Fig. 15.14a shows the tentative detections of a spiral-like feature to the SW and an extended signal to the North. This image was obtained using only 1 principal component ($n_{\rm pc}$) for both the PCA-ADI and PCA-SDI parts of the processing, which minimizes the filtering of extended disk signal. Despite the low number of $n_{\rm pc}$, PCA-ASDI consistently reaches higher contrast than PCA-ADI on the spectrally collapsed cube (Fig. 15.15). The up to 1 mag contrast gain thanks to SDI can be attributed to the high cross-correlation of the (rescaled) stellar halo with wavelength. Aggressive ADI reductions (larger $n_{\rm pc}^{\rm ADI}$) enable to recover a point-like source, but also significantly alters the recovery of azimuthally extended signal, such as spiral arms (Appendix 15.5.1; see also Milli et al. 2012). Both these tests and the PCA-ASDI contrast curve suggest that the extended structures in Fig. 15.14a might be authentic. Since the point-source is not recovered in that reduction, but rather shows up at the tip of an extended spiral-like feature after aggressive processing, we cannot rule out the possibility that it is in fact a filtered portion of the spiral, as was suggested for HD 100546 b (Follette et al. 2017; Rameau et al. 2017). On the other hand, our tests also show that aggressive ADI is most sensitive to the detection of injected fake companions, which leaves the door open to the possibility that both the spiral and point-like features are authentic, but revealed by reductions intrinsically more sensitive to extended and point-like features, respectively. New observations of PDS 70 making use of reference star differential imaging (Racine et al. 1999) could enable to better constrain the nature of the observed signal.

Our reduction using PCA-ADBI reaches a slightly higher contrast than PCA-ASDI and reveals the presence of a compact signal at a 4σ confidence. Using NEGFC with the PCA-ADI reduction, which leads to a more point-like (albeit less significant) signal, we inferred the astrometry of the point-source to be $r = 199.5 \pm 12.5$ mas and PA=$158.0 \pm 2.4^\circ$. A possible way to confirm that this signal traces a companion is through follow-up spectral characterization, which would reveal whether the emission is photospheric, traces thermal emission from heated dust or scattered stellar light, or a combination of the aforementioned. A more detailed spectral analysis will be the subject of a future paper. If the emission turns out to be mostly photospheric, the K-band absolute magnitude ($\sim$ 10.7 mag) and $H-K$ color upper limits ($\gtrsim$ 0.1 mag) are compatible with BT-SETTL models of 4–5 $M_{\rm Jup}$ (resp. $\sim 10 M_{\rm Jup}$)

for a 2 (resp. 10) Myr old object (Allard et al. 2012). Cold-start models rather suggest an object much more massive than $10 M_{\rm Jup}$ (e.g. Marley et al. 2007; Fortney et al. 2008), hence likely in conflict with the core accretion scenario which they are expected to be representative of. Warm-start models, possibly more physically realistic, would lead to intermediate predictions between those of hot and cold-start models (Spiegel & Burrows 2012; Mordasini et al. 2012). If the K-band emission traces a circumplanetary disk, models in Zhu (2015) suggest that the mass times mass accretion rate of the protoplanet is $10^{-5.2\pm0.5} M_{\rm Jup}^2$ yr^{-1} (e.g. a $2 M_{\rm Jup}$ protoplanet accreting at a rate of 10^{-5}-$10^{-6} M_{\rm Jup}$ yr^{-1}). This scenario involves high levels of accretion and very red colors, which should be testable with Hα and L-band observations. The forming planet hypothesis can also be tested with follow-up astrometry. With a separation of $\sim$22.5 au, the tentative *PDS 70 b* would move by $\sim 2.4^\circ$ yr^{-1} (resp. $\sim 3.5^\circ$ yr^{-1}) for a 0.5 $M_\odot$ (resp. 1.1 $M_\odot$) central star. Considering our astrometric uncertainties, this would be testable with any new observation.

Despite the uncertainties on the spiral and point-like features, the possibility that we are observing a planet-disk interaction incited us to further investigate the spiral arm scenario. Our analysis suggests that if the spiral lies in the plane of the outer disk, its deprojected pitch angle would be very large ($27.1 \pm 1.4^\circ$). Comparison with the polarimetric images of Hashimoto et al. (2012) is rendered difficult due to the 0$''$.2 numerical mask they use. However, no significant signal is found at the expected location of the spiral in their images, which might suggest, along with the large pitch angle, that it traces thermal emission from shocks rather than scattered light (e.g. Lyra et al. 2016). Alternatively, the better fit of the spiral trace to Eq. 6.2 in the non-deprojected image could suggest that the spiral arm lies in a different plane as the outer disk. This would be the case if the companion is on a close to polar orbit with respect to the outer disk. This possibility might be supported by tentative shadows seen in recent ALMA images in continuum and gas (Long et al. 2018). In that scenario, the disk and companion would be similar to the case of HD 142527, where the low-mass companion was found on an eccentric and almost polar orbit with respect to the outer disk, dynamically carving a similarly large cavity (Biller et al. 2012; Lacour et al. 2016). This possibility has been further supported by recent numerical simulations suggesting that low-mass companions within the gap of transition disks are prone to both eccentricity and inclination excitation leading to large misalignments (e.g. Owen & Lai 2017; Martin & Lubow 2017). The recent simulations of Price et al. (2018) have shown that such companions are expected to drive spiral-shaped gap-crossing filaments, with a significantly different morphology to what is predicted from simulations considering companions on circular orbits co-planar with the disk (e.g. Dong et al. 2015b; Zhu et al. 2015). Astrometric follow-up of the companion candidate will enable to constrain its orbit, and hence provide new insight on the nature of the possible planet-disk interactions observed here.

Finally, another way to confirm that the point-like source is indeed a companion is by probing the gas kinematics (e.g. Perez et al. 2015). Recent ALMA images of the disk shown in Long et al. (2018) suggest a significant amount of residual gas in the gap. Interestingly, their HCO$^+$ J=4-3 velocity dispersion map reveals a peak in velocity dispersion of ~ 2.5km s^{-1} at the location of our companion candidate (bottom left panel of their Fig. 4), which is the kinematic imprint expected from a $\sim 5 M_{\rm Jup}$ companion (Perez et al. 2015). Furthermore, both their continuum and HCO$^+$ moment 0 images suggest the presence of

a gap-crossing filament at roughly the same PA as our tentative spiral-like feature (their Figs. 1 and 2). Nonetheless, their beam is only slightly smaller than the separations involved with our companion candidate and tentative spiral arm. Therefore new ALMA observations at higher angular resolution are required to confirm the possible connections between features seen in our near-IR image and at sub-mm wavelengths. If the planet nature is confirmed, PDS 70 b would be one of the first protoplanets detected around a young Solar analog.

Appendix A: Fake spiral arm injections

In order to assess the significance of filtering of extended signals, we injected fake spiral arms in copies of our calibrated 4D cube and re-processed these cubes with the different post-processing algorithms used in this work. The synthetic spirals have the same shape as the observed tentative spiral arm seen between 0″.22 and 0″.31 separation to the S-SW in Fig. 15.14a, but are injected mirroring the observed one with respect to axis PA = 275°(this model is best seen in Fig. 15.17d). This enables to check in particular whether the effect of ADI can truncate the spiral. The observed spiral has an estimated contrast of $\sim$ 7.4 mag between PA $\sim 180°$and 225°. We ran two sets of tests, one with a synthetic spiral that is $\sim$2 mag brighter than the observed one that enables to better visualize the effect of filtering (middle row of Fig. 15.17), and a second set of tests where the synthetic spiral is injected at the same level as the observed one (bottom row of Fig. 15.17). For comparison, the first row of Fig. 15.17 corresponds to the images obtained without fake spiral injection. From our tests, we note that only the PCA-ASDI with $n_{\rm pc}^{\rm ADI} = 1$ and $n_{\rm pc}^{\rm SDI} = 1$ recovers almost the full trace of the injected spiral. In particular, the negative ADI artifact associated to the bright edge of the outer disk systematically truncates the spiral in aggressive reductions that enable to detect the companion candidate. Interestingly, panel (i) of Fig. 15.17 shows a bright blob in the arc at the location where the synthetic spiral meets the arc, similar to the blob observed slightly souther along the arc, where the tentative true spiral meets the arc. The similarity between these two features is another possible indication of the authenticity of the observed spiral-like feature.

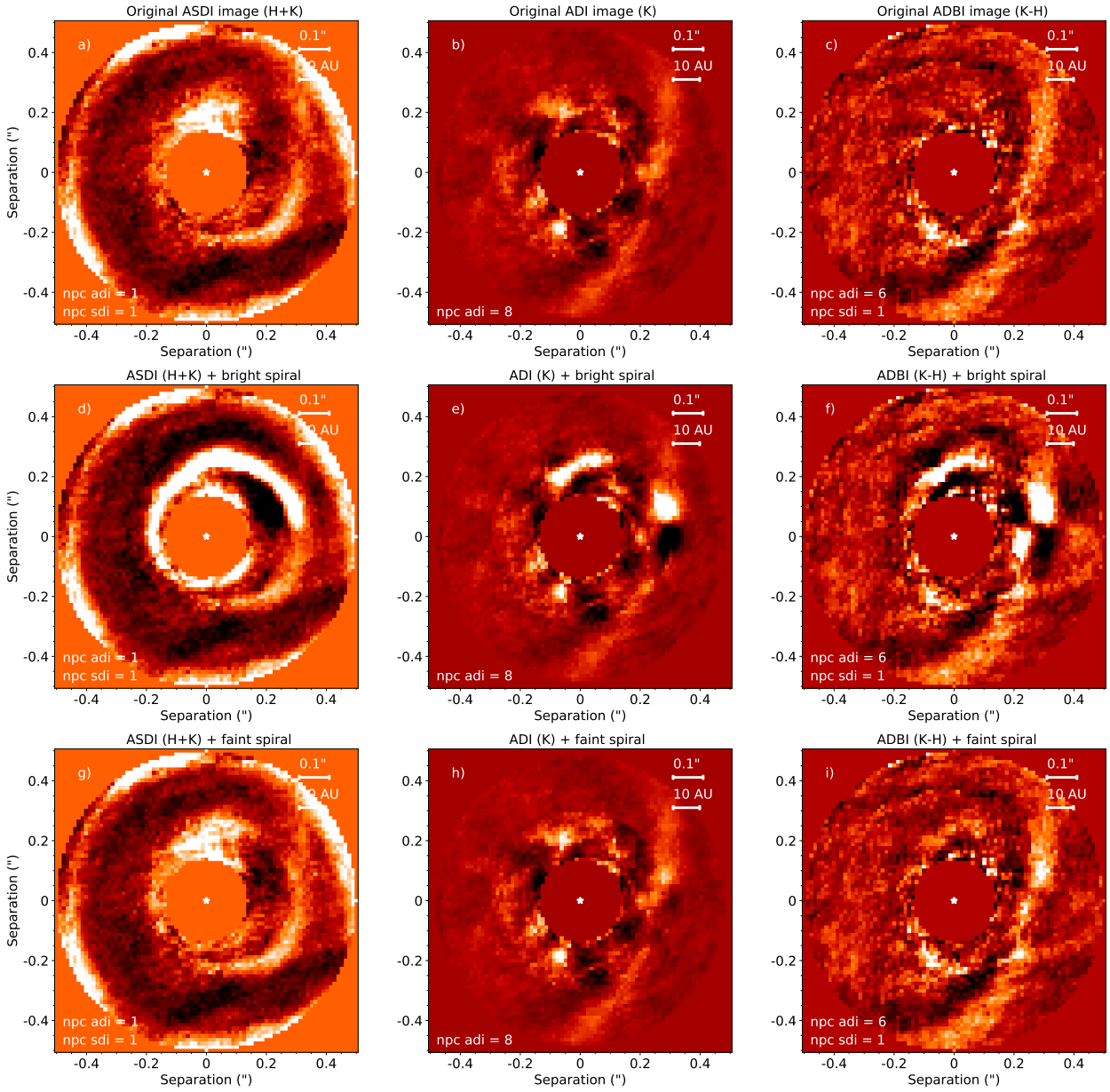

Figure 15.17: Tests of synthetic spiral arm injection. (*Top row*) Final post-processed images obtained without the injection of any synthetic spiral, for the different algorithms tested in this paper: ASDI, ADI (K) and ADBI (K-H). (*Middle row*) Final post-processed images obtained after injection of a synthetic spiral ∼2 mag brighter than the tentative spiral observed towards the S/SW of the star. The spiral model used for injection is the best-fit spiral model shown in Fig. 15.16a, but mirrored along axis PA = 275 °. Its fully recovered only in panel d. (*Bottom row*) Final post-processed images obtained after injection of a synthetic spiral injected at the same level as the tentative observed spiral-like feature. Again, the ASDI reduction (g) is the only one to recover almost the full trace of the injected spiral. Flux scales and limits are fixed in each column of images.

16 Spectral characterization of companions with an IFS

In our SINFONI dataset of HD 142527, we re-detected the companion first identified in Biller et al. (2012) at $\sim$0$''$.08 separation, in each individual spectral channel. This allowed us to retrieve and analyze the spectrum of the companion to infer its physical properties. This is presented in the next section, which consists of the content of our recently accepted A&A paper (Christiaens et al. 2018b). Only Sec. 16.1.3 was summarized compared to the paper version, to minimize redundancy with Secs. 15.2 and 15.3.

16.1 Characterization of low-mass companion HD 142527 B

V. Christiaens, S. Casassus, O. Absil, S. Kimeswenger, C. A. Gomez Gonzalez, J. Girard, R. Ramirez, O. Wertz, A. Zurlo, Z. Wahhaj, C. Flores, V. Salinas, A. Jordan & D. Mawet
A&A, in press

16.1.1 Abstract

The circumstellar disk of the Herbig Fe star HD 142527 is host to several remarkable features including a warped inner disk, a 120 au-wide annular gap, a prominent dust trap and several spiral arms. A low-mass companion, HD 142527 B, was also found orbiting the primary star at $\sim$14 au. This study aims to better characterize this companion, which could help explain its impact on the peculiar geometry of the disk. We observed the source with VLT/SINFONI in H+K band in pupil-tracking mode. Data were post-processed with several algorithms based on angular differential imaging (ADI). HD 142527 B is conspicuously re-detected in most spectral channels, which enables us to extract the first medium-resolution spectrum of a low-mass companion within 0$''$.1 from its central star. Fitting our spectrum with both template and synthetic spectra suggests that the companion is a young M2.5$\pm$1.0 star with an effective temperature of 3500 ± 100 K, possibly surrounded with a hot (1700 K) circum-secondary environment. Pre-main sequence evolutionary tracks pro-

vide a mass estimate of $0.34 \pm 0.06 M_{\odot}$, independent of the presence of a hot environment. However, the estimated stellar radius and age do depend on that assumption; we find a radius of $1.37 \pm 0.05 R_{\odot}$ (resp. $1.96 \pm 0.10 R_{\odot}$) and an age of $1.8^{+1.2}_{-0.5}$ Myr (resp. 0.75 ± 0.25 Myr) in the case of the presence (resp. absence) of a hot environment contributing in H+K. Our new values for the mass and radius of the companion yield a mass accretion rate of 4.1–5.8 $\times 10^{-9}$ $M_{\odot}$ yr^{-1} (2–3% that of the primary). We have constrained the physical properties of HD 142527 B, thereby illustrating the potential for SINFONI+ADI to characterize faint close-in companions. The new spectral type makes HD 142527 B a twin of the well known TW Hya T-Tauri star, and the revision of its mass to higher values further supports its role in shaping the disk.

16.1.2 Introduction

The advents of the Atacama Large Millimeter Array (ALMA) and extreme adaptive optics high-contrast imaging instruments have recently unveiled a wealth of features in protoplanetary disks, including cavities, rings, spiral arms, warps and asymmetric dust distributions (see Casassus 2016, and references therein). A major challenge now is to connect these observed features to the process of planet formation, which is believed to be concomitant. Giant planets must indeed form within the first Myr of the disk life, before all primordial gas is dissipated (Haisch et al. 2001; Hernández et al. 2007). While concentric annular gaps have been observed in protoplanetary disks starting from an early age (e.g. ALMA Partnership et al. 2015; Andrews et al. 2016), a fraction of disks also harbors very large gaps or cavities (> 20 au in radius). This population overlaps with the class of *transition(al) disks* originally identified from their SED (e.g. Strom et al. 1989; Espaillat et al. 2007). Whether a common origin to the large gaps in those disks can be found is still an open debate. Interestingly, most of these disks with very large gaps also show strong mm-flux and significant accretion rates, which would hint towards an origin related to forming planets rather than e.g. photo-evaporation (see Owen 2016, and references therein). Nevertheless, this picture still suffers pitfalls, as the standard disk evolution scenario in the presence of giant planets should lead to a population of mm-bright transition disks with no accretion (e.g. Rosotti et al. 2015), which is not observed.

In this context, the system of HD 142527 constitutes a remarkable case study for protoplanetary disk evolution and possible on-going planet formation. HD 142527 A is an Herbig Fe star surrounded by an inner disk, a gap of 120–130 au in radius seen both in sub-mm and scattered near-IR light, and an outer disk extending up to 700 au (e.g. Fujiwara et al. 2006; Fukagawa et al. 2013; Avenhaus et al. 2017; Christiaens et al. 2014). The inner disk was shown to be inclined by $\sim 70 \pm 5^{\circ}$ with respect to the outer disk (Marino et al. 2015a), and further evidence of this warp was found in the velocity map of CO lines observed with ALMA (Casassus et al. 2015a). In addition to the gap, the outer disk reveals a horseshoe-shaped sub-millimeter continuum (Ohashi 2008; Casassus et al. 2013b) and spiral arms seen in both μm-size dust and CO gas (e.g., Fukagawa et al. 2006; Casassus et al. 2012; Rameau et al. 2012; Avenhaus et al. 2014; Christiaens et al. 2014). The age and mass of the star were estimated to 5.0 ± 1.5 Myr and $\sim$2 $M_{\odot}$ respectively, and the mass accretion rate was constrained to $2 \pm 1 \times 10^{-7}$ $M_{\odot}$ yr^{-1} (Mendigutía et al. 2014; Lacour

et al. 2016). The parallax measured with Gaia corresponds to a distance of 156±6 pc (Gaia Collaboration et al. 2016), which is consistent with the previous estimate of 140 ± 20 pc, based on proximity in the sky and similar proper motion with members of the Upper Centaurus Lupus moving group (de Zeeuw et al. 1999; Teixeira et al. 2000; Fukagawa et al. 2006). We will adopt the Gaia distance throughout this work.

A low-mass companion around HD 142527 was detected using sparse aperture masking (SAM; Biller et al. 2012), and later confirmed with direct imaging in the H_α line (Close et al. 2014) and in Y band (Rodigas et al. 2014). HD 142527 B was found at ~ 88 mas (~ 14 au) from the primary, at the inner edge of the large gap, hence probably shaping the warped inner disk. A recent study suggested that the companion SED could be reproduced by a 3000 K companion with an additional 1700 K circum-secondary disk component (Lacour et al. 2016). Nevertheless, the study did not consider models with other values of effective temperature for the companion and its environment that might also reproduce the observed SED.

More robust information on the nature of low-mass companions can be obtained through low- or medium-resolution spectra. Spectral type classification of young M- and L-type objects can be performed either from comparison to spectral libraries or through the calculation of (gravity-independent) spectral indices (e.g. Allers & Liu 2013; Bonnefoy et al. 2014). Gravity (and hence age) is known to have a significant impact on the spectra of late-type objects (e.g. Lucas et al. 2001; Allers et al. 2007; Cruz et al. 2009; Allers & Liu 2013). For young objects, spectral types can be converted into effective temperatures using a SpT-$T_{\rm eff}$ relationship that is intermediate between those of red giants and red dwarfs (e.g. Luhman et al. 2003). Alternatively, the effective temperature of low-mass companions can also be estimated comparing the observed spectrum to grids of synthetic spectra generated with different atmospheric/photospheric properties (e.g. Fortney et al. 2008; Allard et al. 2012). Using a Hertzsprung-Russel (HR) diagram to compare the effective temperature and absolute magnitude (or total luminosity) with stellar evolution tracks predicted from models allows to estimate the mass and age of young stars (e.g., Siess et al. 2000; Bressan et al. 2012; Baraffe et al. 2015). Finally, near-IR spectra can also provide constraints on the mass accretion rate based on the observed intensity of hydrogen recombination lines (e.g. Muzerolle et al. 1998; Calvet et al. 2004; Mendigutía et al. 2014).

Here, we aim to better characterize low-mass companion HD 142527 B using the integral field spectrograph VLT/SINFONI equipped with its pupil-tracking mode. This analysis will enable to better assess the impact of the companion on the peculiar morphology of the disk in new hydro-dynamical simulations (Price et al. 2018). In Sect. 16.1.3, we describe our observations and subsequent data reduction. Sect. 16.1.4 presents a brief analysis of the spectrum of the primary HD 142527 A. We then detail in Sect. 16.1.4 the procedure to both extract the spectrum of HD 142527 B and estimate photometric and astrometric uncertainties. The companion is analyzed in depth in Sect. 16.1.5, including fits of the spectrum to both synthetic and template spectra, spectral feature identification, and the use of evolutionary models to estimate physical properties of the companion. Results are discussed and compared to previous works in Sect. 16.1.6. Finally, Sect. 16.1.7 summarizes the main conclusions of this work.

16.1.3 VLT/SINFONI observations and data reduction

The observations obtained with SINFONI, along with the four-point dithering pattern used are described in Sec. 15.2. Basic calibration is presented in Sec. 15.3. After this basic reduction, we built ADI cubes for each spectral channel, containing 40 frames each (from the 40 cubes taken in the best conditions), and applied several ADI-based post-processing algorithms on each of them. The post-processing codes were adapted from the open-source Vortex Imaging Post-processing package[1] (VIP; Gomez Gonzalez et al. 2017). Namely, we used (i) classical ADI, where the temporal median is subtracted from each frame pixel by pixel (Marois et al. 2006), (ii) ADI using principal component analysis (PCA-ADI; Amara & Quanz 2012; Soummer et al. 2012) implemented on full frames (hereafter *PCA-full*), (iii) PCA-ADI in several concentric annuli (hereafter *PCA-annuli*), and (iv) PCA-ADI on a single annulus (hereafter *PCA-annulus*). PCA-full is similar to *PynPoint* (Amara & Quanz 2012); the principal components are determined by singular value decomposition of a library consisting of all the ADI frames. With PCA-annuli, each frame is divided in annuli of 2 FWHM width, paving at best the square frames. This time the PCA library is built differently for each annulus, with a frame selection based on a given parallactic angle threshold, instead of admitting all the observed ADI frames. We set this parallactic angle threshold to 0.5 FWHM minimum linear displacement at the radial separation of the companion. This threshold acts to keep out of the PCA library the frames where the companion would not have rotated sufficiently, as these frames would lead to significant self-subtraction of the companion. Finally, PCA-annulus performs PCA with no parallactic angle threshold on a single 2 FWHM-wide annulus. The latter method is much faster than the first ones, but needs a first estimate of the companion location to optimally define the annulus.

16.1.4 Results

The SINFONI spectrum of HD 142527 A

We extracted the raw spectrum of HD 142527 A with aperture photometry performed in each channel after basic calibration; i.e. before ADI post-processing. The radius of the aperture was set to 0.5 FWHM, with the FWHM ranging from 4.9 to 6.4 pixels between the first and last spectral channel as a combined consequence of the power dilution of the PSF with wavelength and a poorer Strehl ratio at shorter wavelength. This raw spectrum was then corrected for telluric lines. Standard stars were observed before and after HD 142527, however either relative humidity or seeing were significantly different from their respective value during the observation of the science target. Therefore, we used the *molecfit* tool (Smette et al. 2015; Kausch et al. 2015) for a refined correction of the telluric lines, based on fitting synthetic transmission spectra to our data. We also applied molecfit to the spectrum of the standard star observed in similar relative humidity but poorer seeing conditions to HD 142527, this allowed us to flag spectral channels where the telluric correction did not perform well and left significant residuals in the spectrum. These channels were

[1] `https://github.com/vortex-exoplanet/VIP`

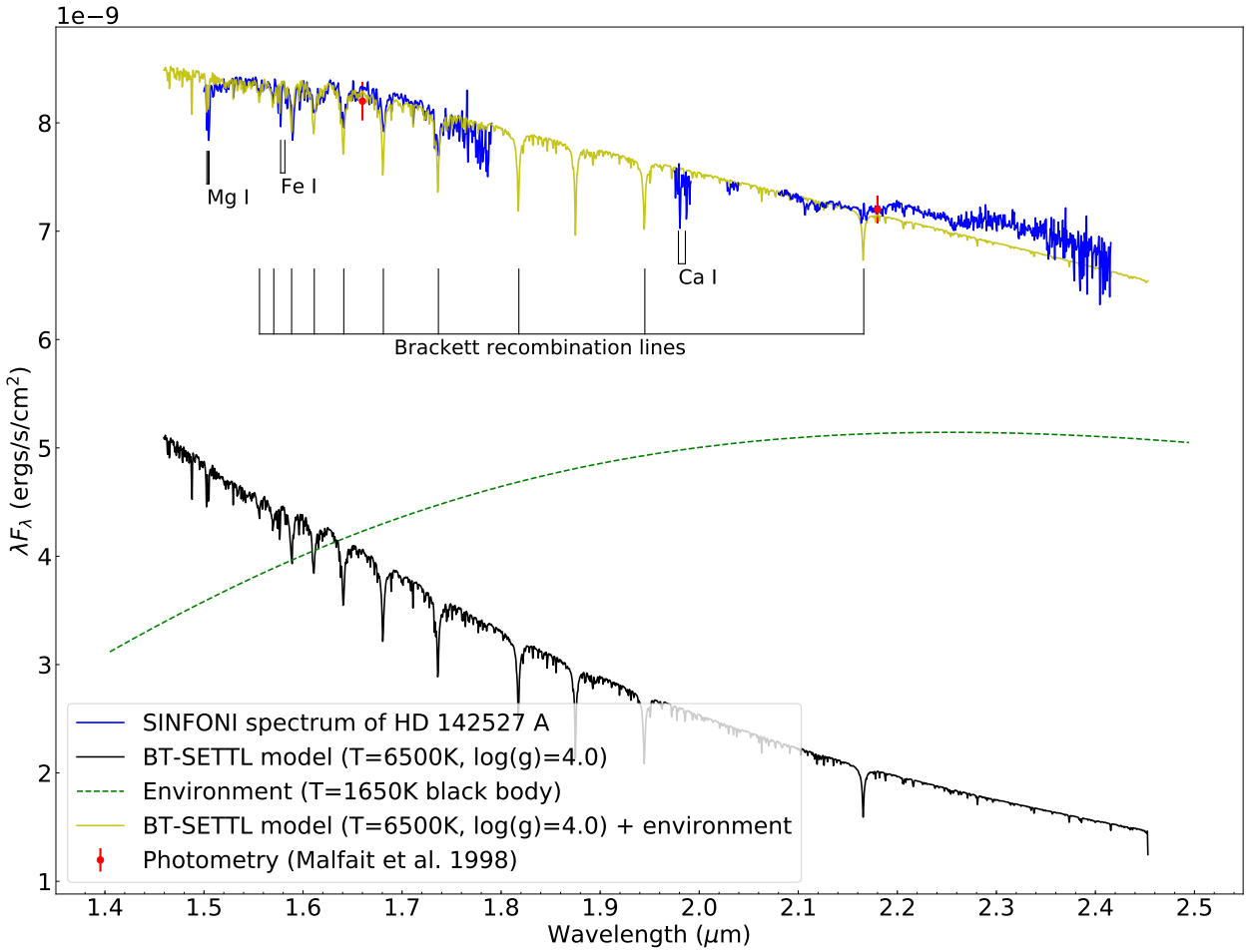

Figure 16.1: Observed spectrum of HD 142527 A after telluric and instrumental response corrections (*blue curve*). The *yellow* curve corresponds to the combination of a BT-SETTL model (T=6500 K, log(g)=4.0; *black curve*) and a black body of 1650 K (*green dashed curve*) representative of the hot inner disk rim. Blanks in the SINFONI spectrum correspond to spectral channels where telluric lines were poorly corrected, and are hence discarded for the rest of the analysis.

removed from the spectrum of HD 142527 A for the rest of the analysis. The spectral slope of our observed spectrum was corrected from instrumental response using the model SED of HD 142527 A used in Casassus et al. (2015b).

The final spectrum of HD 142527 A, provided in Fig. 16.1, is consistent with the H- and K-band photometry reported in Malfait et al. (1998). We compare it to a model spectrum composed of a BT-SETTL model with T= 6500 K and log(g)=4.0, and a dust/hot gas environment with a temperature of 1650 K with an emitting surface area of radius 0.10–0.15 au. The environment temperature and physical extension are in agreement with constraints derived from modeling of near-IR interferometry observations (Lazareff et al. 2017). The BT-SETTL model used for the primary is consistent with the best-fit temperature and gravity inferred from the VLT/XSHOOTER spectrum (Mendigutía et al. 2014). The BT-SETTL model was scaled using a radius of $3.20 R_\odot$, which is consistent with the expected radius of $3.19^{+0.41}_{-0.47} R_\odot$ based on the effective temperature of the star and its measured total luminosity ($16.3 \pm 4.5 L_\odot$; Mendigutía et al. 2014). An extinction of A_V=0.8 was considered

to redden the model (Lazareff et al. 2017). In order to be compared with our H+K spectrum, our model is convolved with a gaussian kernel with a size equal to the spectral PSF of SINFONI in the H+K mode, and smoothed to the spectral resolution of our SINFONI data (5 Å per channel). The observed spectrum shows some excess emission at the red end of K-band with respect to the BT-SETTL + hot environment model, which can be explained by a combination of 2 factors: (i) the contribution of the inner (circumprimary) disk is more significant towards longer wavelengths, and (ii) the FWHM is larger in channels at the red end of the spectrum so that aperture photometry in those spectral channels includes more signal from the inner disk.

Figure 16.1 also labels the main spectral features identified in the VLT/SINFONI spectrum of HD 142527 A. The photospheric recombination lines of the Brackett series (Br14, Br13, Br12, Br11, Br10 and Br7 at 1.588, 1.611, 1.641, 1.681, 1.737 and 2.166 μm resp.) appear mostly veiled, based on the comparison between the observed spectrum and the BT-SETTL+hot environment model. This is an expected consequence from magnetospheric accretion (e.g. Folha & Emerson 1999; Muzerolle et al. 2001), which appears compatible with the significant mass accretion rate inferred in Garcia Lopez et al. (2006) and Mendigutía et al. (2014): $\sim 7 \times 10^{-8}\ M_{\odot}$ yr^{-1} and $2 \pm 1 \times 10^{-7}\ M_{\odot}$ yr^{-1}, respectively. The most significant *emission line* is the strong Brackett-gamma (Br$_{\gamma}$) line (2.16612 μm) that is marginally standing out from the underlying deep photospheric line. This line was already used by Garcia Lopez et al. (2006) and Mendigutía et al. (2014) to estimate the mass accretion rate of HD 142527 A, based on observations of VLT/ISAAC and VLT/X-SHOOTER respectively. The shape of the observed line is in agreement with what would be obtained when degrading the X-SHOOTER spectrum to the spectral resolution of SINFONI. In addition to the Brackett recombination lines, we also note the presence of absorption lines for the Mg I triplet (1.503, 1.504 and 1.505 μm), Fe I doublet (1.577 and 1.582 μm) and Ca I doublet (1.979 and 1.986 μm) in the observed spectrum, which are all stronger than expected from the model. This could suggest that we are witnessing additional absorption by refractory material in the close environment of the primary.

In Appendix 16.1.8, we describe our re-analysis of the VLT/XSHOOTER data used in Mendigutía et al. (2014), which leads to a refined estimate of F6$\pm$0.5III-V for the spectral type of HD 142527 A. This is compatible with the effective temperature estimates suggested both in Mendigutía et al. (2014) and by our comparison of the SINFONI spectrum to a BT-SETTL+hot environment model. The physical characteristics of the primary inferred both in previous works and from our SINFONI and XSHOOTER data analysis are summarized in Table 16.1.

Comparison of our SINFONI spectrum to both the X-SHOOTER spectrum and a BT-SETTL+hot environment model consistent with previous literature indicates that the telluric correction and spectral calibration are valid. Nevertheless, for such low resolution spectrum, the telluric correction is not reliable in some wavelength ranges dominated by atmospheric absorption which we choose to not show in Fig. 16.1 and discard for the rest of our analysis. We are left with 1313 channels out of the 1992 original channels.

Table 16.1: Characteristics of HD 142527 and its close environment

Parameter	Value	Ref.
HD 142527 A		
Right ascension	$15^{\rm h}56^{\rm m}41^{\rm s}.89$	
Declination	$-42°19'23''.5$	
Spectral type	F6±0.5III–Ve	1, 2
$T_{\rm eff}$ [K]	6500 ± 100 / 6550 ± 100	1, 3
Log(g)	3.75 ± 0.10	3
Luminosity [$L_\odot$]	16.3 ± 4.5	3
Age [Myr]	5.0 ± 1.5	3
Mass [$M_\odot$]	2.0 ± 0.3	3
Radius [$R_\odot$]	3.2 ± 0.2	1
Distance [pc]	156 ± 6	4
A_V [mag]	0.60 ± 0.05 / 0.80 ± 0.06	5, 6
Dust/hot gas environment		
Temperature [K]	1650 ± 50 / 1680 ± 100	1, 6
Radius [au]	0.10–0.15 / < 0.15	1, 6

References: (1) This work; (2) Houk (1978); (3) Mendigutía et al. (2014); (4) Gaia Collaboration et al. (2016); (5) Verhoeff et al. (2011); (6) Lazareff et al. (2017).

Extraction of the spectrum of HD 142527 B

Re-detection of the companion The companion is re-detected in most spectral channels after the use of different ADI-based post-processing algorithms. For illustration, the companion detection is shown for the spectral channel corresponding to the Br$_\gamma$ line in Fig. 16.2a, b, c, and d, respectively for classical ADI, PCA-full, PCA-annuli, and PCA-annulus (see Sect. 16.1.3 for a description of the algorithms). The corresponding signal-to-noise ratio (SNR) maps are provided in Fig. 16.2e, f, g and h respectively. The SNR was computed as in Mawet et al. (2014), hence including the small-sample statistics penalty.

For the spectral channel specific to the Br$_\gamma$ line, all post-processing methods provide a SNR > 3 detection of the companion. The PCA algorithms yield a higher SNR than classical ADI, although the exact SNR value depends on the number of principal components n_{pc} used. The companion is recovered with an SNR $\gtrsim 3$ for n_{pc} ranging from 1 to $\sim$20 with either PCA-full or PCA-annuli, and for n_{pc} ranging from 1 to 15 with PCA-annulus. Using either classical ADI or PCA-annuli results in a higher residual speckle noise at the separation of the companion ($\sim$80 mas). The speckle pattern in the frames created with classical ADI or PCA-annuli for PSF subtraction is indeed intrinsically less correlated to the speckle pattern in the science frames than frames created with PCA-full or PCA-annulus. As can be seen in Fig. 16.2a and c, the residual speckle pattern could be triangular with a possible contribution under the location of the companion. For the rest of the analysis in this paper, we favor the PCA-annulus algorithm for ADI processing owing to its reduced computation time, and consider $n_{pc} \in [5, 10]$ to reach a low residual speckle noise level while not over-subtracting the flux of the companion. This choice is confirmed by our SNR estimates of the companion in all spectral channels. The detection is above 3σ in all H+K channels,

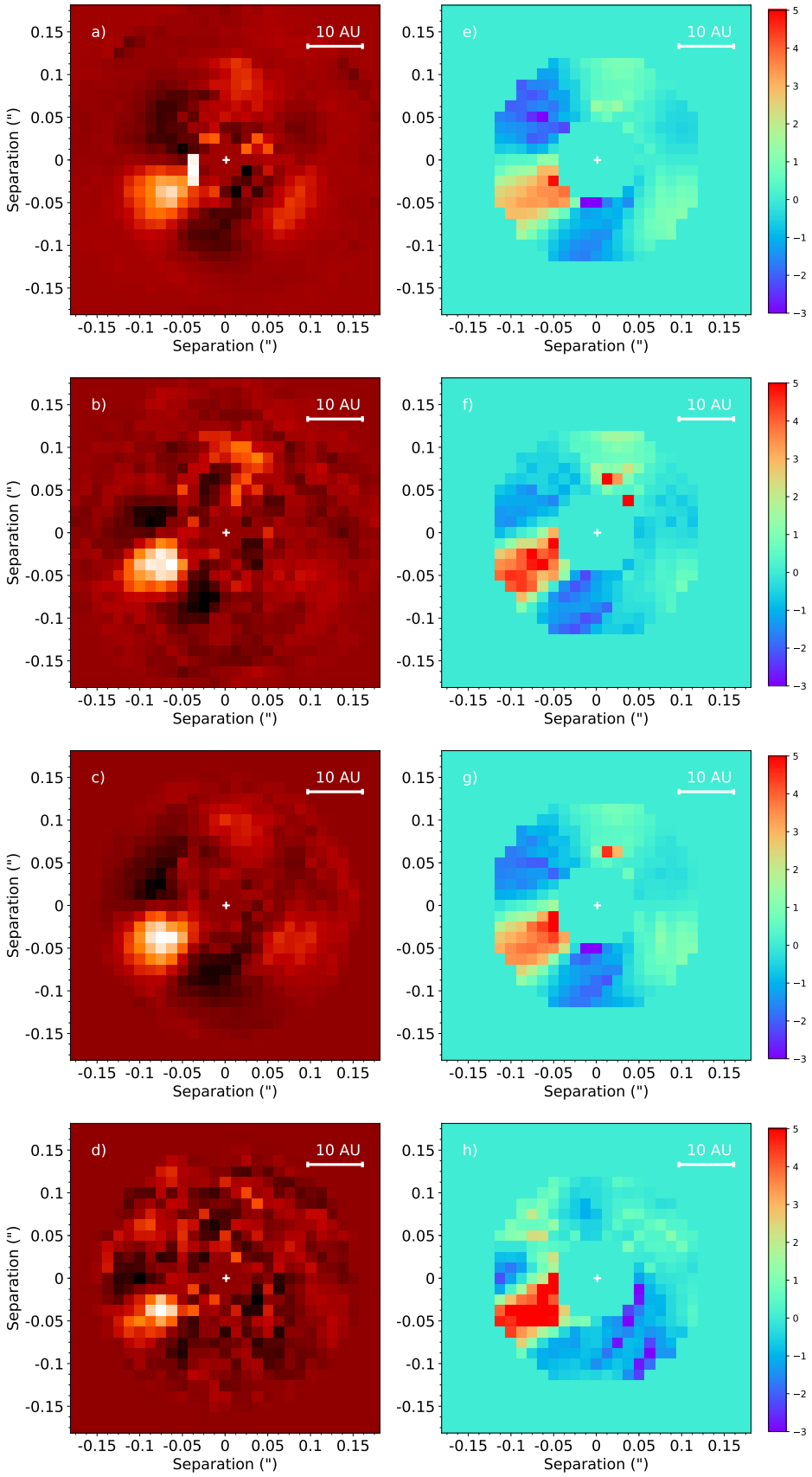

Figure 16.2: Post-processing of the Br$_\gamma$ line spectral channel with **a)** classical ADI; **b)** PCA-full with $n_{pc} = 7$; **c)** PCA-annuli with $n_{pc} = 15$; **d)** PCA-annulus with $n_{pc} = 10$. **e) - h)** SNR map of a) - d) respectively.

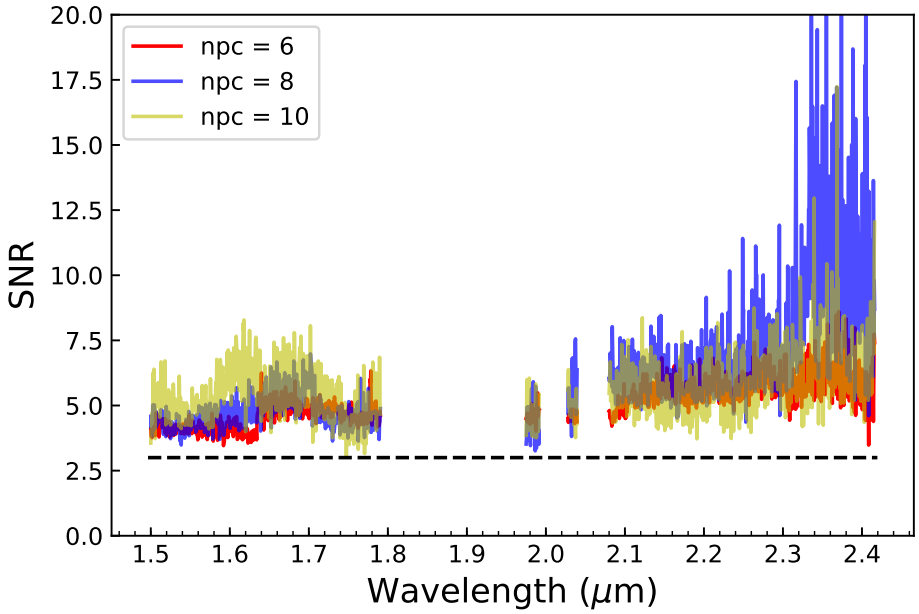

Figure 16.3: SNR of the detection in each channel using PCA-annulus with 6, 8 and 10 principal components. The *black dashed line* corresponds to an SNR of 3.

and above 5σ in most K-band channels (Fig. 16.3).

Photometric and astrometric retrieval Motivated by the conspicuous detection of HD 142527 B in most spectral channels, we used the negative fake companion technique (NEGFC; Marois et al. 2010a; Lagrange et al. 2010) implemented in the VIP package in order to obtain an unbiased estimate of the photometry and astrometry of the companion in all channels (see details in Wertz et al. 2017). It is known that ADI algorithms affect the location and flux of any companion in the processed images. The NEGFC technique circumvents this limitation with the injection of a negative fake companion in the frames before they are processed with ADI. For each spectral channel, we used the normalized median of the stellar PSF across the original 40 cubes as a template PSF for the fake companion to be injected with a negative flux. At each wavelength, the method finds the optimal combination of radial separation r_λ, position angle PA_λ and negative flux $-f_\lambda$ of HD 142527 B that minimizes a specific figure of merit in the ADI-processed frame. The figure of merit consists usually in minimizing either the sum of absolute pixel intensities or the standard deviation of pixel values in a circular aperture centered on the companion location in the post-processed frame.

As described in Wertz et al. (2017), the optimization process of the figure of merit is performed in two steps (see the first two steps of their Sect. 3.2). We first run a grid search on the companion flux, assuming a fixed companion position given by its highest pixel value. The optimal flux and rough companion position are then used as input to run a more precise downward simplex algorithm using the same figure of merit but with three free parameters: r_λ, PA_λ and $-f_\lambda$.

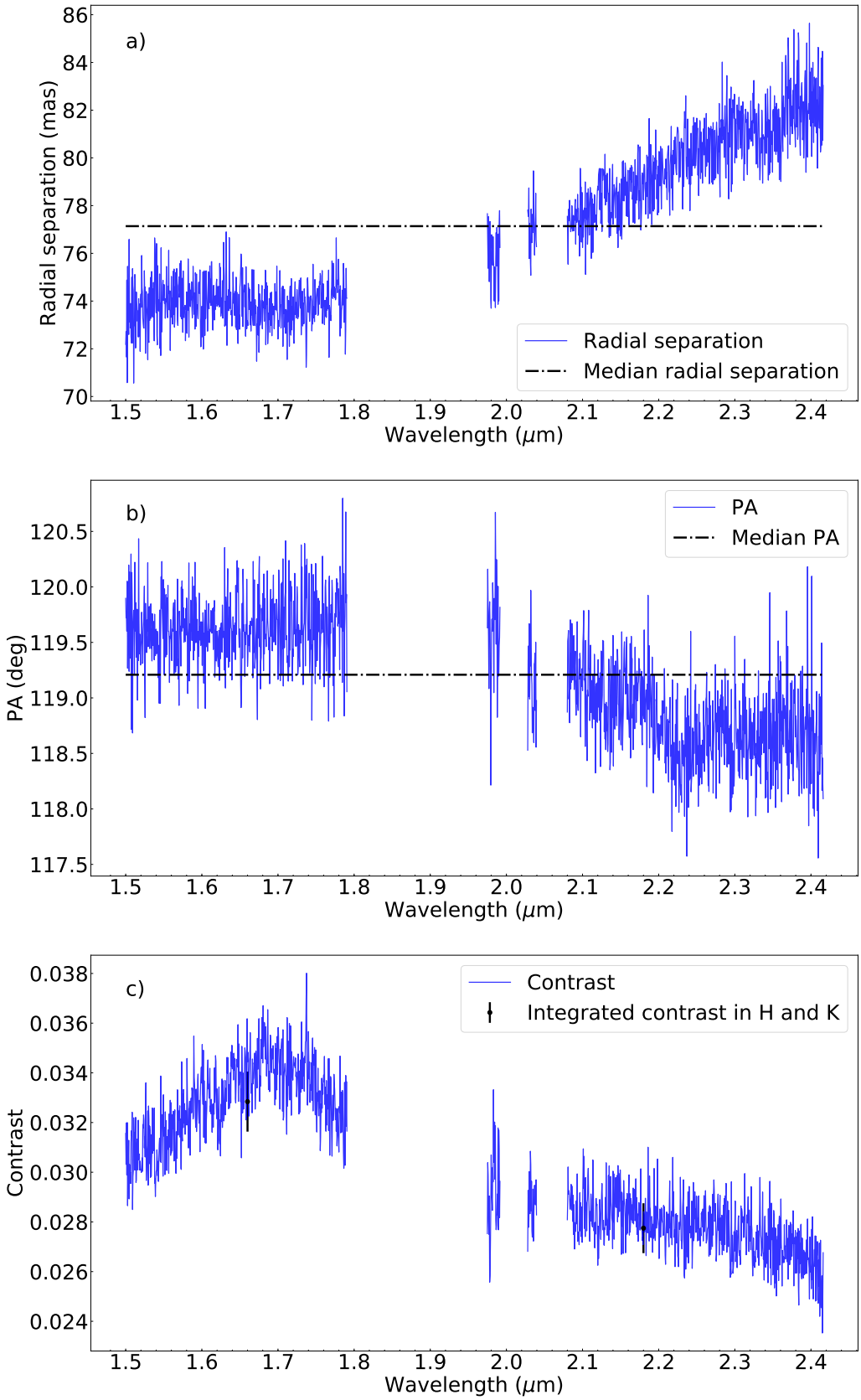

Figure 16.4: **a)** Radial separation, **b)** PA and **c)** contrast of HD 142527 B in all H+K channels, as determined with NEGFC. The median separation and PA over all channels are indicated with *dashed-dot lines*. The contrasts integrated using the H- and K-band filter transmission curves of VLT/NACO, are provided with *black error bars*.

The choice of parameters associated to NEGFC, such as the number of principal components to be used, the size of the aperture and the figure of merit to be optimized, is crucial to obtain reliable results. We noticed that using a single set of parameters led to a significant amount of outliers in estimated r_λ, PA$_\lambda$ and f_λ throughout the 1313 spectral channels of our spectrum. Therefore, we considered different sets of NEGFC parameters within reasonable ranges, constrained as follows:

- For the post-processing ADI algorithm, we chose PCA-annulus, owing to its time-efficiency, with $n_{pc} \in [5, 10]$ as it optimizes the SNR of the companion (Fig. 16.3). This range of n_{pc} also provides a visually low residual speckle noise level while preserving the flux of the companion from significant oversubtraction.
- We considered two different figures of merit: minimizing either the sum of absolute pixel intensities or the standard deviation of pixel values in a circular aperture centered on the companion location in the post-processed frame.
- We used 0.7 and 0.9 FWHM-radius circular apertures for the minimization of the figure of merit. These choices are justified by (i) the requirement for the aperture radius to always be shorter than the radial separation of the companion ($\sim$ 6.4 pixels, or $\sim$ 1 FWHM at the longest wavelength) and (ii) the need for a sufficient number of pixels in the aperture for the figure of merit to be statistically meaningful and hence enable convergence to the correct solution.

For each spectral channel, we considered the median parameters of the companion derived using the $6 \times 2 \times 2 = 24$ different sets of NEGFC parameters. The median enabled to discard all outlier results, which suggests that NEGFC converges in general to a consistent solution in terms of r_λ, PA$_\lambda$ and $-f_\lambda$, but that particular combinations of aperture size, figure of merit and number of principal components can sometimes lead to significant contamination by residual speckle noise. The results are reported in Fig. 16.4. The radial separation and PA of the companion derived in each spectral channel are compared to their median value over all spectral channels. The flux of HD 142527 B is expressed as a contrast with respect to the primary star.

In Fig. 16.4a, we notice that r_λ seems to increase slightly with wavelength in K band (by up to $\sim$10 mas), which is reminiscent of the behavior of a speckle. However, a speckle at that radial distance would move radially by $\sim$50 mas from 1.45 μm to 2.45 μm, and would also be expected to show a more monotonic trend. Nevertheless, a putative speckle located at 60 mas at the short end of H band would lie at less than 1 FWHM from the companion, and would still be unresolved from the companion at the long end of the K band, possibly shifting the centroid of the companion depending on its flux ratio. Another possibility is that the companion emission is radially extended (outward) with a stronger contribution at longer wavelength. This feature was already noted by Rodigas et al. (2014) with polarimetric observations, which could indicate the presence of heated material at larger separation from the companion, shifting the centroid accordingly. The PA variation with wavelength (Fig. 16.4b) appears intimately related to r_λ, in particular at longer wavelengths, where PA$_\lambda$ appears to decrease slightly while r_λ increases (Fig. 16.4b).

The median values of radial separation and PA of HD 142527 B over all H- and K-band channels are 77.1$\pm$3.3 mas and 119.2$\pm$0.6°, respectively. The quoted uncertainties are the

standard deviation of r_λ and PA_λ over all channels, respectively. More robust estimates of the uncertainty on these values are provided in Sect. 16.1.4.

Regarding the contrast ratio with respect to the primary (Fig. 16.4c), we notice a triangular shape throughout the H band with values ranging between 0.030 and 0.036. The contrast ratio in K band shows a monotonically decreasing trend from 0.030 to 0.025 with increasing wavelength. We integrated the derived contrasts using the H- and K-band filter transmission curves of VLT/NACO, and found that the H-band (resp. K-band) contrast is $3.28 \pm 0.12 \times 10^{-2}$ (resp. $2.78 \pm 0.10 \times 10^{-2}$).

Estimation of the uncertainties At such small angular separation from the primary ($\sim$ 77 mas), the residual speckle noise is expected to be the largest source of uncertainty on the radial separation, PA and contrast of HD 142527 B derived by NEGFC. The procedure that we followed to estimate the residual speckle noise uncertainties on the parameters of the companion in each spectral channel is described in Appendix 16.1.9. We used a weighted mean over all spectral channels to estimate the final radial separation and PA of the companion. This leads to $r = 6.24 \pm 0.14$px ($r = 78.0 \pm 1.7$ mas) and PA $= 119.1 \pm 0.8°$.

Nervertheless, a complete astrometric error budget should not only consider the residual speckle noise uncertainties, but also (i) the error associated to the centering of the star in the frames, (ii) the error related to the plate scale (~ 12.5 mas per pixel), and (iii) the errors related to true North and pupil offset (Wertz et al. 2017). The stellar PSF is not saturated in any of our data. Hence, the centering of the star was simply performed with a gaussian fit of the centroid. Comparison with a Moffat fit in all spectral channels provides an agreement of $\sim$0.05 pixel. We do not expect the error associated to stellar centering to be much larger. It has to be noted that we lack appropriate observations to derive a proper estimate of the errors associated to plate scale, true north and pupil offset. However, Meshkat et al. (2015) quoted total uncertainty values (including true north) of 0.4 mas and 0.5° for r and PA for another low-mass companion detected by SINFONI in pupil tracking. The latter companion was found further away from its central star, hence relatively free from speckle noise contamination. As our companion lies at much closer separation, the term associated to the plate scale uncertainty (proportional to r^2) in the error budget is expected to be negligible. Their observations were only a few months apart from ours, so we can assume similar errors on true north and pupil offset as theirs. We conservatively consider their uncertainties and sum them in quadrature to our residual speckle uncertainties. Our final astrometry is thus the following: $r = 78.0 \pm 1.8$ mas and PA $= 119.1 \pm 1.0°$. These values are in agreement with the expected position given by MagAO and GPI data acquired at the same epoch (Rodigas et al. 2014; Lacour et al. 2016).

Our tests in Appendix 16.1.9 suggest that an uncertainty of up to 15% could affect the estimated absolute contrast of the companion if it lies on top of a speckle feature similar to the second brightest artefact (after the companion itself) seen at the same radial separation (Fig. 16.2). However, we also estimated a relative uncertainty $\lesssim 5$% regarding the shape of the contrast spectrum, even when on top of such speckle feature. This suggests that a spectrum of good quality can be extracted for the companion.

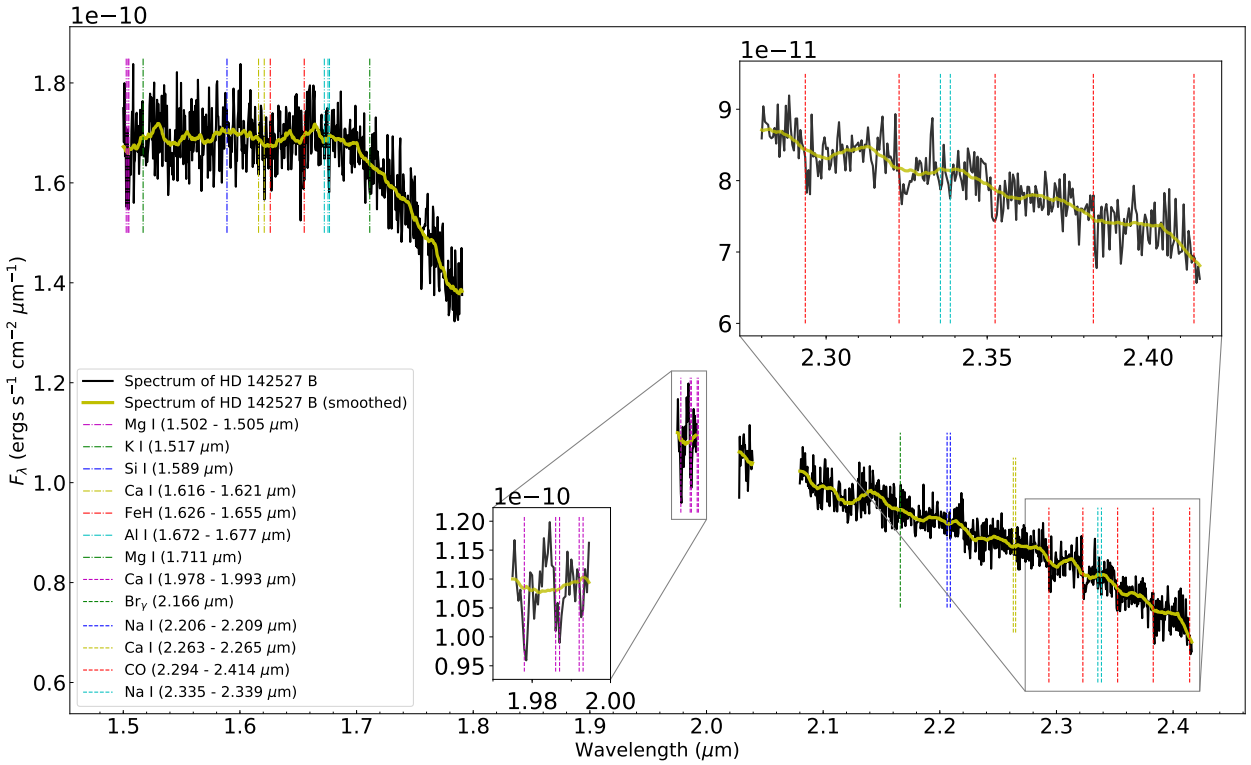

Figure 16.5: Observed H+K spectrum of HD 142527 B (*black curve*) and spectrum after Savitzky-Golay filtering (*yellow curve*), along with expected lines in the spectrum of an early to mid-M dwarf. Lines in H- and K-band are provided with *dashed-dot* and *dashed lines*, respectively. The combined presence of five tentative jumps at expected CO transitions (2.294, 2.323, 2.352, 2.383 and 2.414 μm) makes the detection of the first overtone of CO bandhead significant. The Ca I quintuplet (1.978, 1.986, 1.987, 1.992 and 1.993 μm) also appears to be detected, although this area is bordered by poorly corrected telluric features (not shown) which inspire caution. Insets zooming on the Ca I quintuplet and CO bandhead spectral regions are provided.

Spectrum of HD 142527 B The spectrum of the companion is simply obtained by multiplying the spectrum of HD 142527 A (Fig. 16.1) by the contrast ratio found in each spectral channel (Fig. 16.4c). It is given in Fig. 16.5. Both the absolute and relative flux uncertainty on the spectrum of HD 142527 A are negligible compared to the uncertainty on the contrast of HD 142527 B (Sect. 16.1.4). The absolute flux uncertainty of the primary is very small given the consistency between our spectrum and H- and K-band photometric measurements (Verhoeff et al. 2011, Fig. 16.1). The relative flux uncertainty on the spectrum of HD 142527 A is related to the extraction of the spectrum using aperture photometry in each spectral channel. Based on Poisson statistics, we estimate the latter to be $\lesssim$0.5% in all channels. Therefore, we only consider the uncertainties related to residual speckle noise in the rest of this work, since it is at least an order of magnitude larger than the uncertainties related to the spectrum of HD 142527 A.

We applied a Savitzky-Golay (SG) filter (Savitzky & Golay 1964) with a window size of 51 channels and a polynomial of order 3 to smooth our spectrum. This is shown with the *yellow curve* in Fig. 16.5. We compared the SG-filtered spectrum and the spectrum after a weighted binning of factor 6 (where the weight is inversely proportional to the contrast uncertainty), and noted that the resulting curves are consistent with each other. We favor the SG-smoothing, as it does not suffer from a loss in wavelength resolution and is known

to be more robust to outliers than channel binning (Savitzky & Golay 1964).

16.1.5 Characterization of HD 142527 B

The spectrum of HD 142527 B shows a relatively flat H-band continuum shortward from 1.7 μm followed by a steep drop, turning into a moderate negative slope in K-band. This shape contrasts with the $H + K$ spectrum of young brown dwarfs (spectral type later than M6), characterized by a triangular shape H-band spectrum peaking at $\sim$1.67 μm and a hump in K band centered on 2.25μm, which are the results of broad water absorption bands (Jones et al. 1994; Lucas et al. 2001; Reid et al. 2001; Luhman et al. 2004; McGovern et al. 2004). The absence of these easily identifiable features suggests that HD 142527 B is of earlier spectral type than M6. In Fig. 16.5, we show lines expected to be present in the H+K spectrum of early to mid-M dwarfs. They will be discussed in Sect. 16.1.5. Hereafter, we will carry out an in-depth analysis of the spectrum of the companion in order to better constrain its spectral type, effective temperature, surface gravity, mass and age.

Fit with BT-SETTL models

In order to interpret the H+K spectrum of HD 142527 B, we first compare it to a set of BT-SETTL synthetic spectra[2] (Allard et al. 2012). BT-SETTL models are available for a large range of temperatures and surface gravities. These synthetic spectra are given in flux units at the stellar surface. In consequence, one has to assume a certain distance, stellar radius and extinction to be able to compare the models with our observations. Assuming a distance of 156 pc (Gaia Collaboration et al. 2016), only the stellar radius and extinction are left as free parameters. We choose to not fix the extinction to any value estimated for the primary given the possibility that the companion is self-embedded or surrounded by an optically thick circum-secondary disk. Models are considered on a grid of four free parameters: effective temperature, surface gravity, stellar radius and extinction. In order to reflect the possible near-IR contribution of hot circumsecondary material, we considered a second fit including two additional parameters: the radius and temperature of a hot inner rim (see e.g. Cieza et al. 2005). Free parameters and related assumptions are detailed in Sect. 16.1.5.

Although photometric measurements of the companion are available at other wavelengths, we chose to fit the BT-SETTL models to our H+K spectrum alone. This is motivated by the facts that (i) an arbitrary choice of relative weight given to the spectroscopic and photometric points might change the best-fit result, and (ii) flux calibrations with different instruments used at separate wavelengths could introduce unpredictable biases in the results. For comparison with our H+K spectrum, the BT-SETTL models are convolved with a gaussian kernel with a size equal to the spectral PSF of SINFONI for the mode we used, and smoothed to the spectral resolution of our observations (5 Å per channel).

[2] `http://perso.ens-lyon.fr/france.allard/`

Free parameters

Effective temperature The parameter with the most impact on the shape of the spectrum is the effective temperature of the companion ($T_{\rm eff}$). Its value is intimately related to the slope of the model spectrum between 1.7 and 2.4 μm. The BT-SETTL grid of synthetic spectra ranges from 1200 K to 7000 K in $T_{\rm eff}$, with steps of 100 K. Based on visual similarity of spectral slopes between data and model and on the previous estimate of 3000 K from Lacour et al. (2016), we restricted the grid used for the fit to temperatures between 2600 and 4500 K.

Surface gravity The surface gravity ($\log(g)$) has an impact on the *cuspiness* of the spectrum at around 1.7 μm. This is related to water vapor absorption bands, shortward of 1.55 μm and longward of 1.72 μm, being more significant at lower gravity (e.g. Allers et al. 2007). We tested values of surface gravity from 2.5 to 4.5 with steps of 0.5, hence covering the range in values of $\log(g)$ corresponding to giants and main sequence stars.

Stellar radius The BT-SETTL synthetic spectra are provided in units of emitted flux at the stellar surface. Thus, the stellar radius R_B is adjusted to scale each model to units of observed flux through the dilution factor ($R_B^2/{\rm d}^2$), where the distance d is set to 156 pc. Our grid included 150 values of R_B geometrically spaced between 0.1 and 10.0 $R_\odot$.

Extinction We assumed that extinction can be characterized by only one parameter: A_H, the extinction in H band . This value is then extrapolated to other wavelengths using a total-to-selective extinction ratio R_V = 3.1 following Draine (1989). The extinction that is applied to the different models is adjusted to match the global slope of the continuum from H to K band. We tested values of A_H between 0 and 1.2, per steps of 0.05, hence including the values of $A_V = 0.6$ ($A_H \sim 0.1$), $A_V = 0.8$ and $A_H = 0.3$ suggested in Verhoeff et al. (2011), Lazareff et al. (2017) and Close et al. (2014), respectively.

Circum-secondary disk In view of both the young age of the system and the detection of H_α emission at the location of HD 142527 B (Close et al. 2014), it is conceivable that the companion is surrounded by a circum-secondary disk. Its inner rim could be at sufficiently high temperature to contribute significantly to the near-IR flux (e.g. Cieza et al. 2005). We assumed for simplification that the latter could be represented by a uniform disk emitting as a black body, hence requiring only two parameters for its characterization: the disk radius $R_{\rm d}$ and temperature $T_{\rm d}$. We tested values of temperature ranging from 1000 K to 1700 K per steps of 100 K, with 22 values of radii geometrically spaced between 0.005 and 0.100 au ($\sim$ 1.5 to 20 $R_\odot$). We are not sensitive to temperatures lower than $\sim$ 1000 K, since they do not lead to a significant contribution in H or K band. Temperatures above 1700 K are not considered as the dust would be likely sublimated (see e.g. Meyer et al. 1997). We insist on the fact that this is a very simplistic representation of the inner rim, which aims to answer qualitatively the question of whether the observed spectrum

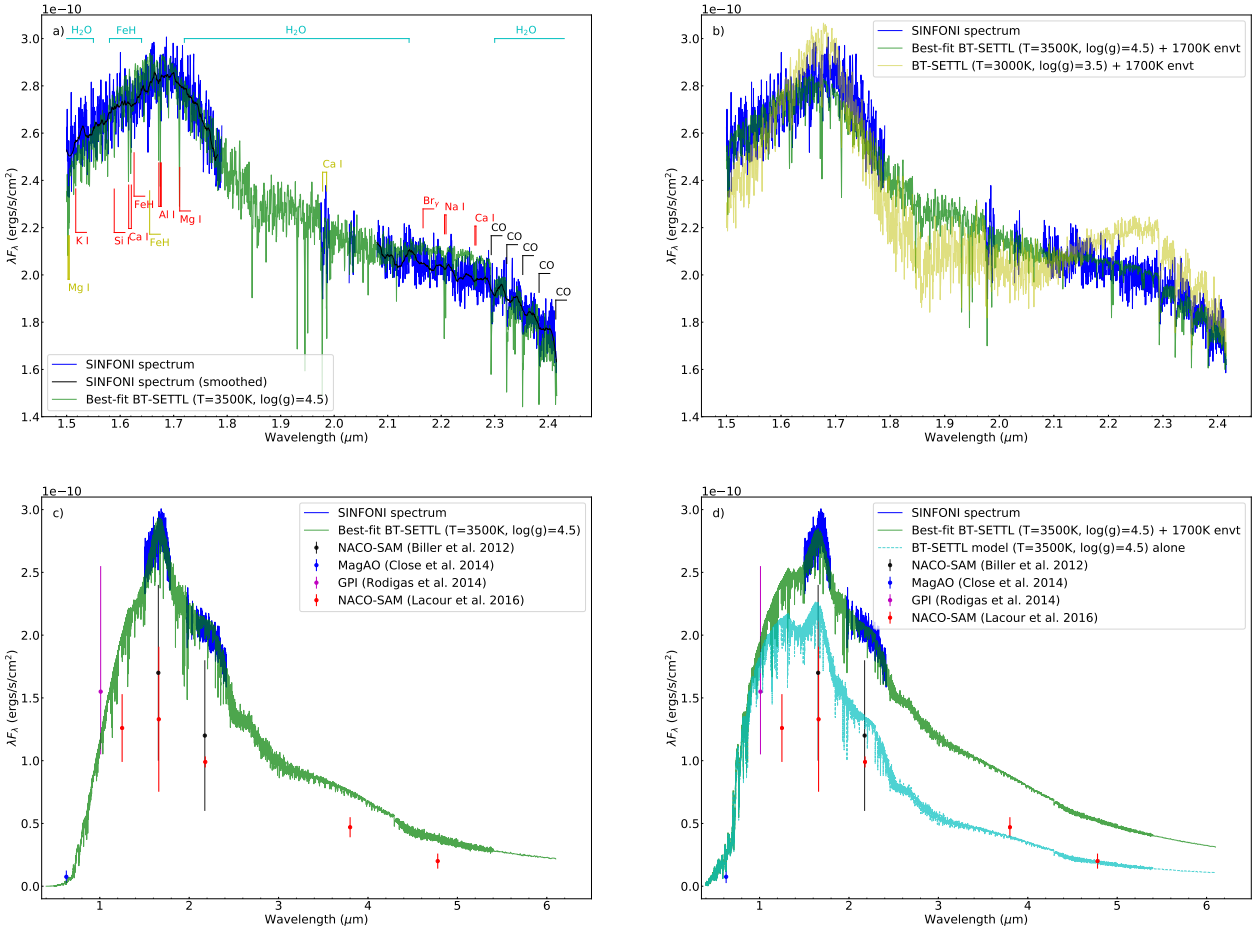

Figure 16.6: **a)** Observed H+K spectrum of HD 142527 B (*blue curve*) and spectrum after Savitzky-Golay filtering (*black curve*). The best-fit BT-SETTL synthetic spectrum is obtained with $T_{\rm eff} = 3500$ K and $\log(g) = 4.5$ (*green curve*). For reference, we provide the location of spectral lines that are expected in the H+K spectrum of M-type stars. Lines labeled in black, yellow and red are detected, tentatively detected and non-detected in the SINFONI spectrum, respectively. **b)** The observed H+K spectrum of HD 142527 B (*blue curve*) is compared to the best-fit BT-SETTL+black body model, representing the photospheric and hot circum-secondary environment contributions, respectively. The best fit is obtained with a $T_{\rm eff} = 3500$ K and $\log(g) = 4.5$ BT-SETTL model, with a 1700 K environment (*green curve*). We also plot the model suggested in Lacour et al. (2016) consisting of a $T_{\rm eff} = 3000$ K and $\log(g) = 3.5$ BT-SETTL model, with a 1700 K environment (*yellow curve*). **c)** Same as a) for a larger wavelength range. **d)** Same as b) for a larger wavelength range, but without the Lacour et al. (2016) model and showing the contribution of the photosphere of the companion (*cyan* curve) in our best-fit BT-SETTL+environment model. In both c) and d), we compare our spectrum with photometric measurements of the companion obtained with different instruments: VLT/NACO-SAM (*black points;* Biller et al. 2012), MagAO (*blue points;* Close et al. 2014), GPI (*magenta points;* Rodigas et al. 2014) and VLT/NACO-SAM (*red points;* Lacour et al. 2016).

suggests the presence of an additional component (apart from the photosphere) or not. A more realistic model would require to consider an annular geometry and hence involve three free parameters (the temperature, radial separation and width of the annulus) where the last two parameters would not be independently constrained by our observations.

Best fit BT-SETTL model We assume that using the χ^2 metric as a goodness-of-fit estimator can provide a reasonable estimate of the effective temperature, surface grav-

ity, extinction and stellar radius. Nevertheless, this estimator is somewhat flawed as the points of our spectrum are not statistically independent – they are significantly affected by the same speckle noise scaled by λ – and do not rigorously follow a Gaussian error distribution (Soummer et al. 2007; Greco & Brandt 2016). Bootstrapping (e.g., Hastie et al. 2009) was hence implemented to estimate the uncertainties on each of the best-fit parameters due to spectral correlation of errors between different channels. We created 5000 bootstrap samples, by drawing 1313 random channels, with repetition, following a uniform probability distribution among our 1313 channels. The first of these samples consists of the 1313 good channels of the actual observed spectrum. For each bootstrap sample, we find the model of our grid that minimizes the residuals, and save the corresponding model parameter values. Histograms reporting the occurrence of each parameter value are then fitted to gaussian functions in order to estimate the 1σ–uncertainty on each parameter.

For R_B and R_d, we propagate an additional uncertainty reflecting the $\sim$15% uncertainty on the absolute flux of the companion (see Appendix 16.1.9 and Fig. 16.10 for details). It is added in quadrature to the uncertainty on these parameters estimated with bootstrapping. Since T_eff, $\log(g)$, A_H and T_d control the shape of the spectrum, i.e. the channel to channel relative flux, but not the absolute flux, these parameters are not affected by the additional uncertainty on the absolute flux.

The best-fit parameters for the companion and a putative hot environment, are compiled in Table 16.2. We distinguish between models consisting of photospheric emission alone (4 free parameters), and of the sum of photospheric and hot circum-secondary material signals (2 additional parameters), in the top and bottom parts of Table 16.2 respectively.

Fitting the whole spectrum with pure photospheric signal (captured by the BT-SETTL synthetic spectra) yields a best-fit effective temperature and surface gravity of $T_\mathrm{eff} = 3500 \pm 100$ K and $\log(g) = 4.5_{-0.5}$, resp. ($\chi^2_r = 0.14$). The corresponding best-fit companion radius R_B and extinction A_H are $R_B = 2.08 \pm 0.18 R_\odot$ and $A_H = 0.75^{+0.05}_{-0.10}$, respectively. The best-fit BT-SETTL synthetic spectrum is shown in Fig. 16.6a and c, in units of λF_λ to better show small changes in spectral slopes. It accounts relatively well for the H-band spectrum of the companion. The K-band spectrum is also qualitatively comparable, although the slope is not perfectly reproduced, either too flat at 2.15–2.28 μm or too steep beyond 2.33 μm.

Adding two additional free parameters representing hot circum-secondary material appears to slightly improve the quality of the fit (best-fit $\chi^2_r = 0.10$). The best-fit effective temperature and surface gravity are consistently $T_\mathrm{eff} = 3500 \pm 100$ K and $\log(g) = 4.5_{-0.5}$. However, the two additional free parameters introduce a degeneracy between the other parameters, as different combinations of R_B, A_H, T_d and R_d can produce very similar quality fits. Therefore, we prefer to provide best-fit parameters R_B, A_H, T_d and R_d as ranges of values, reflecting the different combinations of these parameters leading to $\chi^2_r \approx 0.10$: $R_B \in [1.09, 1.55] R_\odot$, $A_H \in [0.0, 0.2]$, $T_\mathrm{d} \in [1500, 1700]$ K and $R_\mathrm{d} \in [3.0, 13.9] R_\odot$. Among these models, we slightly favor the one associated to $A_H = 0.2$, as it leads to a closer R-band flux to the photometric measurement in Close et al. (2014). This model is shown with the *green curve* in Fig. 16.6b and d and corresponds to the set of best-fit parameters given in parentheses in Table 16.2. Nevertheless, we also note that the best-fit BT-SETTL model

Table 16.2: Best fit parameters for HD 142527 B and a putative hot environment

Parameter	Searching range	Best fit value
Companion alone		
$T_{\rm eff}$ [K]	2600–4500	3500 ± 100
$\log(g)^{\dagger}$	2.5–4.5	$4.5_{-0.5}$
R_B [$R_\odot$]	0.1–10.0	2.08 ± 0.18
A_H [mag]	0.0–1.2	$0.75^{+0.05}_{-0.10}$
χ^2_r		0.14
Companion + hot environment		
$T_{\rm eff}$ [K]	2600–4500	3500 ± 100
$\log(g)^{\dagger}$	2.5–4.5	$4.5_{-0.5}$
R_B [$R_\odot$] ‡	0.1–10.0	1.09–1.55 (1.42)
A_H [mag] ‡	0.0–1.2	0.0–0.2 (0.2)
$T_{\rm d}$ [K] ‡	1000–1700	1500–1700 (1700)
$R_{\rm d}$ [$R_\odot$] ‡	1.5–20.0	3.0–13.9 (11.8)
χ^2_r		0.10

†Missing upper uncertainty limit reflects the fact that the best-fit parameter is found at the limit of the searching range.

‡Given the parameter degeneracy between R_B, A_H, $T_{\rm d}$ and $R_{\rm d}$, we provide parameter ranges for which a similar quality fit can be obtained ($\chi^2_r \sim 0.10$). Values in parentheses correspond to the model shown in Fig. 16.6b and d.

without inclusion of a hot environment still leads to a slightly better agreement in R-band (Fig. 16.6c). This is due to the higher value for the best-fit extinction ($A_H = 0.75^{+0.05}_{-0.10}$).

The H+K spectrum is globally better reproduced when allowing for the additional contribution of a hot black-body environment. For comparison, we also plot the 3000 K BT-SETTL + 1700 K circum-secondary environment model suggested in Lacour et al. (2016) to fit the SED of the companion (*yellow curve* in Fig. 16.6b). It appears incompatible with our SINFONI spectrum, given its more pointy shape H-band continuum and the hump centered at $\sim 2.25\ \mu$m that are both typical of later type objects. We also show the contribution of the photosphere alone in our best-fit BT-SETTL + hot environment model (*cyan curve* in Fig. 16.6d). This will be relevant for the estimation of H- and K-band magnitudes of the companion (without the contribution of the circum-secondary disk), that will be used to locate the position of the companion in HR diagrams.

Figure 16.6c and d compares our best-fit models to the whole SED of the companion, obtained from previous detections with different instruments. Both the best-fit BT-SETTL model alone and best-fit BT-SETTL+environment model are roughly consistent with the R-band and Y-band measurements with MagAO and GPI resp. (Close et al. 2014; Rodigas et al. 2014). However, our observed spectrum and best-fit models are significantly brighter than photometric measurements of the companion obtained using SAM with VLT/NACO (Biller et al. 2012; Lacour et al. 2016). This is further discussed in Sect. 16.1.6.

Fit with template spectra

A common way to estimate the spectral type of a particular source is to compare its spectrum to a spectral sequence of standard stars. This was done in the infrared for field M- and L-dwarfs (e.g. Jones et al. 1994; Cushing et al. 2005). Nevertheless, youth (i.e. low-gravity) is known to affect significantly the shape of the continuum in the near-IR (e.g. Meyer et al. 1998; Gorlova et al. 2003; Lodieu et al. 2008). Considering objects with an estimated age that is similar to our source is critical to not be biased by the effects of gravity in the spectral type estimate.

Allers & Liu (2013) proposed a spectral sequence for very low gravity objects with spectral types ranging from M5 to L3. However the lack of humps at 1.67 and 2.25μm in the spectrum of HD 142527 B suggests that it is of earlier spectral type than M6. Therefore, we built our own sequence of very low gravity early- to mid-M stars from well studied open cluster IC 348, located in the nearby Perseus molecular cloud ($\sim$ 300 pc; Schlafly et al. 2014). This open cluster has an estimated age of 2–6 Myr (e.g. Luhman et al. 2003; Bell et al. 2013), which is similar to the estimate for HD 142527 A (5.0 ± 1.5 Myr old; Mendigutía et al. 2014). Therefore, similar gravity-sensitive spectral features are expected in our very young M-dwarf sequence and in the spectrum of HD 142527 B.

The sequence is shown in Fig. 16.7. It was built using the SpeX Prism library, which is a compilation of near-infrared (0.8–2.5 μm) low-resolution ($\lambda/\Delta\lambda \approx$ 75–120) spectra of red and brown dwarfs obtained with the IRTF SpeX spectrograph (Burgasser 2014). In particular, the SpeX Prism library contains the spectra of 100 low-mass objects identified to be members of IC 348 and whose spectral types were estimated based on combined optical and near-IR spectra (Luhman et al. 2016). Among the IC 348 objects, we chose a template spectrum for each spectral subtype between M1 and M4.5 with steps of 0.5, based on visual inspection of the quality of the spectra, provided in Luhman et al. (2016). Each template spectrum was rescaled to the level of the spectrum of HD 142527 B, and either reddened or unreddened by an amount provided in parenthesis in Fig. 16.7, corresponding to the best fit to our SINFONI spectrum. We chose to let extinction as a free parameter given that the SpeX library consists of spectra that have not been unreddened, and that we are considering very young objects which can be either more or less self-embedded than HD 142527 B. The spectrum of HD 142527 B at the bottom of the figure (represented along the M4.5 template) is at the measured flux, while other occurrences of the spectrum are shifted vertically by steps of 5×10^{-11} ergs s^{-1} cm^{-2} μm^{-1}.

The best fit is obtained with the M2.5 template ($\chi^2_r = 0.27$), closely followed by the M3.5 template ($\chi^2_r = 0.28$). Slightly poorer fits are obtained with the M1.5, M2.0 and M3.0 templates. Earlier spectral types than M1.5 are characterized by discrepant slopes at the end of both the H- and K-bands. Spectral types later than M4 show significant humps at 1.67 and 2.25μm, which are the result of the strengthening of the water absorption bands carving the edges of the H- and K-bands, and are not seen in our spectrum. This analysis suggests that the spectral type of HD 142527 B is M2.5$\pm$1.0. We note that the best-fit spectra were obtained without the necessity of applying significant differential extinction (ΔA_V = 0.3 and 0.0 for the two best-fit templates), which suggests that the extinction towards HD 142527 B is similar to that towards IC 348. Cernis (1993) determined that the mean

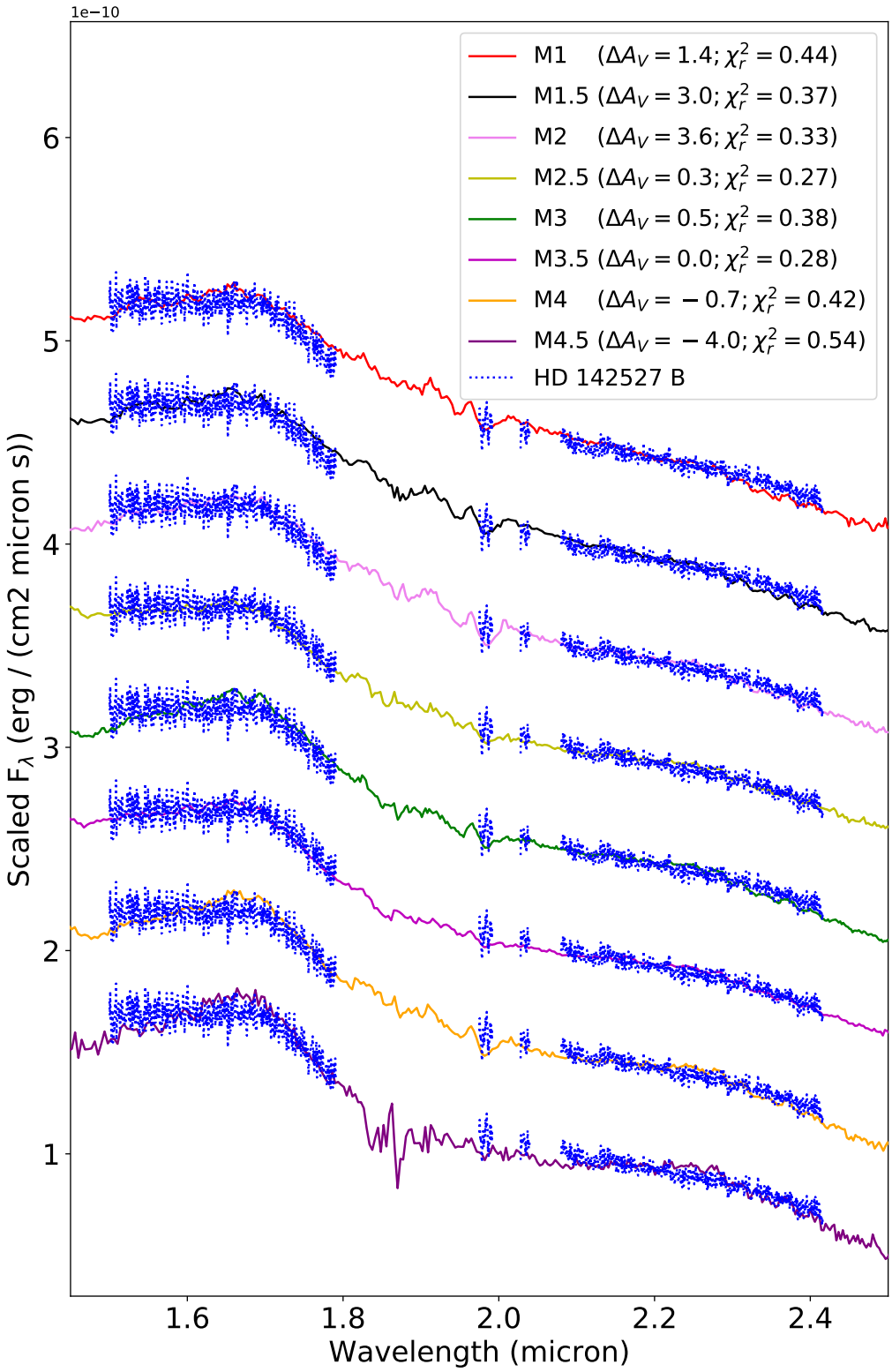

Figure 16.7: Observed $H+K$ spectrum of HD 142527 B (*blue dotted curve*) compared to a sequence of young early-M stars built using the speX Prism library (Burgasser 2014). The best fit to the spectrum of HD 142527 B is obtained with the M2.5 template. Sources are all extracted from young open cluster IC 348 (Luhman et al. 2016): 2MASS J03435953+3215551 (M1), 2MASS J03440216+3219399 (M1.5), 2MASS J03453230+3203150 (M2), 2MASS J03443481+3156552 (M2.5), 2MASS J03430679+3148204 (M3), 2MASS J03435856+3217275 (M3.5), 2MASS J03452021+3217223 (M4) and 2MASS J03450206+3159341 (M4.5).

extinction towards IC 348 was $A_V = 2.5 \pm 0.6$ ($A_H \approx 0.4 \pm 0.1$). This constraint will be further discussed in Sect. 16.1.5.

Luhman et al. (2003) built a relationship to convert spectral type into effective temperature for very young low-mass objects, based on the assumption that the members of the young GG Tau quadruple system, spanning K7 to M7.5 in spectral types, were coeval. This conversion scale is intermediate between those of giants and dwarfs, and yields $T_{\rm eff} = 3480 \pm 130$K for an M2.5±1.0 spectral type. This is in remarkable agreement with the best-fit $T_{\rm eff}$ obtained with BT-SETTL models (3500 ± 100K; Sect. 16.1.5).

In addition to the spectral sequence, we considered another test consisting in finding the best-fit template spectrum in the SpeX Prism library. We considered all objects with a spectral type between M0 and M9 and SNR > 30 in the SpeX library, which totaled to 507 objects. Due to the lower spectral resolution, we interpolated the SpeX spectra with a spline of degree 3 to reach the same resolution as our SINFONI data. The fitting process involved two free parameters, corresponding to flux scaling and relative extinction. The best-fit was obtained with 2MASS J03443481+3156552; i.e. the M2.5 template of the sequence we built in Fig. 16.7. The best-fit template spectrum is shown in Fig. 16.8, along with our spectrum of HD 142527 B smoothed to the resolution of the speX spectrum. We choose the vertical axis to be in units of λF_λ in order to better show small changes in spectral slopes.

We notice a remarkable agreement between our smoothed spectrum and the best-fit template in H-band, where most low-resolution absorption features are reproduced. This casts confidence on the quality of our extracted spectrum. In K-band, the agreement is poorer although most spectral features appear qualitatively reproduced, such as the strong quintuplet of Ca I (1.978–1.986 μm) and the first overtone of the CO bandhead (2.293–2.414 μm). Interestingly, we notice that 2MASS J03443481+3156552 was identified as a transition disk (van der Marel et al. 2016c). Its SED[3] shows indeed a strong mid-IR excess compared to the near-IR (Dunham et al. 2015). Therefore slight discrepancies between the spectra of HD 142527 B and the template might be due to differences in the inner part of the respective disk of each star, which is expected to have a stronger influence at K band than at H band. Finally, we note the presence of the Br$_\gamma$ line in the best-fit template spectrum, absent from the spectrum of HD 142527 B. This is further discussed in Sect. 16.1.5.

Spectral features

Atomic and molecular features can provide insight on the spectral type and gravity of HD 142527 B. However, their identification in our spectrum is complicated by the residual speckle noise affecting the flux of the companion in individual channels. Nevertheless, comparison between our spectrum and BT-SETTL synthetic spectra smoothed at the same spectral resolution (Fig. 16.6) shows that the residual speckle noise is only slightly larger than the intrinsic noise-like signal corresponding to the forest of absorption lines in the photosphere of M-dwarfs. This suggests that more information could be extracted from

[3]Available on the Vizier Photometry viewer: `http://vizier.u-strasbg.fr/vizier/sed/?-c=&-c.r=10&-c.u=arcsec`.

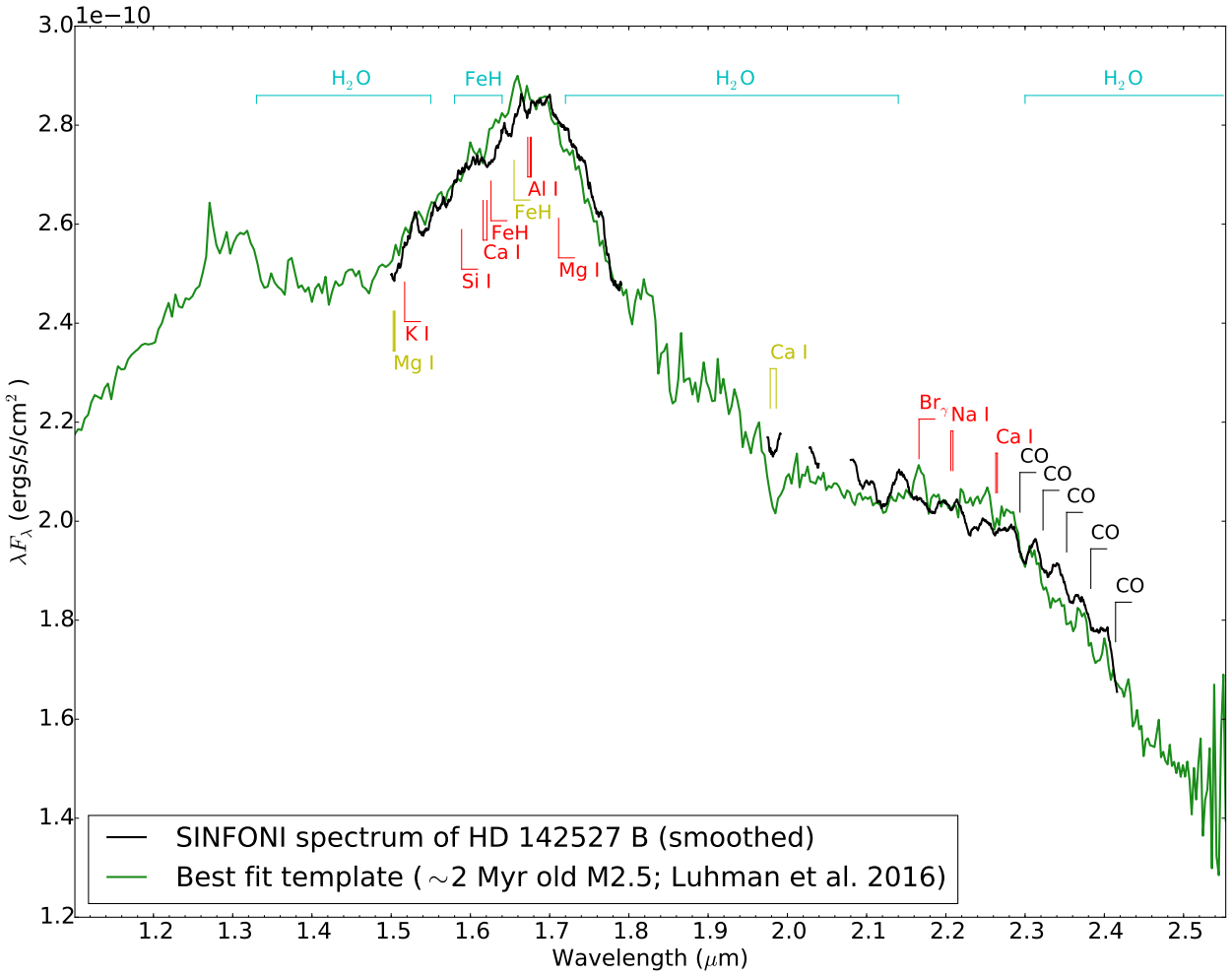

Figure 16.8: Observed H+K spectrum of HD 142527 B (*black curve*) and best-fit SpeX Prism spectrum corresponding to a young M2.5 star (2MASS J03443481+3156552) surrounded by a transition disk in open cluster IC 348 (*green curve*). The SINFONI spectrum was Savitzky-Golay filtered to match the resolution of the SpeX spectrum. The template spectrum was rescaled to match the H-band flux of HD 142527 B.

our spectrum. Therefore, we labeled atomic and molecular lines that are expected in the spectrum of early- to mid-M type stars in Figs. 16.5, 16.6a and 16.8. Most of these lines are predicted by the best-fit BT-SETTL models (*green curves* in Fig. 16.6). In Figs. 16.6a and 16.8, predicted lines that are detected, tentatively detected and non-detected are shown in *black*, *yellow* and *red*, respectively.

The most conspicuous absorption feature in our spectrum appears to be the first overtone of CO bandhead ($\Delta\nu = 2$), with five visible CO transitions, $\nu = 2$–0, 3–1, 4–2, 5–3 and 6–4, at 2.293, 2.323, 2.352, 2.383 and 2.414 μm, respectively. The first overtone of CO bandhead is a common feature in M- and L-dwarfs, both young and in the field (e.g. McLean et al. 2003; Cushing et al. 2005). It has also been associated to the inner disk in $> 23\%$ of T-Tauri stars (Connelley & Greene 2010). Two atomic lines are also tentatively detected in our spectrum: the Mg I triplet (1.502, 1.504 and 1.505 μm) and the Ca I quintuplet (1.978–1.993 μm; inset of Fig. 16.5). The first three lines of the Ca I quintuplet are the strongest absorption features in the K-band spectrum of all M-dwarfs, while the Mg

I triplet is the strongest absorption feature in H band for M1 to M3 dwarfs (e.g. Cushing et al. 2005). For spectral types earlier than M1, Si I (1.589 μm) becomes the dominant absorption feature in H band, while objects with spectral type later than M4 shows a strong K I (1.517 μm) absorption line. The non-detection of those two lines, together with the tentative detection of the Mg I triplet and Ca I quintuplet, appears consistent with an estimated M2.5$\pm$1.0 spectral type.

Nonetheless, we note that all transitions of the CO bandhead, the Mg I triplet and Ca I quintuplet are significantly shallower than predicted by the best-fit BT-SETTL synthetic spectrum. A possible explanation is photospheric line veiling. T-Tauri stars are indeed known to show significant line veiling in near-IR (e.g. Greene & Lada 1996; Folha & Emerson 1999). Veiling at optical wavelengths is likely related to hot accretion streams of gas (e.g. Martin 1996) or accretion shocks at the base of magnetospheric accretion columns (e.g. Calvet & Gullbring 1998). However, the latter are expected to produce a veiling of only $\sim$0.1 in near-IR, insufficient to account for measured veiling ratios $\gtrsim 1.0$ (Folha & Emerson 1999). Signicant sources of line veiling in near-IR might rather be associated to emission from a hot inner rim and/or low-gravity opacity drop of H^- around 1.67 μm in the photosphere (Cieza et al. 2005; Wing & Jorgensen 2003; Vacca & Sandell 2011). The veiling due to the contribution of a 1700 K inner rim can be seen by comparing the depth of the lines in the green curves of Fig. 16.6a and b. However, this effect appears to only partially explain the observed veiling, given that the first three transitions of CO bandhead are still shallower than expected by the best-fit BT-SETTL+hot environment(*green curve* in Fig. 16.6b). Moreover, that model predicts that the Ca I doublet (1.616–1.621 μm), Al I triplet (1.672, 1.676 and 1.677 μm), Mg I (1.711 μm) and the Na I doublet (2.206–2.209 μm) should be detected, while these lines do not appear significant in our spectrum. The youth of the HD 142527 system (and hence the low-gravity of the companion) is likely another factor explaining the non-detection of those lines. A significant H-band excess is indeed expected from the reduction of H^- opacity due to the lower density and gravity in the photosphere of young M-stars (e.g. Wing & Jorgensen 2003). This $H-$band excess was observed in the spectrum of M2.5 T-Tauri star TW Hya in Vacca & Sandell (2011), who suggested that it could be a significant source of line veiling. Specific examples of previously observed veiled lines in the spectrum of M-type objects in young star-forming associations are the Na I doublet (2.206–2.209 μm) and K I (1.517 μm) atomic lines (e.g. Allers et al. 2007; Lodieu et al. 2008).

Finally, we notice another possible line at $\sim$1.65μm which, contrarily to other lines we labeled, is not predicted by the best-fit BT-SETTL model (Fig. 16.6a). We tentatively assign it to the FeH absorption line at 1.655μm, which is one of two major absorption features in the spectra of mid- to late-M dwarfs (the other one being the FeH bandhead at 1.625 μm, also labelled in Fig. 16.6a; Cushing et al. 2003, 2005). Given that this line is not expected to be significant for earlier spectral types than M5, it could rather be a $\sim 2.5\sigma-$outlier in our spectrum; which is statistically possible given that our spectrum is composed of 1313 channels.

Table 16.3: Flux and magnitude of HD 142527 B in H and K band

Band	Case	Flux [mJy]	Apparent magnitude	Absolute magnitude
H	I	151 ± 15	9.63 ± 0.11	$2.92^{+0.15}_{-0.12}$
	II	116 ± 10	9.92 ± 0.16	$3.75^{+0.25}_{-0.16}$
K	I	147 ± 15	9.14 ± 0.11	$2.71^{+0.15}_{-0.12}$
	II	98 ± 8	9.59 ± 0.16	$3.50^{+0.25}_{-0.16}$

Notes: Case I considers that all the observed H+K flux comes from the photosphere of the companion. Case II considers the contribution from the photosphere alone in the best-fit BT-SETTL+hot environment model to the H+K spectrum. The absolute de-reddened magnitudes are computed using $A_H = 0.75$ and 0.2 for cases I and II, respectively.

Flux and magnitude

Three values for the extinction have been suggested for the HD 142527 system: visible extinctions $A_V = 0.60 \pm 0.05$ (corresponding to $A_H \sim 0.1$) and $A_V = 0.80 \pm 0.06$, both based on the fit of the SED of the primary (Verhoeff et al. 2011; Lazareff et al. 2017, resp.), and an H-band extinction $A_H = 0.3$ based on the near-IR colors of the companion (Close et al. 2014). In comparison, our best-fit models to the H+K spectrum (Sect. 16.1.5) suggest values of $A_H = 0.75^{+0.05}_{-0.10}$ in case the H+K signal is composed of photospheric signal alone, and $A_H = 0.0$–0.2 if a hot circum-secondary environment is present. A value of $A_H = 0.75^{+0.05}_{-0.10}$ could suggest that the companion is self-embedded, and suffers much more extinction than the primary. On the contrary, $A_H = 0.0$–0.2 is consistent with the estimate of the extinction towards the primary. The best-fit template spectra (Sect. 16.1.5) suggest that a similar extinction is affecting observations towards HD 142527 B and members of the IC 348 cloud. In the latter case, Cernis (1993) inferred $A_H \approx 0.4 \pm 0.1$. Given that this value lies roughly in the middle of the two best-fit values of A_H found with BT-SETTL models, it does not constrain whether a hot circum-secondary environment is contributing or not to the H+K spectrum. However, among the best-fit BT-SETTL+environment models (consisting in ranges of values in R_B, A_H, R_d and T_d; Table 16.2), the best-fit solution with $A_H = 0.2$ leads to a better agreement with the photometric measurement at R-band, which is the most sensitive to extinction (Fig. 16.6d). Best-fit solutions with $A_H < 0.2$ lead to $\gtrsim 2\sigma$–discrepancy with the R-band photometric point. Therefore, for the rest of the analysis we will favor the best-fit solution with $A_H = 0.2$ (for the case where a hot circum-secondary environment is present), which is also in better agreement with $A_H \approx 0.4 \pm 0.1$ inferred for the IC 348 cloud.

Several indications hint towards the presence of a circum-secondary disk, such as (i) a better quality fit obtained with the inclusion of a hot circum-secondary environment, (ii) the best-fit template obtained with a young M2.5 star surrounded by a transition disk, and (iii) the detection of H_α emission suggesting on-going mass accretion (Close et al. 2014). Nevertheless, we cannot rule out the possibility that the putative circum-secondary disk has a negligible contribution in H+K and that the poorer fit with the synthetic spectra alone is due to the inappropriateness of the BT-SETTL models at such young age. Therefore, we will continue to consider the two possibilities in the rest of the analysis; i.e. the

H+K spectrum is composed of either photospheric signal alone (case I), or the combination of photospheric+hot circum-secondary environment contributions (case II). Table 16.3 compiles the measured flux, measured apparent magnitude and absolute de-reddened magnitude of the companion in each of those two cases. The absolute de-reddened magnitudes are computed using the corresponding best-fit extinction value: $A_H = 0.75$ and 0.2 without and with a circum-secondary environment, respectively. In case II, only the contribution from the photosphere (*cyan curve* in Fig. 16.6d) is provided in Table 16.3. Making this distinction (i.e. subtracting the contribution from the disk) is necessary for an appropriate placement of the companion in HR diagrams (Sect. 16.1.5). The quoted uncertainties in flux and apparent magnitude in Table 16.3 consider a conservative 10% relative flux uncertainty (0.11 mag) and, for case II, an additional error added in quadrature representing the uncertainty on the radius of the companion (Table 16.2). The uncertainty in absolute de-reddened magnitude also includes the uncertainty on A_H (Table 16.2).

The filter transmission curves of CONICA for H and K are overlapping with wavelength areas that are significantly affected by telluric lines, and are hence less reliable. Therefore, the flux and magnitude of the companion derived from our SINFONI spectrum were computed using the H and K filter transmission curves of 2MASS. We do not expect a significant change in the estimation of the magnitude, in particular when compared to other sources of uncertainties on the flux of the companion.

Mass and age

The standard procedure to estimate stellar mass and age consists in comparing the star location with evolutionary tracks in an HR diagram (e.g. Siess et al. 2000; Bressan et al. 2012). Here, we choose to use the Baraffe et al. (2015)[4] evolutionary models, which assume a solar metallicity with the revised heavy element fraction by mass $Z = 0.0153$ from Caffau et al. (2011). Fig. 16.9a and b shows the H- and K-band HR diagram comparing the location of HD 142527 B with the evolutionary tracks of young stellar objects ranging from 0.1 to 0.6 $M_\odot$. Isochrones were considered between 0.5 and 10 Myr. The $T_{\rm eff}$ of HD 142527 B was found to be 3500 ± 100K based on best-fit models using BT-SETTL synthetic spectra (Sect. 16.1.5). This value is consistent with the $T_{\rm eff}$ corresponding to the best-fit spectral type (M2.5±1.0) inferred from young spectral templates: 3480 ± 130K (Sect. 16.1.5). Therefore we consider a single value of $T_{\rm eff} = 3500 \pm 100$K in the HR diagrams. However, we consider two values for the absolute de-reddened magnitude of the companion, corresponding to the cases of the absence or presence of a hot circum-secondary environment (cases I and II in Table 16.3).

In each considered case, we notice that the location of the companion leads to consistent mass and age estimates in the H- and K-band HR diagrams. If all the observed H+K signal is photospheric (case I), the estimated mass and age of HD 142527 B are $0.33 \pm 0.05 M_\odot$ and 0.75 ± 0.25 Myr, respectively. Considering the best-fit photospheric+hot environment model (case II), the mass and age of the companion are $0.34 \pm 0.06 M_\odot$ and $1.8^{+1.20}_{-0.5}$ Myr, respectively. We note that in the first case the very young age is compatible with the signif-

[4]Available at `http://perso.ens-lyon.fr/france.allard/`.

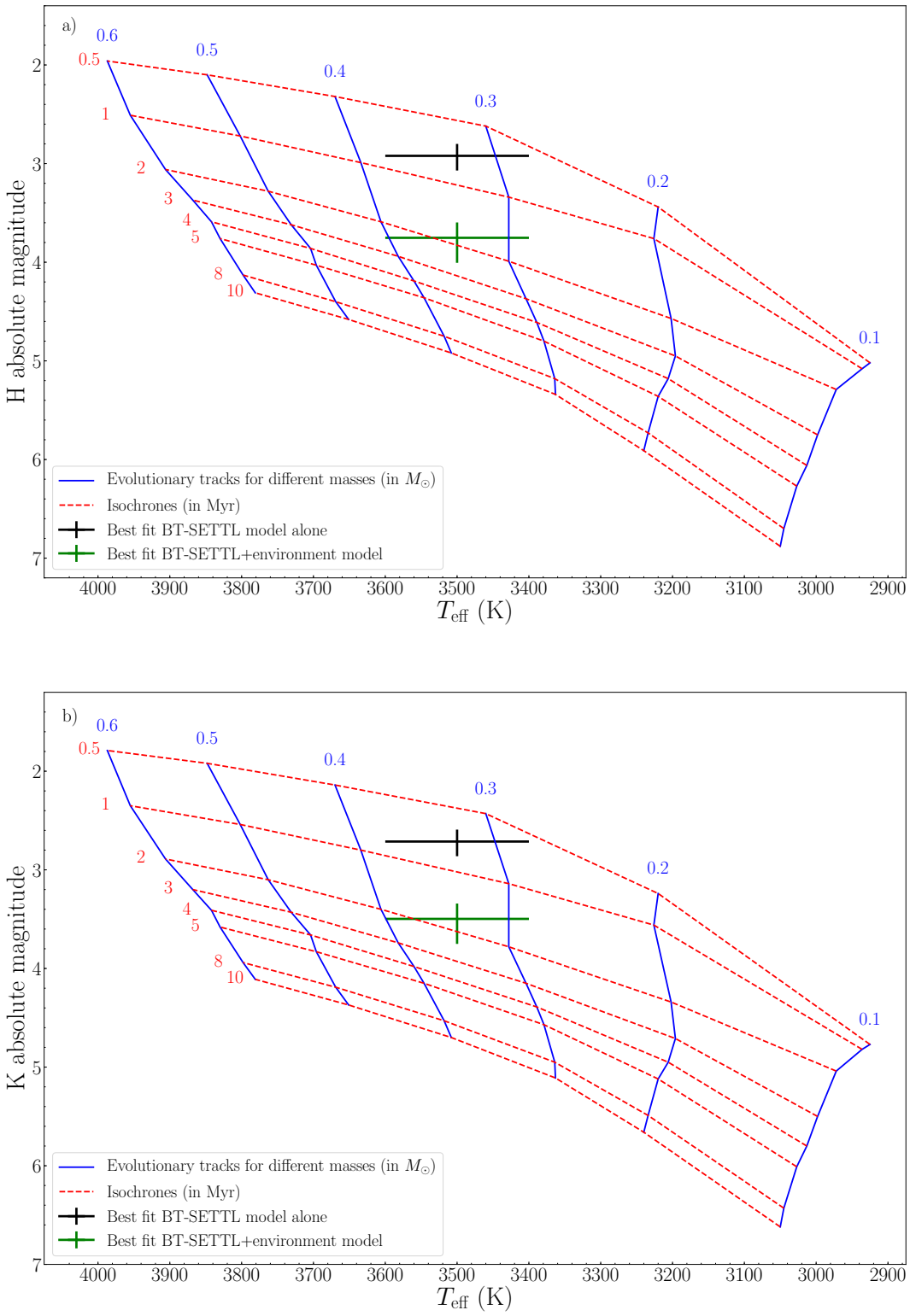

Figure 16.9: HR diagrams in H- (a) and K-band (b) showing stellar tracks for different masses according to the Baraffe et al. (2015) evolutionary models. Isochrones (*red-dashed lines*) range from 0.5 to 10 Myr. The evolutionary paths (*blue lines*) are considered for stellar masses ranging from 0.1 to 0.6 $M_\odot$, per steps of 0.1$M_\odot$. The *black* and *green error bars* correspond to the best-fit $T_{\rm eff}$ and dereddened absolute magnitude of the companion in case all the observed H+K signal is photospheric (case I) or made of a combination of photosphere+hot environment (case II).

icant extinction inferred from the fit to BT-SETTL models ($A_H = 0.75$) conveying the fact that the companion is still embedded in its birth environment. Despite the different age estimates, both cases lead to very similar mass estimates, which is due to the verticality of the Hayashi tracks in the H- and K-band HR diagrams in the considered range of stellar mass and age.

Radius

For the derived mass and age of $0.33 \pm 0.05\ M_\odot$ and 0.75 ± 0.25 Myr (case I), the Baraffe et al. (2015) evolutionary models predict a stellar radius of $1.96 \pm 0.10\ R_\odot$. This is consistent with the best-fit stellar radius obtained independently by calibrating in flux the BT-SETTL model to the H+K spectrum ($2.08 \pm 0.18\ R_\odot$). In case II, the Baraffe et al. (2015) evolutionary models predict a stellar radius of $1.37 \pm 0.05\ R_\odot$ for a mass and age of $0.34 \pm 0.06 M_\odot$ and $1.8^{+1.20}_{-0.5} \pm$ Myr. This is also consistent with the stellar radius value of 1.42 $R_\odot$ found independently from the flux adjustment of the best-fit BT-SETTL+hot circum-secondary environment models to our spectrum. These values of stellar radius indicate that the M2.5±1.0 companion is still gravitationally contracting, as expected in such a young system.

It is also possible to estimate the expected ratio of stellar radii between the primary and the companion:

$$\frac{R_A}{R_B} = \sqrt{\frac{F_A T^4_{\text{eff},B}}{F_B T^4_{\text{eff},A}}}$$

based on the bolometric flux of the best-fit BT-SETTL models for HD 142527 A (F_A) and HD 142527 B (F_B), and the best-fit effective temperatures for the primary ($T_{\text{eff},A}$) and the companion ($T_{\text{eff},B}$). Considering $T_{\text{eff},A} = 6500$ K, $T_{\text{eff},B} = 3500$ K, the model shown in *black* in Fig. 16.1 to compute F_A, and the model shown in green (resp. cyan) in Fig. 16.6c (resp. 16.6d) to calculate F_B leads to $\frac{R_A}{R_B} = 1.52$ (resp. 2.25) in case I (resp. II). These ratios are consistent with $\frac{R_A}{R_B} = 1.63 \pm 0.13$ (resp. 2.34 ± 0.17) considering the respective best-fit BT-SETTL models leading to $R_A = 3.2 \pm 0.2 R_\odot$ (Table 16.1) and $R_B = 1.96 \pm 0.10 R_\odot$ (resp. $1.37 \pm 0.05 R_\odot$) in case I (resp. II).

Surface gravity

For the combinations of mass and age derived in both cases I and II, it is noteworthy that the Baraffe et al. (2015) evolutionary models predict lower values of $\log(g)$ (3.38 ± 0.14 and 3.70 ± 0.18) than inferred from the best-fit BT-SETTL models ($4.5_{-0.5}$ for both cases I and II; Table 16.2). This discrepancy could be due to a significant magnetic field, which is expected to be present for young M-type T-Tauri stars (e.g. Johns-Krull et al. 1999; Johns-Krull 2007). Several studies have indeed shown that not including a strong ($\sim$ kG) magnetic field can lead to $\sim$0.5-1.0 dex difference in the estimated $\log(g)$ due to an improper account of line broadening in the synthetic spectrum (e.g. Doppmann et al. 2003; Sokal et al. 2018, Flores et al. in prep.). However, these conclusions are based on the difference in line widths in normalized spectra and, to our knowledge, the effect on the continuum

shape (which likely dominates our best-fit solutions) has not been studied yet. Nonetheless, given the young age of the system and the fact that BT-SETTL models do not take into account the effect of magnetic fields, we suspect the surface gravity value predicted by evolutionary models ($\log(g) \sim$3.38 and 3.70 in cases I and II, resp.) to be more representative of HD 142527 B, and speculate that a substantial magnetic field ($\sim$1-2 kG, if similar to other M-type T-Tauri stars; Johns-Krull et al. 1999; Johns-Krull 2007) might explain the $\sim$0.5-1.0 dex discrepancy in $\log(g)$.

Mass accretion rate

Meyer et al. (1997) suggested that the observed dereddened $H-K$ color of T-Tauri stars can be related to their mass accretion rate. The absolute H- and K-magnitudes of HD 142527 B yield $H-K \approx 0.2 \pm 0.2$, which leads to a weak constraint of $\dot{M}_B \lesssim 10^{-8} M_\odot \mathrm{yr}^{-1}$ (see Fig. 5 in Meyer et al. 1997).

Calvet et al. (1991) showed that for T-Tauri stars with effective temperature lower than 4000 K, the CO bandhead associated to the disk is expected to be seen in emission for mass accretion rates $\lesssim 10^{-8} M_\odot \mathrm{yr}^{-1}$, which would hence veil the photospheric CO bandhead. In Fig. 16.6a (resp. 16.6b), comparison between the observed depth of the CO bandhead and the expected depth of the CO bands based on the BT-SETTL (resp. BT-SETTL+hot environment) model suggests indeed significant (resp. moderate) veiling. Therefore, similarly to the $H-K$ color, the observed veiling of CO also constrains the mass accretion rate of the companion to be $\dot{M}_B \lesssim 10^{-8} M_\odot \mathrm{yr}^{-1}$.

Connelley & Greene (2010) noted that the presence of veiled photospheric CO was often accompanied with Br_γ emission, a known tracer of mass accretion (e.g. Muzerolle et al. 1998). Nevertheless, our spectrum of HD 142527 B does not show any significant departure from continuum emission around the expected wavelength of the Br_γ line. Considering optimistically a 5% relative uncertainty (Sect. 16.1.4 and Appendix 16.1.9) and a -1 nm equivalent width (the rough value for the Br_γ line of the primary; Mendigutía et al. 2014), the 3σ–upper limit on the line flux is $\sim 1.5 \times 10^{-14}$ ergs s^{-1} cm^2. The Br_γ luminosity is given by $L(\mathrm{Br}_\gamma) = 4\pi D^2 \times F(\mathrm{Br}_\gamma)$, where D is the distance, assumed to be 156 pc, and $F(\mathrm{Br}_\gamma)$ is the total dereddened Br_γ line flux. We find $\log(L(\mathrm{Br}_\gamma)/L_\odot) \lesssim -5.0$. The accretion luminosity is related to the Br_γ line luminosity with the following empirical expression, applicable down to low-mass T-Tauri stars (Calvet et al. 2004):

$$\log(L_{\mathrm{acc}}/L_\odot) = 0.9 \times (\log L(\mathrm{Br}_\gamma)/L_\odot + 4) - 0.7$$

The final accretion luminosity of HD 142527 B is found to be $\lesssim 0.026 L_\odot$. This is compatible with the 0.013 $L_\odot$ estimated from the H_α line detection presented in Close et al. (2014). Therefore, we conclude that residual speckle noise alone can account for the non-detection of Br_γ emission.

Using the accretion luminosity to mass accretion rate relationship $\dot{M}_B = 1.25 L_{\mathrm{acc}} R_B / G M_B$ (Gullbring et al. 1998), with the value of L_{acc} found in Close et al. (2014), but with the new values of mass and radius derived in this work yields $\dot{M}_B \sim 5.8 \times 10^{-9} M_\odot \mathrm{yr}^{-1}$ (resp. $\dot{M}_B \sim 4.1 \times 10^{-9} M_\odot \mathrm{yr}^{-1}$) for the companion in case I (resp. case II). This corresponds to

about 3% (resp. 2%) of the mass accretion rate on the primary, in case I (resp. II). We note that these estimates are consistent with the constraints based on the appearance of the CO bandhead and the dereddened $H-K$ color ($\dot{M}_B \lesssim 10^{-8} M_\odot \mathrm{yr}^{-1}$).

16.1.6 Discussion

Comparison with previous works

The nature and orbit of the companion have recently been investigated by Lacour et al. (2016). They suggest that a low-mass star with an effective temperature of 3000 K and a surface gravity $\log(g) = 3.5$ surrounded by a 1700 K circum-secondary environment can account for the whole SED of the companion, considering a visible extinction A_V=0.6. We compare our H+K spectrum with the model suggested in Lacour et al. (2016) in Fig. 16.6b, and note a disagreement between the shape of our spectrum and their model. We also notice a significant discrepancy between our measured H- and K-band fluxes and the ones measured with SAM (Biller et al. 2012; Lacour et al. 2016). While our measurements are within 2σ compared to the fluxes measured in Biller et al. (2012), they correspond to $> 3\sigma-$differences with the measurements in Lacour et al. (2016). In particular, both the H- and K-band photometric measurements are about twice fainter than our spectrum. Both our tests (Appendix 16.1.9) and the consistency between our estimated radius and the radius predicted by evolutionary models suggest that the absolute flux calibration of our spectrum is of good quality. Even if the uncertainty in absolute flux of our spectrum was slightly larger than 15% (Appendix 16.1.9), it would still be incompatible with the 2016 NACO-SAM H- and K-band measurements. Investigating the possible origins of such difference with the SAM measurements would require an in-depth study which is beyond the scope of this paper. Nevertheless, we note that new measurements with extreme-AO instruments could provide new insight regarding this discrepancy.

Not surprisingly, the significantly fainter SAM photometric measurements led to a much smaller estimated mass for the companion: 0.1 $M_\odot$, corresponding to the lower mass end of the initial estimate of 0.1–0.4 $M_\odot$ (Biller et al. 2012). On the contrary, our new analysis leads to a mass estimate of $\sim 0.35 M_\odot$, hence closer to the upper limit of that range. In the case that all the H+K observed flux is photospheric, our estimated age of HD 142527 B (0.75 ± 0.25 Myr) is significantly younger than the age derived for the primary (5.0 ± 1.5 Myr; Mendigutía et al. 2014; Lacour et al. 2016). This would suggest that the companion formed after the primary, and its extremely young age would be consistent with the significant extinction to be applied to BT-SETTL synthetic spectra to fit the observed spectrum ($A_H = 0.75^{+0.05}_{-0.10}$), conveying that the companion is still embedded in its birth environment. On the contrary, the best-fit model including a hot circum-secondary disk leads to an estimated age of $1.8^{+1.2}_{-0.5}$ Myr, hence only slightly discrepant with the age of the primary.

Based on the measured H_α luminosity of the companion, Close et al. (2014) found a mass accretion rate of $\sim 5.9 \times 10^{-10}$ $\mathrm{M}_\odot$ yr^{-1}. Nevertheless, at that time the mass and radius of the companion were poorly constrained. Our new estimate of the mass accretion rate based on the values of mass and radius inferred in this work is almost an order of

magnitude larger (4.1–5.8×10^{-9} $M_\odot$ yr^{-1}). Given that the new mass ratio between the companion and the primary is $q \sim 1/6$, a mass accretion rate estimate which is 2–3% that of the primary does not appear unreasonable.

Circumbinary or transition disk?

The wealth of features found in the disk of HD 142527 B, including a large gap, a horseshoe-shaped mm-continuum and several spiral arms, have been considered as signposts of planet formation (e.g. Ohashi 2008; Casassus et al. 2013b). Similarly to HD 142527, the majority of large transition disks (with gaps larger than 20 au) show high accretion rates (e.g. Manara et al. 2014), further suggesting that the origin of the gap is not related to photo-evaporation, but possibly to embedded companions (see Owen 2016, and references therein).

Our analysis of the spectrum of HD 142527 B suggests that the mass ratio with respect to the primary is substantial ($q \sim 1/6$). Our new mass estimate was recently considered to inject the binary companion in hydro-dynamical simulations which showed that most of the observed characteristics of the disk could be explained by the interaction of the binary with the disk (Price et al. 2018). One is thus tempted to call HD 142527 a circumbinary disk, even if the term is more often used to refer to equal mass binaries, as in GG Tau A and CoKu Tau 4 (e.g. Ireland & Kraus 2008; Beck et al. 2012). However, we note that for a given mass ratio between the primary and companion, disks around lower mass primaries could show similar features as *circumbinary disks* but still be called *transition disks* due to a substellar companion. Therefore, the distinction between circumbinary disks and (at least a fraction of) transition disks may be purely semantic, as similar physical processes could be at the origin of the observed disk morphologies.

The fact that a $\sim 0.35 M_\odot$ stellar companion evaded detection until recently raises the question of how common are gapped disks where a binary or massive companion has not been detected yet. Could less massive companions (with e.g. $q \sim 0.1$–0.01) be at the origin of similar disk morphologies as HD 142527 with less extreme characteristics (smaller gap, less pronounced dust trap)? Several surveys have investigated the presence of massive companions in transition disks, using two main methods: radial velocities and SAM (e.g. Ghez et al. 1993; Simon et al. 1995; Pott et al. 2010). Recent results from radial velocity surveys, probing the innermost regions of transition disks, suggest that the latter do not host a significantly larger number of spectroscopic binaries than field stars (~ 4%; Kohn et al. 2016). However, the most recent survey making use of SAM led to the conclusion that up to ∼40% of TDs could in fact be circumbinary disks (Ruíz-Rodríguez et al. 2016). Nonetheless, these studies did not make distinctions between e.g. mm-bright and mm-faint disks within the larger class of transition disks. Furthermore, most of these surveys have focused on transition disks in low-mass star forming regions (mostly K and M stars), and hence did not include any Herbig Ae/Be/Fe star. For Herbig stars, detections of companions down to the low-mass end of the stellar regime still remains very challenging (e.g. Duchêne & Kraus 2013b). Here the companion is $\sim 0.35 M_\odot$ and lies at 14 au from the central star, but was only detected in 2012. The companion would likely have been missed if it either lied slightly closer to the primary or was slightly less massive. Large gaps in mm-

bright Herbig disks could thus possibly be carved by close companions (either stellar or massive planetary) falling just below the detection limits in terms of either inner working angle (for direct high-contrast imaging) or achieved contrast (for SAM).

For those gapped disks harboring a binary or massive substellar companion, recent simulations point towards a much more complex disk evolution than previously expected, involving a misalignment between the circumbinary disk and either the binary orbital plane (Martin & Lubow 2017) or the inner disk plane (Owen & Lai 2017). Disks with complex morphologies (inner cavity, spiral arms, asymmetric mm-dust distributions, warp) are thus prime targets to search for companions. As a matter of fact, high-contrast thermal-IR imaging has recently revealed a candidate companion in the gapped disk of Herbig Ae star MWC 758 (Reggiani et al. 2018). The companion is yet poorly characterized, but found in a situation that is reminiscent to HD 142527 B: inside an eccentric sub-mm cavity and internal to both multiple spiral arms and dust traps in the outer disk (e.g. Benisty et al. 2015; Dong et al. 2018a). Detection and characterization of more companions in those disks and subsequent hydrodynamical modeling could answer the question of whether the observed disk morphology can be traced back to a common origin: dynamical interaction with an embedded companion.

16.1.7 Summary

In this paper, we confirmed the spectral type of HD 142527 A to be F6±0.5III-V, based on our VLT/SINFONI spectrum and a re-analysis of VLT/X-SHOOTER data. ADI post-processing algorithms were used on the H+K spectral channels of our VLT/SINFONI observations of the HD 142527 system to obtain the first medium-resolution spectrum of a low-mass companion at less than 0″.1 from its central star. We used the NEGFC technique to derive the position and contrast of HD 142527 B in each channel. A careful estimation of the uncertainties related to speckle noise allowed us to derive robust error bars on our spectrum, typically of order 5–10% relative uncertainty in flux. Our final astrometry is the following: $r = 78.0 \pm 1.8$ mas and PA $= 119.1 \pm 1.0°$ on May 10, 2014. The position is in agreement with previous detections of the companion at similar epoch, however the flux found in H and K bands is not in agreement with previous VLT/NACO sparse aperture masking photometric measurements of the companion.

We compared our spectrum of the companion to BT-SETTL synthetic spectra covering a large range of effective temperature and surface gravity, and considered several additional parameters including the stellar radius, the extinction, and the physical extension and temperature of a putative hot circum-secondary inner rim. Fitting of the H+K spectrum with BT-SETTL synthetic spectra, in the absence of hot circum-secondary material contribution, led to a best-fit effective temperature of 3500 ± 100 K, a surface gravity $\log(g) = 4.5_{-0.5}$, a stellar radius of $2.08 \pm 0.18 R_\odot$ and an H-band extinction $A_H = 0.75^{+0.05}_{-0.10}$ mag. However, the inclusion of two additional free parameters accounting for a hot circum-secondary environment led to a slightly better fit of the observed spectrum. The best-fit effective temperature and surface gravity were found to be the same: 3500±100 K and $\log(g) = 4.5_{-0.5}$. However, we noticed some degeneracy between the stellar radius, H-

band extinction, temperature and radius of the circum-secondary environment (assuming a disk shape for simplification), whose best-fit values range in: $R_B \in [1.09, 1.55] R_\odot$, $A_H \in [0.0, 0.2]$, $T_\mathrm{d} \in [1500, 1700]$ K and $R_\mathrm{d} \in [3.0, 13.9] R_\odot$. Favoring the best-fit model with an H-band extinction $A_H = 0.2$ leads to an estimated stellar radius, circum-secondary environment temperature and physical extension corresponding to $R_B = 1.42 R_\odot$, $T_\mathrm{d} = 1700$K and the area of a disk of $11.8 R_\odot$, respectively. This choice is motivated by the better agreement in R-band with the measured flux in Close et al. (2014).

We also compared our spectrum to a spectral sequence of young low-mass objects taken from the SpeX Prism library. The best fit was obtained with the spectrum of a young M2.5 star surrounded by a transition disk, which remarkably reproduced all the observed spectral features in the H band and qualitatively reproduced the K-band spectrum of HD 142527 B. Using the spectral type to effective temperature conversion scale established in Luhman et al. (2003), we found that an M2.5±1.0 spectral type corresponded to an effective temperature of 3480±130 K, which is in good agreement with the effective temperature inferred from the fit to BT-SETTL models.

We subsequently compared the best-fit effective temperature and the absolute de-reddened magnitudes of HD 142527 B with isochrones of low-mass stars synthesized from the Baraffe et al. (2015) evolutionary models in H- and K-band HR diagrams. This allowed us to derive the following estimates for the mass, age and radius of the companion: 0.34 ± 0.06 $M_\odot$ (resp. 0.33 ± 0.05 $M_\odot$), $1.8^{+1.2}_{-0.5}$ Myr (resp. 0.75 ± 0.25 Myr) and $1.37 \pm 0.05 R_\odot$ (resp. 1.96 ± 0.10 $R_\odot$), in the case of the presence (resp. absence) of a hot circum-secondary environment contributing to the observed H+K band spectrum. We find that the stellar radius estimates obtained from the Baraffe et al. (2015) evolutionary models are consistent with the best-fit stellar radius obtained independently by calibrating in flux the BT-SETTL models to the H+K spectrum. We argue that the corresponding surface gravity value $\log(g) = 3.70 \pm 0.18$ (resp. 3.38±0.14) in the presence (resp. absence) of hot circum-secondary environment is likely to be more representative of the true surface gravity of HD 142527 B than the value inferred from the best-fit BT-SETTL models ($\log(g) = 4.5_{-0.5}$). This is justified by the young age of the system and the fact that the effect of a strong magnetic field, typical of M-type T-Tauri stars (e.g. Johns-Krull 2007), is not taken into account in BT-SETTL synthetic spectra.

The age estimate of the companion in the case of non-significant disk contribution in H and K bands (0.75 ± 0.25 Myr) appears significantly younger than the value of 5.0 ± 1.5 Myr derived for the primary (Mendigutía et al. 2014), suggesting that the companion formed after the primary. However, the age estimate found in the case of the presence of hot circum-secondary environment is only slightly discrepant with the age of the primary. The new mass estimate that we derived (0.34 ± 0.06 $M_\odot$ considering both cases discussed above) is significantly larger than the previous estimate based on SED fitting (0.1 $M_\odot$; Lacour et al. 2016). This suggests that the impact of the companion on the disk morphology could be more significant than previously expected. New hydro-dynamical simulations taking into account the mass derived in this work have recently shown that the peculiar morphology of the disk of HD 142527 could be reproduced by the companion alone considering an inclined and eccentric orbit (Price et al. 2018).

Based on the non-detection of Br_γ emission for the companion, we estimated an upper limit on the accretion luminosity compatible with the value computed from the H_α detection (Close et al. 2014). We provide a new estimate of the mass accretion rate of $\sim$4.1–5.8$\times10^{-9}$ $M_\odot$ yr^{-1} based on the H_α accretion luminosity and using the new values of mass and radius derived for the companion. This is $\sim$2–3% the mass accretion rate of the primary.

We note that the new spectral type of M2.5 makes HD 142527 B a twin of the well known TW Hya T-Tauri star, for which Vacca & Sandell (2011) estimated an effective temperature and mass of 3400 ± 200 K and 0.4 ± 0.1 $M_\odot$, respectively. Although consistent with our estimates for HD 142527 B, the slightly different values they quote is likely due to the fact they used temperature and mass calibrations based on field M-dwarfs (Leggett et al. 1996; Reid & Hawley 2005). The revised age of TW Hya ($\sim$ 3 Myr; Vacca & Sandell 2011) is also similar to the value we inferred for HD 142527 B. The new spectral analysis of TW Hya presented in Sokal et al. (2018) suggests the presence of a strong magnetic field, which is also the interpretation we favor for HD 142527 B to account for the derived values of $\log(g)$. The only major difference in the H+K spectra of both objects is the presence of a significant Br_γ emission line for TW Hya (Vacca & Sandell 2011).

Spectral characterization with extreme-AO might refine the parameters of the companion. In particular, a spectrum in J band could enable a better estimate of the extinction towards the companion and a better diagnostic of the gravity of HD 142527 B (see e.g. Allers & Liu 2013). New observations in thermal-IR might also confirm the presence of a circum-secondary disk. Follow-up observations could hence enable to discriminate between the two possibilities presented in this paper; i.e., whether a putative circum-secondary disk has a significant contribution in the H+K spectrum or not, which would in turn lead to a better estimate of the age of the companion.

From a broader point of view, we demonstrated the efficiency of VLT/SINFONI used in pupil-tracking for the spectral characterization of faint low-mass companions very close to their parent star. While the companion presented in this paper is in the red dwarf regime, using this mode with a fainter primary star could enable the spectral characterization of close-in substellar companions.

16.1.8 Appendix A: Spectral classification of HD 142527 A

The spectral type of HD 142527 A has first been estimated to F6-F7III (Houk 1978; van den Ancker et al. 1998). More recently, based on a VLT/X-SHOOTER spectrum and on an updated distance estimate, Mendigutía et al. (2014) concluded more conservatively that the spectral type must be comprised between F3 and F8. In view of the large uncertainty, we re-analyzed the optical part of their X-SHOOTER spectrum (program 084.C-0952). The data were loaded from the ESO archive, reduced using the ESO X-SHOOTER pipeline v 2.8.4. (Modigliani et al. 2010), and corrected for telluric absorption using *molecfit* (Smette et al. 2015; Kausch et al. 2015). The spectral classification was then obtained by comparing directly the X-SHOOTER spectrum with the spectra of all F stars in the *X-SHOOTER*

Spectral Library DR1 (XSL; Chen et al. 2014). Although Mendigutía et al. (2014) refrained from using any line ratio to infer the MK class due to possible line veiling, the following reasoning led us to a slightly different conclusion. For electron temperatures between 5000 K and 15000 K, the emission line region is expected to have a H_δ:Br_γ ratio of 5:1 (Osterbrock & Ferland 2006). The near-IR spectrum (Fig. 16.1) gives a Br_γ line intensity of at most $\sim 3.4 \times 10^{-10}$ ergs s^{-1} cm^{-2} μm. Therefore, the H_δ from the emission line region of the accretion disk can be at most $\sim 1.7 \times 10^{-9}$ ergs s^{-1} cm^{-2} μm. The X-SHOOTER spectrum in the H_δ region indicates a continuum level of $\sim 3.2 \times 10^{-8}$ ergs s^{-1} cm^{-2} μm, which is thus more than 18 times brighter than the emission line expected from the disk region. Hence, contrarily to the near-IR Br_γ line, the line veiling of H_δ will be negligible. Furthermore, the H_δ absorption line has about 50% of the depth of the local continuum, which is in good agreement with all other XSL F stars with spectral type later than F4. In conclusion, following this line of thought, (i) the low level Paschen lines and ground state Ca II H+K are affected by line veiling due to the line strength; (ii) line veiling in Brackett lines cannot be neglected because the photospheric flux is much weaker at those wavelengths; and (iii) the Ca II IR triplet, the Balmer lines, and the higher level Paschen lines can be assumed to be marginally affected by the ongoing accretion.

Therefore, we used the classical MK standard Fe I (4045Å, 4226Å)/H_δ ratio to estimate the spectral class of HD 142527 A. Fe I (4045Å, 4226Å)/H_δ is < 1 for F5 and earlier, and $\geqslant 1$ for F6 and later (Morgan et al. 1978). These lines are known to be fairly independent from the gravity/luminosity class. The measured line ratio for HD 142527 A is ≈ 1, which indicates a spectral type of F5-6. This is also the case for the XSL comparison stars, so possible instrumental and resolution effects can be excluded. Furthermore, the region of the Ca II IR triplet (8498Å, 8542Å, 8662Å), the Paschen series line (Pa10, Pa11, Pa12, Pa13), and the Mg I (8807Å) were used according to the observational calibrations of stars later than F2 by Marrese et al. (2003) and the synthetic spectra of Zwitter et al. (2004). The parametrization of the F star spectra from the XSL, including our target, was then executed as in Kordopatis et al. (2011). This leads to a spectral type of F6-7. Based on both criteria, we conclude that the spectral type must be F6 with an error of less than one subclass.

The luminosity class was estimated using two methods. First, we computed the classical MK system indicator Fe I (4063Å) for our target and compared it to the F6V and F6III stars of the XSL. Second, we considered the depth of the higher level Paschen lines relative to the Ca II IR triplet, as it also depends strongly on gravity. Both methods indicate a gravity value significantly smaller than that of main sequence stars, but larger than those of giant stars. We hence conclude that the luminosity class must be comprised between III and V, similarly to Mendigutía et al. (2014).

16.1.9 Appendix B: Residual speckle uncertainty on the parameters of HD 142527 B

In order to evaluate the residual speckle uncertainty for the radial separation, PA and contrast of the companion derived with NEGFC, we first subtracted the companion from the original cubes using the optimal companion parameters found with NEGFC in each chan-

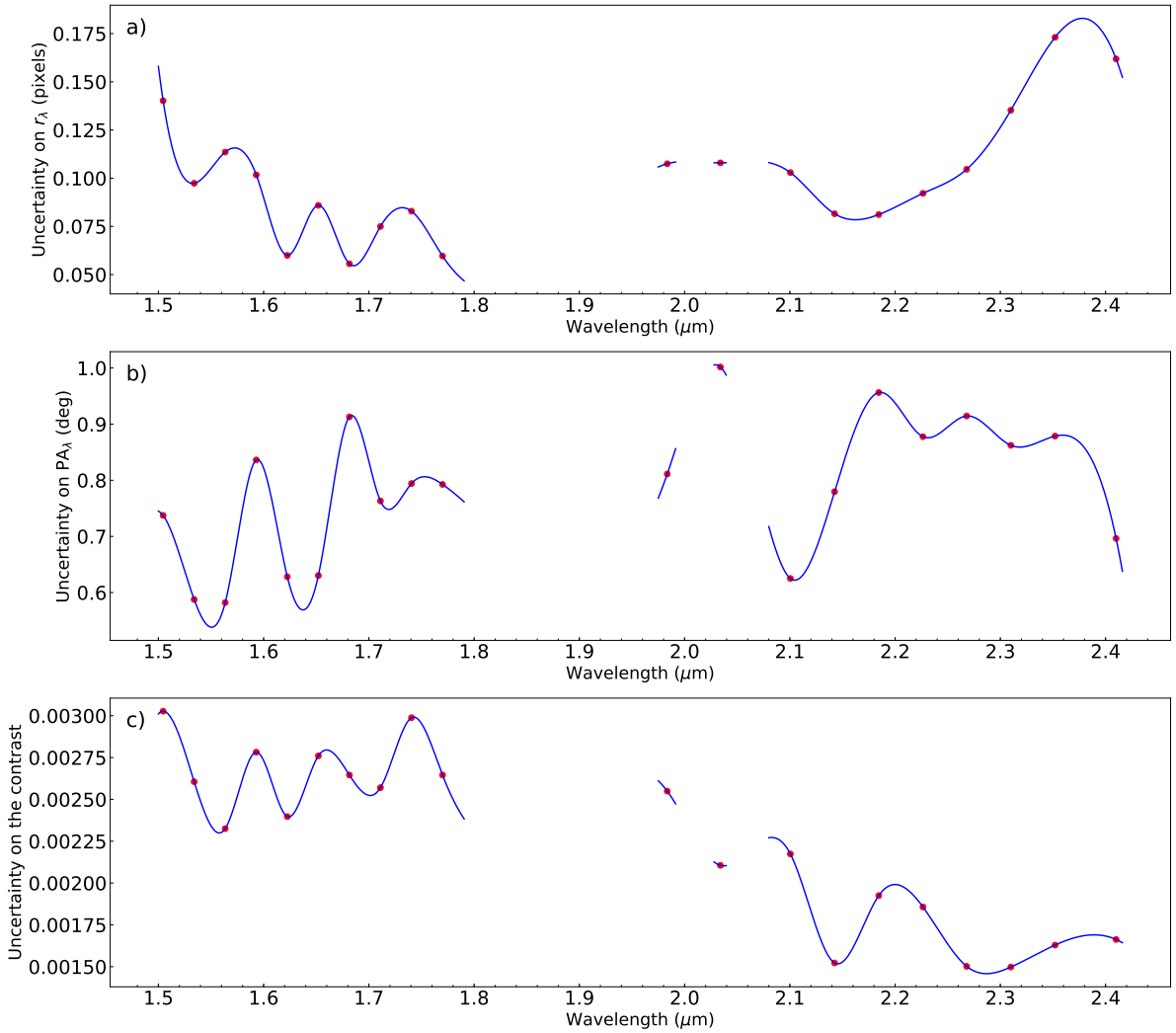

Figure 16.10: Estimated uncertainties on the parameters of HD 142527 B retrieved by NEGFC: **a)** radial separation (in pixels), **b)** position angle (in degrees), and **c)** contrast with respect to the primary in the different spectral channels.

nel (Fig. 16.4). Then, for each channel, we injected one by one a series of 360 (positive) fake companions at the same median radial separation than the companion, equally separated azimuthally by one degree. Each individual fake companion is injected at the inferred contrast of the companion, at a known radial separation and PA. We then run again the NEGFC simplex algorithm with the 24 different sets of parameters detailed in Sect. 16.1.4, spanning different aperture sizes, figures of merit and number of principal components used in PCA. Next, we compute the median difference (over the 24 runs) between the injected companion parameters and the optimal parameters returned by NEGFC. The 1σ–widths of the error histograms over the 360 fake companions can be considered as a good estimate of our residual speckle noise uncertainty (Wertz et al. 2017).

Given the large amount of resources required by the procedure described above, we only applied it to 20 different spectral channels spread over the H+K spectrum. Considering the high correlation between neighboring spectral channels, the estimated uncertainties should be similar in neighboring channels. Therefore, we interpolated the uncertainties to

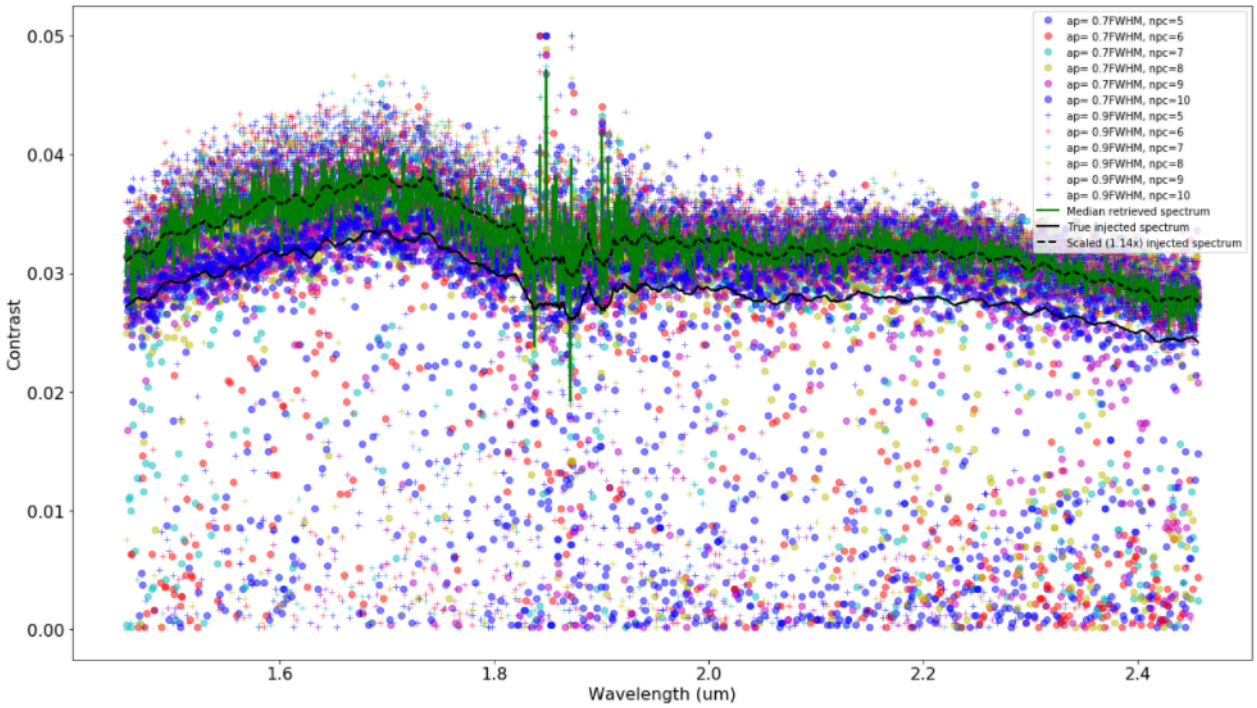

Figure 16.11: Extracted spectrum of an artificially injected companion on top of the strongest speckle feature located at the same radial separation as the companion, at a PA of $240°$. The true injected spectrum is shown with the *solid black curve*. The contrast of the companion is estimated in each spectral channel with different sets of NEGFC parameters: $n_{pc} \in [5, 10]$ and apertures of 0.7 and 0.9 FWHM, using the *standard deviation* as figure of merit (see details in Sect. 16.1.4). For clarity, we do not show the contrast estimates using the *sum* as figure of merit, but do include these results in the median contrast spectrum obtained over all 24 reductions (*green curve*). The median retrieved contrast spectrum follows well the shape of the injected spectrum, but scaled up by a factor 1.14 (*dashed black curve*).

all spectral channels using a cubic spline. The 1σ–uncertainties on the radial separation, PA and contrast of the companion are shown in Fig. 16.10a, b and c respectively.

A possible weakness in this method is that it assumes that the speckle pattern is randomly distributed in the image. Images in Fig. 16.2a to c might suggest a preferential triangular geometry for the speckle pattern, with the companion possibly located on top of one of the vertices. Although this pattern is significantly damped when using PCA-annulus with sufficient principal components (Fig. 16.2d), we considered the worst case scenario and investigated the extraction of the spectrum of an artificially injected companion at the second brightest vertex of that triangle (the brightest after the companion itself). We proceeded as follow. We first subtracted the companion from the original cubes using the optimal companion parameters found with NEGFC in each channel, then injected the artificial companion at the same radial separation but at a PA of 240°. That artificial companion was injected at the same contrast as estimated by NEGFC for the real companion in each spectral channel (Fig. 16.4c), but after smoothing it. The injected spectrum is shown by the *black curve* in Fig. 16.11. We then used NEGFC with the 24 different sets of parameters to estimate the optimal radial separation, PA and contrast of the artificial companion in each spectral channel, in a similar way as for the real companion (see Sect. 16.1.4). For clarity, Fig. 16.11 only shows the 12 reductions corresponding to the *standard deviation* figure of

merit, $n_{pc} \in [5, 10]$ and apertures of 0.7 and 0.9 FWHM. Analogously to the NEGFC reductions for the real companion, we notice the presence of a significant amount of outliers in individual channels, which justify the use of the median of the different runs (*green curve*) to infer the contrast of the companion. The shape of the median contrast spectrum is remarkably similar to the injected spectrum, as can be seen from the comparison to the injected spectrum scaled up by a factor 1.14 (*dashed black curve*). The speckle feature hence only adds a global uncertainty on the flux of the companion of up to 15%, but does not affect significantly the shape of the extracted spectrum ($\sim 5\%$ relative uncertainty). We do not expect the uncertainty on the absolute flux of the true companion to be larger than 15% provided that injecting fake companions at all PA leads to 5–10 % uncertainties on the contrast of all channels (Fig. 16.10c), i.e. slightly more than 5% but less than 15%.

Given that the 15% uncertainty only affects the absolute flux level of the companion, but not the shape of the spectrum, we consider the 5 to 10 % uncertainties mentioned in Fig. 16.10c for the best fit to BT-SETTL models (Sect. 16.1.5) and template spectra (Sect. 16.1.5). However, we conservatively propagate the 15% flux uncertainty to the best fit radius of the companion, since it is the relevant parameter for scaling the BT-SETTL models (provided in units of flux at the stellar surface) to the observed flux of HD 142527 B. In the case of the fit to the photosphere+hot environment model, the 15% uncertainty is included in the best-fit parameter ranges of R_B and $R_{\rm d}$ provided in Table 16.2.

17 Summary and future plans

In Chap. 15, I described the technical aspects and results obtained in a pilot study which aimed to search for young low-mass companions in a selected sample of transition disks using VLT/SINFONI, an AO-fed IFS equipped with a pupil-tracking mode. We coupled PCA with both SDI and ADI in two separate steps (in that order) to take advantage of both the spectral and angular diversity present in the data in order to reach the highest possible contrasts. We compared the results obtained with PCA-ASDI and PCA-ADBI, where the main difference between both algorithms is that the former uses all the spectral channels of the cube for the SDI part, while the latter first collapses the cube spectrally in H and K before applying SDI on the two collapsed bands (more details in Sec. 15.3.2). Taking advantage of the strong correlation of speckles between the numerous spectral channels of SINFONI ($\sim$ 2000), we reached final contrasts that are close to what is obtained with last-generation extreme-AO instruments such as SPHERE; as demonstrated with our PCA-ASDI contrast curves, the final image of the spirals of HD 135344 B (Sec. 15.4.1) and the re-detection of protoplanet candidate PDS 70 b (Sec. 15.5.1). Furthermore, for companions with a contrast that is within reach of that obtained with PCA-ADI in individual spectral channels of SINFONI, its medium spectral resolution enables a more detailed spectral characterization of such companions than based on the IFS of extreme-AO instruments.

17.1 Summary of the results on individual sources

HD 135344 B The spiral pattern is well recovered with PCA-ASDI ($n_{\rm pc}^{ADI}$=1, $n_{\rm pc}^{SDI}$=1), and compare very well with the polarized light image obtained with SPHERE/ZIMPOL (Stolker et al. 2016). When $n_{\rm pc}^{ADI}$ is increased and/or PCA-ADBI is used, the final images show broken spirals suggestive of self-subtraction. A tentative bright extended signal (SNR$\sim$7; 4.0σ detection) is seen right inward from the inner rim of the cavity. If not a speckle artifact, it would likely trace a transient event since it has no counterpart in neither polarimetric images nor L' band images at other epochs.

HD 142527 Applying PCA-ASDI and PCA-ADBI on the recombined 4D cube enables to recover the companion, HD 142527 B. However, the detection is more significant with ADBI (SNR$\sim$7.5; 3.5σ). Using ADI-based algorithms alone in separate spectral channels, we recovered the companion candidate at a separation of $\sim$80 mas in most spectral

channels. This allowed us to extract a spectrum for the companion, which we then compared to synthetic BT-SETTL spectra and template spectra. We inferred the companion to be an M2.5±1.0 star with an effective temperature of 3500±100 K, possibly surrounded with a hot (1700 K) circum-secondary environment. Its mass and age were derived to be 0.34±0.06$M_{\rm Jup}$ and 1-3 Myr, respectively. Altogether the new revision of its mass to higher values further supports its role in shaping the disk.

HD 179218 Using PCA-ADBI, a point-like source detection with an SNR∼8.0 (4.7σ) is obtained at ∼0″.16 separation to the SW of the star. No significant signal is obtained with ASDI, which inspires caution. However, a tentative blob is also seen at roughly the same location in NIRC2 L' data (G. Ruane, private comm.), which is encouraging, but requires further confirmation and a more in-depth analysis.

PDS 70 A tentative detection of a companion candidate was obtained with PCA-ADBI while a tentative spiral-like feature is seen in the PCA-ASDI image, possibly connecting the companion candidate with the outer disk. The companion candidate is also claimed in Keppler et al. (2018, in press) at the same location, where they present detections at several epochs. However, no sign of spiral arm is seen in their polarimetric images which inspires caution.

HD 100546 Back at the time this project started, HD 100546 was the source holding the highest potential of successful protoplanet confirmation given the recent claim of protoplanet candidate presence (Quanz et al. 2013a). It was assigned first priority in this mini-survey. Ironically, it appears to be the only source of the sample that did not lead to any potential detection, of either extended or point-like signal. This can be assigned to a combination of (1) an observing strategy leading to biases difficult to handle in post-processing; (2) a mishap forcing the interruption of the observed sequence; (3) an unusual stellar halo, which did not appear well cross-correlated with all other spectral channels of a same datacube. Nonetheless, I still reached a similar contrast at the location of hypothetical protoplanet HD 100546 as in the NACO K-band observations of Quanz et al. (2015a).

17.2 Strengths and weaknesses of each algorithm

Using PCA-ASDI in two separate steps (PCA-SDI+PCA-ADI) systematically leads to higher contrasts than using PCA with both SDI and ADI handled in one step. Furthermore, the application of PCA-ASDI and PCA-ADBI on the dataset of HD 135344 B suggests that PCA-ASDI preserves better extended structures, since the spiral arms appear more conspicuous and less self-subtracted in the final image. This is also confirmed by our synthetic spiral arm injection tests (Fig. 15.17). We suspect this to be due to the SDI part of PCA-ADBI to be slightly less effective than in PCA-ASDI, possibly caused by a slightly lower cross-

correlation obtained after smearing due to collapse in wavelength. Therefore, to reach similar contrast, the algorithm is more aggressive in the ADI part. Typically, for a given value of $n_{\rm pc}^{SDI}$, $n_{\rm pc}^{ADI}$ has to be slightly larger for PCA-ADBI for both algorithms to reach similar contrasts. Results on HD 142527, HD 179218 and PDS 70 suggest that PCA-ADBI is more appropriate to find point-like sources than PCA-ASDI, as it leads to higher SNR values for the companions found in those datasets. A more in-depth analysis is required to better understand the apparent better sensitivity of PCA-ASDI to recover extended structures, and the better potential of PCA-ADBI to detect point-like sources.

17.3 Future plans

17.3.1 Cross-correlation technique

The *Doppler deconvolution* technique consists in retrieving the spectrum of a known exoplanet based on the cross-correlation of templates to the measured combined (star+exoplanet) spectrum. This technique is most appropriate to very high-resolution spectra, obtained e.g. with VLT/CRIRES, and has enabled the detection of a few molecules in the atmosphere of hot Jupiters (e.g. CO and water; Snellen et al. 2010; Birkby et al. 2013, resp.). Nonetheless, Snellen et al. (2017) have recently shown that the combination of high-pass filtering and template cross-correlation might enable the re-detection of Proxima b using the medium-resolution IFS of JWST (NIRSpec). This idea was further exploited in Hoeijmakers et al. (2018), who used archival SINFONI data to conspicuously re-detect βPic b based on the cross-correlation of both synthetic BT-SETTL spectra and molecular template spectra (CO, CH_4 and H_2O) with each spaxel of the field. The results of this recent investigation brought a lot of optimism regarding the potential of using the SINFONI data of our mini-survey to detect faint companions.

Therefore, I provided my calibrated datasets to Sabyasachi Chattopadhyay, working under the supervision of Dr. Olivier Absil, who implemented the technique described in Hoeijmakers et al. (2018). First results on HD 142527 B were encouraging. The cross-correlation technique using BT-SETTL spectra led to the re-detection of the companion, and the derivation of the same physical parameters as I obtained based on the spectrum retrieved using PCA-ADI in each spectral channel ($T_{\rm eff} \approx 3500$K, $\log(g) \approx 4.5$; Sec. 16.1). These results along with the implementation of a criterion to estimate the detection limits achieved by this technique will be presented in Chattopadhyay et al. (2018, in prep.). At the time this thesis is being written, the technique has been applied to the HD 135344 B and PDS 70 datasets as well, but did not enable to confirm any companion candidate in those disks. The technique still has to be applied to the HD 100546 and HD 179218 datasets.

17.3.2 Frame selection criterion for SDI

The implementation of a PCA-ASDI algorithm with a certain wavelength threshold for the selection of frames to be included in the PCA library might further improve the sensitivity of PCA-ASDI by minimizing self-subtraction, and might possibly help to better understand the different sensitivities of PCA-ASDI and PCA-ADBI towards extended and point-like source. For PCA-ADI in annuli, the common criterion used to minimize self-subtraction is to build the PCA library using frames in which a putative companion at the radial separation of the considered annulus would move by at least 1 FWHM azimuthally, which translates into a criterion of minimum difference in parallactic angle. For SDI, a similar criterion would involve a minimum difference in wavelength, for the radial motion of faint signals of interest to be sufficient during frame rescaling, and hence minimize self-subtraction. In the case of the H+K grating of SINFONI the wavelength ranges from 1.45 to 2.45μm (this is the mode with the most extended wavelength coverage). A 1-FWHM minimum radial motion, even for spectral channels in the middle of that wavelength range, would only be possible beyond $\sim$0$''$.19 separation (considering a typical value of 1 FWHM = 0$''$.07 in the last channel of K band). To extend the range of radial separations where PCA-ASDI would be useful would require the use of the four-points dithering pattern (which would extend it only outward), or to slightly relax the 1-FWHM threshold.

17.3.3 Follow-up of HD 179218

As seen in Sec. 15.4.4, a companion candidate was found around HD 179218. This source was also observed by Gary Ruane using NIRC2+AGPM, who found a tentative blob around the same location. An archival NACO+AGPM dataset in L' is also available on that source, obtained by ISPY in good conditions, with a long integration and a lot of rotation. Therefore, my plan is to reduce the NACO dataset and check if the point-like source obtained using PCA-ADBI on the SINFONI dataset can be recovered at that location. The ISPY dataset will be included in my NACO transition disk survey anyway (Chap. 11). If the point-like source is redetected in the NACO dataset, I will also re-analyze in more details the NIRC2 dataset. As seen in Sec. 11.6.6 in the case of HD 135344 B, speckle tests alone might not be able to provide a clear-cut answer regarding the authenticity of bright close-in signals. However, comparing the results obtained with 3 different instruments is likely to be the best way to check the authenticity of the point-source.

17.3.4 Deeper analysis of PDS 70

Although the detection of the companion is tentative in our data, a study led by the SPHERE consortium led to the detection of a companion at the same location as point b in our images, in multi-epoch observations (Keppler et al. 2018, in press.). This casts confidence for the protoplanet interpretation. With their SPHERE-IFS data in $YJH + K1K2$ bands, the SPHERE team plans to characterize spectrally this companion candidate.

After binning the spectral channels of SINFONI by a factor of 20 and applying PCA-ADI in annuli in those spectral bins, I noticed that the companion is recovered at an almost similar level as in Fig. 15.14b, when the whole K-band spectral channels are collapsed. This suggests that spectral information can be further extracted from the data in a similar way as in Sec. 16.1 but with binned spectral channels. This spectral information would be complementary to what can be retrieved with SPHERE. Therefore, I plan to further exploit the data after completion of my thesis. A collaboration with the SPHERE team will likely be sought where I would contribute with the K-band binned spectrum of the companion. This would enable a more constructive characterization of the companion using a better spectral sampling than with the SPHERE or SINFONI data alone.

V Conclusions and future perspectives

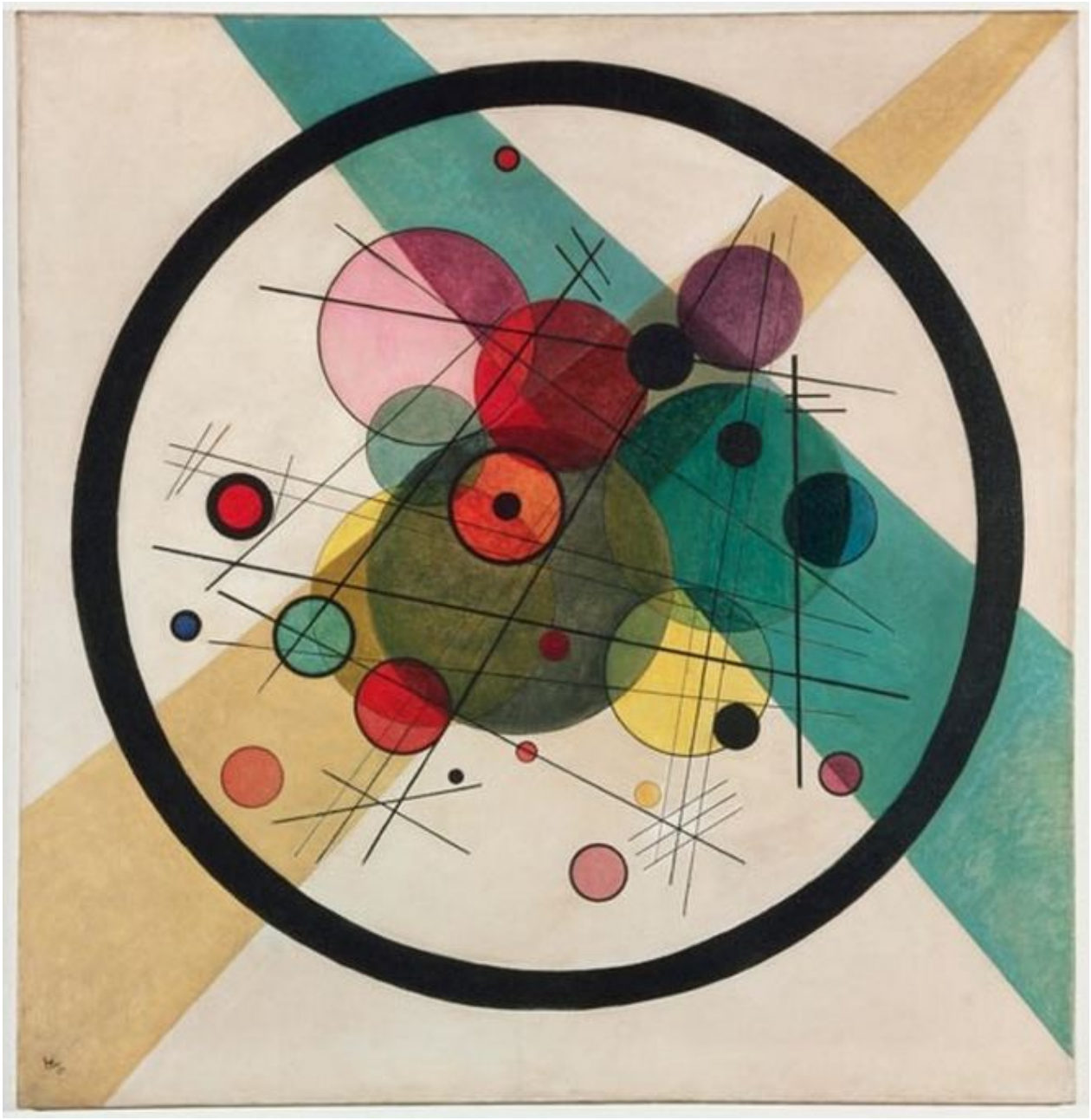

Circles in a circle (Kandinsky, 1923)

This part summarizes the main results obtained throughout this thesis. As exemplified by the results presented in this work, synergy between different techniques is required to put together the missing pieces of the planet formation puzzle. In the last chapter of this thesis, I will discuss future prospects enabled by upcoming space- and ground-based instruments.

I may not have gone where I intended to go,
but I think I have ended up where I needed to be.

Douglas Adams (from *The Long Dark Tea-Time of the Soul*)

18 Main conclusions of this work

In this thesis, I have tackled the issue of constraining the mechanisms involved in the process of planet formation, including the mutual feedback between the planet and its birth environment. To that purpose, I focused on *transition disks with large gaps*, arguably the most promising sources to study the formation of giant planets in-situ and the effects of their interaction with the disk. The topic was approached from three different, yet complementary, angles: the imaging and characterization of structures in transition disks which could be planet signposts, with a particular focus on spiral arms (Part II); the high-contrast imaging search for protoplanets in these disks in the thermal infrared domain (Part III); and the use of an integral field spectrograph to both detection and spectrally characterize young low-mass companions in these disks (Part IV).

18.1 Planet signposts and spiral arms in transition disks

In Part II, I first provided a review of all possible planet signposts observed in transition disks, namely large cavities, annular gaps, asymmetric dust distributions, shadows, warps and spiral arms (Chap. 6). For each of them, I detailed the possible alternative origins. While several different mechanisms could create them, for some of them, there is currently no alternative scenario that can account for their morphology apart from the dynamical interaction with embedded companions. This is the case of large dust cavities with depleted gas content (Sec. 6.1), and warps, which can be inferred from the observation of two sided-shadows (Sec. 6.3).

Among the different planet signposts, I focused in details on spiral arms (Sec. 6.4). I performed a compilation of observed spiral arms in transition disks, and noticed a variety of spiral morphologies (Fig. 6.5), which might be a first hint that not all spirals are produced by a single mechanism. I considered all mechanisms reported in the literature so far (to my knowledge) that were able to lead to the formation of spiral arms in a protoplanetary disk, namely embedded companions, gravitational instability, shadows, stellar flybys, late-envelope infall, warps and dust traps, and investigated ways to discriminate between them based on the expected morphology of the induced spirals. Case by case studies suggest different origins in different systems (Table 6.2). Nonetheless, a larger fraction of spirals do share a grand-design morphology which, in the absence of shadows, suggest

that they are due either to embedded companions or gravitational instability (or a combination of both effects; Pohl et al. 2015). In particular, embedded companions appear as the only explanation for spirals observed in older transition disks (e.g. HD141569; Mawet et al. 2017a), while the effect of gravitational instability might be non-negligible at earlier ages considering in particular that transition disks with large gaps could also correspond to massive protoplanetary disks (Sec. 8.1) and that disk masses are typically underestimated (Sec. 2.1).

Based on the above considerations, I carried out a detailed analysis of the spiral arms observed in MWC 758 (Sec. 7.2). The trace of each spiral was identified and fitted to the spiral equation inferred from density wave theory (Rafikov 2002; Muto et al. 2012), the evolution of the pitch angle was measured for each spiral, the separation angle was measured between each pair of spirals, and a proper motion analysis was performed between observations of the spirals obtained at two different epochs. Based on the results of the spiral characterization, and considering the full morphology of the disk (eccentric cavity+spirals+double dust trap; e.g. Dong et al. 2018a), the most likely scenario involves two companions, one in the cavity (possibly the bright blob identified in Sec. 12.1; Reggiani et al. 2018) and one in the outer disk (possibly truncating it; Dong et al. 2018a).

I also investigated in details the case of HD 142527. We discovered large-scale, very cold, CO spiral arms in ALMA cycle 0 data (Sec. 7.3.2). Their origin is still unsure, they could either be induced by gravitational instability or by the two-sided shadows (or a combination of both; Sec. 7.1). Comparison of the NIR spirals stemming from the edge of the cavity to spirals produced in hydro-dynamical simulations of the disk considering the dynamical effect of the low-mass binary companion allowed us to favor a family of simulated orbits for the injected companion, and hence constrain the orbit of HD 142527 B (Sec. 7.3.3). Another important result from that analysis is that an inner companion appears able to launch one or several spiral arms in the outer disk if it is on an inclined and eccentric orbit. This conclusion incentivizes the exploration of the inclined+eccentric orbit hypothesis in new hydro-dynamical simulations to test whether other observed spiral arms could be due to companions in the cavity rather than in the outer disk, where they have been elusive so far (e.g. Secs. 11.6.6 and 12.1.1; for HD 135344 B and MWC 758, resp.). This is further motivated by recent hydro-dynamical simulations and theoretical work suggesting that eccentricity and inclination excitation might be expected for companions of a certain mass range located within the gap or cavity of a transition disk (Sec. 3.4.2). The results of our hydro-dynamical simulations also suggested that the strongest spiral density wave launched by the companion could trigger the large dust trap seen in the outer disk (Sec. 7.3.3), due to the associated gas surface density bump, instead of requiring a vortex (Sec. 6.2.2). This possibility might deserve more thorough investigation as it could account for the morphology of other systems where a spiral is observed to be coincident with an elongated dust trap (e.g. HD 135344 B and V1642 Ori; van der Marel et al. 2016a; Kraus et al. 2017).

Finally, I briefly discussed in Chap. 8 the results obtained from the first complete resolved study of a disk population, which found that 11% of disks in Lupus were transition disks with a large gap (Ansdell et al. 2016; van der Marel et al. 2018). Whether these results suggest (i) an abundance of giant planets at 5–20 au, (ii) a significant inward migration

during the gas-rich phase, (iii) an overprediction of the luminosity of young giant planets in formation models, or (iv) the presence of a significant fraction low-mass binary companions in these transition disks will require complementary studies. More insight should be brought by similar surveys in other disk populations such as the on-going ODISEA survey in Ophiuchus (Cieza et al., in prep.; Sec. 8.1.1).

18.2 Thermal-IR high-contrast imaging of companions in young disks

In Chap. 10, I first provided a focused review of state-of-the-art HCI techniques. These techniques were then used to conduct a survey of transition disks in thermal IR using VLT/-NACO, whose results are presented in Chap. 11. I detailed the target selection (Sec. 11.2), the observing techniques that were employed (Sec. 11.3) and the pipeline that I implemented to calibrate the biases of NACO (Sec 11.4). Taking advantage of the capabilities of the AGPM coronagraph (Sec. 10.2.1) for the brightest sources of our sample, coupled with advanced post-processing algorithms based on PCA (Sec. 11.5.1), we optimized our chances to detect faint companions around the sources of our survey. Four new companion candidates were identified out of 15 transition disks observed so far, namely around WW Cha (Sec. 11.6.5), HD 135344 B (Sec. 11.6.6), J1622-3724 (Sec. 11.6.7) and J1900-3645 (Sec. 11.6.8). Follow-up observations are nonetheless required to confirm them. In particular, we showed that at small angle, there is currently no clear-cut method to disentangle between the possibilities of speckle and authentic companion signals. The most reliable test so far might consist in re-detecting the companion with different instruments. But even so, the detection obtained in the case of HD 135344 B with two instruments at two different epochs with two different post-processing techniques should still inspire caution since follow-up observations have not enabled to recover the point-like source yet.

Other results from this survey include the (re-)detection of scattered light from the disks around HD 100453 (Sec 11.6.3), T Cha (Sec 11.6.4), and HD 135344 B (Sec 11.6.6). We also applied the technique of binary differential imaging to the dataset of HD 98800, and although we did not reach a high contrast due to overlapping PSFs, we foresee a high potential for more widely separated binary systems (Sec 11.6.9).

Apart from this survey, I also contributed to the detection of a red substellar companion in the debris disk of HD 206893, using NACO+AGPM data in L' band (Sec. 12.2.1). Follow-up observations with SPHERE-IFS confirmed extremely red colors, which might suggest either an extremely dusty atmosphere, or the presence of a very dusty external environment such as a long-lasting circum-companion disk (Sec. 12.2.2).

18.3 Detection and spectral characterization of companions in transition disks with an IFS

In Chap. 15, I presented the mini-survey of transition disks with companion signposts carried out with VLT/SINFONI. We took advantage of the spectral and angular diversity in our data to reach an optimal contrast using a combination of PCA with SDI and ADI, in two consecutive steps (Sec. 15.3.2). In the dataset of HD 135344 B (Sec. 15.4.1), the achieved contrast was similar to that obtained with extreme-AO SPHERE/IRDIFS data (Maire et al. 2017), and the disk image showing the spirals compared well with the ZIMPOL image (Stolker et al. 2016). In the dataset of HD 100546 (Sec. 15.4.2), despite several sources of bias preventing an optimal reduction of the data, we still reached a similar contrast as VLT/NACO in K band at the expected location of protoplanet candidate HD 100546 b (Quanz et al. 2015a). In the dataset of HD 179218 (Sec. 15.4.4), we tentatively detect a companion at a 4.7σ level at a separation of $0''.16$ from the star. A similar point-like source is tentatively seen at roughly the same location in NIRC2 data (G. Ruane, private comm.).

In the SINFONI dataset of PDS 70 (Sec. 15.5.1; Christiaens et al. 2018a), we obtained tentative detections of a companion and a spiral-like feature connecting the companion to the outer disk, using our two algorithms most sensitive to point-like and extended signals; respectively. Our spiral injection tests confirmed that ADI processing could inject significant geometric biases in the final image (Fig. 15.17), and only the least aggressive of our reductions could be trusted to infer the presence of a possible spiral. The presence of a planetary-mass companion around PDS 70, at the exact same position and contrast as our SINFONI candidate companion, was first announced by the SPHERE team (Keppler et al., in press), which casts confidence on the authenticity of the detection. However, the absence of counter-part for the spiral-like feature in their polarized images of the disk is intriguing.

In the dataset of HD 142527 (Sec. 16.1; Christiaens et al. 2018b), a reduction based on the angular diversity was enough to redetect the companion conspicuously in most individual spectral channels, allowing me to retrieve the first medium-resolution spectrum of a low-mass companion at less than $0''.1$ separation. In-depth spectral characterization based on least-squared fits to BT-SETTL models and template spectra enabled to infer the physical parameters for the companion. The effective temperature was constrained to 3500 ± 100 K, with a possible contribution from a hot circumsecondary environment (~ 1700K). The mass and age are estimated to be $0.34 \pm 0.06 M_{\odot}$ and 0.5-3 Myr, resp., based on the comparison of the position of the companion to isochrones from evolutionary models of different stellar masses in HR diagrams (Baraffe et al. 2015). The revised mass (to a higher value) was used in the hydro-dynamical simulations presented in Sec. 7.3.3 to confirm the role of the companion in shaping the disk.

Finally, our results obtained with an IFS originally not originally designed to reach very high contrast suggests that similar architectures for future extreme-AO fed IFS holds high potential to reach even higher contrasts.

In conclusion, this thesis has provided new insights into transition disks with large gaps through synergetic multi-wavelength observations and spiral modeling. The most likely culprit for the peculiar morphology of the transition disk of HD 142527 was narrowed down to its low-mass binary companion. The analysis I carried out for the spirals in MWC 758 as well as other known features of this disk suggest the presence of two embedded companions. Four possible companion detections were obtained in my thermal-IR survey of transition disks, although they require follow-up for confirmation. Both the confirmed companions and the non-detections will feed a statistical analysis on the occurrence of protoplanets in transition disks, which should provide useful constraints on where, when and how giant planets form. The mini-survey carried out with VLT/SINFONI led to a wealth of results, which might be assigned to the combination of (1) the exquisite contrast achieved when exploiting optimally the spectral and angular diversity present in the data, and (2) the target selection, consisting of the transition disks with some of the most conspicuous companion signposts (Chap. 6). Finally, the global approach followed in the case of HD 142527 (multi-wavelength observations, hydro-dynamical simulations, spiral analysis if any) will be pursued for confirmed companions in our NACO and SINFONI surveys. This will provide better insight into companion-disk interactions and better constraints on the companions.

19 Future prospects

19.1 Synergy of direct and indirect protoplanet detection methods

Similarly to indirect methods of exoplanet detection in mature systems, that are based on the scrutiny of the parent star light, indirect methods of protoplanet detections based on the analysis of signals from the disk constitute a promising avenue to complement the weaknesses of HCI.

19.1.1 Kinematics of the disk

Line observations of gas tracers with ALMA enable to probe the kinematics of the disk, based on the different radial velocities of the gas at different locations of the disk. An embedded companion is expected to perturb the gas velocity field in its vicinity, which could leave a detectable signature whose strength (i.e., velocity dispersion amplitude) depends on the mass of the perturber. In a similar way, sampling the kinematics of the disk has been proposed to detect circumplanetary disks, which are comparable to miniature accretion disks within a larger (circumstellar) accretion disk (e.g. Perez et al. 2015).

This technique is particularly appropriate at young age considering that primordial disks are optically thick, and it is unsure whether direct light from embedded protoplanets can be traced at the earliest stages of their formation. First results obtained with the application of this technique on HD 163296 are encouraging, with the possible discovery of several giant planets at large separation (Teague et al. 2018; Pinte et al. 2018). Combination of this technique with high-contrast imaging of protoplanets in transition disks, where there is a higher chance to trace direct light from the nascent planets in the clearing, might reveal particularly synergetic. The two detection methods provide indeed independent luminosity and mass estimates, enabling to discriminate between different planet formation models (provided a good age estimate).

19.1.2 Global hydro-dynamical simulations of disks

The work presented in Price et al. (2018, Sec. 7.3.3) shows that at least in some cases, all the disk features can be qualitatively accounted for by the dynamical interaction between a companion and the disk. While this opens the gate to similar works for other disks presenting similar features as HD 142527, in practice a high degeneracy on the number of parameters involved in the simulations might impede an efficient blind use of it (i.e., without sufficient prior constraints on the companion). This technique appears thus most appropriate in combination with either high-contrast imaging or the disk kinematics technique, which can both provide the location of the companion. The hydro-dynamical simulations can then provide constraints on the mass and orbit of the companion required to reproduce the observed disk features. This technique might reveal useful to confirm promising HCI point-like sources whose authenticity cannot be disentangled from speckles based on HCI alone.

19.2 Future of high-contrast imaging

19.2.1 Promising high-contrast imaging techniques

High Dispersion Coronagraphy is a promising technique to reach extremely high contrast (Riaud & Schneider 2007; Snellen et al. 2015; Wang et al. 2017; Mawet et al. 2017b). The principle consists in combining high-contrast imaging techniques and high spectral resolution spectroscopy, by providing an AO-corrected and coronagraphic beam to the high-resolution spectrograph, e.g. through an optic fiber (Mawet et al. 2017b). Several projects are planned to exploit this concept, such as Keck/KPIC (Mawet et al. 2016) or HiRise (SPHERE+CRIRES; Vigan et al., in prep.), which has the potential to reach the necessary contrast to image nearby Earth-like planets (Snellen et al. 2015).

Even in the case of medium-spectral resolution data, a high-contrast is expected to be achieved using the combination of a high-pass spectral filtering and cross-correlation (Snellen et al. 2017). First results with a SINFONI data set acquired on β Pic showed promising results in terms of sensitivity gains compared to ADI-based techniques alone (Hoeijmakers et al. 2018). Tests on our SINFONI datasets have confirmed that this technique worked well for bright close-in companion HD 142527 B, but could not detect the protoplanet candidate PDS 70 b (Chattopadhyay et al. in prep.). This technique could also find applications in the detection and characterization of exoplanets with the JWST/MIRI medium-resolution integral field spectrograph.

Automatic classification and machine learning have been on the rise in the transit community (e.g. McCauliff et al. 2015; Thompson et al. 2015), culminating recently with Google's AI discovering new transiting exoplanets that were missed by human inspection (Shallue & Vanderburg 2018). Similarly, Gomez Gonzalez et al. (2018) proposed a way to apply it to HCI in order to identify companions that might be missed by human eye or the classically

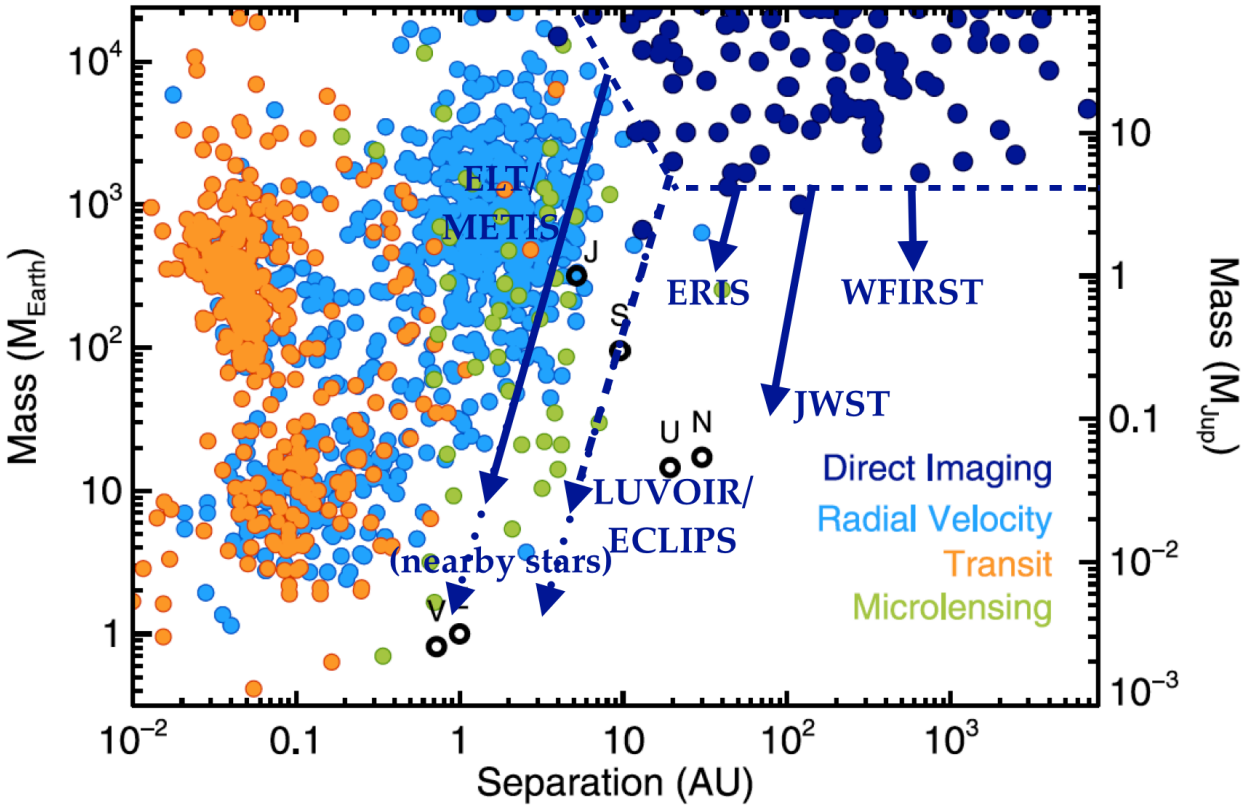

Figure 19.1: Expected sensitivity gain in terms of mass and semi-major axis for future high-contrast imaging instruments. Figure adapted from Bowler (2016).

defined SNR map (Sec. 10.5.1). The proposed technique involves training the machine with large libraries of PSFs obtained with the instrument. When the machine is then confronted to a new dataset, first results suggest that it can identify companions up to 1-2 mag deeper in contrast than classical HCI processing methods (such as PCA). Besides exoplanet detection, machine learning has been proposed recently for spectral characterization as well (e.g. Marquez-Neila et al. 2018). Machine learning is thus a major avenue for the future of HCI (as in other fields).

19.2.2 Future high-contrast imaging instruments

Figure 19.1 shows the predicted sensitivity improvement brought by upcoming high-contrast imaging instruments compared to the current population of directly imaged companions, in a mass versus semi-major axis diagram.

VLT/ERIS (e.g. Amico et al. 2012), the successor of both NACO and SINFONI, will also be equipped with state-of-the-art coronagraphs, such as the AGPM. Given its wavelength coverage up to $\sim 5\mu$m and its enhanced sensitivity, it will likely push the sensitivity limits towards slightly lower masses than currently achieved, in particular in young systems.

JWST, expected for launch in 2019, is the future workhorse of IR astronomy from space

(Gardner et al. 2006). With a 6.5m diameter telescope, it is expected to reach exquisite sensitivity in mid-IR which should significantly improve detection limits in the background-limited range of separations of IR ground-based instruments. It has the potential to detect and characterize young sub-Jupiters at large separation from their star (e.g. Beichman et al. 2010). It might even yield the first direct spectrum of young Neptune-size exoplanets (Schlieder et al. 2017).

WFIRST is another space telescope expected to reach high contrast, based on the inclusion of several state-of-the-art coronagraphs. Its limitation in terms of direct imaging of exoplanets might rather come from its small diameter (2.5 m) and wavelength range (up to 2μm only). However, based on its extreme sensitivity (100-fold improvement with respect to HST), it might be useful for the characterization of self-luminous giant planets at large separation (e.g. Spergel et al. 2015; Lacy et al. 2018).

With a launch date in the mid 2030s, future optical space-based telescopes such as LUVOIR are expected to enable transformative advances across a broad range of astrophysics, with 8 to 15 m in diameter and wavelength coverage from UV to IR (e.g. Crooke et al. 2016; Bolcar et al. 2016). In particular, the ECLIPS coronagraph concept might enable the direct imaging and spectroscopy of Earth-sized exoplanet.

From the ground, the future generation of instruments on 30-m class telescopes (ELTs) are expected to achieve 2–3 orders of magnitude deeper contrast than the current generation of extreme-AO instruments, and reach much closer angular separation (e.g. Gilmozzi & Spyromilio 2007; Quanz et al. 2015a). The Mid-IR ELT Imager and Spectrograph (METIS), equipped with state-of-the-art coronagraphs, should reach unprecedented sensitivity towards exoplanets (Brandl et al. 2014). It is expected to produce the first direct images of nearby (super-)Earths (Quanz et al. 2015b). It would also enable to bridge the gap between indirect and direct techniques in the mass versus semi-major axis diagrams, which implies more possibilities in terms of synergy, such as independent mass/radius estimates with RV/transits versus HCI brightness measurements. Furthermore, combined with high-dispersion coronagraphy, METIS could even lead to the first spectral characterization of nearby exo-Earths, and hence enable the search for bio-signatures (Snellen et al. 2015).

In conclusion, the most exciting times are ahead of us! Soon, the struggle to distinguish between a nascent multi-Jupiter mass exoplanet at tens of AU and a speckle will sound like an old nightmare (although the nightmare might shift to smaller masses and separations).

List of acronyms and symbols

List of acronyms

ADI	Angular Differential Imaging
AGPM	Annular Groove Phase Mask
ALMA	Atacama Large Millimeter Array
AO	Adaptive Optics
BDI	Binary Differential Imaging
CA	Core Accretion
CPD	Circumplanetary Disk
DBI	Dual-Band Imaging
DM	Deformable Mirror
FOV	Field of View
FWHM	Full Width at Half Maximum
GI	Gravitational instability
GPI	Gemini Planet Imager
HCI	High Contrast Imaging
IFS	Integral Field Spectrograph
LOCI	Locally Optimized Combination of Images
MR	Modified Rician (distribution)
NaCo	NAos-COnica
NIR	Near-Infrared
PCA	Principal Component Analysis
PSF	Point Spread Function
RDI	Reference star Differential Imaging
RV	Radial Velocity
SAM	Sparse Aperture Masking
SDI	Spectral Differential Imaging
SINFONI	Spectrograph for INtegral Field Observations in the Near Infrared
SNR	Signal to Noise Ratio
SPHERE	Spectro-Polarimetric High-contrast Exoplanet Research
VLT	Very Large Telescope
WFS	Wavefront Sensor

Physical parameters

$\Sigma(r)$	Surface density (radial) profile
$\Omega(r)$	Angular frequency of the disk
a_p	Semi-major axis of the planet's orbit
c_s	Sound speed
d	Distance from the Solar System
e_p	Eccentricity of the planet's orbit
$H(r)$	Protoplanetary disk scale height (in physical units)
$h(r)$	Protoplanetary disk aspect ratio: $H(r)/r$ (dimensionless)
i_p	Inclination of the planet's orbit (relative to the plane of the sky)
L_*	Luminosity of the parent star
M_*	Mass of the parent star
M_d	Protoplanetary disk mass
M_p	Mass of the planet
PA	Position angle (East from North)
r	Radial separation
R_*	Radius of the parent start
R_c	Protoplanetary disk characteristic radius
R_p	Radius of the planet
T_*	Temperature of the parent star
T_p	Temperature of the planet

Units and physical constants

arcsec	Arc second	$\frac{1}{206265}$ of a radian, or $\frac{1}{3600}$ of a degree
au	Astronomical unit	1.496×10^{11} m
c	Speed of light	2.998×10^8 m s^{-1}
Gyr	Gigayear	10^9 year
kpc	Kilo-parsec	1000 pc
$L_\odot$	Solar luminosity	3.828×10^{26} W m^{-2}
mas	Milli-arcsecond	10^{-3} arcsec
$M_\oplus$	Earth mass	5.972×10^{24} kg
M_Nep	Neptune mass	1.024×10^{26} kg $\approx 20 M_\oplus$
M_Jup	Jupiter mass	1.899×10^{27} kg $\approx 300 M_\oplus$
$M_\odot$	Solar mass	1.989×10^{30} kg $\approx 1000 M_\mathrm{Jup}$
Myr	Megayear	10^6 year
pc	Parsec	3.086×10^{16} m $= 206265$ au
px	Pixel	
$R_\oplus$	Earth radius	6.378×10^6 m
R_Jup	Jupiter radius	7.149×10^7 m $\approx 11 R_\oplus$
$R_\odot$	Solar radius	6.957×10^8 m $\approx 10 R_J$
Sr	Strehl ratio	

Bibliography

Absil, O. & Mawet, D. 2010, A&A Rev., 18, 317

Absil, O., Mawet, D., Karlsson, M., et al. 2016, in Proc. SPIE, Vol. 9908, Ground-based and Airborne Instrumentation for Astronomy VI, 99080Q, mypaper

Absil, O., Milli, J., Mawet, D., et al. 2013, A&A, 559, L12

Acke, B. & van den Ancker, M. E. 2004, A&A, 426, 151

Adams, F. C. & Laughlin, G. 2003, Icarus, 163, 290

Adams, F. C. & Watkins, R. 1995, ApJ, 451, 314

Aime, C. & Soummer, R. 2004, ApJ, 612, L85

Akeson, R. L., Rice, W. K. M., Boden, A. F., et al. 2007, ApJ, 670, 1240

Akiyama, E., Hashimoto, J., Liu, H. B., et al. 2016, AJ, 152, 222

Alexander, R., Pascucci, I., Andrews, S., Armitage, P., & Cieza, L. 2014, Protostars and Planets VI, 475

Alexander, R. D. & Armitage, P. J. 2007, Mon. Not. R. Astron. Soc., 375, 500

Alexander, R. D., Clarke, C. J., & Pringle, J. E. 2006, Mon. Not. R. Astron. Soc., 369, 229

Alibert, Y., Mordasini, C., & Benz, W. 2004, A&A, 417, L25

Allard, F., Homeier, D., & Freytag, B. 2012, Royal Society of London Philosophical Transactions Series A, 370, 2765

Allers, K. N., Jaffe, D. T., Luhman, K. L., et al. 2007, ApJ, 657, 511

Allers, K. N. & Liu, M. C. 2013, ApJ, 772, 79

ALMA Partnership, Brogan, C. L., Pérez, L. M., et al. 2015, ApJ, 808, L3

Amara, A. & Quanz, S. P. 2012, MNRAS, 427, 948

Amico, P., Marchetti, E., Pedichini, F., et al. 2012, in Proc. SPIE, Vol. 8446, Ground-based and Airborne Instrumentation for Astronomy IV, 844620

André, P. 1994, in The Cold Universe, ed. T. Montmerle, C. J. Lada, I. F. Mirabel, & J. Tran Thanh Van, 179

André, P., Ward-Thompson, D., & Greaves, J. 2012, Science, 337, 69

Andrews, S. M., Rosenfeld, K. A., Kraus, A. L., & Wilner, D. J. 2013, ApJ, 771, 129

Andrews, S. M. & Williams, J. P. 2005, ApJ, 631, 1134

Andrews, S. M. & Williams, J. P. 2007, ApJ, 671, 1800

Andrews, S. M., Wilner, D. J., Espaillat, C., et al. 2011, ApJ, 732, 42

Andrews, S. M., Wilner, D. J., Hughes, A. M., Qi, C., & Dullemond, C. P. 2009, ApJ, 700, 1502

Andrews, S. M., Wilner, D. J., Hughes, A. M., Qi, C., & Dullemond, C. P. 2010, ApJ, 723, 1241

Andrews, S. M., Wilner, D. J., Hughes, A. M., et al. 2012, ApJ, 744, 162

Andrews, S. M., Wilner, D. J., Zhu, Z., et al. 2016, ApJ, 820, L40

Ansdell, M., Williams, J. P., van der Marel, N., et al. 2016, ApJ, 828, 46

Ardila, D. R., Golimowski, D. A., Krist, J. E., et al. 2007, ApJ, 665, 512

Armitage, P. J. 2015, ArXiv e-prints

Artymowicz, P., Clarke, C. J., Lubow, S. H., & Pringle, J. E. 1991, ApJ, 370, L35

Artymowicz, P. & Lubow, S. H. 1994, The Astrophysical Journal, 421, 651

Arzamasskiy, L., Zhu, Z., & Stone, J. M. 2018, MNRAS, 475, 3201

Augereau, J. C. & Papaloizou, J. C. B. 2004, A&A, 414, 1153

Aumann, H. H., Beichman, C. A., Gillett, F. C., et al. 1984, ApJ, 278, L23

Avenhaus, H., Quanz, S. P., Garufi, A., et al. 2018, ArXiv e-prints

Avenhaus, H., Quanz, S. P., Schmid, H. M., et al. 2017, AJ, 154, 33

Avenhaus, H., Quanz, S. P., Schmid, H. M., et al. 2014, ApJ, 781, 87

Ayliffe, B. A., Laibe, G., Price, D. J., & Bate, M. R. 2012, MNRAS, 423, 1450

Backman, D. E. & Paresce, F. 1993, in Protostars and Planets III, ed. E. H. Levy & J. I. Lu-

nine, 1253–1304

Bae, J., Hartmann, L., Zhu, Z., & Nelson, R. P. 2014, ApJ, 795, 61

Bae, J. & Zhu, Z. 2017a, ArXiv e-prints

Bae, J. & Zhu, Z. 2017b, ArXiv e-prints

Bae, J., Zhu, Z., & Hartmann, L. 2016, ApJ, 819, 134

Bae, J., Zhu, Z., & Hartmann, L. 2017, ApJ, 850, 201

Balbus, S. A. & Hawley, J. F. 1991, ApJ, 376, 214

Baraffe, I., Chabrier, G., Barman, T. S., Allard, F., & Hauschildt, P. H. 2003, A&A, 402, 701

Baraffe, I., Homeier, D., Allard, F., & Chabrier, G. 2015, A&A, 577, A42

Barenfeld, S. A., Carpenter, J. M., Sargent, A. I., Isella, A., & Ricci, L. 2017, ApJ, 851, 85

Barge, P. & Sommeria, J. 1995, A&A, 295, L1

Barman, T. S., Macintosh, B., Konopacky, Q. M., & Marois, C. 2011, ApJ, 733, 65

Baruteau, C., Crida, A., Paardekooper, S.-J., et al. 2014, Protostars and Planets VI, 667

Baruteau, C., Meru, F., & Paardekooper, S.-J. 2011, MNRAS, 416, 1971

Baruteau, C. & Zhu, Z. 2016, MNRAS, 458, 3927

Beck, T. L., Bary, J. S., Dutrey, A., et al. 2012, ApJ, 754, 72

Beckwith, S. V. W., Sargent, A. I., Chini, R. S., & Guesten, R. 1990, AJ, 99, 924

Beichman, C. A., Krist, J., Trauger, J. T., et al. 2010, PASP, 122, 162

Beichman, C. A., Woolf, N. J., & Lindensmith, C. A. 1999, The Terrestrial Planet Finder (TPF) : a NASA Origins Program to search for habitable planets

Bell, C. P. M., Naylor, T., Mayne, N. J., Jeffries, R. D., & Littlefair, S. P. 2013, MNRAS, 434, 806

Benisty, M., Juhasz, A., Boccaletti, A., et al. 2015, A&A, 578, L6, mypaper

Benisty, M., Stolker, T., Pohl, A., et al. 2017, A&A, 597, A42

Benisty, M., Tatulli, E., Ménard, F., & Swain, M. R. 2010, A&A, 511, A75

Benz, W., Ida, S., Alibert, Y., Lin, D., & Mordasini, C. 2014, Protostars and Planets VI, 691

Bergin, E. A. 2009, ArXiv e-prints

Bergin, E. A., Cleeves, L. I., Gorti, U., et al. 2013, Nature, 493, 644

Bertout, C. 1989, ARA&A, 27, 351

Bertrang, G. H.-M., Avenhaus, H., Casassus, S., et al. 2018, MNRAS, 474, 5105

Beuzit, J.-L., Feldt, M., Dohlen, K., et al. 2008, in Society of Photo-Optical Instrumentation Engineers (SPIE) Conference Series, Vol. 7014, Society of Photo-Optical Instrumentation Engineers (SPIE) Conference Series

Biller, B., Lacour, S., Juhász, A., et al. 2012, ApJ, 753, L38

Biller, B. A., Males, J., Rodigas, T., et al. 2014, ApJ, 792, L22

Binney, J. & Tremaine, S. 1987, Galactic dynamics

Birkby, J. L., de Kok, R. J., Brogi, M., et al. 2013, MNRAS, 436, L35

Birnstiel, T., Andrews, S. M., & Ercolano, B. 2012, A&A, 544, A79

Birnstiel, T., Dullemond, C. P., & Brauer, F. 2010, A&A, 513, A79

Birnstiel, T., Ormel, C. W., & Dullemond, C. P. 2011, A&A, 525, A11

Bitsch, B., Crida, A., Libert, A.-S., & Lega, E. 2013a, A&A, 555, A124

Bitsch, B., Crida, A., Morbidelli, A., Kley, W., & Dobbs-Dixon, I. 2013b, A&A, 549, A124

Bitsch, B. & Johansen, A. 2016, A&A, 590, A101

Bloemhof, E. E. 2004, ApJ, 610, L69

Bloemhof, E. E., Dekany, R. G., Troy, M., & Oppenheimer, B. R. 2001, ApJ, 558, L71

Blum, J. 2018, Space Sci. Rev., 214, 52

Blum, J., Gundlach, B., Krause, M., et al. 2017, MNRAS, 469, S755

Blum, J. & Wurm, G. 2008, Annual Review of Astronomy and Astrophysics, 46, 21

Boccaletti, A., Augereau, J.-C., Lagrange, A.-M., et al. 2012, A&A, 544, A85

Boccaletti, A., Pantin, E., Lagrange, A.-M., et al. 2013, A&A, 560, A20

Boccaletti, A., Thalmann, C., Lagrange, A.-M., et al. 2015, Nature, 526, 230

Boden, A. F., Sargent, A. I., Akeson, R. L., et al. 2005, ApJ, 635, 442

Boehler, Y., Ricci, L., Weaver, E., et al. 2018, ApJ, 853, 162

Boehler, Y., Weaver, E., Isella, A., et al. 2017, ApJ, 840, 60

Boffin, H. M. J., Watkins, S. J., Bhattal, A. S., Francis, N., & Whitworth, A. P. 1998, MNRAS, 300, 1189

Bolcar, M. R., Feinberg, L., France, K., et al. 2016, in Proc. SPIE, Vol. 9904, Space Telescopes and Instrumentation 2016: Optical, Infrared, and Millimeter Wave, 99040J

Bonnefoy, M., Boccaletti, A., Lagrange, A.-M., et al. 2013, A&A, 555, A107

Bonnefoy, M., Chauvin, G., Lagrange, A.-M., et al. 2014, A&A, 562, A127

Bonnefoy, M., Chauvin, G., Rojo, P., et al. 2010, A&A, 512, A52

Bonnet, H., Ströbele, S., Biancat-Marchet, F., et al. 2003, in Society of Photo-Optical Instrumentation Engineers (SPIE) Conference Series, Vol. 4839, Society of Photo-Optical Instrumentation Engineers (SPIE) Conference Series, ed. P. L. Wizinowich & D. Bonaccini, 329–343

Borucki, W., Koch, D., Boss, A., et al. 2004, in ESA Special Publication, Vol. 538, Stellar Structure and Habitable Planet Finding, ed. F. Favata, S. Aigrain, & A. Wilson, 177–182

Borucki, W. J., Koch, D. G., Basri, G., et al. 2011, ApJ, 736, 19

Boss, A. P. 1997, Science, 276, 1836

Boss, A. P. 1998, ApJ, 503, 923

Bouwman, J., de Koter, A., Dominik, C., & Waters, L. B. F. M. 2003, A&A, 401, 577

Bowen, I. S. 1938, ApJ, 88, 113

Bowler, B. P. 2016, PASP, 128, 102001

Bowler, B. P., Liu, M. C., Kraus, A. L., Mann, A. W., & Ireland, M. J. 2011, ApJ, 743, 148

Bracco, A., Chavanis, P. H., Provenzale, A., & Spiegel, E. A. 1999, Physics of Fluids, 11, 2280

Brandl, B. R., Feldt, M., Glasse, A., et al. 2014, in Proc. SPIE, Vol. 9147, Ground-based and Airborne Instrumentation for Astronomy V, 914721

Brandt, T. D., McElwain, M. W., Turner, E. L., et al. 2014, ApJ, 794, 159

Brauer, F., Dullemond, C. P., & Henning, T. 2008, A&A, 480, 859

Bressan, A., Marigo, P., Girardi, L., et al. 2012, MNRAS, 427, 127

Brinch, C. & Hogerheijde, M. R. 2010, A&A, 523, A25

Brittain, S. D., Najita, J. R., & Carr, J. S. 2009, ApJ, 702, 85

Brown, J. M., Blake, G. A., Qi, C., Dullemond, C. P., & Wilner, D. J. 2008, ApJ, 675, L109

Brown, J. M., Blake, G. A., Qi, C., et al. 2009, ApJ, 704, 496

Bryden, G., Beichman, C. A., Trilling, D. E., et al. 2006, ApJ, 636, 1098

Bryden, G., Chen, X., Lin, D. N. C., Nelson, R. P., & Papaloizou, J. C. B. 1999, ApJ, 514, 344

Buenzli, E., Thalmann, C., Vigan, A., et al. 2010, A&A, 524, L1

Burgasser, A. J. 2014, in Astronomical Society of India Conference Series, Vol. 11, Astronomical Society of India Conference Series

Burgasser, A. J., Kirkpatrick, J. D., Brown, M. E., et al. 2002, ApJ, 564, 421

Burrows, A., Hubbard, W. B., Lunine, J. I., & Liebert, J. 2001, Reviews of Modern Physics, 73, 719

Burrows, A., Marley, M., Hubbard, W. B., et al. 1997, ApJ, 491, 856

Burrows, C. J., Stapelfeldt, K. R., Watson, A. M., et al. 1996, ApJ, 473, 437

Caffau, E., Ludwig, H.-G., Steffen, M., Freytag, B., & Bonifacio, P. 2011, Sol. Phys., 268, 255

Calvet, N., D'Alessio, P., Watson, D. M., et al. 2005, ApJ, 630, L185

Calvet, N. & Gullbring, E. 1998, ApJ, 509, 802

Calvet, N., Muzerolle, J., Briceño, C., et al. 2004, AJ, 128, 1294

Calvet, N., Patino, A., Magris, G. C., & D'Alessio, P. 1991, ApJ, 380, 617

Cameron, A. G. W. 1962, Icarus, 1, 13

Cameron, A. G. W. 1973, Icarus, 18, 407

Canovas, H., Hardy, A., Zurlo, A., et al. 2017, A&A, 598, A43

Canovas, H., Ménard, F., Hales, A., et al. 2013, A&A, 556, A123

Canovas, H., Schreiber, M. R., Cáceres, C., et al. 2015, ApJ, 805, 21

Cantalloube, F., Mouillet, D., Mugnier, L. M., et al. 2015, A&A, 582, A89

Carmona, A., Pinte, C., Thi, W. F., et al. 2014, A&A, 567, A51

Casassus, S. 2016, PASA, 33, e013

Casassus, S., Avenhaus, H., Pérez, S., et al. 2018a, MNRAS

Casassus, S., Hales, A., de Gregorio, I., et al. 2013a, A&A, 553, A64

Casassus, S., Marino, S., Lyra, W., et al. 2018b, ArXiv e-prints

Casassus, S., Marino, S., Pérez, S., et al. 2015a, ApJ, 811, 92, mypaper

Casassus, S., Perez M., S., Jordán, A., et al. 2012, ApJ, 754, L31

Casassus, S., van der Plas, G., M, S. P., et al. 2013b, Nature, 493, 191

Casassus, S., Wright, C. M., Marino, S., et al. 2015b, ApJ, 812, 126, mypaper

Cernis, K. 1993, Baltic Astronomy, 2, 214

Chabrier, G., Johansen, A., Janson, M., & Rafikov, R. 2014, Protostars and Planets VI, 619

Chauvin, G., Lagrange, A.-M., Beust, H., et al. 2012, A&A, 542, A41

Chauvin, G., Lagrange, A.-M., Bonavita, M., et al. 2010, A&A, 509, A52

Chauvin, G., Lagrange, A.-M., Dumas, C., et al. 2005a, A&A, 438, L25

Chauvin, G., Lagrange, A.-M., Zuckerman, B., et al. 2005b, A&A, 438, L29

Chen, J. & Kipping, D. 2017, ApJ, 834, 17

Chen, Y.-P., Trager, S. C., Peletier, R. F., et al. 2014, A&A, 565, A117

Chiang, E. & Murray-Clay, R. 2007, Nature Physics, 3, 604

Chiang, E. I. & Goldreich, P. 1997, ApJ, 490, 368

Choquet, É., Perrin, M. D., Chen, C. H., et al. 2016, ApJ, 817, L2

Choquet, É., Pueyo, L., Hagan, J. B., et al. 2014, in Proc. SPIE, Vol. 9143, Space Telescopes and Instrumentation 2014: Optical, Infrared, and Millimeter Wave, 914357

Christiaens, V., Casassus, S., Absil, O., et al. 2018a, subm. to MNRAS

Christiaens, V., Casassus, S., Absil, O., et al. 2018b, A&A in press, ArXiv e-prints

Christiaens, V., Casassus, S., Perez, S., van der Plas, G., & Ménard, F. 2014, ApJ

Cieza, L. A., Casassus, S., Pérez, S., et al. 2017, ApJ, 851, L23

Cieza, L. A., Kessler-Silacci, J. E., Jaffe, D. T., Harvey, P. M., & Evans, II, N. J. 2005, ApJ, 635, 422

Clampin, M., Krist, J. E., Ardila, D. R., et al. 2003, AJ, 126, 385

Clarke, C. J., Gendrin, A., & Sotomayor, M. 2001, MNRAS, 328, 485

Clarke, C. J. & Pringle, J. E. 1991, MNRAS, 249, 584

Clarke, C. J. & Pringle, J. E. 1993, MNRAS, 261, 190

Close, L. M., Follette, K. B., Males, J. R., et al. 2014, ApJ, 781, L30

Cockell, C. S., Léger, A., Fridlund, M., et al. 2009, Astrobiology, 9, 1

Connelley, M. S. & Greene, T. P. 2010, AJ, 140, 1214

Content, R. 1997, in Proc. SPIE, Vol. 2871, Optical Telescopes of Today and Tomorrow, ed. A. L. Ardeberg, 1295–1305

Corder, S., Eisner, J., & Sargent, A. 2005, ApJ, 622, L133

Crida, A., Morbidelli, A., & Masset, F. 2006, Icarus, 181, 587

Crooke, J. A., Roberge, A., Domagal-Goldman, S. D., et al. 2016, in Proc. SPIE, Vol. 9904, Space Telescopes and Instrumentation 2016: Optical, Infrared, and Millimeter Wave, 99044R

Cruz, K. L., Kirkpatrick, J. D., & Burgasser, A. J. 2009, AJ, 137, 3345

Cumming, A., Butler, R. P., Marcy, G. W., et al. 2008, PASP, 120, 531

Currie, T., Muto, T., Kudo, T., et al. 2014, ApJ, 796, L30

Currie, T., Rodigas, T. J., Debes, J., et al. 2012, ArXiv e-prints

Cushing, M. C., Rayner, J. T., Davis, S. P., & Vacca, W. D. 2003, ApJ, 582, 1066

Cushing, M. C., Rayner, J. T., & Vacca, W. D. 2005, ApJ, 623, 1115

Daemgen, S., Todorov, K., Silva, J., et al. 2017, A&A, 601, A65

D'Alessio, P., Calvet, N., & Hartmann, L. 2001, ApJ, 553, 321

D'Alessio, P., Hartmann, L., Calvet, N., et al. 2005, ApJ, 621, 461

D'Angelo, G., Lubow, S. H., & Bate, M. R. 2006, ApJ, 652, 1698

David, T. J. & Hillenbrand, L. A. 2015, ApJ, 804, 146

Dawson, R. I., Murray-Clay, R. A., & Fabrycky, D. C. 2011, ApJ, 743, L17

de Gregorio-Monsalvo, I., Ménard, F., Dent, W., et al. 2013, A&A, 557, A133

de Juan Ovelar, M., Min, M., Dominik, C., et al. 2013, A&A, 560, A111

de Zeeuw, P. T., Hoogerwerf, R., de Bruijne, J. H. J., Brown, A. G. A., & Blaauw, A. 1999, AJ, 117, 354

Delacroix, C., Absil, O., Forsberg, P., et al. 2013, A&A, 553, A98, mypaper

Delorme, P., Schmidt, T., Bonnefoy, M., et al. 2017, A&A, 608, A79

Dent, W. R. F., Wyatt, M. C., Roberge, A., et al. 2014, Science, 343, 1490

Dipierro, G., Lodato, G., Testi, L., & de Gregorio Monsalvo, I. 2014, MNRAS, 444, 1919

Dodson-Robinson, S. E. & Salyk, C. 2011, ApJ, 738, 131

Dominik, C., Dullemond, C. P., Waters, L. B. F. M., & Walch, S. 2003, A&A, 398, 607

Dong, R. & Dawson, R. 2016, ApJ, 825, 77

Dong, R. & Fung, J. 2017a, ApJ, 835, 38

Dong, R. & Fung, J. 2017b, ApJ, 835, 146

Dong, R., Hall, C., Rice, K., & Chiang, E. 2015a, ApJ, 812, L32

Dong, R., Hashimoto, J., Rafikov, R., et al. 2012, ApJ, 760, 111

Dong, R., Liu, S.-y., Eisner, J., et al. 2018a, ArXiv e-prints

Dong, R., Najita, J. R., & Brittain, S. 2018b, ArXiv e-prints

Dong, R., Rafikov, R. R., & Stone, J. M. 2011, ApJ, 741, 57

Dong, R., Zhu, Z., Fung, J., et al. 2016, ApJ, 816, L12

Dong, R., Zhu, Z., Rafikov, R. R., & Stone, J. M. 2015b, ApJ, 809, L5

Dong, R., Zhu, Z., & Whitney, B. 2015c, ApJ, 809, 93

Doppmann, G. W., Jaffe, D. T., & White, R. J. 2003, AJ, 126, 3043

D'Orazio, D. J., Haiman, Z., Duffell, P., MacFadyen, A., & Farris, B. 2016, MNRAS, 459, 2379

Draine, B. T. 1989, in ESA Special Publication, Vol. 290, Infrared Spectroscopy in Astronomy, ed. E. Böhm-Vitense

Draine, B. T. 2006, ApJ, 636, 1114

Duchêne, G. & Kraus, A. 2013a, ARA&A, 51, 269

Duchêne, G. & Kraus, A. 2013b, ARA&A, 51, 269

Duffell, P. C. & Chiang, E. 2015, ApJ, 812, 94

Duffell, P. C., Haiman, Z., MacFadyen, A. I., D'Orazio, D. J., & Farris, B. D. 2014, ApJ, 792, L10

Dullemond, C. P. & Dominik, C. 2004a, A&A, 417, 159

Dullemond, C. P. & Dominik, C. 2004b, A&A, 421, 1075

Dullemond, C. P. & Dominik, C. 2005, A&A, 434, 971

Dullemond, C. P., Hollenbach, D., Kamp, I., & D'Alessio, P. 2007, Protostars and Planets V, 555

Dunham, M. M., Allen, L. E., Evans, II, N. J., et al. 2015, ApJS, 220, 11

Dunhill, A. C., Alexander, R. D., & Armitage, P. J. 2013, MNRAS, 428, 3072

Durisen, R. H., Boss, A. P., Mayer, L., et al. 2007, Protostars and Planets V, 607

Dürmann, C. & Kley, W. 2017, A&A, 598, A80

Dutrey, A., Semenov, D., Chapillon, E., et al. 2014, Protostars and Planets VI, 317

Eiroa, C., Marshall, J. P., Mora, A., et al. 2013, A&A, 555, A11

Eisenhauer, F., Abuter, R., Bickert, K., et al. 2003, in Proc. SPIE, Vol. 4841, Instrument Design and Performance for Optical/Infrared Ground-based Telescopes, ed. M. Iye & A. F. M. Moorwood, 1548–1561

Eisner, J. A. 2015, ApJ, 803, L4

Eisner, J. A., Graham, J. R., Akeson, R. L., & Najita, J. 2009, ApJ, 692, 309

Esau, C. F., Harries, T. J., & Bouvier, J. 2014, MNRAS, 443, 1022

Espaillat, C., Calvet, N., D'Alessio, P., et al. 2007, ApJ, 670, L135

Espaillat, C., Muzerolle, J., Najita, J., et al. 2014, Protostars and Planets VI, 497

Evans, II, N. J., Dunham, M. M., Jørgensen, J. K., et al. 2009, ApJS, 181, 321

Fairlamb, J. R., Oudmaijer, R. D., Mendigutía, I., Ilee, J. D., & van den Ancker, M. E. 2015, MNRAS, 453, 976

Faramaz, V., Beust, H., Augereau, J.-C., Kalas, P., & Graham, J. R. 2015, A&A, 573, A87

Farris, B. D., Duffell, P., MacFadyen, A. I., & Haiman, Z. 2014, ApJ, 783, 134

Fedele, D., Tazzari, M., Booth, R., et al. 2018, A&A, 610, A24

Fedele, D., Carney, M., Hogerheijde, M. R., et al. 2017, A&A, 600, A72

Fernandez, J. A. & Ip, W.-H. 1984, Icarus, 58, 109

Fitzgerald, M. P. & Graham, J. R. 2006, ApJ, 637, 541

Flock, M., Ruge, J. P., Dzyurkevich, N., et al. 2015, A&A, 574, A68

Folha, D. F. M. & Emerson, J. P. 1999, A&A, 352, 517

Follette, K. B., Rameau, J., Dong, R., et al. 2017, AJ, 153, 264

Follette, K. B., Tamura, M., Hashimoto, J., et al. 2013, ApJ, 767, 10

Forgan, D., Parker, R. J., & Rice, K. 2015, MNRAS, 447, 836

Forgan, D. & Rice, K. 2013, MNRAS, 432, 3168

Forgan, D. H., Hall, C., Meru, F., & Rice, W. K. M. 2018, MNRAS, 474, 5036

Fortney, J. J., Marley, M. S., Saumon, D., & Lodders, K. 2008, ApJ, 683, 1104

Fouchet, L., Gonzalez, J.-F., & Maddison, S. T. 2010, A&A, 518, A16

Fujiwara, H., Honda, M., Kataza, H., et al. 2006, ApJ, 644, L133

Fukagawa, M., Hayashi, M., Tamura, M., et al. 2004, ApJ, 605, L53

Fukagawa, M., Tamura, M., Itoh, Y., et al. 2006, ApJ, 636, L153

Fukagawa, M., Tsukagoshi, T., Momose, M., et al. 2013, PASJ, 65

Fung, J. & Dong, R. 2015, ApJ, 815, L21

Fung, J., Shi, J.-M., & Chiang, E. 2014, ApJ, 782, 88

Furlan, E., Sargent, B., Calvet, N., et al. 2007, ApJ, 664, 1176

Fusco, T., Petit, C., Rousset, G., et al. 2006, in Society of Photo-Optical Instrumentation Engineers (SPIE) Conference Series, Vol. 6272, Society of Photo-Optical Instrumentation Engineers (SPIE) Conference Series

Gagné, J., Allers, K. N., Theissen, C. A., et al. 2018, ApJ, 854, L27

Gaia Collaboration, Brown, A. G. A., Vallenari, A., et al. 2016, ArXiv e-prints

Gaia Collaboration, Brown, A. G. A., Vallenari, A., et al. 2018, ArXiv e-prints

Galicher, R., Marois, C., Macintosh, B., et al. 2016, A&A, 594, A63

Gammie, C. F. 2001, ApJ, 553, 174

Gárate, M., Cuadra, J., & Montesinos, M. 2017, ArXiv e-prints

Garcia Lopez, R., Natta, A., Testi, L., & Habart, E. 2006, A&A, 459, 837

Gardner, J. P., Mather, J. C., Clampin, M., et al. 2006, Space Sci. Rev., 123, 485

Garufi, A., Quanz, S. P., Avenhaus, H., et al. 2013, A&A, 560, A105

Gerard, B. L., Marois, C., & Galicher, R. 2018, ArXiv e-prints

Ghez, A. M., Neugebauer, G., & Matthews, K. 1993, AJ, 106, 2005

Gilmozzi, R. & Spyromilio, J. 2007, The Messenger, 127

Girard, J. 2011, Very Large Telescope NaCo User Manual, ESO - European Southern Observatory, Karl-Schwarzschild-Str.2, 85748 Garching bei Munchen, Germany

Girardi, L., Barbieri, M., Groenewegen, M. A. T., et al. 2012, Astrophysics and Space Science Proceedings, 26, 165

Goldreich, P. & Tremaine, S. 1979, ApJ, 233, 857

Gomez Gonzalez, C. A., Absil, O., & Van Droogenbroeck, M. 2018, A&A, 613, A71

Gomez Gonzalez, C. A., Wertz, O., Absil, O., et al. 2017, AJ, 154, 7, mypaper

Goodman, J. & Rafikov, R. R. 2001, ApJ, 552, 793

Gorlova, N. I., Meyer, M. R., Rieke, G. H., & Liebert, J. 2003, ApJ, 593, 1074

Grady, C. A., Muto, T., Hashimoto, J., et al. 2013, ApJ, 762, 48

Grady, C. A., Polomski, E. F., Henning, T., et al. 2001, AJ, 122, 3396

Grady, C. A., Schneider, G., Sitko, M. L., et al. 2009, ApJ, 699, 1822

Grady, C. A., Woodgate, B., Bruhweiler, F. C., et al. 1999, ApJ, 523, L151

Grady, C. A., Woodgate, B., Heap, S. R., et al. 2005, ApJ, 620, 470

Greco, J. P. & Brandt, T. D. 2016, ApJ, 833, 134

Greene, T. P. & Lada, C. J. 1996, AJ, 112, 2184

Gregorio-Hetem, J. & Hetem, A. 2002, MNRAS, 336, 197

Grether, D. & Lineweaver, C. H. 2006, ApJ, 640, 1051

Groff, T., Chilcote, J., Brandt, T., et al. 2017, in Society of Photo-Optical Instrumentation Engineers (SPIE) Conference Series, Vol. 10400, Society of Photo-Optical Instrumentation Engineers (SPIE) Conference Series, 1040016

Guillot, T., Lin, D. N. C., Morel, P., Havel, M., & Parmentier, V. 2014, in EAS Publications Series, Vol. 65, EAS Publications Series, 327–336

Guilloteau, S. & Dutrey, A. 1998, A&A, 339, 467

Guilloteau, S., Dutrey, A., & Simon, M. 1999, A&A, 348, 570

Guimarães, M. M., Alencar, S. H. P., Corradi, W. J. B., & Vieira, S. L. A. 2006, A&A, 457, 581

Gullbring, E., Hartmann, L., Briceño, C., & Calvet, N. 1998, ApJ, 492, 323

Gutermuth, R. A., Megeath, S. T., Myers, P. C., et al. 2009, ApJS, 184, 18

Guyon, O. 2004, ApJ, 615, 562

Haisch, Jr., K. E., Lada, E. A., & Lada, C. J. 2001, ApJ, 553, L153

Hall, S. M. 1997, MNRAS, 287, 148

Hall, S. M., Clarke, C. J., & Pringle, J. E. 1996, MNRAS, 278, 303

Hartmann, L., Calvet, N., Gullbring, E., & D'Alessio, P. 1998, ApJ, 495, 385

Hashimoto, J., Dong, R., Kudo, T., et al. 2012, ApJ, 758, L19

Hashimoto, J., Tamura, M., Muto, T., et al. 2011, ApJ, 729, L17

Hashimoto, J., Tsukagoshi, T., Brown, J. M., et al. 2015, ApJ, 799, 43

Hastie, T. J., Tibshirani, R. J., & Friedman, J. H. 2009, The elements of statistical learning : data mining, inference, and prediction, Springer series in statistics (New York: Springer), autres impressions : 2011 (corr.), 2013 (7e corr.)

Hatzes, A. P. & Rauer, H. 2015, ApJ, 810, L25

Heap, S. R., Lindler, D. J., Lanz, T. M., et al. 2000, ApJ, 539, 435

Hennebelle, P. & Chabrier, G. 2013, ApJ, 770, 150

Henning, T. & Meeus, G. 2011, Dust Processing and Mineralogy in Protoplanetary Accretion Disks, ed. P. J. V. Garcia, 114–148

Henning, T. & Semenov, D. 2013, Chemical Reviews, 113, 9016

Hernández, J., Hartmann, L., Megeath, T., et al. 2007, ApJ, 662, 1067

Hersant, F., Wakelam, V., Dutrey, A., Guilloteau, S., & Herbst, E. 2009, A&A, 493, L49

Hinkley, S., Bowler, B. P., Vigan, A., et al. 2015, ApJ, 805, L10

Hinkley, S., Oppenheimer, B. R., Soummer, R., et al. 2007, ApJ, 654, 633

Hoeijmakers, H. J., Schwarz, H., Snellen, I. A. G., et al. 2018, ArXiv e-prints

Holland, W. S., Greaves, J. S., Zuckerman, B., et al. 1998, Nature, 392, 788

Hopkins, P. F. 2013, MNRAS, 430, 1653

Hord, B., Lyra, W., Flock, M., Turner, N. J., & Mac Low, M.-M. 2017, ApJ, 849, 164

Houk, N. 1978, Michigan catalogue of two-dimensional spectral types for the HD stars, ed. U. of Michigan (University Microfilms International)

Howard, A. W., Marcy, G. W., Johnson, J. A., et al. 2010, Science, 330, 653

Huby, E., Baudoz, P., Mawet, D., & Absil, O. 2015, A&A, 584, A74

Huby, E., Bottom, M., Femenia, B., et al. 2017, ArXiv e-prints

Huélamo, N., Lacour, S., Tuthill, P., et al. 2011, A&A, 528, L7

Hueso, R. & Guillot, T. 2005, A&A, 442, 703

Hughes, A. M., Duchene, G., & Matthews, B. 2018, ArXiv e-prints

Hughes, A. M., Wilner, D. J., Qi, C., & Hogerheijde, M. R. 2008, ApJ, 678, 1119

Hunziker, S., Quanz, S. P., Amara, A., & Meyer, M. R. 2017, ArXiv e-prints

Huygens, C. 1698, The celestial worlds discover'd:

Ida, S. & Lin, D. N. C. 2004a, ApJ, 604, 388

Ida, S. & Lin, D. N. C. 2004b, ApJ, 616, 567

Ida, S., Lin, D. N. C., & Nagasawa, M. 2013, ApJ, 775, 42

Ireland, M. J. 2013, MNRAS, 433, 1718

Ireland, M. J., Kraus, A., Martinache, F., Law, N., & Hillenbrand, L. A. 2011, ApJ, 726, 113

Ireland, M. J. & Kraus, A. L. 2008, ApJ, 678, L59

Isella, A., Carpenter, J. M., & Sargent, A. I. 2009, ApJ, 701, 260

Isella, A., Chandler, C. J., Carpenter, J. M., Pérez, L. M., & Ricci, L. 2014, ApJ, 788, 129

Isella, A., Guidi, G., Testi, L., et al. 2016, Physical Review Letters, 117, 251101

Isella, A., Natta, A., Wilner, D., Carpenter, J. M., & Testi, L. 2010, ApJ, 725, 1735

Isella, A., Pérez, L. M., Carpenter, J. M., et al. 2013, ApJ, 775, 30

Isella, A., Tatulli, E., Natta, A., & Testi, L. 2008, A&A, 483, L13

Isella, A., Testi, L., & Natta, A. 2006, A&A, 451, 951

Itoh, Y., Hayashi, M., Tamura, M., et al. 2005, ApJ, 620, 984

Itoh, Y., Oasa, Y., Kudo, T., et al. 2014, Research in Astronomy and Astrophysics, 14, 1438

Itoh, Y., Tamura, M., Hayashi, S. S., et al. 2002, PASJ, 54, 963

Janson, M., Brandt, T. D., Kuzuhara, M., et al. 2013, ApJ, 778, L4

Janson, M., Carson, J. C., Lafrenière, D., et al. 2012, ApJ, 747, 116

Jensen-Clem, R., Mawet, D., Gomez Gonzalez, C. A., et al. 2018, AJ, 155, 19

Johansen, A., Oishi, J. S., Mac Low, M.-M., et al. 2007, Nature, 448, 1022

Johns-Krull, C. M. 2007, ApJ, 664, 975

Johns-Krull, C. M., Valenti, J. A., & Koresko, C. 1999, ApJ, 516, 900

Jones, H. R. A., Longmore, A. J., Jameson, R. F., & Mountain, C. M. 1994, MNRAS, 267, 413

Juhász, A., Benisty, M., Pohl, A., et al. 2015, MNRAS, 451, 1147

Juhász, A. & Rosotti, G. P. 2018, MNRAS, 474, L32

Kalas, P. G., Rajan, A., Wang, J. J., et al. 2015, ApJ, 814, 32

Kausch, W., Noll, S., Smette, A., et al. 2015, A&A, 576, A78

Kikuta, H., Ohira, Y., & Iwata, K. 1997, Appl. Opt., 36, 1566

Kim, H. 2011, ApJ, 739, 102

Klahr, H. H. & Henning, T. 1997, Icarus, 128, 213

Kluska, J., Kraus, S., Davies, C. L., et al. 2018, ApJ, 855, 44

Köhler, R. 2011, A&A, 530, A126

Kohn, S. A., Shkolnik, E. L., Weinberger, A. J., Carlberg, J. K., & Llama, J. 2016, ApJ, 820, 2

Kokubo, E. & Ida, S. 1998, Icarus, 131, 171

Konishi, M., Grady, C. A., Schneider, G., et al. 2016, ApJ, 818, L23

Kordopatis, G., Recio-Blanco, A., de Laverny, P., et al. 2011, A&A, 535, A106

Kozai, Y. 1962, AJ, 67, 591

Kratter, K. & Lodato, G. 2016, ARA&A, 54, 271

Kratter, K. M., Murray-Clay, R. A., & Youdin, A. N. 2010, ApJ, 710, 1375

Kraus, A. L. & Ireland, M. J. 2012, ApJ, 745, 5

Kraus, A. L., Ireland, M. J., Cieza, L. A., et al. 2014, ApJ, 781, 20

Kraus, A. L., Ireland, M. J., Martinache, F., & Lloyd, J. P. 2008, ApJ, 679, 762

Kraus, S., Kreplin, A., Fukugawa, M., et al. 2017, ApJ, 848, L11

Krauss, O., Wurm, G., Mousis, O., et al. 2007, A&A, 462, 977

Kuhn, J. R., Potter, D., & Parise, B. 2001, ApJ, 553, L189

Kurucz, R. L. 1993, VizieR Online Data Catalog, 6039

Lacour, S., Biller, B., Cheetham, A., et al. 2016, A&A, 590, A90

Lacy, B., Shlivko, D., & Burrows, A. 2018, ArXiv e-prints

Lada, C. J. & Wilking, B. A. 1984, ApJ, 287, 610

Lafrenière, D., Jayawardhana, R., & van Kerkwijk, M. H. 2010, ApJ, 719, 497

Lafrenière, D., Marois, C., Doyon, R., & Barman, T. 2009, ApJ, 694, L148

Lafrenière, D., Marois, C., Doyon, R., Nadeau, D., & Artigau, É. 2007, ApJ, 660, 770

Lagrange, A.-M., Boccaletti, A., Milli, J., et al. 2012, A&A, 542, A40

Lagrange, A.-M., Bonnefoy, M., Chauvin, G., et al. 2010, Science, 329, 57

Lagrange, A.-M., Gratadour, D., Chauvin, G., et al. 2009, A&A, 493, L21

Lambrechts, M. & Johansen, A. 2012, A&A, 544, A32

Larkin, J. E., Quirrenbach, A., Krabbe, A., et al. 2003, in Proc. SPIE, Vol. 4841, Instrument Design and Performance for Optical/Infrared Ground-based Telescopes, ed. M. Iye & A. F. M. Moorwood, 1600–1610

Larwood, J. D. & Kalas, P. G. 2001, MNRAS, 323, 402

Lavie, B., Mendonça, J. M., Mordasini, C., et al. 2017, AJ, 154, 91

Lazareff, B., Berger, J.-P., Kluska, J., et al. 2017, A&A, 599, A85

Leggett, S. K., Allard, F., Berriman, G., Dahn, C. C., & Hauschildt, P. H. 1996, ApJS, 104, 117

Lesur, G. & Papaloizou, J. C. B. 2009, A&A, 498, 1

Li, H., Colgate, S. A., Wendroff, B., & Liska, R. 2001, ApJ, 551, 874

Li, H., Finn, J. M., Lovelace, R. V. E., & Colgate, S. A. 2000, ApJ, 533, 1023

Lidov, M. L. 1962, Planet. Space Sci., 9, 719

Ligi, R., Vigan, A., Gratton, R., et al. 2017, ArXiv e-prints

Lin, D. N. C. & Papaloizou, J. 1979, MNRAS, 186, 799

Lin, D. N. C. & Papaloizou, J. C. B. 1993, in Protostars and Planets III, ed. E. H. Levy & J. I. Lunine, 749–835

Lin, S.-Y., Ohashi, N., Lim, J., et al. 2006, ApJ, 645, 1297

Lissauer, J. J. 1993, ARA&A, 31, 129

Lodieu, N., Hambly, N. C., Jameson, R. F., & Hodgkin, S. T. 2008, MNRAS, 383, 1385

Lomax, J. R., Wisniewski, J. P., Grady, C. A., et al. 2016, ApJ, 828, 2

Long, Z. C., Akiyama, E., Sitko, M., et al. 2018, ArXiv e-prints

Lovelace, R. V. E., Li, H., Colgate, S. A., & Nelson, A. F. 1999, ApJ, 513, 805

Lubow, S. H., Seibert, M., & Artymowicz, P. 1999, ApJ, 526, 1001

Lucas, P. W., Roche, P. F., Allard, F., & Hauschildt, P. H. 2001, MNRAS, 326, 695

Luhman, K. L. 2012, ARA&A, 50, 65

Luhman, K. L., Esplin, T. L., & Loutrel, N. P. 2016, ApJ, 827, 52

Luhman, K. L., Peterson, D. E., & Megeath, S. T. 2004, ApJ, 617, 565

Luhman, K. L., Stauffer, J. R., Muench, A. A., et al. 2003, ApJ, 593, 1093

Lunine, J. I. & Stevenson, D. J. 1982, Icarus, 52, 14

Lyo, A.-R., Ohashi, N., Qi, C., Wilner, D. J., & Su, Y.-N. 2011, AJ, 142, 151

Lyra, W., Johansen, A., Klahr, H., & Piskunov, N. 2008, A&A, 491, L41

Lyra, W., Johansen, A., Klahr, H., & Piskunov, N. 2009a, A&A, 493, 1125

Lyra, W., Johansen, A., Zsom, A., Klahr, H., & Piskunov, N. 2009b, A&A, 497, 869

Lyra, W. & Klahr, H. 2011, A&A, 527, A138

Lyra, W. & Lin, M.-K. 2013, ApJ, 775, 17

Lyra, W., Richert, A. J. W., Boley, A., et al. 2016, ApJ, 817, 102

Ma, B. & Ge, J. 2014, MNRAS, 439, 2781

Maaskant, K. M., Honda, M., Waters, L. B. F. M., et al. 2013, A&A, 555, A64

Macintosh, B., Graham, J. R., Barman, T., et al. 2015, Science, 350, 64

Macintosh, B., Graham, J. R., Ingraham, P., et al. 2014, Proceedings of the National Academy of Science, 111, 12661

Macintosh, B., Poyneer, L., Sivaramakrishnan, A., & Marois, C. 2005, in Society of Photo-Optical Instrumentation Engineers (SPIE) Conference Series, Vol. 5903, Society of Photo-Optical Instrumentation Engineers (SPIE) Conference Series, ed. R. K. Tyson & M. Lloyd-Hart, 170–177

Maire, A.-L., Stolker, T., Messina, S., et al. 2017, A&A, 601, A134

Maldonado, J. & Villaver, E. 2017, A&A, 602, A38

Males, J. R., Belikov, R., & Bendek, E. 2015, in Proc. SPIE, Vol. 9605, Techniques and Instrumentation for Detection of Exoplanets VII, 960518

Malfait, K., Bogaert, E., & Waelkens, C. 1998, A&A, 331, 211

Malhotra, R. 1995, AJ, 110, 420

Mamajek, E. E. 2009, in American Institute of Physics Conference Series, Vol. 1158, American Institute of Physics Conference Series, ed. T. Usuda, M. Tamura, & M. Ishii, 3–10

Manara, C. F., Testi, L., Natta, A., et al. 2014, A&A, 568, A18

Marechal, Y., Coulomb, J. L., Meunier, G., & Touzot, G. 1994, IEEE Transactions on Magnetics, 30, 3558

Marino, S., Casassus, S., Perez, S., et al. 2015a, ApJ, 813, 76

Marino, S., Perez, S., & Casassus, S. 2015b, ApJ, 798, L44

Marleau, G.-D. & Cumming, A. 2014, MNRAS, 437, 1378

Marley, M. S., Fortney, J. J., Hubickyj, O., Bodenheimer, P., & Lissauer, J. J. 2007, ApJ, 655, 541

Marley, M. S., Saumon, D., Cushing, M., et al. 2012, ArXiv e-prints

Marois, C., Correia, C., Véran, J.-P., & Currie, T. 2014, in IAU Symposium, Vol. 299, Exploring the Formation and Evolution of Planetary Systems, ed. M. Booth, B. C. Matthews, & J. R. Graham, 48–49

Marois, C., Doyon, R., Nadeau, D., et al. 2005, PASP, 117, 745

Marois, C., Doyon, R., Racine, R., & Nadeau, D. 2000, PASP, 112, 91

Marois, C., Lafrenière, D., Doyon, R., Macintosh, B., & Nadeau, D. 2006, ApJ, 641, 556

Marois, C., Macintosh, B., Barman, T., et al. 2008, Science, 322, 1348

Marois, C., Macintosh, B., & Véran, J.-P. 2010a, in Proc. SPIE, Vol. 7736, Adaptive Optics Systems II, 77361J

Marois, C., Zuckerman, B., Konopacky, Q. M., Macintosh, B., & Barman, T. 2010b, Nature, 468, 1080

Marquez-Neila, P., Fisher, C., Sznitman, R., & Heng, K. 2018, ArXiv e-prints

Marrese, P. M., Boschi, F., & Munari, U. 2003, A&A, 406, 995

Marsh, K. A. & Mahoney, M. J. 1992, ApJ, 395, L115

Marsh, K. A. & Mahoney, M. J. 1993, ApJ, 405, L71

Martin, R. G. & Lubow, S. H. 2011, MNRAS, 413, 1447

Martin, R. G. & Lubow, S. H. 2017, ApJ, 835, L28

Martin, S. C. 1996, ApJ, 470, 537

Marzari, F. & Weidenschilling, S. J. 2002, Icarus, 156, 570

Masset, F. 2000, A&AS, 141, 165

Masset, F. & Snellgrove, M. 2001, MNRAS, 320, L55

Masset, F. S. & Papaloizou, J. C. B. 2003, ApJ, 588, 494

Mata Sánchez, D., González Hernández, J. I., Israelian, G., et al. 2014, A&A, 566, A83

Mauron, N. & Dole, H. 1998, A&A, 337, 808

Mawet, D., Absil, O., Girard, J. H., et al. 2013, The Messenger, 152, 8, mypaper

Mawet, D., Choquet, É., Absil, O., et al. 2017a, AJ, 153, 44, mypaper

Mawet, D., Milli, J., Wahhaj, Z., et al. 2014, ApJ, 792, 97

Mawet, D., Pueyo, L., Lawson, P., et al. 2012, in Proc. SPIE, Vol. 8442, Space Telescopes and Instrumentation 2012: Optical, Infrared, and Millimeter Wave, 844204

Mawet, D., Riaud, P., Absil, O., & Surdej, J. 2005, ApJ, 633, 1191

Mawet, D., Ruane, G., Xuan, W., et al. 2017b, ApJ, 838, 92

Mawet, D., Serabyn, E., Liewer, K., et al. 2009, Optics Express, 17, 1902

Mawet, D., Wizinowich, P., Dekany, R., et al. 2016, in Proc. SPIE, Vol. 9909, Adaptive Optics Systems V, 99090D

Mayama, S., Hashimoto, J., Muto, T., et al. 2012, ApJ, 760, L26

Mayor, M., Marmier, M., Lovis, C., et al. 2011, ArXiv e-prints

Mayor, M. & Queloz, D. 1995, Nature, 378, 355

McCaughrean, M. J. & O'dell, C. R. 1996, AJ, 111, 1977

McCauliff, S. D., Jenkins, J. M., Catanzarite, J., et al. 2015, ApJ, 806, 6

McGovern, M. R., Kirkpatrick, J. D., McLean, I. S., et al. 2004, ApJ, 600, 1020

McGregor, P. J., Hart, J., Conroy, P. G., et al. 2003, in Proc. SPIE, Vol. 4841, Instrument Design and Performance for Optical/Infrared Ground-based Telescopes, ed. M. Iye & A. F. M. Moorwood, 1581–1591

McLean, I. S., McGovern, M. R., Burgasser, A. J., et al. 2003, ApJ, 596, 561

Meeus, G., Montesinos, B., Mendigutía, I., et al. 2012, A&A, 544, A78

Meeus, G., Waters, L. B. F. M., Bouwman, J., et al. 2001, A&A, 365, 476

Mendigutía, I., Fairlamb, J., Montesinos, B., et al. 2014, ApJ, 790, 21

Meshkat, T., Bonnefoy, M., Mamajek, E. E., et al. 2015, MNRAS, 453, 2378

Meshkat, T., Kenworthy, M. A., Quanz, S. P., & Amara, A. 2014, ApJ, 780, 17

Meshkat, T., Mawet, D., Bryan, M., et al. 2017, ArXiv e-prints, mypaper

Meyer, M. R., Calvet, N., & Hillenbrand, L. A. 1997, AJ, 114, 288

Meyer, M. R., Edwards, S., Hinkle, K. H., & Strom, S. E. 1998, ApJ, 508, 397

Meyer, M. R. & Wilking, B. A. 2009, PASP, 121, 350

Milli, J., Hibon, P., Christiaens, V., et al. 2017a, A&A, 597, L2, mypaper

Milli, J., Mawet, D., Pinte, C., et al. 2015, A&A, 577, A57

Milli, J., Mouillet, D., Lagrange, A.-M., et al. 2012, A&A, 545, A111

Milli, J., Vigan, A., Mouillet, D., et al. 2017b, A&A, 599, A108

Min, M., Stolker, T., Dominik, C., & Benisty, M. 2017, A&A, 604, L10

Miotello, A., van Dishoeck, E. F., Kama, M., & Bruderer, S. 2016, A&A, 594, A85

Mittal, T. & Chiang, E. 2015, ApJ, 798, L25

Mizuno, H. 1980, Progress of Theoretical Physics, 64, 544

Modigliani, A., Goldoni, P., Royer, F., et al. 2010, in Proc. SPIE, Vol. 7737, Observatory Operations: Strategies, Processes, and Systems III, 773728

Molyarova, T., Akimkin, V., Semenov, D., et al. 2017, ApJ, 849, 130

Montesinos, M., Cuadra, J., Perez, S., Baruteau, C., & Casassus, S. 2015, ApJ, 806, 253

Montesinos, M. & Cuello, N. 2018, MNRAS, 475, L35

Montesinos, M., Perez, S., Casassus, S., et al. 2016, ApJ, 823, L8, mypaper

Moór, A., Ábrahám, P., Derekas, A., et al. 2006, ApJ, 644, 525

Mordasini, C. 2018, ArXiv e-prints

Mordasini, C., Alibert, Y., Klahr, H., & Henning, T. 2012, A&A, 547, A111

Morgan, W. W., Abt, H. A., & Tapscott, J. W. 1978, Revised MK Spectral Atlas for stars earlier than the sun

Morton, T. D., Bryson, S. T., Coughlin, J. L., et al. 2016, ApJ, 822, 86

Mouillet, D., Larwood, J. D., Papaloizou, J. C. B., & Lagrange, A. M. 1997, MNRAS, 292, 896

Mulders, G. D., Paardekooper, S.-J., Panić, O., et al. 2013, A&A, 557, A68

Müller, A., van den Ancker, M. E., Launhardt, R., et al. 2011, A&A, 530, A85

Müller, S., Helled, R., & Mayer, L. 2018, ApJ, 854, 112

Murakami, N., Nishikawa, J., Traub, W. A., et al. 2012, in Proc. SPIE, Vol. 8442, Space Telescopes and Instrumentation 2012: Optical, Infrared, and Millimeter Wave, 844205

Muto, T., Grady, C. A., Hashimoto, J., et al. 2012, ApJ, 748, L22

Muto, T., Tsukagoshi, T., Momose, M., et al. 2015, PASJ, 67, 122

Muzerolle, J., Allen, L. E., Megeath, S. T., Hernández, J., & Gutermuth, R. A. 2010, ApJ, 708, 1107

Muzerolle, J., Calvet, N., & Hartmann, L. 2001, ApJ, 550, 944

Muzerolle, J., Hartmann, L., & Calvet, N. 1998, AJ, 116, 2965

Natta, A., Testi, L., & Randich, S. 2006, A&A, 452, 245

Nayakshin, S. 2010, MNRAS, 408, L36

Nayakshin, S. 2017a, MNRAS, 470, 2387

Nayakshin, S. 2017b, PASA, 34, e002

Nielsen, E. L., De Rosa, R. J., Rameau, J., et al. 2017, ArXiv e-prints

Nixon, C. J. & Pringle, J. E. 2010, MNRAS, 403, 1887

Nordin, G. P. & Deguzman, P. C. 1999, Optics Express, 5, 163

O'dell, C. R., Wen, Z., & Hu, X. 1993, ApJ, 410, 696

Ogihara, M., Kokubo, E., Suzuki, T. K., & Morbidelli, A. 2018, ArXiv e-prints

Ogilvie, G. I. & Lubow, S. H. 2002, MNRAS, 330, 950

Ohashi, N. 2008, Ap&SS, 313, 101

Ohta, Y., Fukagawa, M., Sitko, M. L., et al. 2016, PASJ, 68, 53

Olofsson, J., Benisty, M., Le Bouquin, J.-B., et al. 2013, A&A, 552, A4

Oppenheimer, B. R., Baranec, C., Beichman, C., et al. 2013, ApJ, 768, 24

Ormel, C. W., Ida, S., & Tanaka, H. 2012, ApJ, 758, 80

Osterbrock, D. E. & Ferland, G. J. 2006, Astrophysics of gaseous nebulae and active galactic nuclei, ed. Osterbrock, D. E. & Ferland, G. J. (University Science Books)

Ostriker, E. C. 1994, ApJ, 424, 292

Owen, J. E. 2016, PASA, 33, e005

Owen, J. E., Clarke, C. J., & Ercolano, B. 2012, MNRAS, 422, 1880

Owen, J. E. & Lai, D. 2017, MNRAS, 469, 2834

Paardekooper, S.-J. & Johansen, A. 2018, Space Sci. Rev., 214, 38

Paardekooper, S.-J. & Mellema, G. 2004, A&A, 425, L9

Padoan, P. & Nordlund, Å. 2002, ApJ, 576, 870

Palla, F. & Stahler, S. W. 1999, ApJ, 525, 772

Panić, O., Ratzka, T., Mulders, G. D., et al. 2014, A&A, 562, A101

Papaloizou, J. C. B. & Nelson, R. P. 2005, A&A, 433, 247

Papaloizou, J. C. B., Nelson, R. P., & Masset, F. 2001, A&A, 366, 263

Patience, J., King, R. R., De Rosa, R. J., et al. 2012, A&A, 540, A85

Payne, M. J. & Lodato, G. 2007, MNRAS, 381, 1597

Pérez, L. M., Carpenter, J. M., Andrews, S. M., et al. 2016, Science, 353, 1519

Pérez, L. M., Isella, A., Carpenter, J. M., & Chandler, C. J. 2014, ApJ, 783, L13

Perez, S., Dunhill, A., Casassus, S., et al. 2015, ApJ, 811, L5

Perrin, M. D., Sivaramakrishnan, A., Makidon, R. B., Oppenheimer, B. R., & Graham, J. R. 2003, ApJ, 596, 702

Perryman, M., Hartman, J., Bakos, G. Á., & Lindegren, L. 2014, ApJ, 797, 14

Pfalzner, S. 2003, ApJ, 592, 986

Pfalzner, S., Umbreit, S., & Henning, T. 2005, ApJ, 629, 526

Piétu, V., Dutrey, A., & Guilloteau, S. 2007, A&A, 467, 163

Pinilla, P., Benisty, M., & Birnstiel, T. 2012a, A&A, 545, A81

Pinilla, P., Birnstiel, T., Ricci, L., et al. 2012b, A&A, 538, A114

Pinilla, P., de Boer, J., Benisty, M., et al. 2015a, A&A, 584, L4

Pinilla, P., de Juan Ovelar, M., Ataiee, S., et al. 2015b, A&A, 573, A9

Pinilla, P., Flock, M., Ovelar, M. d. J., & Birnstiel, T. 2016, A&A, 596, A81

Pinilla, P., Tazzari, M., Pascucci, I., et al. 2018, ArXiv e-prints

Pinilla, P., van der Marel, N., Pérez, L. M., et al. 2015c, A&A, 584, A16

Pinte, C., Harries, T. J., Min, M., et al. 2009, A&A, 498, 967

Pinte, C., Ménard, F., Duchêne, G., & Bastien, P. 2006, A&A, 459, 797

Pinte, C., Price, D. J., Ménard, F., et al. 2018, ApJ, 860, L13

Pohl, A., Benisty, M., Pinilla, P., et al. 2017a, ApJ, 850, 52

Pohl, A., Pinilla, P., Benisty, M., et al. 2015, MNRAS, 453, 1768

Pohl, A., Sissa, E., Langlois, M., et al. 2017b, A&A, 605, A34

Pollack, J. B., Hubickyj, O., Bodenheimer, P., et al. 1996, Icarus, 124, 62

Pontoppidan, K. M., Blake, G. A., van Dishoeck, E. F., et al. 2008, ApJ, 684, 1323

Posselt, W., Holota, W., Kulinyak, E., et al. 2004, in Proc. SPIE, Vol. 5487, Optical, Infrared, and Millimeter Space Telescopes, ed. J. C. Mather, 688–697

Pott, J.-U., Perrin, M. D., Furlan, E., et al. 2010, ApJ, 710, 265

Potter, D., Baudoz, P., Guyon, O., et al. 2001, in Bulletin of the American Astronomical Society, Vol. 33, American Astronomical Society Meeting Abstracts #198, 812

Price, D. J., Cuello, N., Pinte, C., et al. 2018, MNRAS, 477, 1270

Price, D. J., Wurster, J., Nixon, C., et al. 2017, ArXiv e-prints

Pueyo, L., Crepp, J. R., Vasisht, G., et al. 2012, ApJS, 199, 6

Qi, C., D'Alessio, P., Öberg, K. I., et al. 2011, ApJ, 740, 84

Qi, C., Öberg, K. I., Wilner, D. J., et al. 2013, Science, 341, 630

Quanz, S. P., Amara, A., Meyer, M. R., et al. 2015a, ApJ, 807, 64

Quanz, S. P., Amara, A., Meyer, M. R., et al. 2013a, ApJ, 766, L1

Quanz, S. P., Avenhaus, H., Buenzli, E., et al. 2013b, ApJ, 766, L2

Quanz, S. P., Crossfield, I., Meyer, M. R., Schmalzl, E., & Held, J. 2015b, International Journal of Astrobiology, 14, 279

Quanz, S. P., Schmid, H. M., Geissler, K., et al. 2011, ApJ, 738, 23

Quillen, A. C. 2006, ApJ, 640, 1078

Quillen, A. C., Varnière, P., Minchev, I., & Frank, A. 2005, AJ, 129, 2481

Racine, R., Walker, G. A. H., Nadeau, D., Doyon, R., & Marois, C. 1999, PASP, 111, 587

Rafikov, R. R. 2002, ApJ, 569, 997

Rafikov, R. R. 2016, ApJ, 831, 122

Ragusa, E., Dipierro, G., Lodato, G., Laibe, G., & Price, D. J. 2017, MNRAS, 464, 1449

Ragusa, E., Lodato, G., & Price, D. J. 2016, MNRAS, 460, 1243

Rameau, J., Chauvin, G., Lagrange, A.-M., et al. 2013, ApJ, 772, L15

Rameau, J., Chauvin, G., Lagrange, A.-M., et al. 2015, A&A, 581, A80

Rameau, J., Chauvin, G., Lagrange, A.-M., et al. 2012, A&A, 546, A24

Rameau, J., Follette, K. B., Pueyo, L., et al. 2017, AJ, 153, 244

Reche, R., Beust, H., & Augereau, J.-C. 2009, A&A, 493, 661

Regály, Z., Juhász, A., Sándor, Z., & Dullemond, C. P. 2012, MNRAS, 419, 1701

Regály, Z., Sándor, Z., Csomós, P., & Ataiee, S. 2013, MNRAS, 433, 2626

Reggiani, M., Christiaens, V., Absil, O., et al. 2018, A&A, 611, A74

Reggiani, M., Quanz, S. P., Meyer, M. R., et al. 2014, ApJ, 792, L23

Reid, I. N., Burgasser, A. J., Cruz, K. L., Kirkpatrick, J. D., & Gizis, J. E. 2001, AJ, 121, 1710

Reid, I. N. & Hawley, S. L. 2005, New light on dark stars : red dwarfs, low-mass stars, brown dwarfs

Ren, B., Dong, R., Esposito, T. M., et al. 2018, ApJ, 857, L9

Riaud, P., Mawet, D., Absil, O., et al. 2006, A&A, 458, 317

Riaud, P. & Schneider, J. 2007, A&A, 469, 355

Ricci, L., Testi, L., Natta, A., et al. 2014, ApJ, 791, 20

Rice, W. K. M., Armitage, P. J., Wood, K., & Lodato, G. 2006, MNRAS, 373, 1619

Rice, W. K. M., Wood, K., Armitage, P. J., Whitney, B. A., & Bjorkman, J. E. 2003, MNRAS, 342, 79

Richert, A. J. W., Lyra, W., Boley, A., Mac Low, M.-M., & Turner, N. 2015, ApJ, 804, 95

Rigaut, F. 2015, PASP, 127, 1197

Rodigas, T. J., Follette, K. B., Weinberger, A., Close, L., & Hines, D. C. 2014, ApJ, 791, L37

Rodigas, T. J., Weinberger, A., Mamajek, E. E., et al. 2015, ApJ, 811, 157

Roe, H. G. 2002, PASP, 114, 450

Romero, G. A., Schreiber, M. R., Cieza, L. A., et al. 2012, ApJ, 749, 79

Rosenfeld, K. A., Chiang, E., & Andrews, S. M. 2014, ApJ, 782, 62

Rosenthal, E. D., Gurwell, M. A., & Ho, P. T. P. 1996, Nature, 384, 243

Rosotti, G. P., Ercolano, B., & Owen, J. E. 2015, MNRAS, 454, 2173

Rosotti, G. P., Ercolano, B., Owen, J. E., & Armitage, P. J. 2013, MNRAS, 430, 1392

Rouan, D., Riaud, P., Boccaletti, A., Clénet, Y., & Labeyrie, A. 2000, PASP, 112, 1479

Ruane, G., Mawet, D., Kastner, J., et al. 2017, ArXiv e-prints

Rucinski, S. M. 1985, AJ, 90, 2321

Ruge, J. P., Flock, M., Wolf, S., et al. 2016, A&A, 590, A17

Ruíz-Rodríguez, D., Ireland, M., Cieza, L., & Kraus, A. 2016, MNRAS, 463, 3829

Safronov, V. S. 1969, Evoliutsiia doplanetnogo oblaka.

Safronov, V. S. 1972, Evolution of the protoplanetary cloud and formation of the earth and planets.

Sahlmann, J., Ségransan, D., Queloz, D., et al. 2011, A&A, 525, A95

Sallum, S., Follette, K. B., Eisner, J. A., et al. 2015, Nature, 527, 342

Sándor, Z., Lyra, W., & Dullemond, C. P. 2011, ApJ, 728, L9

Sargent, A. I. & Beckwith, S. 1987, ApJ, 323, 294

Savitzky, A. & Golay, M. J. E. 1964, Anal. Chem., 36, 1627

Schlafly, E. F., Green, G., Finkbeiner, D. P., et al. 2014, ApJ, 786, 29

Schlaufman, K. C. 2018, ApJ, 853, 37

Schlieder, J. E., Meyer, M., Beichman, C. A., et al. 2017, in American Astronomical Society Meeting Abstracts, Vol. 230, American Astronomical Society Meeting Abstracts #230, 114.07

Schneider, G., Grady, C. A., Hines, D. C., et al. 2014, AJ, 148, 59

Schneider, G., Grady, C. A., Stark, C. C., et al. 2016, AJ, 152, 64

Schneider, G. & Silverstone, M. 2003, in Society of Photo-Optical Instrumentation Engineers (SPIE) Conference Series, Vol. 4860, Society of Photo-Optical Instrumentation Engineers (SPIE) Conference Series, ed. A. B. Schultz, 1–9

Schneider, J., Dedieu, C., Le Sidaner, P., Savalle, R., & Zolotukhin, I. 2011, A&A, 532, A79, the online database was checked for the last time on 2012, June 30th.

See, T. J. J. 1896, AJ, 16, 17

Seok, J. Y. & Li, A. 2017, ApJ, 835, 291

Serabyn, E., Huby, E., Matthews, K., et al. 2017, AJ, 153, 43

Shallue, C. J. & Vanderburg, A. 2018, AJ, 155, 94

Siess, L., Dufour, E., & Forestini, M. 2000, A&A, 358, 593

Silber, J., Gledhill, T., Duchêne, G., & Ménard, F. 2000, ApJ, 536, L89

Simon, J. B., Armitage, P. J., Li, R., & Youdin, A. N. 2016, ApJ, 822, 55

Simon, M., Ghez, A. M., Leinert, C., et al. 1995, ApJ, 443, 625

Skemer, A. J., Hinz, P., Montoya, M., et al. 2015, in Proc. SPIE, Vol. 9605, Techniques and Instrumentation for Detection of Exoplanets VII, 96051D

Skrutskie, M. F., Dutkevitch, D., Strom, S. E., et al. 1990, AJ, 99, 1187

Smette, A., Sana, H., Noll, S., et al. 2015, A&A, 576, A77

Smith, B. A. & Terrile, R. J. 1984, Science, 226, 1421

Smith, N., Bally, J., Licht, D., & Walawender, J. 2005, AJ, 129, 382

Smith, W. H. 1987, PASP, 99, 1344

Snellen, I., de Kok, R., Birkby, J. L., et al. 2015, A&A, 576, A59

Snellen, I. A. G., de Kok, R. J., de Mooij, E. J. W., & Albrecht, S. 2010, Nature, 465, 1049

Snellen, I. A. G., Désert, J.-M., Waters, L. B. F. M., et al. 2017, AJ, 154, 77

Sokal, K. R., Deen, C. P., Mace, G. N., et al. 2018, ApJ, 853, 120

Solomon, P. M., Rivolo, A. R., Barrett, J., & Yahil, A. 1987, ApJ, 319, 730

Soummer, R., Ferrari, A., Aime, C., & Jolissaint, L. 2007, ApJ, 669, 642

Soummer, R., Pueyo, L., & Larkin, J. 2012, ApJ, 755, L28

Sparks, W. & Ford, H. 2002, ApJ, 578, 543

Spergel, D., Gehrels, N., Baltay, C., et al. 2015, ArXiv e-prints

Spezzi, L., Vernazza, P., Merín, B., et al. 2011, ApJ, 730, 65

Spiegel, D. S. & Burrows, A. 2012, ApJ, 745, 174

Spiegel, D. S., Burrows, A., & Milsom, J. A. 2011, ApJ, 727, 57

Stamatellos, D. 2015, ApJ, 810, L11

Stapelfeldt, K. R., Krist, J. E., Menard, F., et al. 1998, ApJ, 502, L65

Stevenson, D. J. 1991, ARA&A, 29, 163

Stolker, T., Dominik, C., Avenhaus, H., et al. 2016, A&A, 595, A113

Stolker, T., Sitko, M., Lazareff, B., et al. 2017, ApJ, 849, 143

Strom, K. M., Strom, S. E., Edwards, S., Cabrit, S., & Skrutskie, M. F. 1989, AJ, 97, 1451

Su, K. Y. L., MacGregor, M. A., Booth, M., et al. 2017, AJ, 154, 225

Su, K. Y. L., Rieke, G. H., Stansberry, J. A., et al. 2006, ApJ, 653, 675

Suzuki, T. K. & Inutsuka, S.-i. 2009, ApJ, 691, L49

Szulágyi, J., van der Plas, G., Meyer, M. R., et al. 2017, ArXiv e-prints

Takami, M., Bailey, J., Gledhill, T. M., Chrysostomou, A., & Hough, J. H. 2001, MNRAS, 323, 177

Tamura, M. 2009, in American Institute of Physics Conference Series, Vol. 1158, American Institute of Physics Conference Series, ed. T. Usuda, M. Tamura, & M. Ishii, 11–16

Tanaka, H., Takeuchi, T., & Ward, W. R. 2002, ApJ, 565, 1257

Tang, Y.-W., Guilloteau, S., Dutrey, A., et al. 2017, ApJ, 840, 32

Tang, Y.-W., Guilloteau, S., Piétu, V., et al. 2012, A&A, 547, A84

Tanga, P., Babiano, A., Dubrulle, B., & Provenzale, A. 1996, Icarus, 121, 158

Tatulli, E., Benisty, M., Ménard, F., et al. 2011, Astronomy & Astrophysics, 531, A1

Teague, R., Bae, J., Bergin, E. A., Birnstiel, T., & Foreman-Mackey, D. 2018, ApJ, 860, L12

Teixeira, R., Ducourant, C., Sartori, M. J., et al. 2000, A&A, 361, 1143

Telesco, C. M., Fisher, R. S., Wyatt, M. C., et al. 2005, Nature, 433, 133

Terquem, C. & Papaloizou, J. C. B. 2002, MNRAS, 332, L39

Thalmann, C., Grady, C. A., Goto, M., et al. 2010, ApJ, 718, L87

Thalmann, C., Janson, M., Garufi, A., et al. 2016, ApJ, 828, L17

Thalmann, C., Mulders, G. D., Hodapp, K., et al. 2014, A&A, 566, A51

Thommes, E. W., Duncan, M. J., & Levison, H. F. 2003, Icarus, 161, 431

Thompson, S. E., Mullally, F., Coughlin, J., et al. 2015, ApJ, 812, 46

Tielens, A. G. G. M., Tokunaga, A. T., Geballe, T. R., & Baas, F. 1991, ApJ, 381, 181

Tobin, J. J., Hartmann, L., Chiang, H.-F., et al. 2011, ApJ, 740, 45

Tobin, J. J., Kratter, K. M., Persson, M. V., et al. 2016, Nature, 538, 483

Tomida, K., Machida, M. N., Hosokawa, T., Sakurai, Y., & Lin, C. H. 2017, ApJ, 835, L11

Toomre, A. 1964, ApJ, 139, 1217

Traub, W. A. & Oppenheimer, B. R. 2010, Direct Imaging of Exoplanets, ed. S. Seager, 111–156

Troup, N. W., Nidever, D. L., De Lee, N., et al. 2016, AJ, 151, 85

Turner, N. J., Fromang, S., Gammie, C., et al. 2014, Protostars and Planets VI, 411

Tuthill, P. G., Monnier, J. D., Danchi, W. C., Wishnow, E. H., & Haniff, C. A. 2000, PASP, 112, 555

Udry, S. 2010, in In the Spirit of Lyot 2010

Uyama, T., Hashimoto, J., Muto, T., et al. 2018, ArXiv e-prints

Vacca, W. D. & Sandell, G. 2011, ApJ, 732, 8

van de Kamp, P. 1969, AJ, 74, 757

van den Ancker, M. E., de Winter, D., & Tjin A Djie, H. R. E. 1998, A&A, 330, 145

van der Marel, N., Cazzoletti, P., Pinilla, P., & Garufi, A. 2016a, ApJ, 832, 178

van der Marel, N., Pinilla, P., Tobin, J., et al. 2015, ApJ, 810, L7

van der Marel, N., van Dishoeck, E. F., Bruderer, S., et al. 2016b, A&A, 585, A58

van der Marel, N., van Dishoeck, E. F., Bruderer, S., et al. 2013, Science, 340, 1199

van der Marel, N., Verhaar, B. W., van Terwisga, S., et al. 2016c, A&A, 592, A126

van der Marel, N., Williams, J. P., Ansdell, M., et al. 2018, ApJ, 854, 177

van der Plas, G., Ménard, F., Canovas, H., et al. 2017a, A&A, 607, A55

van der Plas, G., van den Ancker, M. E., Acke, B., et al. 2009, A&A, 500, 1137

van der Plas, G., Wright, C. M., Ménard, F., et al. 2017b, A&A, 597, A32

van Dishoeck, E. F. & Black, J. H. 1988, ApJ, 334, 771

van Dishoeck, E. F., van der Marel, N., Bruderer, S., & Pinilla, P. 2015, in Astronomical Society of the Pacific Conference Series, Vol. 499, Revolution in Astronomy with ALMA: The Third Year, ed. D. Iono, K. Tatematsu, A. Wootten, & L. Testi, 281

van Leeuwen, F. 2007, A&A, 474, 653

van Terwisga, S. E., van Dishoeck, E. F., Ansdell, M., et al. 2018, ArXiv e-prints

Vargas Catalán, E., Huby, E., Forsberg, P., et al. 2016, A&A, 595, A127

Varnière, P. & Tagger, M. 2006, A&A, 446, L13

Verhoeff, A. P., Min, M., Pantin, E., et al. 2011, A&A, 528, A91

Vicente, S., Merín, B., Hartung, M., et al. 2011, Astronomy & Astrophysics, 533, A135

Vicente, S. M. & Alves, J. 2005, A&A, 441, 195

Vigan, A., Bonavita, M., Biller, B., et al. 2017, A&A, 603, A3

Vigan, A., Langlois, M., Moutou, C., & Dohlen, K. 2008, in Proc. SPIE, Vol. 7014, Ground-based and Airborne Instrumentation for Astronomy II, 70144M

Vorobyov, E. I. & Basu, S. 2010a, ApJ, 714, L133

Vorobyov, E. I. & Basu, S. 2010b, ApJ, 719, 1896

Waelkens, C., Waters, L. B. F. M., de Graauw, M. S., et al. 1996, A&A, 315, L245

Wagner, K., Apai, D., Kasper, M., & Robberto, M. 2015, ApJ, 813, L2

Wagner, K., Dong, R., Sheehan, P., et al. 2018, ApJ, 854, 130

Wahhaj, Z., Liu, M. C., Biller, B. A., et al. 2013, ApJ, 779, 80

Walsh, K. J., Morbidelli, A., Raymond, S. N., O'Brien, D. P., & Mandell, A. M. 2011, Nature, 475, 206

Wang, J., Mawet, D., Ruane, G., Hu, R., & Benneke, B. 2017, AJ, 153, 183

Waters, L. B. F. M. & Waelkens, C. 1998, ARA&A, 36, 233

Weidenschilling, S. J. 1977, MNRAS, 180, 57

Weitzel, L., Krabbe, A., Kroker, H., et al. 1996, A&AS, 119, 531

Wertz, O., Absil, O., Gómez González, C. A., et al. 2017, A&A, 598, A83

Westmoquette, M. S., Exter, K. M., Christensen, L., et al. 2009, ArXiv e-prints

Whitney, B. A., Robitaille, T. P., Bjorkman, J. E., et al. 2013, ApJS, 207, 30

Williams, J. P. & Cieza, L. A. 2011, ARA&A, 49, 67

Wing, R. F. & Jorgensen, U. G. 2003, Journal of the American Association of Variable Star

Observers (JAAVSO), 31, 110

Winn, J. N. & Fabrycky, D. C. 2015, ARA&A, 53, 409

Wolff, S. G., Perrin, M., Millar-Blanchaer, M. A., et al. 2016, ApJ, 818, L15

Wolszczan, A. 1994, Science, 264, 538

Wolszczan, A. & Frail, D. A. 1992, Nature, 355, 145

Wright, E. L., Eisenhardt, P. R. M., Mainzer, A. K., et al. 2010, AJ, 140, 1868

Wright, J. T., Marcy, G. W., Howard, A. W., et al. 2012, ApJ, 753, 160

Wu, Y.-L., Close, L. M., Eisner, J. A., & Sheehan, P. D. 2017, AJ, 154, 234

Wu, Y.-L. & Sheehan, P. D. 2017, ApJ, 846, L26

Wyatt, M. C. 2018, ArXiv e-prints

Wyatt, M. C., Panić, O., Kennedy, G. M., & Matrà, L. 2015, Ap&SS, 357, 103

Yorke, H. W., Bodenheimer, P., & Laughlin, G. 1993, ApJ, 411, 274

Youdin, A. & Johansen, A. 2007, ApJ, 662, 613

Youdin, A. N. & Goodman, J. 2005, ApJ, 620, 459

Yu, M., Evans, II, N. J., Dodson-Robinson, S. E., Willacy, K., & Turner, N. J. 2017, ApJ, 841, 39

Zakhozhay, O. V., Zapatero Osorio, M. R., Béjar, V. J. S., & Boehler, Y. 2017, MNRAS, 464, 1108

Zanazzi, J. J. & Lai, D. 2018, MNRAS, 473, 603

Zhang, K., Isella, A., Carpenter, J. M., & Blake, G. A. 2014, ApJ, 791, 42

Zhou, Y., Herczeg, G. J., Kraus, A. L., Metchev, S., & Cruz, K. L. 2014, ApJ, 783, L17

Zhu, Z. 2015, ApJ, 799, 16

Zhu, Z., Andrews, S. M., & Isella, A. 2017, ArXiv e-prints

Zhu, Z., Dong, R., Stone, J. M., & Rafikov, R. R. 2015, ApJ, 813, 88

Zhu, Z., Hartmann, L., & Gammie, C. 2009, ApJ, 694, 1045

Zhu, Z., Nelson, R. P., Dong, R., Espaillat, C., & Hartmann, L. 2012, ApJ, 755, 6

Zhu, Z., Nelson, R. P., Hartmann, L., Espaillat, C., & Calvet, N. 2011, ApJ, 729, 47

Zhu, Z., Stone, J. M., & Rafikov, R. R. 2013a, ApJ, 768, 143

Zhu, Z., Stone, J. M., & Rafikov, R. R. 2013b, ApJ, 768, 143

Zuckerman, B., Song, I., & Bessell, M. S. 2004, ApJ, 613, L65

Zurlo, A., Vigan, A., Galicher, R., et al. 2016, A&A, 587, A57

Zwitter, T., Castelli, F., & Munari, U. 2004, A&A, 417, 1055